



---

# Using Unmanned Aircraft Systems for Crash Reconstructions during Suboptimal Conditions

Technical Report 0-7063-R1

---

Cooperative Research Program

TEXAS A&M TRANSPORTATION INSTITUTE  
COLLEGE STATION, TEXAS

in cooperation with the  
Federal Highway Administration and the  
Texas Department of Transportation  
<https://tti.tamu.edu/documents/0-7063-R1.pdf>



1. Report No. FHWA/TX-21/0-7063-R1		2. Government Accession No.		3. Recipient's Catalog No.	
4. Title and Subtitle USING UNMANNED AIRCRAFT SYSTEMS FOR CRASH RECONSTRUCTIONS DURING SUBOPTIMAL CONDITIONS				5. Report Date Published: October 2021	
				6. Performing Organization Code	
7. Author(s) Cesar Quiroga, Michael J. Starek, Jorge Maldonado, Edgar Kraus, Stanton Taylor, Youngjib Ham, and Tianxing Chu				8. Performing Organization Report No. Report 0-7063-R1	
9. Performing Organization Name and Address Texas A&M Transportation Institute The Texas A&M University System College Station, Texas 77843-3135				10. Work Unit No. (TRAIS)	
				11. Contract or Grant No. Project 0-7063	
12. Sponsoring Agency Name and Address Texas Department of Transportation Research and Technology Implementation Office 125 E. 11 <sup>th</sup> Street Austin, Texas 78701-2483				13. Type of Report and Period Covered Technical Report: January 2020–August 2021	
				14. Sponsoring Agency Code	
15. Supplementary Notes Project performed in cooperation with the Texas Department of Transportation and the Federal Highway Administration. Project Title: Guidance for the Use of UAS during Suboptimal Environmental Conditions URL: <a href="https://tti.tamu.edu/documents/0-7063-R1.pdf">https://tti.tamu.edu/documents/0-7063-R1.pdf</a>					
16. Abstract The Texas Department of Transportation (TxDOT) has a strategic interest in using unmanned aircraft systems (UASs) to support a variety of initiatives, including traffic incident management. TxDOT is interested in identifying and documenting UAS uses to determine to what degree UASs can be used to streamline the process to clear and document fatal crash scenes. Environmental conditions such as wind, rain, and limited ambient light affect both UAS flight operations and the quality of the data collected. Fatal crashes can occur at any time, which means that UAS flights might need to occur during conditions that are less than optimal. To better understand the feasibility of using UASs under these conditions, this research documented key challenges and developed and tested procedures for data collection and processing. The research included reviewing historical crash data trends in Texas to establish correlations with environmental factors, simulating the effect of environmental factors on the quality of data collected with UASs, performing field tests of UAS-based crash data collection activities under a variety of conditions, and developing recommendations for updates of the TxDOT <i>Unmanned Aircraft System (UAS) Flight Operations and User's Manual</i> . Evaluated environmental factors include impact of wind speed and direction on UAS flight operations, impact of aerial imaging network design on 3D crash scene reconstructions using commercial structure-from-motion (SfM) software, impact of ambient lighting and low visibility on UAS-SfM reconstructions, self-calibration versus preflight calibration procedures for consumer-grade nonmetric digital RGB cameras, impact of suboptimal conditions on visual image quality, and impact of camera properties on UAS image quality to guide crash scene imaging.					
17. Key Words Crash reconstruction, digital surface model, GCP, orthomosaic, point cloud, PPK, RTK, SfM, traffic incident management, UAS			18. Distribution Statement No restrictions. This document is available to the public through NTIS: National Technical Information Service Alexandria, Virginia 22312 <a href="https://www.ntis.gov">https://www.ntis.gov</a>		
19. Security Classif. (of this report) Unclassified		20. Security Classif. (of this page) Unclassified		21. No. of Pages 458	22. Price



# **USING UNMANNED AIRCRAFT SYSTEMS FOR CRASH RECONSTRUCTIONS DURING SUBOPTIMAL CONDITIONS**

by

Cesar Quiroga, Ph.D., P.E.  
Senior Research Engineer, Texas A&M Transportation Institute

Michael J. Starek, Ph.D.  
Associate Professor of Geospatial Engineering, Texas A&M University-Corpus Christi

Jorge Maldonado  
Software Developer, Texas A&M Transportation Institute

Edgar Kraus, P.E.  
Research Engineer, Texas A&M Transportation Institute

Stanton Taylor  
Adjunct Instructor, Center for Public Safety, Northwestern University

Youngjib Ham, Ph.D.  
Assistant Professor of Construction Science, Texas A&M University

and

Tianxing Chu, Ph.D.  
Assistant Professor of Geospatial Engineering, Texas A&M University-Corpus Christi

Report 0-7063-R1  
Project 0-7063  
Project Title: Guidance for the Use of UAS during Suboptimal Environmental Conditions

Performed in cooperation with the  
Texas Department of Transportation  
and the  
Federal Highway Administration

Published: October 2021

TEXAS A&M TRANSPORTATION INSTITUTE  
The Texas A&M University System  
College Station, Texas 77843-3135



## **DISCLAIMER**

This research was performed in cooperation with the Texas Department of Transportation (TxDOT) and the Federal Highway Administration (FHWA). The contents of this report reflect the views of the authors, who are responsible for the facts and the accuracy of the data presented herein. The contents do not necessarily reflect the official view or policies of FHWA or TxDOT. This report does not constitute a standard, specification, or regulation.

This report is not intended for construction, bidding, or permit purposes. The engineer in charge of the project was Cesar Quiroga, P.E. (Texas Registration #84274).

The United States Government and the State of Texas do not endorse products or manufacturers. Trade or manufacturers' names appear herein solely because they are considered essential to the object of this report.

## ACKNOWLEDGMENTS

This research was conducted in cooperation with TxDOT and FHWA. The research team gratefully acknowledges the advice and assistance of the project advisors at TxDOT. The research team appreciates the input provided by numerous individuals at TxDOT and other agencies to complement information needed for the analysis, in particular members of the National Association of Professional Accident Reconstruction Specialists and members of the American Association of State Highway and Transportation Officials' Aviation Council and Committee on Transportation Systems.

The researchers gratefully acknowledge the valuable contribution by other members of the research team. In particular, the research team recognizes Jacob Berryhill and Mohammad Pashaei at the Conrad Blucher Institute for Surveying and Science at Texas A&M University-Corpus Christi, Mirsalar Kamari and Jaeyoon Kim at the Construction Science Department at Texas A&M University, and Adam Hyde at the Northwestern University Center for Public Safety. The research team also recognizes the contribution of Marcie Perez at the Center for Transportation Safety at TTI and the staff at the TTI Proving Ground for facilitating access to Texas A&M University's RELLIS Campus in College Station to conduct test UAS flights. In addition, the research team is grateful to Lieutenant Aaron Fritch at the Texas Department of Public Safety (TxDPS) for the insights and information provided throughout the research and for facilitating access to the TxDPS Tactical Training Facility in Florence to conduct test UAS flights.



# TABLE OF CONTENTS

	Page
LIST OF FIGURES .....	xi
LIST OF TABLES .....	xix
LIST OF ACRONYMS AND ABBREVIATIONS .....	xxiii
LIST OF TERMS.....	xxvi
CHAPTER 1. INTRODUCTION .....	1
CHAPTER 2. LITERATURE REVIEW .....	3
INTRODUCTION .....	3
FEDERAL AND STATE REGULATIONS .....	3
Federal Requirements .....	3
State Requirements .....	5
UAS FLIGHT PLANNING AND MANAGEMENT .....	7
Equipment Preparations .....	7
Flight Planning.....	7
Preflight Checklist .....	9
Onsite Flight Authorization Procedures.....	10
Ground Control .....	12
Flight Design.....	15
Postflight Checklist.....	21
STRUCTURE-FROM-MOTION PHOTOGRAMMETRY .....	21
Sparse Point Cloud Generation .....	23
Dense Point Cloud Generation.....	24
Ground Control Points .....	25
Measurement Assessment and Reliability .....	26
Processing Quality Reports.....	27
UAS-SfM Accuracy.....	27
UAS-BASED CRASH INVESTIGATIONS.....	30
COMMONLY USED UAS EQUIPMENT FOR CRASH INVESTIGATIONS .....	32
OTHER TRAFFIC INCIDENT MANAGEMENT APPLICATIONS.....	34
NATIONAL SURVEY FINDINGS .....	34
Survey of National Association of Professional Accident Reconstruction Specialists .....	34
Survey of State DOTs .....	35
CASE STUDIES.....	41
Case Study 1—Daylight Conditions .....	41
Case Study 2—Nighttime Conditions.....	45
OPERATIONAL EXPERIENCE OF PUBLIC SAFETY AGENCIES.....	47
CHAPTER 3. CRASH DATA ANALYSIS .....	51

INTRODUCTION .....	51
CRASH DATA .....	51
GENERAL TRENDS .....	54
High-Level Statistical Analysis .....	56
Daylight versus Nighttime Crashes .....	57
Crashes by Weather Condition .....	61
Crashes by Surface Condition.....	65
Crashes by Manner of Collision .....	69
SPATIAL AND TEMPORAL DISTRIBUTIONS OF CRASHES .....	71
General Observations.....	73
Overall Trends for Fatal Crashes .....	84
CHAPTER 4. SIMULATIONS TO ASSESS IMPACTS OF SUBOPTIMAL ENVIRONMENTAL CONDITIONS .....	85
INTRODUCTION .....	85
IMPACT OF WIND SPEED AND DIRECTION ON UAS FLIGHT OPERATIONS .....	85
General Concepts .....	85
Methods.....	86
Results.....	100
Lessons Learned.....	118
IMPACT OF AERIAL IMAGING NETWORK DESIGN ON 3D CRASH SCENE RECONSTRUCTIONS .....	120
General Concepts .....	120
Methods.....	123
Results.....	131
Lessons Learned.....	152
IMPACT OF AMBIENT LIGHTING AND LOW VISIBILITY ON UAS-SfM RECONSTRUCTIONS .....	154
General Concepts .....	155
Methods.....	155
Results.....	167
Lessons Learned.....	193
SELF-CALIBRATION VERSUS PREFLIGHT CALIBRATION PROCEDURES FOR CONSUMER-GRADE NONMETRIC DIGITAL RGB CAMERAS.....	196
General Concepts .....	196
Methods.....	199
Results.....	204
Lessons Learned.....	216
IMPACT OF SUBOPTIMAL CONDITIONS ON VISUAL IMAGE QUALITY .....	219
General Concepts .....	219
Methods.....	222
Results.....	225
Lessons Learned.....	231
IMPACT OF CAMERA PROPERTIES ON UAS IMAGE QUALITY TO GUIDE CRASH SCENE IMAGING .....	232
Methods.....	232

Results.....	233
Lessons Learned.....	237
CHAPTER 5. FIELD TESTING OF UAS FLIGHT OPERATIONS .....	239
INTRODUCTION .....	239
TEST LOCATIONS .....	240
Test 1 (08/09/2020): Crash Scene in Abbott, Texas .....	240
Test 2 (08/25/2020): Simulated Crash at Phil Hardberger Park, San Antonio, Texas.....	240
Test 3 (09/30/2020): Crash Test at the RELLIS Campus, College Station, Texas.....	242
Test 4 (10/07/2020): Crash Test at The RELLIS Campus, College Station, Texas .....	243
Test 5 (12/07/2020): Delivery Truck Crash Test at the RELLIS Campus, College Station, Texas .....	244
Test 6 (01/15/2021): Simulated Passenger Car Crash Test at the TxDPS Tactical Training Facility in Florence, Texas.....	245
Test 7 (03/20/2021): Simulated Passenger Car Crash Test at the TxDPS Tactical Training Facility in Florence, Texas.....	246
DATA COLLECTION EQUIPMENT .....	247
DJI Mavic 2 Pro .....	247
DJI Matrice 300 RTK .....	247
DJI Phantom 4 RTK.....	248
Wingtra WingtraOne.....	249
RIEGL-VZ 2000i TLS .....	250
LiBackpack DG50 LiDAR .....	251
GNSS Equipment.....	251
FIELD TESTING—TAMUCC .....	252
Test 1 (08/09/2020): Crash Scene in Abbott, Texas .....	252
Test 4 (10/07/2020): Crash Test at the RELLIS Campus, College Station, Texas.....	265
Test 5 (12/07/2020): Delivery Truck Crash Test at the RELLIS Campus, College Station, Texas .....	288
Test 6 (01/15/2021): Simulated Passenger Car Crash Test at the TxDPS Tactical Training Facility in Florence, Texas.....	305
Test 7 (03/20/2021): Simulated Passenger Car Crash Test at The TxDPS Tactical Training Facility in Florence, Texas.....	311
FIELD TESTING—TTI .....	343
Test 2 (08/25/2020): Simulated Crash at Phil Hardberger Park, San Antonio, Texas.....	353
Test 3 (09/30/2020): Crash Test at the RELLIS Campus, College Station, Texas.....	357
Test 4 (10/07/2020): Crash Test at The RELLIS Campus, College Station, Texas .....	362
Test 5 (12/07/2020): Delivery Truck Crash Test at the RELLIS Campus, College Station, Texas .....	368
Test 6 (01/15/2021): Simulated Passenger Car Crash Test at the TxDPS Tactical Training Facility in Florence, Texas.....	373
Test 7 (03/20/2021): Simulated Passenger Car Crash Test at the TxDPS Tactical Training Facility in Florence, Texas.....	381
General Trends.....	388
CHAPTER 6. CONCLUSIONS AND RECOMMENDATIONS .....	397

CONCLUSIONS.....	397
Crash Data Analysis.....	397
Simulations to Assess Impacts of Suboptimal Environmental Conditions.....	399
Field Tests of UAS-Based Data Collection Activities.....	404
RECOMMENDATIONS.....	411
REFERENCES .....	415
APPENDIX. VALUE OF RESEARCH.....	425
QUANTITATIVE BENEFITS .....	425
QUALITATIVE BENEFITS .....	426

## LIST OF FIGURES

	Page
Figure 1. Sample DJI GEO Zone Map in the Vicinity of the San Antonio Airport. ....	9
Figure 2. Matrice 300 RTK’s Health Management System (29).....	10
Figure 3. AirMap Authorization Request Interface (31). ....	11
Figure 4. TxDOT RTN as of June 2021 (34).....	12
Figure 5. UAS Flight Patterns—Adapted from (38).....	17
Figure 6. Survey, Evidence, and Overview Passes Used by NUCPS.....	19
Figure 7. UAS Flight Plan for a 2D Orthomosaic Production.....	20
Figure 8. UAS Flight Plan for a 3D Model.....	21
Figure 9. UAS-SfM Workflow to Process UAS Image Sequences into Mapping Products. ....	23
Figure 10. Different Types of Targets for Aerial Control. ....	25
Figure 11. Relationship between GSD, Focal Length, Pixel Pitch, and Flight Height.....	29
Figure 12. UAS Placement and Camera Angles.....	42
Figure 13. Orthomosaic of the Crash Scene. ....	42
Figure 14. 3D Textured Mesh.....	43
Figure 15. Virtual Survey Markings. ....	44
Figure 16. Points Displayed in Crash Reconstruction Software.....	44
Figure 17. Evidence Markup.....	45
Figure 18. UAS Image Capture Placements. ....	46
Figure 19. Overview Diagram Prepared from UAS Data.....	47
Figure 20. Electric Transmission Towers in Waukegan, Illinois.....	49
Figure 21. Crash Index—All Crashes and All Fatal Crashes. ....	55
Figure 22. Crash Index—Daylight vs. Nighttime Crashes. ....	60
Figure 23. Crash Index—Daylight vs. Nighttime <i>Fatal</i> Crashes.....	61
Figure 24. Top 10 Manners of Collision for <i>All</i> Crashes (2010–2019 Crash Data). ....	70
Figure 25. Top 10 Manners of Collision for <i>Fatal</i> Crashes (2010–2019 Crash Data). ....	71
Figure 26. 2019 Austin Area (Travis County) Crashes—Heat Map (All Crashes) and Fatal Crash Locations. ....	74
Figure 27. 2019 Dallas Area (Dallas County) Crashes—Heat Map (All Crashes) and Fatal Crash Locations. ....	75
Figure 28. 2019 Fort Worth Area (Tarrant County) Crashes—Heat Map (All Crashes) and Fatal Crash Locations.....	76
Figure 29. 2019 Houston Area (Harris County) Crashes—Heat Map (All Crashes) and Fatal Crash Locations. ....	77
Figure 30. 2019 San Antonio Area (Bexar County) Crashes—Heat Map (All Crashes) and Fatal Crash Locations.....	78
Figure 31. 2010–2019 Daylight/Nighttime Fatal Crashes in the Austin Area (Travis County).....	79
Figure 32. 2010–2019 Daylight/Nighttime Fatal Crashes in the Dallas Area (Dallas County). ....	80
Figure 33. 2010–2019 Daylight/Nighttime Fatal Crashes in the Fort Worth Area (Tarrant County). ....	81
Figure 34. 2010–2019 Daylight/Nighttime Fatal Crashes in the Houston Area (Harris County).....	82

Figure 35. 2010–2019 Daylight/Nighttime Fatal Crashes in the San Antonio Area (Bexar County).....	83
Figure 36. Mission Area Polygon.....	87
Figure 37. Mission Parameters of Simulation Runs.....	87
Figure 38. Overview of Flight Lines, Waypoints, and Action Information.....	88
Figure 39. Screen in Mission Planner Where Simulation Starts and Craft Type Is Selected.....	89
Figure 40. Settings of Environmental Parameters for a Simulation Run.....	91
Figure 41. Image of Mission Planner during an Example Simulation Mission Execution.....	92
Figure 42. Image of Mission Planner during Flight Log Download.....	93
Figure 43. CAM .txt File.....	94
Figure 44. CAM .txt File after Conversion to UTM via VDatum.....	94
Figure 45. Flight Path for Single Altitude of 80 m (262 ft) AGL.....	97
Figure 46. Flight Path for Dual Altitudes of 80 m (262 ft) and 10 m (33 ft) AGL.....	99
Figure 47. Wind Rose Plot of Average 3D Errors for No-Turbulence Runs.....	104
Figure 48. Wind Rose Plot of Average 3D Errors for All Simulation Runs with Turbulence.....	105
Figure 49. Wind Rose Plot of Standard Deviations for No-Turbulence Runs.....	109
Figure 50. Wind Rose Plot of Standard Deviations for All Simulation Runs with Turbulence.....	110
Figure 51. Wind Rose Plot of Flight Times for All Turbulence-Free Runs.....	114
Figure 52. Wind Rose Plot of Flight Times for All Simulation Runs with Turbulence.....	115
Figure 53. Summary of the Entire UAS Imaging Simulation and Processing Framework.....	123
Figure 54. Top View of the 3D Textured Mesh.....	125
Figure 55. 3D View of the Crash Scene.....	125
Figure 56. UAS Image Acquisition Framework in Blender.....	126
Figure 57. Postprocessing Steps Applied to Raw Images Rendered by Blender.....	126
Figure 58. Pix4D’s Initial Processing and Densification Settings Used for Simulations.....	129
Figure 59. Cloud-to-Cloud Distance (93).....	131
Figure 60. Overlapping Images for E60-S60 and E80-S80 Scenarios.....	132
Figure 61. Overlap and DSM Maps for E60-S60 and E80-S80 Scenarios.....	133
Figure 62. Total Number of 2D Keypoints and 3D Points by Overlap.....	134
Figure 63. Average Number of 2D Keypoints and Matched Keypoints per Image.....	135
Figure 64. Average Number of Images Observed for a 2D Keypoint Used to Reconstruct a 3D Point in the Sparse Point Cloud.....	136
Figure 65. Mean Reprojection Error by Overlap.....	137
Figure 66. Mean Absolute Camera <i>Position</i> Uncertainty.....	138
Figure 67. Mean Absolute Camera <i>Orientation</i> Uncertainty.....	138
Figure 68. Absolute Camera Geolocation Error.....	139
Figure 69. Absolute Camera Orientation Error.....	140
Figure 70. RMSE of the Checkpoint Error.....	140
Figure 71. Mean Checkpoint Error with Error Bars.....	141
Figure 72. Total Number of Points in Densified Point Cloud.....	142
Figure 73. Average Point Density of Densified Point Cloud.....	142
Figure 74. Cloud-to-Cloud Distance RMSE Trends for Total Scene.....	143
Figure 75. Cloud-to-Cloud Distance RMSE Trends for Crash Scene.....	143

Figure 76. Correlation between Different Quality Factor Values and Sidelap/Endlap. ....	144
Figure 77. Pix4D SfM Initial Processing Time and Densification Time by Overlap. ....	145
Figure 78. Simulated Flight Time Based on Percent Sidelap and Flight Height. ....	146
Figure 79. Absolute Camera Orientation and Geolocation Errors for the UAS Flight in Corpus Christi. ....	148
Figure 80. Mean Absolute Camera <i>Position</i> Uncertainty. ....	150
Figure 81. Absolute Camera <i>Orientation</i> Uncertainty. ....	150
Figure 82. Absolute Camera <i>Geolocation</i> Error. ....	151
Figure 83. Absolute Camera <i>Orientation</i> Error. ....	151
Figure 84. Mean Checkpoint Error with Error Bars. ....	152
Figure 85. Cloudy Sky (100% Coverage) in Late Evening (7:00 PM). ....	157
Figure 86. Dark Sky (11:00 PM). ....	158
Figure 87. Dark Sky with Lamp Posts at Full Illumination (11:00 PM). ....	158
Figure 88. Dark Sky with Lamp Posts with Partial Illumination (11:00 PM). ....	159
Figure 89. Civil Twilight (8:34 PM). ....	159
Figure 90. Dusk (8:08 PM). ....	160
Figure 91. Afternoon (5:00 PM). ....	160
Figure 92. Solar Noon (1:27 PM). ....	161
Figure 93. Solar Noon on the Summer Solstice (1:32 PM). ....	161
Figure 94. Fog Condition with High Visibility. ....	163
Figure 95. Fog Condition with Low Visibility. ....	163
Figure 96. Wet Asphalt Road and Related Node Tree in the Shader Editor Window. ....	164
Figure 97. Pix4D Initial Processing and Densification Settings. ....	165
Figure 98. Total Number of 2D Keypoints and 3D Points by Lighting Scenario. ....	167
Figure 99. Average Number of 2D Keypoints and Matched Keypoints per Image. ....	168
Figure 100. Mean Reprojection Error. ....	169
Figure 101. Mean Absolute Camera Position Uncertainty with Error Bars. ....	170
Figure 102. Mean Absolute Camera Orientation Uncertainty with Error Bars. ....	170
Figure 103. Absolute Camera Geolocation Error. ....	171
Figure 104. Absolute Camera Orientation Error. ....	172
Figure 105. RMSE of the Checkpoint Error. ....	172
Figure 106. Orthomosaic Showing Low-Visibility Fog and High-Visibility Fog Scenarios at E80-S80 Overlap. ....	174
Figure 107. Total Number of 2D Keypoints and 3D Points by Fog and Overlap Scenario. ....	175
Figure 108. Mean Absolute Camera Position Uncertainties by Fog and Overlap Scenario. ....	175
Figure 109. Mean Absolute Camera Orientation Uncertainties by Fog and Overlap Scenario. ....	176
Figure 110. RMSE of the Checkpoint Error by Fog and Overlap Scenario. ....	176
Figure 111. Orthomosaic for Dark Sky Scenario at E60-S60 and E80-S80 Overlap Scenarios. ....	177
Figure 112. Total Number of 2D Keypoints and 3D Points by Overlap Scenario. ....	178
Figure 113. RMSE of the Checkpoint Error by Overlap Scenario. ....	178
Figure 114. Orthomosaic for Partial Illumination and Full Illumination Lamp Post Scenarios at E80-S80 Overlap. ....	180
Figure 115. Total Number of 2D Keypoints and 3D Points by Illumination Scenario. ....	181
Figure 116. Mean Absolute Camera Position Uncertainties by Illumination Scenario. ....	181

Figure 117. Mean Absolute Camera Orientation Uncertainties by Illumination Scenario.....	182
Figure 118. RMSE of the Checkpoint Error by Illumination Scenario. ....	182
Figure 119. Orthomosaic for Dry Asphalt Surface and Wet Asphalt Surface at E80-S80.....	184
Figure 120. Mean Number of 2D Keypoints and Matched 2D Keypoints Per Image for Dry and Wet Surface.....	185
Figure 121. Mean Reprojection Error for Dry and Wet Surface. ....	185
Figure 122. Mean Absolute Camera Position Uncertainty for Dry and Wet Surface.....	186
Figure 123. Mean Checkpoint Error for Dry and Wet Surface.....	186
Figure 124. Total Number of Points in the Densified Point Cloud. ....	188
Figure 125. Average Point Density.....	188
Figure 126. Cloud-to-Cloud Distance RMSE for Total Scene. ....	189
Figure 127. Cloud-to-Cloud Distance RMSE for Crash Scene. ....	189
Figure 128. Cloud-to-Cloud Distance RMSE for Different Fog and Overlap Scenarios. ....	190
Figure 129. Total Number of Points in Densified Cloud for Dark Sky Scenario by Overlap.....	190
Figure 130. Total Number of Points in Densified Point Cloud for Dry and Wet Surface.....	191
Figure 131. Cloud-to-Cloud Distance RMSE for Dry and Wet Surface. ....	191
Figure 132. Correlation Coefficient Matrix between Different Quality Factors and Brightness and Darkness Indexes. ....	192
Figure 133. Example Orthomosaic of the Crash Scene Derived from Simulated UAS Imagery Using a Textured Mesh Created from Real-World UAS Data. ....	199
Figure 134. Example of Pix4D Initial Processing Settings for Fixed Geolocation with Optimization of External Camera Parameters Set to None. ....	201
Figure 135. Digital Calibration Target in Metashape ( <i>112</i> ). ....	202
Figure 136. Calibration Images of the Checkerboard Pattern Projected onto a 165-cm (65- inch) TV. ....	203
Figure 137. ECDC Building on the TAMUCC Campus. ....	203
Figure 138. Pix4D Calibration Results for the Six Different Self-Calibration Scenarios. ....	205
Figure 139. Initial vs. Optimized Focal Length for the Six Calibration Scenarios. ....	205
Figure 140. Initial vs. Optimized Principal Point for the Six Calibration Scenarios.....	206
Figure 141. Correlation between Camera Internal Parameters. ....	207
Figure 142. Absolute Camera Geolocation Error for the Six Calibration Scenarios.....	208
Figure 143. Absolute Camera Orientation Error for the Six Calibration Scenarios. ....	209
Figure 144. Mean Checkpoint Error with Error Bars for the Six Calibration Scenarios.....	209
Figure 145. RMSE of the Checkpoint Error for the Six Calibration Scenarios.....	210
Figure 146. Digital Surface Models Generated from Scenarios 1 and 2. ....	211
Figure 147. Estimated Camera Lens Distortion for Each Calibration Scenario. ....	214
Figure 148. Sparse Point Clouds of the ECDC Building on the TAMUCC Campus Generated from the Different Calibration Processing Scenarios with Metashape. ....	215
Figure 149. Workflow to Simulate and Analyze Fog Impacts. ....	223
Figure 150. Workflow to Simulate and Analyze Motion Blur Impacts.....	224
Figure 151. Original UAS Imagery. ....	225
Figure 152. Original UAS Imagery with Different MOR Values. ....	226
Figure 153. Simulated Early Morning Imagery with Different MOR Values.....	227
Figure 154. Original UAS Imagery Feature Matching (MOR = 1000 m).....	228
Figure 155. Effect of Wind Speed on Motion Blur for Different Exposure Times. ....	230



Figure 156. Image Quality Degradation for Different Exposure Times and UAS Speeds.....	234
Figure 157. Variance of Laplacian for Orthomosaics Obtained in Abbott, Texas (Flight Altitudes: 25 m, 50 m, and 75 m). .....	235
Figure 158. Variance of Laplacian for Orthomosaics Obtained at the RELLIS Campus (Orthomosaics Obtained with Pix4D and Metashape).....	236
Figure 159. Variance of Laplacian for Orthomosaics Obtained in Florence, Texas (Orthomosaics Obtained from 01/15/2021 and 03/20/2021 Flights).....	236
Figure 160. Test Site Location (08/09/2020).....	240
Figure 161. Test Site Location (08/25/2020).....	241
Figure 162. Vehicle Location (08/25/2020).....	241
Figure 163. Test Site Location (09/30/2020).....	242
Figure 164. Crash Scene 3D Model (09/30/2020).....	242
Figure 165. Test Site Location (10/07/2020).....	243
Figure 166. Crash Scene 3D Model (10/07/2020).....	243
Figure 167. Crash Site Location (12/07/2020) .....	244
Figure 168. Crash Scene 3D Model (12/07/2020).....	244
Figure 169. Crash Site Location (01/15/2021) .....	245
Figure 170. Crash Scene 3D Model (01/15/2021).....	245
Figure 171. Crash Site Location (03/20/2021). .....	246
Figure 172. Crash Scene 3D Model (03/20/2021).....	246
Figure 173. DJI Mavic 2 Pro.....	247
Figure 174. DJI Matrice 300 RTK.....	248
Figure 175. DJI Phantom 4 RTK. ....	249
Figure 176. WingtraOne UAS Platform. ....	249
Figure 177. RIEGL VZ-2000i.....	250
Figure 178. LiBackpack DG50 Mobile 3D Mapping System. ....	251
Figure 179. Static Observation GNSS Receiver Being Set Up. ....	252
Figure 180. TxDPS Target (left) and Research Team’s Target (right).....	253
Figure 181. RTK Surveying of Targets. ....	253
Figure 182. Example Mission Plan for Low-Altitude Flight.....	254
Figure 183. UAS Flight Image Locations.....	255
Figure 184. Profile View of Image Locations with the Low-Altitude Flight in Blue. ....	255
Figure 185. Lidar Field Testing Site near Abbott, Texas. ....	256
Figure 186. Testing Trajectory Recovered in SLAM Mode Using the LiBackpack DG50. ....	257
Figure 187. Field Testing Site and Point Cloud Processed in SLAM Mode. ....	258
Figure 188. Checkpoint Locations Overlaid on an Orthomosaic Generated from the Combined Flights Processed with Metashape. ....	260
Figure 189. Point Cloud from Combined Flights Solution Processed in Pix4D. ....	262
Figure 190. Point Cloud from Mid-Altitude Flight Processed in Pix4D. ....	263
Figure 191. Point Cloud from Mid-Altitude Flight Processed in Metashape.....	263
Figure 192. Comparison of Point Clouds (Metashape in Red and Pix4D in Green).....	264
Figure 193. 3D Mesh Model Generated from Pix4D for the Combined Flight Solution. ....	264
Figure 194. 3D Mesh Model Generated from Pix4D for the Combined Flight Solution. ....	265
Figure 195. Test 4 Aerial Control Network for Accuracy Assessment. ....	266
Figure 196. UAS Flight Design for the WingtraPilot. ....	267
Figure 197. Zoomed-in View of an Orthomosaic Image Created with the WingtraOne.....	267

Figure 198. Example of a Merged Point Cloud Showing the Four TLS Scan Positions.....	268
Figure 199. Example MSA Adjustment Result from a RiSCAN Pro Processing Report.....	271
Figure 200. Colorized TLS Scan of the Crashed Vehicle.....	272
Figure 201. Example of 25-cm Radius Point Patches Extracted from UAS and TLS Data. ....	273
Figure 202. Circular Patches for Computing Surface Roughness (not to scale). ....	273
Figure 203. Segmented Car Region of Interest.....	274
Figure 204. Orthometric View of the Entire Scanned Area of the TLS Point Cloud. ....	276
Figure 205. Comparison of UAS Point Cloud Created with Metashape and Pix4D. ....	276
Figure 206. Comparison of UAS and TLS Point Cloud for Car Scene. ....	277
Figure 207. Surface Roughness. ....	279
Figure 208. Distance from UAS Points to TLS Points for Car Segment Region of Interest.....	280
Figure 209. Mean Distance in Z for UAS Point Patches to TLS Point Patches. ....	281
Figure 210. Cloud-to-Cloud Distances in Meters for Large Scene (Metashape). ....	282
Figure 211. Cloud-to-Cloud Distances in Meters for Car Scene (Metashape and Pix4D). ....	282
Figure 212. Geometry of Triangular Facets in the Scene. ....	283
Figure 213. Top-Down View of TLS Point Cloud Showing Ground Control Layout. ....	291
Figure 214. Oblique View of TLS Point Cloud of Crashed Vehicle. ....	291
Figure 215. Mavic 2 Pro with LEDs Dense Point Cloud.....	292
Figure 216. Matrice 300 RTK with LEDs Dense Point Cloud. ....	294
Figure 217. Matrice 300 RTK with LEDs and Spotlight Dense Point Cloud.....	295
Figure 218. Region of Interest Overlaid on Mavic 2 Pro with LEDs Point Cloud.....	296
Figure 219. Distances from Mavic 2 Pro and Matrice 300 RTK Point Sets to TLS Point Set within the Region of Interest. ....	297
Figure 220. Mean Distance in Z for UAS Point Patches to TLS Point Patches. ....	298
Figure 221. Cloud-to-Cloud Distances for Large Region of Interest. ....	299
Figure 222. Cloud-to-Cloud Distances for Crash Scene Region of Interest.....	300
Figure 223. Orthomosaics and DSMs from Pix4D Processing Report.....	303
Figure 224. Image from Phantom 4 RTK Flight Showing Excessive Motion Blur. ....	304
Figure 225. Example of the Poor Sparse Point Cloud Reconstruction Quality in Pix4D.....	305
Figure 226. Top-Down View of TLS Point Cloud Showing Ground Control Layout. ....	308
Figure 227. Oblique View of TLS Point Cloud of Staged Vehicle. ....	308
Figure 228. Example Image Acquired at 1/500-Second Exposure Time. ....	311
Figure 229. TxDOT’s Instrument Point and Checkpoint Locations.....	312
Figure 230. Marks to Indicate TxDOT’s Instrument Points and Checkpoints. ....	312
Figure 231. Camera Positions and Orientations for Phantom 4 RTK Night Flight.....	314
Figure 232. TLS Target Setup on Instrument Points and an Additional Target Tie Point. ....	315
Figure 233. GCP and TxDOT Survey Control Overlaid on Merged TLS Point Cloud.....	316
Figure 234. 2D View of Target Fine Scan.....	318
Figure 235. Cylinder Shape Fit to a Tie Point Target.....	318
Figure 236. Colorized TLS Point Cloud Showing Tie Points and Scan Positions. ....	318
Figure 237. Before Noise Filtering. ....	320
Figure 238. After Noise Filtering.....	320
Figure 239. Colorized TLS Point Cloud View of Staged Car Scene.....	321
Figure 240. Surface Roughness. ....	324
Figure 241. Region of Interest for TLS Point Cloud (Oblique View).....	325
Figure 242 Region of Interest for the UAS Point Clouds (Daytime). ....	325

Figure 243. Distance from UAS Points to TLS Points within the Region of Interest. ....	326
Figure 244. Mean Distance in Z for UAS Point Patches within the Region of Interest. ....	327
Figure 245. Point Patches Overlaid on Phantom 4 RTK Point Cloud. ....	328
Figure 246. Phantom 4 RTK Point Clouds at Night. ....	329
Figure 247. Distance from Phantom 4 RTK Points to TLS Points within the Region of Interest.....	330
Figure 248. Mean Distance in Z for Nighttime Result within the Region of Interest. ....	331
Figure 249. Cloud-to-Cloud Distances in Car Scene Region of Interest (Daytime Flights). ....	332
Figure 250. Cloud-to-Cloud Distances for Phantom 4 RTK Night Flight.....	334
Figure 251. Cloud-to-Cloud Distances for Phantom 4 RTK Night Flight for Large Region of Interest. ....	335
Figure 252. Orthomosaics and DSMs from Pix4D Processing Report.....	341
Figure 253. Phantom 4 RTK Orthomosaic and DSM from Pix4D Processing Report.....	342
Figure 254. DSM from Metashape Processing Report for Phantom 4 RTK Night Flight.....	342
Figure 255. Google Elevation Data Point Locations (08/25/2020). ....	353
Figure 256. Point Locations (08/25/2020). ....	354
Figure 257. Orthomosaic (08/25/2020).....	355
Figure 258. Digital Surface Model (08/25/2020). ....	356
Figure 259. Google Elevation Data Point Locations (09/30/2020). ....	358
Figure 260. Scene’s Manual Point Locations (09/30/2020). ....	358
Figure 261. Orthomosaic for Run 1, Scenario 1a (09/30/2020). ....	360
Figure 262. Digital Surface Model for Run 1, Scenario 1a (09/30/2020). ....	361
Figure 263. Google Elevation Data Point Locations (10/07/2020). ....	363
Figure 264. Scene’s Manual Point Locations (10/07/2020). ....	364
Figure 265. Orthomosaic (10/07/2020).....	366
Figure 266. Digital Surface Model (10/07/2020). ....	367
Figure 267. Scene’s Manual Point Locations (12/07/2020). ....	369
Figure 268. Run 2, Scenario 1a Model (12/07/2020). ....	371
Figure 269. Mavic 2 Pro Nighttime Run Model (12/07/2020). ....	372
Figure 270. Orthomosaic: Mavic 2 Pro Night Model vs. Matrice 300 RTK (12/07/2020). ....	372
Figure 271. Digital Surface Model: Mavic 2 Pro Night Model vs. Matrice 300 RTK (12/07/2020).....	373
Figure 272. Google Elevation Data (01/15/2021).....	375
Figure 273. Scene’s Manual Point Locations (01/15/2021). ....	375
Figure 274. Matrice 300 RTK Night Model (01/15/2021). ....	377
Figure 275. Mavic 2 Pro Scene with Built-In LEDs and High-Mast Lights (01/15/2021). ....	378
Figure 276. Nighttime Mavic 2 Pro Model with Google Elevation Data (01/15/2021).....	378
Figure 277. Nighttime Orthomosaic (01/15/2021). ....	379
Figure 278. Nighttime Digital Surface Model (01/15/2021). ....	379
Figure 279. Daytime Orthomosaic (01/15/2021).....	380
Figure 280. Daytime Digital Surface Model (01/15/2021).....	380
Figure 281. Google Elevation Data (03/20/2021).....	383
Figure 282. Scene’s Manual Point Locations (03/20/2021). ....	383
Figure 283. Mavic 2 Pro Nighttime Model (03/20/2021).....	386
Figure 284. Ray Cloud Views for Mavic 2 Pro Nighttime Run. ....	387
Figure 285. 3D Distance Deltas with Respect to Base Scenario Coordinates. ....	389

Figure 286. 3D Distance Deltas with Respect to Surveyed Checkpoint Coordinates. .... 390

Figure 287. Normalized 3D Distance Deltas with Respect to Distance between  
Checkpoints A and B. .... 391

Figure 288. Effect of Using the Accurate Geolocation and Orientation Setting in Pix4D..... 393

Figure 289. Deltas for Distances between Points with and without Scale Constraint..... 395

Figure 290. VOR Calculation (Case: 25,000 AADT and 15 Minutes Saved per Driver). .... 427

## LIST OF TABLES

	Page
Table 1. GCP Checkpoint Errors from a Sample Pix4D Quality Report.....	27
Table 2. UAS Manufacturer among Public Safety Agencies in the United States. ....	33
Table 3. UAS Manufacturer Models among Public Safety Agencies in the United States. ....	33
Table 4. Summary of UASs Usage as Reported by State DOTs. ....	36
Table 5. Summary of UASs Usage as Reported by State Public Safety Agencies.....	37
Table 6. Plans for UAS Use by State Agencies <i>Currently Using</i> UASs. ....	39
Table 7. Plans for UAS Use by State Agencies <i>Not Currently Using</i> UASs.....	40
Table 8. Model vs. Field Measurement Table. ....	43
Table 9. Points with Coordinates and Description (Using a Local Coordinate System).....	44
Table 10. Counties Selected for Analysis of Five Metro Areas. ....	51
Table 11. Number of Crashes—Statewide.....	52
Table 12. Number of Crashes—Austin Area (Travis County). ....	52
Table 13. Number of Crashes—Dallas Area (Dallas County).....	52
Table 14. Number of Crashes—Fort Worth Area (Tarrant County). ....	53
Table 15. Number of Crashes—Houston Area (Harris County).....	53
Table 16. Number of Crashes—San Antonio Area (Bexar County). ....	53
Table 17. Number of Fatal Crashes—Statewide and Metro Area Counties. ....	54
Table 18. Indicators of Select Crash Attributes for Fatal Crash Prediction Modeling. ....	57
Table 19. Grouping of Crashes into Daylight and Nighttime Crashes. ....	57
Table 20. Statewide Count of Daylight and Nighttime <i>Nonfatal</i> Crashes.....	58
Table 21. Statewide Count of Daylight and Nighttime <i>Fatal</i> Crashes. ....	58
Table 22. Number of <i>All</i> Crashes by Weather Condition—Statewide. ....	62
Table 23. Number of <i>All</i> Crashes by Weather Condition (2010–2019). ....	62
Table 24. Percentage of <i>All</i> Crashes by Weather Condition (2010–2019). ....	62
Table 25. Number of <i>All</i> Crashes by Aggregated Weather Condition (2010–2019).....	62
Table 26. Percentage of <i>All</i> Crashes by Aggregated Weather Condition (2010–2019). ....	63
Table 27. Number of <i>Fatal</i> Crashes by Weather Condition—Statewide. ....	63
Table 28. Number of <i>Fatal</i> Crashes by Weather Condition (2010–2019). ....	63
Table 29. Percentage of <i>Fatal</i> Crashes by Weather Condition (2010–2019). ....	63
Table 30. Number of <i>Fatal</i> Crashes by Aggregated Weather Condition (2010–2019).....	64
Table 31. Percentage of <i>Fatal</i> Crashes by Aggregated Weather Condition (2010–2019). ....	64
Table 32. Number of <i>All</i> Crashes by Surface Condition—Statewide.....	65
Table 33. Number of <i>All</i> Crashes by Surface Condition (2010–2019).....	65
Table 34. Percentage of <i>All</i> Crashes by Surface Condition (2010–2019). ....	66
Table 35. Number of <i>All</i> Crashes by Aggregated Surface Condition (2010–2019). ....	66
Table 36. Percentage of <i>All</i> Crashes by Aggregated Surface Condition (2010–2019).....	66
Table 37. Number of <i>Fatal</i> Crashes by Surface Condition—Statewide.....	67
Table 38. Number of <i>Fatal</i> Crashes by Surface Condition (2010–2019).....	67
Table 39. Percentage of <i>Fatal</i> Crashes by Surface Condition (2010–2019). ....	67
Table 40. Number of <i>Fatal</i> Crashes by Aggregated Surface Condition (2010–2019). ....	67
Table 41. Percentage of <i>Fatal</i> Crashes by Aggregate Surface Condition (2010–2019).....	68
Table 42. Turbulence Levels.....	90
Table 43. Tailwind, Headwind, and Crosswind Scenarios. ....	96

Table 44. Simulations for Single Altitude of 80 m (262 ft) AGL.....	97
Table 45. Simulations for Dual Altitudes of 80 m (262 ft) and 10 m (33 ft) AGL. ....	99
Table 46. Average 3D Errors (m) for 58 Single-Altitude Simulation Runs. ....	101
Table 47. Normalized Average 3D Errors for 58 Single Altitude-Simulation Runs. ....	101
Table 48. Average 3D Errors (m) by Flight Course for 58 Single-Altitude Simulation Runs. ....	102
Table 49. Normalized Average 3D Errors by Flight Course for 58 Single-Altitude Simulation Runs.....	103
Table 50. Standard Deviations (m) for 58 Single-Altitude Simulation Runs. ....	106
Table 51. Normalized Standard Deviations for 58 Single Altitude-Simulation Runs.....	106
Table 52. Standard Deviations (m) by Flight Course for 58 Single-Altitude Simulation Runs. ....	107
Table 53. Normalized Standard Deviations by Flight Course for 58 Single-Altitude Simulation Runs.....	108
Table 54. Total Flight Times (s) for 58 Single-Altitude Simulation Runs. ....	111
Table 55. Normalized Total Flight Times (s) for 58 Single-Altitude Simulation Runs. ....	111
Table 56. Flight Times (s) by Flight Course for 58 Single-Altitude Simulation Runs.....	112
Table 57. Normalized Flight Times (s) by Flight Course for 58 Single-Altitude Simulation Runs.....	113
Table 58. Battery Use (mAh) for 58 Single-Altitude Simulation Runs.....	116
Table 59. Normalized Battery Use (mAh) for 58 Single-Altitude Simulation Runs.....	116
Table 60. Results for Six Dual-Altitude Simulation Runs.....	117
Table 61. Disaggregated Results by Headwind, Tailwind, and Crosswind.....	117
Table 62. Disaggregated Results by Headwind, Tailwind, Crosswind, and Flight Altitude. ....	118
Table 63. Number of Images That See a Point as a Function of the Overlap.....	122
Table 64. Parameters for Image Lens Distortion and Vignetting Effects.....	127
Table 65. Camera Settings. ....	127
Table 66. Overlap Scenarios. ....	128
Table 67. Number of Images Acquired Based on Percent Sidelap and Flight Height.....	147
Table 68. Geolocation and Orientation Uncertainty Parameters for Wind Simulation. ....	148
Table 69. Natural and Artificial Lighting Scenarios Evaluated.....	157
Table 70. Fog Simulation Conditions. ....	162
Table 71. Overall Brightness and Darkness Index Values for Different Scenarios.....	166
Table 72. Sony A6500 Camera Specifications. ....	202
Table 73. Camera Calibration Solutions in Metashape for Pre-Calibration and Self- Calibration Run 1.....	212
Table 74. Camera Calibration Solutions in Metashape for Pre-Calibration and Self- Calibration Run 2.....	212
Table 75. Relationship between Attenuation Coefficient, MOR, and Visibility.....	220
Table 76. Number of Points in the 3D Point Cloud (original UAS Imagery). ....	228
Table 77. Number of Points in the 3D Point Cloud (Early Morning Imagery). ....	228
Table 78. Reduction in the Number of Pairwise Matches and Sparse Point Cloud Points.....	231
Table 79. Reduction in the Number of Points in the 3D Point Cloud at Different UAS Speed and Exposure Time Levels.....	235
Table 80. Example of Final Image Locations for Import to SfM Software.....	259
Table 81. Checkpoint Residuals for the Combined Flight Solution in Pix4D.....	260

Table 82. Checkpoint Residuals for the Combined Flight Solution in Metashape.....	261
Table 83. RMSE of Checkpoint Residuals (Pix4D Solution).....	261
Table 84. RMSE of Checkpoint Residuals (Metashape Solution).....	262
Table 85. TLS Survey Parameters Used for Each Scan Position. ....	268
Table 86. PPK-Corrected WingtraOne UAS Image Positions.....	269
Table 87. TLS Estimated Scan Position Accuracy. ....	271
Table 88. General Information about Point Cloud Data for Entire Scene.....	275
Table 89. General Information about Point Cloud Data for Surrounding Scene.....	275
Table 90. General Information about Point Cloud Data for Car Scene Only. ....	275
Table 91. Magnitude of Surface Height Error Relative to RTK GNSS (Developed Method).....	277
Table 92. Magnitude of Surface Height Error Relative to RTK GNSS (LAStools Method).....	277
Table 93. Statistics for Point-to-Point Distance Comparisons.....	280
Table 94. Cloud-to-Cloud Distance Statistics.....	283
Table 95. Measured Distances within TLS and UAS Point Clouds. ....	284
Table 96. Measured Angles within TLS and UAS Point Clouds. ....	284
Table 97. Summary of SfM Processing Report Results for Checkpoint Error. ....	285
Table 98. Difference in RMSE between Processing Runs and PPK-Only Solution in Pix4D. ....	285
Table 99. Pix4D SfM Checkpoint Error (Autonomous GNSS and 7 GCPs).....	285
Table 100. Pix4D SfM Checkpoint Error (PPK). ....	286
Table 101. Pix4D SfM Checkpoint Error (PPK and 1 GCP).....	286
Table 102. Pix4D SfM Checkpoint Error (PPK and 3 GCPs).....	287
Table 103. Pix4D SfM Checkpoint Error (PPK and 5 GCPs).....	287
Table 104. Metashape SfM Checkpoint Error (PPK). ....	288
Table 105. Test 5 TLS Survey Parameters Used for Each Scan Position.....	289
Table 106. UAS Flights and SfM Processing Runs.....	290
Table 107. TLS Estimated Scan Position Accuracy. ....	291
Table 108. Mavic 2 Pro with LEDs Surface Height Error.....	293
Table 109. Matrice 300 RTK with LEDs Surface Height Error. ....	294
Table 110. Matrice 300 RTK with LEDs + Spotlight Surface Height Error. ....	295
Table 111. Cloud-to-Cloud Distance Statistics for Mavic 2 Pro with LEDs.....	300
Table 112. Cloud-to-Cloud Distance Statistics for Matrice 300 RTK with LEDs. ....	300
Table 113. Cloud-to-Cloud Distance Statistics for Matrice 300 RTK with LEDs and Spotlight.....	300
Table 114. Pix4D Processing Quality Results for Mavic 2 Pro with LEDs. ....	301
Table 115. Pix4D Processing Quality Results for Matrice 300 RTK with LEDs.....	301
Table 116. Pix4D Processing Quality Results for Matrice 300 RTK with LEDs + Spotlight.....	301
Table 117. Checkpoint Errors for Matrice 300 RTK with LEDs. ....	302
Table 118. Checkpoint Errors for Matrice 300 RTK with LEDs and Spotlight. ....	302
Table 119. Pix4D Processing Quality Results for Phantom 4 RTK. ....	305
Table 120. TLS Survey Parameters Used for Each Scan Position. ....	306
Table 121. UAS Flights and SfM Processing Runs.....	307
Table 122. TLS Estimated Scan Position Accuracy. ....	307

Table 123. TLS Surface Height Error.....	309
Table 124. Pix4D Processing Quality Results (Shutter: 1/1000 Seconds). ....	310
Table 125. Pix4D Processing Quality Results (Shutter: 1/500 Seconds). ....	310
Table 126. Test 7 TLS Survey Parameters Used for Each Scan Position.....	315
Table 127. Test 7 UAS Flights and SfM Processing Runs. ....	317
Table 128. Statistical Results from MSA for Control Points.....	319
Table 129. Statistical Results from MSA for Single Tie Point.....	319
Table 130. Surface Height Error Relative to TxDOT Control.....	322
Table 131. Surface Height Error Relative to RTK GNSS GCPs.....	322
Table 132. Cloud-to-Cloud (C2C) Distance Statistics for WingtraOne. ....	333
Table 133. Cloud-to-Cloud (C2C) Distance Statistics for Phantom 4 RTK.....	333
Table 134. Cloud-to-Cloud (C2C) Distance Statistics for Phantom 4 RTK (night flight). ....	334
Table 135. Cloud-to-Cloud (C2C) Distance Statistics for Phantom 4 RTK (night flight). ....	335
Table 136. Pix4D SfM Checkpoint Error for WingtraOne PPK. ....	337
Table 137. Checkpoint RMSE for WingtraOne Based on Control Method. ....	337
Table 138. Pix4D SfM Checkpoint Error for Phantom 4 RTK (Daytime).....	338
Table 139. Checkpoint RMSE for Phantom 4 RTK Based on Control Method (Daytime). ....	338
Table 140. Pix4D SfM Checkpoint Error for Phantom 4 RTK (Nighttime). ....	339
Table 141. Checkpoint RMSE for Phantom 4 RTK Based on Control Method (Nighttime).....	339
Table 142. GCP Errors for WingtraOne PPK Processed in Pix4D.....	340
Table 143. GCP Errors for Phantom 4 RTK Processed in Pix4D (Daytime). ....	340
Table 144. Vertical RMSE for TxDOT Checkpoints with and without GCPs.....	340
Table 145. Checkpoint Errors from Metashape Report for Phantom 4 RTK Night Flight. ....	343
Table 146. Tests, Runs, and Scenarios Completed. ....	345
Table 147. Summary of Results for Each Scenario. ....	347
Table 148. Deltas Associated with the Location of Five Points for Each Scenario. ....	349
Table 149. Deltas Associated with Distances between Five Points for Each Scenario. ....	351
Table 150. Summary of VOR Calculations. ....	427



## LIST OF ACRONYMS AND ABBREVIATIONS

2D	Two-dimensional
3D	Three-dimensional
AADT	Annual average daily traffic
AASHTO	American Association of State Highway and Transportation Officials
AGL	Aboveground level
API	Application programming interface
ASPRS	American Society for Photogrammetry and Remote Sensing
AT	Aerial triangulation
ATC	Air traffic control
B	Blue
BA	Bundle adjustment
BIM	Building information modeling
CBR	Cost-benefit ratio
CFL	Calibrated focal length
CFR	Code of Federal Regulations
CMOS	Complementary metal-oxide semiconductor
CORS	Continuously operating reference station
CRIS	Crash Record Information System
DGNSS	Differential Global Navigation Satellite System
DOD	U.S. Department of Defense
DSM	Digital surface model
ECDC	Early Childhood Development Center
EGM96	Earth Geodetic Model 96
EMI	Electromagnetic induction
EO	Exterior orientation
EXIF	Exchangeable image file format
FAA	Federal Aviation Administration
FCU	Flight control unit
FOV	Field-of-view
FTN	FAA tracking number
G	Green
GCP	Ground control point
GCS	Ground control station
GEO	Geospatial Environment Online
GIS	Geographic information system
GNSS	Global Navigation Satellite System
GPR	Ground penetrating radar
GPS	Global Positioning System
GRS80	Geodetic Reference System of 1980
GSD	Ground sample distance
IACRA	Integrated Airman Certification and Rating Application
IMU	Inertial measurement unit
IO	Interior orientation
ISO	International Standards Organization

ISP	Iowa State Patrol
LAANC	Low Altitude Authorization and Notification Capability
LAS	LASer (format)
LAZ	Compressed LAS format
LCSO	Lake County Sheriff Office
LED	Light-emitting diode
LiDAR	Light detection and ranging
LS	Least squares
mAh	Milliamp hour
MCAT	Major Crash Assistance Team
MEMS	Microelectromechanical system
MOR	Meteorological optical range
MP	Megapixel
MSA	Multi-station adjustment
MSL	Mean sea level
MVS	Multi-view stereo
NAD83	North American Datum of 1983
NAPARS	National Association of Professional Accident Reconstruction Specialists
NAVD 88	North American Vertical Datum of 1988
NGS	National Geodetic Survey
NOAA	National Oceanic and Atmospheric Administration
NOTAM	Notice to Airmen
NUCPS	Northwestern University Center for Public Safety
OPUS	Online Positioning User Service
OSP	Oklahoma State Patrol
PPK	Postprocessed kinematic
R	Red
RGB	Red green blue
RMSE	Root mean square error
RRP	Regional reference point
RTCM	Radio Technical Commission for Maritime
RTK	Real-time kinematic
RTN	Real-Time Network
SfM	Structure-from-motion
SIFT	Scale invariant feature transform
SIM	Subscriber identity module
SITL	Software-in-the-loop
SLAM	Simultaneous localization and mapping
TAMUCC	Texas A&M University-Corpus Christi
TIM	Traffic incident management
TIN	Triangulated irregular network
TLS	Terrestrial laser scanner
TTI	Texas A&M Transportation Institute
TxDOT	Texas Department of Transportation
TxDPS	Texas Department of Public Safety
UAS	Unmanned aircraft system

UAV	Unmanned aerial vehicle
USB	Universal serial bus
USGS	United States Geological Survey
UTM	Universal Transverse Mercator
VLOS	Visual line-of-sight
VO	Visual observer
VOR	Value of research
WGS84	World Geodetic System 1984
WSP	Washington State Patrol

## LIST OF TERMS

**Absolute positional accuracy:** Degree to which a point or feature in a map or 3D reconstructed model corresponds to its true position in a fixed coordinate system in the real world.

**Aerial triangulation (AT):** Process of determining the X-Y-Z ground coordinates of individual points based on photo coordinate measurements.

**Altitude:** Vertical distance of the UAS with respect to the terrain where the UAS is flying. To distinguish between several types of altitude normally used in aviation, UAS altitudes frequently include a modifier (e.g., aboveground level [AGL]). Altitude and height are used interchangeably.

**Angular orientation angle:** Rotations between the image coordinate system and the geodetic coordinate system. There are angular orientation angles: phi (with respect to the X axis), omega (with respect to the Y axis), and kappa (with respect to the Z axis).

**3D error:** Difference in geolocation (i.e., 3D Euclidean distance) between a calculated or observed 3D location and its associated true 3D location.

**3D point:** Point in 3D space with associated X-Y-Z coordinates in a local or geodetic coordinate system.

**Bundle adjustment (BA):** Photogrammetric and computational procedure implemented by the SfM software to simultaneously solve for camera interior orientation (IO) parameters (e.g., focal length) and camera exterior orientation (EO) parameters (e.g., camera positions and angular orientations at the time of each image).

**Calibrated focal length (CFL):** Focal length that produces an overall mean distribution of lens distortion. For digital cameras, this is typically reported in pixel units for calibration purposes within the SfM software.

**Checkpoint:** Control point, such as a painted mark or aerial survey target, with accurately surveyed horizontal and vertical coordinates that is used to assess the accuracy of the SfM reconstruction. Checkpoints are technically ground control points not used during optimization of the SfM solution for camera positions and orientations.

**Civil twilight:** Brightest of the three twilight periods when the sun is just below the horizon and there is enough natural light to carry out outdoor activities.

**Crosswind:** Wind component that blows to the side of an aircraft.

**Dense point cloud:** Collection of 3D tie point coordinates within a defined coordinate system that is based on a densification process that matches corresponding points in stereo image pairs and then expands on point measurements between the sparse point cloud by enforcing epipolar geometry constraints obtained from the BA solution and later filtering the outliers.

**Depth map:** Representation of the depth information associated with a given image that is used as an intermediate source of information for generation of dense point clouds. It is a grayscale image having intensity values typically ranging from 0 to 255. Objects closer to the camera have higher intensity values in the depth map (255 for objects located nearest to the camera), and objects farther from the camera have lower intensity values (0 for objects located farthest from the camera). A depth map is calculated by measuring disparity in stereo vision, which is a shift in the position of a corresponding point in one image relative to its position in another image that is dependent on its distance in the scene to the camera.

**Elevation:** Height of a point or object above mean sea level (MSL).

**Endlap:** frontal overlap within the same flight line. Endlap is a function of flight speed and the time interval (i.e., distance) between image exposure stations.

**Exposure time:** Length of time the digital sensor inside a camera is exposed to light. Shutter speed is a commonly used term when referring to exposure time.

**Epipolar geometry:** Geometry of stereo vision.

**Flight course:** Desired direction in which an aircraft is to be steered. For example, east represents the flight course for an eastbound aircraft. The course is not necessarily the direction the aircraft actually travels due to wind disturbance.

**Flight line:** Individual trajectory within the flight plan where the aircraft is flying. Flight plans usually have multiple flight lines. For example, a flight plan could have several east-west flight lines and several perpendicular north-south flight lines, with each flight line having a specific flight course.

**Focal length:** Distance from the focal point on the camera sensor frame to the center of a lens.

**Geolocation error:** Difference between the initial positions (X-Y-Z coordinates) and computed positions for a camera position at the time of image acquisition or GCP. Image geolocation error stems from the geolocation error of camera positions.

**Global Navigation Satellite System (GNSS):** Constellation of satellites providing signals from space that transmit positioning and timing data to GNSS receivers. Examples of GNSSs are the Global Positioning System (GPS), GLONASS, Galileo, and BeiDou.

**Ground control point (GCP):** painted mark, aerial survey target, or identifiable feature in the scene whose horizontal and vertical coordinates have been accurately surveyed, such as with RTK GNSS. A GCP is used to georeference or improve the georeferencing of an SfM reconstruction.

**Ground sample distance (GSD):** Projected pixel area on the ground. It is a function of the camera focal length, physical size of the individual sensor elements inside the camera (called pixel pitch), and flight height AGL. GSD is a measure of the spatial resolution of the imagery.

**Headwind:** Wind component that blows against the direction of travel of an aircraft.

**Height:** Vertical distance between an object or point and a reference datum. Altitude and height are used interchangeably.

**Keypoint:** Point of interest (e.g., features of high contrast, interesting texture) in the UAS images that can be easily recognized by the SfM software's automated feature (keypoint) extraction and feature-matching algorithms.

**Lambertian surface:** Diffuse surface that scatters incident illumination equally in all directions.

**Least squares (LS):** Computational technique that minimizes the sum of the squares of differences between observed values and estimated values. It is used to estimate the optimal value of a parameter or set of parameters based on the minimization criteria.

**Meteorological optical range (MOR):** Distance needed to reduce the luminous flux of a collimated beam (i.e., a light that emits parallel rays) from a 2700-K color temperature to 5 percent of the original value.

**Metric camera:** Camera with known and stable interior orientation (i.e., known focal length and internal dimensions) defined with the help of fiducial marks and calibration.

**Nonmetric camera:** Camera with unknown or unstable interior orientation, typically lacking fiducial marks.

**Pearson's correlation coefficient:** Bivariate correlation. It is a statistic that measures linear correlation between two variables. It has a value between +1 and -1.

**Pixel pitch:** Distance from the center of a pixel to the center of the next pixel in a camera sensor.

**Postprocessed kinematic (PPK):** Technique to correct GNSS positions using carrier-based ranging calculations, as well as corrections from sources such as ephemerides and ionospheric and tropospheric delays. As opposed to real-time kinematic (RTK) techniques, PPK corrections are made after the data are collected in the field.

**Precision:** Degree of closeness of measurements of a quantity with respect to a central tendency metric. Precision refers to how closely repeated measurements or observations come to duplicating measured or observed values.

**Principal point location:** X-Y image coordinates of the principal point in pixels. Principal point is the point on the image plane onto which the perspective center of the lens is projected. For a digital camera, the principal point is where the optical axis intersects the image plane, nominally located at the center of the sensor frame. Due to imperfections, it is often not perfectly aligned with the optical center of the lens. Calibration can determine the offset from this location.

**Radial lens distortion:** Symmetric component of lens distortion that occurs along lines radially away from the principal point. Radial distortion occurs when light rays bend more near the edges of a lens than they do at its optical center. Although the amount may be negligible, this type of distortion is theoretically always present even if the lens system is perfectly manufactured to design specifications. Consumer-grade digital cameras are prone to radial distortion.

Real-time kinematic: Technique to correct GNSS positions using real-time, carrier-based ranging calculations, as well as corrections from sources such as ephemerides and ionospheric and tropospheric delays. Network RTK relies on a network of spatially distributed permanent stations that broadcast RTK correction data to rover stations in real time.

Relative positional accuracy: Degree to which a point or feature in a map or 3D reconstructed model is accurate in location relative to other points within that same map or model.

Reprojection error: Distance between the initially detected keypoint location and the 3D point's reprojected location in the same image. This error depends on the quality of the camera calibration and BA result for resolving exterior camera parameters (position and orientation), as well as the quality of the keypoint detection in the images.

Root mean square error (RMSE): Standard deviation of the residuals (i.e., prediction errors). RMSE accounts for both the mean error (bias) and standard deviation (uncertainty) components of error. In cases of 0 bias, standard deviation and RMSE are equivalent.

Sidelap: Side overlap between flight lines. Sidelap is a function of the distance between flight lines.

Skew coefficient: Nonzero coefficients that can sometimes be used in calibration to compensate for image axes that are skewed (not perpendicular) within a digital camera.

Standard deviation or sigma: Square root of the average of the squared differences from the mean value. It is the square root of the variance.

Sparse point cloud: Collection of 3D tie point coordinates within a defined coordinate system, which is based on the automated feature-matching algorithm performed by the SfM software to extract and correspond features between images.

Surface roughness: Standard deviation of the Z component in a point cloud.

Tailwind: Wind component that blows in the direction of travel of an aircraft.

Tangential lens distortion: Lens distortion that remains after compensation for symmetric radial lens distortion. Sometimes referred to as decentering distortion, tangential distortion occurs when the physical elements of a lens are not perfectly parallel and aligned with the image plane.

Tie point: Feature that can be clearly identified in two or more images and can be selected as a reference point. In Pix4Dmapper™ terminology, an *automatic* tie point refers to a 3D point and its corresponding 2D keypoints that were automatically detected in the images and used to compute its 3D position. A *manual* tie point is a point without 3D coordinates that is marked by the user in the images.

Turbulence: Random changes in wind speed, direction, and pressure.

Uncertainty: Expression of the statistical dispersion of the values attributed to a measured quantity, often reported as the standard deviation based on a set of repeated observations. In the

context of LS estimation, it represents the theoretical error, which is based on the estimated standard deviation for an adjusted parameter value.

Unmanned aircraft system (UAS): Aircraft system that includes an aircraft without any human pilot, crew, or passengers onboard and the equipment necessary to control and communicate with the aircraft. Small UASs are UASs in which the aircraft weighs less than 25 kg (55 lb) on takeoff, inclusive of all components that are either onboard or attached to the aircraft.

Variance: Average of the squared differences from the mean value.

Visibility: Measure of the distance at which a target object can be clearly discerned.

Voxel: Element or data point of a grid in 3D space. The concept of a voxel is similar to that of a pixel in 2D space. In 3D computer graphics, voxels are used for rendering and visualization purposes and frequently for describing spatial resolution.

Wind direction: Direction from which the wind is coming with respect to north in a clockwise fashion. For example, 0 degrees represents north wind blowing from the north and 90 degrees represents east wind blowing from the east.



## CHAPTER 1. INTRODUCTION

The Texas Department of Transportation (TxDOT) has a strategic interest in using unmanned aircraft systems (UASs) to support a variety of initiatives, including traffic incident management (TIM). TxDOT is interested in identifying and documenting UAS uses to determine to what degree UASs can be used to streamline the process to clear and document fatal crash scenes.

UASs represent a new frontier in surveying and mapping. Improvements in the availability and accuracy of miniaturized positioning and orientation sensors, autonomous navigation, image postprocessing software and algorithms, and the quality of consumer-grade digital cameras and miniaturized sensors have resulted in an explosion of public and private sector uses of UASs for geospatial applications. Advantages of UASs for surveying and mapping instead of traditional piloted aircraft and satellites include the following (1, 2):

- Ability to fly at much lower altitudes enabling higher image detail (e.g., cm to sub-cm scales).
- Flexible and repeatable data acquisition to achieve high temporal resolution, target ideal weather conditions and events, or provide rapid response in certain scenarios with proper preparation and planning.
- Data acquisition efficiency for mapping at localized geographic scales.

High image overlap enables the use of automated photogrammetric techniques to postprocess the imagery and derive accurate two-dimensional (2D) orthorectified image products and three-dimensional (3D) reconstructions of a scene for planimetric mapping and 3D mensuration, respectively. Spectral data can also be acquired from multispectral sensors onboard the UAS to perform traditional remote sensing tasks. With these capabilities, UASs are being used for a variety of surveying and remote sensing tasks in support of various industries and applications including land surveying, emergency response, oil and gas development, civil engineering, and inspection surveying (3).

A major benefit of using UASs to improve TIM practices, including clearing a crash scene or fatal crash scene reconstruction, is the ability to replace traditional forensic “feet on the ground” surveying methods using a total station or terrestrial laser scanner with a method that involves the use of photogrammetric techniques. The photogrammetric aspect of the UAS survey method allows for documenting and cataloging enormous amounts of geospatial data quickly in comparison to traditional survey methods.

Several challenges exist regarding the effective use of UASs for this type of application. Operational challenges include current and evolving regulations, limitations in platform endurance, difficulty operating UASs along interstate highways and urban corridors, and suboptimal environmental conditions, such as high winds, rain, low ambient lighting, or fog. Additional challenges reside on the data processing and photogrammetry side of the process. To overcome these challenges, it is necessary to better understand the impacts of suboptimal conditions on data acquisition and image quality and how these factors affect geospatial data fidelity, including measurement accuracy and repeatability. This improved understanding is needed to optimize standard operating procedures and refine best practices for UAS surveying of crash scenes under suboptimal conditions.

To better understand the feasibility of using UASs under these conditions, this research documented key challenges and developed and tested procedures for data collection and processing. The research included (a) review of historical crash data trends in Texas to establish correlations with environmental factors, (b) simulation of the effect of environmental factors on the quality of data collected with UASs, (c) field tests of UAS-based crash data collection activities under a variety of conditions, (d) development of recommendations and guidelines for UAS operations under suboptimal environmental conditions, and (e) development of recommendations for updates of the TxDOT *Unmanned Aircraft System (UAS) Flight Operations and User's Manual (4)*.

The evaluation of environmental factors included these elements:

- Impact of wind speed and direction on UAS flight operations.
- Impact of aerial imaging network design on 3D crash scene reconstructions using commercial SfM software.
- Impact of ambient lighting and low visibility on UAS-SfM reconstructions.
- Self-calibration versus preflight calibration procedures for consumer-grade nonmetric digital RGB cameras.
- Impact of suboptimal conditions on visual image quality.
- Impact of camera properties on UAS image quality to guide crash scene imaging.

This report summarizes the work completed throughout the research. Subsequent chapters cover the following topics:

- Chapter 2 includes a literature review of basic UAS concepts, relevant federal and state regulations, structure-from-motion (SfM) photogrammetry, use of UASs for crash investigations, and commonly used UASs for crash investigations.
- Chapter 3 includes an analysis of spatial and temporal trends in the occurrence of crashes on Texas highways. The crash data analysis focused on the Austin, Dallas, Fort Worth, Houston, and San Antonio metro areas.
- Chapter 4 describes computer simulations to assess impacts of suboptimal environmental conditions when performing UAS-SfM photogrammetric data collection and processing for crash reconstruction applications.
- Chapter 5 describes the activities undertaken to collect and process UAS data under a variety of scenarios depicting vehicle crashes. The research team performed UAS data collection at the following locations in Texas: IH-35 near Abbott, Phil Hardberger Park in San Antonio, Texas A&M University's RELLIS Campus in College Station, and Texas Department of Public Safety's (TxDPS's) Tactical Training Facility in Florence.
- Chapter 6 includes conclusions and recommendations for implementation.

A separate, standalone deliverable includes the recommendations for updates to the TxDOT *Unmanned Aircraft System (UAS) Flight Operations and User's Manual*.

## CHAPTER 2. LITERATURE REVIEW

### INTRODUCTION

This chapter includes a literature review of relevant federal and state regulations, basic UAS flight planning and management concepts, SfM photogrammetry, use of UASs for crash investigations, national survey findings, and case studies.

### FEDERAL AND STATE REGULATIONS

#### Federal Requirements

A critical regulation at the federal level for the operation of UASs is 14 Code of Federal Regulations (CFR) 107, which was enacted in 2016 (5). The Federal Aviation Administration (FAA) has different rules based on the type of UAS mission and the type of remote pilot that is commanding the UAS. FAA's 2018 Advisory Circular 00-1.1B, *Public Aircraft Operations—Manned and Unmanned*, provides guidance on relevant roles and regulations (6).

#### *UAS Registration*

According to Part 107, a small unmanned aircraft is an unmanned aircraft that weighs less than 25 kg (55 lb) on takeoff, inclusive of everything that is onboard or attached to the aircraft. The UASs used in this research fall under this category (5). If the total weight on takeoff is 25 kg (55 lb) or more, the unmanned aircraft must be registered in accordance with 14 CFR 47 (7).

FAA requires pilots to register UASs on the FAA DroneZone webpage using the online registration process (8). FAA issues FA numbers for UASs less than 25 kg (55 lb) and N numbers for UASs 25 kg (55 lb) or heavier. After creating an account, the pilot provides information about the unmanned aircraft, such as description, model, and serial number. With this information, FAA issues a registration number that must be permanently affixed to the outside of the unmanned aircraft and is valid for three years. FAA also issues a Certificate of Registration that must be carried with the UAS whenever the UAS is being used.

#### *Pilot License*

Under Part 107 rules, the UAS pilot, or remote pilot in command, must obtain a remote pilot certificate from FAA (9). Requirements include that the pilot must be at least 16 years old; be able to understand, speak, read, and write English; be in physical and mental condition to fly a drone safely; and pass an initial aeronautical knowledge exam. The certificate is valid for two years and must be available during all UAS operations.

The first step is for the pilot to obtain an FAA tracking number (FTN) by creating an Integrated Airman Certification and Rating Application (IACRA) account. The FTN is necessary to schedule an aeronautical knowledge exam (as well as recurring exams). The exam covers topics such as regulations on UAS flight operations and limitations, airspace classification and operating requirements, flight restrictions, and aviation weather sources and effects on UASs.

After passing the test, the pilot submits the FAA Airman Certificate and/or Rating Application form through the IACRA system (9). It usually takes two to three weeks for FAA to review and issue the certificate.

### *Operational Limitations*

Part 107 imposes several limitations on UAS operations, including:

- The UAS must weigh less than 25 kg (55 lb).
- Only flights within visual line-of-sight (VLOS) are allowed. The UAS must remain within VLOS of the remote pilot in command and the person manipulating the flight controls of the UAS. Alternatively, the UAS must remain within VLOS of the visual observer. The remote pilot in command and the person manipulating the flight controls must be able to see the UAS with vision unaided by any device other than corrective lenses.
- The UAS may not fly over people, except if a waiver is granted (see below). The UAS may fly over a person without a waiver if that person is participating directly in the operation, is under a covered structure, or is inside a covered stationary vehicle providing reasonable protection. Flight over people is also allowed if the UAS fits one of four risk categories specified in Part 107 Subpart D that became effective April 21, 2021. These categories cover criteria such as UAS weight, protection against human skin laceration, and level of kinetic energy capable of causing injury upon impact.
- Beginning April 21, 2021, UAS operations at night are permitted if the pilot has completed an initial knowledge test or training after March 1, 2021, and the UAS has anti-collision lighting that is visible from at least 5 km (3 mi) and has a flash rate deemed sufficient to avoid a collision.
- The remote pilot in command must yield the right of way to other aircraft.
- A visual observer (VO) may be used but is not required.
- The UAS maximum ground speed is 161 km/h (100 mph).
- The UAS maximum height is 120 m (400 ft) aboveground level (AGL) or, if higher than 120 m (400 ft) AGL, remain within 120 m (400 ft) of a structure.
- The minimum weather visibility is 5 km (3 mi) from the UAS control station.
- Operations in Class B, C, D and E airspace are allowed with the required air traffic control (ATC) permission. Operations in Class G airspace are allowed without ATC permission.
- A remote pilot in command or VO may not operate more than one UAS at the same time.
- Operations from a moving aircraft are not allowed. Operations from a moving vehicle are not allowed unless the operation is over a sparsely populated area.

These requirements are evolving. For example, in April 2021, FAA updated Part 107 to allow UAS operations at night or over people without the need for a waiver under certain conditions. The rulemaking process started officially in February 2019 through a notice of proposed rulemaking and ended with the publication of the new rules in January 2021 (10, 11). Similarly, in March 2021, FAA established requirements for the remote identification of unmanned aircraft, including three options to comply with those requirements (12, 13). Unmanned aircraft produced beginning September 16, 2022, must comply with this rule, and unmanned aircraft produced

before that date must comply with the rule by September 16, 2023. Several federal regulations were affected by this new rule, including Part 107.

### *Part 107 Waivers*

Certain UAS operations require a waiver of operations from FAA. Examples for which an FAA Certificate of Waiver is required under Part 107 include (14):

- Operation from a moving vehicle or aircraft (14 CFR 107.25).
- Nighttime operation (14 CFR 107.29).
- Visual line of sight aircraft operation (14 CFR 107.31).
- Visual observer (14 CFR 107.33).
- Operation of multiple UASs (14 CFR 107.35).
- Operation over people (14 CFR 107.39).
- Operating limitations (14 CFR 107.51).
- Operation over moving vehicles (14 CFR 107.145).

The FAA DroneZone system provides guidance for the application process. As of this writing, FAA's commitment is to review requests and issue decisions within 90 days of submission. FAA publishes all approved Part 107 waiver certifications online (15). The waiver application must specify the relevant regulation section(s) for which a waiver is being requested, describe the proposed operation and justification, and identify operational risks and how the risk will be mitigated. A useful reference is FAA Advisory Circular 107-2, which documents operational risks, risk assessments, and risk mitigations (16).

Two waivers under Part 107 that are relevant to this research include flying UASs at night (14 CFR 107.29) and flying UASs with a visibility of less than 5 km (3 mi) (14 CFR 107.51). FAA approved the request for a waiver under 14 CFR 107.29 (nighttime operations) in November 2020 but denied the request for a waiver under 14 CFR 107.51(c) (operating limitations: minimum visibility). The nighttime waiver expired when the new rule for nighttime operations became effective on April 21, 2021.

### **State Requirements**

Title 4, Chapter 423 of the Texas Government Code includes provisions for the operation of UASs in Texas (17). This chapter includes an extensive list of situations where it is lawful to operate UASs. Examples include research and development; management of utility facilities; collection of imagery with the consent of the individual who owns or lawfully occupies the real property captured in the imagery; and law enforcement, including crash scene investigations. The chapter also describes situations where it is illegal to use UASs. Examples include unauthorized surveillance and unauthorized flights over correctional facilities and critical infrastructure such as dams, refineries, and oil or gas drilling sites.

Under the law, political subdivisions (such as counties and municipalities) are allowed to regulate the use of UASs for their own use, for special events, and near facilities owned by the political subdivision. However, they may not adopt other regulations regarding the use of UASs.

### *TxDOT Flight Rules and Authorization Process*

TxDOT's *Unmanned Aircraft System Flight Operations and User's Manual* provides a high-level description of requirements for UAS operations (4). The manual requires the following to be completed prior to using UASs on the TxDOT right-of-way or on TxDOT property:

- Flight plan providing information about the proposed flight, including a map that shows the limits of the UAS operating area, planned maneuvers, turning areas, and proposed take-off and landing sites.
- Project risk assessment.
- liability insurance.

All projects require the submittal of a flight plan. Flights that do not have the risk factors listed in the manual can proceed after submitting the flight plan to TxDOT (18). Flights with any of the risk factors listed in the manual require the submission of a flight preapproval form (19). In addition to the flight authorization process, the manual includes requirements for flight and ground operations. Examples of requirements include requirements for the flight crew, a recommended process for the project risk assessment, general rules for flight planning, required components of the flight plan, requirements for traffic control, safety procedures specific to UAS operations, required steps for an in-flight emergency plan, a downed aircraft recovery plan, and rules for UAS maintenance, logs, and accident reporting.

### *The Texas A&M University System Flight Rules and Authorization Process*

The research team conducted UAS flights at the RELIS campus in College Station. Like TxDOT, the A&M System requires the submission of an application form, copies of UAS pilot certificates, a signed liability release, copies of applicable FAA waiver certificates, and copies of local airspace authorizations (if applicable). For all UASs used in the proposed flight, the application requires a copy of maintenance records, records of previously reportable accidents, the operational emergency plan, pictures of the UASs and the FAA registration number, and evidence of liability insurance (20, 21, 22, 23). Further, the application requests information about the type of UAS flown, manufacturer and model, weights, frequencies used, flight locations, flight dates, flight purpose, agency property asset identification, type of flight authorization, export controls, type of airspace, related research project information, and acknowledgements of compliance with applicable rules, including Texas Government Code Title 4 Chapter 423 (24).

The operational emergency plan must include provisions on procedures in case of emergencies (e.g., interference with commercial aircraft or loss of control or communication with the UAS). Review of the application usually takes about two weeks. The Texas A&M University Environmental Health and Safety Department manages UAS operations within the A&M System property and reviews UAS flight applications. UAS flights conducted as part of a research project administered through the A&M System must be approved by the Environmental Health and Safety Department regardless of flight location.

## UAS FLIGHT PLANNING AND MANAGEMENT

Conducting UAS flight missions involves a great deal of preparation beyond regulatory requirements. Preparation involves equipment preparations, flight planning, onsite flight management, and postflight activities.

### Equipment Preparations

Each UAS and associated electronic equipment, such as battery charging stations, mobile surveying stations, and remote controllers, receive firmware updates from the manufacturer on a regular basis. In some cases, if all electronic components do not have the same firmware version, the UAS might not start. As a result, it is critical to check before each flight mission that the firmware of each component is up to date and compatible with each other.

UAS equipment can receive firmware updates wirelessly or by connecting the equipment to a computer via a universal serial bus (USB) cable. Depending on the UAS equipment, it might also be necessary to download and install software to assist with the firmware updating process. For example, as described in Chapter 5, the research team used DJI™ Mavic 2 Pro™ and Matrice 300 Real-Time Kinematic (RTK)™ UASs. For the Mavic 2 Pro, updating the firmware involved connecting the remote controller to a Wi-Fi network and then connecting the controller to each UAS equipment component, including the UAS, to complete the firmware update. For the Matrice 300 RTK, it was necessary to download a program called DJI Assistant™, connect the aircraft via a USB cable, and then load the latest firmware.

UASs might require system calibrations. Depending on the system, some of the calibrations can be performed quickly in the field. Examples of calibration include:

- **Compass.** If the remote controller is exposed to electromagnetic interference, the remote controller's compass might need to be recalibrated.
- **Vision System.** The vision system is factory calibrated but might need recalibration (e.g., using a visual calibration plate) if the aircraft experiences a collision or if the working temperature has changed significantly.
- **Center of Gravity.** The center of gravity shifts when the aircraft's payloads change. If there is a change of payload, the center of gravity must be recalibrated.

UASs normally use flight batteries that stop charging at the maximum charge level. In addition, to preserve battery life, batteries have a feature that reduces the battery charge automatically after several days. It is critical to check the batteries of all UAS components (including the aircraft, the remote controller, and other battery-operated components) the day before a flight.

### Flight Planning

Most flight authorizations require the submission of a flight plan, which typically includes information about the location, purpose, maximum flight altitude, need for an FAA waiver, airspace class, need for a Notice to Airmen (NOTAM), and date of the flight. The flight plan should also include a map of the area, including nearby towns, roadways, and cultural features to help locate the flight area. As mentioned, TxDOT flight authorizations require a project map that

shows the limits of the UAS operating area, including planned maneuvers, turning areas, and proposed take-off and landing sites.

Airspace restrictions can be checked using a variety of available web resources. For example, FAA provides maps that show the maximum altitude around airports where Part 107 flight operations might be authorized (25). Other websites (e.g., SkyVector) provide complete aeronautical charts, including NOTAMs (26).

UAS vendors provide additional support to guide pilots. For example, DJI UASs use the DJI Geospatial Environment Online (GEO) system, which provides the pilot with current information about the area where the pilot will fly the UAS (27). GEO shows where it is safe to fly, where a flight might raise concerns, and where flights are restricted. Restricted zones include airports, power plants, and correctional facilities. The system also shows temporary flight restrictions around major stadium events, forest fires, and other emergency situations. DJI defines seven GEO zones, as shown in Figure 1 (27):

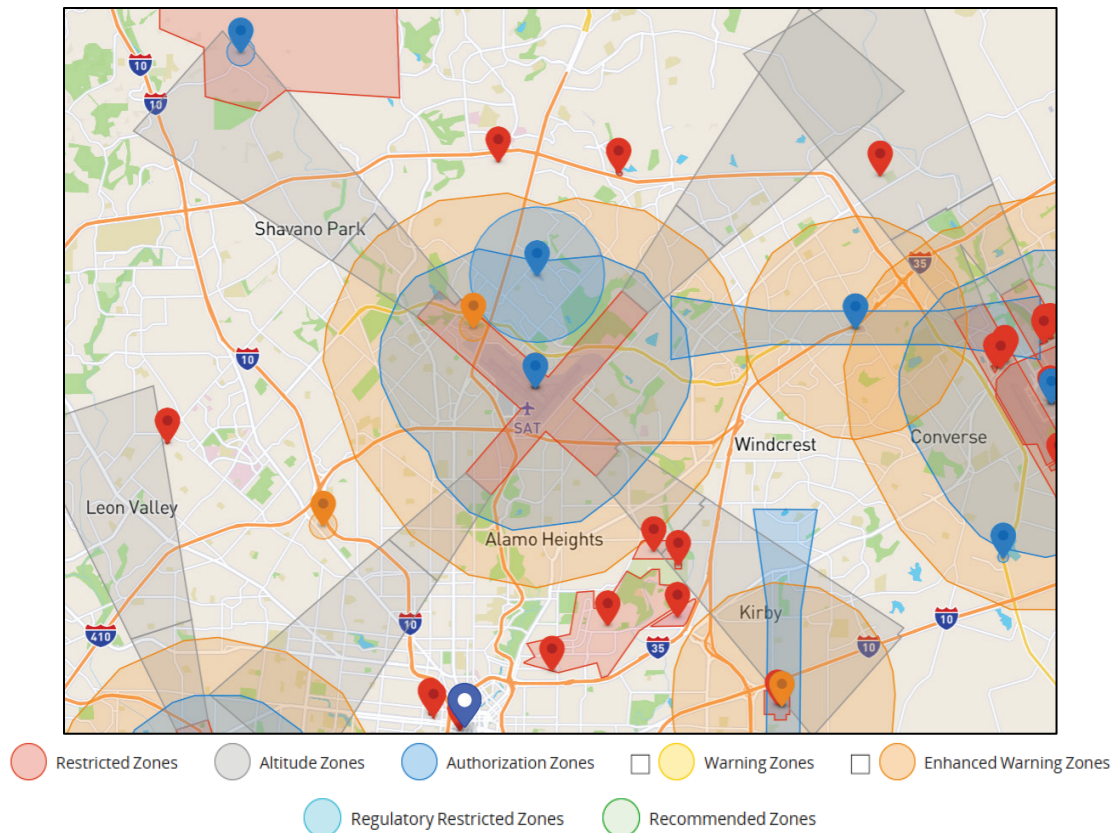
- Restricted Zones. In these zones, the flight does not take place.
- Altitude Zones. In these zones, flight height is limited.
- Authorization Zones. In these zones, the flight is limited by default. Authorization zones may be unlocked by authorized users using a DJI-verified account.
- Warning Zones. In these zones, users are prompted with a warning message. Class E airspace is an example of a warning zone.
- Enhanced Warning Zones. In these zones, the pilot must unlock the zone using the same steps as in an Authorization Zone, but the pilot does not require a verified account or an internet connection at the time of flight.
- Regulatory Restricted Zones. In these zones, flights are prohibited because of local regulations and policies.
- Recommended Flight Zones. These zones do not have special restrictions.

Authorization zones can be unlocked using the self-unlocking process by using the online system or using the remote controller if connected to the internet. Using the online system, unlocking a zone, which remains unlocked for three days, can be scheduled if no internet connection is available to unlock the zone onsite using the remote controller.

Restricted zones, which appear in red in Figure 1, can be unlocked using a custom unlocking process if the pilot has the appropriate flight authorization and submits that information in writing to DJI. However, custom unlocking might disable certain autonomous features, such as waypoint navigation, and might require the pilot to fly the UAS manually.

DJI now enables users to fly UASs without restrictions under certain conditions. For government and public safety agencies, it is now possible to have the UAS altitude and geo-fencing limitations unlocked for an extended period of time and for a larger area (28).





**Figure 1. Sample DJI GEO Zone Map in the Vicinity of the San Antonio Airport.**

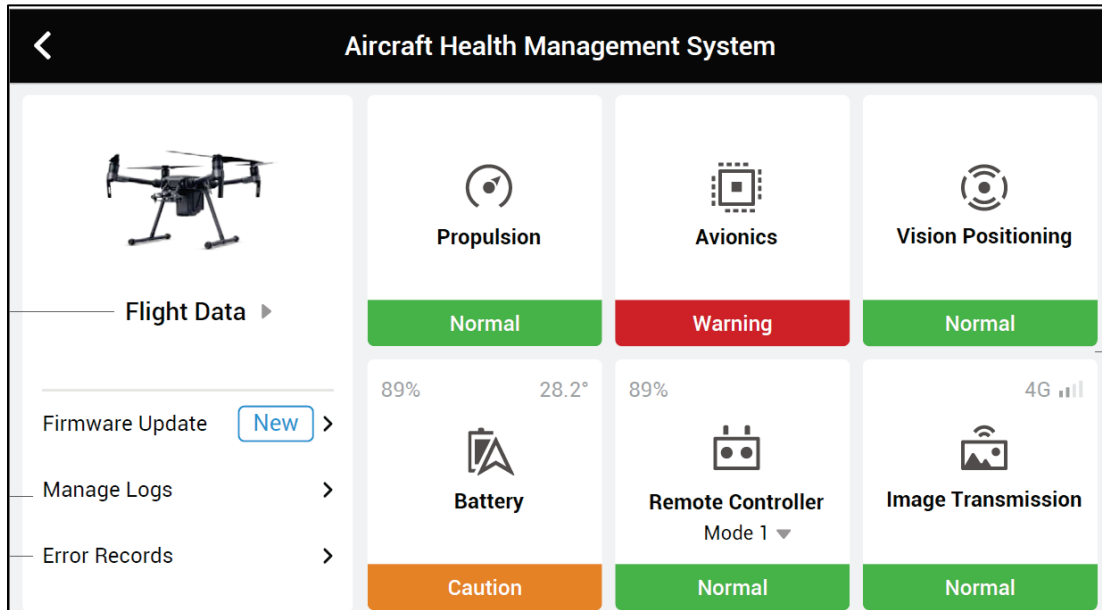
### **Preflight Checklist**

It is critical to check that each UAS component is working properly prior to operating the UAS in the field. Examples of elements to check include the following:

- The batteries of all UAS components, including the aircraft, remote controller, base station, and spare batteries are fully charged.
- All battery connectors face in the correct direction.
- The UAS frame arms are unfolded and locked firmly, the landing gears are mounted firmly, and the batteries are locked firmly.
- All devices have up-to-date firmware.
- The microSD card has been inserted (if used).
- All gimbal components are functioning normally.
- The aircraft motors start and are functioning normally.
- The remote controller is successfully connected to the aircraft.
- Sensors for the vision and infrared sensing systems are clean.
- Anti-collision lighting is properly working and securely attached to the UAS (if used and if flying at night or during civil twilight).

UAS vendors provide additional support to conduct equipment checks. For example, the Matrice 300 RTK includes a tool that checks propulsion, avionics, vision positioning, battery, remote

controller, and image transmission systems, and shows the corresponding status in green (normal operation), yellow (notice), orange (caution), or red (warning) (Figure 2) (29). The tool also alerts the pilot if a firmware update is available or necessary.



**Figure 2. Matrice 300 RTK’s Health Management System (29).**

### Onsite Flight Authorization Procedures

Depending on the area and type of UAS authorization needed, it may be necessary to follow different on-site authorization procedures. For example, at the Texas A&M University RELLIS Campus, the Texas A&M flight authorization required notification to the Easterwood ATC Tower at Easterwood Airport (located about 10 km [6 mi] southeast of the RELLIS Campus) and Texas A&M Police Dispatch 30 minutes before starting the UAS flight and upon conclusion of the flight.

At other locations (e.g., at Phil Hardberger Park in San Antonio), the research team used the Low Altitude Authorization and Notification Capability (LAANC) system (30). The system provides near real-time access to controlled airspace within the federal rules for flying UASs. However, LAANC authorizations only cover daylight operations with a hard ceiling of 120 m (400 ft), even near tall structures, and cannot be used for flying under an FAA-authorized waiver.

Several smartphone apps (e.g., AirMap and Aloft) are FAA-approved UAS service suppliers. These apps enable users to request flight authorizations using LAANC. For example, for AirMap (although the process is similar for apps such as Aloft), after creating an account, the pilot provides information about the UAS (31). The pilot then uses the app to create a new flight plan onsite immediately before takeoff. The app uses the UAS takeoff location and checks for air space restrictions. For example, Figure 3 shows a screenshot of the application requesting LAANC authorization at Phil Hardberger Park. The screenshot shows that due to proximity to the San Antonio airport, flight height is limited to 60 m (200 ft) AGL. The pilot must then answer a series of flight-related questions. The brief provides weather information such as wind,

visibility, temperature, dew point, and air pressure in one-hour intervals. The brief also provides an overview of flight advisories, which might include one or more of the following:

- Temporary flight restrictions.
- Special use airspace.
- Controlled airspace.
- Restricted parks.

After completing the flight plan, the user submits the authorization request, which the app checks against multiple airspace data sources in the FAA UAS Data Exchange, such as facility maps, special use airspace data, airports and airspace classes, temporary flight restrictions, and NOTAMs. If approved, pilots receive an authorization within seconds. Unless the authorization specifies otherwise, pilots do not need to notify airport towers before they fly. Pilots are still required to check available NOTAMs and weather conditions. As of this writing, 735 airports in the United States were participating in the LAANC program (32).

Several apps can be used in the field to review weather information (e.g., Unmanned Aerial Vehicle [UAV] Forecast™, Drone Buddy™, and Drone Start™). The research team used UAV Forecast.

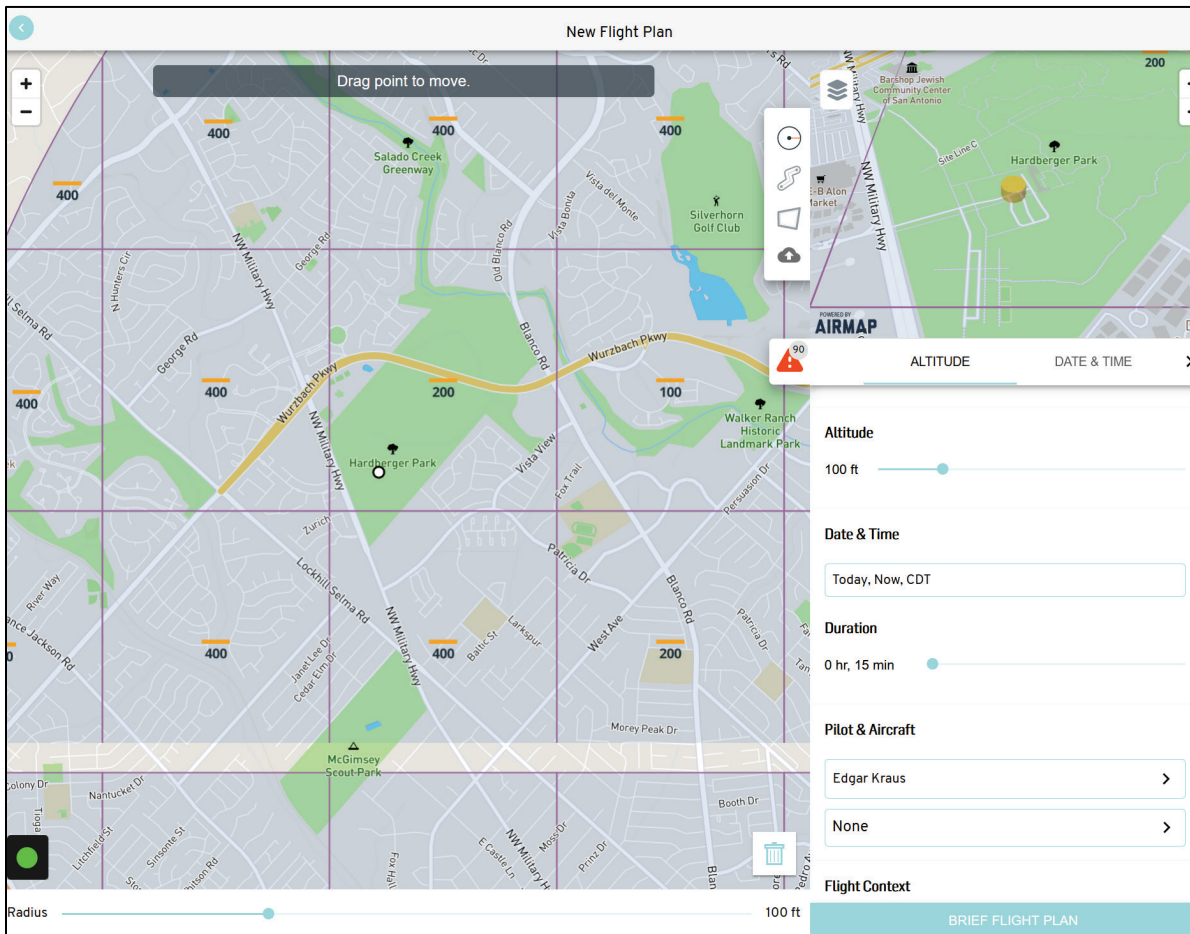


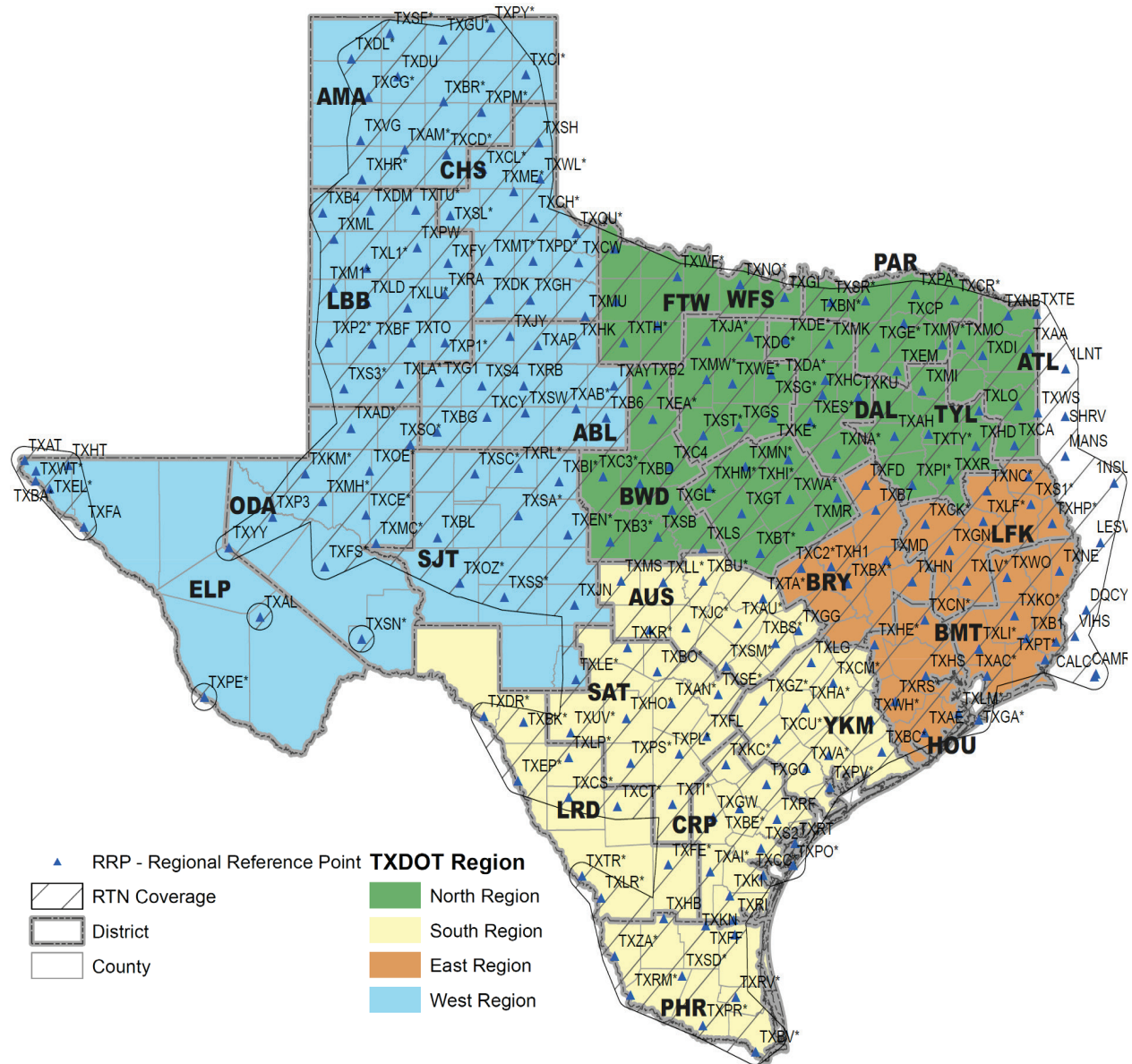
Figure 3. AirMap Authorization Request Interface (31).

## Ground Control

Part of the planning process involves determining whether the UAS will be operated in a standalone mode or if the operation will include ground control.

### *TxDOT Real-Time Network*

The National Spatial Reference System includes a network of continuously operating reference stations (CORSS) (33). TxDOT operates most CORSS in Texas. Figure 4 provides an overview of the TxDOT Regional Reference Points (RRPs) and Real-Time Network (RTN) (34).



**Figure 4. TxDOT RTN as of June 2021 (34).**

The TxDOT *Survey Manual* lists nine different methods to conduct Global Navigation Satellite System (GNSS) surveys, among them RTK surveys and Networked RTK or Virtual Reference Station surveys (35). RTK surveys use a base station and a rover unit and are limited to the maximum communication range between the two. High positional accuracy is attainable up to 10 km (6 mi), after which it drops sharply due to atmospheric errors.

Networked RTK relies on the CORSs, which are connected to a central computer that can be accessed remotely by the survey equipment or rover using a cell phone internet connection. The rover receives a correction from a virtual base station that is determined by the computer from the network of CORS base stations and is never more than 5 km (3 mi) away from the location of the rover. If the rover exceeds this distance, the system automatically redefines the position. The accuracy at the rover is comparable to working within a short distance of an actual base station.

Access to the TxDOT RTN is reserved for TxDOT staff and authorized consultants and researchers. The research team received authorization from TxDOT to access the network and received the corresponding IP address, username, and password.

The RTK function in the Matrice 300 RTK works by connecting the controller to the internet, typically through a cell phone connection. Depending on whether a mobile station is also connected to the controller, the RTK function can work as follows: (a) the UAS is connected to the RTK network through the controller, (b) a mobile station is connected to the RTK network, or (c) a mobile station is placed at a location with a known position. If a mobile station is not used, the UAS uses its own internal RTK processing unit. For flight planning purposes, it is important to determine if both RTK network coverage and cellular network coverage are available for the location where the flight will take place.

The cell phone connection can be set up through a cell phone network modem that connects to the remote controller or the base station using a USB port. The modem usually requires a subscriber identity module (SIM) card along with a data plan provided by a cell phone network provider. Alternatively, the UAS remote controller can be connected wirelessly to a Wi-Fi hotspot provided by a cell phone.

A critical piece of information for the RTN connection is the mount point name of the RRP. The mount point of a CORS RRP is the connection point on the RRP that can exchange data with the rover equipment wirelessly. The mount point provides unique settings for different types of rover equipment. TxDOT uses mount points for equipment using the Radio Technical Commission for Maritime (RTCM) Services standard, which is a format used by many manufacturers (including DJI), and the compact measurement record format, which is specific to Trimble® equipment.

If a smartphone hotspot connection is used to provide network access, the smartphone needs to stay close to the remote controller. In one of the earlier tests the research team conducted, the smartphone owner moved away from the UAS pilot to aid with visual navigation, and the connection between smartphone and remote controller was temporarily lost. The Matrice 300 RTK continued to fly normally, but the location data recorded with the imagery lost the positional accuracy provided by the RTN.

### *Texas A&M University-Corpus Christi (TAMUCC) Ground Control Points*

The research team used survey-grade Septentrio NR3 GNSS receivers. One antenna was used to record static observations while the other antenna was tied to TxDOT's RTN and used as a rover to collect ground control data. The research team assessed accuracy relative to a series of ground control targets used as checkpoints and terrestrial laser scanner (TLS) 3D point cloud data of the crash scenes. The research team set up the static observation receiver to log GNSS observations for postprocessed kinematic (PPK) corrections. At the different test locations, the result was over two hours of static observations for processing base station coordinate data using the National Geodetic Survey Online Positioning User Service (36).

At each test location, the research team laid out several aerial control targets in a grid pattern on the perimeter of the simulated crash scene. The team collected additional topo points for accuracy assessment. At each aerial control target, the research team gathered 5–10 seconds of observations at a frequency of 1 Hz and calculated the average of those observations to obtain the X-Y-Z coordinates for that target.

The TAMUCC ground control points (GCPs) were in the following coordinate system:

- Datum: North American Datum of 1983 (NAD83) 2011 realization. This realization or adjustment is frequently called NAD83(2011).
- Horizontal coordinates: State Plane Texas Central (meters).
- Vertical coordinates: Geoid height above Geodetic Reference System of 1980 (GRS80) ellipsoid: 0 meters.

The research team used ellipsoid heights to ensure a consistent comparison of vertical coordinates to the SfM processing workflows using PPK image geotags, which are in NAD83(2011) ellipsoid heights. Although these tags can be converted to the North American Vertical Datum of 1988 (NAVD 88) using a hybrid geoid model, the research team's standard practice is to convert derived mapping products to NAVD 88 outside of the SfM software environment.

### *TxDOT GCPs*

As described in Chapter 5, the last UAS flights involved a simulated passenger car crash test with nighttime data collection at the TxDPS Tactical Training Facility in Florence, Texas. TxDOT surveyed the location and produced a set of highly accurate horizontal and vertical coordinates that the research team then used as GCPs. For this activity, TxDOT used traditional optical and light detection and ranging (LiDAR) surveying equipment as follows:

- Conducted a reconnaissance of the skid pad area to determine the optimal location of instrument points, where the ground surveying equipment would be located during data collection. TxDOT also identified eight checkpoint locations.
- Marked each instrument point and checkpoint using a fading yellow spray paint. Each mark was 8 cm (3 inches) long and 1.3 cm (0.5 inches) wide.
- Ran a digital level loop through the points, holding the elevation of one of the instrument points as the true "take-off" elevation.

- Using a Trimble SX10™ total station, measured the horizontal coordinates of the instrument points by using a closed traverse.
- Measured checkpoint horizontal coordinates as side shots from the traverse.
- From each instrument point, collected a scanned point cloud and digital imagery covering the simulated crash scene.

The TxDOT instrument point and checkpoint coordinates were in the following coordinate system:

- Datum: NAD83(2011).
- Horizontal coordinates: State Plane Texas Central (U.S. survey ft).
- Vertical coordinates: NAVD 88 GEOID12B.

### *Google Elevation Data*

For flights that did not have GCPs, the research team used Google elevation data to enhance standalone coordinates obtained with the UASs. Typically, the process involved selecting point locations that could be used for georeferencing and obtaining the corresponding horizontal and vertical coordinates. The research team used Aerial Metrics Maptools as follows (37):

- Imported the images of the desired scene into Aerial Metrics Maptools. The corresponding geotags enabled the software to load a map showing the scene location.
- Selected three points that could be easily seen in the processed model.
- Saved a comma delimited .csv file containing the latitude, longitude, and altitude of each point.
- Imported the file into Pix4Dmapper as GCPs.

The Google Elevation Data coordinates were in the following coordinate system:

- Datum: World Geodetic System 1984 (WGS84).
- Horizontal coordinates: WGS84.
- Vertical coordinates: Mean Sea Level (MSL) Earth Geodetic Model 96 (EGM96) Geoid.

### **Flight Design**

A variety of flight designs may be possible depending on the purpose and size of the UAS data collection activity. A flight design includes the trajectory the UAS will follow, endlap and sidelap requirements, and whether the operation of the aircraft will be autonomous or manual. Examples of potential flight designs recommended by Pix4D include (38):

- General case (Figure 5a): At least 75 percent endlap and at least 60 percent sidelap. It is recommended to take images using a regular grid pattern.
- Forest and dense vegetation (Figure 5a): Same grid pattern as for the general case but increase the overlap to at least 85 percent endlap. Flying higher can also improve the results.
- Flat terrain with homogeneous visual content (e.g., agriculture fields and asphalt roadways) (Figure 5a): Same grid image acquisition plan as for the general case but

increase the overlap to at least 85 percent endlap and at least 70 percent sidelap. In such cases, flying higher can also improve the results.

- Sand and snow: Use at least 85 percent endlap and set the exposure settings to obtain as much contrast in each image as possible. Water surfaces are difficult to reconstruct.
- Corridor mapping (e.g., roads or railways) (Figure 5b): Dual track flight path with a forward and return track, using at least 85 percent endlap and at least 60 percent sidelap. If a dual-track image acquisition plan is not possible, a single-track image acquisition plan may be adequate if the overlap is sufficiently high (at least 85 percent endlap).
- Building reconstruction (Figure 5c): Fly around the building at different heights. Orient the pitch of the camera to ensure most of the image frame is filled with the object being captured. At each height, modify the oblique angle (with respect to the horizon) in such a way that the oblique angle decreases as height decreases.
- City reconstruction with visible facades (Figure 5d): Grid flight pattern with perpendicular flight lines (also known as a double grid). This pattern helps to improve reconstruction of building edges and facades from all directions. The recommended overlap is the same as for the general case. For the facades to be visible, take oblique images with an oblique angle between 55 degrees and 80 degrees with respect to the horizon.
- Large vertical object reconstruction (Figure 5e): Fly close to the structure in a circular pattern at different heights. At each height, take pictures of the structure using at least 90 percent endlap and 60 percent overlap between images taken at different heights. Ensure all objects are in focus, including background objects.
- Multiple flights: Make sure each individual flight plan captures images with enough overlap and that there is sufficient overlap between the two flight plans. As much as possible, the different plans should be acquired under the same ambient conditions (e.g., sun direction, weather conditions, and building patterns).



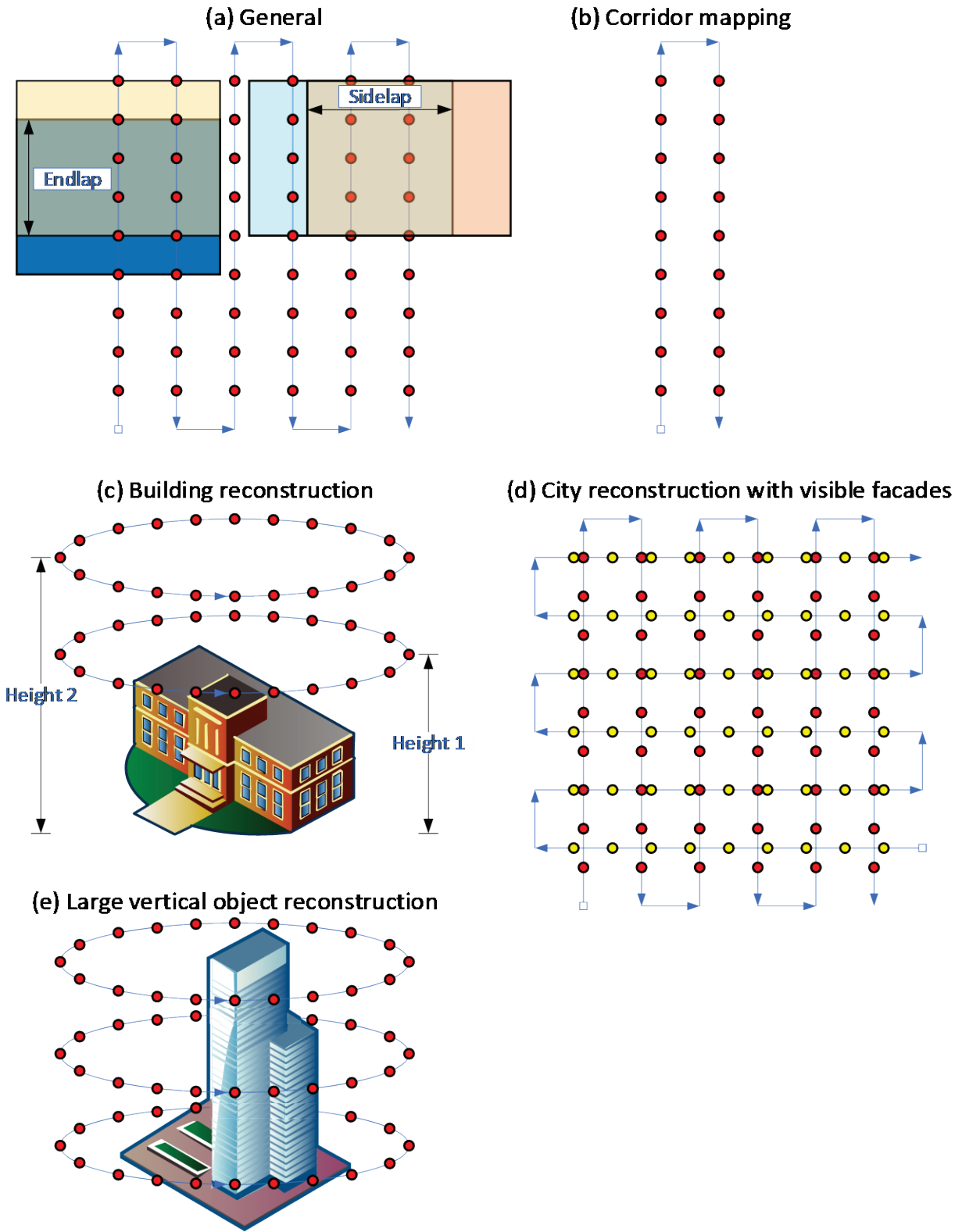
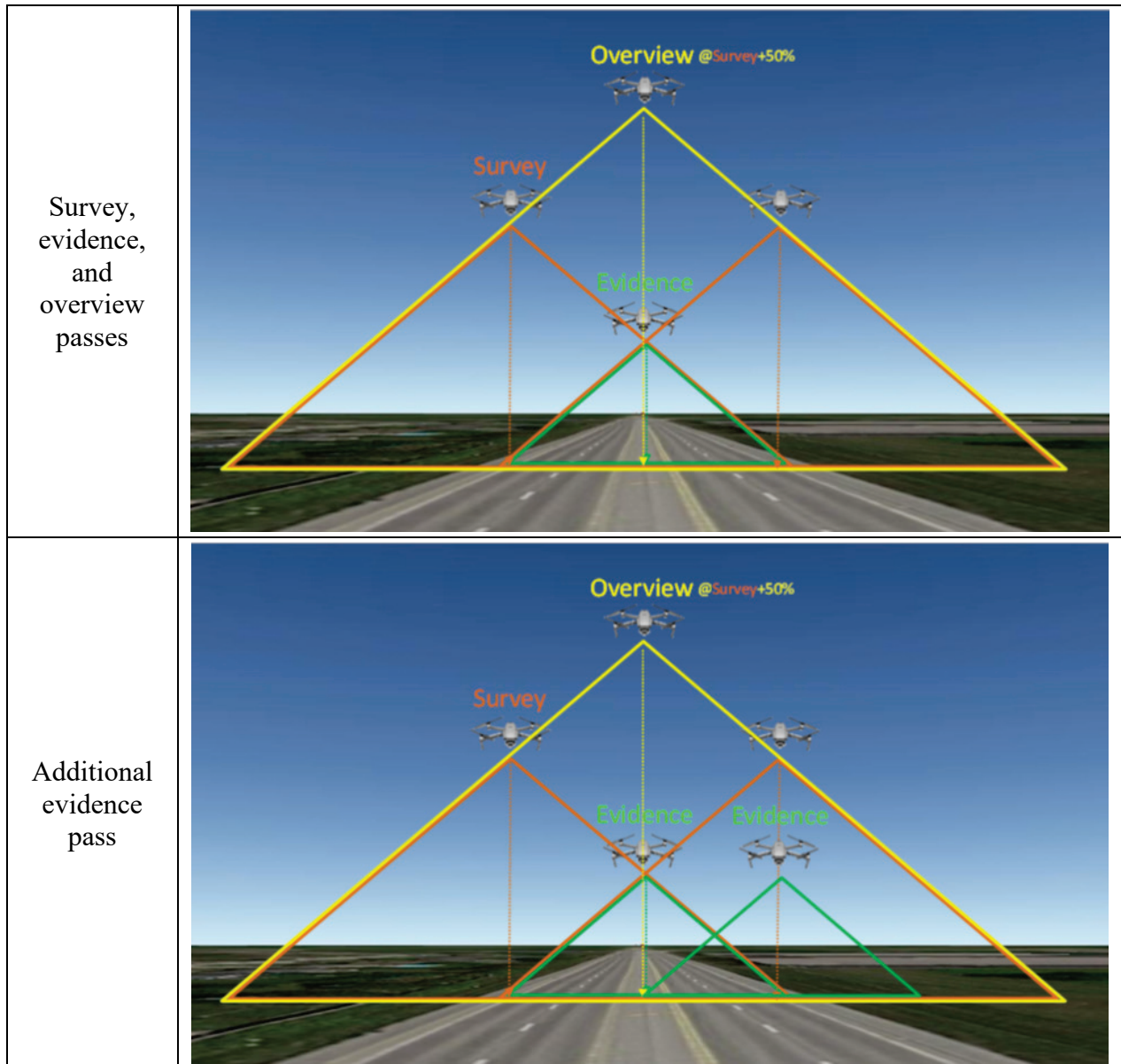


Figure 5. UAS Flight Patterns—Adapted from (38).

For crash reconstructions, the Northwestern University Center for Public Safety (NUCPS) frequently uses a diamond shape flight configuration that involves operating the UAS manually to collect several passes of nadir and oblique imagery, as follows:

- Place the UAS directly above the line that separates the outer travel lane from the shoulder and then ascend the aircraft until the edge line on the other side of the road comes into view (Figure 6a). The height of the aircraft at this point is the *survey height*.
- Traverse the UAS along the edge line and take nadir pictures using an 80 percent endlap (i.e., move the field visible in the remote controller by 20 percent before taking a new picture). This pass is called a *survey (or grid) pass*.
- Move the UAS to the opposite side of the roadway, vertically above the other edge line, and complete a second *survey pass* using an 80 percent endlap.
- Move the UAS to the center of the road and increase the height to 150 percent of the survey height. Collect imagery as for the other passes. This pass is called an *overview pass*.
- If there is visible evidence (e.g., tire marks, scrapes, and gouges), keep the UAS in the center of the road and reduce the height of the UAS to 50 percent of the survey height recorded previously.
- Collect imagery for the extent of the area of interest using an 80 percent endlap. This pass is called an *evidence pass*. Additional passes may be necessary if evidence is identified within the scene or off the roadway (Figure 6b).
- Collect oblique imagery of the crashed vehicles and other objects that should appear as 3D objects in the model at about 50 percent of the survey height. The oblique angle should be at least 45 degrees from a horizontal plane such that the horizon is not viewable and the background is kept within the survey area. A rule of thumb is to capture at least 12 images of the objects of interest while the UAS follows a circular pattern. If additional vehicle detail is needed (e.g., for crush analysis), conduct a second circular oblique pass at a slightly increased height, for example at 75 percent of the survey height.

This manual data collection protocol involves stopping the aircraft at every location along each path where the pilot takes pictures. For nighttime operations, NUCPS recommends gathering two images at each location where the UAS stops.



**Figure 6. Survey, Evidence, and Overview Passes Used by NUCPS.**

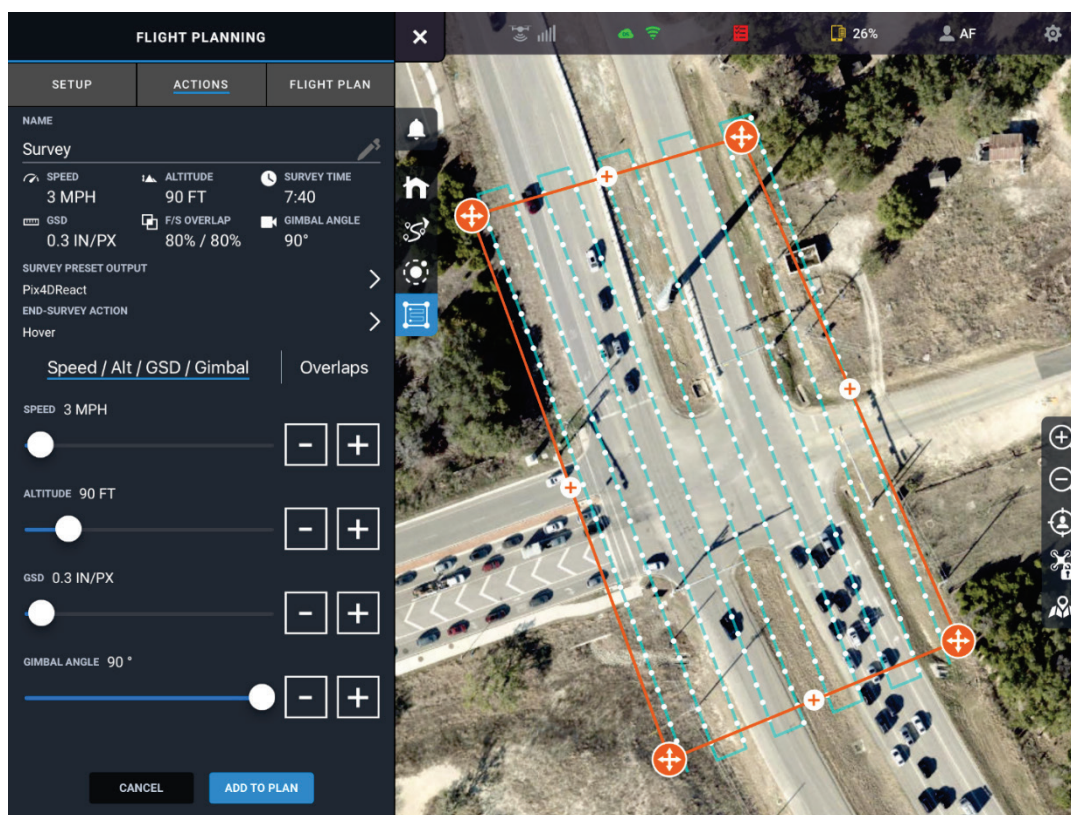
*Texas Department of Public Safety*

For crash reconstructions, TxDPS uses a variety of flight patterns depending on the purpose of the crash reconstruction. For example, if only a 2D depiction of the crash area is of interest, pilots use a grid pattern similar to the general case in Figure 5a. If the crash reconstruction involves a 3D point cloud and a 3D model of the crash scene, pilots use a pattern similar to that shown in Figure 5d, along with gathering oblique imagery at a single height using a pattern similar to that shown in Figure 5c.

TxDPS uses DroneSense™ to manage its fleet of UASs (39). TxDPS uses DroneSense to plan missions, track the maintenance of its UAS fleet, and store relevant information such as pilot

information, flight logs, and NOTAMs. TxDPS also uses the platform for training activities, video streaming, and tracking UASs during flight operations.

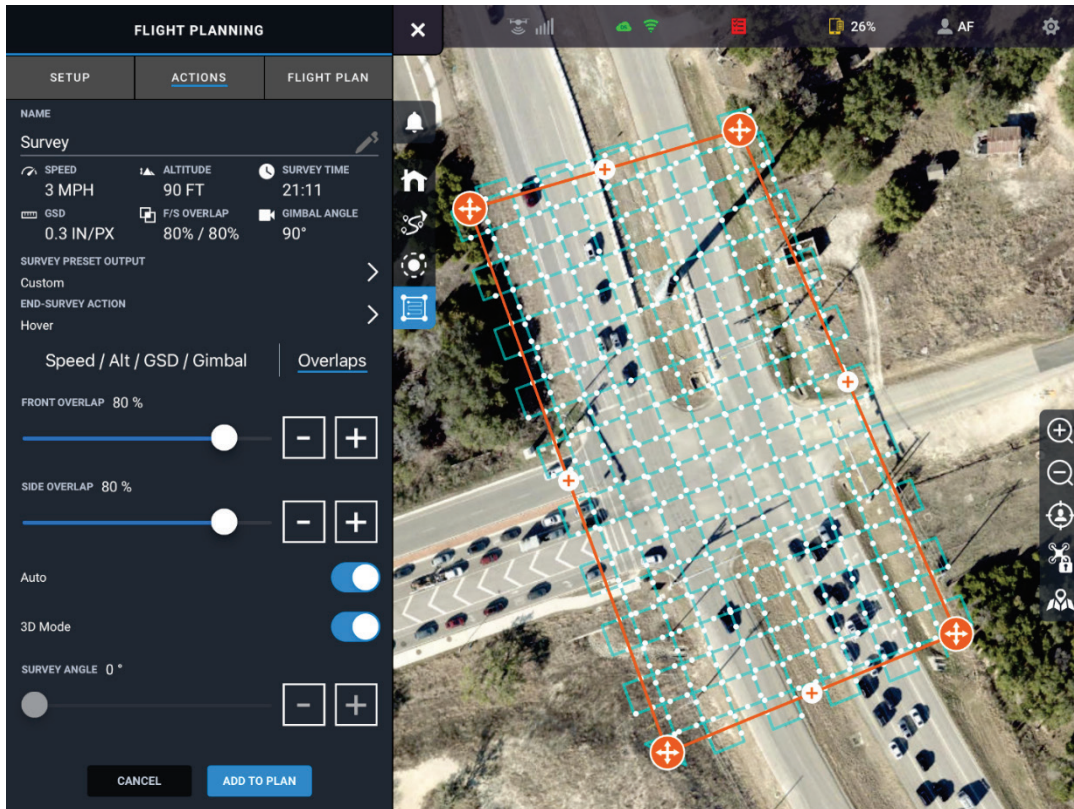
Most UAS flights at TxDPS are completed using an autonomous flight protocol that enables pilots to take pictures while the aircraft is moving at a low speed, typically around 5 km/h (3 mph). The pilot identifies the flight boundary area, selects endlap and sidelap (typically 80 percent), and specifies parameters such as flight height and ground sample distance (GSD). In areas that require a high-altitude flight because of obstructions such as tall trees or power poles, the pilot also flies at a lower altitude a second time to focus on a much smaller area of the crash scene. If needed, the pilot also collects oblique imagery using a manual flight protocol. As an example, Figure 7 shows a flight plan that uses a general grid pattern when the only data collection outcome is a 2D orthomosaic. Figure 8 shows a flight plan where the desired outcome is a 3D model.



**Figure 7. UAS Flight Plan for a 2D Orthomosaic Production.**

TxDPS uses the autonomous flight protocol with UASs in motion for daylight flights. For nighttime data collection, an autonomous flight protocol is normally not possible because most if not all images are blurry. For nighttime data collection, TxDPS normally uses a manual flight protocol that involves stopping the aircraft at each location and taking at least two pictures. To minimize the risk of blurriness, the pilot might use a bracketing technique that involves capturing a sequence of pictures with different camera settings and returning the UAS to the ground to decide on the most favorable settings before conducting the actual data collection flight. TxDPS has had positive experiences illuminating nighttime crash scenes using the onboard light-emitting diode (LED) lights. However, in most cases TxDPS illuminates crash scenes with other

available light sources, such as vehicle headlights and other lights equipped on TxDPS vehicles. Nighttime data collection works reasonably well up to an altitude of about 15 m (50 ft).



**Figure 8. UAS Flight Plan for a 3D Model.**

## Postflight Checklist

Activities conducted during a flight should be entered into a logbook for the UAS. What to include in the log depends on several factors, but in general, the information should include items such as flight date and location, flight duration, batteries used, environmental conditions, unexpected behavior of the UAS, and UAS crashes. If a crash results in serious injury to a person or any loss of consciousness, or if the crash results in property damage costing more than \$500, the crash must be reported to the FAA (e.g., using the FAA DroneZone webpage [8]).

## STRUCTURE-FROM-MOTION PHOTOGRAMMETRY

UAS photogrammetric surveys are processed using SfM/multi-view stereo (MVS) techniques. Traditional photogrammetry requires precisely calibrated metric cameras. Metric cameras are those with known and stable interior orientation (IO) (i.e., known focal length and internal dimensions), typically with the help of fiducial marks and calibration. However, metric cameras are expensive and not conducive for widespread use of UASs for mapping applications. SfM uses information from multiple overlapping images to extract 3D object information and negates the need for metric cameras that must be precisely calibrated in a laboratory setting through automated self-calibration. SfM derives 3D structures from 2D image sequences through movement of the camera, thereby providing different perspective views of the scene. By using

the UAS as the moving platform, SfM can be implemented with an onboard camera by acquiring images with sufficient overlap (40, 41, 42).

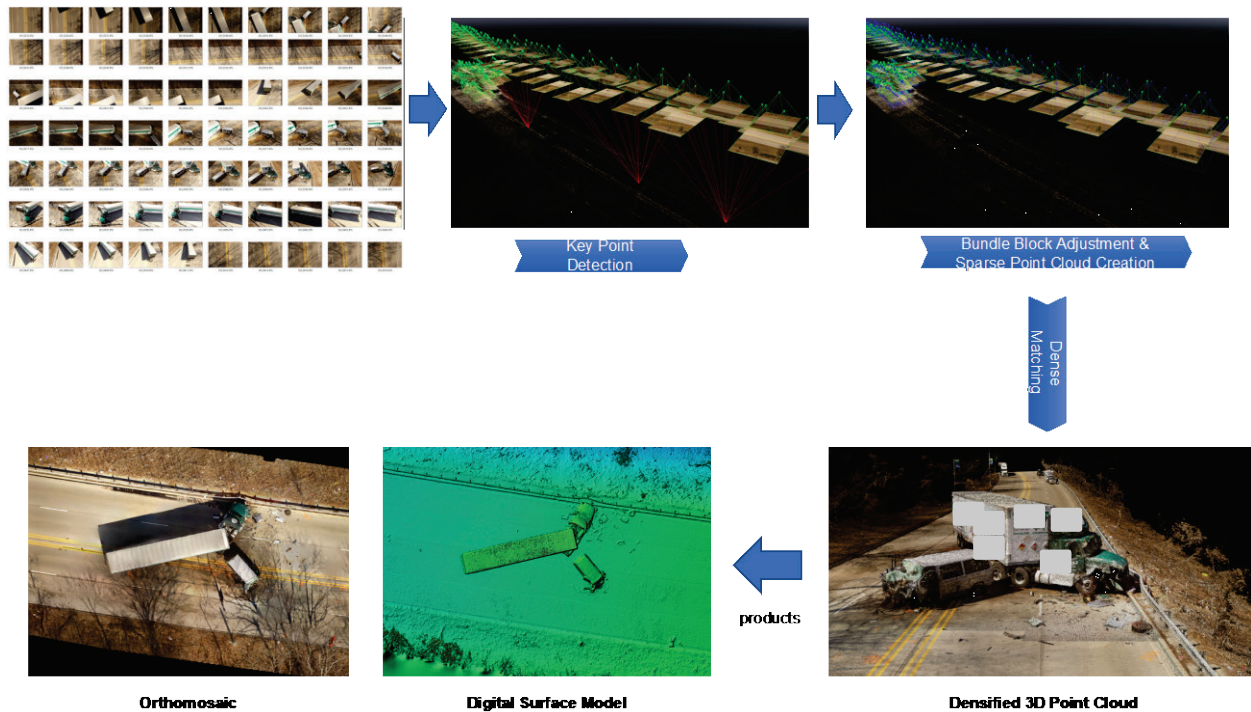
Several commercial and open-source SfM software suites are available for processing UAS imagery to derive mapping products. Two of the most widely used commercial suites at present are Agisoft Metashape and Pix4D™ Pix4Dmapper™ (also commonly known as Pix4D). Alternatively, OpenDroneMap is an open-source toolkit that chains together multiple open-source SfM and MVS packages for processing UAS imagery. Each software offers advantages and disadvantages, and its use depends on end-user comfort level and desired processing workflows or needs.

Although each software package has its own interface, workflows, and internal algorithms, most SfM software packages follow similar processing steps. The typical SfM image processing workflow is as follows (40, 41, 42, 43):

- **Stage 1 (Keypoint Extraction and Matching)**—Image sequences are input into the software and a keypoint detection algorithm, such as the scale invariant feature transform (SIFT), is used to automatically extract features and find keypoint correspondences between overlapping images using a keypoint descriptor. Keypoints are points of interest (e.g., features of high-contrast, interesting texture) on the UAS images that can be easily recognized by the SfM software’s automated keypoint extraction and correspondence algorithms. SIFT is a well-known computer vision algorithm that allows for feature detection regardless of scale, camera rotations, camera perspectives, and changes in illumination (44).
- **Stage 2 (Bundle Adjustment and Sparse Point Cloud Creation)**— A least squares (LS) iterative bundle adjustment (BA) is performed to minimize the errors in the keypoint correspondences by automatically solving for camera IO parameters and performing aerial triangulation (AT) to resolve (i.e., calculate) the relative position and angular orientation parameters of the camera at the time of image acquisition. Based on this reconstruction, the matching points are verified and their 3D coordinates simultaneously calculated to generate a sparse point cloud. Without any other spatial information, the coordinate system is arbitrary in translation and rotation and has inaccurate scale.
  - **Sub Step (Point Cloud Georeferencing)**—To further constrain the problem and develop a georectified point cloud, camera geolocations from an onboard GNSS receiver and GCPs (if available) are introduced to constrain the solution. This process resolves the exterior orientation (EO) parameters of the camera and the coordinates of the sparse point cloud with respect to a real-world coordinate system. The solution can rely solely on the direct georeferencing provided by the onboard GNSS receiver, or GCPs can be applied to optimize the solution. Orientation information provided by an onboard inertial measurement unit (IMU) can also be used by the SfM software to weigh the solution and potentially aid it, but in general, this information is not necessary because orientation is solved directly via BA in Stage 2.
- **Stage 3 (3D Point Cloud Densification)**—Finally, the IO and EO parameters for each image are used as input into an MVS algorithm that attempts to densify the point cloud by projecting every pixel at the full image scale or projecting pixels at a reduced image scale. Image scale refers to the size of the image at which additional 3D points are

generated. For example, half-image scale densification uses images that are half the size of the original image size.

The basic output of the UAS-SfM image processing workflow is a densified set of X-Y-Z coordinates of the imaged scene. This set, called a point cloud, is typically colored by the red, green, and blue (RGB) pixel values of the digital camera. UAS-SfM point clouds can have high point density (easily exceeding 1000 points/m<sup>2</sup>) due to the high camera resolutions and typical low altitudes at which data are collected. The 3D point cloud can then be used to generate a digital surface model (DSM) of the terrain, which can then be used to orthorectify the images and produce an orthomosaic image or a 3D textured mesh. Output for these derivative mapping products is commonly performed by commercial SfM software. Figure 9 summarizes the UAS-SfM processing workflow for a real crash scene processed with Pix4D.



**Figure 9. UAS-SfM Workflow to Process UAS Image Sequences into Mapping Products.**

### Sparse Point Cloud Generation

During the BA stage of the SfM processing workflow (Figure 9), the initial geometry of the scene (i.e., the sparse point cloud), internal camera parameters, and external camera position and orientations are established and finalized. The accuracy of all subsequent generated data products is determined during this stage. If GCPs are used during the survey, these can be integrated to resolve for the internal and external camera parameters and refine the sparse point cloud. In addition to georeferencing the SfM point clouds, GCPs can improve the accuracy of the model during the BA by performing a nonlinear optimization. In this step, the camera IO and EO parameters and the constructed geometry are resolved again (i.e., reoptimized) by minimizing the reprojection error of feature matches in the sparse point cloud after importing the GCPs (45).

The sparse point cloud itself is a collection of 3D tie point coordinates that is based on the automated feature-matching algorithm performed by the SfM software. Most SfM software applications include a method to filter these sparse cloud points to only include points of acceptable quality. Sometimes automated feature-matching algorithms can become confused, typically when acquiring imagery over dynamic environments or low texture. An example of this situation is a UAS survey conducted along a roadway over a river, where water movement in the scene can cause spurious feature matches and result in erroneous sparse point cloud measurements in certain places.

Some software applications filter out noisy features or keypoints automatically with little or no user input. This is the approach that Pix4D uses. The advantage of this method is that users do not need to worry about the internal workings of the SfM software, enabling a more efficient, easier processing workflow. The disadvantage is having to depend on the capability of the software to automatically and accurately filter out noisy point features, which can vary for different environments. Alternatively, some software allows the user to filter out the points based on a set of accuracy metrics. This feature enables the user to tune the feature matching and removal of spurious points based on the terrain being mapped. Agisoft Metashape uses this approach. Whichever software suite is used for SfM processing, it is necessary to follow proper software guidelines and select proper processing settings.

### **Dense Point Cloud Generation**

Generating a dense point cloud involves using an MVS photogrammetric technique in which the camera IO and EO parameters, resolved from the previous step, are used to generate a point cloud that is much denser than the previously created sparse point cloud (46). Densification works by matching corresponding points in stereo image pairs, expanding on point measurements between the sparse point cloud by enforcing epipolar geometry (i.e., stereo vision geometry) constraints obtained from the BA solution, and then filtering the outliers (47, 48, 49). Performance of MVS algorithms and corresponding results and accuracies can vary by commercial SfM software. Densification includes generating a depth map for the pixels of the images that contains information about the distance from the camera to the objects. A depth map represents distances or depth information by using intensity values (e.g., 0 to 255) such that objects that are closer to the camera have higher intensity values.

The dense point cloud generated at this step is then used to create subsequent geospatial data products such as DSMs or textured meshes. Because the densification algorithm used depends on the camera interior and exterior parameters estimated during the previous step of sparse point cloud generation, it is important that the sparse point cloud generation be performed well. SfM software exports the dense point cloud to an appropriate file format, such as LASer (LAS) or LAZ (which refers to compressed LAS format), for use in external software for further analysis and product generation. LAS is a commonly used file format for exchanging 3D point cloud data that was originally developed for exchanging airborne LiDAR data. Color information (pixel values) from the images is typically exported with the point coordinates of the dense cloud. Furthermore, many SfM software suites give users the capability to classify dense clouds into different objects, such as ground and building points, and this action may be useful for removing certain features.



## Ground Control Points

GCPs can consist of painted marks, aerial survey targets, or identifiable features in the scene whose horizontal and vertical coordinates have been accurately surveyed, such as by RTK GNSS (Figure 10). GCPs should be as evenly distributed across the survey area as feasible.

Several studies show that the number of GCPs required for a given project depends on the size of area, terrain, GCP distribution, and image network geometry (50, 51, 52). The appropriate number of GCPs also becomes important when processing uncalibrated cameras with unknown or inaccurate camera parameters and when SfM self-calibration might fail due to poor keypoint feature correspondence or other factors.



**Figure 10. Different Types of Targets for Aerial Control.**

GCP targets laid out during the UAS survey can be identified in the SfM software to improve georeferencing accuracy. The process involves assigning image coordinates of each GCP to each control coordinate. Commercial SfM software packages include methods to expedite this process. For example, a method involves generating a sparse cloud to establish the scene and camera geometries, after which the software narrows down the images in which each target should appear. Another method is to allow auto identification of targets after manually locating those targets in a certain number of overlapping images. Some software packages also enable users to select specific targets as GCPs. The software can then auto-identify these targets within the UAS images without any manual identification. In any case, it is always advisable to verify any automated GCP selection because of the risk of misidentification. Error in the identification of the GCP coordinate origin directly propagates in the form of horizontal and vertical errors in the photogrammetric solution.

For crash scene reconstructions, setting up a rigorous ground control network with GCPs may not be feasible due to the labor and time required and is generally not warranted unless demands for high absolute accuracy and/or independent accuracy validation exist. Of primary importance for crash scene reconstruction is relative accuracy (i.e., accuracy within the crash scene, regardless of the coordinate system used for georeferencing). In some cases, relative accuracy of UAS-SfM mapping products can be of survey-grade quality, even when relying solely on an autonomous (i.e., noncorrected) GNSS receiver for image locations, as is the case with most consumer-level UASs. Distance measurements of higher-order accuracy acquired at the scene can be applied within the SfM software to scale and improve the overall relative accuracy. This is often done for UAS crash scene mapping by laying out at least three aerial control targets

(forming an L) and measuring distances between them using a tape rather than laying out a network of GCPs whose coordinates are accurately surveyed using RTK GNSS or other means.

Finally, an increasing number of UASs designed for surveying applications are now being equipped with RTK or PPK GNSS receivers. These receivers can eliminate or greatly reduce the workload required for establishing a control network where high absolute and relative accuracy is still required (53, 54).

### **Measurement Assessment and Reliability**

UAS-SfM photogrammetric measurements are only as reliable as the established control network or direct georeferencing method used for acquiring image geolocations. For example, if the absolute accuracy of the GCP vertical coordinates is  $\pm 5$  cm (2 inches) based on the survey method used, the absolute UAS vertical error cannot be better than  $\pm 5$  cm (2 inches). In general, measurements away from the control network tend to be less reliable. The area of high accuracy is constrained by the boundary of the GCPs. This is a major advantage of using UASs equipped with onboard RTK/PPK capabilities because the differential correction is only constrained by distance from the correction source or local GNSS base station.

A recommended practice for standard UAS surveying applications is to include additional GCPs as independent checkpoints not used in the SfM BA for evaluating the accuracy of SfM-derived 3D point cloud data or other mapping products (e.g., orthomosaics). This method should also be considered a standard practice when relying solely on differentially corrected RTK/PPK GNSS measurements for image geolocations without ground control and when an understanding of the measurement error is important for subsequent analyses. Including GCPs as checkpoints or other independent survey measurements (e.g., field tape measurements between identifiable marks or targets in the scene) enables an independent evaluation of the UAS-SfM measurement error in the scene.

The American Society for Photogrammetry and Remote Sensing (ASPRS) Positional Accuracy Standards for Digital Geospatial Data (55) recommends a minimum of 20 checkpoints to conduct a statistical evaluation of absolute positional errors of point cloud or elevation data derived from photogrammetry or LiDAR. ASPRS also recommends that the survey accuracy of the checkpoints be at least three times more accurate than the data they are evaluating. However, meeting this level of accuracy is not always practical. For example, RTK GNSS is a commonly accepted method for field validation of UAS-SfM accuracy, which may not meet this requirement in the vertical dimension for some UAS-SfM survey scenarios.

In practice, the number of checkpoints needed to evaluate mapping products derived from UAS-SfM surveys depends on the size of the area, degree of heterogeneity of the topography and land cover, and project requirements for accuracy validation. The ASPRS guideline stresses the need to develop a quantitative methodology to characterize and specify the spatial distribution of checkpoints across project extents but also recognizes that, in the absence of such a methodology, the density and distribution of checkpoints must depend on empirical results and simplified area-based methods (55).

For surveying crash scenes, setting up aerial control targets to be used as GCPs for aiding in SfM reconstruction or as independent checkpoints for accuracy evaluation depends heavily on logistical considerations, such as time and effort to install them, feasibility of installation, size and complexity of the scene, and survey capabilities for acquiring accurate coordinates. This is one of the reasons it is important to use a tape to measure distances between identifiable features in the scene.

### Processing Quality Reports

Commercial SfM software packages typically generate reports to assist in evaluating SfM processing results and the quality and accuracy of the generated survey products. Information typically includes feature matching and BA results for sparse point cloud creation, camera calibration results, and dense point cloud information. If GCPs and checkpoints are used in the survey, the processing report includes a table showing the error residuals for each GCP or checkpoint. In most cases, reported GCP error residuals are low because the software uses these points to constrain the location of the processed data. As a result, GCP error residuals do not necessarily provide a fair assessment of positional errors. Checkpoint error residuals provide a better overall assessment of UAS-SfM survey accuracy. Table 1 shows an example of checkpoint error statistics from a Pix4D processing report.

**Table 1. GCP Checkpoint Errors from a Sample Pix4D Quality Report.**

Check Point Name	Accuracy XYZ [m]	Error X [m]	Error Y [m]	Error Z [m]	Projection Error [pixel]	Verified/Marked
GCP_1		0.170	0.326	0.121	0.350	63 / 63
GCP_2		0.111	0.362	0.109	0.319	132 / 132
GCP_3		0.168	0.398	0.116	0.418	36 / 36
GCP_4		0.040	0.296	0.105	0.298	110 / 110
GCP_6		-0.007	0.352	0.118	0.371	88 / 88
GCP_7		-0.085	0.255	0.106	0.324	99 / 99
GCP_8		-0.175	0.255	0.103	0.396	44 / 44
GCP_9		-0.122	0.314	0.123	0.310	96 / 96
<b>Mean [m]</b>		0.012371	0.319693	0.112711		
<b>Sigma [m]</b>		0.123851	0.047361	0.007277		
<b>RMS Error [m]</b>		0.124468	0.323182	0.112946		

Other important rubrics to consider include the results of the camera calibration between initial and optimized parameter settings and reprojection errors. These metrics can be used to identify issues in the SfM reconstruction result when no checkpoints or other sources of independent accuracy assessment are available or if visual inspection suggests less than satisfactory results, such as a noticeable warping of the point cloud. Understanding the details and metrics included in a software’s processing report is an important part of being able to produce quality survey products with UAS-SfM photogrammetry.

### UAS-SfM Accuracy

Multiple factors can influence the accuracy of UAS-SfM data. Factors mentioned in the literature include accuracy of camera and GCP locations, geometry and spatial distribution of GCPs and cameras, image resolution, image noise or blur, lighting condition, shadow effect, scene

complexities, standoff distances, image-matching performance, moving objects in the scene, poor image overlap, inadequate modeling of lens distortion, and flight conditions (42, 56, 57).

Scene texture also plays a role on SfM reconstruction accuracy. The quality and uniqueness of detected keypoints in an image and on an object is subject to scene texture as represented by the image. Image texture describes the spatial arrangement of color or intensities in an image or selected region of an image. The lack of texture within a terrain scene, as represented by an image, has been shown to have one of the largest impacts on the accuracy of UAS-SfM point clouds (49, 58). Understanding this relationship is complex. Suboptimal environmental conditions, such as low ambient lighting or fog, can reduce scene texture significantly. Similarly, certain pavement types, such as dark asphalt, may be more homogeneous in appearance—lacking distinct or identifiable texture compared to other types—and can potentially result in reduced feature correspondence (i.e., matching of distinct keypoints shared between overlapping images) in certain areas. Although not practical for TIM or crash scene mapping where flights are often in response to unforeseen incidents, a common recommendation is to plan UAS surveys during midday times to maximize lighting potential and reduce shadows.

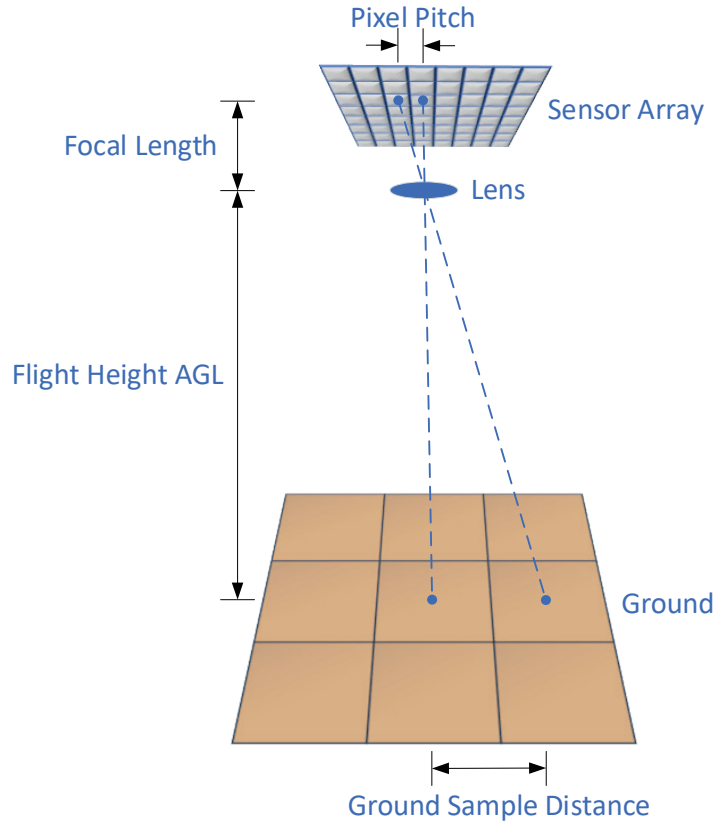
Handling of scene texture also depends on the software’s internal algorithms and the image quality stemming from camera specifications and settings. For the same UAS image set, different SfM software applications might produce differences in point cloud characteristics and geospatial fidelity due to the inherent differences in the automated feature-matching and correspondence algorithms (59).

Relative accuracy depends on the quality of the reconstruction of the UAS-SfM project, which depends highly on the amount of overlap between images, the visual content of the images, and other parameters as described above. Relative accuracy can vary spatially. A measure of spatial resolution of a sensor is GSD (60). As shown in Figure 11, GSD is the projected pixel pitch (or distance from the center of a pixel to the center of the next pixel) on the ground and can be estimated as follows:

$$GSD = \frac{p \times H}{f} \tag{1}$$

where:

$p$  = pixel pitch or distance from the center of a pixel to the center of the next pixel ( $\mu\text{m}$ ),  
 $H$  = flight height AGL (m); and  
 $f$  = focal length of the respective camera (mm).



**Figure 11. Relationship between GSD, Focal Length, Pixel Pitch, and Flight Height.**

During flight design, mission planning software enables users to specify the specific camera model and focal length. Alternatively, the software might detect these parameters automatically. The software then allows the user to adjust the nominal flight height AGL to achieve a desired GSD for a given camera model. Maintaining a constant flight height above the ground or object helps to ensure the same level of spatial detail or resolution for the images. Changes in relief and camera perspective alter the GSD for a set flight height. If the camera pointing direction is not at its nadir, the GSD must be corrected by the factor  $\cos^{-1} \theta$ , where  $\theta$  is the angle between the ground and the sensor line-of-sight (61).

According to Pix4D, one can expect an error of one to three times the GSD value for the relative position of a point in a project that is correctly scaled and reconstructed (62). This error is not global and can vary. Some points are more accurate than others based on the number of images on which they are visible (overlap), how close they are to a GCP (if used), and what the GSD is in this area. For sub-centimeter GSD projects, it is hard to reach the ideal error conditions because problems with perspective, vibrations of the camera, and blur effect are magnified.

Absolute accuracy increases significantly when using GCPs or an RTK/PPK-enabled GNSS receiver onboard the UAS. When using ground control, accuracy depends on the accuracy of the survey method used to measure the GCP coordinates, number of GCPs, and their distribution in the scene. According to Pix4D, the expected accuracy of a correctly reconstructed project is one to two times the GSD of the original images horizontally (X-Y coordinates) and one to three times the GSD vertically (Z coordinate) (62). For example, a project with a GSD of 5 cm

(2 inches) has an expected horizontal accuracy of 5–10 cm (2–4 inches) and a vertical accuracy of 5–15 cm (2–6 inches). In theory, this error can be reached at any scale. However, for sub-centimeter GSD projects, which might be the case for low-altitude crash scene flights, it is hard to achieve the ideal conditions due to the same problems mentioned above for relative accuracy. It is important to emphasize that the absolute accuracy of the results cannot exceed the accuracy of the GCP coordinates or GNSS method used for image geolocation.

GCPs not only improve absolute positional accuracy, but they can also improve relative positional accuracy of the 3D reconstruction, especially in areas with lower overlap or with difficult image content (41, 62). For example, as opposed to doing a standard rigid or scaled 3D transformation, Pix4D allows GCPs to be used within the BA process to reoptimize the sparse cloud solution for IO and EO parameters.

Numerous studies have shown that UAS-SfM implemented with consumer-grade digital cameras can be a reliable, repeatable method to generate accurate survey products at a low cost (40, 41, 60, 63, 64, 65). For example, studies have reported UAS-SfM point cloud accuracies for topographic surveying comparable to TLS (i.e., survey-grade quality) with proper use of ground control and a well-designed image acquisition plan (40, 63). For a crash scene study, key features in a crash scene mapped from UAS-SfM imagery processed with Pix4D had a root mean square error (RMSE) of 3.7 cm (1.5 inches) with respect to field tape measurements (64). Another case study involved comparing UAS-SfM and FARO® TLS data for a crash scene by conducting flights at five different altitudes and four different flight patterns for multiple platforms (65). The UAS-SfM data across all flights and platforms had a mean RMSE of 33 mm (1.3 inches) compared to 2.6 mm (0.1 inches) for the FARO scanner point cloud. RMSE values decreased at lower flight heights, and the most accurate results were associated with a UAS equipped with a 20-megapixel (MP) digital camera (compared to other, lower resolution cameras tested). A 100 m (328 ft) flight height AGL yielded the most precision and accuracy across platforms and flight patterns. Mean distances between point locations in the SfM point clouds and the TLS point cloud were less than 10 mm (0.4 inches) for some flights. The study conclusion was that UAS-SfM could provide crash scene data of sufficient quality and detail for investigative purposes.

## **UAS-BASED CRASH INVESTIGATIONS**

Millions of car crashes, most of which are minor, happen throughout the country every year. Police conduct extensive investigations of over 50,000 serious crashes in the United States annually. The *Manual on Classification of Motor Vehicle Traffic Crashes* defines an injury crash as a road vehicle crash that results in one or more injuries, and a fatal crash as an injury crash that results in one or more fatal injuries (66). Before the COVID-19 pandemic, the United States was experiencing 34,000 fatal motor vehicle crashes per year, resulting in 37,000 fatalities (67). In Texas, the total was 3,300 fatal crashes (or almost 10 percent of U.S. fatal crashes) resulting in more than 3,600 fatalities (67, 68). Each of these crashes (and many more when injuries are severe and the outcome is unknown at the time of incident) result in a police investigation to determine cause, fault, and potential criminality. The quality and extent of the investigation vary by agency, resource availability, and specific incident circumstances. Chapter 3 provides a more detailed description of spatial and temporal trends in the occurrence of crashes on Texas highways, with a particular focus on fatal crashes.

Crash investigations can take one to six hours or even longer depending on scene size, complexity, equipment used, and investigation quality. Roadways are typically closed to public traffic throughout the investigation both for evidence preservation and for officer safety. The result is delays on the affected roadways as well as higher traffic volumes on alternate routes.

Extended road closures can also result in secondary incidents, such as secondary crashes, engine stalls, overheating, and running out of fuel. Particularly in urban areas and major highway systems, secondary incidents can affect thousands of vehicles and result in serious congestion issues over multiple corridors. It is estimated that 20 percent of all incidents are secondary incidents, and the likelihood of a secondary crash increases by 2.8 percent for each additional minute of clearance of the primary incident (69, 70). Secondary incidents must be handled by the same agency responding to the primary incident and thus consume additional resources that could be applied to other agency activities. Reducing investigation times and opening roads sooner deliver benefits to public safety and reduce agency expenditures on activities related to secondary incidents.

In 2015, crash investigation instructors from NUCPS, who were also active members of the Major Crash Assistance Team (MCAT) in Lake County, Illinois, launched an initiative to assess the feasibility of using UASs and photogrammetry for crash scene data collection and crash reconstruction efforts.

In 2016, after an initial research and development period, MCAT deployed UASs to all MCAT major crash scenes in parallel with preexisting mapping techniques based on traditional optical-based surveying equipment (i.e., total stations). MCAT used UASs to determine vehicle speed, identify and locate evidence, and measure relevant roadway characteristics. This strategy enabled the team to assess how well the technique would work across a wide variety of crash scenes and operating conditions, including rural, suburban, and urban crashes, in both daylight and nighttime conditions, and in weather conditions such as high winds, cold temperatures, and precipitation.

MCAT used both data collection approaches on 40 actual crash scenes for a full year. For these investigations, a comparison between UAS-generated data and data from total stations revealed that the accuracy of the UAS data was at least equal to that collected with total stations. MCAT did not observe significant measurement or plotting discrepancies between the UAS and total station collection methods. However, MCAT did notice that using UASs to collect and process data required less time than traditional methods.

Based on the positive results of the UAS-based approach after a full year of parallel scene mapping, MCAT stopped using total stations in 2017. Since then, MCAT has only used UASs as the primary method of crash scene data capture. In 2017, MCAT refined the UAS mapping technique and formalized a training program as part of the NUCPS crash investigation curriculum. At about the same time, the Lake County Sheriff Office (LCSO) switched to UASs for crash mapping, with results similar to the results experienced by MCAT.

In Lake County, Illinois, serious crashes are the responsibility of LCSO, MCAT, or the Waukegan Police Department, depending on the jurisdiction. The three accident investigation teams have used UASs for all major crash investigations since 2017—some 150 investigations in

total—for both daylight and nighttime hours. Other counties and municipal agencies in Illinois have also started using UASs and photogrammetry for crash reconstructions. For example, McHenry County, Grundy County, and the Elgin Police Department used them to document 33 fatal crashes in 2019.

The number of state public safety agencies, county sheriffs, and municipal police departments around the country that have received training and use UASs as their primary scene-mapping technique is increasing rapidly. The following is a small sample of agencies actively using UASs as part of their incident management programs. Officers at those agencies provided feedback to the research team.

- The Washington State Patrol's (WSP's) Major Accident Investigation Team started with training from NUCPS in August 2017. Initially, nine pilots were trained on the use of UASs for crash investigations and the subsequent development of 3D photogrammetric models for crash documentation and analysis. As of September 2019, WSP had 150 UASs, and 111 troopers had received training as UAS pilots. WSP flew 126 scenes in 2018 and over 250 in 2019. Recent feedback from WSP indicates that WSP now uses UASs for at least 75 percent of all major crash scenes. WSP also indicated that the program has been successful for delivering on the primary goal of getting traffic moving sooner and reducing officer time spent on crash scene investigations.
- In September 2019, 16 Iowa State Patrol (ISP) troopers completed the same UAS training program as what WSP had received previously. ISP's first deployment was on December 9, 2019, investigating a 50-vehicle pileup on I-80 in Des Moines. Using a UAS, officers completed the scene survey in 30 minutes. ISP's statewide UAS deployment went operational on January 6, 2020.
- The Oklahoma State Patrol (OSP) reported using UASs for 259 crash investigations in 2019. In OSP's experience, using total stations usually takes one to two hours (three to four hours on more complicated incidents when using laser scanners). Using UASs for crash scene investigations instead of these other methods resulted in a reduction of about 75 percent in time spent at the scene and road closures.

Elsewhere, the use of UASs is also increasing. For example, officers at Tippecanoe County in Indiana received training from Purdue University and began using UASs for crash reconstructions (71). Using traditional ground-based and UAS-based photogrammetric mapping for two crashes in July 2018, officers noted discrepancies within 8.8 cm (0.29 ft) between UAS-based measurements and field tape measurements.

## **COMMONLY USED UAS EQUIPMENT FOR CRASH INVESTIGATIONS**

The Center for the Study of the Drone at Bard College published a report in 2018 (updated in March 2020) that surveyed the use of UASs at public safety agencies in the United States (72). The survey included 1,578 state and local police, sheriff, fire, and emergency services agencies. The research team prepared Table 2 and Table 3 based on the trends reported in the 2018 and 2020 reports.



**Table 2. UAS Manufacturer among Public Safety Agencies in the United States.**

UAS Manufacturer	Number of Agencies			Market Share		
	2018	2020	Change	2018	2020	Change
DJI	523	924	+401	88%	90%	+2%
Yuneec™	31	46	+15	5%	4%	-1%
Physical Sciences	14	17	+3	3%	2%	0%
Draganfly™	10	11	+1	2%	1%	-1%
Parrot	8	11	+3	1%	1%	<1%
Leptron	8			1%		
Autel Robotics		21			2%	

**Table 3. UAS Manufacturer Models among Public Safety Agencies in the United States.**

UAS Brand	Model	Number of Agencies <sup>1</sup>			Market Share <sup>1</sup>		
		2018	2020	Change	2018	2020	Change
DJI	Phantom	260	336	76	39%	28%	-11%
DJI	Inspire	211	291	80	31%	24%	-7%
DJI	Matrice	61	226	165	9%	19%	10%
DJI	Mavic	42	246	204	6%	21%	15%
Yuneec	Typhoon	30	34	4	4%	3%	-1%
Physical Sciences	InstantEye	14	17	3	2%	1%	-1%
Draganfly	Draganflyer	10			1%		
3DR	Solo	9			1%		
Leptron	RDASS	8			1%		
Aeryon	Skyranger	6			1%		
Parrot	AR Drone	5			1%		
Lockheed Martin	Indago	5			1%		
Autel Robotics	X-Star Premium	5	12	7	1%	1%	<1%
Maxsur	Seeker	4			1%		
GoPro	Karma	3			0%		
Yuneec	H520		12			1%	
Draganfly Innovations	Draganflyer		11			1%	
Autel Robotics	Evo		9			1%	

<sup>1</sup> Numbers do not match those in Table 2 because agencies might have more than one different UAS model.

According to Table 2, UASs in use at public safety agencies were primarily from six manufacturers. Leptron appeared in the 2018 survey but not in the 2020 survey. Autel Robotics did not appear in the 2018 survey but appeared in the 2020 survey. DJI, a Chinese manufacturer, had a market share of 88 percent in 2018 and increased it to 90 percent in 2020.

Table 3 provides a more in-depth look at UAS use at public safety agencies in the United States, providing an overview of the UAS models in use by manufacturer. Four DJI models dominate the UAS market at public safety agencies: a consumer-level model (Mavic™) and three professional-level models (Phantom™, Inspire™, and Matrice™). In 2018, DJI UASs were typically Phantom and Inspire, but the use of Matrice and Mavic increased from 2018 to 2020. In 2020, DJI UAS use is now similar among these four models. Several UAS models from other manufacturers in use in 2018 were no longer in use in 2020.

The UAS market is evolving quickly, partly because of changes in the regulatory environment. In January 2021, the federal government through the General Services Administration decided to

remove all UASs from multiple award schedule contracts, except those UASs approved by the U.S. Department of Defense (DOD). As of this writing, DOD had approved five manufacturers: four American manufacturers (Skydio, Altavian, Teal Drones, and Vantage Robotics) and one French manufacturer (Parrot) (73). It is unclear what effects this decision will have on the UAS marketplace in the United States.

## **OTHER TRAFFIC INCIDENT MANAGEMENT APPLICATIONS**

Other than crash data collection and reconstruction activities, relatively little in the technical literature documents the use of UASs for TIM. In 2016, the Colorado DOT conducted a demonstration project involving a tethered UAS for traffic control and emergency management (74, 75). Reported advantages of the tethered UAS included providing continuous power to the UAS and continuously sending and receiving data using the tether cable. The tether was limited to 120 m (400 ft), allowing only 6 m (20 ft) of drift of the UASs in any direction at maximum altitude.

In 2017, the Texas A&M Transportation Institute (TTI) conducted a two-day demonstration on the use of UASs in the Houston area. The purpose of the demonstration was to monitor traffic, detect incidents, respond to incidents, and provide situational awareness in support of TxDOT's TranStar operations (75). The demonstration in Houston included a tethered UAS for traffic monitoring (Cyphy Works Persistent Aerial Reconnaissance and Communications) and an untethered UAS (DJI Inspire 2) as a response unit. Traffic monitoring involved launching and landing the tethered UAS from a Metropolitan Transit Authority of Harris County park-and-ride to monitor AM and PM peak traffic on a nearby freeway and at the park-and-ride. For incident detection, the data collection involved simulating a stalled vehicle in the US 290 high-occupancy vehicle lane and then using the tethered UAS to detect the stalled vehicle. The stalled vehicle information was provided to Metropolitan Transit Authority of Harris County crews to initiate the tow operation. For crash mapping, the data collection involved simulating a crash in a parking lot and using the untethered UAS and photogrammetry software to develop a 3D map of the simulated crash scene.

## **NATIONAL SURVEY FINDINGS**

### **Survey of National Association of Professional Accident Reconstruction Specialists**

In January 2020, the research team conducted a survey of industry professionals in the traffic crash investigation and reconstruction field to gain an understanding of the current use of UASs for crash reconstructions. The research team disseminated the survey to all members of the National Association of Professional Accident Reconstruction Specialists (NAPARS). NAPARS is the largest professional organization of its kind and includes over 800 professionals from across the globe. Traffic safety professions represented in the membership include but are not limited to professional engineers, law enforcement officers, and insurance specialists. The survey included the following questions:

- Have you used a drone for crash investigations? If yes, how many times?
- If you use a drone, do you use it for mapping or just photography?
- If you have not used a drone, do you have plans within the next 12 months to do so?

A total of 165 respondents, or 21 percent of NAPARS members, completed the survey. A summary of the responses, which suggest a rapid increase in deployment of UASs across the country, is as follows:

- 64 percent of respondents have used UASs for crash investigations; 21 percent of those who have used UASs for crash investigations have used them frequently, with 19 percent reporting using UASs up to 50 times.
- 54 percent of respondents indicated that they use UASs for both photography and mapping crash scenes. Some 12 percent of respondents use them only for photography.
- Of the 36 percent of respondents who had not yet used a UAS for crash investigations, 27 percent have plans to do so within the next year. When asked about plans for deployment in the next 12 months, only 26 percent responded that they do not have plans to do so.

### **Survey of State DOTs**

The research team contacted 82 members of the American Association of State Highway and Transportation Officials (AASHTO) Aviation Council, representing 43 states, and 111 members of the AASHTO Committee on Transportation Systems, representing 50 states and the District of Columbia. The survey was available from January 27, 2020, to February 20, 2020. In total, there were 50 responses from 27 states. The research team combined responses from the same state agency. The survey included three questions/requests:

- Does your state DOT use UASs for traffic incident management?
- If yes, please provide a summary of UASs equipment used for traffic incident management, examples of usage, and lessons learned.
- What are the current plans at your state DOT regarding the use of UASs for traffic incident management?

A total of 27 states responded to the first question, of which nine responded that they use UASs for TIM (18 percent of states), and 18 responded that they do not use UASs for TIM (36 percent of states). Twenty-three states and the District of Columbia (46 percent of states) did not respond to the survey.

Of the nine states that responded affirmatively to the first question, five responses were from state DOTs (Alabama, Delaware, Georgia, Indiana, and New Jersey), one response was from a state DOT (Alaska) responding on behalf of a state law enforcement agency (the Alaska Department of Public Safety), and three responses were from state public safety agencies (the Kentucky State Police, Maine State Police, and WSP). Although the survey was intended for state DOTs, it was clear that the survey invitation was forwarded to a few state public safety agencies.

Table 4 summarizes the responses from state DOTs. Table 5 summarizes the responses from state law enforcement agencies, including the response from the Alaska DOT on behalf of the Alaska Department of Public Safety. Table 5 also includes six responses from agencies that responded “no” to the first question but, when asked about plans, mentioned the use of UASs.

**Table 4. Summary of UASs Usage as Reported by State DOTs.**

<b>Agency</b>	<b>Response</b>
Alabama DOT	We used a senseFly eBee and Phantom 4 to fly an accident scene on I-65, which consisted of nadir and oblique imagery. We achieved these flights by using a rolling roadblock. We had 12 minutes to fly the project site, and it was completed in eight minutes.
Delaware DOT	The Delaware DOT uses a variety of UASs for incident management. We have 21 drones in our inventory; all of them are DJI. We use the Matrice 210 with thermal and zoom sensors for large-scale events. The Phantom 4 Pro and the Mavic 2 Enterprise are the day-to-day drones; the smaller Mavic Airc we use for indoor training and flying near trees and obstacles. We have used the drones to provide video downlink capability during major freeway closures over extended periods of time. We use them during special events such as NASCAR, music festivals, and marathons.
Georgia DOT	The Georgia DOT is utilizing UASs to monitor traffic conditions, hazmat detection, and problem detection. We use DroneSense to send remote feeds back to the traffic management center and the Georgia Emergency Management and Homeland Security Agency in Atlanta. During the 2019 I-16 contraflow, UASs were positioned at the interstate crossovers to monitor traffic in real time. Assets were also deployed to Tybee Island to monitor conditions on the island and the causeway.
Indiana DOT	We have started deploying UASs to gather data. We just filmed a bridge damaged by an oversize truck. The data have been sent to our Bridge Division. Lessons learned are proper coordination and having proper individuals operating the UASs. The bridge we just filmed was close to a nonhub primary airport, and we had coordination with the airport before the flight took place.
New Jersey DOT	The New Jersey DOT UAS program was used as an in-house resource under the NJ-495 Construction Traffic Operations Plan. We used a stationary Inspire 2 and Matrice 210 to livestream traffic data during peak times into the Woodbridge Traffic Management Center and the NJ-495 Project Command Post. This was a very high-priority project for the department, and we had to contend with livestreaming bandwidth issues and trying to maintain almost constant coverage without a tether system. In addition, we had to scramble to coordinate a Part 107 Airspace Authorization to fly in a presidential temporary flying restriction under short notice.

**Table 5. Summary of UASs Usage as Reported by State Public Safety Agencies.**

<b>Agency</b>	<b>Response</b>
Alaska DOT and Public Facilities	Response to traffic incidents with UASs is conducted by the Alaska Department of Public Safety. The data collected by UASs are used to create a 3D model for scene recreation, speed calculations, and accurate measurement for areas of interest. By collecting multiple forms of data, the average time on scene goes from three hours to 30 minutes. By using UAS with the FARO scanner, absolute accuracies range from $\pm 0.2$ cm. This has proven to be a fantastic tool for collecting more data than we need, with the ability to analyze the site in greater detail after the initial acquisition. The only problems we have run into are mapping in the dark and data storage.
Arkansas Department of Public Safety	The Arkansas State Police, part of the Arkansas Department of Public Safety, has UASs to reconstruct major crash scenes. This has substantially cut down on the time it takes to measure and document crash scenes, allowing incident clearance times to improve.
Illinois State Police	The Illinois State Police Crash Reconstruction Unit has started to implement some use of UASs.
Kentucky State Police	Crash reconstruction, forensic diagramming, and aerial photography. Pix4D for point cloud and ortho production.
Maine State Police	The Maine State Police currently has six UASs (DJI Matrice 200 and 210) and six Part 107 certified remote pilots assigned to the crash analysis unit. The UASs are used to document crash scenes and assist with the crash reconstruction. The photos are processed using Pix4D software, and the UASs replace the traditional mapping methods. The UAS mapping takes minutes and often does not involve a complete road closure, compared to the hours and complete closures involved in traditional mapping.
Michigan State Police	The Michigan State Police uses UASs for mapping crash scenes.
New Hampshire State Police	Currently, the New Hampshire State Police has a UAS program for law enforcement and accident survey. The program is one year old.
North Dakota State Police	The Highway Patrol and other law enforcement agencies currently in the state perform reconstruction and other traffic-incident-related operations.
Washington State Patrol	We use DJI Matrice 200 series, and Mavic 1 and 2. We use these to take high-quality top-down photographs to be used in photogrammetry software, which produces a 3D model. That model is then used in collision reconstruction software to create a diagram of the scene. We have noticed an approximate 80 percent reduction in on-scene measurement times.
Wisconsin State Patrol	The Wisconsin State Patrol uses UASs for crash reconstruction and assisting other law enforcement.

Of the five responses that state DOTs provided (Table 4), one of the responses (from the Alabama DOT) indicated using UASs for a crash scene, raising the question of whether it was the state DOT or a public safety agency conducting the UAS-based data collection. For the other state DOTs, the response provided was more in line with the kind of TIM activities that a state DOT would conduct, such as monitoring traffic conditions or special events.

The responses provided by state public safety agencies (Table 5) confirm or expand the results of the survey of NAPARS members, as discussed in the previous section. For example, agencies indicated using UAS data to develop 3D models for crash scene recreation or crash reconstruction and forensic diagramming. Several agencies mentioned using various DJI™ models, and one agency mentioned using a SenseFly™ UAS. The most frequently mentioned UASs was the DJI Matrice quadcopter. Two agencies mentioned using the Pix4D™ photogrammetry software suite, and one respondent mentioned using the DroneSense software platform.

Benefits of UAS use described by respondents included faster data collection than traditional data collection using ground-based equipment, faster clearance of incident sites, production of data with higher accuracy, and avoidance of road closures in certain situations. Issues that survey respondents mentioned were mapping and data collection in the dark, as well as the storage of large datasets.

With respect to plans, Table 6 shows the responses from agencies that were using UASs. Table 7 shows the responses from agencies that did not use UASs. Agencies already using UASs were working on standardizing data collection procedures, improving nighttime photogrammetry, finding ways to expand the UAS fleet, and determining procedures to coordinate the use of UASs among state agencies. Of the agencies that did not use UASs, three agencies (Kansas, Oklahoma, and Pennsylvania) were actively developing UAS programs, and two agencies were expanding existing UAS programs to include TIM (Idaho and Illinois). The North Dakota DOT did not use UASs for TIM but did for other DOT-related activities. Four states were evaluating the feasibility of UAS programs or conducting preliminary research for UAS programs (California, Louisiana, Nebraska, and Vermont), and four states had no plans and were not actively working on the implementation of UAS program (Mississippi, Minnesota, Montana, and Rhode Island).

**Table 6. Plans for UAS Use by State Agencies *Currently Using UASs.***

<b>Agency</b>	<b>Response</b>
Alabama DOT	We currently handle the incidents on a case-by-case basis, and the Alabama Law Enforcement Agency is starting its own UAS program to handle accident sites.
Alaska DOT and Public Facilities	Further development for nighttime photogrammetry with UASs and creating reference cards for the best capture settings. Because many accidents happen outside wireless coverage, the use of offline documentation and checklists will allow for proper acquisition of data.
Delaware DOT	The Delaware DOT has standard operating procedures for the UAS program. There are no plans specifically for traffic incident management. Our program was initially built around the Delaware DOT's response to traffic incidents or special events. Lately, we have branched out and have started to implement survey work into our UAS uses.
Georgia DOT	Expand our fleet from two to five aircraft to give 24/7 coverage for emergency incident response. Our FLIR cameras are made available to local agencies, and future plans call for upgrading to the latest sensor package.
Indiana DOT	We plan to be able to assist with any requests to provide UASs for our Indiana DOT counterparts. Our office is planning to add staff to increase our ability to meet additional UAS activity.
Kentucky State Police	No plans.
Maine State Police	The DOT just purchased three UASs for the State Police to assist with quick clearance. These three UASs were placed in a high-crash region where no UAS was available before. The UASs will be used to assist in quick clearance methods.
New Jersey DOT	The UAS program continues to support the TIM section as needed.
Washington State Patrol	Continue what we are doing. No plans for expansion with UASs other than current deployment.

**Table 7. Plans for UAS Use by State Agencies *Not Currently Using* UASs.**

<b>Agency</b>	<b>Response</b>
California DOT	At the current time, the DOT is creating training for potential UAS pilots to help obtain the Part 107 licensing as well as to understand the DOT’s rules and regulations as set forth by our Aeronautics Division. We are also conducting research on UASs as a communication platform to use in our remote areas that do not currently have adequate cellular coverage. The DOT has a policy in place to use UASs but not specifically for traffic incident management. They can be used by consultants if we do a “temp” contract with them for that, but not in our current practice/policy.
Idaho Transportation Department	Preliminary research. We will continue to advance UAS operations within our state DOT on an as needed/requested basis. Working with law enforcement to see how we can incorporate it.
Illinois DOT	The bureau of aeronautics is still developing policies for use of UASs. The bureau has used them in regard to flooding issues throughout the state but not specifically for TIM.
Kansas DOT	Just starting a program.
Louisiana Department of Transportation and Development	Investigating possible usage. We plan to explore that capability in the near future.
Minnesota DOT	None. Our Department of Public Safety has concerns regarding evidentiary chain of custody if the DOT does incident management.
Mississippi DOT	Currently have no plans to use for this purpose.
Montana DOT	Unknown
Nebraska DOT	The DOT has had preliminary discussions on concepts and gathered some data from other state DOTs on their use.
North Dakota DOT	We currently have 12 UASs within the DOT for other DOT-related types of processes.
Oklahoma DOT	We are in the process of purchasing 12 drones for incident management to be used by the Oklahoma Department of Public Safety. We expect to operational in six months.
Pennsylvania DOT	A program for UAS for incident management is currently in development. We anticipate having the full program implemented by June 2020. The program will drive the use of UASs for incident management in cases such as traffic incidents, flood scaling, earth slides, etc., and other needs as necessary.
Rhode Island DOT	The Rhode Island DOT has no plans to use UASs at this time to my knowledge.
Vermont Agency of Transportation	We have discussed ways to use UASs in TIM but have not implemented yet.



## CASE STUDIES

The following two case studies describe the use of UASs to support crash investigations and provide an overview of techniques used and forensic mapping results. A daylight crash and a nighttime crash are presented to demonstrate the applicability of the technique across the spectrum of lighting conditions. Both cases were conducted by NUCPS's research team members and members of the Lake County, Illinois, MCAT.

### Case Study 1—Daylight Conditions

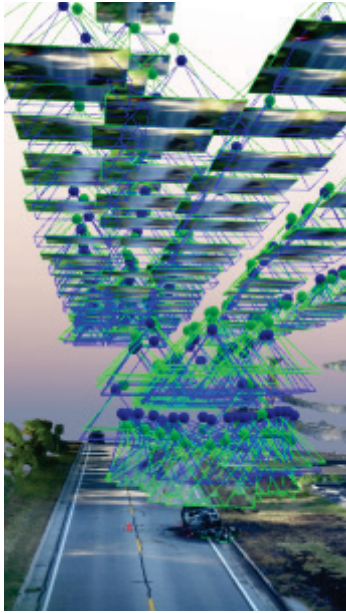
On the afternoon of July 16, 2016, a collision occurred between a southbound pickup truck and a group of motorcyclists traveling together northbound on a two-lane county road. The driver of the pickup truck lost control. The vehicle crossed the center line, struck two motorcycles, and burst into flames. A third motorcycle was not struck by the pickup truck but slid down on the road as the motorcyclist maneuvered to avoid the crash. Because injuries were significant, a thorough crash investigation was requested, and four MCAT members of Lake County, Illinois, were dispatched to the scene.

The use of photogrammetry for this crash scene enabled MCAT to bypass the time-consuming, hazardous task of conducting extensive field measurements. At the same time, it provided a richer and more detailed record of the crash scene and surrounding area than using traditional crash reconstruction methods.

#### *UAS Data Collection*

MCAT officials marked evidence with florescent paint. At 6:05 PM, they deployed a DJI Inspire/1 UAS to gather aerial imagery. During the 14-minute total flight time, the UAS pilot collected 186 images covering a 91 m (300 ft) section of roadway using the Inspire/1's Zenmuse X3 12.4-MP camera. The pilot took pictures from altitudes ranging from 30 m (100 ft) to ensure complete area coverage to 5 m (15 ft) to capture specific evidence detail. Figure 12 provides an overview of where the pilot positioned the UASs while capturing images of the scene. Before deploying the UAS, MCAT officials arranged three evidence markers orthogonally 15 m (50 ft) apart within the scene. The officials then measured the distances between the markers using a tape. The flight took five minutes for setup, 14 minutes for data collection, and about five minutes for packing up the UASs, for a total on-scene time of under 25 minutes.

The UAS data collection included multiple passes at progressively lower altitudes. The initial pass included 13 nadir pictures at 30 m (100 ft) in a single line and served as a backup against lower altitude coverage gaps. This pass covered areas adjacent to the primary scene. The second pass included 125 nadir pictures in a  $5 \times 25$  grid at 15 m (50 ft) and served as the primary survey. Imagery at 15 m (50 ft) provided adequate image and model detail to accurately map typical road features such as lane lines, pavement edges, and road markings. The third pass included 25 nadir pictures in two rows at 8 m (25 ft) directly over evidence markings. This pass yielded greater visual detail, enabling accurate mapping and measurement of evidence features such as skids, scrapes, and gouges. A final pass included 23 oblique pictures at 5m (15 ft) in a circular pattern around the pickup truck and two of the motorcycles and provided visual detail of the vehicles from multiple perspectives.



**Figure 12. UAS Placement and Camera Angles.**

### *Orthomosaic Production*

Figure 13 is a scaled orthomosaic based on 186 overlapping aerial images collected at the crash scene. A technician processed the 186 aerial images using Pix4Dmapper. The software used the GNSS image coordinates to place the crash scene in the correct geographic context, in this case a county road in northern Illinois.



**Figure 13. Orthomosaic of the Crash Scene.**

The embedded GNSS data also provided an initial scale to the crash scene model, which enabled the technician to compare it against the actual distances measured in the field and rescale the model. The initial model of the crash scene was 6 cm (0.2 ft) longer than the actual field measurement: 23.99 m (78.7 ft) in the model versus 23.93 m (78.5 ft) in the field (Table 8). After rescaling the model to the known field measurement, the scaled model's observed measurements

were consistently within 0.1 percent of those taken in the field. This level of accuracy is typical for the technique used and is sufficient for scene documentation purposes.

**Table 8. Model vs. Field Measurement Table.**

Markers	Field Measurement (m)	Initial Model Measurement	Initial Error (m)	Scaled Model Measurement (m)
A-C	23.93	23.99	0.06	23.93
A-B	9.11	9.14	0.03	9.11

*Point Cloud and 3D Textured Mesh*

The technician used Pix4D to generate a dense 3D point cloud and corresponding 3D textured mesh (Figure 14). The technician then conducted a virtual survey to identify evidence and road features needed to prepare accurate, scaled crash diagrams. The virtual survey identified the X-Y-Z coordinates of over 500 points of interest, including highway features, vehicle locations, tire marks, and pavement gouges. Figure 15 shows green dots where points were identified and recorded in the computer model similarly to how they previously would have been identified with a total station in the field.

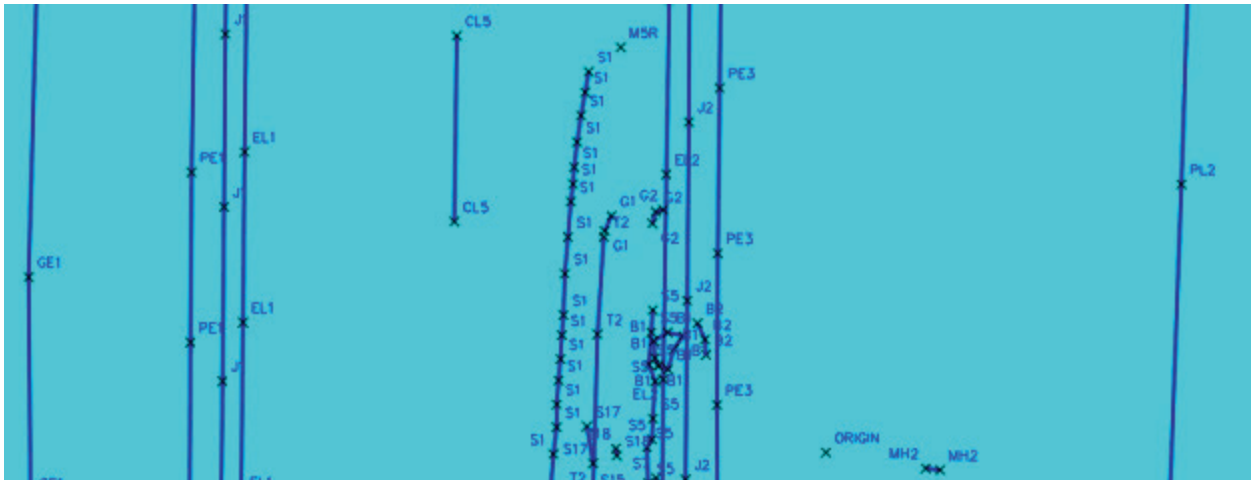


**Figure 14. 3D Textured Mesh.**



**Figure 15. Virtual Survey Markings.**

The points marked in the virtual survey were then exported to AutoCAD™ in drawing exchange format, and as a point list in Microsoft™ Excel™ format for documentation purposes. The point file is the equivalent of what previously would have been downloaded from a total station. Figure 16 shows how the collected data appear once imported into a typical crash reconstruction software package. Table 9 shows the same data in the commonly used easting/northing tabular format.



**Figure 16. Points Displayed in Crash Reconstruction Software.**

**Table 9. Points with Coordinates and Description (Using a Local Coordinate System).**

<u>POINT #</u>	<u>EASTING</u>	<u>NORTHING</u>	<u>ELEVATION</u>	<u>CODE</u>	<u>DESCRIPTION</u>
425	-11.57	-3.99	-0.65	S16	Scrape 16
426	-11.56	-2.44	-0.61		
427	-5.90	-54.52	-0.93	M4F	Motorcycle 4 front wheel
428	-10.39	-52.74	-0.86	M4R	Motorcycle 4 rear wheel
429	-6.99	-52.65	-0.73	M3R	Motorcycle 3 rear wheel
430	-11.74	28.71	1.96	M5F	Motorcycle 5 front wheel
431	-11.70	23.08	1.62	M5R	Motorcycle 5 rear wheel
432	-7.47	-42.30	-1.91	LR	Pickup truck left rear
433	-12.84	-52.00	-2.09	FR	Pickup truck front right
434	-13.14	-42.03	-1.76	RR	Pickup truck rear right
435	0.00	0.00	0.00	ORIGIN	Total Station base

## Case Study 2—Nighttime Conditions

On March 15, 2019, at 10:15 PM, there was a two-vehicle crash with a fatality on a four-lane divided highway in Lake County, Illinois. A sedan traveling south on Route 12 crossed the center median into the northbound lanes and collided with another sedan occupied by four teenagers.

Mapping 380 m (1,250 ft) of divided highway with a total station would have been time consuming and disruptive to traffic. Collecting data in unlit areas at night would also have been dangerous to first responders. Using a UAS reduced the overall road closure time and increased safety for investigators by allowing many of the mapping tasks to be performed from a safer position off the roadway.

### *UAS Data Collection*

The crash occurred on a dark stretch of roadway with no overhead lighting. In accordance with the procedure for investigating scenes at night, MCAT dispatched two towable light towers to illuminate the scene, facilitate the investigation, and increase safety.

MCAT officials marked evidence with florescent paint, placed three reference points orthogonally, and measured distances between the reference points. Because high speed was a suspected contributing factor, the area to be documented was extended to 380 m (1,250 ft). Figure 17 shows a sample image captured by the UAS.

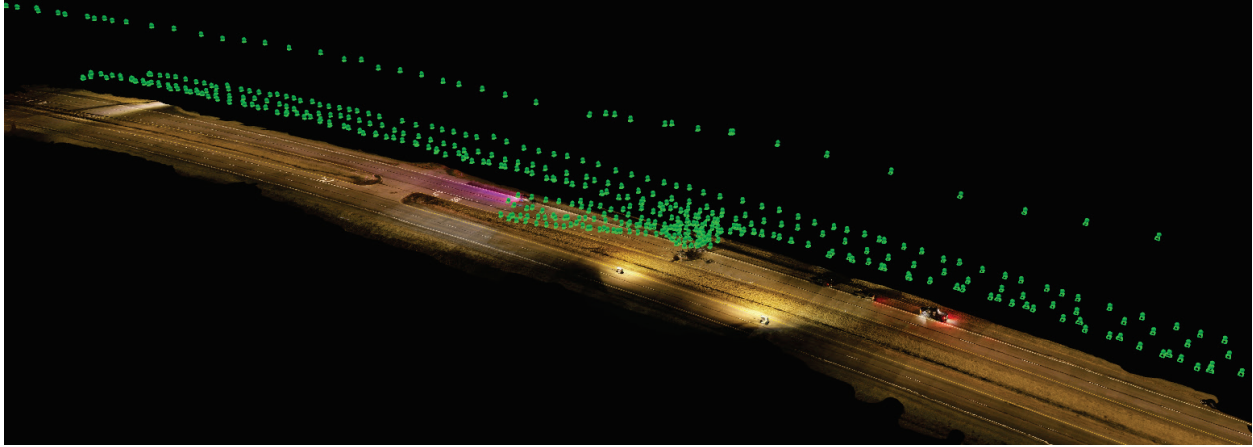


**Figure 17. Evidence Markup.**

Per MCAT preflight checklists, the UAS pilot recorded weather conditions ( $-1^{\circ}\text{C}$  or  $30^{\circ}\text{F}$  with 16–29 km/h or 10–18 mph winds) and checked for airspace restrictions. Because the flight was conducted at night, a flashing beacon visible from 5 km (3 mi) away was activated and affixed to the UAS prior to takeoff. The MCAT team had a four-year waiver by FAA to operate at night under Part 107 regulations, as well as annual controlled airspace authorizations to operate near airports in northern Illinois.

The pilot used a Mavic 2 Pro with an integrated 20-MP Hasselblad L1D-20C camera to collect 505 pictures from altitudes between 8 m (25 ft) and 38 m (125 ft), covering a 380 m (1,250 ft) section of both northbound and southbound lanes and the central median area. The flight

operation took 50 minutes, including brief stops for battery changes. Figure 18 provides an overview of where the pilot positioned the UAS while capturing images of the scene.



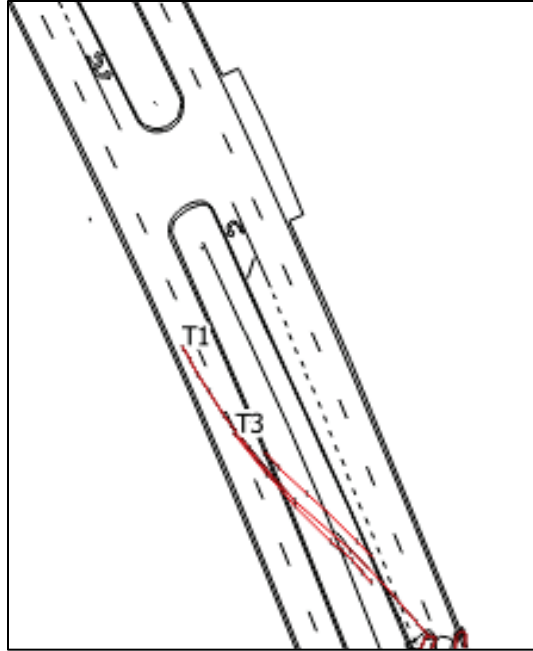
**Figure 18. UAS Image Capture Placements.**

The vehicle area and immediate vicinity were well illuminated by portable lighting, but the remaining 305 m (1,000 ft) of roadway was in complete darkness. To capture imagery in the unlit areas, the pilot used the built-in, downward-facing UAS LEDs.

#### *Merging of Daylight Aerial Photography*

An officer returned to the scene the following morning and determined that the tire yaw markings found on the southbound lanes extended further back to the north. The additional evidence proved useful in determining the speed of the southbound vehicle when first losing control and before entering the center median area. With the newly discovered evidence marked, the official deployed a UAS for nine minutes to capture an additional 54 pictures of the area. By positioning the UAS flight path off the shoulder of the roadway, it was not necessary to close the road for the additional data collection activity.

The 505 nighttime and 54 daylight aerial photos of the scene were processed into a single model using Pix4Dmapper to produce a georeferenced 2D orthomosaic, 3D point cloud, and triangle mesh model. It was also possible to generate scaled diagrams of the crash scene (Figure 19).



**Figure 19. Overview Diagram Prepared from UAS Data.**

## **OPERATIONAL EXPERIENCE OF PUBLIC SAFETY AGENCIES**

A growing number of public safety agencies use UASs for crash reconstruction purposes. The operational experience of these teams, as observed by crash investigation instructors at NUCPS, has produced several lessons learned, including but not limited to the following:

- **Use of consumer-grade UASs for crash investigations.** The primary justification for using photogrammetry is imagery with sufficient quality. Consumer UASs now have 20-MP cameras that can capture the required imagery. Early-adopting agencies have reported success in a wide range of weather conditions.
- **FAA Part 107 regulations.** In 2016, FAA enacted rules designed to enable and regulate the use of UASs by private and public pilots, as well as rules for safe operations and pilot licensing requirements (5). Many of these restrictions, such as daylight-only operations, can be waived. UAS-licensed pilots for public safety agencies who obtain the proper waivers can fly crash scenes day or night and in controlled airspaces, such as near airports.
- **Manual flight control.** Public safety agencies such as TxDPS routinely fly UASs on autonomous mode. For autonomous UAS flights, FAA requires a licensed pilot to supervise the flights and be ready to take control if needed. Most public safety agencies that use UASs for crash investigations on a consistent basis tend to gather imagery manually. Stated reasons include the need to capture evidence that is obscured or blocked by trees or other obstructions and the need to fly lower over key evidence areas with traffic signals, streetlights, overhead utility cables, and other hazards that lie beyond the obstacle avoidance capability of current UASs on the market. Additional reasons include the need to comply with FAA safety regulations, such as not flying directly over people or moving vehicles, and the need to develop and maintain pilot skills.

- **Crash investigation officer training and licensing.** Officers can master the necessary piloting and photogrammetry skills to be effective in the field. The typical training curriculum to prepare an officer who is new to the technology is about one week, including learning the FAA Part 107 knowledge required to obtain an FAA UAS pilot license. As pilot experience increases, the time required to process a crash scene decreases significantly.
- **Nighttime data collection.** A variety of techniques for collecting data at night using UASs have been successfully demonstrated. Examples include:
  - Street lighting, when combined with high-contrast paint, chalk, or evidence markers, can be sufficient.
  - Light towers, when angled horizontally, can illuminate a dark stretch of roadway.
  - Vehicle headlights, when strategically placed, can illuminate the roadway and evidence areas.
  - Downward-looking LEDs are built into some UAS models or can be attached to many UAS platforms. Built-in light sources frequently provide sufficient illumination at flight heights up to 30 m (100 ft).
  - Daylight and nighttime UAS imagery can be combined to extend scene coverage.
  - In all cases, care must be taken to keep the UAS still when the camera shutter is activated to avoid motion blur caused by the required longer exposure times. Issues using UASs for nighttime data collection have been raised (76), but techniques such as those discussed previously appear to effectively address those issues.
- **Use of UASs under mild to moderate precipitation conditions.** Several agencies have reported success using UASs in mild to moderate rain or snow conditions. The limiting factor is not the UAS's flight capabilities but the degradation in image quality because of rain or snow preventing a clear, unobstructed view of the ground from the UAS. UAS-mounted lighting exacerbates the effect. Under these conditions, it is better to use other light sources for night scenes during rain or snowfall.
- **Limiting UAS use to crash investigations to avoid public criticism.** A few police departments have run into public criticism when introducing UASs as a new general-purpose tool for police use. Departments that have restricted the use of police UASs to crash investigation and search-and-rescue applications have received more favorable media and public reception (77).
- **Aboveground utility lines.** Utility lines can complicate the use of UASs at a crash scene. In most situations, utility wires do not emit enough electromagnetic radiation to interfere with UAS flight control signals. It is possible to operate UASs within 3 m (10 ft) of high-voltage wires before electromagnetic interference becomes an issue. In practice, the challenge with multiple utility lines is the difficulty navigating around those lines and acquiring the necessary images. However, this is not an impossible task. As an illustration, the accident investigation team at the Waukegan Police Department in Lake County, Illinois, successfully completed a nighttime UAS mission in January 2020 to capture a fatal hit-and-run crash scene. The mission involved flying the UAS below, above, and between 50 utility lines, including high-voltage wires (Figure 20).





**Figure 20. Electric Transmission Towers in Waukegan, Illinois.**



## CHAPTER 3. CRASH DATA ANALYSIS

### INTRODUCTION

The research team conducted an analysis to identify spatial and temporal trends in the occurrence of crashes on Texas highways, with a particular focus on fatal crashes. It was also of interest to identify any potential effect of environmental factors on those trends. As requested by TxDOT, the crash data analysis focused on the Austin, Dallas, Fort Worth, Houston, and San Antonio metro areas.

### CRASH DATA

The research team gathered and processed 10 years (2010 to 2019) of crash data from TxDOT's Crash Record Information System (CRIS). The data included all the records from the crash, unit, primary person, and person tables. Consistent with protocols between TTI and TxDOT for the release of historical crash data, the research team worked through a designated official at the TTI Traffic Safety Center to download and furnish relevant crash data.

Although the crash data include a city ID attribute, the five metro areas include several cities. The crash data also include a county ID attribute. For this reason, the research team decided to use county boundaries to group crashes within each region. Table 10 lists the counties selected.

**Table 10. Counties Selected for Analysis of Five Metro Areas.**

<b>Metro Area</b>	<b>County</b>
Austin	Travis County
Dallas	Dallas County
Fort Worth	Tarrant County
Houston	Harris County
San Antonio	Bexar County

Table 11 provides a summary of the total number of crashes in Texas from 2010 to 2019. The table includes the total number of fatal crashes as well as different injury levels. Table 12 through Table 16 provide corresponding summaries for each of the counties associated with the five metro areas listed in Table 10. Table 17 provides a summary of fatal crashes, both statewide and for each metro area. It is worth noting that the data used for the analysis correspond to a CRIS database query conducted on February 26, 2020. CRIS is a live system, which means that a query conducted on a different day is likely to produce a different result. In general, query result differences decrease rapidly as the data age increases.

**Table 11. Number of Crashes—Statewide.**

Year	Fatal	Suspected Serious Injury	Non-Incapacitating	Possible Injury	Not Injured	Unknown	Total
2010	2,781	11,746	48,166	81,384	232,356	15,614	<b>392,047</b>
2011	2,802	11,693	46,330	81,065	226,817	15,720	<b>384,427</b>
2012	3,037	12,824	50,602	88,317	245,951	17,013	<b>417,744</b>
2013	3,063	13,387	51,985	88,591	270,870	18,197	<b>446,093</b>
2014	3,192	13,639	52,866	92,014	296,684	19,307	<b>477,702</b>
2015	3,193	13,700	54,650	96,805	331,124	23,264	<b>522,736</b>
2016	3,424	14,195	58,854	102,987	349,294	24,579	<b>553,333</b>
2017	3,347	14,284	58,408	97,893	342,015	22,848	<b>538,795</b>
2018	3,313	12,179	54,229	101,535	350,052	23,224	<b>544,532</b>
2019	3,224	12,818	53,821	105,123	360,580	21,655	<b>557,221</b>

**Table 12. Number of Crashes—Austin Area (Travis County).**

Year	Fatal	Suspected Serious Injury	Non-Incapacitating	Possible Injury	Not Injured	Unknown	Total
2010	75	481	3,066	3,045	6,819	575	<b>14,061</b>
2011	75	497	3,194	3,262	6,587	591	<b>14,206</b>
2012	98	609	3,729	3,664	7,358	664	<b>16,122</b>
2013	103	611	3,784	3,519	7,441	595	<b>16,053</b>
2014	85	553	3,516	3,639	7,242	484	<b>15,519</b>
2015	134	549	3,348	3,836	9,172	688	<b>17,727</b>
2016	114	650	3,621	4,284	10,441	792	<b>19,902</b>
2017	106	614	3,474	3,793	10,688	729	<b>19,404</b>
2018	114	595	3,631	3,802	10,870	712	<b>19,724</b>
2019	113	620	3,659	4,199	10,913	623	<b>20,127</b>

**Table 13. Number of Crashes—Dallas Area (Dallas County).**

Year	Fatal	Suspected Serious Injury	Non-Incapacitating	Possible Injury	Not Injured	Unknown	Total
2010	172	951	4,908	9,934	17,946	1,744	<b>35,655</b>
2011	173	976	4,763	9,555	18,076	1,670	<b>35,213</b>
2012	192	1,128	4,929	9,535	18,862	1,784	<b>36,430</b>
2013	206	1,224	5,230	9,672	22,212	2,261	<b>40,805</b>
2014	222	1,234	5,230	9,763	24,027	2,403	<b>42,879</b>
2015	240	1,235	5,771	10,873	27,827	2,959	<b>48,905</b>
2016	289	1,439	6,585	12,661	31,443	3,267	<b>55,684</b>
2017	263	1,421	6,453	11,576	27,957	2,897	<b>50,567</b>
2018	286	1,266	5,639	11,474	28,275	2,812	<b>49,752</b>
2019	251	1,322	5,976	11,915	32,540	3,024	<b>55,028</b>

**Table 14. Number of Crashes—Fort Worth Area (Tarrant County).**

<b>Year</b>	<b>Fatal</b>	<b>Suspected Serious Injury</b>	<b>Non-Incapacitating</b>	<b>Possible Injury</b>	<b>Not Injured</b>	<b>Unknown</b>	<b>Total</b>
2010	123	1,002	3,607	5,843	13,157	1,280	<b>25,012</b>
2011	137	891	3,448	5,769	12,700	1,308	<b>24,253</b>
2012	116	1,033	3,738	5,824	14,164	1,160	<b>26,035</b>
2013	128	1,037	3,876	6,054	15,470	1,402	<b>27,967</b>
2014	138	1,090	3,858	6,130	15,658	1,400	<b>28,274</b>
2015	142	1,040	3,878	6,741	17,445	1,585	<b>30,831</b>
2016	158	1,045	4,444	7,769	19,613	1,698	<b>34,727</b>
2017	170	946	4,056	7,617	19,809	1,707	<b>34,305</b>
2018	159	764	3,724	7,676	19,149	1,548	<b>33,020</b>
2019	148	754	3,740	7,765	18,415	1,429	<b>32,251</b>

**Table 15. Number of Crashes—Houston Area (Harris County).**

<b>Year</b>	<b>Fatal</b>	<b>Suspected Serious Injury</b>	<b>Non-Incapacitating</b>	<b>Possible Injury</b>	<b>Not Injured</b>	<b>Unknown</b>	<b>Total</b>
2010	338	1,598	6,413	14,206	42,353	2,590	<b>67,498</b>
2011	353	1,483	5,950	14,208	42,217	2,417	<b>66,628</b>
2012	334	1,739	6,851	17,241	48,660	2,961	<b>77,786</b>
2013	351	1,698	7,198	18,821	55,566	3,455	<b>87,089</b>
2014	381	1,926	7,865	20,802	67,372	3,686	<b>102,032</b>
2015	367	1,935	8,116	21,259	75,512	4,333	<b>111,522</b>
2016	429	1,918	8,736	21,146	76,430	4,265	<b>112,924</b>
2017	431	1,785	8,741	19,725	73,834	4,082	<b>108,598</b>
2018	369	1,674	7,940	20,608	72,795	4,400	<b>107,786</b>
2019	385	1,945	8,141	21,545	75,638	4,305	<b>111,959</b>

**Table 16. Number of Crashes—San Antonio Area (Bexar County).**

<b>Year</b>	<b>Fatal</b>	<b>Suspected Serious Injury</b>	<b>Non-Incapacitating</b>	<b>Possible Injury</b>	<b>Not Injured</b>	<b>Unknown</b>	<b>Total</b>
2010	138	683	2,793	8,522	19,731	1,949	<b>33,816</b>
2011	145	640	2,666	8,698	18,706	1,992	<b>32,847</b>
2012	151	911	3,459	9,139	20,179	2,075	<b>35,914</b>
2013	173	956	3,487	8,741	24,047	2,285	<b>39,689</b>
2014	169	865	3,590	9,127	26,545	2,416	<b>42,712</b>
2015	173	946	3,950	10,289	29,952	2,985	<b>48,295</b>
2016	207	987	4,394	11,020	32,623	3,410	<b>52,641</b>
2017	158	993	4,686	10,552	31,168	2,997	<b>50,554</b>
2018	174	657	4,151	10,345	30,952	2,910	<b>49,189</b>
2019	171	708	3,923	10,604	32,260	2,899	<b>50,565</b>

**Table 17. Number of Fatal Crashes—Statewide and Metro Area Counties.**

Year	Statewide	Austin	Dallas	Fort Worth	Houston	San Antonio
2010	2,781	75	172	123	338	138
2011	2,802	75	173	137	353	145
2012	3,037	98	192	116	334	151
2013	3,063	103	206	128	351	173
2014	3,192	85	222	138	381	169
2015	3,193	134	240	142	367	173
2016	3,424	114	289	158	429	207
2017	3,347	106	263	170	431	158
2018	3,313	114	286	159	369	174
2019	3,224	113	251	148	385	171

## GENERAL TRENDS

Based on the data compiled in Table 11 through Table 17 as well as basic crash attribute data, the research team prepared a series of figures and charts to develop a high-level understanding of crash locations and trends. This section includes a small sample of charts and figures to highlight general trends. Additional materials can be prepared as needed.

Figure 21 shows the annual relative variation in the number of crashes from 2010 to 2019, using 2010 as the base year, both statewide and for each metro area. The figure shows trends for both total crashes and fatal crashes. In the figure, an index value of 1.0 is associated with the number of crashes in 2010. Any index value higher than 1.0 means that the number of crashes for that year was higher than the number of crashes in 2010. Likewise, any index value lower than 1.0 means that the number of crashes for that year was lower than the number of crashes in 2010.

With respect to all crashes, Figure 21 shows the following:

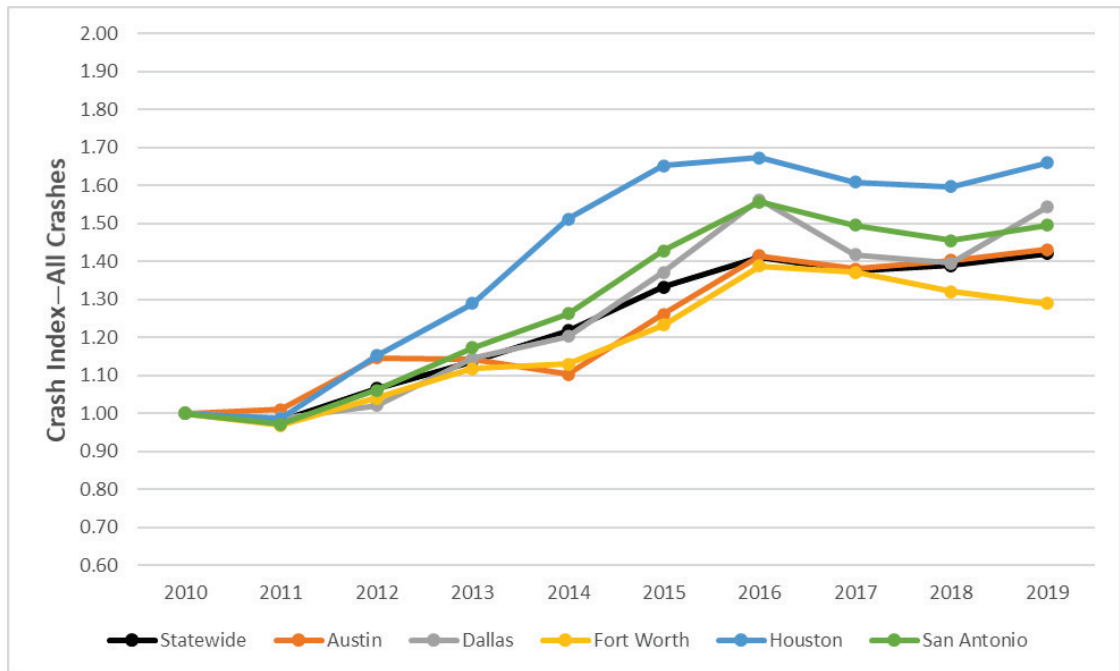
- The number of crashes increased statewide until about 2016, and then it remained roughly at the same level. Statewide, the increase was about 40 percent from 2010 to 2016, which corresponds to an annual growth rate of about 6 percent. The crash index value for 2019 was 1.42 (i.e., only slightly higher than the index value in 2010).
- All five metro areas followed the overall statewide trend. However, crashes in the Austin, Dallas, Houston, and San Antonio areas increased faster than the statewide trend. The Houston area experienced the fastest growth in the number of crashes of all five metro areas. By comparison, crashes in the Fort Worth area increased more slowly than the statewide trend. Fort Worth was the only metro area that experienced a steady decline in crashes since 2016.

With respect to fatal crashes, Figure 21 shows the following:

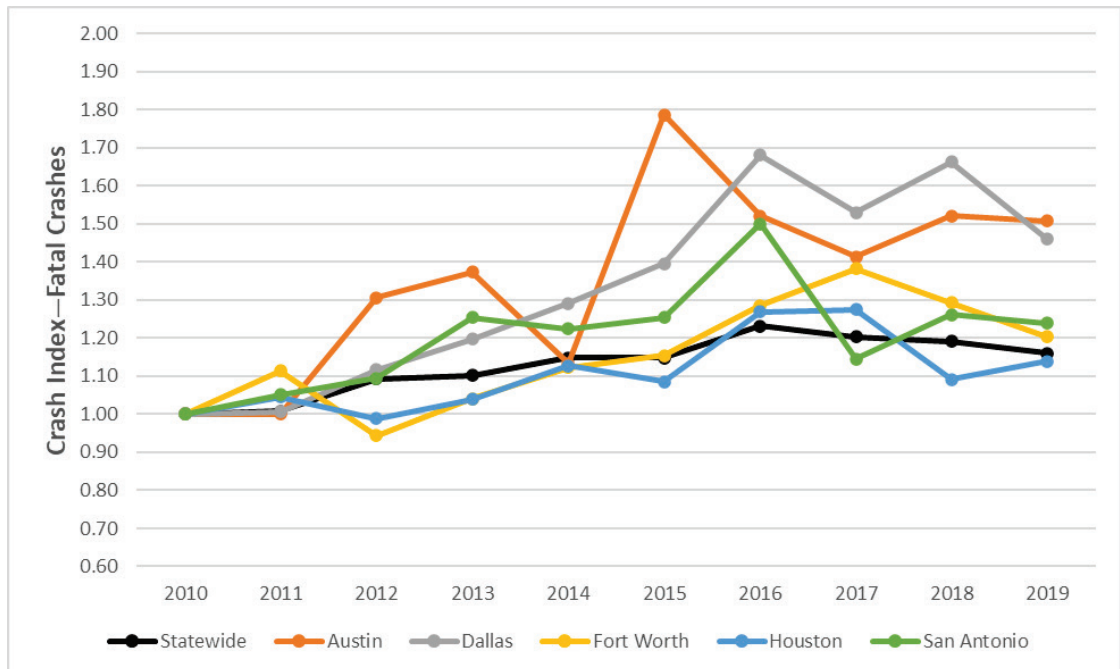
- The number of fatal crashes increased statewide until 2016, at which point there was a steady decline.
- All metro areas showed a decrease in the number of fatal crashes from 2016 to 2019.

- Fatal crashes in all metro areas grew faster than the statewide trend except for Houston, which had a fatal crash index value similar to the statewide trend in 2019.

All crashes



Fatal crashes



**Figure 21. Crash Index—All Crashes and All Fatal Crashes.**

## High-Level Statistical Analysis

The research team conducted a high-level statistical analysis to determine potential correlations between a variety of factors and fatal crashes. For the analysis, the research team calculated the sample Pearson correlation coefficient as:

$$r_{xy} = \frac{\sum_1^n (x(i) - \bar{x})(y(i) - \bar{y})}{(n-1)s_x s_y} \quad (2)$$

where:

$r_{xy}$  = sample Pearson correlation coefficient,

$x(i)$  =  $i^{\text{th}}$  value of Attribute 1,

$\bar{x}$  = sample mean of Attribute 1,

$y(i)$  =  $i^{\text{th}}$  value of Attribute 2,

$\bar{y}$  = sample mean of Attribute 2,

$n$  = sample size or number of value pairs for Attributes 1 and 2,

$s_x$  = sample standard deviation of Attribute 1, and

$s_y$  = sample standard deviation of Attribute 2.

Correlation coefficients can vary between -1 and +1. Higher correlation values (positive or negative) mean a higher level of linear correlation between attributes.

For the analysis, the research team correlated crash attributes and the crash fatal flag attribute (i.e., [CRASH\_FATAL\_FL]). Table 18 shows the results of the analysis for a selection of attributes of interest. The table also shows ID-Ness (which measures the degree to which an attribute resembles an ID), Stability (which measures how stable an attribute is), and Missing (which is the number of missing values as a fraction of the total number of records).

The results in Table 18 were for all crash records in Texas in 2019. As Table 18 shows, the correlation between the crash fatal flag attribute and the death count attribute was 0.9177. This finding was expected, considering that fatal crash records usually have an entry in the death count field. The correlation coefficient for all other attributes in the database was very low, meaning that those attributes were poor predictors of whether a crash would involve a fatality. The highest ranked environmental attribute was light condition, but even the corresponding correlation coefficient was only 0.0007. The second highest environmental attribute was weather condition, but the corresponding correlation coefficient was only 0.0001.

Results for other years were similar. Even when considering regions, results were not drastically different. For example, for the San Antonio metro area, the correlation coefficient for light condition in 2010 was only 0.0021.



**Table 18. Indicators of Select Crash Attributes for Fatal Crash Prediction Modeling.**

	<b>Correlation Coefficient</b>	<b>ID-Ness</b>	<b>Stability</b>	<b>Missing</b>
Death Count	0.9177	0.00%	99.48%	0.00%
Rural Urban Type	0.0051	0.00%	60.39%	48.02%
Population Group	0.0019	0.00%	39.74%	1.32%
Surface Width	0.0019	0.02%	24.74%	48.02%
Crash Speed Limit	0.0019	0.00%	16.29%	0.00%
Object Struck	0.0019	0.01%	78.67%	0.00%
Number of Lanes	0.0018	0.00%	39.28%	48.02%
Road Type	0.0017	0.00%	60.04%	48.02%
Commercial Vehicle Involvement	0.0009	0.00%	93.16%	0.00%
Intersection Related	0.0009	0.00%	51.31%	0.00%
Collision Type	0.0008	0.01%	21.59%	0.00%
Light Condition	0.0007	0.00%	68.76%	0.00%
Harmful Event	0.0007	0.00%	74.82%	0.00%
Weather Condition	0.0001	0.03%	74.46%	0.00%
Surface Condition	<0.0001	0.03%	83.13%	0.00%

### Daylight versus Nighttime Crashes

Although light condition by itself is not a strong predictor of whether a crash is a fatal crash, the research team conducted a more detailed analysis to identify trends and patterns that could be of interest. For the analysis, the research team grouped light conditions into two broad categories, as shown in Table 19: daylight and nighttime.

**Table 19. Grouping of Crashes into Daylight and Nighttime Crashes.**

<b>ID</b>	<b>Description</b>	<b>Grouping</b>
0	Unknown	Daylight
1	Daylight	Daylight
2	Dawn	Daylight
3	Dark, not lighted	Nighttime
4	Dark, lighted	Nighttime
5	Dusk	Daylight
6	Dark, unknown lighting	Nighttime
8	Other (explain in narrative)	Daylight
94	Reported invalid	Excluded from analysis
95	Not reported	Excluded from analysis

Table 20 shows the total number of daylight and nighttime *nonfatal* crashes in the state from 2010 to 2019. During this period, 71 percent of all nonfatal crashes occurred during daylight hours and 29 percent occurred during nighttime hours. Percentages for individual years varied from 70–71 percent for daylight nonfatal crashes and from 29–30 percent for nighttime crashes.

**Table 20. Statewide Count of Daylight and Nighttime *Nonfatal* Crashes.**

<b>Year</b>	<b>Daylight</b>	<b>Nighttime</b>	<b>Total</b>
2010	277,120	112,146	<b>389,266</b>
2011	268,977	112,648	<b>381,625</b>
2012	293,256	121,451	<b>414,707</b>
2013	313,107	129,923	<b>443,030</b>
2014	335,141	139,369	<b>474,510</b>
2015	364,751	154,792	<b>519,543</b>
2016	390,266	159,643	<b>549,909</b>
2017	380,489	154,959	<b>535,448</b>
2018	383,371	157,848	<b>541,219</b>
2019	395,008	158,989	<b>553,997</b>
<b>Total</b>	<b>3,401,486</b>	<b>1,401,768</b>	<b>4,803,254</b>
<b>% of Total</b>	<b>71%</b>	<b>29%</b>	

Table 21 shows the total number of *fatal* daylight and nighttime crashes in the state from 2010 to 2019. During this period, 46 percent of all fatal crashes occurred during daylight hours and 54 percent occurred during nighttime hours. Percentages for individual years varied from 44–47 percent for daylight fatal crashes and from 53–56 percent for nighttime crashes.

**Table 21. Statewide Count of Daylight and Nighttime *Fatal* Crashes.**

<b>Year</b>	<b>Daylight</b>	<b>Nighttime</b>	<b>Total</b>
2010	1,311	1,470	<b>2,781</b>
2011	1,306	1,496	<b>2,802</b>
2012	1,437	1,600	<b>3,037</b>
2013	1,439	1,624	<b>3,063</b>
2014	1,445	1,747	<b>3,192</b>
2015	1,447	1,746	<b>3,193</b>
2016	1,534	1,890	<b>3,424</b>
2017	1,545	1,802	<b>3,347</b>
2018	1,469	1,844	<b>3,313</b>
2019	1,468	1,756	<b>3,224</b>
<b>Total</b>	<b>14,401</b>	<b>16,975</b>	<b>31,376</b>
<b>% of Total</b>	<b>46%</b>	<b>54%</b>	

The analysis of nonfatal versus fatal crashes reveals that more nonfatal crashes occurred during daylight hours than during nighttime hours and that more fatal crashes occurred during nighttime hours than during daylight hours. More precisely, less than a third of nonfatal crashes occurred during nighttime hours compared to more than half of fatal crashes.

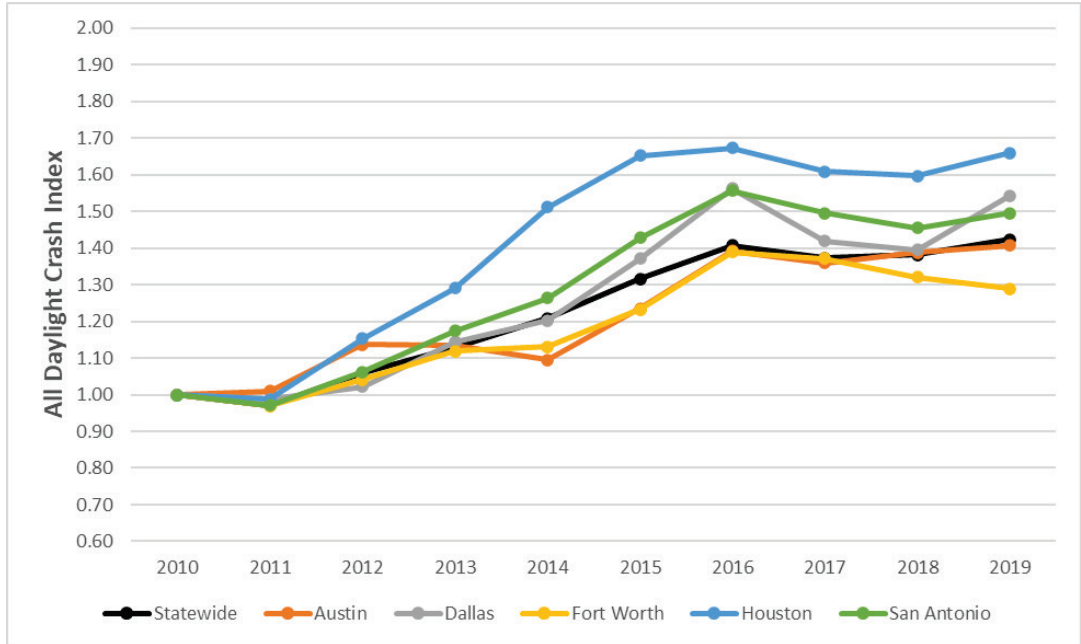
Using year 2010 as the base year for each metro area and the entire state, Figure 22 shows the annual relative variation in the number of *all* crashes. The figure shows separate charts for daylight crashes and nighttime crashes. Overall, Figure 22 shows the following:

- Statewide, daylight and nighttime crashes increased similarly (i.e., by about 40 percent).
- Changes for daylight crashes compared to changes for nighttime crashes from one year to the next were very similar in each metro area.
- Daylight crashes increased faster in Dallas, Houston, and San Antonio than the statewide trend. By comparison, daylight crashes increased more slowly in Fort Worth than the statewide trend and were about equal in Austin to the statewide trend.
- Nighttime crashes increased faster in Austin, Dallas, Houston, and San Antonio than the statewide trend. By comparison, nighttime crashes increased more slowly in Fort Worth than the statewide trend.

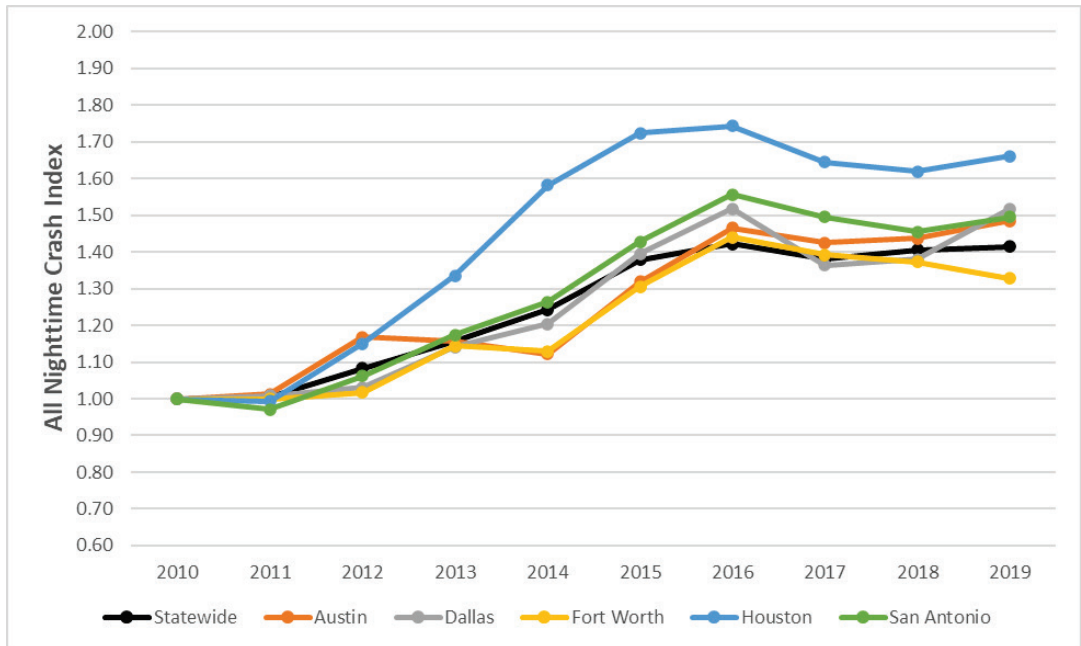
Using year 2010 as the base year for each metro area and the entire state, Figure 23 shows the annual relative variation in the number of *fatal* crashes. The figure shows separate charts for daylight crashes and nighttime crashes. Overall, Figure 23 shows the following:

- Statewide, daylight fatal crashes increased by about 12 percent from 2010 to 2019. However, daylight fatal crashes increased from 2010 to 2016, but then began to decrease.
- All five metro areas followed a trend similar to the statewide trend. However, daylight fatal crashes increased faster in all metro areas than the statewide trend. Daylight fatal crashes were about 45 percent higher in the Dallas area and about 52 percent higher in the Austin area.
- Statewide, nighttime fatal crashes increased by about 20 percent from 2010 to 2019. During the same period, nighttime fatal crashes increased faster in Austin, Dallas, and San Antonio than the statewide trend. Nighttime fatal crashes increased slower in Fort Worth and Houston than the statewide trend.
- From year to year, there were wide variations in the number of fatal crashes in each of the metro areas, but the variations were considerably wider for nighttime fatal crashes than for daylight fatal crashes. From the information available at this point, it is not clear why such wide yearly variations exist in the number of fatal crashes.

Daylight  
crashes

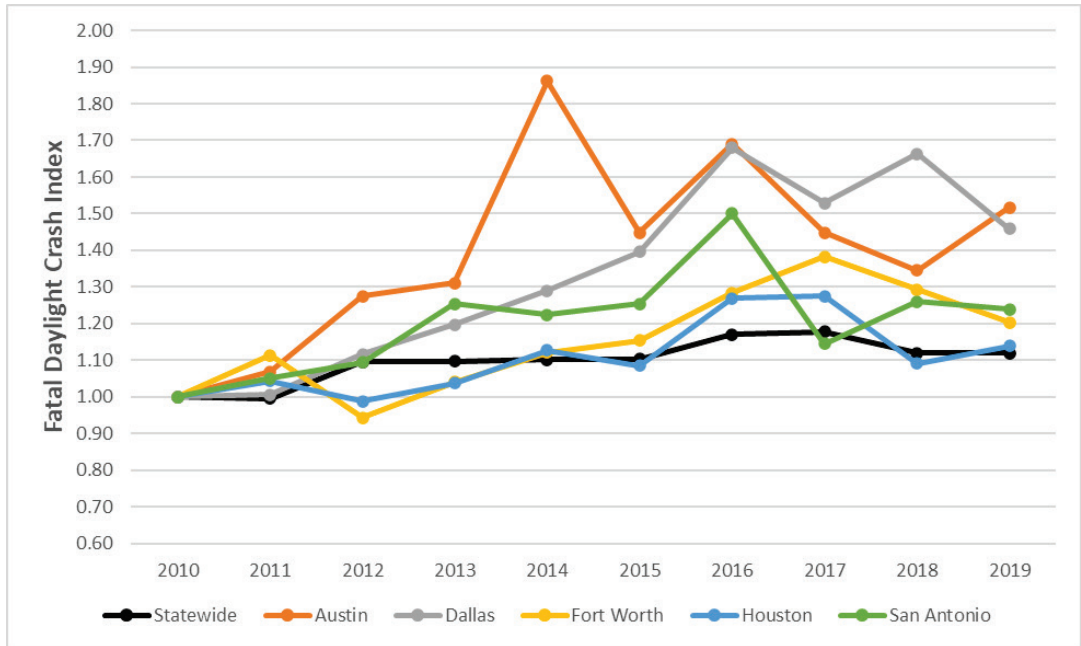


Nighttime  
crashes

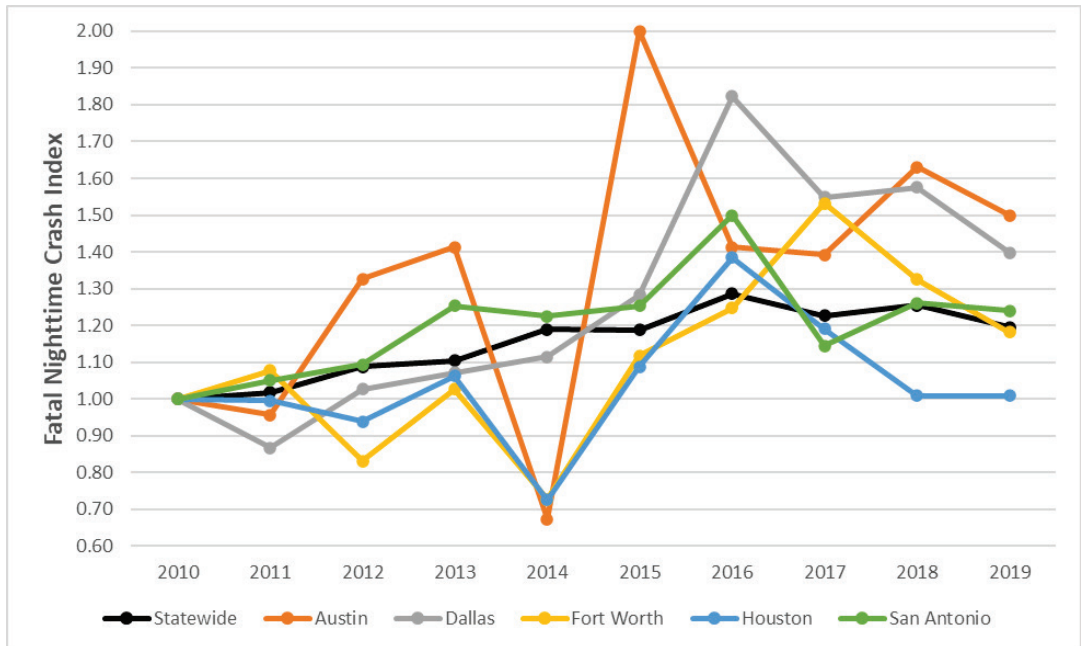


**Figure 22. Crash Index—Daylight vs. Nighttime Crashes.**

Daylight  
fatal  
crashes



Nighttime  
fatal  
crashes



**Figure 23. Crash Index—Daylight vs. Nighttime *Fatal* Crashes.**

### Crashes by Weather Condition

Most crashes occur when the weather is clear. Nevertheless, it was of interest to identify whether weather conditions might be associated with changes in the frequency of crashes (and fatal crashes).

Table 22 shows the distribution of crashes in Texas for all the weather conditions listed in the crash database from 2010 to 2019. Table 23 shows the total number of crashes statewide and in the five metro areas for each weather condition. Table 24 shows the corresponding percentages of crashes by weather condition. Table 25 shows the distribution of crashes in Texas after grouping weather conditions into three aggregated categories: one category for clear or cloudy weather conditions; a second category called inclement weather for rain, sleet, hail, snow, blowing sand or snow, severe crosswinds, and other weather conditions; and a third category for unknown weather conditions. Table 26 shows the corresponding distribution of percentages of crashes.

**Table 22. Number of All Crashes by Weather Condition—Statewide.**

Year	Clear	Cloudy	Rain	Sleet/Hail	Snow	Fog	Blowing Sand/Snow	Severe Crosswinds	Other	Unknown	Total
2010	290,656	55,737	38,254	431	2,390	1,512	165	257	303	2,342	<b>392,047</b>
2011	304,232	48,649	23,642	1,423	2,535	1,619	320	295	377	1,335	<b>384,427</b>
2012	318,630	59,548	33,088	359	1,046	2,273	235	247	232	2,086	<b>417,744</b>
2013	325,740	71,412	40,944	2,089	1,034	1,997	171	274	355	2,077	<b>446,093</b>
2014	343,207	83,209	40,468	3,108	2,047	2,459	253	260	439	2,252	<b>477,702</b>
2015	360,864	93,352	58,363	2,193	2,578	2,584	162	177	311	2,152	<b>522,736</b>
2016	406,863	90,690	50,145	179	228	2,437	130	231	211	2,219	<b>553,333</b>
2017	402,676	83,817	44,624	729	1,294	2,920	169	259	234	2,073	<b>538,795</b>
2018	387,908	89,930	58,100	1,655	619	2,842	201	261	312	2,704	<b>544,532</b>
2019	410,206	88,119	50,561	610	271	3,562	192	613	285	2,802	<b>557,221</b>
<b>Total</b>	<b>3,550,982</b>	<b>764,463</b>	<b>438,189</b>	<b>12,776</b>	<b>14,042</b>	<b>24,205</b>	<b>1,998</b>	<b>2,874</b>	<b>3,059</b>	<b>22,042</b>	<b>4,834,630</b>
<b>%</b>	<b>73.45%</b>	<b>15.81%</b>	<b>9.06%</b>	<b>0.26%</b>	<b>0.29%</b>	<b>0.50%</b>	<b>0.04%</b>	<b>0.06%</b>	<b>0.06%</b>	<b>0.46%</b>	<b>100.00%</b>

**Table 23. Number of All Crashes by Weather Condition (2010–2019).**

Region	Clear	Cloudy	Rain	Sleet/Hail	Snow	Fog	Blowing Sand/Snow	Severe Crosswinds	Other	Unknown	Total
Statewide	3,550,982	764,463	438,189	12,776	14,042	24,205	1,998	2,874	3,059	22,042	<b>4,834,630</b>
Austin Area	129,475	24,437	16,993	217	114	725	17	31	134	702	<b>172,845</b>
Dallas Area	331,851	69,148	44,537	1,064	1,653	962	99	115	391	1,098	<b>450,918</b>
Fort Worth Area	219,748	44,341	28,720	753	974	643	53	369	204	870	<b>296,675</b>
Houston Area	681,405	171,009	89,970	942	227	2,942	15	72	312	6,928	<b>953,822</b>
San Antonio Area	310,773	80,131	39,409	701	149	1,916	14	83	311	2,735	<b>436,222</b>

**Table 24. Percentage of All Crashes by Weather Condition (2010–2019).**

Region	Clear	Cloudy	Rain	Sleet/Hail	Snow	Fog	Blowing Sand/Snow	Severe Crosswinds	Other	Unknown	Total
Statewide	73.45%	15.81%	9.06%	0.26%	0.29%	0.50%	0.04%	0.06%	0.06%	0.46%	<b>100.00%</b>
Austin Area	74.91%	14.14%	9.83%	0.13%	0.07%	0.42%	0.01%	0.02%	0.08%	0.41%	<b>100.00%</b>
Dallas Area	73.59%	15.33%	9.88%	0.24%	0.37%	0.21%	0.02%	0.03%	0.09%	0.24%	<b>100.00%</b>
Fort Worth Area	74.07%	14.95%	9.68%	0.25%	0.33%	0.22%	0.02%	0.12%	0.07%	0.29%	<b>100.00%</b>
Houston Area	71.44%	17.93%	9.43%	0.10%	0.02%	0.31%	0.00%	0.01%	0.03%	0.73%	<b>100.00%</b>
San Antonio Area	71.24%	18.37%	9.03%	0.16%	0.03%	0.44%	0.00%	0.02%	0.07%	0.63%	<b>100.00%</b>

**Table 25. Number of All Crashes by Aggregated Weather Condition (2010–2019).**

Region	Clear or Cloudy	Inclement Weather	Unknown	Total
Statewide	4,315,445	497,143	22,042	<b>4,834,630</b>
Austin	153,912	18,231	702	<b>172,845</b>
Dallas	400,999	48,821	1,098	<b>450,918</b>
Fort Worth	264,089	31,716	870	<b>296,675</b>
Houston	852,414	94,480	6,928	<b>953,822</b>
San Antonio	390,904	42,583	2,735	<b>436,222</b>

**Table 26. Percentage of *All* Crashes by Aggregated Weather Condition (2010–2019).**

Region	Clear or Cloudy	Inclement Weather	Unknown	Total
Statewide	89.26%	10.28%	0.46%	<b>100.00%</b>
Austin	89.05%	10.55%	0.41%	<b>100.00%</b>
Dallas	88.93%	10.83%	0.24%	<b>100.00%</b>
Fort Worth	89.02%	10.69%	0.29%	<b>100.00%</b>
Houston	89.37%	9.91%	0.73%	<b>100.00%</b>
San Antonio	89.61%	9.76%	0.63%	<b>100.00%</b>

Table 27 shows the distribution of *fatal* crashes in Texas for all the weather conditions listed in the crash database from 2010 to 2019. Table 28 shows the total number of fatal crashes statewide and in the five metro areas for each weather condition. Table 29 shows the corresponding percentages of crashes by weather condition. Table 30 shows the distribution of crashes in Texas after grouping weather conditions into the three aggregated categories mentioned previously. Table 31 shows the corresponding distribution of percentages of crashes.

**Table 27. Number of *Fatal* Crashes by Weather Condition—Statewide.**

Year	Clear	Cloudy	Rain	Sleet/Hail	Snow	Fog	Blowing Sand/Snow	Severe Crosswinds	Other	Unknown	Total
2010	2,117	424	180	3	8	35	-	3	4	7	<b>2,781</b>
2011	2,254	363	113	12	8	20	4	7	6	15	<b>2,802</b>
2012	2,358	452	142	1	5	52	3	8	5	11	<b>3,037</b>
2013	2,297	480	211	17	5	36	3	4	4	6	<b>3,063</b>
2014	2,330	583	191	10	2	54	2	9	4	7	<b>3,192</b>
2015	2,218	617	281	12	7	44	2	2	1	9	<b>3,193</b>
2016	2,537	606	222	1	1	45	1	2	2	7	<b>3,424</b>
2017	2,488	523	241	5	5	64	2	4	6	9	<b>3,347</b>
2018	2,363	606	270	7	3	48	2	5	3	6	<b>3,313</b>
2019	2,323	588	230	1	-	69	2	2	5	4	<b>3,224</b>
<b>Total</b>	<b>23,285</b>	<b>5,242</b>	<b>2,081</b>	<b>69</b>	<b>44</b>	<b>467</b>	<b>21</b>	<b>46</b>	<b>40</b>	<b>81</b>	<b>31,376</b>
<b>%</b>	<b>74.21%</b>	<b>16.71%</b>	<b>6.63%</b>	<b>0.22%</b>	<b>0.14%</b>	<b>1.49%</b>	<b>0.07%</b>	<b>0.15%</b>	<b>0.13%</b>	<b>0.26%</b>	<b>100.00%</b>

**Table 28. Number of *Fatal* Crashes by Weather Condition (2010–2019).**

Region	Clear	Cloudy	Rain	Sleet/Hail	Snow	Fog	Blowing Sand/Snow	Severe Crosswinds	Other	Unknown	Total
Statewide	23,285	5,242	2,081	69	44	467	21	46	40	81	<b>31,376</b>
Austin Area	762	170	68	3	-	7	-	3	-	4	<b>1,017</b>
Dallas Area	1,709	402	157	1	2	10	-	1	7	5	<b>2,294</b>
Fort Worth Area	1,090	211	98	5	-	1	-	1	3	10	<b>1,419</b>
Houston Area	2,634	848	213	1	-	29	-	1	2	10	<b>3,738</b>
San Antonio Area	1,206	311	115	1	-	17	-	-	2	7	<b>1,659</b>

**Table 29. Percentage of *Fatal* Crashes by Weather Condition (2010–2019).**

Region	Clear	Cloudy	Rain	Sleet/Hail	Snow	Fog	Blowing Sand/Snow	Severe Crosswinds	Other	Unknown	Total
Statewide	74.21%	16.71%	6.63%	0.22%	0.14%	1.49%	0.07%	0.15%	0.13%	0.26%	<b>100.00%</b>
Austin Area	74.93%	16.72%	6.69%	0.29%	0.00%	0.69%	0.00%	0.29%	0.00%	0.39%	<b>100.00%</b>
Dallas Area	74.50%	17.52%	6.84%	0.04%	0.09%	0.44%	0.00%	0.04%	0.31%	0.22%	<b>100.00%</b>
Fort Worth Area	76.81%	14.87%	6.91%	0.35%	0.00%	0.07%	0.00%	0.07%	0.21%	0.70%	<b>100.00%</b>
Houston Area	70.47%	22.69%	5.70%	0.03%	0.00%	0.78%	0.00%	0.03%	0.05%	0.27%	<b>100.00%</b>
San Antonio Area	72.69%	18.75%	6.93%	0.06%	0.00%	1.02%	0.00%	0.00%	0.12%	0.42%	<b>100.00%</b>

**Table 30. Number of *Fatal* Crashes by Aggregated Weather Condition (2010–2019).**

Region	Clear or Cloudy	Inclement Weather	Unknown	Total
Statewide	28,527	2,768	81	<b>31,376</b>
Austin	932	81	4	<b>1,017</b>
Dallas	2,111	178	5	<b>2,294</b>
Fort Worth	1,301	108	10	<b>1,419</b>
Houston	3,482	246	10	<b>3,738</b>
San Antonio	1,517	135	7	<b>1,659</b>

**Table 31. Percentage of *Fatal* Crashes by Aggregated Weather Condition (2010–2019).**

Region	Clear or Cloudy	Inclement Weather	Unknown	Total
Statewide	90.92%	8.82%	0.26%	<b>100.00%</b>
Austin	91.64%	7.96%	0.39%	<b>100.00%</b>
Dallas	92.02%	7.76%	0.22%	<b>100.00%</b>
Fort Worth	91.68%	7.61%	0.70%	<b>100.00%</b>
Houston	93.15%	6.58%	0.27%	<b>100.00%</b>
San Antonio	91.44%	8.14%	0.42%	<b>100.00%</b>

Table 22 through Table 26 reveal the following:

- Of the 4.8 million crashes in Texas from 2010–2019, 4.3 million crashes (or 89.3 percent) occurred under clear or cloudy weather conditions. Only 10.3 percent of crashes occurred under any kind of inclement weather.
- Other than clear or cloudy, the most common weather condition both statewide and for each metro area was rain. Between 9 and 10 percent of crashes in the state occurred under rainy weather conditions. All other weather conditions combined were associated with less than 1 percent of all crashes.
- Certain weather conditions were related to a geographic location. For example, the percentage of all crashes that occurred under sleet, hail, or snow was considerably higher in Dallas and Fort Worth than in Austin, Houston, or San Antonio. Overall, the percentage of inclement weather-related crashes was slightly higher in Dallas and Fort Worth (10.8 percent and 10.7 percent, respectively) than in Austin (10.6 percent), Houston (9.9 percent), and San Antonio (9.8 percent).

Table 27 through Table 31 show the following:

- Of the 31,376 fatal crashes in Texas from 2010–2019, 28,527 fatal crashes (or 90.9 percent) occurred under clear or cloudy weather conditions. Only 8.8 percent of fatal crashes occurred under any kind of inclement weather. This percentage was lower than the corresponding percentage for all crashes in the state (i.e., 10.3 percent).
- Other than clear or cloudy, the most common weather condition both statewide and for each metro area was rain. Between 5.7 and 6.9 percent of fatal crashes in the state occurred under rainy weather conditions. This percentage was lower than the corresponding percentage for all crashes in the state (i.e., between 9 and 10 percent).



- All other weather conditions combined were associated with roughly 2 percent of fatal crashes. This percentage was higher than the corresponding percentage for all crashes in the state (i.e., less than 1 percent).
- No consistent trend was observed regarding geographic location with respect to weather conditions and fatal crashes. For example, the lowest percentage for rain was in Houston (5.7 percent), but the highest percentage for fog was in San Antonio (1 percent).

### Crashes by Surface Condition

Most crashes occur when the road surface is dry. As in the case of weather conditions, it was of interest to identify whether road surface conditions could be associated with changes in the frequency of crashes (and fatal crashes).

Table 32 shows the distribution of crashes in Texas for all the road surface conditions listed in the crash database from 2010 to 2019. Table 33 shows the total number of crashes statewide and in the five metro areas for each surface condition. Table 34 shows the corresponding percentages of crashes by surface condition. Table 35 shows the distribution of crashes in Texas after grouping surface conditions into three aggregated categories: one category for dry surface conditions; a second category called abnormal surface for wet, standing water, slush, ice, snow, sand, mud, dirt and other surface conditions; and a third category for unknown surface conditions. Table 36 shows the corresponding distribution of percentages of crashes.

**Table 32. Number of All Crashes by Surface Condition—Statewide.**

Year	Dry	Wet	Standing Water	Slush	Ice	Snow	Sand, Mud, Dirt	Other	Unknown	Total
2010	329,571	51,889	1,915	859	2,443	1,040	1,538	544	2,248	<b>392,047</b>
2011	339,594	33,062	979	475	5,915	919	1,614	629	1,240	<b>384,427</b>
2012	364,303	45,496	1,840	260	1,192	447	1,651	676	1,879	<b>417,744</b>
2013	378,375	55,985	2,069	488	4,582	461	1,538	752	1,843	<b>446,093</b>
2014	406,545	57,037	1,973	307	6,516	1,088	1,505	722	2,009	<b>477,702</b>
2015	428,727	78,448	3,981	790	5,610	1,159	1,441	700	1,880	<b>522,736</b>
2016	475,418	70,104	3,164	45	382	109	1,395	788	1,928	<b>553,333</b>
2017	467,040	62,772	2,497	157	1,956	516	1,360	724	1,773	<b>538,795</b>
2018	451,294	81,468	3,482	264	3,182	236	1,431	984	2,191	<b>544,532</b>
2019	476,023	72,174	2,861	96	1,259	118	1,376	636	2,678	<b>557,221</b>
<b>Total</b>	<b>4,116,890</b>	<b>608,435</b>	<b>24,761</b>	<b>3,741</b>	<b>33,037</b>	<b>6,093</b>	<b>14,849</b>	<b>7,155</b>	<b>19,669</b>	<b>4,834,630</b>
<b>%</b>	<b>85.15%</b>	<b>12.58%</b>	<b>0.51%</b>	<b>0.08%</b>	<b>0.68%</b>	<b>0.13%</b>	<b>0.31%</b>	<b>0.15%</b>	<b>0.41%</b>	<b>100.00%</b>

**Table 33. Number of All Crashes by Surface Condition (2010–2019).**

Region	Dry	Wet	Standing Water	Slush	Ice	Snow	Sand, Mud, Dirt	Other	Unknown	Total
Statewide	4,116,890	608,435	24,761	3,741	33,037	6,093	14,849	7,155	19,669	<b>4,834,630</b>
Austin Area	147,101	24,031	435	40	334	37	100	139	628	<b>172,845</b>
Dallas Area	381,992	60,167	2,453	453	3,722	622	269	315	925	<b>450,918</b>
Fort Worth Area	252,089	38,976	1,295	274	2,331	486	196	237	791	<b>296,675</b>
Houston Area	816,305	123,550	4,409	87	1,567	59	372	450	7,023	<b>953,822</b>
San Antonio Area	372,260	57,246	1,983	36	962	64	270	433	2,968	<b>436,222</b>

**Table 34. Percentage of *All* Crashes by Surface Condition (2010–2019).**

Region	Dry	Wet	Standing Water	Slush	Ice	Snow	Sand, Mud, Dirt	Other	Unknown	Total
Statewide	85.15%	12.58%	0.51%	0.08%	0.68%	0.13%	0.31%	0.15%	0.41%	100.00%
Austin Area	85.11%	13.90%	0.25%	0.02%	0.19%	0.02%	0.06%	0.08%	0.36%	100.00%
Dallas Area	84.71%	13.34%	0.54%	0.10%	0.83%	0.14%	0.06%	0.07%	0.21%	100.00%
Fort Worth Area	84.97%	13.14%	0.44%	0.09%	0.79%	0.16%	0.07%	0.08%	0.27%	100.00%
Houston Area	85.58%	12.95%	0.46%	0.01%	0.16%	0.01%	0.04%	0.05%	0.74%	100.00%
San Antonio Area	85.34%	13.12%	0.45%	0.01%	0.22%	0.01%	0.06%	0.10%	0.68%	100.00%

**Table 35. Number of *All* Crashes by Aggregated Surface Condition (2010–2019).**

Region	Dry	Abnormal	Unknown	Total
Statewide	4,116,890	698,071	19,669	4,834,630
Austin	147,101	25,116	628	172,845
Dallas	381,992	68,001	925	450,918
Fort Worth	252,089	43,795	791	296,675
Houston	816,305	130,494	7,023	953,822
San Antonio	372,260	60,994	2,968	436,222

**Table 36. Percentage of *All* Crashes by Aggregated Surface Condition (2010–2019).**

Region	Dry	Abnormal	Unknown	Total
Statewide	85.15%	14.44%	0.41%	100.00%
Austin	85.11%	14.53%	0.36%	100.00%
Dallas	84.71%	15.08%	0.21%	100.00%
Fort Worth	84.97%	14.76%	0.27%	100.00%
Houston	85.58%	13.68%	0.74%	100.00%
San Antonio	85.34%	13.98%	0.68%	100.00%

Table 37 shows the distribution of *fatal* crashes in Texas for all the surface conditions listed in the crash database from 2010 to 2019. Table 38 shows the total number of fatal crashes statewide and in the five metro areas for each surface condition. Table 39 shows the corresponding percentages of crashes by surface condition. Table 40 shows the distribution of crashes in Texas after grouping surface conditions into the three aggregated categories mentioned previously. Table 41 shows the corresponding distribution of percentages of crashes.

**Table 37. Number of *Fatal* Crashes by Surface Condition—Statewide.**

Year	Dry	Wet	Standing Water	Slush	Ice	Snow	Sand, Mud, Dirt	Other	Unknown	Total
2010	2,444	270	11	4	7	4	25	10	6	<b>2,781</b>
2011	2,548	176	6	3	22	4	18	12	13	<b>2,802</b>
2012	2,753	223	16	2	5	2	24	4	8	<b>3,037</b>
2013	2,688	292	11	2	28	3	25	9	5	<b>3,063</b>
2014	2,839	280	10	1	25	1	20	12	4	<b>3,192</b>
2015	2,695	410	20	2	29	3	16	6	12	<b>3,193</b>
2016	3,038	332	14	-	-	-	22	10	8	<b>3,424</b>
2017	2,957	330	19	-	12	-	12	6	11	<b>3,347</b>
2018	2,838	397	23	1	18	-	22	8	6	<b>3,313</b>
2019	2,799	375	16	2	7	-	16	5	4	<b>3,224</b>
<b>Total</b>	<b>27,599</b>	<b>3,085</b>	<b>146</b>	<b>17</b>	<b>153</b>	<b>17</b>	<b>200</b>	<b>82</b>	<b>77</b>	<b>31,376</b>
<b>%</b>	<b>87.96%</b>	<b>9.83%</b>	<b>0.47%</b>	<b>0.05%</b>	<b>0.49%</b>	<b>0.05%</b>	<b>0.64%</b>	<b>0.26%</b>	<b>0.25%</b>	<b>100.00%</b>

**Table 38. Number of *Fatal* Crashes by Surface Condition (2010–2019).**

Region	Dry	Wet	Standing Water	Slush	Ice	Snow	Sand, Mud, Dirt	Other	Unknown	Total
Statewide	27,599	3,085	146	17	153	17	200	82	77	<b>31,376</b>
Austin Area	896	109	4	-	4	-	1	1	2	<b>1,017</b>
Dallas Area	2,034	230	7	-	5	-	1	11	6	<b>2,294</b>
Fort Worth Area	1,249	140	3	1	9	-	2	8	7	<b>1,419</b>
Houston Area	3,369	341	12	-	4	1	-	1	10	<b>3,738</b>
San Antonio Area	1,471	178	2	-	-	-	-	1	7	<b>1,659</b>

**Table 39. Percentage of *Fatal* Crashes by Surface Condition (2010–2019).**

Region	Dry	Wet	Standing Water	Slush	Ice	Snow	Sand, Mud, Dirt	Other	Unknown	Total
Statewide	87.96%	9.83%	0.47%	0.05%	0.49%	0.05%	0.64%	0.26%	0.25%	<b>100.00%</b>
Austin Area	88.10%	10.72%	0.39%	0.00%	0.39%	0.00%	0.10%	0.10%	0.20%	<b>100.00%</b>
Dallas Area	88.67%	10.03%	0.31%	0.00%	0.22%	0.00%	0.04%	0.48%	0.26%	<b>100.00%</b>
Fort Worth Area	88.02%	9.87%	0.21%	0.07%	0.63%	0.00%	0.14%	0.56%	0.49%	<b>100.00%</b>
Houston Area	90.13%	9.12%	0.32%	0.00%	0.11%	0.03%	0.00%	0.03%	0.27%	<b>100.00%</b>
San Antonio Area	88.67%	10.73%	0.12%	0.00%	0.00%	0.00%	0.00%	0.06%	0.42%	<b>100.00%</b>

**Table 40. Number of *Fatal* Crashes by Aggregated Surface Condition (2010–2019).**

Region	Dry	Abnormal	Unknown	Total
Statewide	27,599	3,700	77	<b>31,376</b>
Austin	896	119	2	<b>1,017</b>
Dallas	2,034	254	6	<b>2,294</b>
Fort Worth	1,249	163	7	<b>1,419</b>
Houston	3,369	359	10	<b>3,738</b>
San Antonio	1,471	181	7	<b>1,659</b>

**Table 41. Percentage of *Fatal* Crashes by Aggregate Surface Condition (2010–2019).**

Region	Dry	Abnormal	Unknown	Total
Statewide	87.96%	11.79%	0.25%	<b>100.00%</b>
Austin	88.10%	11.70%	0.20%	<b>100.00%</b>
Dallas	88.67%	11.07%	0.26%	<b>100.00%</b>
Fort Worth	88.02%	11.49%	0.49%	<b>100.00%</b>
Houston	90.13%	9.60%	0.27%	<b>100.00%</b>
San Antonio	88.67%	10.91%	0.42%	<b>100.00%</b>

Table 32 through Table 36 reveal the following:

- Of the 4.8 million crashes in Texas from 2010–2019, 4.1 million crashes (or 85.2 percent) occurred under dry surface conditions. Only 14.4 percent of crashes occurred under any kind of abnormal surface conditions.
- The most common surface condition both statewide and for each metro area was dry. Between 13 and 13.9 percent of crashes in the metro areas occurred under wet surface conditions. All other surface conditions combined were associated with less than 2 percent of all crashes.
- Certain weather conditions were related to a geographic location. For example, the percentage of all crashes that occurred under slush, ice, or snow was considerably higher in Dallas and Fort Worth than in Austin, Houston, or San Antonio. Overall, the percentage of abnormal surface -related crashes was slightly higher in Dallas and Fort Worth (15.1 percent and 14.8 percent, respectively) than in Austin (14.5 percent), Houston (13.7 percent), and San Antonio (14.0 percent).

Table 37 through Table 41 show the following:

- Of the 31,376 fatal crashes in Texas from 2010–2019, 27,599 fatal crashes (or 88.0 percent) occurred under dry surface conditions. Only 11.8 percent of fatal crashes occurred under any kind of abnormal surface conditions. This percentage was lower than the corresponding percentage for all crashes in the state (i.e., 14.4 percent).
- The most common abnormal surface condition both statewide and for each metro area was wet. Between 9.1 and 10.7 percent of fatal crashes in the metro areas occurred under wet surface conditions. This percentage was lower than the corresponding percentage for all crashes in the metro areas (i.e., between 13 and 13.9 percent).
- All other abnormal surface conditions combined were associated with between 0.2 and 1.6 percent of fatal crashes. This percentage was lower than the corresponding percentage for all crashes in the state (i.e., less than 2 percent).
- No consistent trend was observed regarding geographic location with respect to surface conditions and fatal crashes. For example, the lowest percentage for wet surface was in Houston (9.1 percent), but the percentage for ice was higher in Austin (0.4 percent) than in Dallas (0.2 percent).

## Crashes by Manner of Collision

CRIS contains data regarding manners of collision and crash-contributing factors for individual crashes, according to information included in the crash reports. This information is based on the responding officer's interpretation of what happened at the crash sites, not based on forensic or engineering analyses. Despite these caveats, a high-level review of the data offers insight as to potential crash causes.

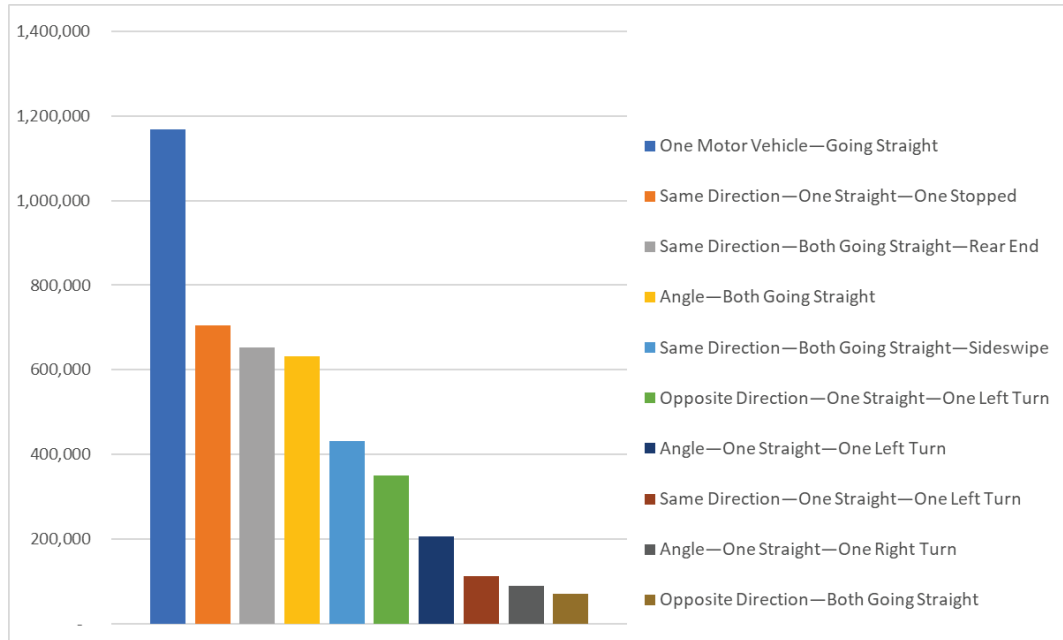
Figure 24 shows the top 10 manners of collision for *all* crashes from 2010 to 2019. By far, the most common manner of collision was a single motor vehicle going straight. Statewide, the second and third most common manners of collision were two vehicles going straight in the same direction, with either "one straight—one stopped" or "both going straight—rear end." Readers should note that a vehicle going straight does not mean the road alignment was straight. It just means the vehicle was not making a turn. A more detailed analysis is necessary to clarify the impact of roadway characteristics, such as horizontal and vertical alignments, curvature, cross-section characteristics, visibility restrictions, and pavement conditions.

The trends for individual metro areas were similar to the statewide trend. The exception was the Houston area, where one vehicle going straight was in third place behind two vehicles in the same direction with "both going straight—rear end" (most frequent manner of collision) and two vehicles at an angle with both going straight (second most frequent manner of collision).

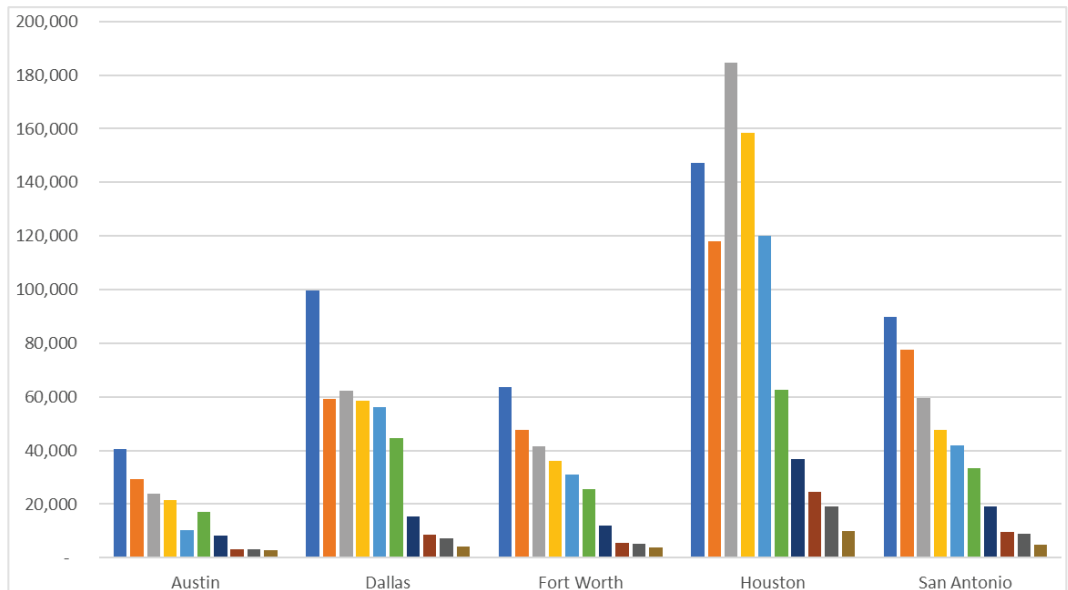
Figure 25 shows the top 10 manners of collision for *fatal* crashes from 2010 to 2019. By far, the most common manner of collision was a single motor vehicle going straight, as for all crashes. Other top 10 manners of collision ranked differently for fatal crashes than for all crashes. For fatal crashes, the second most common manner of collision was two vehicles going straight in the opposite direction. The third most common manner of collision was two vehicles going straight and crashing at an angle.

The trends for individual metro areas were similar to the statewide trend. The exceptions were the Houston and Dallas areas, where more fatal crashes had a manner of collision labeled "angle—both going straight" than "opposite direction—both going straight."

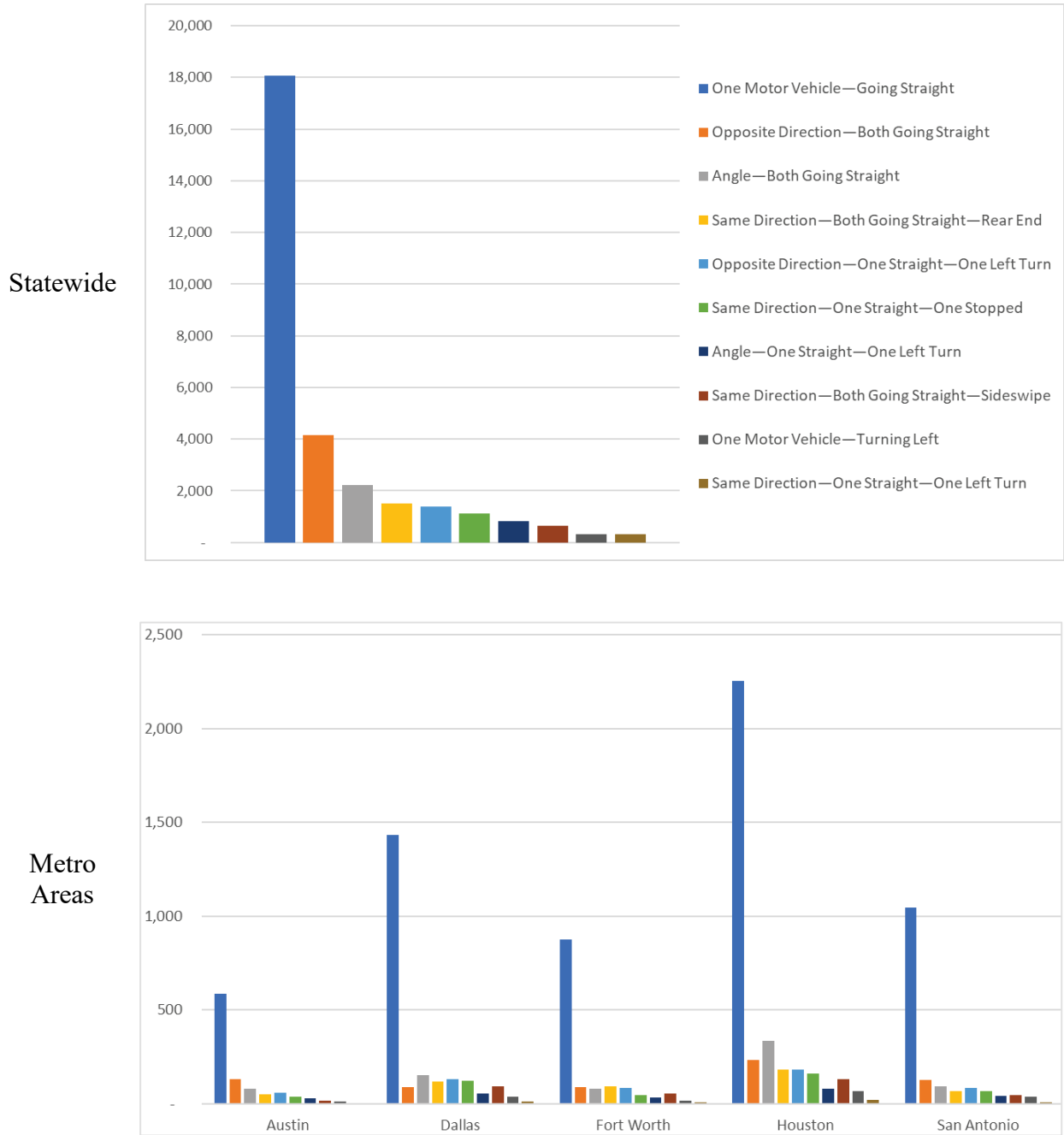
Statewide



Metro Areas



**Figure 24. Top 10 Manners of Collision for All Crashes (2010–2019 Crash Data).**



**Figure 25. Top 10 Manners of Collision for *Fatal* Crashes (2010-2019 Crash Data).**

**SPATIAL AND TEMPORAL DISTRIBUTIONS OF CRASHES**

The research team complemented the tabular crash data analysis in the previous section with an analysis in a geographic information system (GIS)–based environment to identify potential spatial and temporal trends in the occurrence of crashes. Because of the difficulty in observing meaningful trends at the statewide level, the focus of the GIS-based analysis was the five metro areas. The research team conducted the analysis using Esri™ ArcGIS™ Pro.

The research team prepared six series of maps as follows:

- Austin metro area (Travis County):
  - Separate maps for each year from 2010 to 2019.
  - For each year, heat maps representing the spatial distribution of all crashes.
  - Location of all fatal crashes overlaying the heat maps.
  - Separate maps for daylight and nighttime crashes.
- Dallas metro area (Dallas County):
  - Separate maps for each year from 2010 to 2019.
  - For each year, heat maps representing the spatial distribution of all crashes.
  - Location of all fatal crashes overlaying the heat maps.
  - Separate maps for daylight and nighttime crashes.
- Fort Worth metro area (Tarrant County):
  - Separate maps for each year from 2010 to 2019.
  - For each year, heat maps representing the spatial distribution of all crashes.
  - Location of all fatal crashes overlaying the heat maps.
  - Separate maps for daylight and nighttime crashes.
- Houston metro area (Harris County):
  - Separate maps for each year from 2010 to 2019.
  - For each year, heat maps representing the spatial distribution of all crashes.
  - Location of all fatal crashes overlaying the heat maps.
  - Separate maps for daylight and nighttime crashes.
- San Antonio metro area (Bexar County):
  - Separate maps for each year from 2010 to 2019.
  - For each year, heat maps representing the spatial distribution of all crashes.
  - Location of all fatal crashes overlaying the heat maps.
  - Separate maps for daylight and nighttime crashes.
- Fatal crashes from 2010 to 2019:
  - Heat maps representing the spatial distribution of all fatal crashes from 2010 to 2019.
  - Separate maps for daylight and nighttime fatal crashes.
  - Separate maps for clear weather and inclement weather fatal crashes.
  - Separate maps for dry surface and abnormal surface fatal crashes.

In total, the research team prepared 130 maps. To visualize trends more easily, the research team also prepared a PowerPoint file, with each slide containing a separate map. For all heat maps, the colors provided a visual representation of the spatial proximity between crashes (i.e., the spatial density of crashes). In the GIS, each crash was represented by an inverted 3D bell having a constant height and radius. With this information, the GIS generated a 3D surface for all crashes on the map. The colors represent all points on the map having the same combined elevation on the 3D surface. Yellow represents the highest density. Light blue represents the lowest density.



Due to space constraints, it is not possible to include all 130 maps. As an illustration, this report includes the following maps:

- 2019 crashes in the Austin metro area (Travis County) (Figure 26).
- 2019 crashes in the Dallas metro area (Dallas County) (Figure 27).
- 2019 crashes in the Fort Worth metro area (Tarrant County) (Figure 28).
- 2019 crashes in the Houston metro area (Harris County) (Figure 29).
- 2019 crashes in the San Antonio metro area (Bexar County) (Figure 30).
- 2010–2019 distribution of daylight and nighttime fatal crashes in the Austin metro area (Travis County) (Figure 31).
- 2010–2019 distribution of daylight and nighttime fatal crashes in the Dallas metro area (Dallas County) (Figure 32).
- 2010–2019 distribution of daylight and nighttime fatal crashes in the Fort Worth metro area (Tarrant County) (Figure 33).
- 2010–2019 distribution of daylight and nighttime fatal crashes in the Houston metro area (Harris County) (Figure 34).
- 2010–2019 distribution of daylight and nighttime fatal crashes in the San Antonio metro area (Bexar County) (Figure 35).

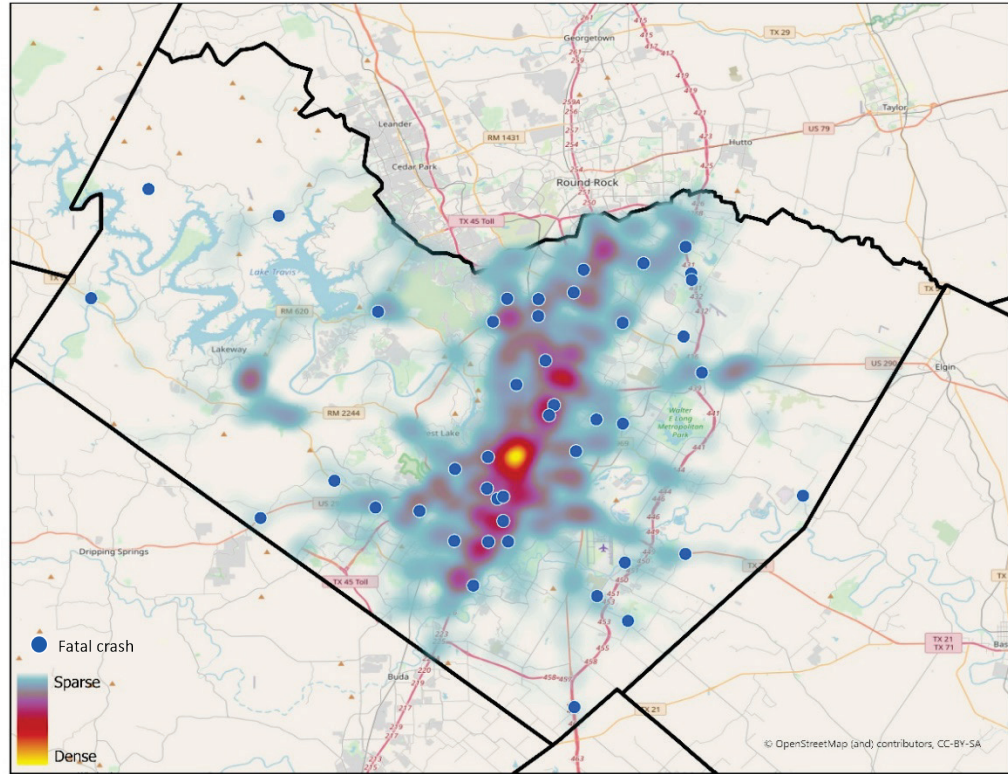
### **General Observations**

For all metro areas, differences existed between the heat maps representing daylight crashes and the heat maps representing nighttime crashes. Generally speaking, red and yellow areas representing a higher density of crashes occurred along major highways and the downtown area.

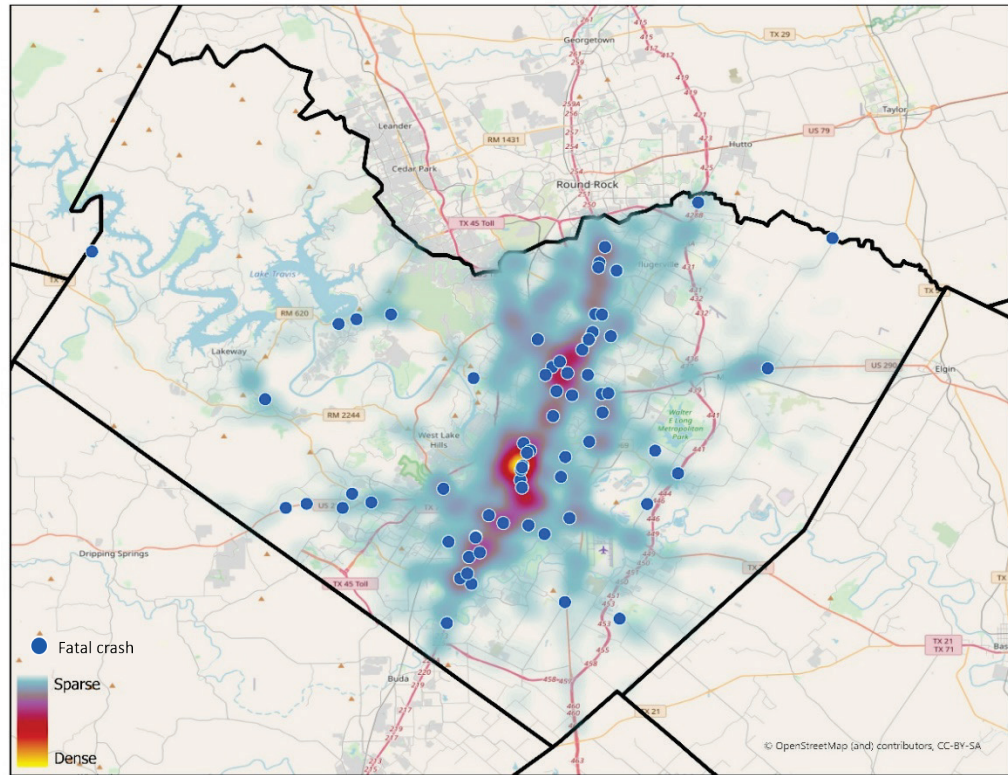
For all metro areas, crashes were widely distributed. The exception was the Austin area, where crashes were more concentrated within a relatively narrow zone around the IH-35 corridor.

For each year (regardless of metro area), the location of individual fatal crashes indicated a high degree of variability, confirming that fatal crashes are random events. In some cases, it was possible to identify some trends (e.g., some fatal crashes located along the same highway). However, just by looking at individual years, it is not possible to draw generalized conclusions.

Daylight  
Crashes

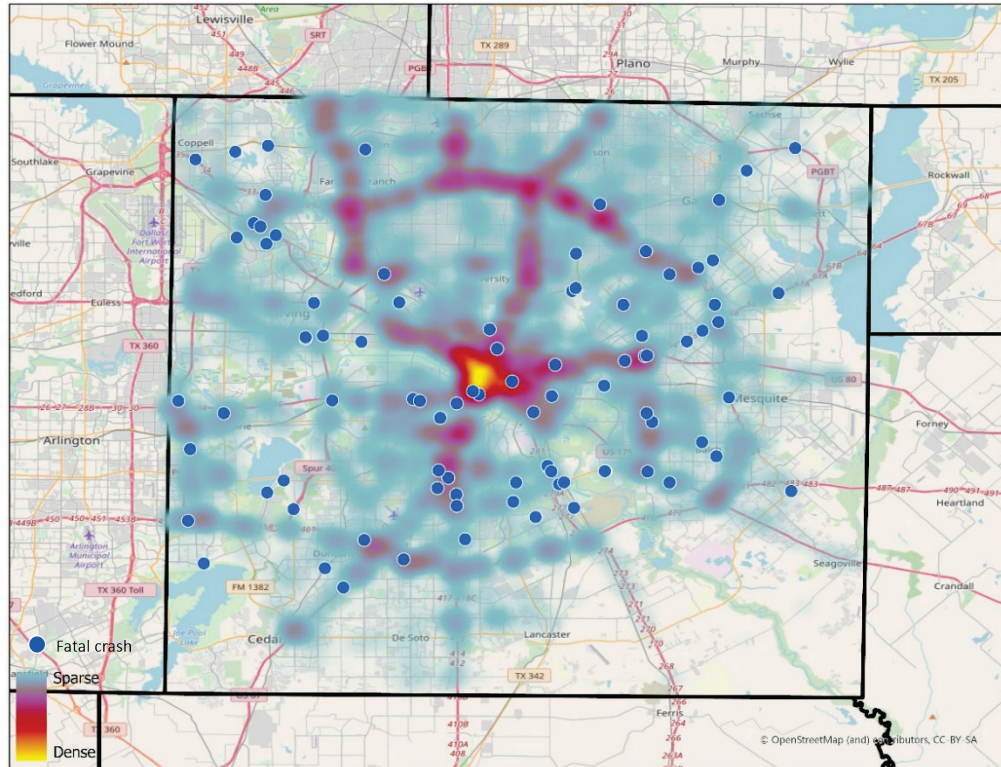


Nighttime  
Crashes

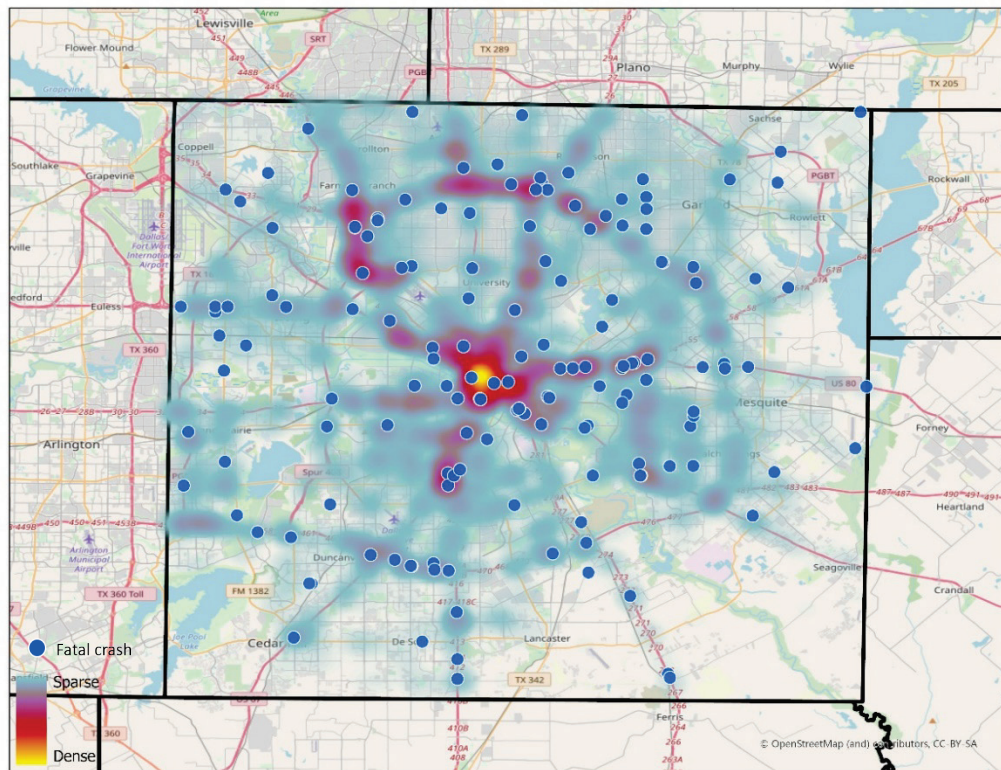


**Figure 26. 2019 Austin Area (Travis County) Crashes—Heat Map (All Crashes) and Fatal Crash Locations.**

Daylight  
Crashes

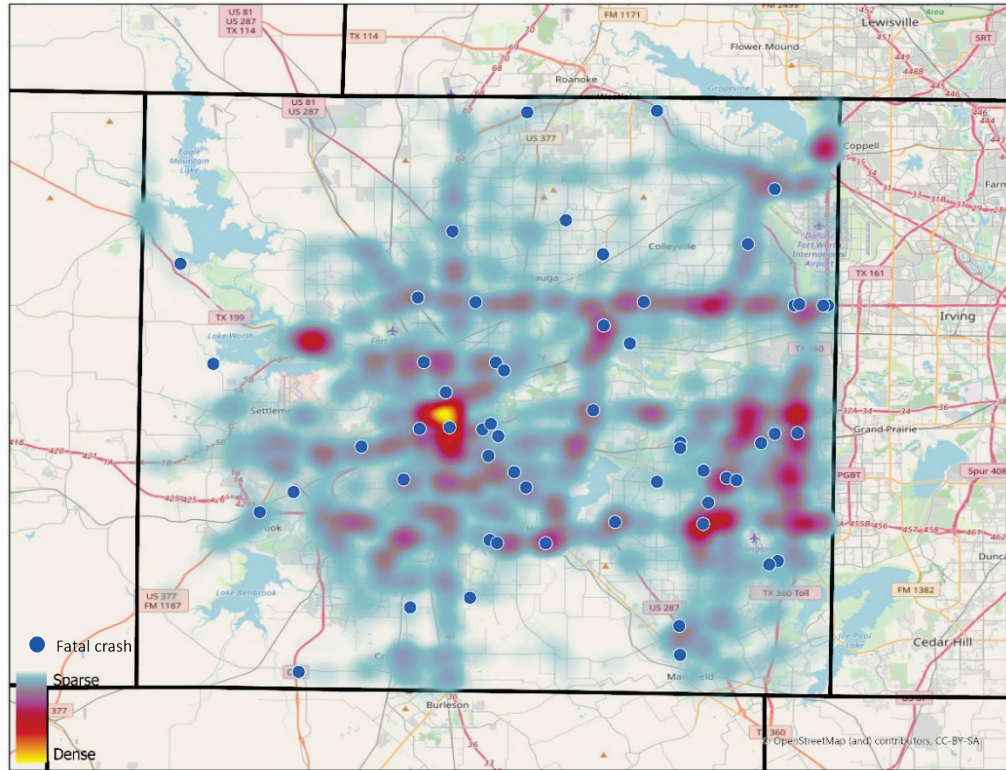


Nighttime  
Crashes

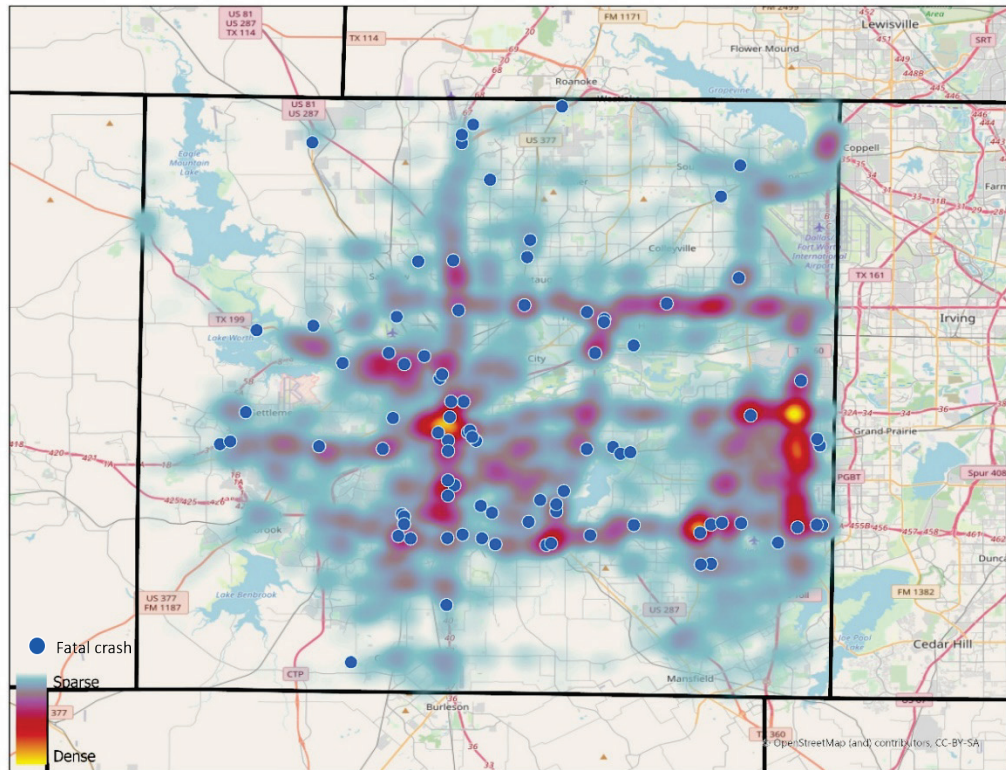


**Figure 27. 2019 Dallas Area (Dallas County) Crashes—Heat Map (All Crashes) and Fatal Crash Locations.**

Daylight  
Crashes

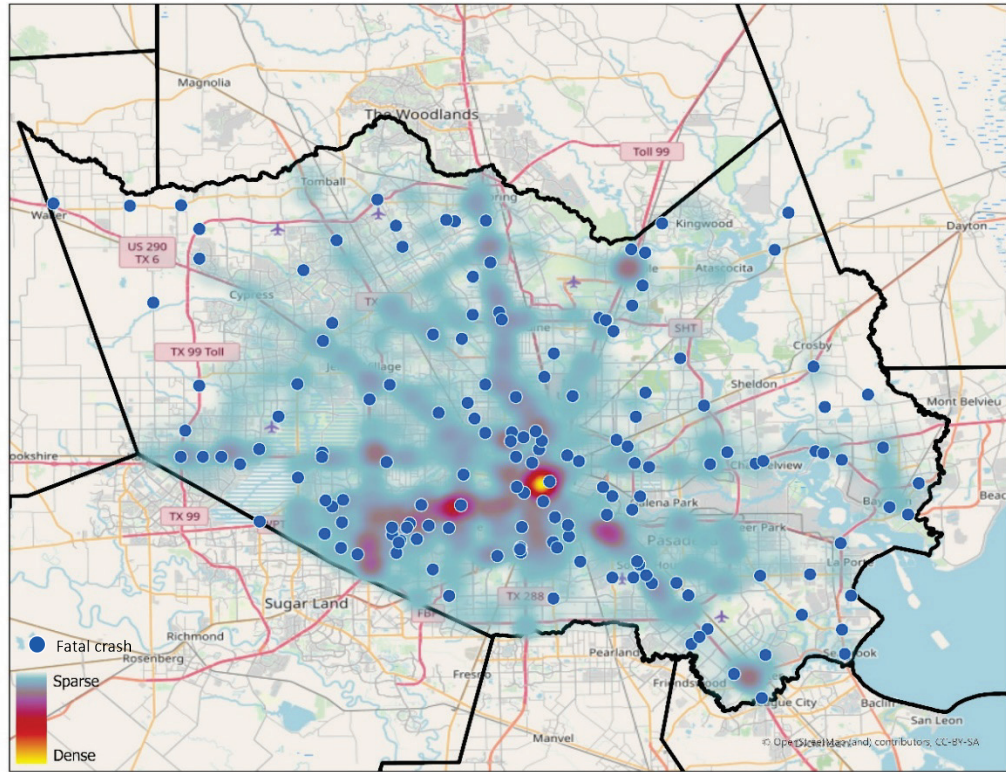


Nighttime  
Crashes

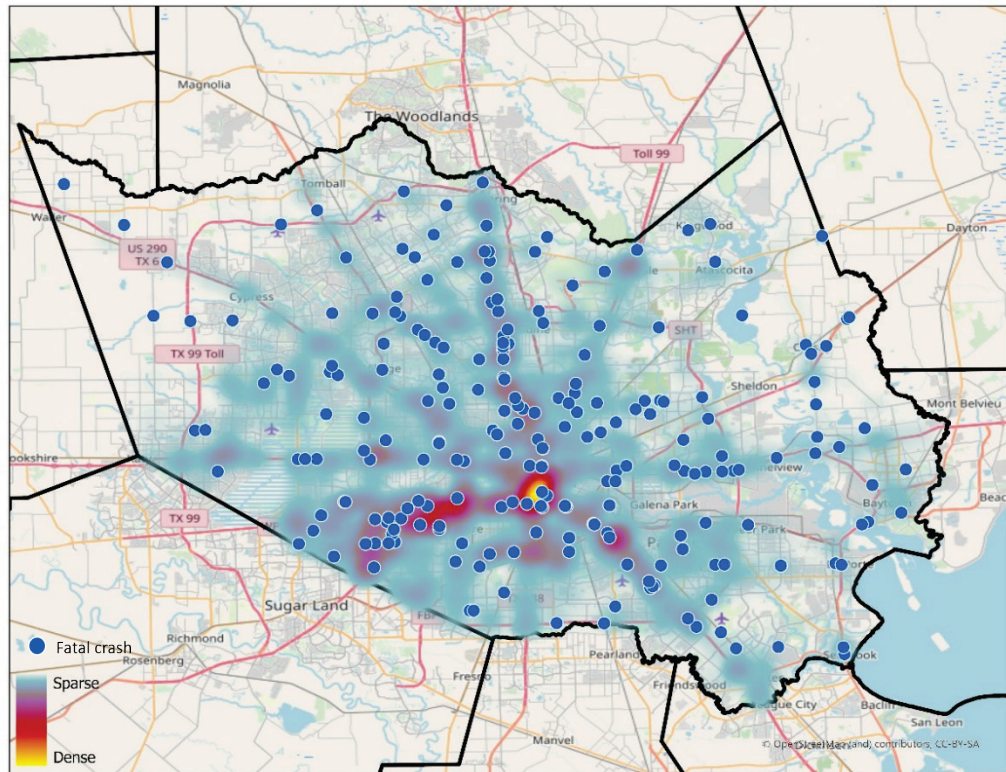


**Figure 28. 2019 Fort Worth Area (Tarrant County) Crashes—Heat Map (All Crashes) and Fatal Crash Locations.**

Daylight  
Crashes

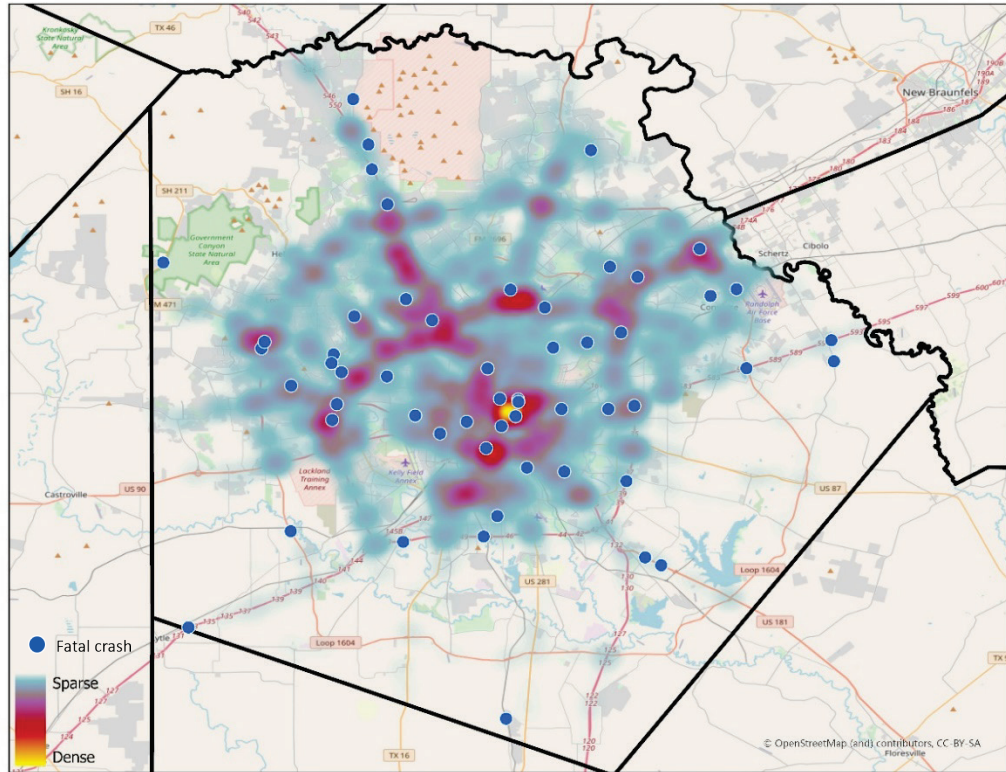


Nighttime  
Crashes

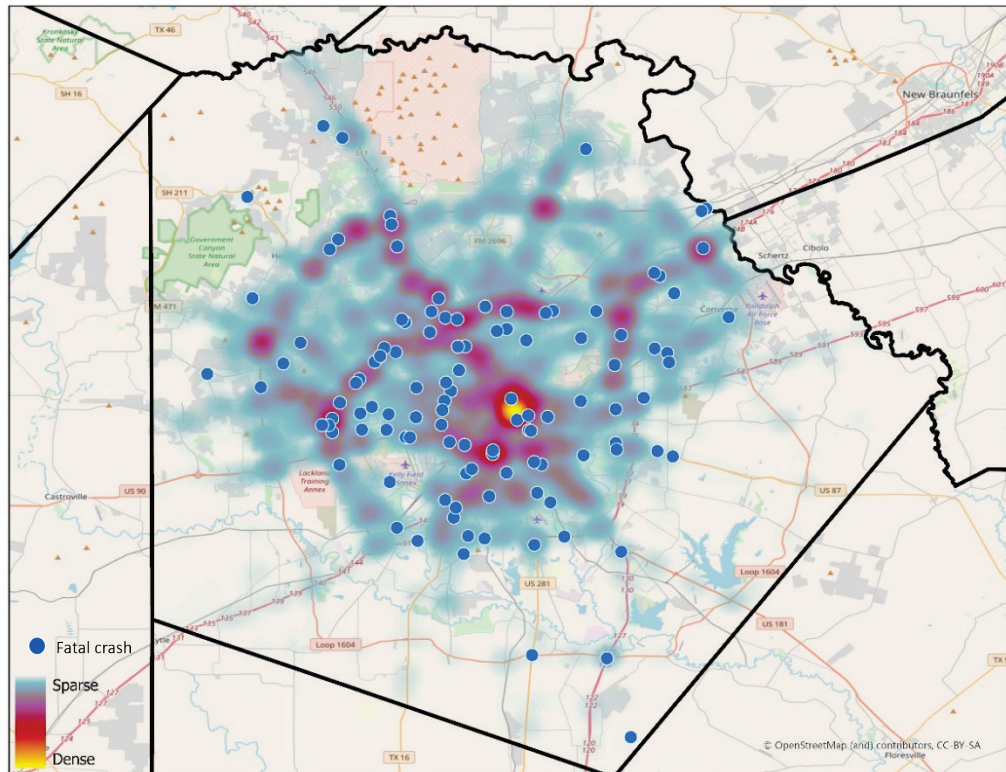


**Figure 29. 2019 Houston Area (Harris County) Crashes—Heat Map (All Crashes) and Fatal Crash Locations.**

Daylight  
Crashes

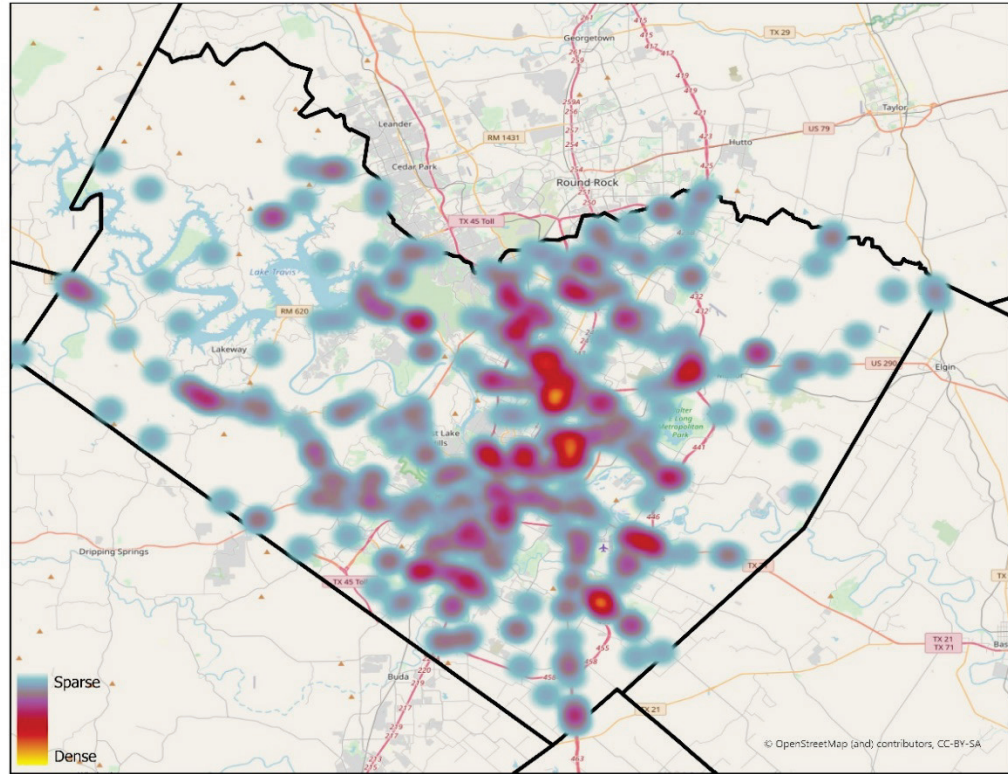


Nighttime  
Crashes

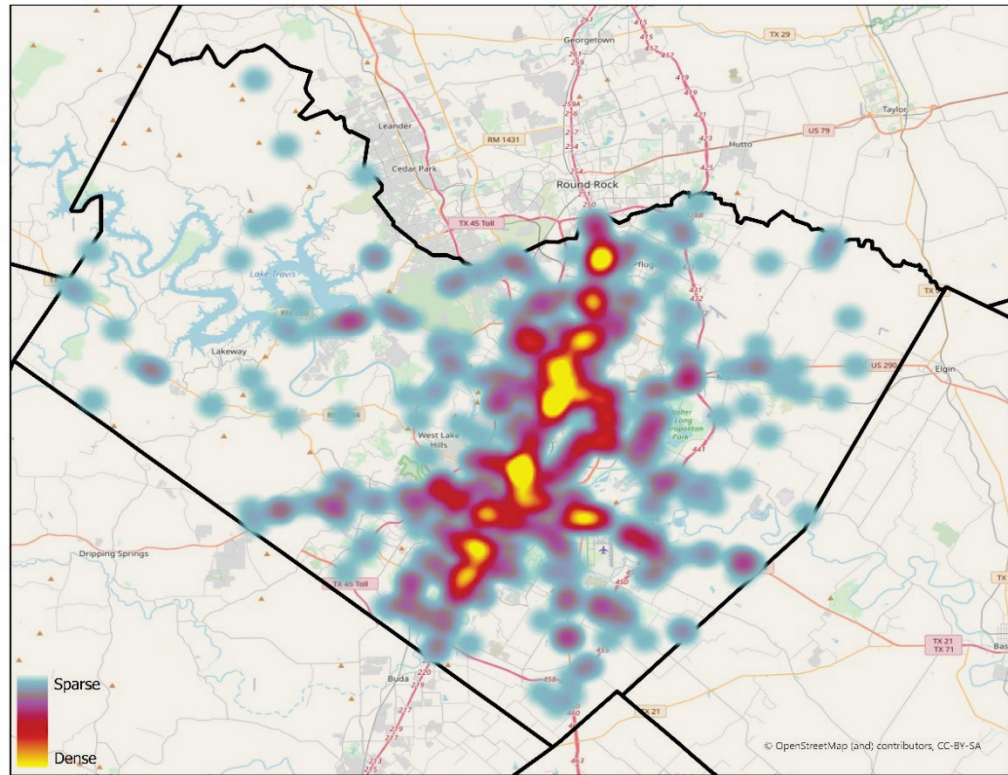


**Figure 30. 2019 San Antonio Area (Bexar County) Crashes—Heat Map (All Crashes) and Fatal Crash Locations.**

Daylight  
Fatal  
Crashes

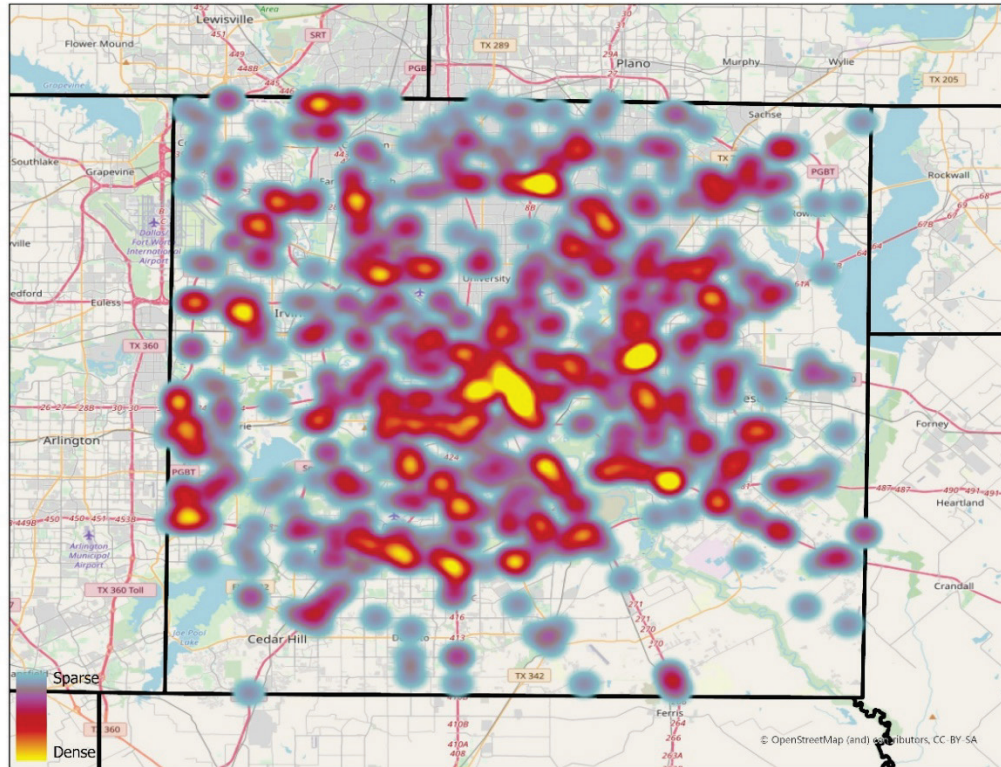


Nighttime  
Fatal  
Crashes

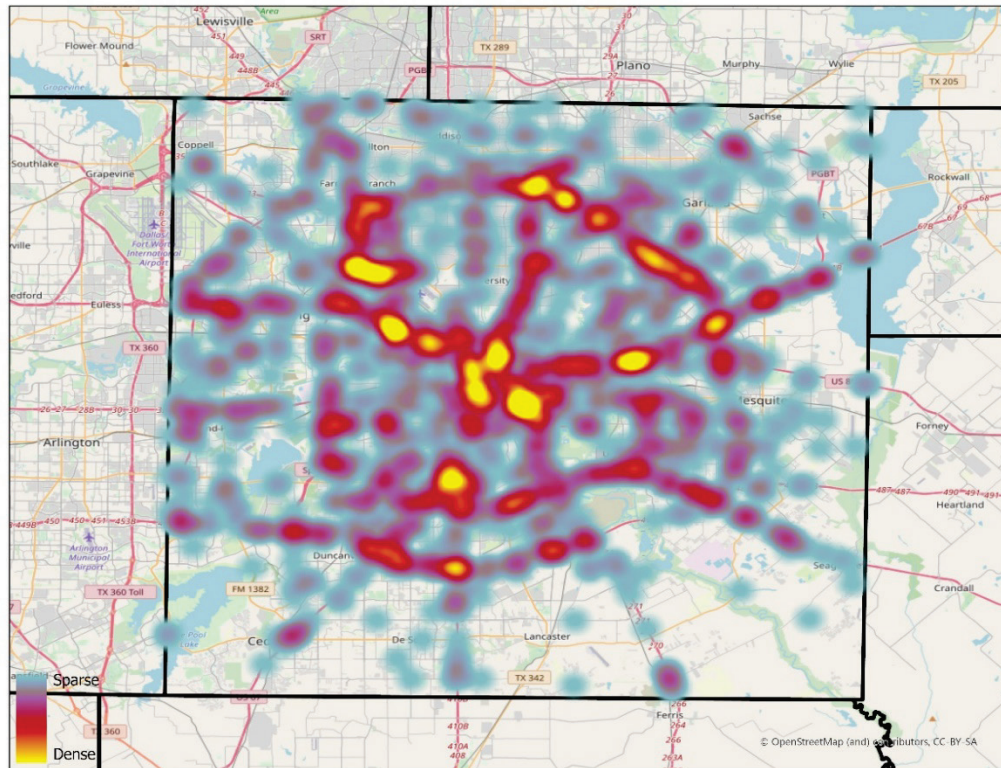


**Figure 31. 2010–2019 Daylight/Nighttime Fatal Crashes in the Austin Area (Travis County).**

Daylight  
Fatal  
Crashes



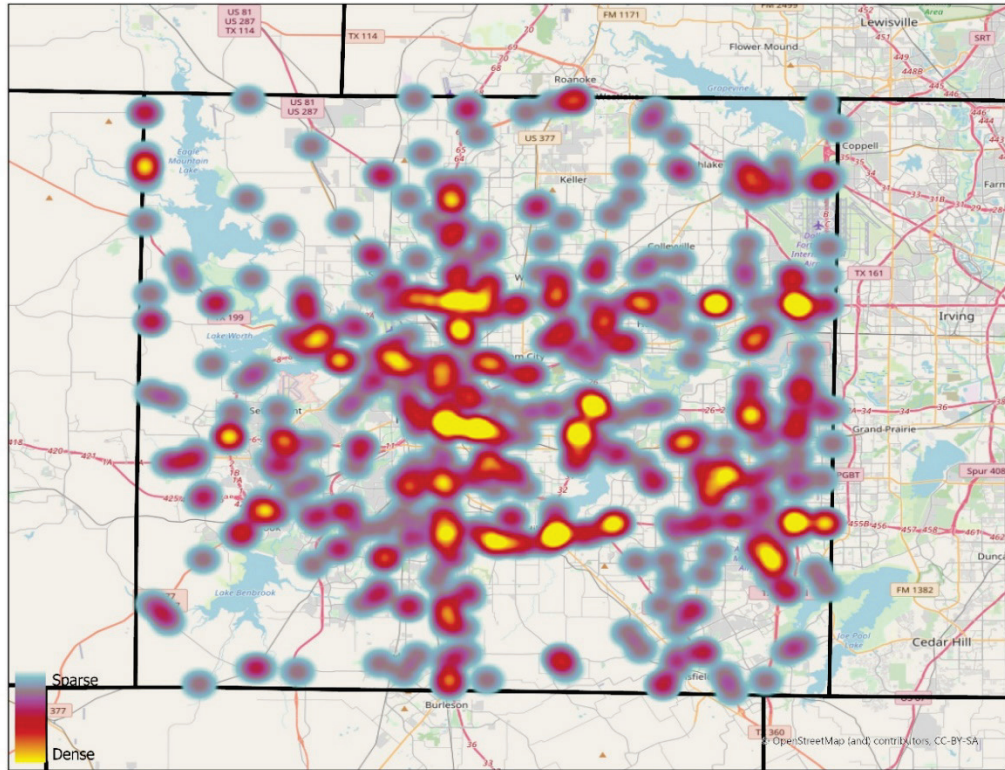
Nighttime  
Fatal  
Crashes



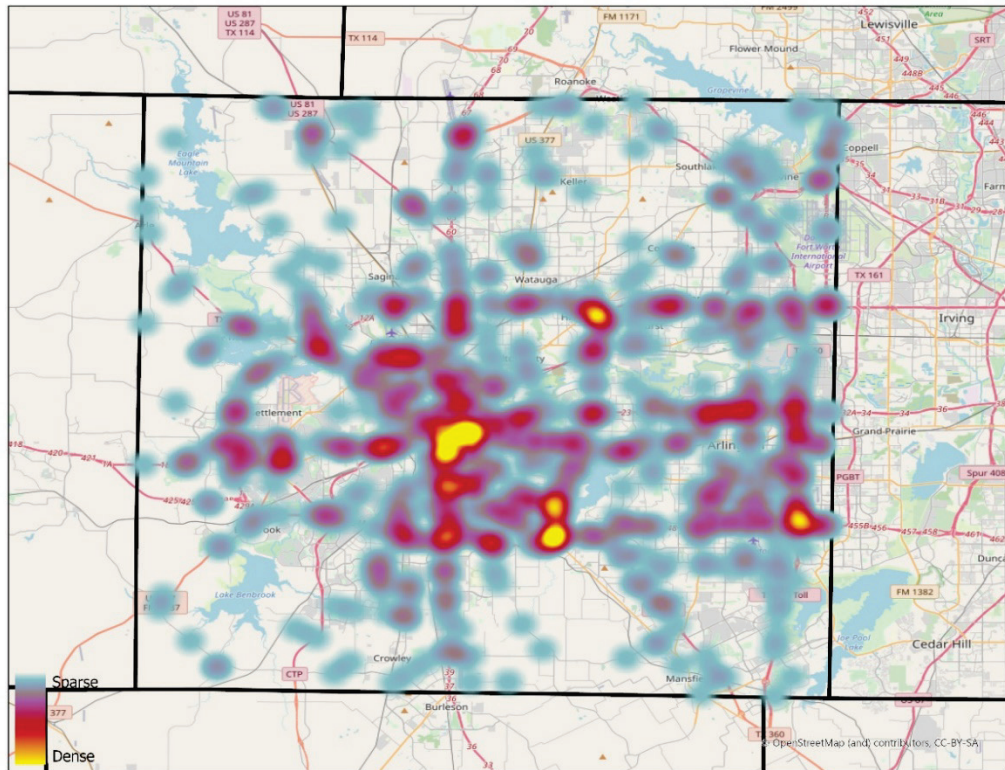
**Figure 32. 2010–2019 Daylight/Nighttime Fatal Crashes in the Dallas Area (Dallas County).**



Daylight  
Fatal  
Crashes

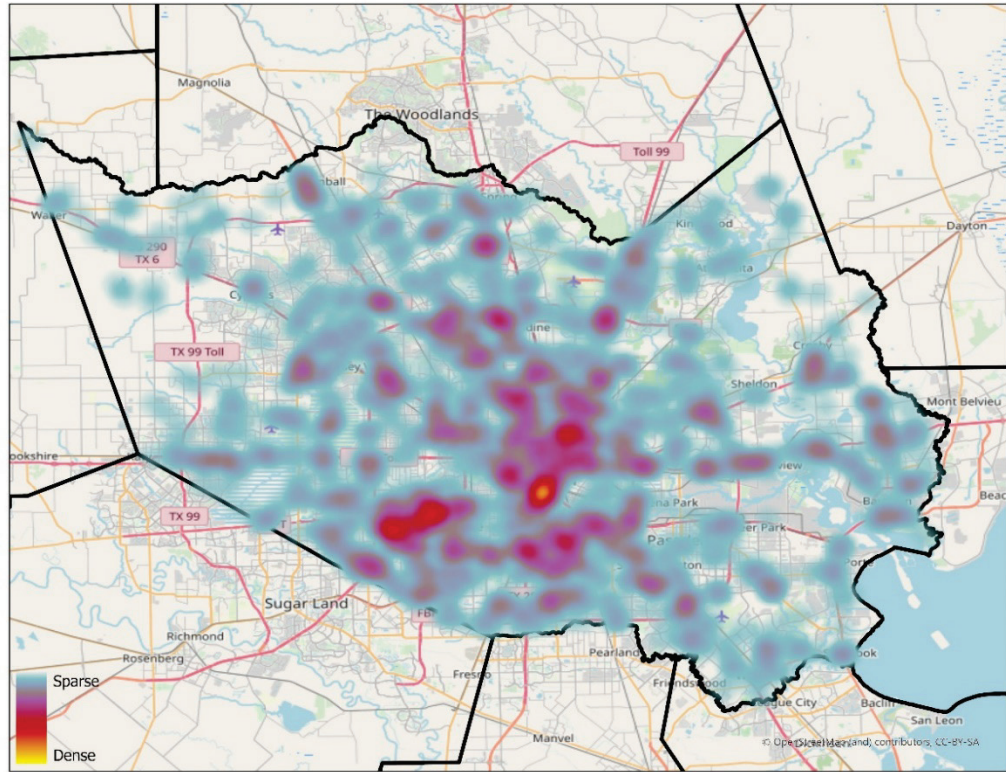


Nighttime  
Fatal  
Crashes

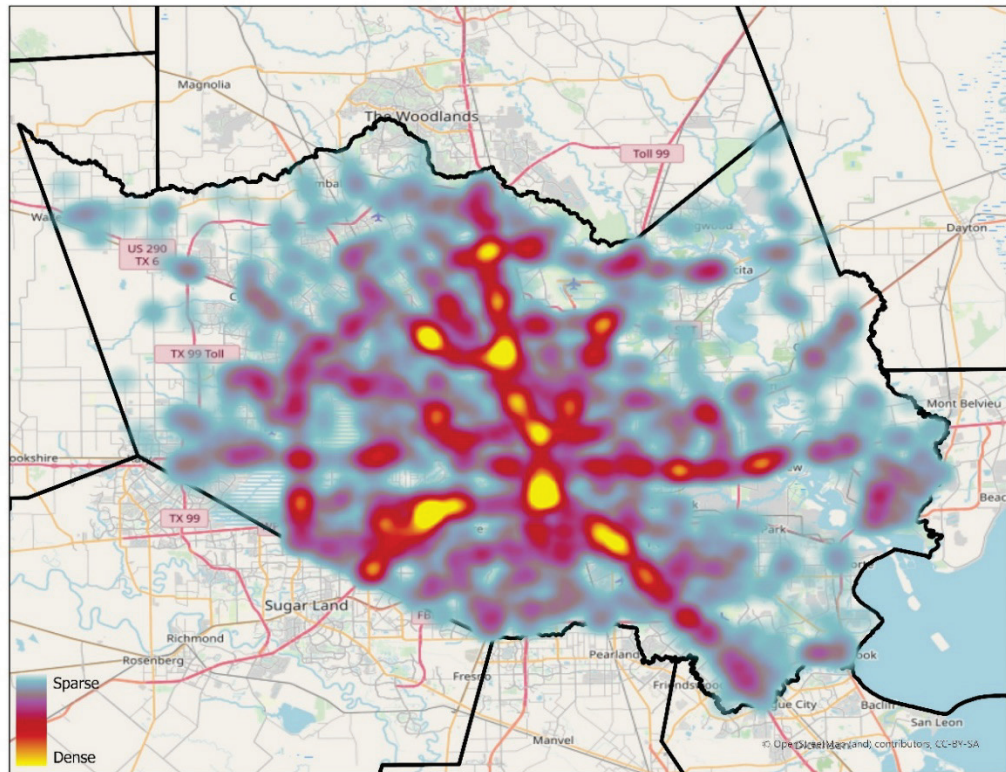


**Figure 33. 2010–2019 Daylight/Nighttime Fatal Crashes in the Fort Worth Area (Tarrant County).**

Daylight  
Fatal  
Crashes

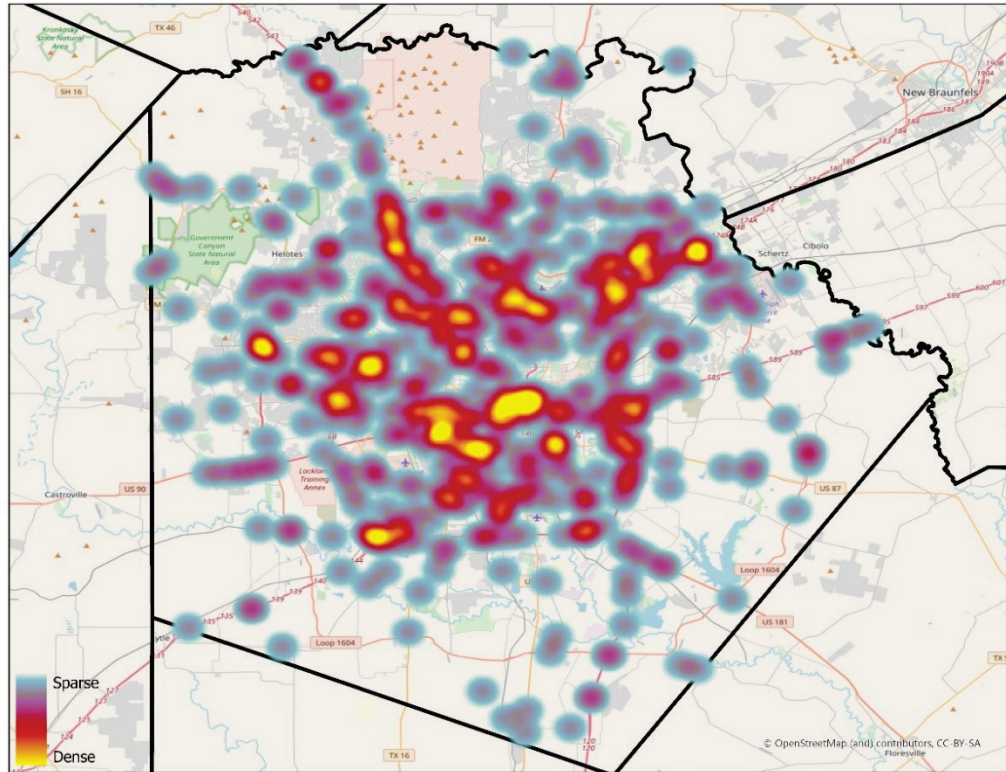


Nighttime  
Fatal  
Crashes

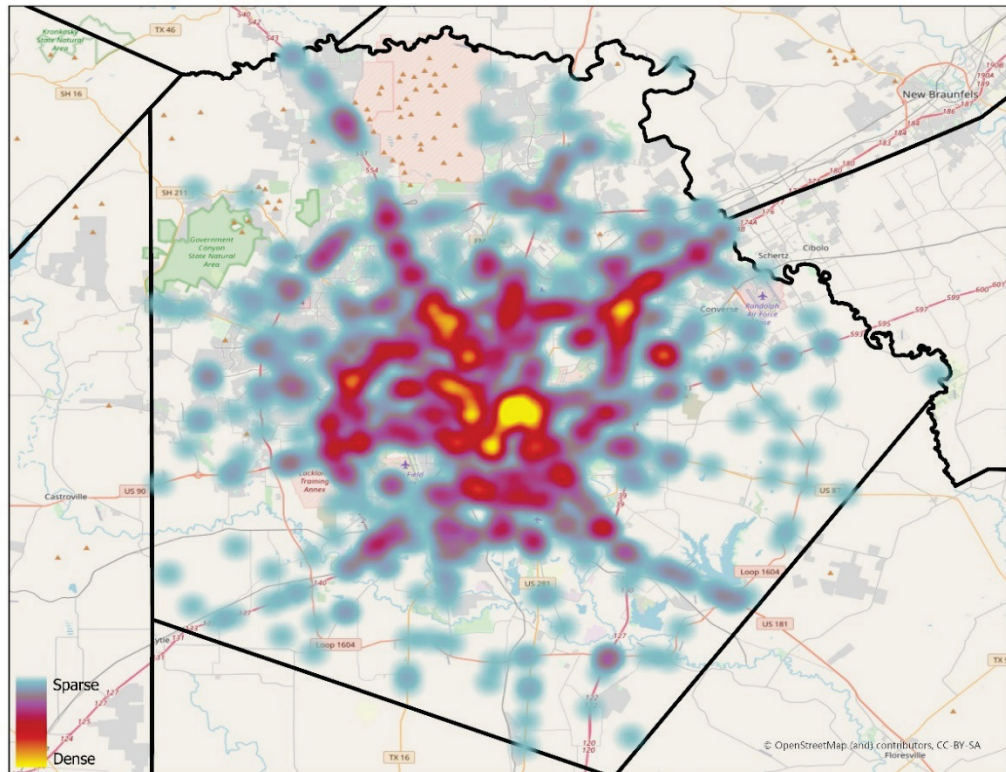


**Figure 34. 2010–2019 Daylight/Nighttime Fatal Crashes in the Houston Area (Harris County).**

Daylight  
Fatal  
Crashes



Nighttime  
Fatal  
Crashes



**Figure 35. 2010–2019 Daylight/Nighttime Fatal Crashes in the San Antonio Area (Bexar County).**

## Overall Trends for Fatal Crashes

When all fatal crashes were analyzed separately (more specifically, one series for daylight fatal crashes and separate series for nighttime crashes, inclement weather crashes, and abnormal surface crashes), different patterns became apparent for each metro area:

- Austin metro area: Daylight fatal crashes were widely distributed over the Austin area. However, nighttime fatal crashes were heavily concentrated within a relatively narrow zone around the IH-35 corridor.
- Dallas metro area: Daylight fatal crashes were widely distributed, but there were also a high number of pockets with a high density of fatal crashes. Nighttime fatal crashes were also widely distributed, but these crashes were more concentrated along major highways between IH-20 to the south and IH-635 to the north.
- Fort Worth metro area: Daylight fatal crashes were widely distributed, but there were also a high number of pockets with a high density of fatal crashes. Nighttime fatal crashes were also widely distributed, but these crashes tended to be more concentrated in downtown areas.
- Houston metro area: Daylight fatal crashes were widely distributed, with relatively few pockets with a moderate density of fatal crashes. Nighttime fatal crashes were also widely distributed, with a significant concentration around downtown and along several major highways, particularly IH-45 and IH-69.
- San Antonio metro area: Daylight fatal crashes were widely distributed, but there were also a high number of pockets with a high density of fatal crashes. Nighttime fatal crashes were also widely distributed, but these crashes tended to be concentrated in certain areas inside Loop 410 and along Loop 1604.
- For all metro areas, the spatial distribution of fatal crashes under clear or cloudy weather conditions was much more similar to the spatial distribution of nighttime fatal crashes than to the spatial distribution of daylight fatal crashes.
- For all metro areas, the spatial distribution of crashes under inclement weather conditions was similar to the spatial distribution of crashes under abnormal surface conditions. This finding was expected considering that most inclement weather crashes are related to rain and most abnormal surface crashes are related to wet surface conditions.
- For all metro areas, most fatal crashes under inclement weather conditions had the same location as fatal crashes under wet surface conditions.
- For all metro areas, the location of fatal crashes under inclement weather conditions did not appear to be strongly correlated with the spatial distribution of all inclement weather conditions.
- For all metro areas, the location of fatal crashes under abnormal surface conditions did not appear to be strongly correlated with the spatial distribution of all abnormal surface weather conditions.

## **CHAPTER 4. SIMULATIONS TO ASSESS IMPACTS OF SUBOPTIMAL ENVIRONMENTAL CONDITIONS**

### **INTRODUCTION**

This chapter summarizes the results of a series of computer simulations to assess impacts of suboptimal environmental conditions when performing UAS-SfM photogrammetric data collection and processing for crash reconstruction applications. The research team used the results of this analysis to document the impact of field operating conditions during the field test data collection and processing (see Chapter 5). The focus of the analysis was the typical nonmetric RGB digital cameras (e.g., 20-MP, 2.5-cm [1-inch] complementary metal-oxide semiconductor [CMOS] sensor, global shutter) used for surveying crash scenes with UASs. The simulation and tests covered the following areas:

- Impact of wind speed and direction on UAS flight operations.
- Impact of aerial imaging network design on 3D crash scene reconstructions using commercial SfM software.
- Impact of ambient lighting and low visibility on UAS-SfM reconstructions.
- Self-calibration versus preflight calibration procedures for consumer-grade nonmetric digital RGB cameras.
- Impact of suboptimal conditions on visual image quality.
- Impact of camera properties on UAS image quality to guide crash scene imaging.

### **IMPACT OF WIND SPEED AND DIRECTION ON UAS FLIGHT OPERATIONS**

The research team used commercial and open-source UAS flight simulation software to analyze the impacts of wind speed, direction, and turbulence on the endurance of the mission, safety of the craft, and flight design for SfM mapping missions. The research team evaluated scenarios using typical flight performance capabilities of UASs increasingly used for crash data collection and reconstruction. The research team (a) performed a series of quadcopter simulations to evaluate incremental increases in wind speed, direction, and turbulence versus altitude; (b) used simulation results to derive statistical analytics and visual analytics of the impacts of wind speed, direction, and turbulence on UAS flight operations; and (c) used average 3D error, standard deviation, battery use, and flight time to parameterize the impacts of wind on mission planning and operations.

#### **General Concepts**

UAS vendors include maximum wind speeds in the equipment specifications. However, while it is possible to operate the aircraft at those speed levels, such conditions are not ideal for mapping missions. Some UASs can operate in high wind speeds, but their battery life and flight time is reduced as wind speeds increase (78, 79). High wind speed can also negatively affect the photogrammetry and derived mapping products. If winds are too strong, even if the aircraft can hold its position, the gimbal may be adversely tilted or disturbed, preventing the collection of quality images for photogrammetric purposes. Wind direction and turbulence are also important variables to consider because they affect the flight path geometry and overall flight stability.

Recent studies have documented the impact of wind on UAS flight performance. Wang et al. examined the effects of various types of wind affecting UASs at low altitudes (80). Their analysis included recommendations for mitigating negative effects of wind on UAS operations. Siqueira evaluated software-based and mathematical modeling of wind effects on small UAS trajectory tracking (81).

Two important UAS components are the flight control unit (FCU) and the ground control station (GCS). The FCU is onboard the craft and works in real time to maintain flight and execute user-desired inputs. The GCS can be as simple as a remote controller that one flies in real time, or in the case of photogrammetry, the GCS can be software that creates a set of instructions that are executed by the FCU without any real-time user input. The radio communication between the GCS and the FCU uses the micro air vehicle link protocol.

It is common to use open-source UAS autopilot software to conduct simulation runs. Prior studies used ArduPilot Mission Planner and software-in-the-loop (SITL) to analyze the impact of wind. Hentati et al. provided an overview of different UAS flight simulators, including Mission Planner and SITL (82). Biradar used Mission Planner and SITL to run simulations with a fixed-wing aircraft (83). The research team decided to use Mission Planner because of its versatility as a full-featured ground station software for ArduPilot open-source autopilot applications. Mission Planner enabled the research team to define waypoints, flight lines, and overlaps on the digital map; configure autopilot settings for the UAS platform; select commands for flight missions; download mission log files; and simulate a UAS through an SITL module as a virtual FCU to conduct predefined simulation runs.

## **Methods**

The research team generated 58 single-altitude and six dual-altitude simulation runs to evaluate flight performance by incrementally increasing wind speed, direction, and turbulence values. The metrics used included average 3D error, standard deviation, flight time, and battery use to evaluate the impacts of wind speed, direction, and turbulence on mission planning and operations. The average 3D error and the standard deviation provided metrics for the differences in location between planned waypoint locations and the corresponding camera trigger locations. Flight time provided a metric for the total time needed to complete a mission as wind conditions changed with respect to a reference zero-speed, no-turbulence wind scenario. Battery use provided a metric for the cumulative use of battery power as wind conditions changed with respect to a reference zero-speed, no-turbulence wind scenario.

### *Simulation Setup*

The research team identified a rectangular area at the Texas A&M Flight Test Station Airport in Bryan, Texas, to define the boundary of the survey mission (Figure 36). The rectangular area was  $105 \times 70$  m ( $344 \times 230$  ft) and centered over an airfield intersection at 30 degrees, 38 minutes, 16.50 seconds N and 96 degrees 28 minutes 54.70 seconds W. Within Mission Planner, the research team used a survey grid tool to create mission flight lines. Figure 37 shows the parameters of the flights within this tool. Figure 38 shows the mission flight lines and waypoints.

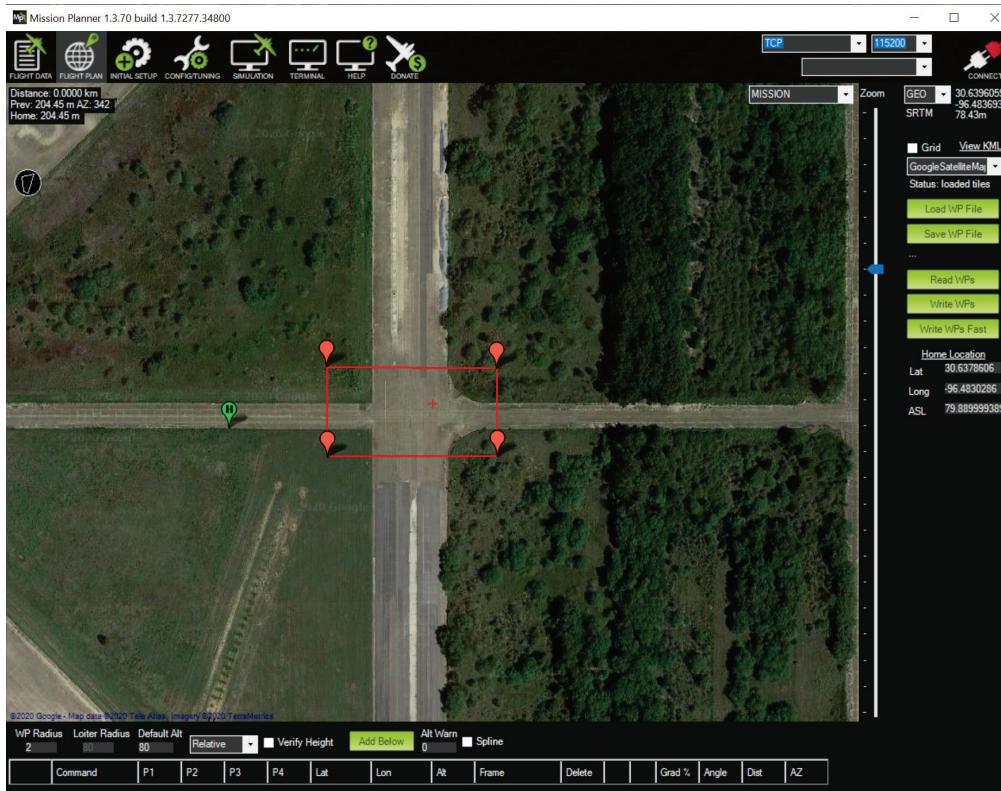


Figure 36. Mission Area Polygon.

Stats					
Area:	12890 m <sup>2</sup>	Pictures:	48	Flight Time (est):	3:23 Minutes
Distance:	0.81 km	No of Strips:	4	Photo every (est):	2.80 Seconds
Dist between images:	14 m	Footprint:	105 x 70 m	Turn Dia (at 45d):	7 m
Ground Resolution:	1.92 cm	Dist between lines:	21.01 m	Ground Elevation:	79-81 m

**Simple Options**

Camera: Mavic 2 Pro

Altitude (m): 80

Angle (deg): 90

Camera top facing forward

Flying Speed (est) (m/s): 5

Use speed for this mission

Add Takeoff and Land WPs

Use RTL

Split into x segments: 1

**Display**

Boundary

Markers

Grid

Internals

Footprints

Advanced Options

**Grid Options**

Distance between lines [m]: 23.87

OverShoot [m]: 0

OverShoot [m]: 0

Leadin [m]: 0

StartFrom: Home

Overlap [%]: 80.0

Sidelap [%]: 80.0

Cross Grid  Corridor  Spiral

Corridor Width [m]: 100.0

**Copter Options**

Delay at WP (sec): 1.0

Heading Hold 80

Spline Exit/Entries

**Camera Options**

Focal Length [mm]: 10.0

Image Width [Pixels]: 5472

Image Height [Pixels]: 3648

Sensor Width [mm]: 13.13

Sensor Height [mm]: 8.75

Load Sample Photo

Save

Calculated Values

cm/pixel: 1.92 cm

Field of View Horizontal [m]: 105

Field of View Vertical [m]: 70

**Trigger Method**

CAM\_TRIGG\_DIST  Breakup starts

DO\_DIGICAM\_CONTROL

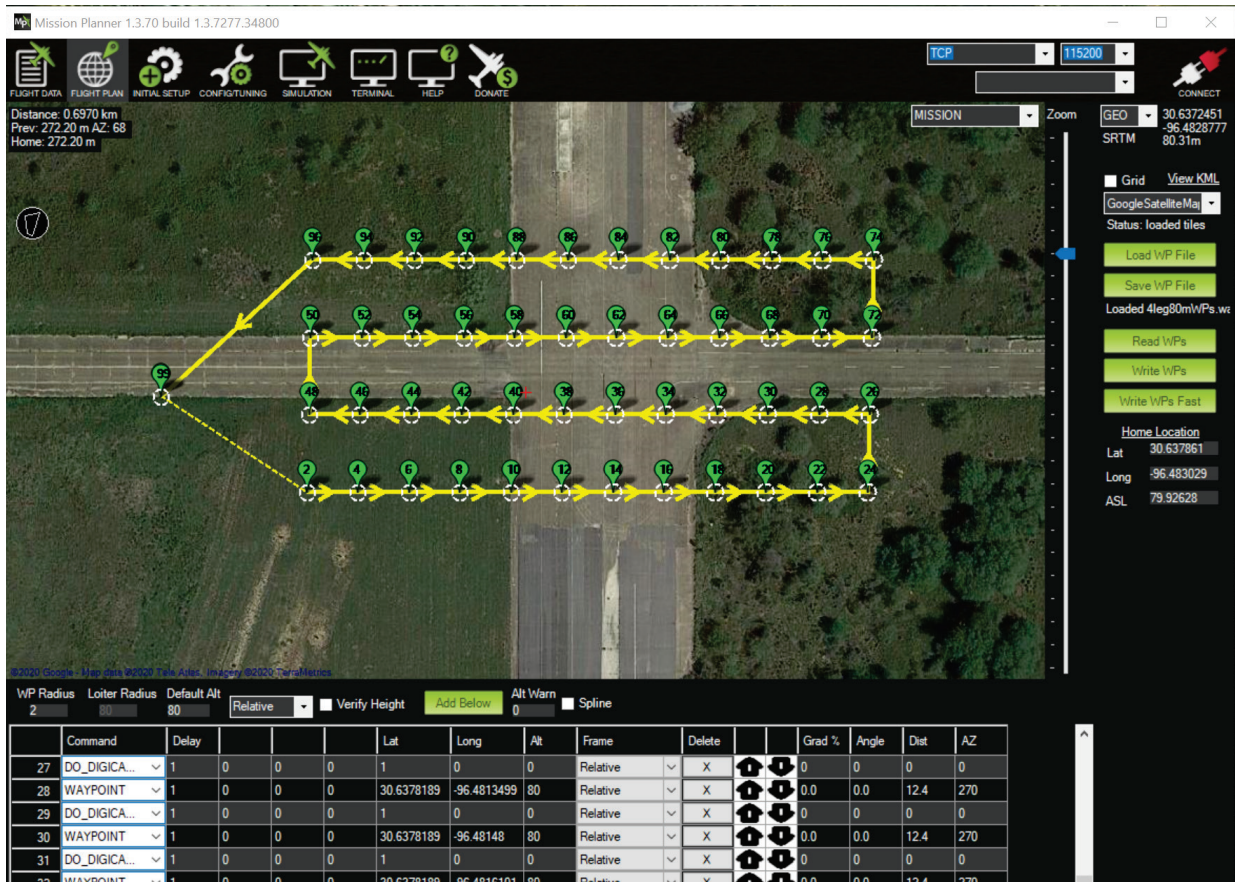
DO\_REPEAT\_SERVO

Servo: 5 PWM: 1100 Cycle Time [s]: 2

DO\_SET\_SERVO

Servo: 5 PWM L: 1100 PWM H: 1900

Figure 37. Mission Parameters of Simulation Runs.



**Figure 38. Overview of Flight Lines, Waypoints, and Action Information.**

The mission consisted of 48 photo locations taken along four flight lines consisting of 12 photo locations each. The flight plan included the UAS stopping at each planned waypoint location to capture an image before moving to the next waypoint. The spacing between photo locations was 80 percent endlap and 80 percent sidelap. Mission Planner used the calculated field of view of the camera used along with the mission altitude over the ground to calculate the appropriate photo locations to achieve the desired overlap. For this task, the research team used the focal length and sensor size of a DJI Mavic 2 Pro camera as parameters for calculating the field of view. SITL did not specify the characteristics of the simulated quadcopter. However, it was possible to edit the MAVProxy parameter list. For example, the parameter for battery capacity was set at 3300 milliamp hours (mAh). Additional information about simulated quadcopters in SITL is available elsewhere (84).

Mission Planner loaded the SITL software and placed the simulated craft at the home position (Figure 39). The software ran a simulated flight controller within a virtual aircraft that was awaiting commands while at a home location. The research team then uploaded the mission into the simulated airframe via the simulated ground control station link the same way it would be done in a real flight with an actual craft. The interface then set environmental factors, such as wind speed and direction values, for each simulation run.





**Figure 39. Screen in Mission Planner Where Simulation Starts and Craft Type Is Selected.**

The software simulates turbulence by adding 3D random vectors and magnitudes to the existing wind conditions. In the software, turbulence is a combination of high pass and low pass filters in both horizontal and vertical directions satisfying the following conditions (85):

$$t_h^n = 0.98 t_h^{n-1} + 10 \cdot (1 - 0.98) t_i r_g \quad (3)$$

$$t_v^n = 0.98 t_v^{n-1} + 10 \cdot (1 - 0.98) t_i r_g \quad (4)$$

where:

$t_h$  and  $t_v$  = horizontal and vertical turbulences, respectively (in m/s),  
 $n$  and  $n - 1$  = current and previous time instances,  
 $r_g$  = random number following a  $\mathcal{N}(0,1)$  Gaussian distribution, and  
 $t_i$  = turbulence index: 0, 5, 10 or 20.

The National Weather Service defines four levels of turbulence for operating aircraft, depending on variations in air speed and vertical gust velocity (Table 42) (86). Gust denotes a local maximum above a certain threshold above the mean wind speed within a certain amount of time such as one or two minutes (87).

**Table 42. Turbulence Levels.**

Turbulence Level	Variation in Air Speed			Vertical Gust Velocity		
	(m/s)	(knots)	(mph)	(m/s)	(ft/s)	(mph)
Light	3–7	5–14	6–16	2–6	5–19	3–13
Moderate	8–12	15–24	17–28	6–11	20–35	14–24
Severe	$\geq 13$	$\geq 25$	$\geq 29$	11–15	36–49	25–33
Extreme	$\geq 13$	$\geq 25$	$\geq 29$	$\geq 15$	$\geq 50$	$\geq 34$

The research team simulated light turbulence (i.e., turbulent index 5), moderate turbulence (turbulence index 10), and extreme turbulence (turbulence index 20). It was not necessary to simulate severe turbulence because the only difference between severe and extreme turbulence was the vertical turbulence component. Turbulence index 5 included randomized horizontal and vertical air speed fluctuations up to 5 m/s (10 knots or 11 mph). Turbulence index 10 included randomized horizontal and vertical air speed fluctuations up to 10 m/s (20 knots or 23 mph). Turbulence index 20 included randomized horizontal and vertical air speed fluctuations up to 20 m/s (39 knots or 45 mph).

The research team then set up wind parameters through the parameter tree under simulation settings. The parameter tree is one of the ways that Mission Planner gives access to the tunable parameters and variables within a flight control unit. In an actual craft, these parameters need to be accessible for craft setup and tuning. When a session is active, the environmental parameters for the simulation runs are also accessible in Mission Planner. Figure 40 highlights the environmental parameters concerned with the simulation runs in the parameter tree.

After setting up environmental parameters, the simulated craft was then armed and flown in autopilot mode. Figure 41 shows an image of a simulated flight in progress. Once the simulated craft landed and disarmed its motors the flight log was downloaded from the flight controller via the simulated radio link. Each flight log was stored in a folder for dissemination.

Mission Planner 1.3.70 build 1.3.7277.34800 ArduCopter V4.1.0-dev (be3a2cc2)

FLIGHT DATA FLIGHT PLAN INITIAL SETUP CONFIG/TUNING SIMULATION TERMINAL HELP DONATE **ARDUPILOT** Stats... TCP5760-1-QUADROTOR DISCONNECT

Flight Modes  
 GeoFence  
 Basic Tuning  
 Extended Tuning  
 Standard Params  
 Advanced Params  
 User Params  
 Full Parameter List  
**Full Parameter Tree**  
 Planner

Command	Value	Unit	Range	Description
SIM_VIB_MOT_MULT	1			
SIM_VICON_FAIL	0			
SIM_VICON_GLIT_X	0			
SIM_VICON_GLIT_Y	0			
SIM_VICON_GLIT_Z	0			
SIM_VICON_POS_X	0			
SIM_VICON_POS_Y	0			
SIM_VICON_POS_Z	0			
SIM_VICON_TMASK	3			
SIM_VICON_VGLJ_X	0			
SIM_VICON_VGLJ_Y	0			
SIM_VICON_VGLJ_Z	0			
SIM_VICON_YAW	0			
SIM_VICON_YAWERR	0			
SIM_WAVE_AMP	0.5			
SIM_WAVE_DIR	0			
SIM_WAVE_ENABLE	0			
SIM_WAVE_LENGTH	10			
SIM_WAVE_SPEED	0.5			
SIM_WIND_DELAY	0			
SIM_WIND_DIR	0			
SIM_WIND_DIR_Z	0			
SIM_WIND_SPD	5			
SIM_WIND_T	0			
SIM_WIND_T_ALT	1			
SIM_WIND_T_COEF	0.01			
SIM_WIND_TURB	0			
SIM_WOW_PIN	-1			
SIMPLE	0			Bitmask which holds which flight modes use simple heading mode (eg bit 0 = 1 means Flight Mode 0 uses simple mode)
SPRAY_ENABLE	0		0:Disabl ed 1:En_	Allows you to enable (1) or disable (0) the sprayer
SR0				
SR1				
SR2				
SR3				
SRTL				
STAT				
SUPER_SIMPLE	0		0:Disabl ed 1:M...	Bitmask to enable Super Simple mode for some flight modes. Setting this to Disabled(0) will disable Super Simple Mode
SYSID				
TCAL_ENABLED	0		0:Disabl ed 1:En_	Enable temperature calibration. Set to 0 to disable. Set to 1 to use learned values. Set to 2 to learn new values and use the values
TELEM_DELAY	0	s	0 30	The amount of time (in seconds) to delay radio telemetry to prevent an Xbee bricking on power up

Load from file  
 Save to file  
 Write Params  
 Refresh Params  
 Compare Params

All Units are in raw format with no scaling

3DR\_Iris+\_AC34  
 Load Presaved  
 Reset to Default  
 Search  
 Modified

Figure 40. Settings of Environmental Parameters for a Simulation Run.



**Figure 41. Image of Mission Planner during an Example Simulation Mission Execution.**

### *Flight Log Dissemination and Parsing*

The flight log downloaded in the previous step contained the status of the flight control unit recorded at 5 Hz throughout the flight (Figure 42). This led to a log containing 150,000 to 200,000 lines of information in each simulation run. For this task, the research team was interested in the position and attitude of the craft at the time of image acquisition and the battery power consumed at the end of the mission. To meet these needs, the research team wrote a Python script that read the flight log and output a text file containing the desired information. First, the script looked for flight log messages beginning with a CAM tag and wrote them to a

text file in a designated format. As Figure 43 shows, the CAM messages contained the attitude and positional information of the airframe when the camera was triggered. The CAM file contained position coordinates in WGS84 coordinates. For analysis, the research team converted the coordinates to the Universal Transverse Mercator (UTM) coordinate system using National Oceanic and Atmospheric Administration (NOAA) VDatum software (Figure 44). All altitudes were left in their original AGL format. Next, the script found the last flight log message containing a BAT tag and wrote it to a separate text file. The BAT message contained information on the total power consumed during the mission.



**Figure 42. Image of Mission Planner during Flight Log Download.**

```

CAMFMT,TimeUS,GPSTime,GPSWeek,Lat,Lng,RelAlt,Roll,Pitch,Yaw
CAM,115588746,250292200,2099,30.6376503,-96.4826566,79.99,-10.37,12.62,124.12
CAM,122248581,250299000,2099,30.6376472,-96.4825271,80,-12.58,5.71,93.72
CAM,128888424,250305600,2099,30.6376445,-96.4823975,80,-12.42,5.97,95.34
CAM,135488283,250312200,2099,30.6376417,-96.4822672,79.99,-12.35,6.13,95.81
CAM,142088975,250318800,2099,30.6376388,-96.4821372,80,-12.31,6.2,95.78
CAM,148688834,250325400,2099,30.6376359,-96.482007,79.99,-12.37,6.29,95.92
CAM,155308685,250332000,2099,30.637633,-96.4818768,79.99,-12.34,6.31,96.08
CAM,161928536,250338600,2099,30.6376302,-96.4817467,79.99,-12.27,6.3,96.25
CAM,168548387,250345200,2099,30.6376273,-96.4816167,80,-12.19,6.28,95.96
CAM,175148246,250351800,2099,30.6376243,-96.4814865,80,-12.19,6.55,96.84
CAM,181748938,250358400,2099,30.6376214,-96.4813565,80,-12.18,6.42,96.46
CAM,188348797,250365000,2099,30.6376186,-96.4812263,79.99,-12.14,6.55,96.77
CAM,197088633,250373800,2099,30.6377863,-96.4812189,80,0.74,-7.89,355.46
CAM,203988372,250380600,2099,30.6377906,-96.4813484,79.99,12.86,5.42,269.01
CAM,210628215,250387400,2099,30.6377917,-96.4814785,80,13.98,3.29,276.91
CAM,217228907,250394000,2099,30.6377945,-96.4816088,80,14.14,3.05,278.33
CAM,223848758,250400600,2099,30.6377975,-96.4817388,80,14.17,3.27,277.97
CAM,230448617,250407200,2099,30.6378002,-96.4818689,79.99,14.27,3.06,278.69
CAM,237048476,250413800,2099,30.6378031,-96.4819991,79.99,14.33,3.07,279
CAM,243668327,250420400,2099,30.637806,-96.4821292,80,14.36,3.06,279.18
CAM,250288178,250427000,2099,30.6378088,-96.4822593,79.99,14.47,3.02,279.43
CAM,256908862,250433600,2099,30.6378118,-96.4823895,79.99,14.41,3.07,279.52
CAM,263548705,250440200,2099,30.6378146,-96.4825198,79.99,14.46,3.04,279.97

```

**Figure 43. CAM .txt File.**

```

CAMFMT,TimeUS,GPSTime,GPSWeek,Lat,Lng,RelAlt,Roll,Pitch,Yaw
CAM,115588746,250292200,2099,3392147.63932,741262.33462,79.99000,-10.37,12.62,124.12
CAM,122248581,250299000,2099,3392147.57378,741274.75748,80.00000,-12.58,5.71,93.72
CAM,128888424,250305600,2099,3392147.55282,741287.18892,80.00000,-12.42,5.97,95.34
CAM,135488283,250312200,2099,3392147.52230,741299.68773,79.99000,-12.35,6.13,95.81
CAM,142088975,250318800,2099,3392147.48005,741312.15803,80.00000,-12.31,6.2,95.78
CAM,148688834,250325400,2099,3392147.43825,741324.64750,79.99000,-12.37,6.29,95.92
CAM,155308685,250332000,2099,3392147.39647,741337.13697,79.99000,-12.34,6.31,96.08
CAM,161928536,250338600,2099,3392147.36557,741349.61661,79.99000,-12.27,6.3,96.25
CAM,168548387,250345200,2099,3392147.32338,741362.08692,80.00000,-12.19,6.28,95.96
CAM,175148246,250351800,2099,3392147.27056,741374.57664,80.00000,-12.19,6.55,96.84
CAM,181748938,250358400,2099,3392147.22840,741387.04695,80.00000,-12.18,6.42,96.46
CAM,188348797,250365000,2099,3392147.19777,741399.53618,79.99000,-12.14,6.55,96.77
CAM,197088633,250373800,2099,3392165.80670,741399.82881,80.00000,0.74,-7.89,355.46
CAM,203988372,250380600,2099,3392166.00514,741387.40298,79.99000,12.86,5.42,269.01
CAM,210628215,250387400,2099,3392165.84751,741374.92758,80.00000,13.98,3.29,276.91
CAM,217228907,250394000,2099,3392165.87795,741362.42879,80.00000,14.14,3.05,278.33
CAM,223848758,250400600,2099,3392165.93122,741349.95826,80.00000,14.17,3.27,277.97
CAM,230448617,250407200,2099,3392165.95103,741337.47889,79.99000,14.27,3.06,278.69
CAM,237048476,250413800,2099,3392165.99281,741324.98944,79.99000,14.33,3.07,279
CAM,243668327,250420400,2099,3392166.03483,741312.50957,80.00000,14.36,3.06,279.18
CAM,250288178,250427000,2099,3392166.06577,741300.02996,79.99000,14.47,3.02,279.43
CAM,256908862,250433600,2099,3392166.11868,741287.54026,79.99000,14.41,3.07,279.52
CAM,263548705,250440200,2099,3392166.14922,741275.04148,79.99000,14.46,3.04,279.97

```

**Figure 44. CAM .txt File after Conversion to UTM via VDatum.**

### *Data Aggregation and Statistical Metrics*

The research team imported the CAM and BAT files into a master Microsoft Excel file. The file included metrics and aggregate statistics to determine the effect of wind on the UAS's capability to trigger its camera at the intended location. The basic metric was the deviation from the actual camera trigger locations to the intended waypoint trigger locations. The aggregate statistics included average, minimum, maximum, range, standard deviation, and RMSE for the 2D and 3D evaluation metrics from each planned waypoint to its actual camera trigger location. The research team also calculated the mission flight time (from the first to the last image taken) and the total power consumed during the mission.

The average 3D error between intended waypoints and actual camera trigger locations for each individual simulation run is:

$$d = \frac{\sum_{n=1}^m \|p_n - q_n\|}{m} \quad (5)$$

where:

$d$  = average 3D error between intended waypoints and actual camera trigger locations (m);  
 $m$  = number of planned waypoints where the camera is supposed to be triggered;  
 $p$  and  $q$  = waypoint location vector and corresponding actual camera trigger location vector, respectively; and  
 $\|p - q\|$  = 3D Euclidean distance.

A normalized average 3D error for individual simulation runs is:

$$n_{s,d,t} = \frac{d_{s,d,t}}{d_{0,0}} \quad (6)$$

where:

$n_{s,d,t}$  = normalized average 3D error for wind speed  $s$ , wind direction  $d$ , and turbulence index  $t$ ;  
 $d_{s,d,t}$  = average 3D error for wind speed  $s$ , wind direction  $d$ , and turbulence index  $t$ ; and  
 $d_{0,0}$  = average 3D error for a reference zero-speed, no-turbulence wind scenario.

The standard deviation of 3D errors between intended waypoints and actual camera trigger locations for each individual simulation run can be expressed as:

$$s = \sqrt{\frac{\sum_{n=1}^m (d_n - \bar{d})^2}{m-1}} \quad (7)$$

where:

$s$  = standard deviation of 3D errors between intended waypoints and actual camera trigger locations,  
 $m$  = number of planned waypoints where the camera is triggered (in this case,  $m = 48$ ),  
 $d_m$  = 3D error between a planned waypoint and its associated camera trigger location, and  
 $\bar{d}$  = mean error of  $d_m$  for the 48 waypoints.

### *Overview of Simulation Runs*

The simulated UAS was a light-weight quadcopter with flight lines primarily in the east-west direction, as shown in Figure 39. The research team evaluated the following wind conditions:

- Wind speed: Up to 14 m/s (50 km/h or 31 mph). The research team simulated five wind speed values: 0, 3.5 m/s (7.8 mph), 7 m/s (16 mph), 10.5 m/s (23 mph), and 14 m/s (31 mph).

- Turbulence: Up to 20 m/s (72 km/h or 45 mph), using four turbulence index values: 0, 5, 10, and 20. As the turbulence index increased, the turbulence magnitude increased. The simulation accounted for light, moderate, and extreme turbulence conditions. It was not necessary to simulate severe turbulence conditions because the only difference between severe and extreme turbulence was the vertical turbulence component.
- Wind direction: 0 degrees, 22.5 degrees, 45 degrees, 67.5 degrees, and 90 degrees. Wind direction is the direction from which the wind is coming. For instance, north wind is wind that comes from the north. The corresponding wind direction is 0 degrees. Similarly, east wind is wind that comes from the east. The corresponding wind direction is 90 degrees. It was of interest to evaluate the effect of headwind, tailwind, and crosswind from all directions. The simulated flight lines followed an east-west alignment (Figure 38). As a result, it was only necessary to consider the effect of wind direction in the first quadrant (i.e., from 0–90 degrees) to cover all directions. Table 43 summarizes the various scenarios the research team included in the simulation effort.

**Table 43. Tailwind, Headwind, and Crosswind Scenarios.**

Type	Wind Direction <sup>a</sup>	Flight Course <sup>b</sup>	Angle <sup>c</sup>
Headwind	90°	E	0°
Tailwind	90°	W	180°
Crosswind	0°	E	90°
Crosswind	0°	W	270°
Crosswind	22.5°	E	67.5°
Crosswind	22.5°	W	247.5°
Crosswind	45°	E	45°
Crosswind	45°	W	225°
Crosswind	67.5°	E	22.5°
Crosswind	67.5°	W	202.5°

Notes:

<sup>a</sup> Direction from which the wind is coming.

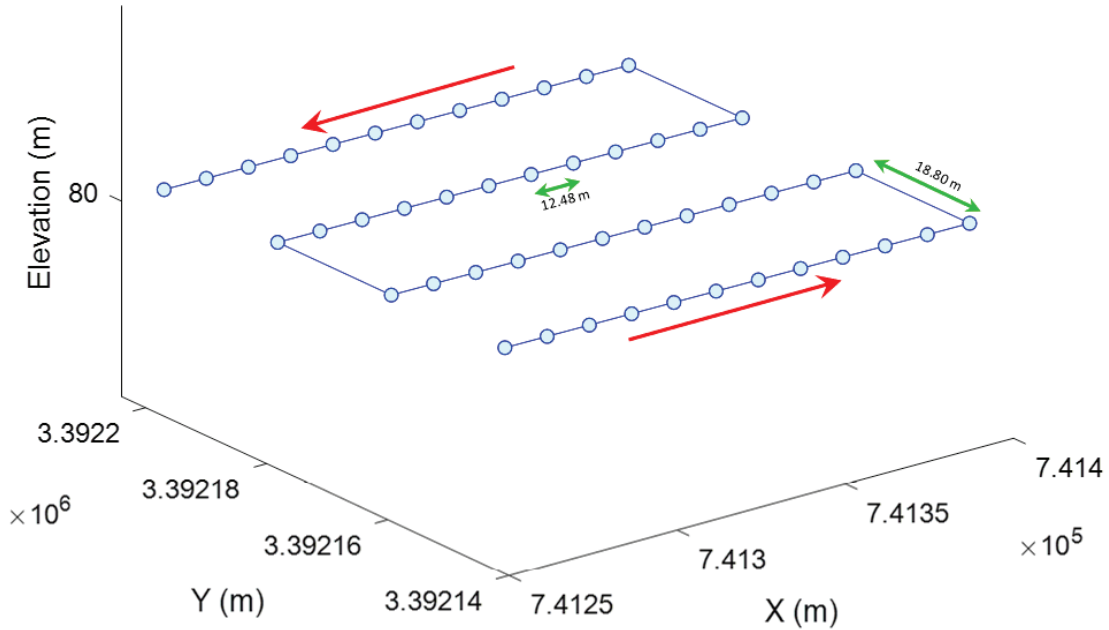
<sup>b</sup> Desired direction in which the aircraft is to be steered.

<sup>c</sup> Angle from the wind direction to the flight course in a clockwise fashion.

The flight plan included the quadcopter stopping at each waypoint location to capture an image before moving to the next waypoint. The spacing between image locations included 80 percent endlap and 80 percent sidelap between images.

The simulation included two flight elevations: 80 m and 10 m (or 262 ft and 33 ft) AGL. Most runs were at a single altitude of 80 m (262 ft) (Figure 45). The red lines indicate the flight path. There were 48 planned waypoints located on four equal-length flight lines. The spacing between waypoints was 12.5 m (41 ft). The spacing between flight lines was 18.8 m (62 ft). Table 44 summarizes all 58 individual simulation runs performed at this altitude. The research team used a wind speed of 14 m/s (31 mph) only under no turbulence conditions. Adding turbulence at this level would have resulted in unsafe flying conditions. Simulation runs for a turbulence index of 5 included wind speeds of 10.5 m/s (23 mph). The reason was that the results for turbulence indices of 0 and 5 were similar.





**Figure 45. Flight Path for Single Altitude of 80 m (262 ft) AGL.**

**Table 44. Simulations for Single Altitude of 80 m (262 ft) AGL.**

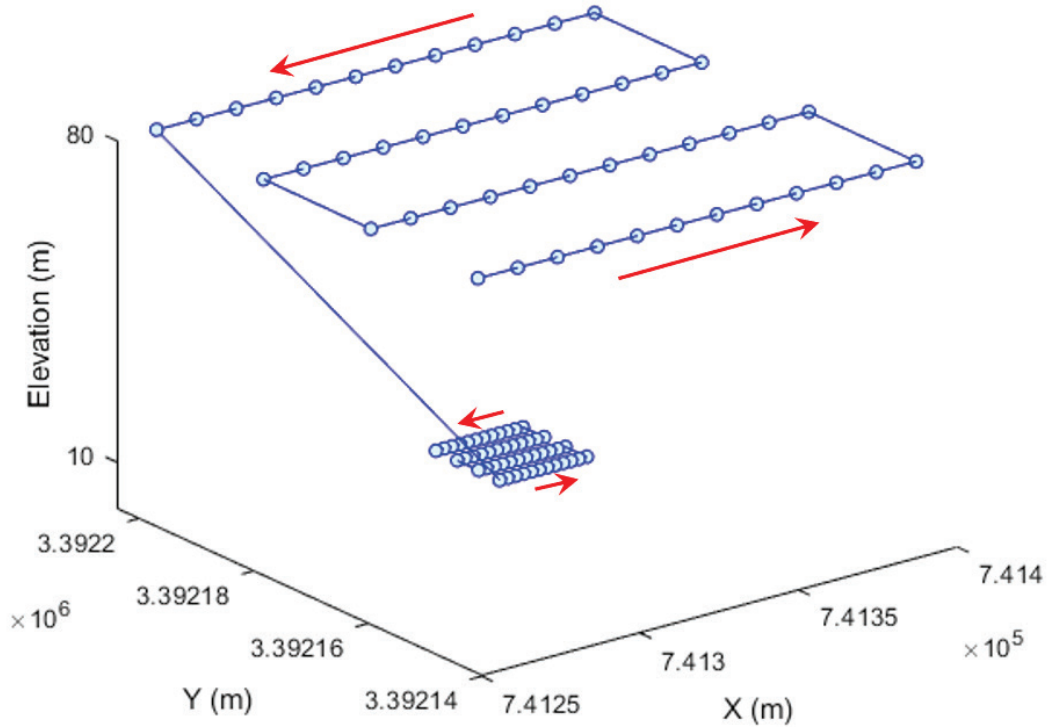
Wind Direction (°)	Wind Speed		Turbulence Index	Flight Height (AGL)	
	(m/s)	(mph)		(m)	(ft)
N/A	0.0	0.0	0	80	262
0	3.5	7.8	0	80	262
0	7.0	15.7	0	80	262
0	10.5	23.5	0	80	262
0	14.0	31.3	0	80	262
22.5	3.5	7.8	0	80	262
22.5	7.0	15.7	0	80	262
22.5	10.5	23.5	0	80	262
22.5	14.0	31.3	0	80	262
45	3.5	7.8	0	80	262
45	7.0	15.7	0	80	262
45	10.5	23.5	0	80	262
45	14.0	31.3	0	80	262
67.5	3.5	7.8	0	80	262
67.5	7.0	15.7	0	80	262
67.5	10.5	23.5	0	80	262
67.5	14.0	31.3	0	80	262
90	3.5	7.8	0	80	262
90	7.0	15.7	0	80	262
90	10.5	23.5	0	80	262
90	14.0	31.3	0	80	262

**Table 44. Simulations for Single Altitude of 80 m (262 ft) AGL (Continued).**

Wind Direction (°)	Wind Speed		Turbulence Index	Flight Height (AGL)	
	(m/s)	(mph)		(m)	(ft)
0	10.5	23.5	5	80	262
22.5	10.5	23.5	5	80	262
45	10.5	23.5	5	80	262
67.5	10.5	23.5	5	80	262
90	10.5	23.5	5	80	262
0	0.0	0.0	10	80	262
0	3.5	7.8	10	80	262
0	7.0	15.7	10	80	262
0	10.5	23.5	10	80	262
22.5	3.5	7.8	10	80	262
22.5	7.0	15.7	10	80	262
22.5	10.5	23.5	10	80	262
45	3.5	7.8	10	80	262
45	7.0	15.7	10	80	262
45	10.5	23.5	10	80	262
67.5	3.5	7.8	10	80	262
67.5	7.0	15.7	10	80	262
67.5	10.5	23.5	10	80	262
90	3.5	7.8	10	80	262
90	7.0	15.7	10	80	262
90	10.5	23.5	10	80	262
0	0.0	0.0	20	80	262
0	3.5	7.8	20	80	262
0	7.0	15.7	20	80	262
0	10.5	23.5	20	80	262
22.5	3.5	7.8	20	80	262
22.5	7.0	15.7	20	80	262
22.5	10.5	23.5	20	80	262
45	3.5	7.8	20	80	262
45	7.0	15.7	20	80	262
45	10.5	23.5	20	80	262
67.5	3.5	7.8	20	80	262
67.5	7.0	15.7	20	80	262
67.5	10.5	23.5	20	80	262
90	3.5	7.8	20	80	262
90	7.0	15.7	20	80	262
90	10.5	23.5	20	80	262

The research team also conducted six simulation runs that involved flying the UAS at both altitudes of 80 m (262 ft) and 10 m (33 ft) as part of the same simulation run. As Figure 46 shows, in each simulation, after completing a set of runs at 80 m (262 ft), the UAS descended

and continued the mission at 10 m (33 ft) AGL. At this lower altitude, the flight path configuration was the same, but the flight lines were scaled down. The spacing between waypoints was 2.48 m (8.1 ft). The spacing between flight lines was 3.73 m (12 ft). Table 45 provides a summary of the six simulation runs.



**Figure 46. Flight Path for Dual Altitudes of 80 m (262 ft) and 10 m (33 ft) AGL.**

**Table 45. Simulations for Dual Altitudes of 80 m (262 ft) and 10 m (33 ft) AGL.**

Simulation Run	Wind Direction (°)	Wind Speed		Turbulence Index	Flight Height (AGL)	
		(m/s)	(mph)		(m)	(ft)
1	0	10.5	23.5	0	80	262
	0	3.5	7.8	0	10	33
2	45	10.5	23.5	0	80	262
	45	3.5	7.8	0	10	33
3	90	10.5	23.5	0	80	262
	90	3.5	7.8	0	10	33
4	0	10.5	23.5	10	80	262
	0	3.5	7.8	0	10	33
5	45	10.5	23.5	10	80	262
	45	3.5	7.8	0	10	33
6	90	10.5	23.5	10	80	262
	90	3.5	7.8	0	10	33

## Results

### *Performance Evaluation for Single Altitude Simulation Runs*

The following tables and figures summarize the results obtained:

- Average 3D errors between intended waypoints and actual camera trigger locations:
  - Table 46 shows average 3D errors (in m) in response to wind speed, direction, and turbulence variations.
  - Table 47 shows normalized average 3D errors, where the reference value was 0.19 m (0.62 ft), which corresponded to a reference zero-speed, no-turbulence wind scenario.
  - Table 48 shows average 3D errors by flight course.
  - Table 49 shows normalized average 3D errors by flight course with respect to a reference zero-speed, no-turbulence wind scenario.
  - Figure 47 shows a wind rose plot of average 3D errors for no-turbulence runs.
  - Figure 48 shows a wind rose plot of average 3D errors for all the simulation runs that included turbulence.
- Standard deviations of 3D errors:
  - Table 50 shows standard deviations (in m).
  - Table 51 shows normalized standard deviations, where the reference value was 0.04 m (0.13 ft), corresponding to a reference zero-speed, no-turbulence wind scenario.
  - Table 52 shows standard deviations by flight course.
  - Table 53 shows normalized standard deviations with respect to a reference zero-speed, no-turbulence wind scenario.
  - Figure 49 shows a wind rose plot of standard deviations for no-turbulence runs.
  - Figure 50 shows a wind rose plot of standard deviations for all the simulation runs that included turbulence.
- Flight times:
  - Table 54 shows total flight times (from the first image to the last image) for each simulation run.
  - Table 55 shows normalized total flight times, where the reference value was 318 seconds, corresponding to a reference zero-speed, no-turbulence wind scenario.
  - Table 56 shows flight times by flight course.
  - Table 57 shows normalized flight times by flight course. In this case, the reference value was 146 seconds, which corresponded to a reference scenario that included a headwind speed of 3.5 m/s (8 mph) and no turbulence.
  - Figure 51 shows a wind rose plot of flight times for no-turbulence runs.
  - Figure 52 shows a wind rose plot of flight times for all the simulation runs that included turbulence.
- Battery use:
  - Table 58 shows total battery use (in mAh).
  - Table 59 shows normalized total battery use with respect to a reference zero-speed, no-turbulence wind scenario.

**Table 46. Average 3D Errors (m) for 58 Single-Altitude Simulation Runs.**

Wind Speed		Wind Direction				
(m/s)	(mph)	0°	22.5°	45°	67.5°	90°
Turbulence Index = 0						
0.0	0	0.19				
3.5	8	0.19	0.19	0.2	0.19	0.19
7.0	16	0.19	0.19	0.2	0.19	0.2
10.5	23	0.19	0.2	0.2	0.21	0.24
14.0	31	0.24	0.34	0.66	0.71	0.66
Turbulence Index = 5						
10.5	23	0.26	0.26	0.26	0.28	0.3
Turbulence Index = 10						
0.0	0	0.26				
3.5	8	0.27	0.28	0.27	0.27	0.25
7.0	16	0.36	0.36	0.33	0.37	0.39
10.5	23	0.55	0.56	0.45	0.53	0.53
Turbulence Index = 20						
0.0	0	0.66				
3.5	8	0.67	0.62	0.56	0.6	0.54
7.0	16	0.78	0.9	0.71	0.8	0.83
10.5	23	1.25	1.28	1.36	1.21	1.09

**Table 47. Normalized Average 3D Errors for 58 Single Altitude-Simulation Runs.**

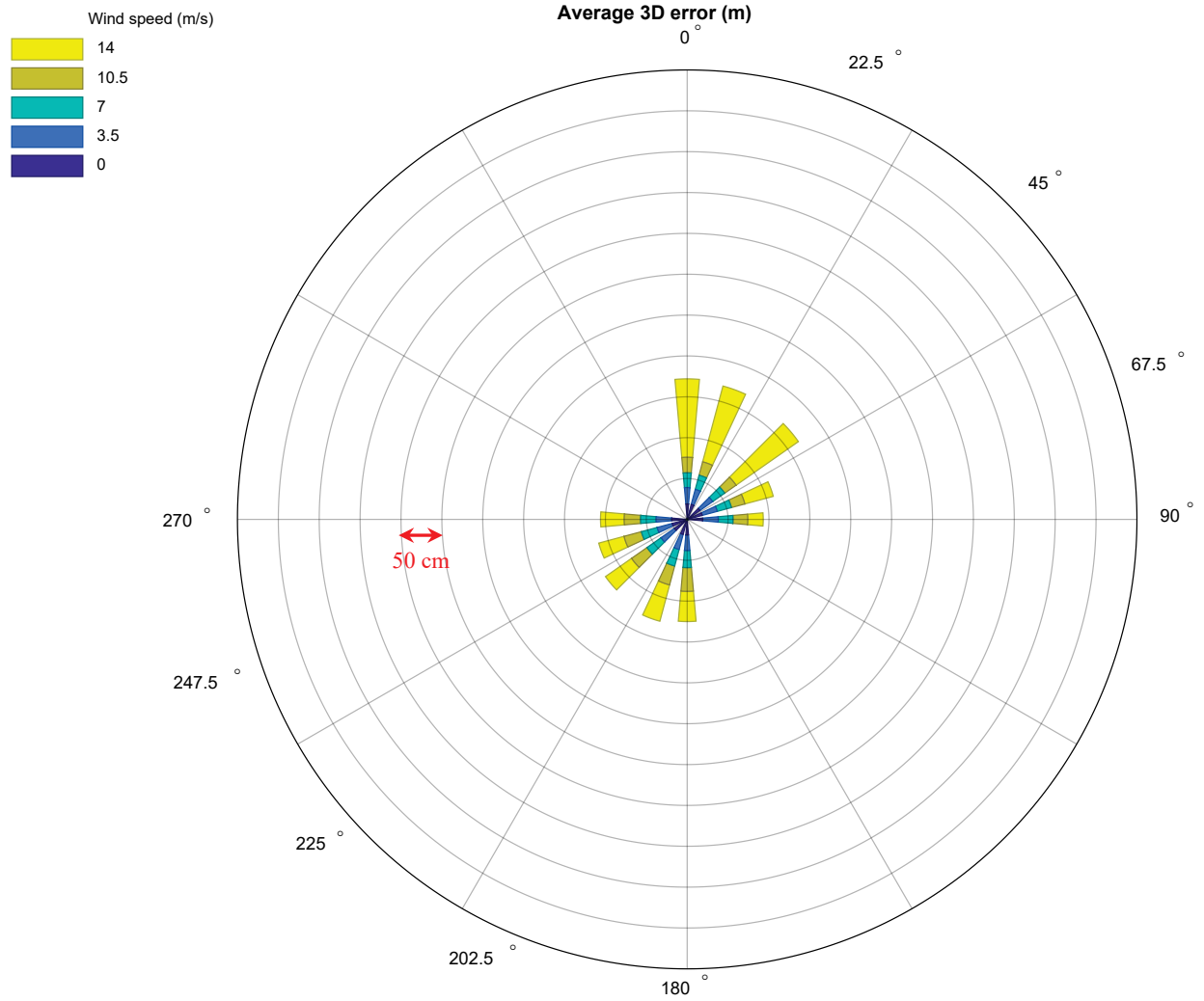
Wind Speed		Wind Direction				
(m/s)	(mph)	0°	22.5°	45°	67.5°	90°
Turbulence Index = 0						
0.0	0	1.00				
3.5	8	1.00	1.00	1.05	1.00	1.00
7.0	16	1.00	1.00	1.05	1.00	1.05
10.5	23	1.00	1.05	1.05	1.11	1.26
14.0	31	1.26	1.79	3.47	3.74	3.47
Turbulence Index = 5						
10.5	23	1.37	1.37	1.47	1.58	0.3
Turbulence Index = 10						
0.0	0	1.37				
3.5	8	1.42	1.47	1.42	1.42	1.32
7.0	16	1.89	1.89	1.74	1.95	2.05
10.5	23	2.89	2.95	2.37	2.79	2.79
Turbulence Index = 20						
0.0	0	3.47				
3.5	8	3.53	3.26	2.95	3.16	2.84
7.0	16	4.11	4.74	3.74	4.21	4.37
10.5	23	6.58	6.74	7.16	6.37	5.74

**Table 48. Average 3D Errors (m) by Flight Course for 58 Single-Altitude Simulation Runs.**

Wind Speed		Headwind	Tailwind	Crosswind							
(m/s)	(mph)			90°	270°	67.5°	247.5°	45°	225°	22.5°	202.5°
Turbulence Index = 0											
0.0	0	0.19									
3.5	8	0.20	0.19	0.19	0.19	0.19	0.19	0.19	0.20	0.19	0.19
7.0	16	0.18	0.21	0.18	0.19	0.18	0.20	0.18	0.21	0.18	0.21
10.5	23	0.19	0.29	0.18	0.20	0.17	0.22	0.17	0.23	0.17	0.24
14.0	31	0.96	0.37	0.19	0.29	0.36	0.32	0.93	0.39	0.96	0.46
Turbulence Index = 5											
10.5	23	0.30	0.30	0.23	0.30	0.25	0.27	0.22	0.30	0.30	0.26
Turbulence Index = 10											
0.0	0	0.26									
3.5	8	0.24	0.25	0.27	0.28	0.28	0.29	0.23	0.31	0.28	0.26
7.0	16	0.37	0.41	0.34	0.38	0.37	0.35	0.28	0.37	0.37	0.37
10.5	23	0.53	0.52	0.54	0.55	0.59	0.53	0.43	0.48	0.51	0.55
Turbulence Index = 20											
0.0	0	0.66									
3.5	8	0.54	0.54	0.72	0.62	0.53	0.72	0.55	0.57	0.60	0.61
7.0	16	0.84	0.81	0.70	0.86	1.06	0.73	0.74	0.67	0.82	0.78
10.5	23	1.14	1.03	1.35	1.16	1.14	1.42	1.20	1.52	1.10	1.31

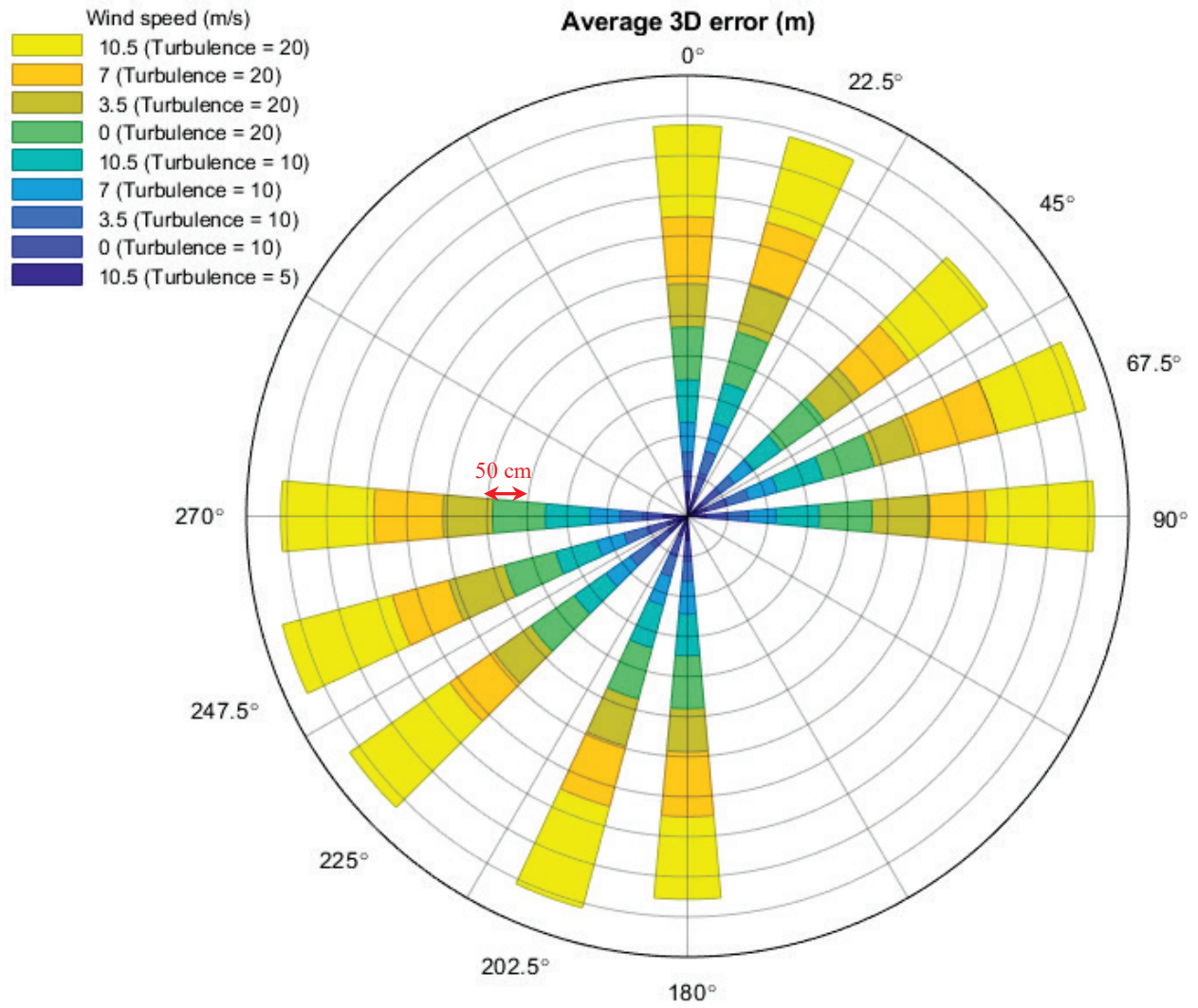
**Table 49. Normalized Average 3D Errors by Flight Course for 58 Single-Altitude Simulation Runs.**

Wind Speed		Headwind	Tailwind	Crosswind							
(m/s)	(mph)			90°	270°	67.5°	247.5°	45°	225°	22.5°	202.5°
Turbulence Index = 0											
0.0	0	1.00									
3.5	8	1.05	1.00	1.00	1.00	1.00	1.00	1.00	1.05	1.00	1.00
7.0	16	0.95	1.11	0.95	1.00	0.95	1.05	0.95	1.11	0.95	1.11
10.5	23	1.00	1.53	0.95	1.05	0.89	1.16	0.89	1.21	0.89	1.26
14.0	31	5.05	1.95	1.00	1.53	1.89	1.68	4.89	2.05	5.05	2.42
Turbulence Index = 5											
10.5	23	1.58	1.58	1.21	1.58	1.32	1.42	1.16	1.58	1.58	1.37
Turbulence Index = 10											
0.0	0	1.37									
3.5	8	1.26	1.32	1.42	1.47	1.47	1.53	1.21	1.63	1.47	1.37
7.0	16	1.95	2.16	1.79	2.00	1.95	1.84	1.47	1.95	1.95	1.95
10.5	23	2.79	2.74	2.84	2.89	3.11	2.79	2.26	2.53	2.68	2.89
Turbulence Index = 20											
0.0	0	3.47									
3.5	8	2.84	2.84	3.79	3.26	2.79	3.79	2.89	3.00	3.16	3.21
7.0	16	4.42	4.26	3.68	4.53	5.58	3.84	3.89	3.53	4.32	4.11
10.5	23	6.00	5.42	7.11	6.11	6.00	7.47	6.32	8.00	5.79	6.89



**Figure 47. Wind Rose Plot of Average 3D Errors for No-Turbulence Runs.**





**Figure 48. Wind Rose Plot of Average 3D Errors for All Simulation Runs with Turbulence.**

**Table 50. Standard Deviations (m) for 58 Single-Altitude Simulation Runs.**

Wind Speed		Wind Direction				
(m/s)	(mph)	0°	22.5°	45°	67.5°	90°
Turbulence Index = 0						
0.0	0	0.04				
3.5	8	0.03	0.03	0.04	0.04	0.03
7.0	16	0.03	0.04	0.04	0.04	0.04
10.5	23	0.04	0.05	0.05	0.05	0.07
14.0	31	0.18	0.18	0.31	0.29	0.34
Turbulence Index = 5						
10.5	23	0.11	0.09	0.15	0.11	0.16
Turbulence Index = 10						
0.0	0	0.10				
3.5	8	0.11	0.11	0.10	0.11	0.1
7.0	16	0.18	0.19	0.14	0.24	0.26
10.5	23	0.39	0.37	0.27	0.42	0.43
Turbulence Index = 20						
0.0	0	0.39				
3.5	8	0.48	0.42	0.32	0.49	0.34
7.0	16	0.65	0.62	0.41	0.50	0.50
10.5	23	0.55	0.71	0.82	0.8	0.59

**Table 51. Normalized Standard Deviations for 58 Single Altitude-Simulation Runs.**

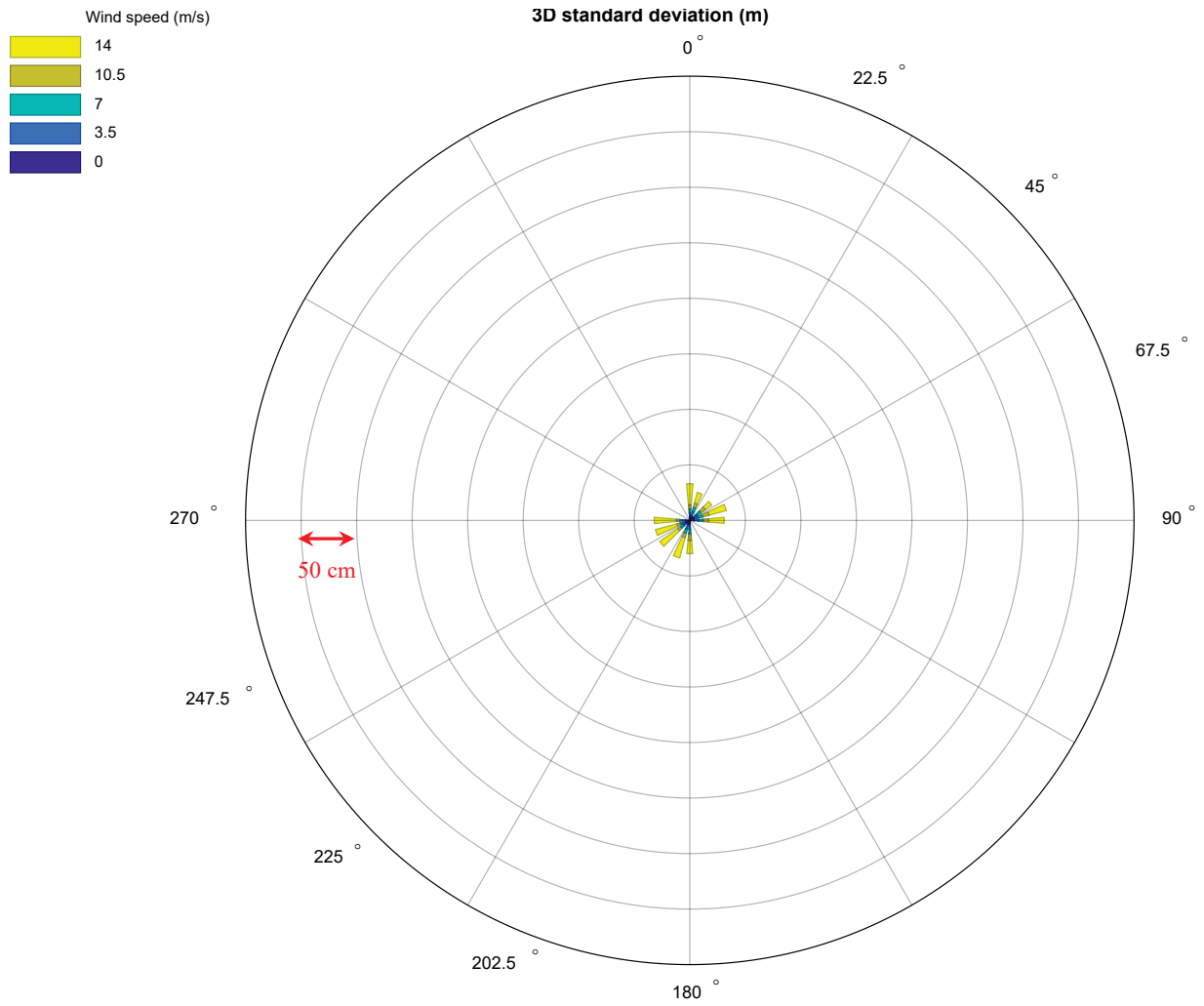
Wind Speed		Wind Direction				
(m/s)	(mph)	0°	22.5°	45°	67.5°	90°
Turbulence Index = 0						
0.0	0	1.00				
3.5	8	0.75	0.75	1.00	1.00	0.75
7.0	16	0.75	1.00	1.00	1.00	1.00
10.5	23	1.00	1.25	1.25	1.25	1.75
14.0	31	4.50	4.50	7.75	7.25	8.50
Turbulence Index = 5						
10.5	23	2.75	2.25	3.75	2.75	4.00
Turbulence Index = 10						
0.0	0	2.50				
3.5	8	2.75	2.75	2.50	2.75	2.50
7.0	16	4.50	4.75	3.50	6.00	6.50
10.5	23	9.75	9.25	6.75	10.50	10.75
Turbulence Index = 20						
0.0	0	9.75				
3.5	8	12.00	10.50	8.00	12.25	8.50
7.0	16	16.25	15.50	10.25	12.50	12.50
10.5	23	13.75	17.75	20.50	20.00	14.75

**Table 52. Standard Deviations (m) by Flight Course for 58 Single-Altitude Simulation Runs.**

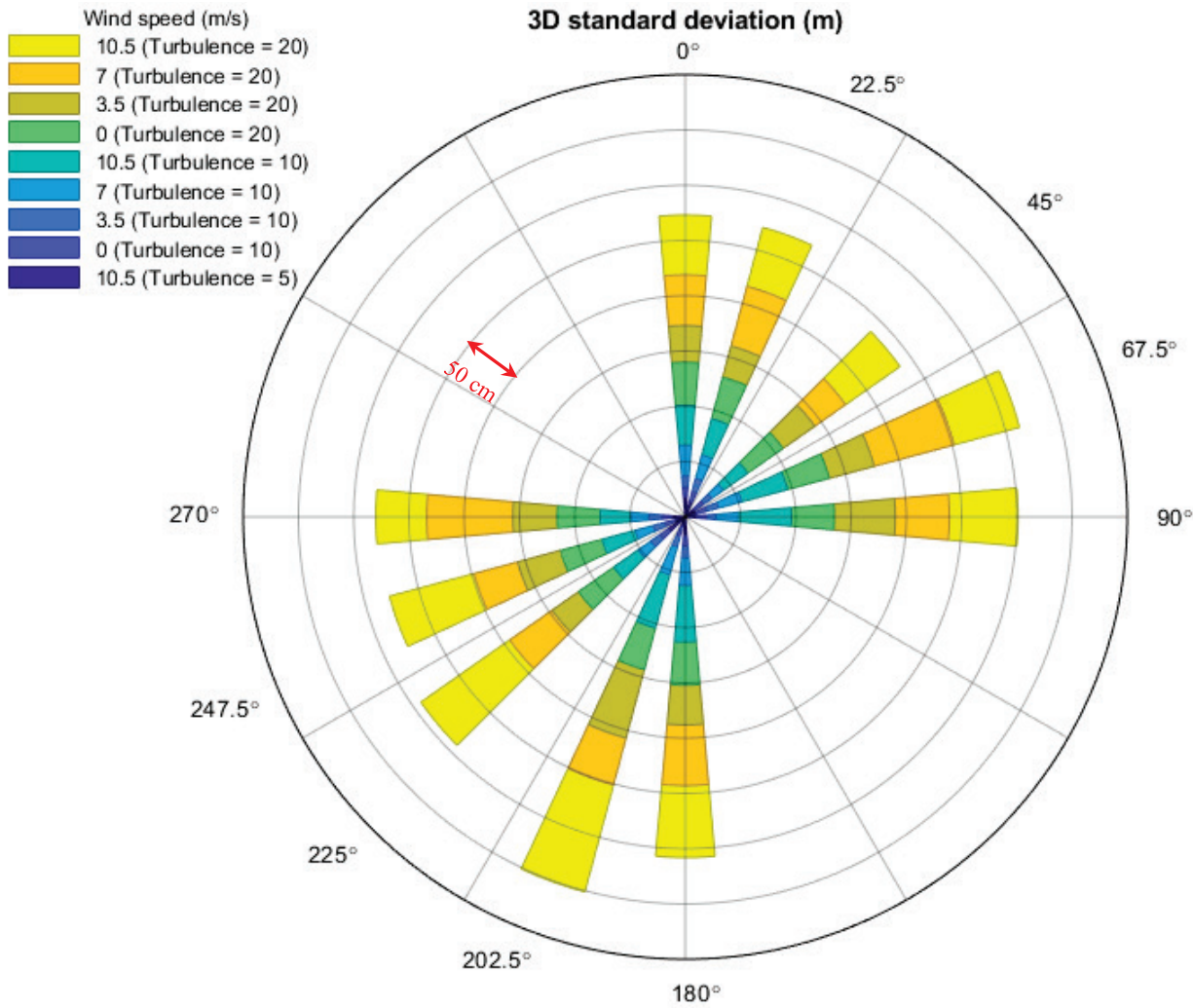
Wind Speed		Headwind	Tailwind	Crosswind							
(m/s)	(mph)			90°	270°	67.5°	247.5°	45°	225°	22.5°	202.5°
Turbulence Index = 0											
0.0	0	0.04									
3.5	8	0.03	0.04	0.04	0.03	0.04	0.03	0.04	0.03	0.04	0.04
7.0	16	0.03	0.04	0.04	0.02	0.04	0.02	0.04	0.03	0.04	0.04
10.5	23	0.04	0.06	0.05	0.03	0.06	0.03	0.05	0.03	0.04	0.04
14.0	31	0.19	0.12	0.14	0.20	0.16	0.20	0.07	0.20	0.10	0.19
Turbulence Index = 5											
10.5	23	0.17	0.16	0.09	0.11	0.10	0.09	0.10	0.18	0.14	0.08
Turbulence Index = 10											
0.0	0	0.10									
3.5	8	0.10	0.11	0.09	0.12	0.11	0.11	0.09	0.10	0.12	0.10
7.0	16	0.28	0.25	0.20	0.16	0.22	0.17	0.13	0.14	0.22	0.26
10.5	23	0.36	0.51	0.48	0.28	0.43	0.31	0.27	0.27	0.34	0.50
Turbulence Index = 20											
0.0	0	0.39									
3.5	8	0.33	0.36	0.55	0.40	0.42	0.40	0.35	0.29	0.29	0.64
7.0	16	0.46	0.55	0.49	0.78	0.75	0.41	0.34	0.47	0.56	0.44
10.5	23	0.54	0.65	0.62	0.46	0.61	0.79	0.60	0.98	0.55	1.00

**Table 53. Normalized Standard Deviations by Flight Course for 58 Single-Altitude Simulation Runs.**

Wind Speed		Headwind	Tailwind	Crosswind							
(m/s)	(mph)			90°	270°	67.5°	247.5°	45°	225°	22.5°	202.5°
Turbulence Index = 0											
0.0	0	1.00									
3.5	8	0.75	1.00	1.00	0.75	1.00	0.75	1.00	0.75	1.00	1.00
7.0	16	0.75	1.00	1.00	0.50	1.00	0.50	1.00	0.75	1.00	1.00
10.5	23	1.00	1.50	1.25	0.75	1.50	0.75	1.25	0.75	1.00	1.00
14.0	31	4.75	3.00	3.50	5.00	4.00	5.00	1.75	5.00	2.50	4.75
Turbulence Index = 5											
10.5	23	4.25	4.00	2.25	2.75	2.50	2.25	2.50	4.50	3.50	2.00
Turbulence Index = 10											
0.0	0	2.50									
3.5	8	2.50	2.75	2.25	3.00	2.75	2.75	2.25	2.50	3.00	2.50
7.0	16	7.00	6.25	5.00	4.00	5.50	4.25	3.25	3.50	5.50	6.50
10.5	23	9.00	12.75	12.00	7.00	10.75	7.75	6.75	6.75	8.50	12.50
Turbulence Index = 20											
0.0	0	9.75									
3.5	8	8.25	9.00	13.75	10.00	10.50	10.00	8.75	7.25	7.25	16.00
7.0	16	11.50	13.75	12.25	19.50	18.75	10.25	8.50	11.75	14.00	11.00
10.5	23	13.50	16.25	15.50	11.50	15.25	19.75	15.00	24.50	13.75	25.00



**Figure 49. Wind Rose Plot of Standard Deviations for No-Turbulence Runs.**



**Figure 50. Wind Rose Plot of Standard Deviations for All Simulation Runs with Turbulence.**

**Table 54. Total Flight Times (s) for 58 Single-Altitude Simulation Runs.**

Wind Speed		Wind Direction				
(m/s)	(mph)	0°	22.5°	45°	67.5°	90°
Turbulence Index = 0						
0.0	0	318				
3.5	8	318	318	318	318	318
7.0	16	318	318	318	318	318
10.5	23	319	318	318	318	319
14.0	31	358	359	416	448	456
Turbulence Index = 5						
10.5	23	320	323	325	325	325
Turbulence Index = 10						
0.0	0	320				
3.5	8	320	320	320	323	321
7.0	16	322	323	323	326	324
10.5	23	339	341	344	357	356
Turbulence Index = 20						
0.0	0	351				
3.5	8	360	346	357	353	362
7.0	16	377	374	390	391	397
10.5	23	635	635	665	635	657

**Table 55. Normalized Total Flight Times (s) for 58 Single-Altitude Simulation Runs.**

Wind Speed		Wind Direction				
(m/s)	(mph)	0°	22.5°	45°	67.5°	90°
Turbulence Index = 0						
0.0	0	1.00				
3.5	8	1.00	1.00	1.00	1.00	1.00
7.0	16	1.00	1.00	1.00	1.00	1.00
10.5	23	1.00	1.00	1.00	1.00	1.00
14.0	31	1.13	1.13	1.31	1.41	1.43
Turbulence Index = 5						
10.5	23	1.01	1.01	1.02	1.02	1.02
Turbulence Index = 10						
0.0	0	1.01				
3.5	8	1.01	1.00	1.01	1.01	1.01
7.0	16	1.01	1.02	1.02	1.02	1.02
10.5	23	1.07	1.07	1.08	1.12	1.12
Turbulence Index = 20						
0.0	0	1.10				
3.5	8	1.13	1.09	1.12	1.11	1.14
7.0	16	1.18	1.18	1.22	1.23	1.25
10.5	23	1.99	2.00	2.09	2.00	2.07

**Table 56. Flight Times (s) by Flight Course for 58 Single-Altitude Simulation Runs.**

Wind Speed		Headwind	Tailwind	Crosswind							
(m/s)	(mph)			90°	270°	67.5°	247.5°	45°	225°	22.5°	202.5°
Turbulence Index = 0											
0.0	0	N/A									
3.5	8	146	146	146	146	146	146	146	146	146	146
7.0	16	146	146	146	146	146	146	146	146	146	146
10.5	23	146	147	146	146	146	146	146	146	146	146
14.0	31	284	145	146	146	152	147	218	147	262	146
Turbulence Index = 5											
10.5	23	153	146	146	146	147	146	151	145	151	148
Turbulence Index = 10											
0.0	0	N/A									
3.5	8	148	146	146	147	148	146	148	146	151	146
7.0	16	153	145	148	147	150	146	151	145	152	147
10.5	23	178	151	150	158	156	152	170	146	177	150
Turbulence Index = 20											
0.0	0	N/A									
3.5	8	172	160	159	164	159	159	158	164	168	157
7.0	16	202	163	168	172	177	166	197	163	196	166
10.5	23	442	177	313	256	340	219	397	194	403	174

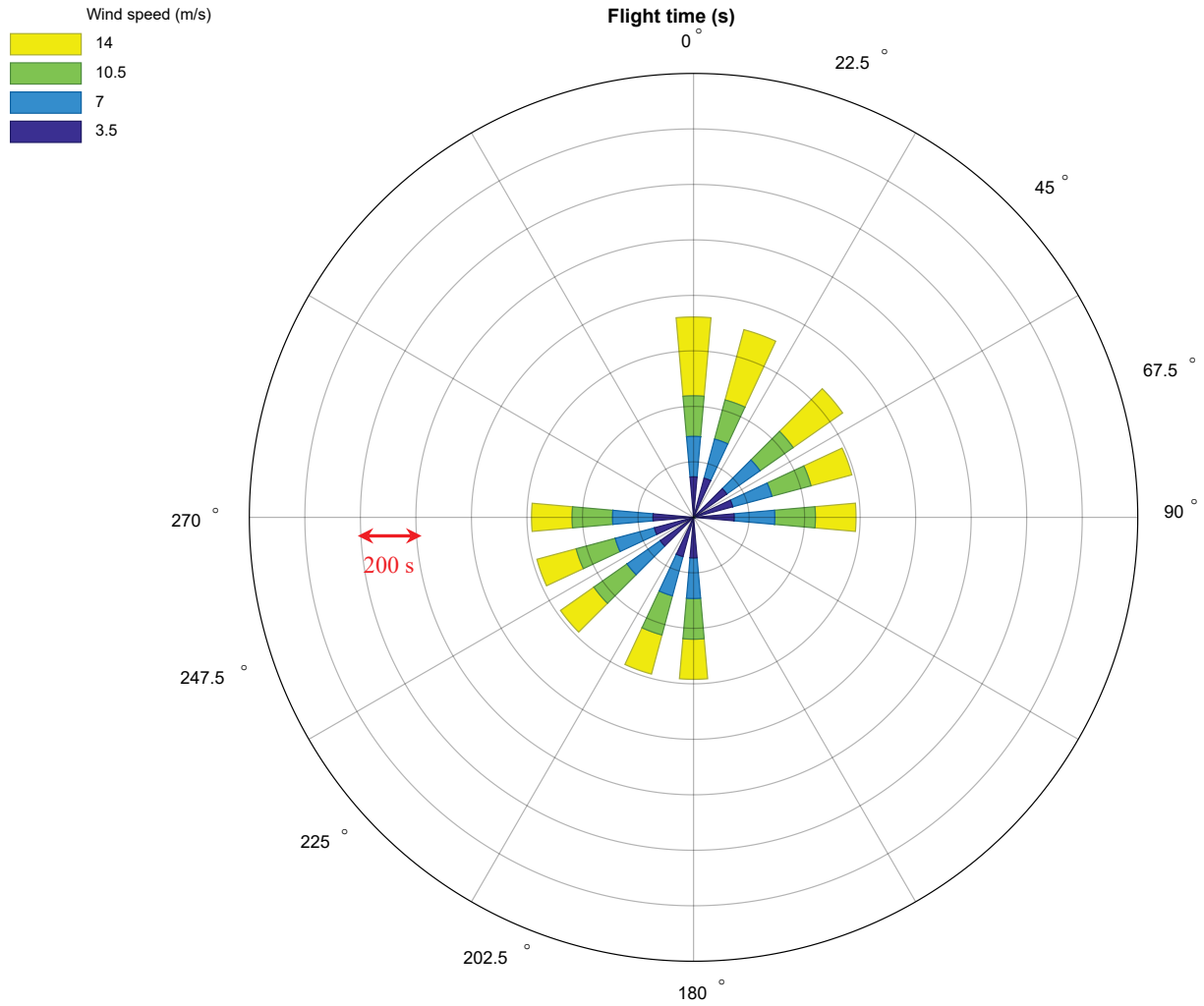
Note: This table excluded transit times between flight lines. This table did not include flight time information for all zero-speed simulation runs because they did not have headwind, tailwind or crosswind components.



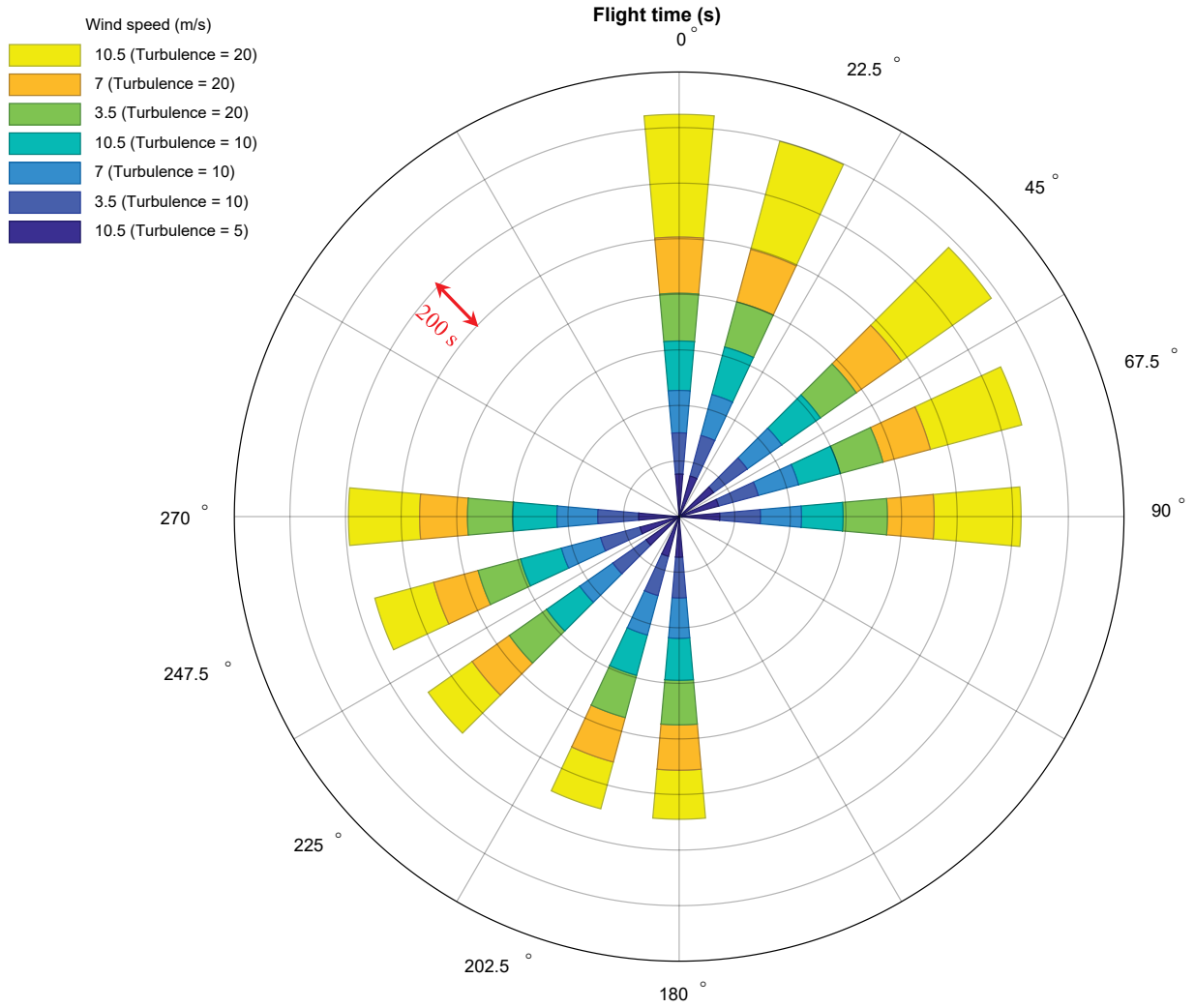
**Table 57. Normalized Flight Times (s) by Flight Course for 58 Single-Altitude Simulation Runs.**

Wind Speed		Headwind	Tailwind	Crosswind							
(m/s)	(mph)			90°	270°	67.5°	247.5°	45°	225°	22.5°	202.5°
Turbulence Index = 0											
0.0	0	N/A									
3.5	8	1.00	1.00	1.00	1.00	1.00	1.00	1.00	1.00	1.00	1.01
7.0	16	1.00	1.01	1.01	1.00	1.00	1.00	1.00	1.00	1.00	1.01
10.5	23	1.00	1.01	1.00	1.00	1.00	1.00	1.00	1.00	1.00	1.00
14.0	31	1.95	0.99	1.01	1.00	1.05	1.01	1.50	1.01	1.80	1.00
Turbulence Index = 5											
10.5	23	1.05	1.00	1.00	1.00	1.01	1.00	1.04	0.99	1.04	1.02
Turbulence Index = 10											
0.0	0	N/A									
3.5	8	1.02	1.01	1.00	1.01	1.01	1.00	1.02	1.00	1.04	1.00
7.0	16	1.05	1.00	1.02	1.01	1.03	1.00	1.04	1.00	1.05	1.01
10.5	23	1.22	1.04	1.03	1.09	1.07	1.04	1.16	1.00	1.22	1.03
Turbulence Index = 20											
0.0	0	N/A									
3.5	8	1.18	1.10	1.09	1.12	1.09	1.09	1.08	1.12	1.16	1.08
7.0	16	1.39	1.12	1.16	1.18	1.21	1.14	1.35	1.12	1.34	1.14
10.5	23	3.03	1.21	2.15	1.76	2.34	1.51	2.72	1.33	2.77	1.20

Note: The reference value was 146 seconds, which corresponded to a reference scenario that included a headwind speed of 3.5 m/s (8 mph) and no turbulence. This table did not include flight time information for all zero-speed simulation runs because they did not have headwind, tailwind, or crosswind components.



**Figure 51. Wind Rose Plot of Flight Times for All Turbulence-Free Runs.**



**Figure 52. Wind Rose Plot of Flight Times for All Simulation Runs with Turbulence.**

**Table 58. Battery Use (mAh) for 58 Single-Altitude Simulation Runs.**

Wind Speed		Wind Direction				
(m/s)	(mph)	0°	22.5°	45°	67.5°	90°
Turbulence Index = 0						
0.0	0	2601				
3.5	8	2661	2660	2660	2659	2659
7.0	16	2917	2910	2915	2921	2928
10.5	23	3214	3212	3217	3220	3224
14.0	31	3874	3883	4377	4707	4774
Turbulence Index = 5						
10.5	23	3233	3177	3188	3206	3274
Turbulence Index = 10						
0.0	0	2572				
3.5	8	2644	2639	2643	2657	2658
7.0	16	2953	2955	2943	2970	2952
10.5	23	3385	3323	3339	3511	3492
Turbulence Index = 20						
0.0	0	2726				
3.5	8	2904	2816	2865	2941	2893
7.0	16	3248	3219	3411	3413	3483
10.5	23	5537	5641	5849	5746	5822

**Table 59. Normalized Battery Use (mAh) for 58 Single-Altitude Simulation Runs.**

Wind Speed		Wind Direction				
(m/s)	(mph)	0°	22.5°	45°	67.5°	90°
Turbulence Index = 0						
0.0	0	1.00				
3.5	8	1.02	1.02	1.02	1.02	1.02
7.0	16	1.12	1.12	1.12	1.12	1.13
10.5	23	1.24	1.23	1.24	1.24	1.24
14.0	31	1.49	1.49	1.68	1.81	1.84
Turbulence Index = 5						
10.5	23	1.24	1.22	1.23	1.23	1.26
Turbulence Index = 10						
0.0	0	0.99				
3.5	8	1.02	1.01	1.02	1.02	1.02
7.0	16	1.14	1.14	1.13	1.14	1.13
10.5	23	1.30	1.28	1.28	1.35	1.34
Turbulence Index = 20						
0.0	0	1.05				
3.5	8	1.12	1.08	1.10	1.13	1.11
7.0	16	1.25	1.24	1.31	1.31	1.34
10.5	23	2.13	2.17	2.25	2.21	2.24

*Performance Evaluation for Dual Altitude Simulation Runs*

Table 60 shows summarized results for the six simulation runs that involved flying the UAS first at 80 m (262 ft) and then 10 m (33 ft) AGL as part of the same simulation run. The results include the case where the turbulence index was zero at both altitudes as well as the case where the turbulence index was different at either altitude. The results show the overall effect of changing wind direction and turbulence index on average 3D error, standard deviation of the 3D error, total flight time, and battery use.

**Table 60. Results for Six Dual-Altitude Simulation Runs.**

Evaluation Metric	Wind Direction		
	0°	45°	90°
Turbulence Index = 0 at both 10 m and 80 m			
Average 3D Error (m)	0.20	0.21	0.23
Standard Deviation (m)	0.05	0.05	0.06
Total Flight Time (s)	473	471	473
Battery Use (mAh)	4418	4418	4425
Turbulence Index = 0 at 10 m, Turbulence Index = 10 at 80 m			
Average 3D Error (m)	0.38	0.34	0.37
Standard Deviation (m)	0.33	0.23	0.35
Total Flight Time (s)	494	497	509
Battery Use (mAh)	4590	4539	4693

Note: The total flight time does not include the transition time from 80 m to 10 m.

Table 61 and Table 62 show disaggregated results. Table 61 shows evaluation metrics by disaggregating wind direction into headwind, tailwind, and four crosswind levels. As in the case of Table 60, Table 61 shows results that include the case where the turbulence index was zero at both altitudes as well as the case where the turbulence index was different at either altitude. For example, Table 60 shows 0.23 as the average 3D error for a wind direction of 90° and a turbulence index of zero both at 10 m (33 ft) and 80 m (262 ft). The two corresponding values in Table 61 are 0.21 and 0.25, which correspond to headwind and tailwind, respectively.

**Table 61. Disaggregated Results by Headwind, Tailwind, and Crosswind.**

Evaluation Metric	Headwind	Tailwind	Crosswind			
			90°	270°	45°	225°
Turbulence Index = 0 at both 10 m and 80 m						
Average 3D Error (m)	0.21	0.25	0.19	0.21	0.19	0.23
Standard Deviation (m)	0.05	0.07	0.06	0.04	0.05	0.04
Total Flight Time (s)	212	213	212	212	212	212
Turbulence Index = 0 at 10 m, Turbulence Index = 10 at 80 m						
Average 3D Error (m)	0.38	0.36	0.37	0.38	0.32	0.35
Standard Deviation (m)	0.30	0.39	0.38	0.26	0.22	0.23
Total Flight Time (s)	244	218	216	224	236	212

Note: The total flight time does not include the transition time from 80 m to 10 m or the transition time between flight lines.

Table 62 shows even more disaggregated results by considering subsets of images at each altitude separately. For example, the average 3D error was 0.53 (headwind) and 0.52 (tailwind) for the flight at 80 m (262 ft) and a turbulence index of 10. This error was considerably higher than the 3D error at the same altitude, assuming a turbulence index of zero.

**Table 62. Disaggregated Results by Headwind, Tailwind, Crosswind, and Flight Altitude.**

Evaluation Metric	Headwind	Tailwind	Crosswind			
			90°	270°	45°	225°
Turbulence Index = 0 at 80 m						
Average 3D Error (m)	0.19	0.29	0.18	0.20	0.17	0.23
Standard Deviation (m)	0.04	0.06	0.05	0.03	0.05	0.03
Total Flight Time (s)	146	147	146	146	146	146
Turbulence Index = 10 at 80 m						
Average 3D Error (m)	0.53	0.52	0.54	0.55	0.43	0.48
Standard Deviation (m)	0.36	0.51	0.48	0.28	0.27	0.27
Total Flight Time (s)	178	151	150	158	170	146
Turbulence Index = 0 at 10 m						
Average 3D Error (m)	0.22	0.20	0.19	0.21	0.22	0.22
Standard Deviation (m)	0.05	0.04	0.07	0.05	0.05	0.04
Total Flight Time (s)	66	66	67	67	66	66

Note: The total flight time does not include the transition time from 80 m to 10 m or the transition time between flight lines.

## Lessons Learned

Major lessons learned from the simulation exercise included the following:

- The average 3D error and corresponding standard deviation between planned waypoints and the actual camera trigger locations increased as the wind speed increased. The magnitude of the impact varied significantly as a function of the turbulence level. Specifically, as the turbulence level increased, the impact on the 3D error became more noticeable at lower speeds. The results were similar for the standard deviation. For example:
  - For low turbulence levels (i.e., turbulence index of 0 or 5), the average 3D error did not increase significantly if the wind speed was up to 10.5 m/s (23 mph). If the speed increased to 14 m/s (or 31 mph), the 3D error was 26 percent higher than the average 3D error for speeds up to 10.5 m/s (or 23 mph).
  - For a turbulence index of 10, the average 3D error began to vary significantly at lower speeds: 42 percent higher for a speed of 3.5 m/s (8 mph), 89 percent higher for a speed of 7.0 m/s (or 16 mph), and 189 percent higher for a speed of 10.5 m/s (or 23 mph).
  - For a turbulence index of 20, the average 3D error began to vary at even lower speeds: 253 percent higher for a speed of 3.5 m/s (8 mph), 311 percent higher for a speed of 7.0 m/s (or 16 mph), and 558 percent higher for a speed of 10.6 m/s (or 23 mph).

- Wind direction played a lesser role on the average 3D error and corresponding standard deviation than turbulence. However, the impact of wind direction increased as the wind speed and turbulence increased. For example:
  - For a turbulence index of zero, if the wind speed was up to 7.0 m/s (16 mph), the variation in average 3D error due to differences in wind direction was up to 16 percent. Compared to a reference zero-speed, no-turbulence wind scenario, the average 3D error varied from –5 percent (90 degrees crosswind) to 11 percent (225 degrees crosswind). The impact was more noticeable as the wind speed increased. If the wind speed was 10.5 m/s (23 mph), the variation in average 3D error due to differences in wind direction was up to 64 percent. At 14 m/s (31 mph), the variation in average 3D error due to differences in wind direction was up to 405 percent.
  - For a turbulence index of 10, if the wind speed was up to 7.0 m/s (16 mph), the variation in average 3D error due to differences in wind direction was up to 69 percent. If the wind speed was 10.5 m/s (23 mph), the variation in average 3D error due to differences in wind direction was up to 85 percent.
  - For a turbulence index of 20, if the wind speed was up to 7.0 m/s (16 mph), the variation in average 3D error due to differences in wind direction was up to 205 percent. If the wind speed was 10.5 m/s (23 mph), the variation in average 3D error due to differences in wind direction was up to 258 percent.
- The total flight time (or time to complete a mission) was less sensitive to changes in wind speed, direction, and turbulence conditions than the average 3D error and standard deviation. In general:
  - If the wind speed was up to 7.0 m/s (16 mph) and the turbulence index was up to 10, the flight time varied less than 5 percent compared to a reference zero-speed, no-turbulence wind scenario. At this wind speed, even if the turbulence index was 20, the total flight time varied less than 25 percent compared to a reference zero-speed, no-turbulence wind scenario.
  - If the wind speed was 10.5 m/s (or 23 mph) and the turbulence index was up to 10, the total flight time varied less than 12 percent. However, if the turbulence level was 20, the total flight time varied 109 percent compared to a reference zero-speed, no-turbulence wind scenario.
  - If the wind speed was up to 7.0 m/s (16 mph) and the turbulence index was up to 10, the variation in total flight time between tailwind and headwind conditions was no larger than 5 percent. Headwind conditions produced a higher total flight time.
  - The effect due to differences between headwind and tailwind conditions was more noticeable for higher speeds and turbulence levels. If the wind speed was 10.5 m/s (or 23 mph) and the turbulence index was 10, the total flight time was 18 percent higher under headwind conditions than under tailwind conditions. However, if the wind speed was 14 m/s (or 31 mph) and the turbulence index was 20, the total flight time was 182 percent higher under headwind conditions than under tailwind conditions (which was already 21 percent higher than for a reference zero-speed, no-turbulence wind scenario).
- Battery use was also less sensitive to changes in wind speed, direction, and turbulence conditions than the average 3D error and standard deviation. In general:

- If the wind speed was up to 7.0 m/s (16 mph) and the turbulence index was up to 10, the flight time varied less than 14 percent compared to a reference zero-speed, no-turbulence wind scenario. At this wind speed, even if the turbulence index was 20, the total battery use varied less than 34 percent compared to a reference zero-speed, no-turbulence wind scenario.
- If the wind speed was 10.5 m/s (or 23 mph) and the turbulence index was up to 10, the battery use varied less than 14 percent. However, if the turbulence level was 20, the battery use varied 125 percent compared to a reference zero-speed, no-turbulence wind scenario.

In general, the simulations confirm the accepted practice of operating UASs if the wind is no more than 30 mph and under light to moderate turbulence levels. As wind conditions depart from the ideal zero-speed, no-turbulence wind scenario, equipment performance is affected, as measured in terms of positional accuracy, required flight time, and battery use.

## **IMPACT OF AERIAL IMAGING NETWORK DESIGN ON 3D CRASH SCENE RECONSTRUCTIONS**

The research team ran a series of experiments to evaluate the effects of aerial imaging network design (with an emphasis on the percentage of overlap) on the capability of commercial SfM software to generate 3D crash scene reconstructions. The analysis focused on the influence of different amounts of overlap on the automated feature matching, BA results, densified point cloud quality, flight time, and processing time using simulated data generated from a real-world crash scene. Additional simulations examined how random perturbations to camera position and orientation provided by an onboard GNSS and IMU, respectively, impacted SfM crash scene reconstruction results under high wind conditions.

### **General Concepts**

An operational challenge is how to achieve an optimal UAS-SfM flight design for a given sensor configuration without increasing flight and image processing time excessively (88, 89). For a crash scene reconstruction, two key aspects determine the image reconstruction quality: (a) the detail captured in the reconstruction and (b) the location precision of these reconstructed points in a 3D space. Finding a balance between detail and efficiency requires the UAS pilot to make choices about flight height, image overlap, and flight speed. The pilot can also set sensor parameters such as exposure time and camera perspective that determine the field-of-view (FOV). These parameters influence flight design and imaging conditions during a survey.

### *Flight Design*

For conducting SfM photogrammetry missions with UASs, the two main parameters that govern flight design are GSD and image overlap. As discussed, the mission height AGL determines the GSD for any given camera. Height also affects the number of batteries and flight time required to complete a mission. Flight control software typically provides an estimated GSD for a chosen height to aid in making this decision. For manual flying of crash scenes, experienced pilots use estimates of GSD to target specific flight heights based on their manual flight procedure.



GSD is the primary factor that determines the spatial resolution of an image. Because GSD depends on the UAS flight height, the choice in flight height for a given camera setting directly impacts the size of detectable features in the acquired imagery. Finer details can be seen in a higher resolution image with a smaller GSD. Conversely, a low-resolution image has a larger GSD, but only coarser features can be seen. A frequently used rule of thumb is that an object needs to be at least four times the size of the area represented by the GSD.

The spatial resolution of an image is not only a function of the GSD. Digital cameras convert light energy that falls on the sensor array into electrical signals. The capability of a camera to accomplish this task is affected by several factors, including the quality of the sensor, radiometric resolution, camera settings such as International Standards Organization (ISO) sensitivity, and ambient conditions such as natural lighting at the time of imaging (88).

For SfM reconstruction, GSD affects the overall density of the point cloud during the MVS densification phase of the SfM processing workflow. Densification of the point cloud can occur at the highest resolution (i.e., smallest average GSD) obtained throughout the imaging survey. High camera resolutions and typical low altitudes at which UAS data are normally collected can result in point densities exceeding several hundreds or even thousands of points per square meter. To compensate, SfM software allows the output of the densified point cloud at a reduced point density.

GSD also plays an important role in feature extraction and the keypoint matching process during the initial phase of the SfM workflow and generation of the sparse point cloud. Higher resolution images enable more potential feature matches and may result in higher image texture, which is beneficial for SfM, but that relationship is complex and depends heavily on the homogeneity or lack thereof in the features visible in the imagery.

### *Image Overlap*

Two types of overlap are of interest: frontal overlap within the same flight line (or endlap) and side overlap between flight lines (or sidelap). endlap is a function of flight speed and the time interval (i.e., distance) between image exposure stations, while sidelap is a function of the distance between flight lines. Both depend on height AGL and sensor size. The amount of overlap is expressed as (89, 90):

$$O_{endlap} = \left(1 - \frac{d_{end}f}{Hh}\right) \times 100 \quad (8)$$

$$O_{sidelap} = \left(1 - \frac{d_{side}f}{Hw}\right) \times 100 \quad (9)$$

where:

$O_{endlap}$  = endlap (in percentage),

$O_{sidelap}$  = sidelap (in percentage),

$d_{end}$  = distance between exposure stations,

$d_{side}$  = distance between flight lines,

$f$  = focal length,

$H$  = distance from the camera projection center to the ground,  
 $h$  = height of the sensor frame, and  
 $w$  = width of the sensor frame oriented perpendicular to the flight course.

Another way to express overlap is in terms of the number of images that are necessary to see a point (78):

$$O = \left(1 - \frac{1}{n}\right) \times 100 \quad (10)$$

where:

$O$  = overlap (in percentage), and  
 $n$  = number of images that see a point.

Table 63 lists the overlap percentage as a function of the number of images that see a point.

**Table 63. Number of Images That See a Point as a Function of the Overlap.**

Number of Images (n)	Overlap Percentage
2	50.0%
3	66.7%
4	75.0%
5	80.0%
6	83.3%
7	85.7%
8	87.5%

In practice, image acquisition plans may vary depending on project requirements and UAS capabilities, as well as environmental conditions such as weather. Additional information about flight design for UAS mapping is available elsewhere (91).

#### *Operational Tradeoffs for UAS Flight Design of Crash Scenes*

GSD, image overlap, and flight parameters have an impact on SfM reconstruction. Trade-offs exist between these factors. A common example is the trade-off between flight height and area covered during the flight, which is affected by the sensor's FOV and the UAS battery life (which determines the UAS flight time). As the height increases, the area that can be covered by the UAS on a single battery charge increases, and the number of images that need to be processed decreases. However, increasing height also affects the GSD and, therefore, the spatial details that can be detected from the imagery (89).

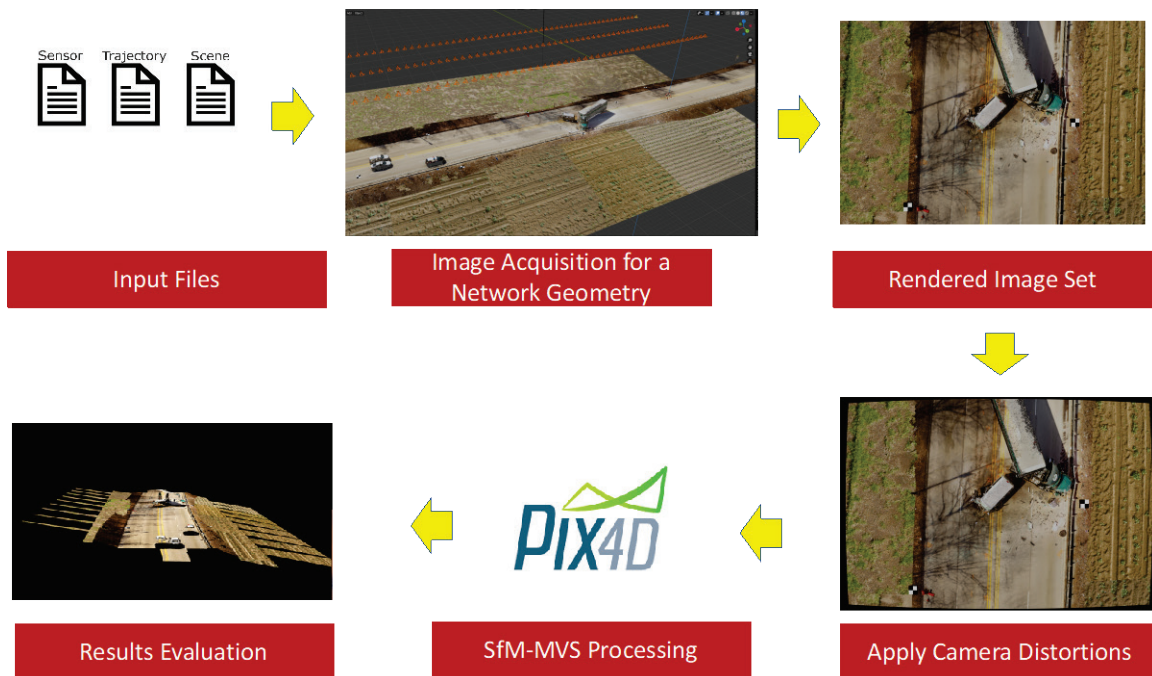
Similar trade-offs exist between endlap and sidelap. Although the endlap can be managed by varying the number of images per second within the flight line, the sidelap is based on parallel flight lines and a key variable in UAS flight planning. Greater height AGL enables more separation distance between images in the along-track direction and allows more separation distance between parallel flight lines while helping to maintain desired endlap and sidelap percentages, thereby reducing flight times.

For crash scene reconstruction, data collection time is critical. Therefore, a mission objective is to reduce flight time while maintaining sufficient GSD and overlap settings for high fidelity reconstruction. Suboptimal conditions, such as high wind or poor lighting, provide another layer of operational complexity to this problem, forcing the UAS pilot to make flight decisions based on factors that may not be ideal for photogrammetric reconstruction, such as flying in low light conditions or reducing overlap coverage due to high winds.

## Methods

### Simulation Framework

Figure 53 summarizes the UAS imaging network simulation and processing framework. The research team imported a 3D model from an actual crash into a 3D modeling and simulation environment to generate synthetic images representing different flight height, endlap, and sidelap conditions. The research team then fed the simulated imagery directly into SfM-MVS photogrammetry software to examine impacts on 3D reconstruction. The framework developed here is based on a method called simUAS (42). The team adapted the method to enable the simulation of any combination of overlap settings, allowing the evaluation of myriad combinations of flight designs not practical in the field.



**Figure 53. Summary of the Entire UAS Imaging Simulation and Processing Framework.**

For the analysis, the research team used a real-world crash scene provided by NUCPS. The data is representative of optimal ambient lighting and weather conditions. The dataset consisted of 409 images acquired using a DJI FC350 camera onboard a multi-rotor platform flying at 20 m (66 ft) AGL. The image resolution was  $4000 \times 3000$  pixels, resulting in a GSD of about 8.5 mm.

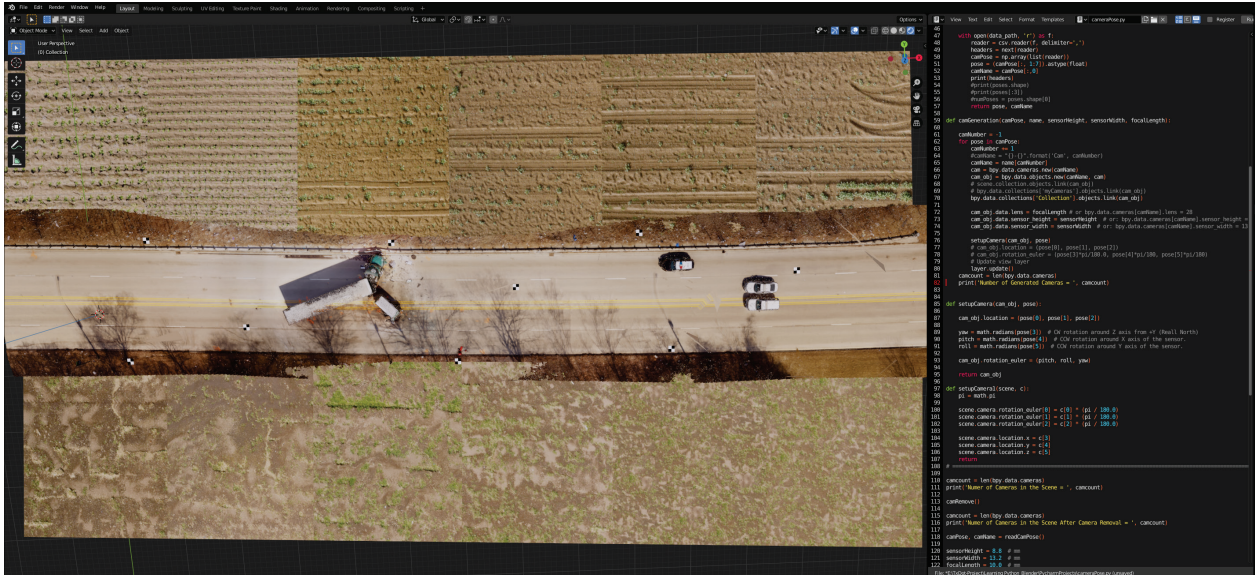
The research team processed the data using a commercial SfM photogrammetry software, Agisoft Metashape, to create a dense point cloud containing 219,949,507 points. From the dense

point cloud, further processing created a  $278 \times 26$  m ( $912 \times 85$  ft) texturized mesh (i.e., a 3D model) at a resolution of 7.60 mm/pixel and a point density of 1.73 points/cm<sup>2</sup>. The 26 m (85 ft) cross section included the road (16 m or 52 ft) and two 5 m (16 ft) shoulder lanes. To reduce the computational burden of image rendering, preprocessing, and SfM postprocessing tasks, the research team used half of the reconstructed real scene including the crash scene. This resulted in a  $156 \times 26$  m ( $512 \times 85$  ft) scene.

The research team used *Blender*—a free open-source 3D modeling, simulation, and visualization software—to develop a framework to simulate the acquisition and rendering of UAS images under a variety of flight height, endlap, and sidelap conditions. The research team imported the 3D model from the actual crash into Blender using a local coordinate system consistent with the real-world dimensions. The roadway was aligned in the east-west direction in this local system. The research team introduced eight virtual square control targets as GCPs distributed evenly throughout the scene. The dimension of each target was  $1 \times 1 \times 0.05$  m ( $3.28 \times 3.28 \times 0.16$  ft).

To ensure adequate texture on the edges of the scene while allowing enough area to simulate various aerial imaging geometries in Blender, the research team added rectangular  $150 \times 30$  m ( $492 \times 98$  ft) mesh patches to both sides of the road. To texturize the additional mesh patches, the research team used ten  $1000 \times 1000$ -pixel images that created an effective texture element (or texel) of  $1.5 \times 1.8$  cm in size (in the X and Y directions, respectively).

The rendering operation modeled objects as perfect Lambertian reflecting surfaces. A Lambertian surface is a diffuse surface that scatters incident illumination equally in all directions. Scene illumination applied a lamp model that simulated sun-style lighting with parallel light rays. Placement of the light source vertically in the middle of the scene at 90 degrees with respect to the horizon reduced the length of shadows in the scene. Figure 54 shows the high-resolution 3D mesh model imported with the additional flat surfaces. Figure 54 also shows the text editor environment used with the Blender Python application programming interface (API) to set up the required parameters for defining the scene structure, scene illumination, camera specifications, and rendering constraints. Figure 55 shows a 3D view of the crash scene.



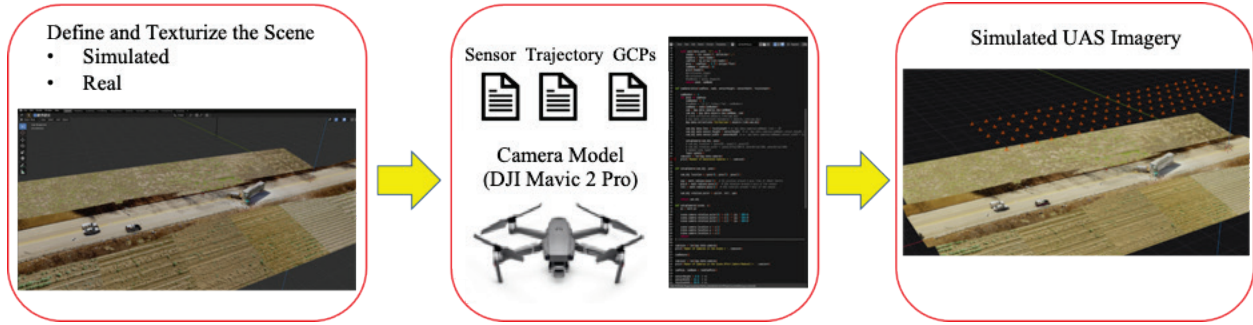
**Figure 54. Top View of the 3D Textured Mesh.**

The simulation framework used the Blender Python API to calculate all the parameters required for the simulation and subsequently render images using the Blender Internal Render Engine. After setting the required UAS flight mission parameters, including endlap and sidelap values, flight height, and camera internal parameters (such as focal length and sensor size), the simulation rendered images from each camera position and orientation. Figure 56 shows a simplified overview of the image rendering framework within Blender used to simulate different UAS imaging networks.



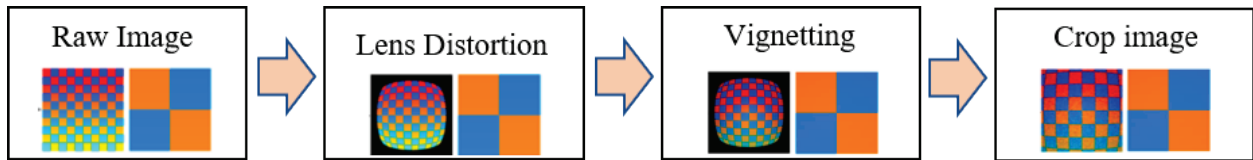
Note: Identifiable information was masked for the purpose of preparing this picture.

**Figure 55. 3D View of the Crash Scene.**



**Figure 56. UAS Image Acquisition Framework in Blender.**

The rendered image sets corresponding to each overlap scenario underwent postprocessing in MATLAB to apply distortions to the pixels of each individual image within each image set. This step was necessary because the Blender Internal Render Engine used an approximately perfect pinhole camera model to render images from the 3D scene. Real-world cameras produce image aberrations and geometric distortions due to imperfections in optical components and sensors. The resulting images (referred to as distorted images) represented real-world imagery acquired from a consumer-grade digital camera more accurately. Figure 57 shows a flowchart depicting this postprocessing step.



**Figure 57. Postprocessing Steps Applied to Raw Images Rendered by Blender.**

The distortion applied in MATLAB was a nonlinear Brown distortion that shifted the raw image coordinates and interpolated pixel intensities in the distorted image space, as follows (92):

$$r = \sqrt{(x - c_x)^2 + (y - c_y)^2} \quad (11)$$

$$x' = x \left( 1 + \frac{K_1}{f^2} r^2 + \frac{K_2}{f^4} r^4 + \frac{K_3}{f^6} r^6 + \frac{K_4}{f^8} r^8 \right) + \frac{P_1}{f} (r^2 + 2x^2) + \frac{2P_2}{f} xy \quad (12)$$

$$y' = y \left( 1 + \frac{K_1}{f^2} r^2 + \frac{K_2}{f^4} r^4 + \frac{K_3}{f^6} r^6 + \frac{K_4}{f^8} r^8 \right) + \frac{P_2}{f} (r^2 + 2y^2) + \frac{2P_1}{f} xy \quad (13)$$

where:

$(c_x, c_y)$  = principal point coordinates (in pixels);

$(x, y)$  = pixel coordinates in the undistorted image;

$(x', y')$  = corresponding pixel coordinates in the distorted image;

$K_1, K_2, K_3, K_4, P_1,$  and  $P_2$  = radial and tangential lens distortion coefficients; and

$f$  = focal length.

A vignetting effect was then applied to each distorted image to reduce the image brightness toward the periphery, as follows (42):

$$I_{corr} = I_{raw} + \vartheta_1 + \vartheta_2 r + \vartheta_3 r^2 \quad (14)$$

where:

$I_{raw}$  = original pixel digital number, and

$I_{corr}$  = corrected pixel digital number after applying the vignetting effect.

Table 64 shows the constants used in the process.

**Table 64. Parameters for Image Lens Distortion and Vignetting Effects.**

Parameter	Value	Units
$c_x$	50	pixel
$c_y$	50	pixel
$K_1$	-0.001	pixel <sup>2</sup>
$K_2$	0.000	pixel <sup>4</sup>
$K_3$	0.000	pixel <sup>6</sup>
$K_4$	0.000	pixel <sup>8</sup>
$P_1$	0.000	pixel <sup>2</sup>
$P_2$	0.000	pixel <sup>2</sup>
$\vartheta_1$	10.00	pixel
$\vartheta_2$	0.200	unitless
$\vartheta_3$	0.000	pixel <sup>-1</sup>

### *Simulation Scenarios*

The simulation evaluated 16 overlap scenarios ranging from 60 percent endlap (E60) and 60 percent sidelap (S60) to 90 percent endlap (E90) and 90 percent sidelap (S90), with 10 percent incremental steps. All simulations used a 20-MP 2.5-cm (1-inch) sensor frame Hasselblad camera model, which is carried onboard a DJI Mavic 2 Pro. The flight height was 30 m (98 ft). Table 65 lists the camera settings. Table 66 shows the number of images rendered for each overlap scenario.

**Table 65. Camera Settings.**

Setting	Value
Focal Length	10 mm
Sensor Size	13.2 x 8.8 mm
Pixel Pitch	2.42 $\mu$ m
Resolution	5472x3648 pixels
Flight Height	29.9 m (98 ft)
GSD	7.2 mm

**Table 66. Overlap Scenarios.**

<b>Overlap Scenario</b>	<b>Description</b>	<b>Number of Images Rendered</b>
E60-S60	60% endlap and 60% sidelap	36
E60-S70	60% endlap and 70% sidelap	45
E60-S80	60% endlap and 80% sidelap	56
E60-S90	60% endlap and 90% sidelap	133
E70-S60	70% endlap and 60% sidelap	46
E70-S70	70% endlap and 70% sidelap	61
E70-S80	70% endlap and 80% sidelap	76
E70-S90	70% endlap and 90% sidelap	181
E80-S60	80% endlap and 60% sidelap	64
E80-S70	80% endlap and 70% sidelap	85
E80-S80	80% endlap and 80% sidelap	106
E80-S90	80% endlap and 90% sidelap	253
E90-S60	90% endlap and 60% sidelap	154
E90-S70	90% endlap and 70% sidelap	205
E90-S80	90% endlap and 80% sidelap	256
E90-S90	90% endlap and 90% sidelap	603

*SfM Data Processing*

Photogrammetric processing of all rendered image sets used commercial SfM photogrammetry software, Pix4Dmapper Version 4.5.6 (i.e., Pix4D). More specifically, the research team used Pix4D’s standard 3D mapping template (with a few modifications as described below). This template relies on self-calibration of the camera’s internal parameters and uses several default settings for calibration and aerial triangulation, sparse point cloud generation, and densification. The purpose of using the standard 3D mapping template was to replicate as much as possible the typical workflow that practitioners follow when using photogrammetry software for crash reconstructions. In other words, the simulation assumed a user with a basic level of photogrammetry concepts and procedures.

The exact camera position and orientation values were known from the simulation environment. However, to ensure consistency with a real-world scenario, the research team used a standard setting in Pix4D for geolocation uncertainty based on a typical single-frequency, nondifferential GNSS receiver, such as onboard a DJI Mavic 2 Pro. This setting in Pix4D’s standard mapping template equates to a geolocation uncertainty of  $\pm 5$  m (16 ft) horizontally and  $\pm 10$  m (33 ft) vertically for image geolocations. Note that uncertainty here, and in Pix4D terminology, refers to the standard deviation of a parameter’s expected value.

The camera calibration and distortion values were also known from the simulation environment. To ensure consistency with a real-world scenario, all simulations used the default camera model values for the Hasselblad camera stored in the Pix4D standard camera library.

Calibration of the internal parameters used the “all prior” setting in Pix4D, which told Pix4D to provide more weight to the initial camera values in the BA. This condition constrained the optimized solution to remain close to the initial values. Strictly speaking, using the all prior



setting was not part of the Pix4D standard mapping template, but the justification to use it here was to ensure consistent behavior during the calibration and to reduce any undesirable variability resulting from the use of the simulated images that were created in Blender. Although Blender enabled the production of controlled imagery that was suitable for simulation, the simulation still used as input an artificial 3D-textured mesh of a real 3D scene generated from UAS imagery acquired at a certain time and under certain conditions.

Reduced scene texture and artifacts in the scene, such as shadowing in the pixels stemming from the real shadows during the actual UAS flight, could have caused unexpected behavior during the initial BA and calibration phase. Using the all prior setting helped to control this potential behavior while still ensuring a fair assessment of the different stages of the SfM processing workflow for different overlap scenarios.

The end product resulting from processing each overlap scenario is a densified 3D point cloud that is within a localized, properly scaled coordinate system. Figure 58 shows Pix4D’s initial processing and point cloud densification settings.

(a) Initial processing settings

Detected Template	No Template Available
Keypoints Image Scale	Full, Image Scale: 1
Advanced: Matching Image Pairs	Aerial Grid or Corridor
Advanced: Matching Strategy	Use Geometrically Verified Matching: no
Advanced: Keypoint Extraction	Targeted Number of Keypoints: Automatic
Advanced: Calibration	Calibration Method: Standard Internal Parameters Optimization: All prior External Parameters Optimization: All Rematch: Auto, yes

(b) Point cloud densification settings

Image Scale	multiscale, 1/2 (Half image size, Default)
Point Density	Optimal
Minimum Number of Matches	3
3D Textured Mesh Generation	no
LOD	Generated: no
Advanced: Image Groups	group1
Advanced: Use Processing Area	yes
Advanced: Use Annotations	yes
Time for Point Cloud Densification	05m:11s
Time for Point Cloud Classification	NA
Time for 3D Textured Mesh Generation	NA

**Figure 58. Pix4D’s Initial Processing and Densification Settings Used for Simulations.**

### *Evaluation Metrics*

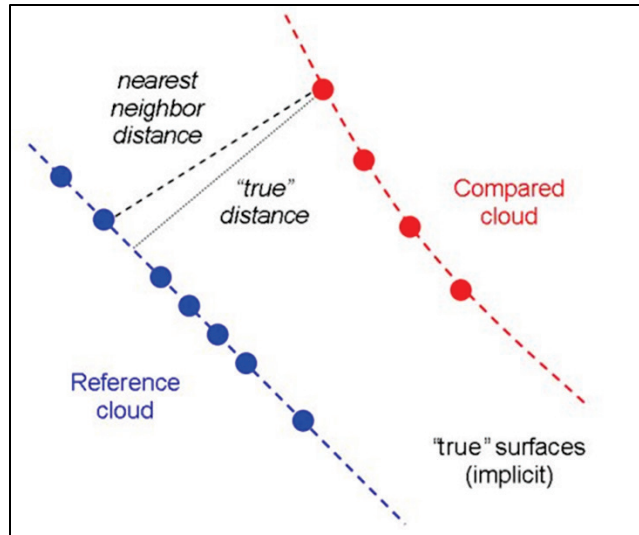
The research team evaluated the influence of different overlap scenarios on the quality of the 3D reconstruction results by examining quality factors at each of the three key stages of the full SfM workflow implemented by the Pix4D software:

- Stage 1: Keypoint extraction and matching.
- Stage 2: Calibration and bundle block adjustment (i.e., sparse point cloud phase).
- Stage 3: Dense point cloud generation.

For Stages 1 and 2, the research team focused on quality factors that were available from the Pix4D processing report and included metrics such as reprojection error, estimated camera position and orientation uncertainty, and checkpoint geolocation error. For the latter, the processing workflow set all GCPs as checkpoints to assess SfM reconstruction accuracy and none were used to constrain the SfM solution during the bundle block adjustment. The camera positions with respect to the local coordinate system used in Blender were tagged to the imagery and used within Pix4D for SfM processing. This procedure allowed the absolute camera EO to be resolved within the local coordinate system via the SfM BA without needing to use the GCP coordinates within the local system for constraining (i.e., georeferencing) the solution. This process is analogous to real-world cases where image geolocations are assigned to the imagery from a GNSS onboard the platform, except in this case the exact camera geolocations and orientations were known from the simulation, which allowed the team to directly assess the impact of overlap on the accuracy of the SfM reconstruction (i.e., sparse point cloud) by using the GCPs as checkpoints while eliminating any additional variability that might result from GNSS positional uncertainty in real-world scenarios.

For Stage 3, the evaluation of dense point cloud quality consisted of computing cloud-to-cloud distances between the 3D-densified point cloud created from the rendered imagery of the scene and the 3D point cloud of the mesh model used in the simulation and created from the real-world UAS data. This latter point cloud is considered a ground truth point cloud for the purposes of the simulation analysis. The mean cloud-to-cloud distance error and standard deviation of the error served as the dense point cloud quality factors in addition to point density. The research team used the open-source software CloudCompare to compute cloud-to-cloud distances.

Figure 59 shows the cloud-to-cloud distance computation. The method works by searching for the nearest neighbor in the reference cloud for each point of the compared cloud and computing their Euclidean distance (93). For dense enough point clouds, as is the case here, this method provides an overall assessment of the similarity between the two clouds. Larger deviations suggest a less accurate 3D reconstruction result. Cloud-to-mesh signed distances can also be computed based on the surface normal from the reference mesh surface to the compared cloud.

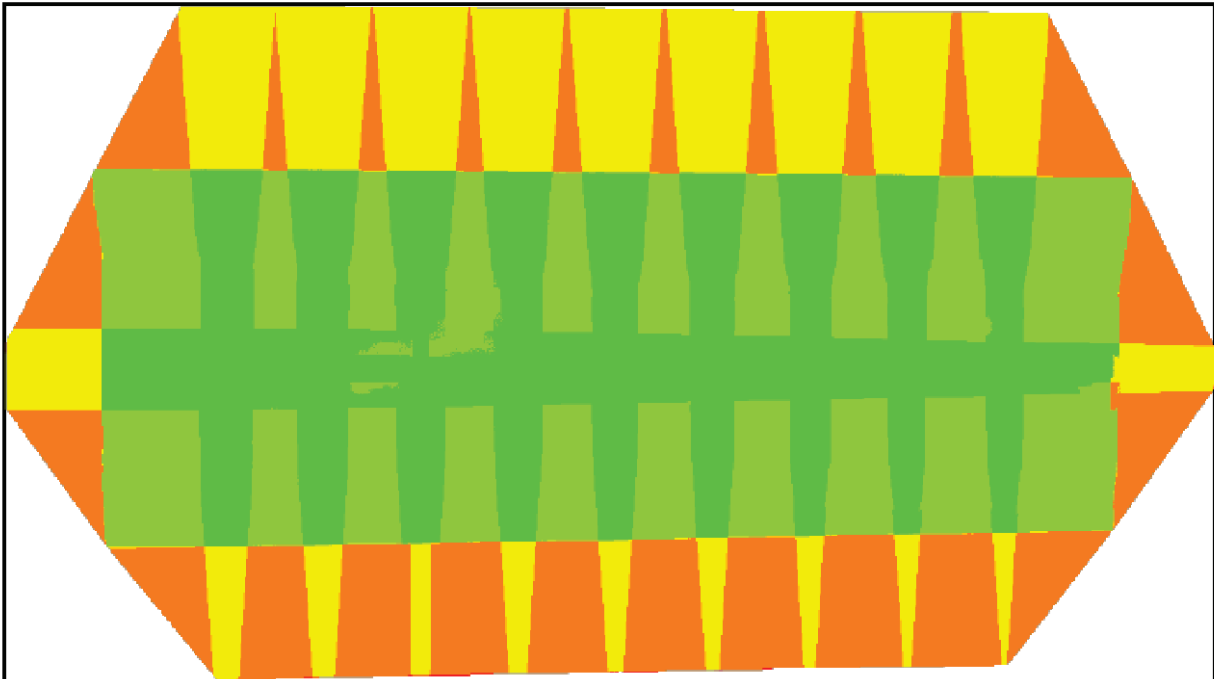


**Figure 59. Cloud-to-Cloud Distance (93).**

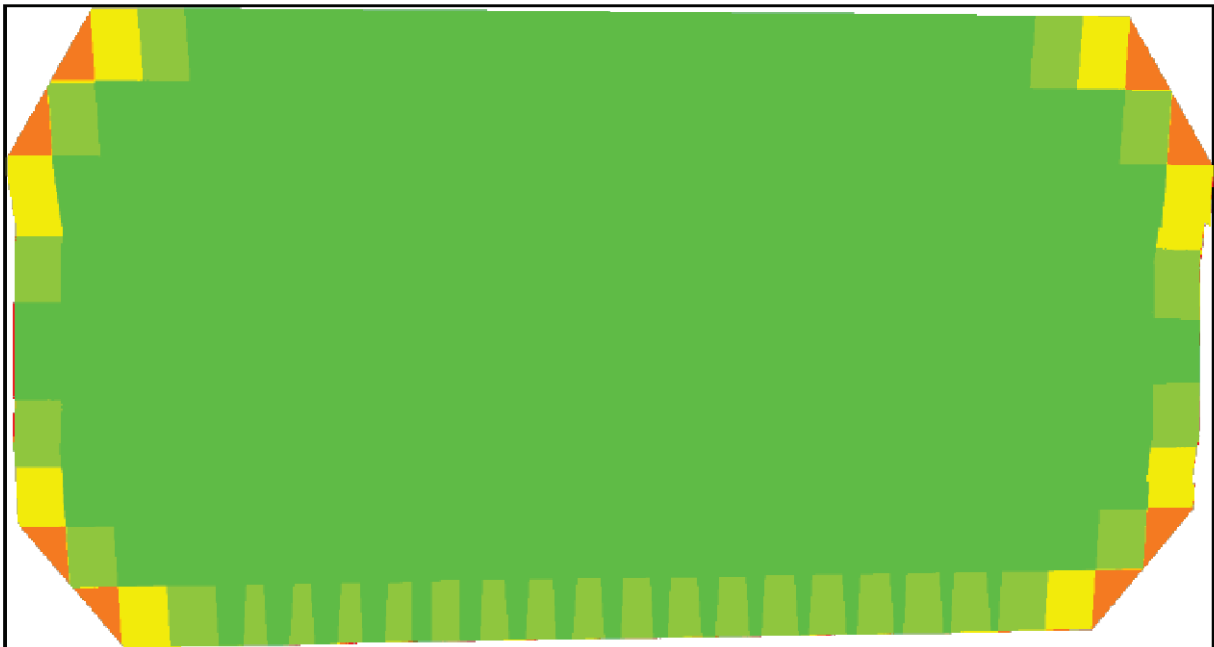
## Results

To validate the functionality of the simulation framework, Figure 60 shows the difference in the number of overlapping images between the E60-S60 and E80-S80 scenarios. Figure 61 shows the corresponding differences between the first-order DSM maps. The number of overlapping images was significantly lower on the edges for the E60-S60 scenario (Figure 60a) than the E80-S80 scenario (Figure 60b). The impact was a drop in detail and the appearance of artifacts on the edges of the DSM for the E60-S60 scenario (Figure 61a) compared to the E80-S80 scenario (Figure 61b). It is important to mention that the DSMs shown here are based on the sparse point cloud. The densification stage of the SfM processing workflow in Pix4D densified the sparse cloud to provide a more detailed point cloud and subsequent DSM.

(a) Overlap for E60-S60 scenario



(b) Overlap for E80-S80 scenario

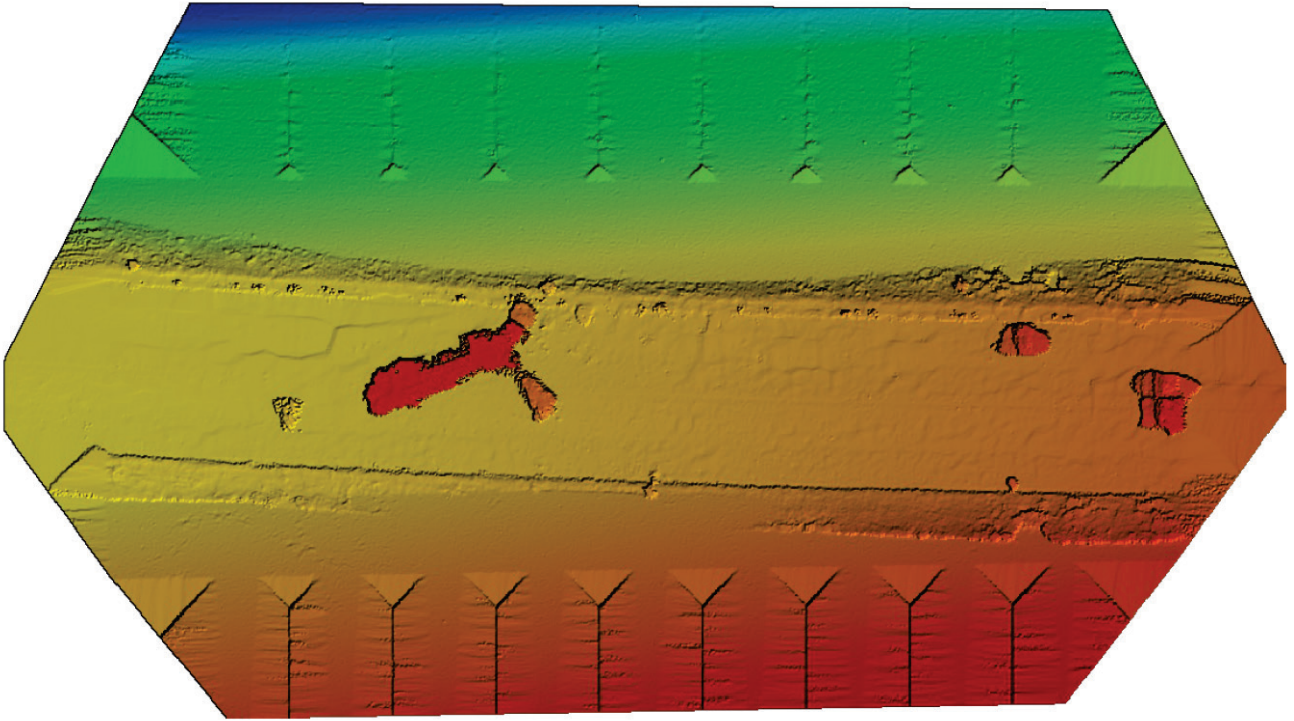


(b)

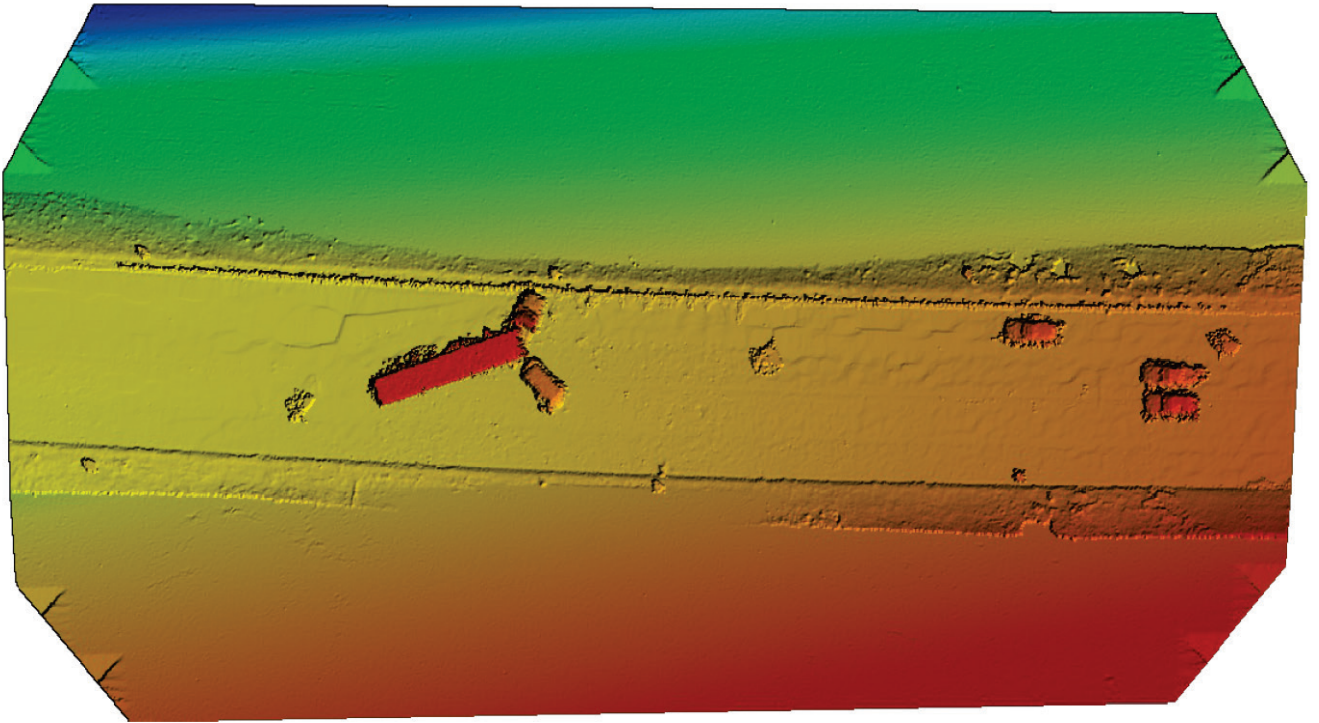
Number of overlapping images: 1 2 3 4 5+

Figure 60. Overlapping Images for E60-S60 and E80-S80 Scenarios.

(a) DSM map for E60-S60 scenario



(b) DSM map for E80-S80 scenario

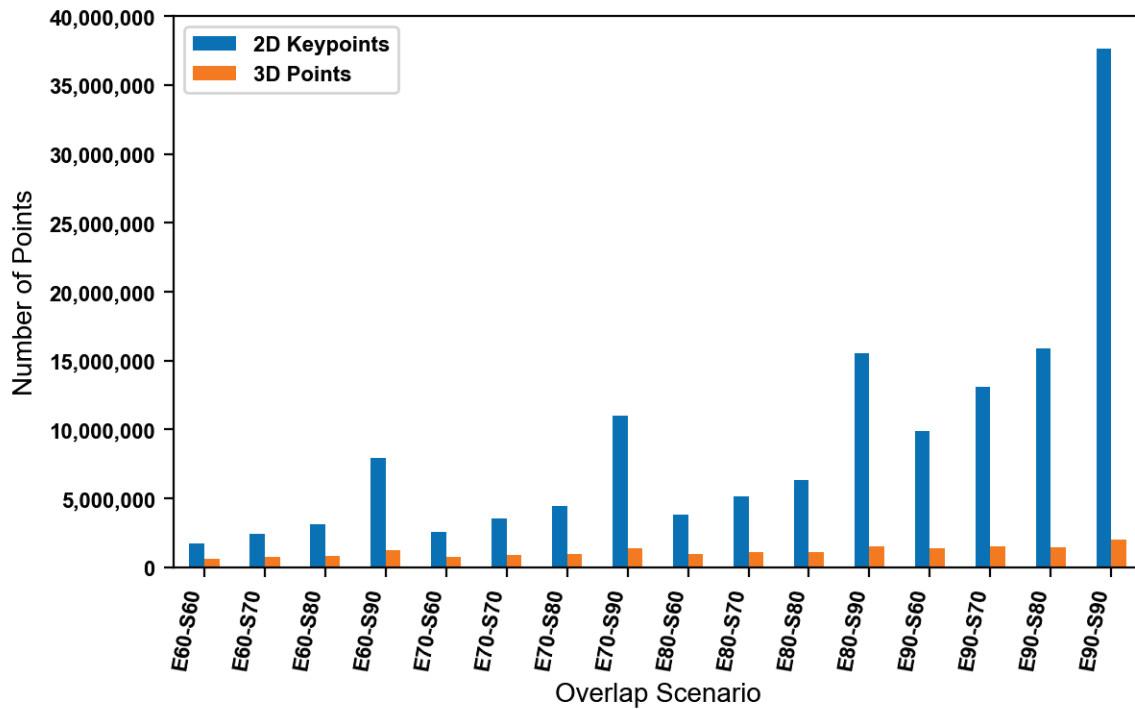


**Figure 61. Overlap and DSM Maps for E60-S60 and E80-S80 Scenarios.**

### Keypoint Extraction and Matching Quality Factors

The first stage of the Pix4D SfM workflow automatically extracts features (keypoints) and finds keypoint correspondences between overlapping image sequences using a keypoint descriptor algorithm, such as SIFT or some variant. The entire process of 3D reconstruction through aero-triangulation and BA relies on the number, quality, and consistency of these keypoint matches, which is heavily influenced by overlap settings. The quality of that result directly influences the quality of point cloud densification.

Figure 62 shows the total number of 2D keypoints and 3D points extracted across the entire scene. The number of 2D keypoints are the automatic tie points on all images that are used for the BA. According to Pix4D, this number corresponds to the number of all keypoints that could be matched on at least two images. The number of 3D points are all the points that were generated by matching 2D points on the images. As Figure 62 shows, increasing both sidelap and endlap produced an increasing number of 2D keypoints and 3D points. However, the number of 2D keypoints increased at a much faster rate than the number of 3D points. The reason is that the total number of 2D keypoints is computed by summing up all keypoints for each image that were matched to at least one other keypoint in another image. By comparison, a 3D point is only counted once for a respective keypoint match, whether that match consisted of keypoints corresponding between two images, three images, four images, and so on.

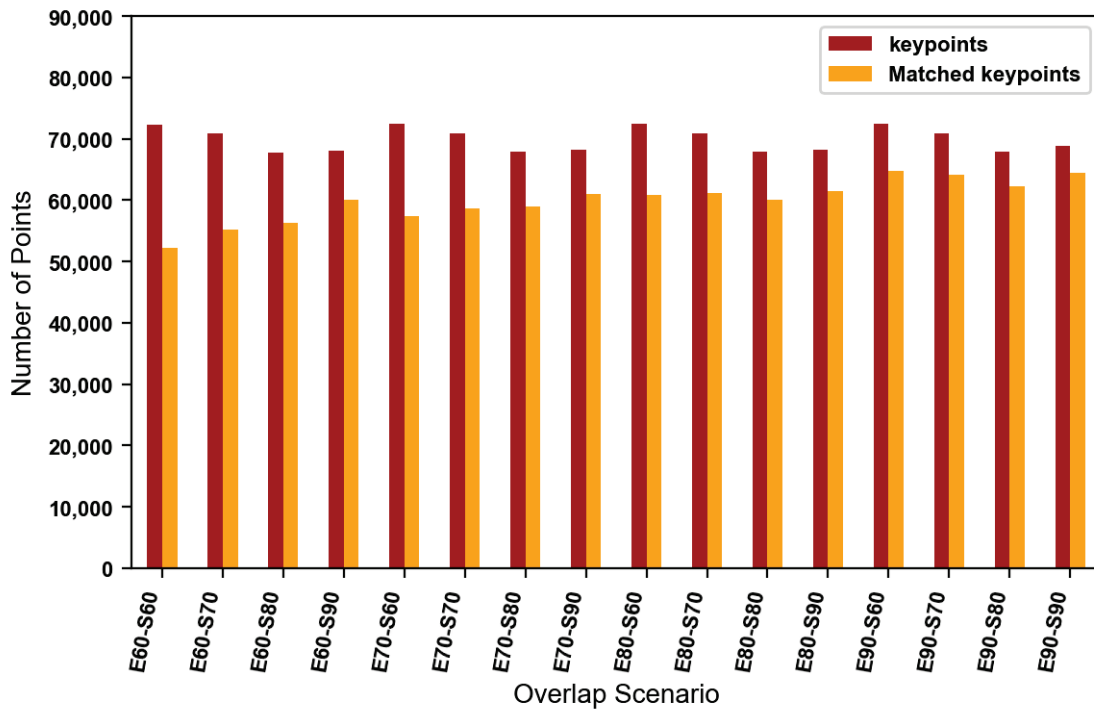


**Figure 62. Total Number of 2D Keypoints and 3D Points by Overlap.**

One notable trend was the sharp rise in the number of keypoints when the sidelap was at least 80 percent. Another observation was the similarity between the number of 2D keypoints for several endlap-sidelap combinations, which could be used for mission planning purposes. For example, the number of 2D keypoints for the E60-S90 scenario was only slightly lower than the

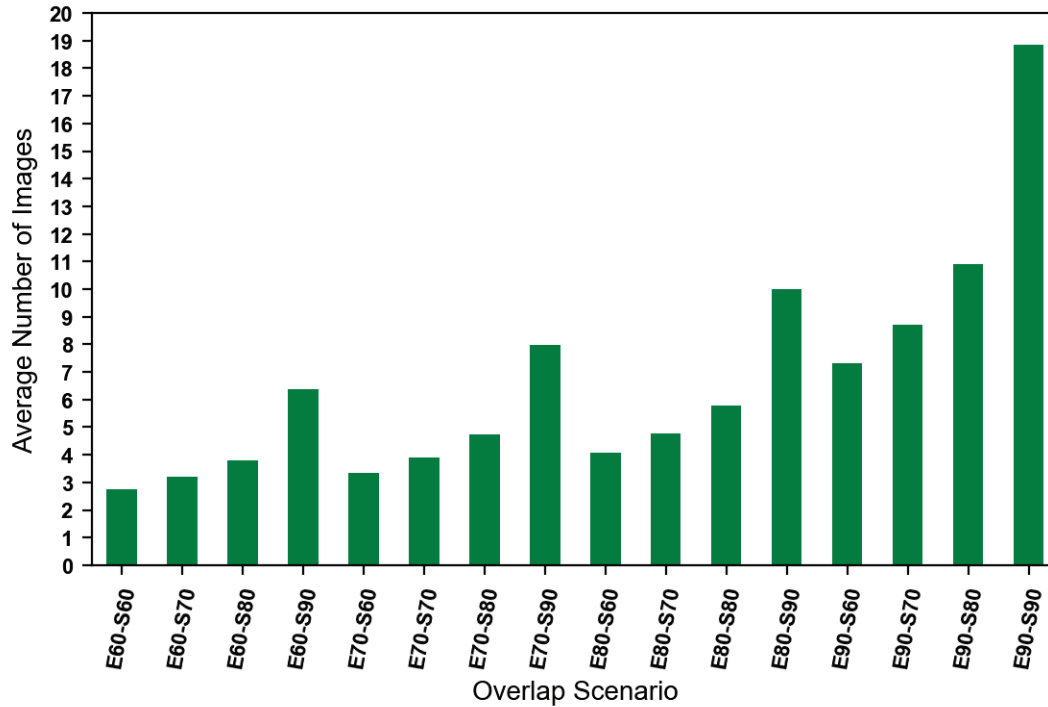
number of the 2D keypoints for the E90-S60 scenario, but as discussed, more endlap is preferable because the result is a shorter flight time (which is desirable).

Figure 63 shows the average number of 2D keypoints and matched keypoints per image. (Note: When two keypoints on two different images are found to be the same, they are considered matched keypoints. Keypoints are always considered 2D because they are associated with specific image locations, not 3D space.) The number of keypoints per image depends on image size and the visual content or texture. Increasing combinations of sidelap and endlap do not necessarily affect the average number of 2D keypoints per image. However, based on the Pix4D processing settings used, the results indicate that increasing overlap does result in a subtle increase in the average number of matched keypoints per image, which is desirable.



**Figure 63. Average Number of 2D Keypoints and Matched Keypoints per Image.**

Figure 64 shows more compelling evidence of the value of increasing overlap for SfM. Higher endlap-sidelap combinations increased the average number of images observed for a 2D keypoint used to reconstruct a 3D point in the sparse point cloud. The higher the number of images on which a 3D point is visible, the more observations and constraints in the BA. In return, 3D points reconstructed from keypoints observed in more images relative to those reconstructed from less images should have better accuracy (i.e., less uncertainty) in their LS estimation and provide for a more robust sparse point cloud in that vicinity.



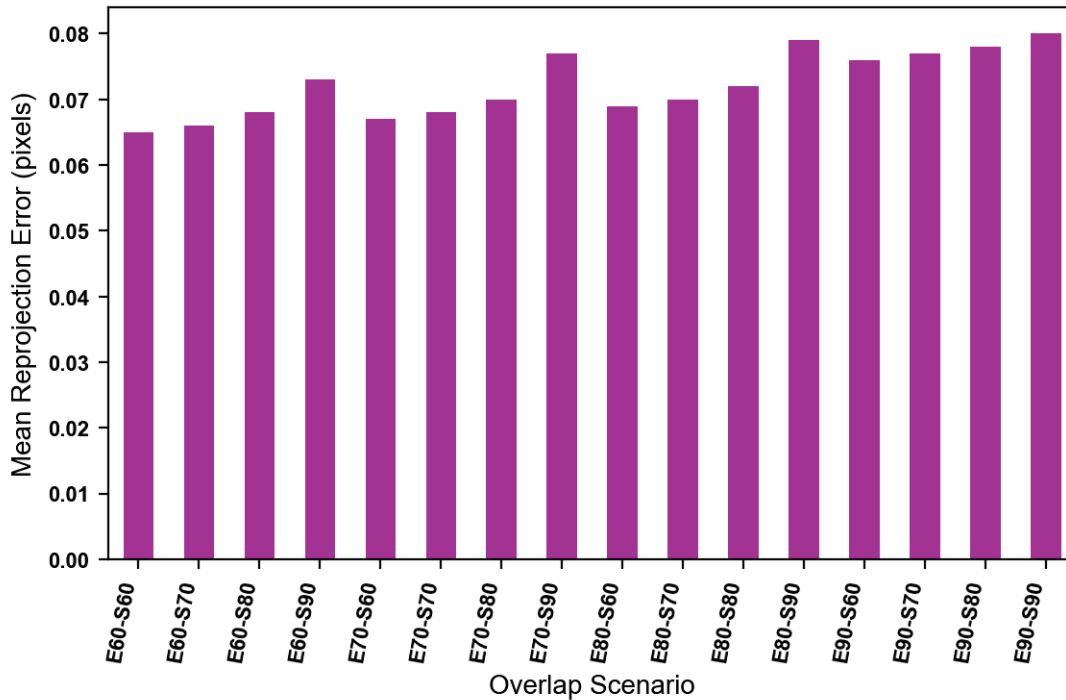
**Figure 64. Average Number of Images Observed for a 2D Keypoint Used to Reconstruct a 3D Point in the Sparse Point Cloud.**

### *BA Quality Factors*

At this stage of the SfM processing workflow in Pix4D, the keypoints obtained in the previous stage are input into a LS bundle block adjustment to minimize errors while automatically solving for camera IO and EO parameters. Based on this reconstruction, the matching points are verified and their 3D coordinates are calculated to generate a sparse point cloud. GCPs can be used here for reoptimization or as checkpoints. The accuracies of all subsequent data products are largely determined during this stage.

Figure 65 shows the mean reprojection error by overlap measured in pixel space. When the software computes a 3D point using the matched keypoints, the 3D coordinates of this point are computed using the estimated camera’s internal and external parameters as well as the specific location of the keypoint in the images. The reprojection error is the distance between the initially detected keypoint location and the 3D point’s reprojected location in the same image. This error depends on the quality of the camera calibration and BA result for resolving exterior camera parameters (position and orientation), as well as the quality of the keypoint detection in the images. Reprojection errors should be less than one pixel. As Figure 65 shows, all overlap scenarios were well below this threshold. Readers should note that the main reason was that this simulation provided perfectly known camera pose information provided to Pix4D. A slight trend of increasing mean reprojection error with increasing overlap exists, but it may be due to the increasing number of 3D keypoints. This trend is negligible.

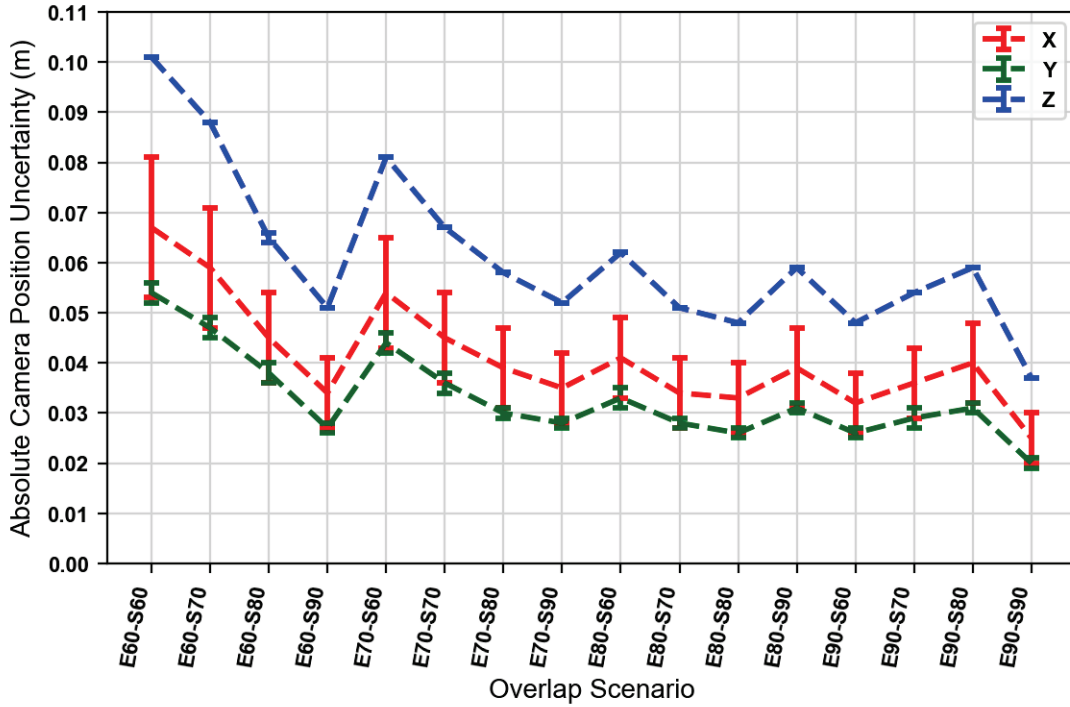




**Figure 65. Mean Reprojection Error by Overlap.**

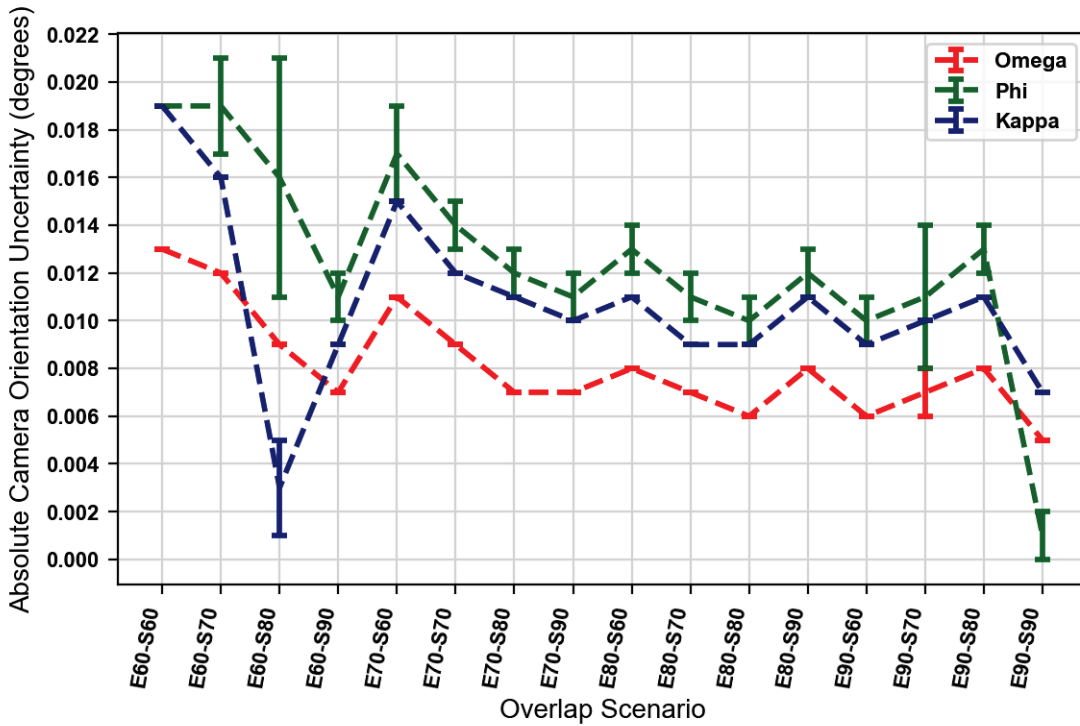
Figure 66 shows uncertainty trends in the mean absolute camera position, based on the BA. The more images observed for a keypoint, the more beneficial it is for reducing uncertainty in the minimization procedure used to estimate the geolocations and orientations. Figure 66 shows an overall downward trend in geolocation uncertainty (preferred) as the overlap increases. Not surprisingly, the level of uncertainty for Z coordinates is significantly higher than the uncertainties for X-Y coordinates.

Figure 67 shows uncertainty trends in the phi, omega, and kappa angular orientation angles. These angles define rotations between the image coordinate system and the geodetic coordinate system (X axis, Y axis, and Z axis, respectively). In general, an overall decrease in uncertainty occurred with increasing overlap. Phi and kappa angles (rotation around the X axis and Z axis, respectively) were more uncertain to resolve at a specific overlap scenario than the omega angle (i.e., rotation around the Y axis). There were anomalous drops in kappa angle uncertainty for the E60-S80 and E90-S90 scenarios, which might be an effect of more favorable keypoint matching geometry resulting from differing imaging perspectives of the artificial scene at those overlaps.



Note: The dashed lines are used for overall visualization, not to suggest linear trends between adjacent data points.

**Figure 66. Mean Absolute Camera *Position* Uncertainty.**



Note: The dashed lines are used for overall visualization, not to suggest trends between adjacent data points.

**Figure 67. Mean Absolute Camera *Orientation* Uncertainty.**

Figure 68, Figure 69, Figure 70, and Figure 71 show RMSE trends. Figure 68 shows RMSE trends for absolute camera geolocation errors. The geolocation error is the difference between the initial camera positions (i.e., input image geolocations) and their computed positions from the AT and BA procedure. Technically, the errors should be zero because the exact camera position and orientation values from the simulation were fed to Pix4D. However, the camera pose information was not locked within Pix4D and was allowed to vary to mimic a realistic scenario based on standard GNSS uncertainties. Figure 69 shows RMSE trends for absolute camera orientation errors between initial and computed orientations. Figure 70 and Figure 71 show RMSE trends for checkpoint error and mean of the checkpoint error, respectively, based on the artificial GCPs introduced to the rendered scene. The coordinates of the GCPs were known and fed into Pix4D. During Pix4D processing, the GCPs were tagged and only used for assessing error, not reoptimization.

In general, the results in Figure 68, Figure 69, Figure 70, and Figure 71 show a decreasing error trend with more overlap, particularly in the case of endlap. More noise is associated with sidelap.

The analysis also included an evaluation of variations in focal length and principal point offsets. Very little variation occurred in these parameters as a function of the endlap and sidelap scenario.

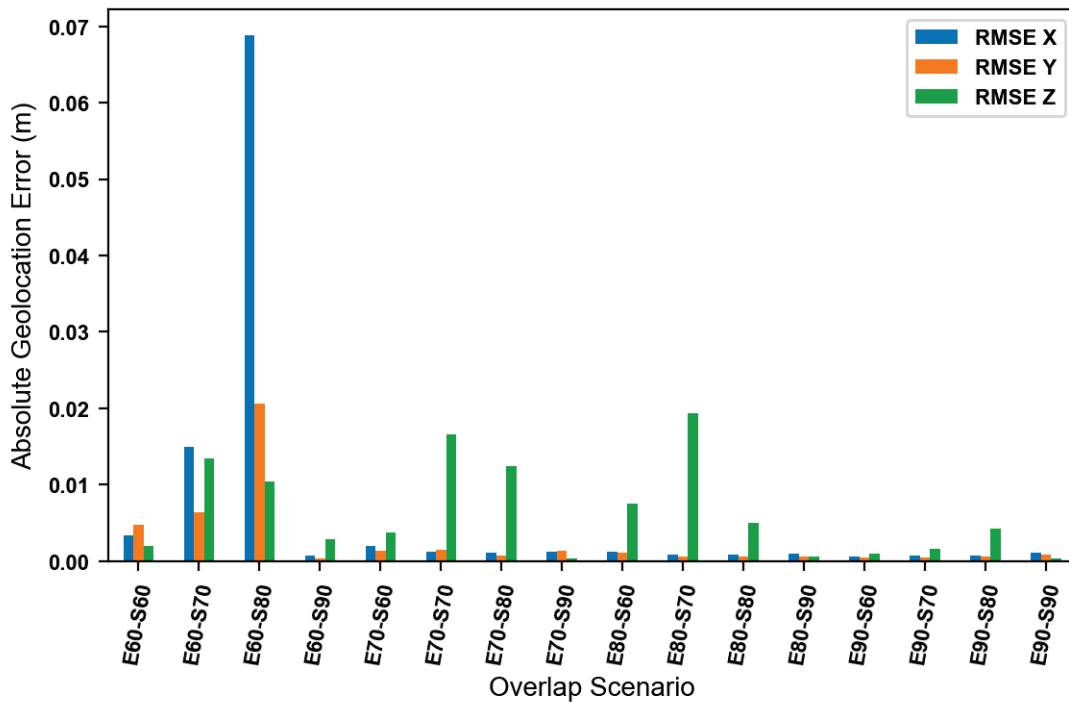


Figure 68. Absolute Camera Geolocation Error.

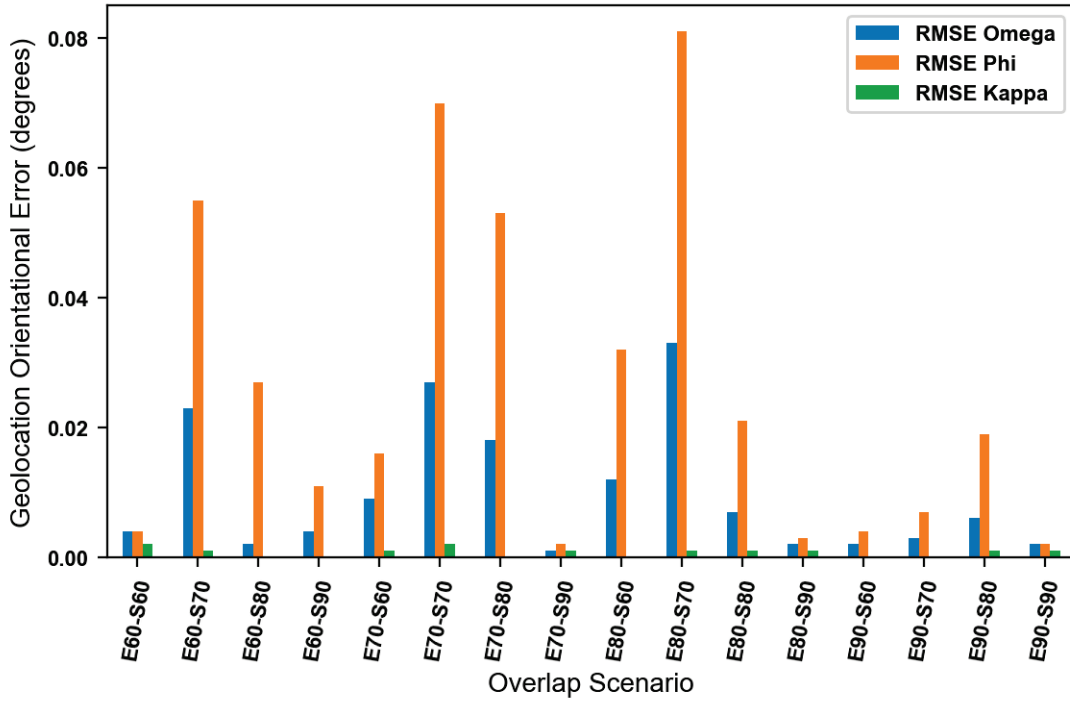


Figure 69. Absolute Camera Orientation Error.

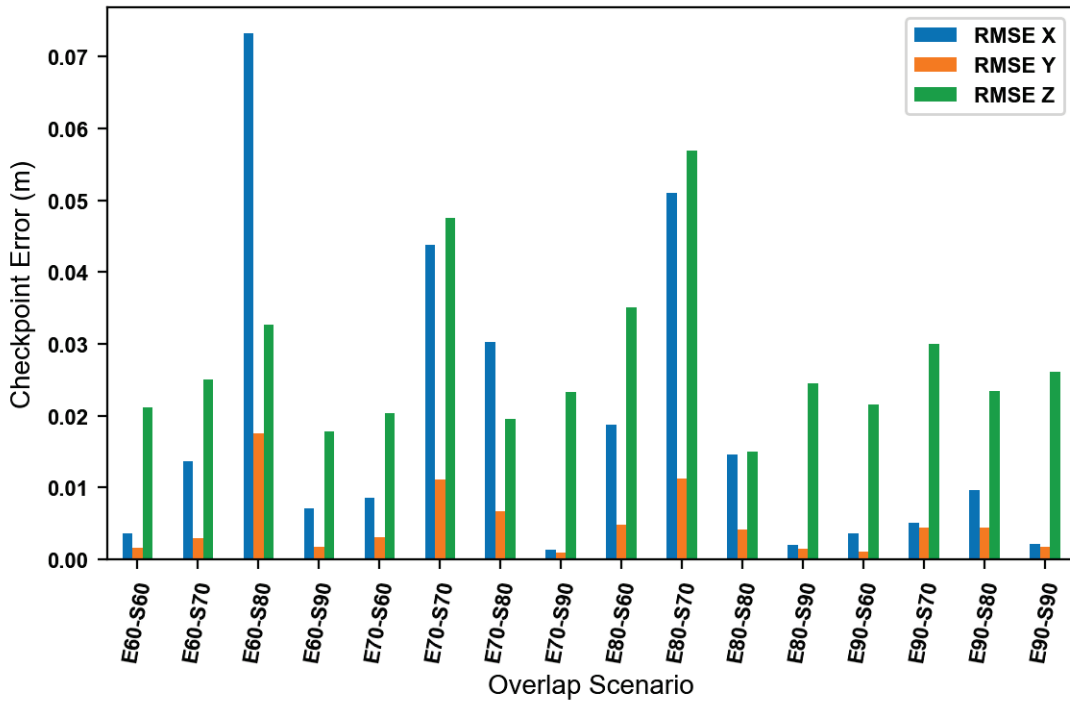
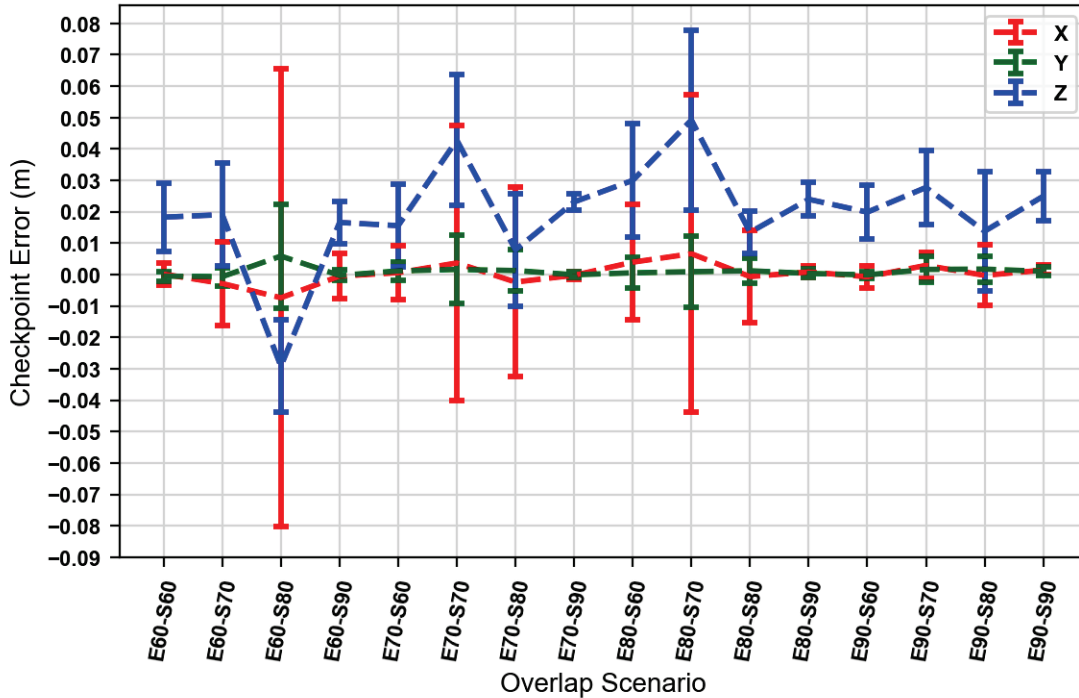


Figure 70. RMSE of the Checkpoint Error.



Note: The dashed lines are used for overall visualization, not to suggest trends between adjacent data points.

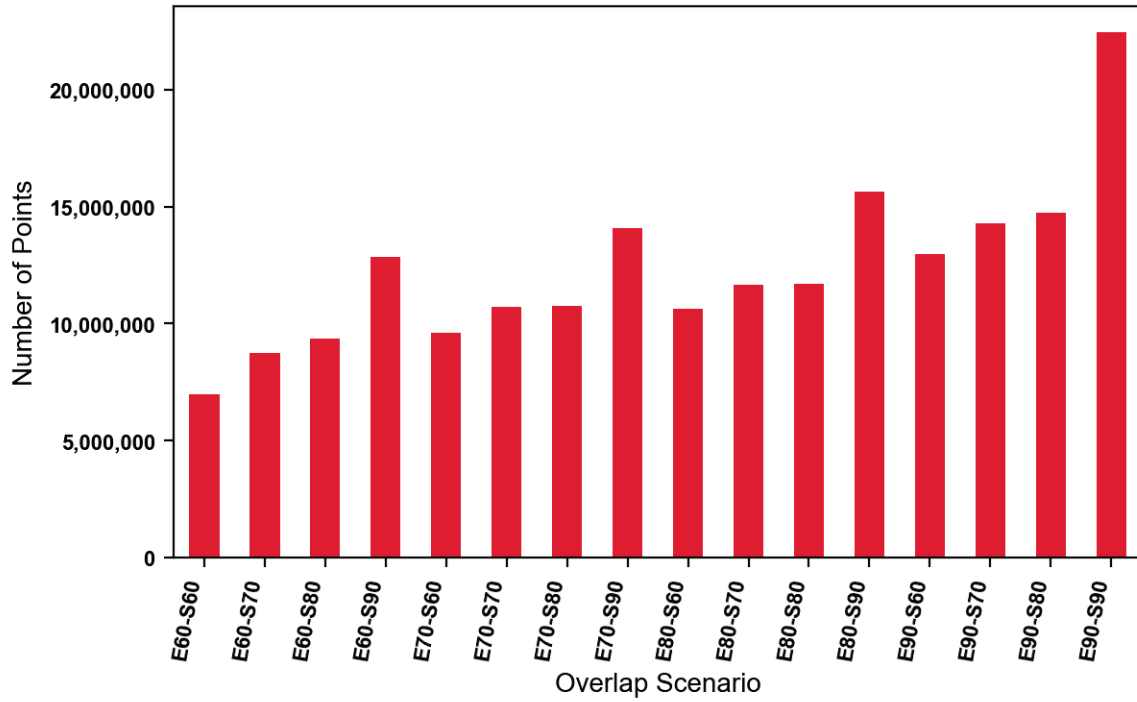
**Figure 71. Mean Checkpoint Error with Error Bars.**

### *Dense Point Cloud Quality Factors*

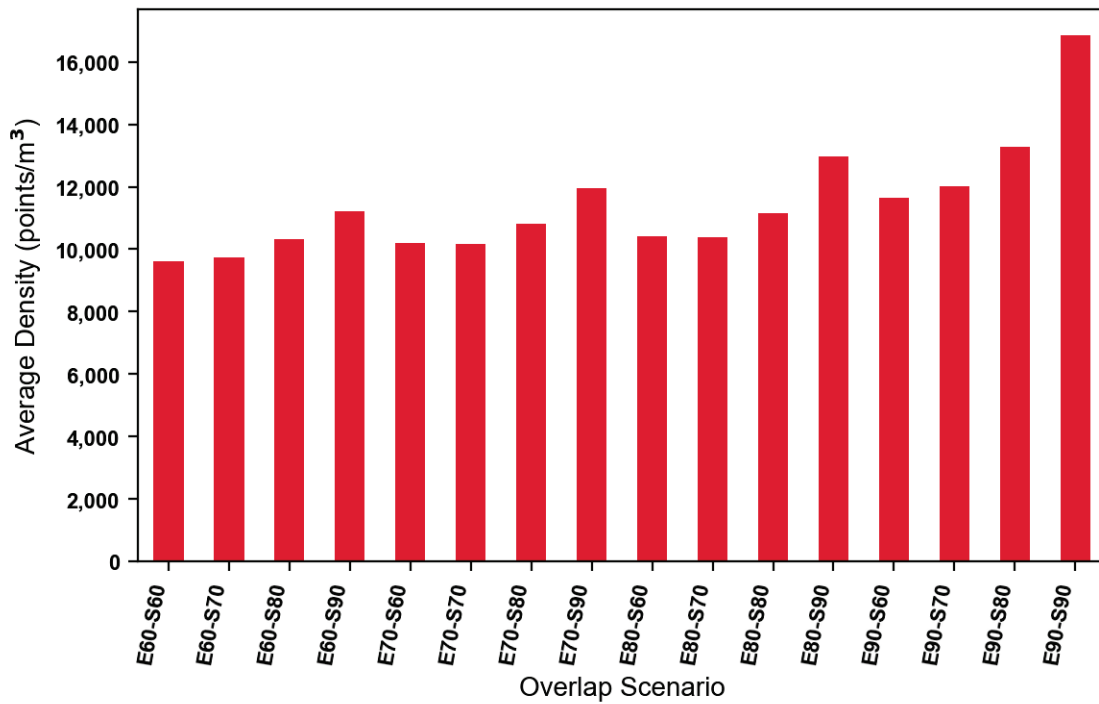
The final step in the Pix4D SfM processing workflow is the generation of a dense point cloud using MVS photogrammetry techniques. The camera IO and EO parameters resolved from the BA step are used to generate a point cloud that is much denser than the previously created sparse point cloud. MVS densification uses stereo correspondence from multiple images and relies on the resolved camera IO and EO parameters from the sparse point cloud, which themselves are affected by overlap settings. Therefore, densification is directly affected by overlap variations.

Figure 72 and Figure 73 show the total number of points and average point density, respectively, for the densified point clouds based on the 16 overlap scenarios. The total number of points and point density increased with overlap. However, even at low overlap levels, the density exceeded several thousand points per cubic meter, which was expected considering the small GSD of 7.2 mm (0.28 inches) associated with the low flight height of 30 m (98 ft) and resolution of the Mavic 2 Pro camera used for the image rendering.

Figure 74 and Figure 75 show RMSE trends for cloud-to-cloud distances based on the total scene and the crash scene, respectively. No major patterns were discerned in either case, mainly because of the parameters of the simulation. The simulation used a textured mesh created from the ground truth point cloud. Furthermore, all overlap scenarios tested produced very dense clouds comparable to, or exceeding in some cases, the density of the ground truth point cloud.



**Figure 72. Total Number of Points in Densified Point Cloud.**



**Figure 73. Average Point Density of Densified Point Cloud.**

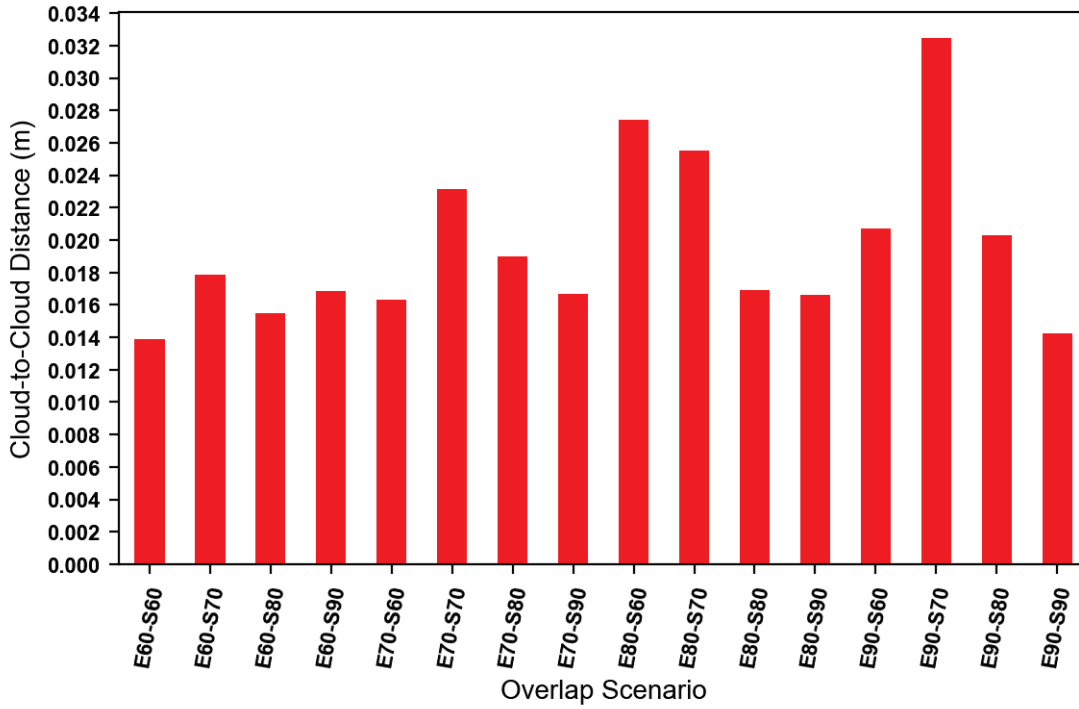


Figure 74. Cloud-to-Cloud Distance RMSE Trends for Total Scene.

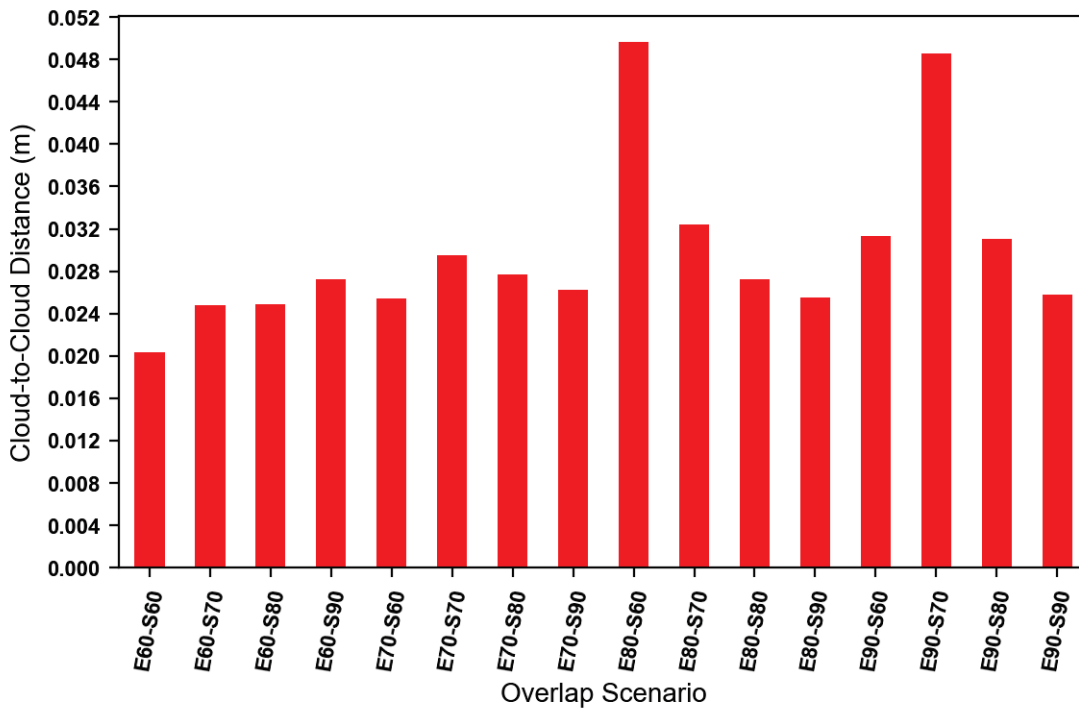
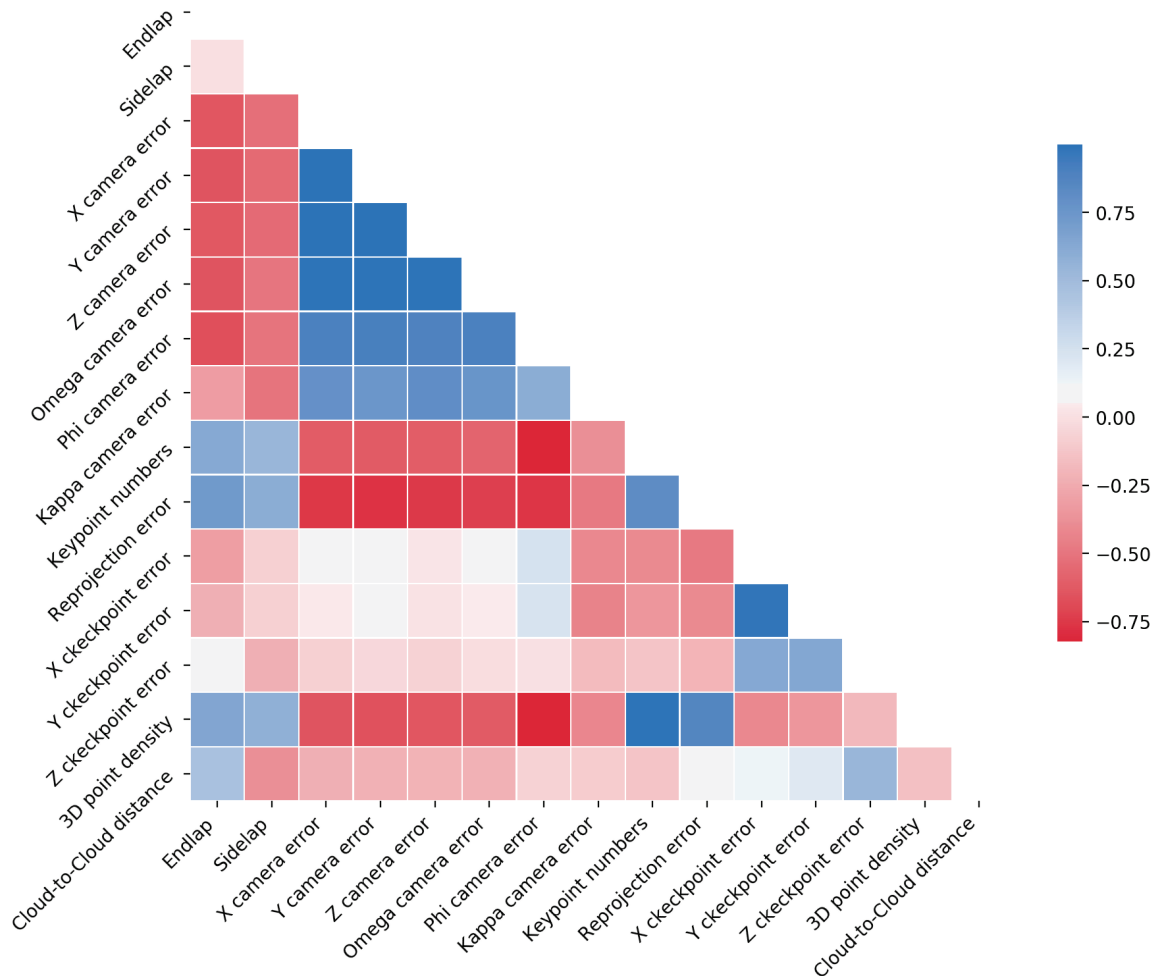


Figure 75. Cloud-to-Cloud Distance RMSE Trends for Crash Scene.

## Correlation Analysis

Figure 76 shows the Pearson’s correlation coefficient between the various quality factors previously examined for the different stages of the SfM processing workflow. In the figure, values range from +1 (dark blue) to -1 (dark red). Positive values correspond to a positive linear correlation (i.e., increasing the value of one parameter increases the value of another). Negative values correspond to a negative linear correlation (i.e., increasing the value of one parameter decreases the value of another). For example, the correlation between endlap and 3D point density was positive. The corresponding correlation coefficient was around 0.6.



**Figure 76. Correlation between Different Quality Factor Values and Sidelap/Endlap.**

Trends in Figure 76 related to endlap and sidelap include the following:

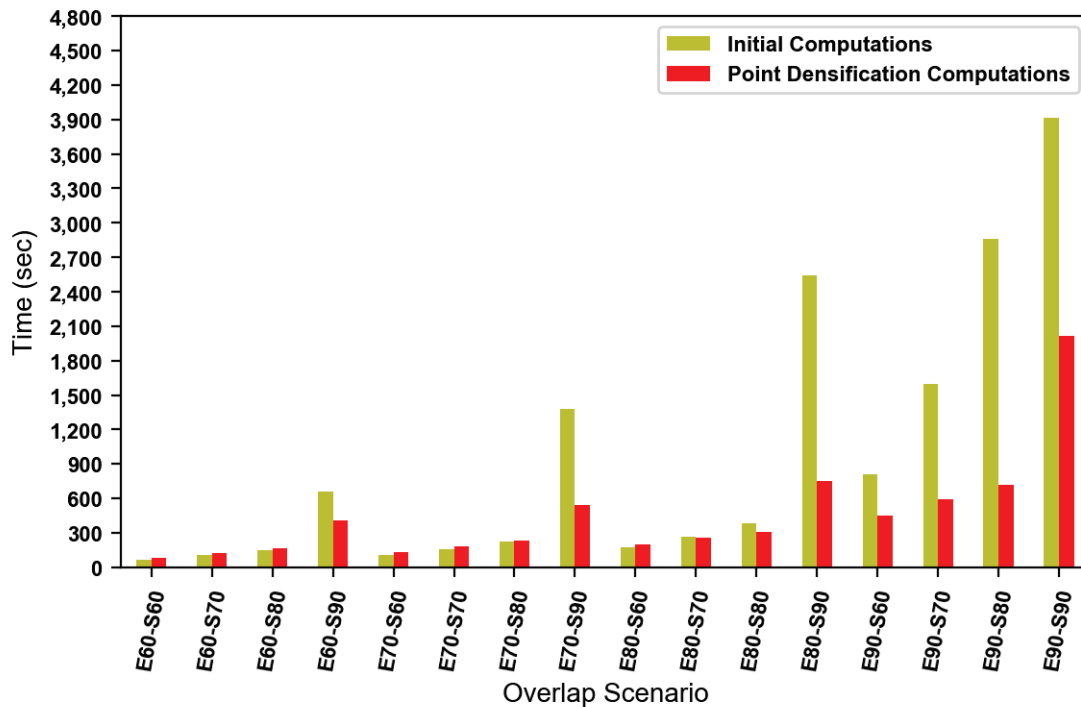
- Both endlap and sidelap had a positive correlation with keypoint extraction and 3D point density. Increasing either endlap or sidelap increases the number of potential keypoints within the Pix4D software, which has a positive impact on the final point density. The correlation associated with the endlap was slightly stronger.



- Both endlap and sidelap had a negative correlation with the absolute geolocation and orientation parameters. Endlap showed a stronger negative correlation, suggesting that, for this scene and simulation, it had more influence on the reduction in AT uncertainty. A similar pattern was observed for the X-Y checkpoint errors. Interestingly, the Z-checkpoint error appeared to show little correlation with either sidelap or endlap.
- Both endlap and sidelap had a positive correlation with the mean reprojection error.
- Endlap had a positive correlation with the cloud-to-cloud distance RMSE. In contrast, sidelap had a negative correlation with the cloud-to-cloud distance RMSE. The added oblique perspectives gained from increasing sidelap enabled more reconstruction on the sides of the crash scene, thereby reducing cloud-to-cloud disparities.

### *Impact of Image Overlap on Data Processing Time*

Figure 77 shows the impact of image overlap on Pix4D processing time, including initial computations and point densification computations. As a reference, the computer system used for the simulation had an Intel® Core™ i7-6950X @ 3 GHz CPU and 64 GB of RAM. The operating system was Windows 10 Enterprise. In general, the processing time increased as the amount of overlap increased. In relative terms, the initial computations took longer to complete than the point densification computations as the amount of overlap increased. Not surprisingly, given that the number of images did not increase linearly as a function of the endlap-sidelap scenario, the processing time did not increase linearly either.

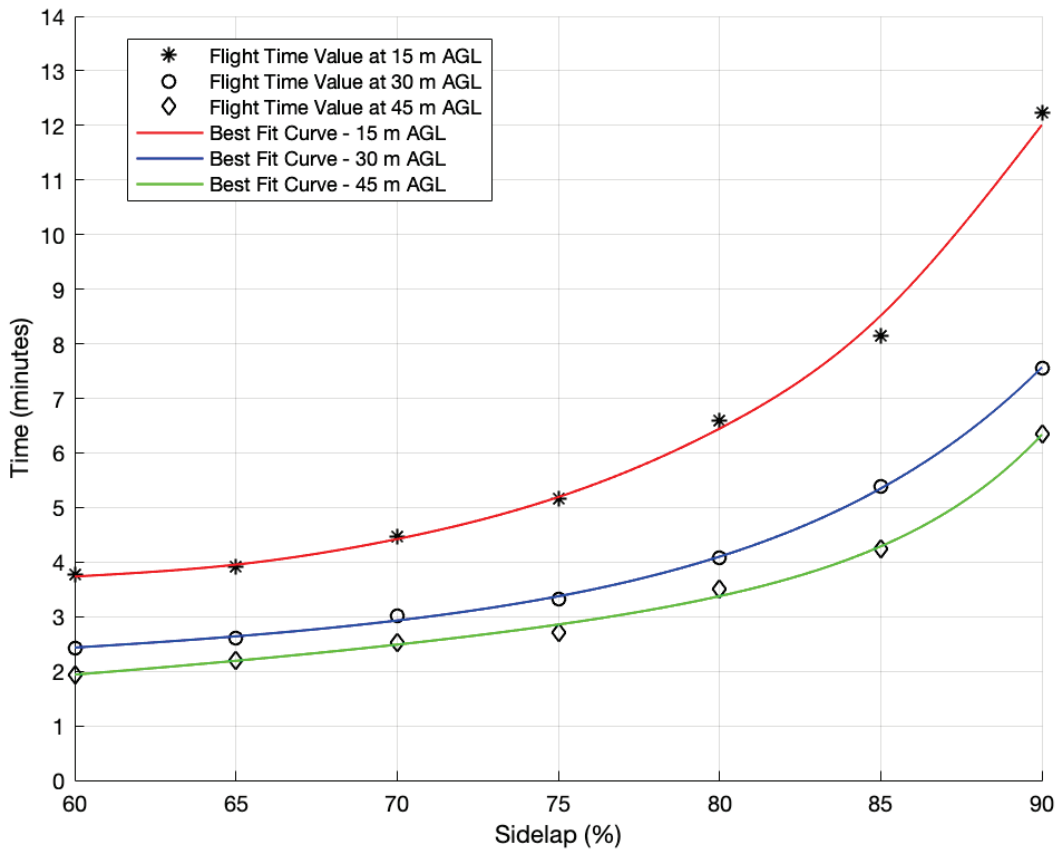


**Figure 77. Pix4D SfM Initial Processing Time and Densification Time by Overlap.**

### Impact of Image Overlap on Flight Time

To investigate the impact of overlap on flight time, the research team conducted a flight time simulation for different sidelap values at three different flight heights. The simulation used a representative crash scene area of 50×100 m (164×328 ft) and a flight speed of 5 m/s (11 mph) with no wind. The simulation set the endlap at 75 percent and varied sidelap in 5 percent increments.

Figure 78 shows results of the flight time simulation. Table 67 shows the number of images acquired for each simulation scenario. Not surprisingly, flight time increased as the percentage of sidelap increased. The increase in flight time shows a semi-exponential growth with increasing sidelap based on the best fit curves shown in Figure 78. The effect was more noticeable as the sidelap increased to 85 or 90 percent. Likewise, flight time decreased as the flight height increased. The larger field-of-view of the camera as the flight height increased enabled more overlap with greater spacing between adjacent flight lines, thus reducing the total flight time. With changing height, the GSD increased from 3.6 mm (0.14 inches) at 15 m (49 ft) AGL to 10.9 mm (0.43 inches) at 45 m (148 ft) AGL.



**Figure 78. Simulated Flight Time Based on Percent Sidelap and Flight Height.**

**Table 67. Number of Images Acquired Based on Percent Sidelap and Flight Height.**

Sidelap	Flight Height AGL		
	15 m (49 ft) (GSD = 3.6 mm)	30 m (98 ft) (GSD = 7.2 mm)	45 m (148 ft) (GSD = 10.9 mm)
60%	288	85	48
65%	320	102	60
70%	352	119	60
75%	416	136	72
80%	544	170	96
85%	704	221	120
90%	1056	323	180

*Impact of Wind on UAS Image Geolocations and SfM Reconstruction*

As a final component of this subtask, the research team examined the impact of high wind conditions on input camera position and orientation values used by Pix4D during SfM reconstruction. This activity entailed using one of the simulated image sets at a set overlap setting (E80-S80) and then perturbing the input image geolocation and orientation values. These values come exactly known from the simulation, and previous analyses used the exact values for input into Pix4D for SfM processing. By changing the values prior to input into Pix4D, the research team simulated the effect of wind impact on the geolocation and orientation values and subsequently assessed the impact of these changed values on Pix4D SfM processing.

To get a sense of the order of magnitude of the geolocation and orientation errors that were expected due to high wind, the research team used the Pix4D photogrammetric SfM quality report associated with a DJI Phantom 4 Pro flight mission conducted on September 7<sup>th</sup>, 2017. The Phantom platform was flown 70 m (230 ft) above Newport Pass Road in Corpus Christi, Texas. Reasons for selecting this mission included that the UAS platform was a small quadcopter, the wind speed reached 32 mph from a southerly direction during flight, and ground control targets laid out before flight enabled an accurate determination of the uncertainties of absolute camera position and orientation.

Figure 79 shows the RMSE of the orientation angles and geolocation errors associated with the Corpus Christi flight as well as the mean error (bias) and standard deviation (sigma) for the geolocation errors. The RMSE of the orientation angles reflects the difference between the initial and computed image orientation angles. The RMSE of the geolocation errors reflects the difference between the initial and computed image positions. Most of the orientation error was related to the kappa angle (i.e., rotation around the Z axis). This error was five times the error related to the phi angle (i.e., rotation about the X axis) and 10 times the error related to the omega angle (i.e., rotation around the Y axis). The geolocation error in the Z direction was also significantly higher than in the X and Y directions (29 times and 11 times, respectively). The uncertainty in the Y direction was higher than the uncertainty in the X direction, quite likely reflecting a higher impact due to wind in the Y direction, which is evidenced by the larger mean geolocation error (bias) shown in Figure 79 for the Y direction compared to the X direction. The RMSE of the Z direction was large (i.e., 40 m [131 ft]) due to a systematic altitude error

introduced by DJI on geotagged images. This factor is evidenced by the large mean error (bias) for the Z direction shown in Figure 79. For this reason, the research team used the Z direction standard deviation (i.e.,  $\pm 4.2$  m [14 ft]), which is more realistic considering that the planned flight height did not change at such extreme distances during the entire mission.

(a) RMSE of orientation angles

Geolocation Orientational Variance	RMS [degree]
Omega	0.428
Phi	0.914
Kappa	4.489

(b) Geolocation errors

Mn Error [m]	Max Error [m]	Geolocation Error X [%]	Geolocation Error Y [%]	Geolocation Error Z [%]
-	-15.00	0.00	0.00	0.00
-15.00	-12.00	0.00	0.00	0.00
-12.00	-9.00	0.00	0.00	0.55
-9.00	-6.00	0.00	0.00	6.64
-6.00	-3.00	0.00	8.57	14.82
-3.00	0.00	51.38	35.34	29.04
0.00	3.00	46.90	50.88	25.11
3.00	6.00	1.71	5.20	12.94
6.00	9.00	0.00	0.00	10.90
9.00	12.00	0.00	0.00	0.00
12.00	15.00	0.00	0.00	0.00
15.00	-	0.00	0.00	0.00
<b>Mean [m]</b>		1.144509	3.117393	-39.870534
<b>Sigma [m]</b>		0.903622	2.121635	4.199664
<b>RMS Error [m]</b>		1.458229	3.770871	40.091105

**Figure 79. Absolute Camera Orientation and Geolocation Errors for the UAS Flight in Corpus Christi.**

The research team used the E80-S80 simulated image set and perturbed the exact input image geolocation and orientation values using random Gaussian noise based on the determined uncertainty (sigma) values from the Pix4D processing report for the Corpus Christi flight. Table 68 summarizes the camera position and orientation uncertainties used to perturb the input image geolocations and orientations. The research team then processed the simulated image set using the perturbed image geolocation and orientation values in Pix4D based on the same processing settings as those used for the overlap analysis. Processing considered two scenarios: (a) geolocation perturbation only and (b) geolocation and orientation perturbation.

**Table 68. Geolocation and Orientation Uncertainty Parameters for Wind Simulation.**

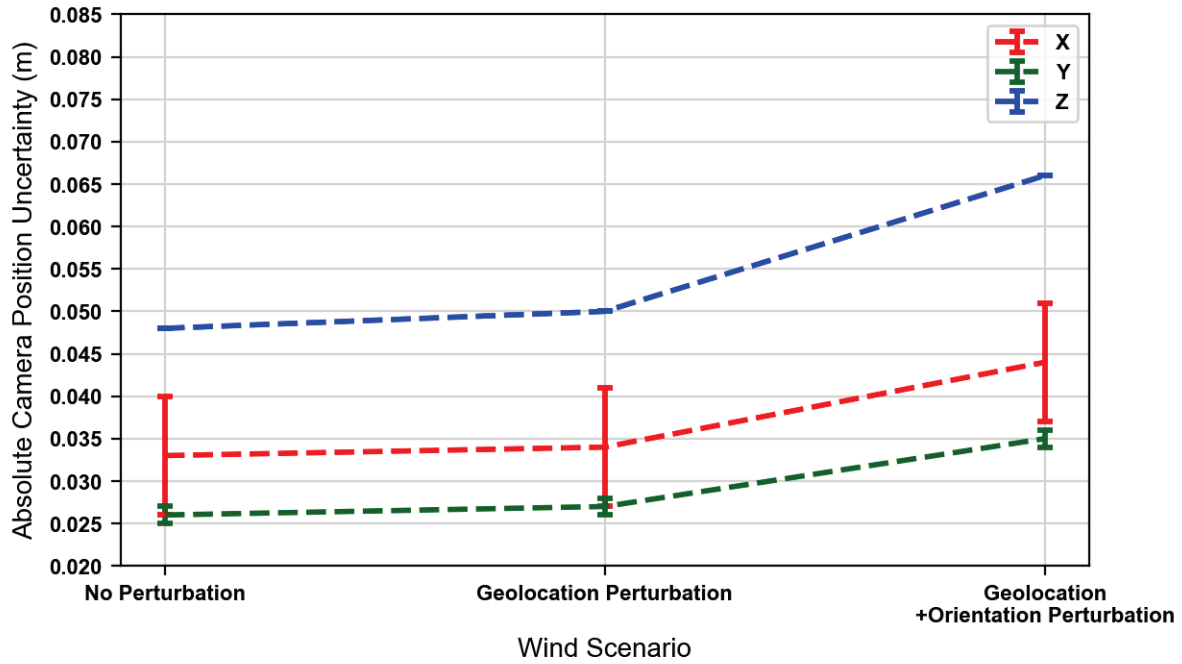
<b>X</b>	<b>Y</b>	<b>Z</b>	<b>Omega</b>	<b>Phi</b>	<b>Kappa</b>
$\pm 2.5$ m	$\pm 2.5$ m	$\pm 4.2$ m	$\pm 1.0^\circ$	$\pm 1.0^\circ$	$\pm 4.5^\circ$

For the sake of brevity, only a few examples of the various SfM quality factors previously evaluated are presented here to demonstrate the effect of wind-induced position and orientation

uncertainty on Pix4D SfM processing results. Figure 80 and Figure 81 show the mean absolute camera position and orientation estimation uncertainty, respectively, along with error bars showing the variation in the mean uncertainty values. These values are constrained by the integrity of the automated keypoint matches and are largely defined by overlap perspective, which are the same for all three image sets. With respect to the no-perturbation scenario, geolocation perturbation only had a slight impact on absolute camera position uncertainty. The impact was more noticeable for the geolocation + orientation perturbation scenario. The impact of only geolocation perturbation was more noticeable on absolute camera orientation uncertainty.

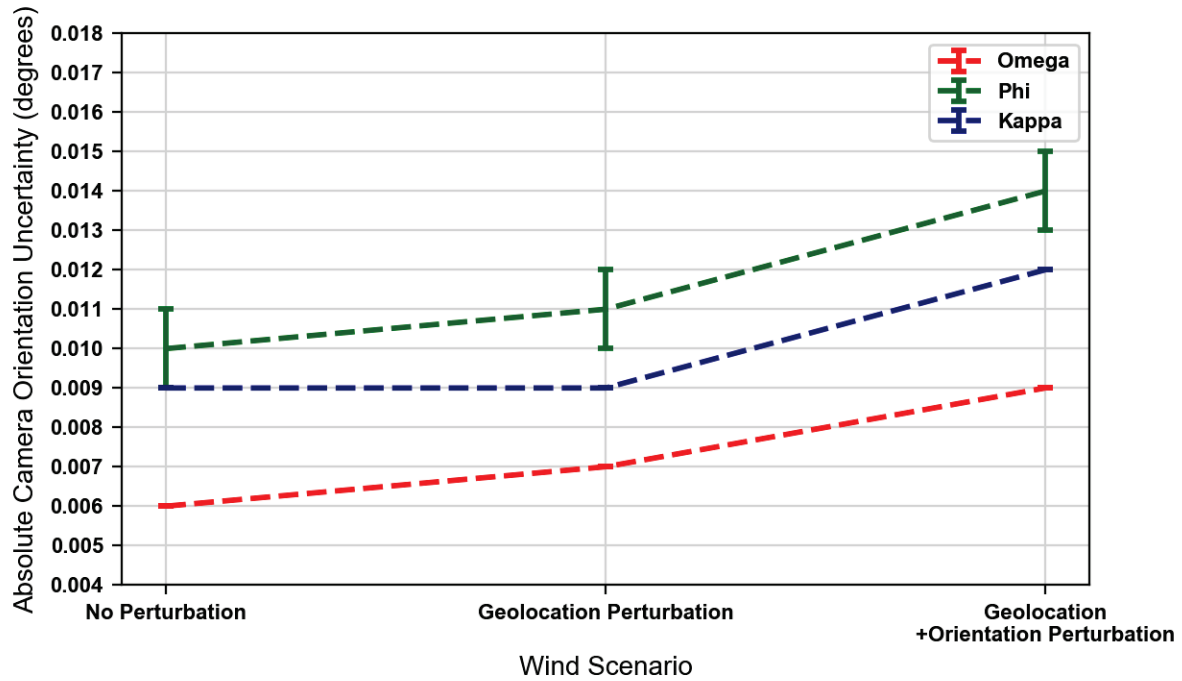
Figure 82 and Figure 83 show the RMSE of the absolute camera position errors and orientation errors, respectively. These errors were computed based on the difference between the initial (input) camera pose values and computed values from the BA during the sparse point cloud generation phase. Figure 82 shows that the absolute camera geolocation errors were similar to the uncertainty values used to perturb the input locations (Table 68), which is expected and more realistic of a typical UAS SfM processing scenario with high geolocation variability due to high wind. Similarly, Figure 83 shows an increase in absolute camera orientation error due to wind perturbation. For the geolocation + orientation perturbation scenario, the error values were in the range of uncertainty values used to perturb the  $\omega$ ,  $\phi$ , and  $\kappa$  angular values of the input image sequence (Table 68). Interestingly, the geolocation perturbation also increased the absolute orientation error, which can potentially propagate as additional error into the densified point cloud.

Figure 84 shows the mean checkpoint error for the various scenarios along with error bars. As expected, without the use of GCPs or more accurate image geolocations such as from RTK or PPK GNSS, checkpoint errors increased significantly due to geolocation perturbation relative to no perturbation. The additional impact due to orientation perturbation was relatively minor. Pix4D does not need to use the orientation values because Pix4D can resolve camera orientation completely from the keypoint matching constraints and BA procedure optimized by image geolocations. This result is interesting and suggests that Pix4D uses input orientation values to weigh the adjustment procedure to some degree, which is also supported by the trend shown in Figure 81. Further investigation may be necessary to better understand how Pix4D applies orientation values and orientation uncertainty into the SfM procedure because this will have implications for processing direct georeferencing and IMU data.



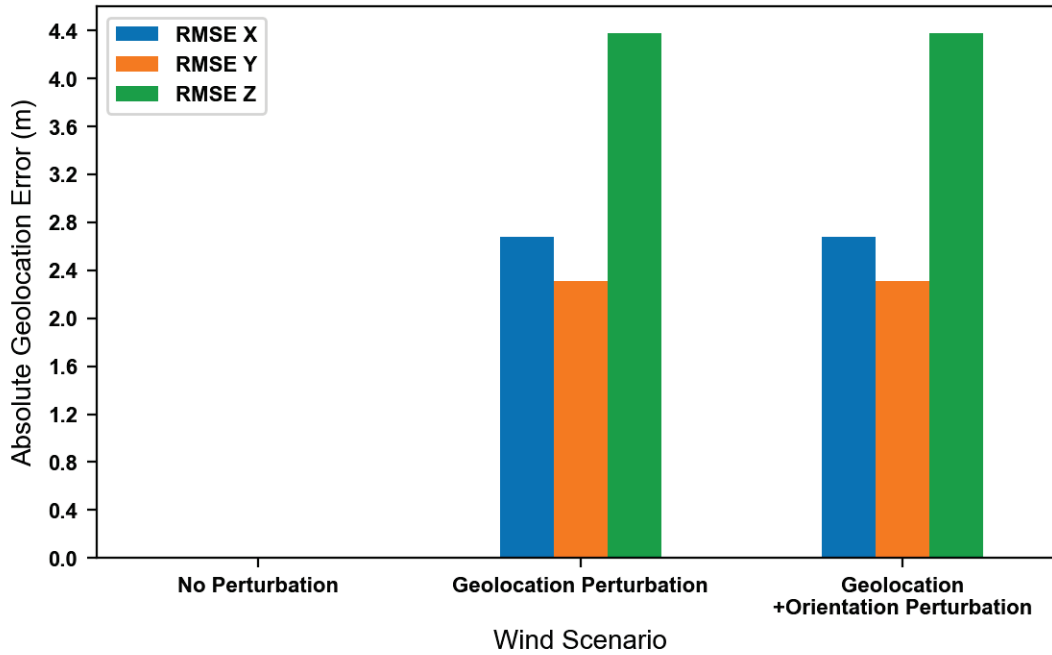
Note: The dashed lines are used for overall visualization, not to suggest linear trends between adjacent data points.

**Figure 80. Mean Absolute Camera *Position* Uncertainty.**

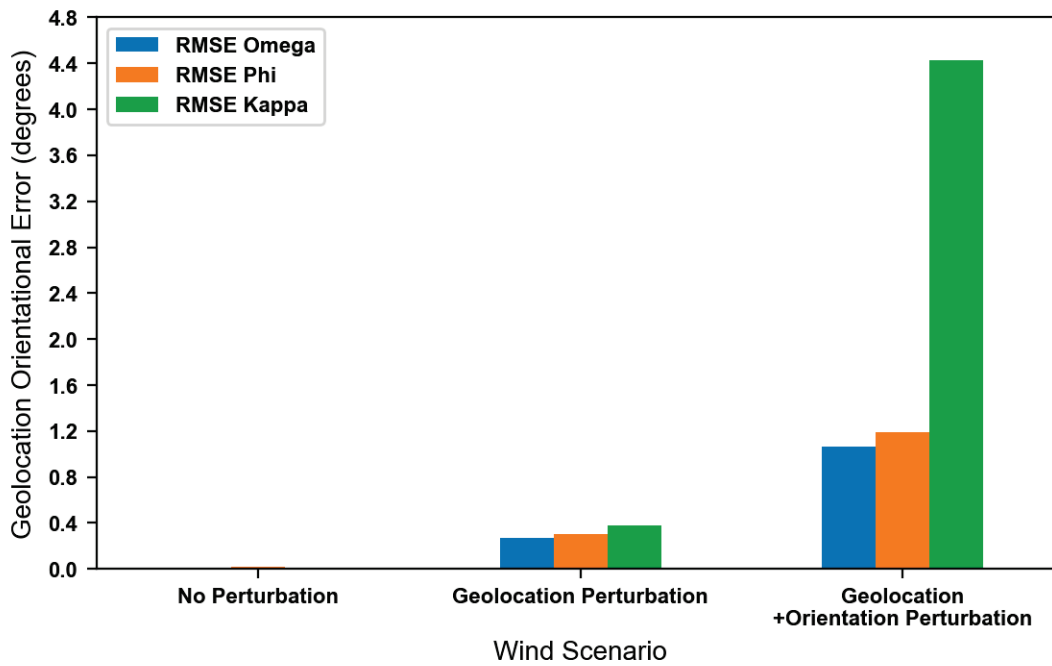


Note: The dashed lines are used for overall visualization, not to suggest linear trends between adjacent data points.

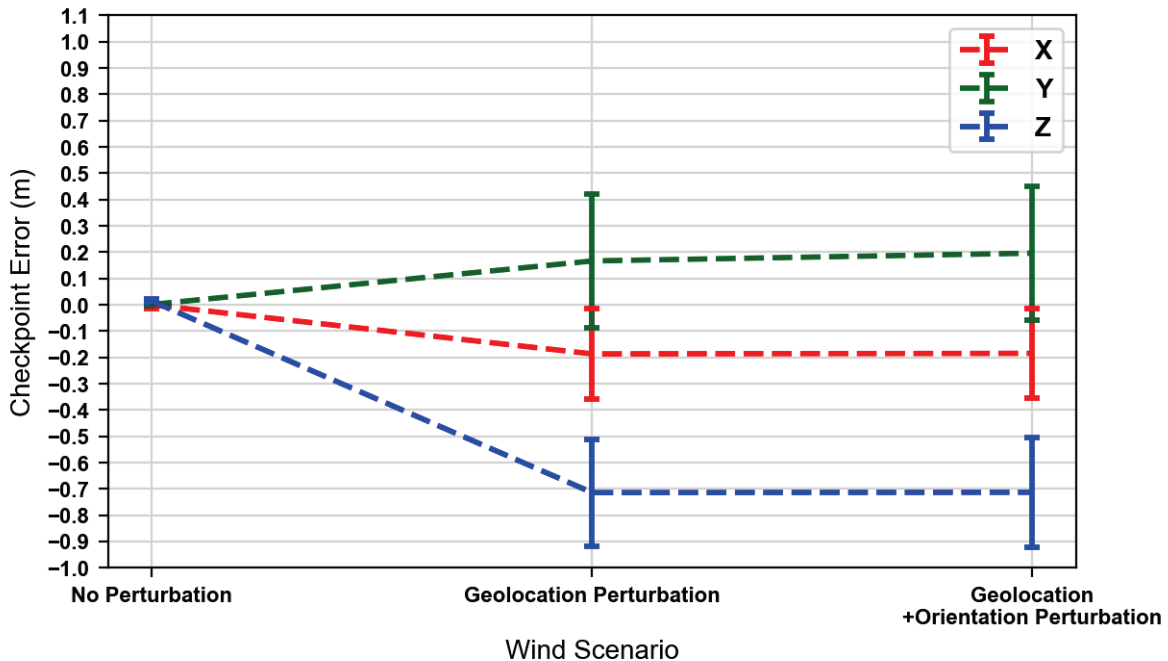
**Figure 81. Absolute Camera *Orientation* Uncertainty.**



**Figure 82. Absolute Camera *Geolocation* Error.**



**Figure 83. Absolute Camera *Orientation* Error.**



Note: The dashed lines are used for overall visualization, not to suggest linear trends between adjacent data points.

**Figure 84. Mean Checkpoint Error with Error Bars.**

## Lessons Learned

Major lessons learned from the simulation exercise included the following:

- Sidelap and endlap were positively correlated with keypoint extraction. Increasing either one increases the number of potential keypoints within Pix4D. A sharp rise in the number of keypoints at 90 percent endlap for lower sidelap scenarios shows that the endlap can be used to maintain a high number of keypoints (which is desirable) for flight lines oriented along roadway corridors. Increasing keypoints can be beneficial under suboptimal lighting conditions to help ensure sufficient keypoint correspondences for reconstruction.
- Higher endlap or sidelap percentages substantially increased the average number of images observed for a keypoint used to reconstruct a 3D point in the sparse point cloud. The higher the image number on which a 3D point is visible, the more observations and constraints in the BA (which is desirable). In return, 3D point measurements reconstructed from keypoints observed in more images will, in general, have better relative accuracy (i.e., less uncertainty) in their LS estimation and provide for a more robust sparse point cloud in that vicinity.
- Sidelap and endlap were negatively correlated with the uncertainty associated with estimated camera geolocation and orientation, demonstrating the direct benefit of overlap on improving reconstruction of accurate camera position and orientation (also known as camera pose). This feature can be beneficial in adverse weather, such as high wind speed, when input positional uncertainty may be high. Endlap showed a stronger negative correlation relative to sidelap for the scene examined, which means that increasing the percentage of endlap, relative to sidelap at the same percentage, provided a greater



decrease in the uncertainty of the estimated camera position and orientation values. Decreasing this uncertainty is desirable.

- Reconstruction of the Z coordinate for camera geolocations and checkpoint locations showed a larger error than for horizontal X-Y coordinates. This result is expected given that GNSS image geolocation uncertainty tends to be greater in the Z-dimension. It is worth noting that SfM software such as Pix4D automatically assigns greater uncertainty to Z coordinates. For example, when importing simulated UAS image sets into Pix4D for SfM processing, Pix4D's default setting for a standard, low-accuracy GNSS receiver is 5 m (16 ft) horizontally and 10 m (33 ft) vertically.
- Variation in overlap directly affected point densification. The total number of points and point density increased with overlap because of the increase in the number of images and coverage of the scene from multiple camera perspectives. Regardless, all overlap scenarios produced dense point clouds. The simulation used a 30 m (98 ft) flight height AGL, which resulted in a GSD of 7.2 mm (0.2 in) for the respective DJI Mavic 2 Pro camera model tested. Because densification occurs at or near the resolution of the imagery GSD, this small GSD still enabled dense clouds to be generated at lower overlap scenarios. All dense point clouds generated from each overlap scenario provided low RMSE values for cloud-to-cloud distances relative to the point cloud of the 3D mesh model of the crash scene used in the simulation and generated from the real-world UAS data. This point cloud is considered a ground truth point cloud for the purposes of the simulation analysis.
- SfM processing times for sparse point cloud generation and densification increased with the number of images processed, which stems from increasing sidelap or endlap. Major jumps in processing time occur when the number of images increase dramatically due to an incremental increase in sidelap adding additional flight lines.
- Simulation results showed that the major factor that governs flight time for UAS survey design is sidelap. UAS survey design for crash scenes should consider the impact of increasing sidelap on flight time while also keeping a balance in overlap requirements for SfM 3D reconstruction. This goal is achievable by optimizing endlap, which can be managed by varying the number of images per second along the flight course. Reducing UAS flight time may help reduce the time needed for road closures. Reducing flight time is also important under suboptimal weather conditions when longer time in the air might result in potentially encountering more unstable weather or degraded lighting conditions.
- Simulation results showed the value of increasing overlap to increase keypoint extraction and matching across multiple image perspectives. In most cases, increasing overlap reduces the uncertainty in SfM reconstruction of 3D point measurements within the regions of high overlap. For corridor mapping along roadways, a strategy to consider is to align the sensor frame's aspect ratio (i.e., the width dimension) with the flight course as opposed to perpendicular to it (which is typical). This strategy would enable more imagery to focus along the roadway or crash scene of interest while increasing endlap, thereby focusing the keypoint extraction and overlap scenarios to the roadway. The benefit of this approach for SfM reconstruction depends on size or width of the area to map, camera dimensions, and requirements of the scene for oblique perspectives.
- Examination of real-world UAS data collected during high wind conditions in Corpus Christi, Texas, and processed in Pix4D revealed that most of the orientation uncertainty rested with the yaw angle. The gimbaled camera on the DJI Phantom platform was set to

nadir view during imagery collection. The roll and pitch angles were kept low, reaching an uncertainty up to  $\pm 1.0$  degree. It is worth noting that the capability of a gimbal to maintain its pointing direction in response to high wind varies by platform.

- As expected, simulation of the effect of high wind on Pix4D processing by perturbing the input image geolocation and orientation values increased the error associated with absolute camera geolocation and checkpoints. Simulation results also showed that geolocation and orientation perturbation increased the estimated uncertainty of camera position and orientation during the BA phase in Pix4D. This occurrence may result in reduced relative point cloud accuracy in places of higher estimation uncertainty. In general, including GCPs or more accurate image geolocations should result in better absolute accuracy in high wind scenarios.
- Pix4D can resolve camera orientation without any IMU information through the SfM procedure. However, wind simulation results showed that Pix4D is influenced by the input orientation values—like it is with the input image geolocation values—and is likely using them to affect the adjustment procedure. Further investigation is probably necessary to better understand how Pix4D applies orientation values and orientation uncertainty into the SfM procedure because this will have implications for processing of accurate direct georeferencing and IMU data.
- Pix4D can use GCPs to improve both the relative positional accuracy and absolute positional accuracy of the 3D reconstruction of a scene. It applies the coordinates during the BA phase to reoptimize the estimation of camera IO and EO parameters. Accurate image geolocations using real-time kinematic/postprocessed kinematic (RTK/PPK) GNSS can also help constrain the BA. Use of GCPs as checkpoints is a valuable component to assess the absolute positional accuracy of the 3D reconstruction during SfM processing. However, it is worth noting that time and logistics may not allow use of GCPs for UAS mapping of crash scenes, especially under suboptimal conditions and reduced time constraints.
- Although not encountered here during simulation runs, bowling of the point cloud, often referred to as the “bowl effect,” is a commonly observed effect when processing UAS flights along corridors. It can be caused by unstable and inaccurate internal camera geometries, low overlap between images, and other factors, but typically stems from poor solutions of radial distortion parameters. Adding oblique angle camera perspectives, perpendicular flights lines, inclusion of control points or accurate image geolocations, and higher combinations of overlap can help mitigate this effect.

## **IMPACT OF AMBIENT LIGHTING AND LOW VISIBILITY ON UAS-SfM RECONSTRUCTIONS**

The research team used the UAS image acquisition simulation tool developed in the prior subtask to generate imagery suitable to evaluate effects of ambient lighting and visibility on SfM processing. The research team conducted simulation runs to produce overlapping images (i.e., image networks) subject to low lighting (typical of early morning or late in the day); bright lighting (e.g., midday); low visibility from mist, fog, or clouds; artificial lighting; and wet surfaces after rainfall events. The research team then fed the simulated image networks through a typical SfM processing workflow using Pix4D to evaluate effects of suboptimal lighting on 3D

reconstruction. In addition, this work examined the impact of low overlap (E60-S60) versus enough overlap for grid flight patterns (E80-S80).

Note that this section handles fog at two general visibility levels: high visibility and low visibility. A subsequent section provides a much more granular view by evaluating the effect of different fog levels on the number of pairwise matches and number of points in the 3D point cloud.

## **General Concepts**

Scene texture plays a key role in SfM reconstruction accuracy. The success in measuring keypoints on objects in an image is dependent on image texture. Image texture describes the spatial arrangement of color or intensities in an image or selected region of an image (94). The lack of texture within a terrain scene, as represented by an image, has been shown to have one of the largest impacts on the accuracy of UAS-SfM point clouds (42, 49, 58).

Suboptimal environmental conditions, such as fog or low lighting at twilight, can reduce or alter scene texture. A degraded scene texture can potentially result in reduced keypoint correspondence and spurious keypoint matches in certain areas. It can also degrade the quality of the SfM sparse point cloud reconstruction, including the estimation of camera position and orientation as well as automated calibration of internal camera parameters. Performing point cloud densification by the MVS algorithms implemented within an SfM software is also problematic in featureless and nontextured regions (e.g., in areas of low reflectance, strong shadows, or saturated or homogenous areas that may be bright or overly exposed) (49).

An environment with balanced ambient and direct light is preferable for UAS data collection (e.g., a uniformly bright cloudy day). Shadows are shortest at local noon time but also strongest. Data acquired during this time may have less shadowing, but where shadows occur, 3D reconstruction can be poor (49).

Effect of scene texture on an SfM solution also depends on the camera, camera settings, and software algorithms. For example, for the same UAS image set, one SfM software relative to another may produce differences in point cloud characteristics and geospatial fidelity due to the inherent differences in the automated keypoint matching and correspondence algorithms (59).

## **Methods**

The research team used the UAS image acquisition simulation tool developed in the prior subtask to generate imagery suitable to evaluate effects of ambient lighting and visibility on SfM processing. The research team conducted simulation runs to produce overlapping images (i.e., image networks) subject to low lighting (typical of early morning or late in the day); bright lighting (e.g., midday); low visibility from mist, fog, or clouds; artificial lighting; and wet surfaces after rainfall events.

The lighting conditions that were simulated represent various levels of overall scene darkness and brightness-producing conditions more favorable to underexposure or overexposure within the scene. Underexposure and overexposure occur when a camera sensor does not record enough

details in the darkest and brightest part of the images, respectively. Such conditions can potentially degrade or enhance image texture.

Daytime simulation conditions also examined sensitivity of the SfM-MVS process to variations in incoming sun intensity (brightness conditions) and strength of shadowing within the scene due to sun altitude and heading. The research team simulated lighting conditions in Austin, Texas, on May 1, 2020, and an additional scenario on the summer solstice at solar noon (June 20, 2020). Although the actual crash scene was from another location, the simulation environment (Blender) allows simulated lighting in different conditions and locations.

It is worth noting that Blender includes computer graphics techniques to provide 3D visualizations based on physical principles of illumination, sunlight, light propagation, and light scattering. Although Blender is a simulation environment and therefore does not replicate real-world scenarios perfectly, it does provide a controlled environment with which to look at the impacts of various types of suboptimal lighting conditions on SfM reconstruction. Achieving this goal would be difficult and impractical if having to rely solely on data collected in the field.

Blender includes a path-tracing rendering engine (called Cycles) that simulates light. For each pixel, path tracing follows rays from the camera through the scene until the rays hit a light source. Using unbiased Monte Carlo sampling, this process is repeated several times for each pixel (95, 96, 97). Each time the ray takes a different path, providing a different contribution to the radiance the surface emits. With this approach, the software emulates the way photons take from a light source to the camera, only backwards.

Blender handles light rays but not polarization. Blender does include a radiosity renderer (98). Radiosity is a global illumination algorithm that accounts for illumination that comes from surfaces that reflect light diffusely. This algorithm takes into account the light generated by diffuse emitters and its interaction with the environment. The physical principle behind the radiosity algorithm is thermal radiation, which enables the simulation of the amount of light energy transferred among surfaces.

The technical literature includes reports on the use of the ray tracing engine in Blender for applications such as simulating radar and its interaction with targets, realistically simulating natural atmospheric lighting phenomena, and generating photo-realistic images of space objects to simulate light curves that are then compared with actual light curves extracted from telescope imagery (99, 100, 101). The literature also includes reports of the use of Blender to recreate crash scene geometry and lighting conditions (102).

### *Lighting Conditions*

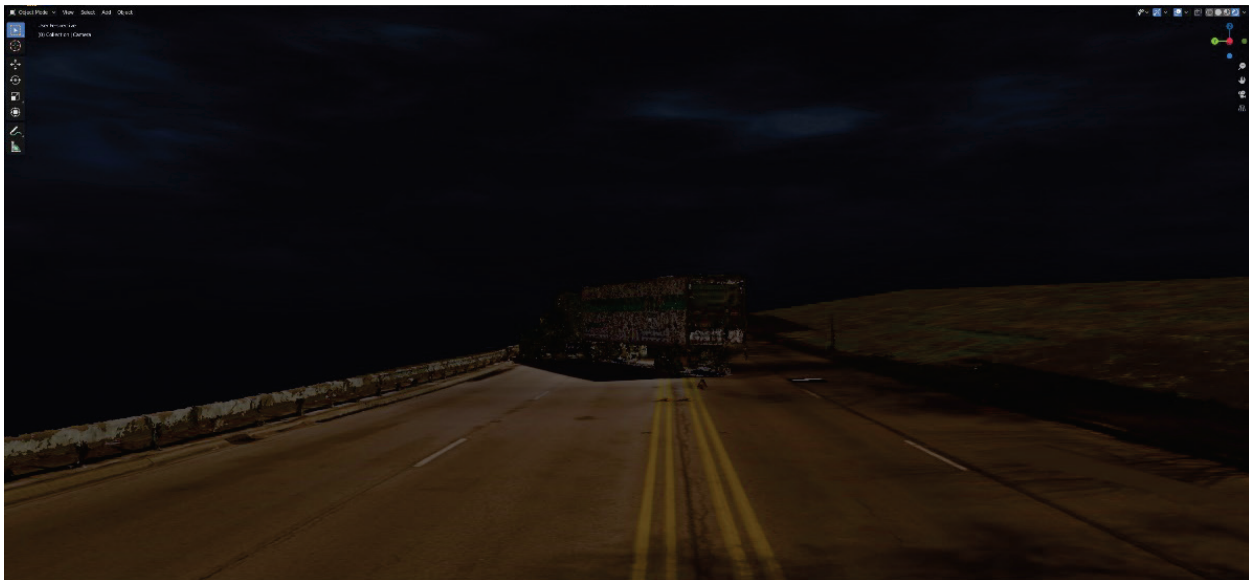
The research team used a combination of internal objects in Blender, such as lamp and sun objects. The research team also used an external add-on called Dynamic Sky to modify settings such as sky color, sky brightness, horizon color, cloud color and density, and some controls on the sun direction and brightness. Sun parameters included solar elevation angle and azimuth, which were based on a specific geographic location (Austin, Texas) and date (May 1, 2020). The simulation also included solar noon at the summer solstice (June 20, 2020).

Renderings of artificial lighting under dark sky conditions used lamp posts placed on both sides of the road directly across from each other and on either side of the crash scene. Spacing between lamp posts was 30 m (98 ft). For each lamp post, simulated lighting in Blender used a 1000-watt lamp at 30 m (98 ft) AGL. Table 69 shows the various lighting scenarios examined. Note that the cloudy sky scenario was for late evening conditions (7:00 PM). For simulations of dark sky with lamp posts, the research team added a second, more critical scenario, in which only two lamp posts were on and the sky was completely dark.

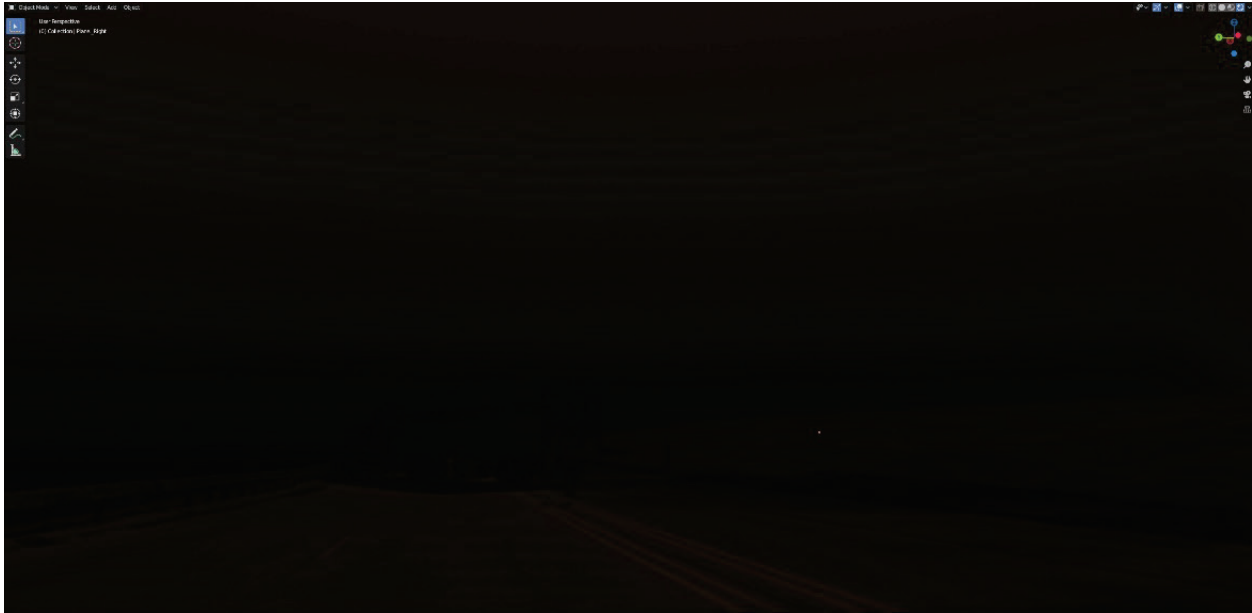
**Table 69. Natural and Artificial Lighting Scenarios Evaluated.**

Lighting Scenario	Time	Solar Elevation Angle	Solar Azimuth	Cloud Coverage	Lamp Post Power (Watts)
Cloud	7:00 PM	14°	280°	100%	None
Dark	11:00 PM	-32°	317°	20%	None
Dark with Lamp Posts (Full and Partial Illumination)	11:00 PM	-32°	317°	20%	1000
Civil twilight	8:34 PM	-6°	292°	20%	None
Dusk	8:08 PM	0°	288°	20%	None
Afternoon	5:00 PM	39°	265°	20%	None
Solar Noon	1:27 PM	75°	180°	20%	None
Solar Noon (Summer Solstice)	1:32 PM	83°	180°	20%	None

Figure 85 through Figure 93 show the scene rendered for each lighting scenario in Blender.



**Figure 85. Cloudy Sky (100% Coverage) in Late Evening (7:00 PM).**



**Figure 86. Dark Sky (11:00 PM).**



**Figure 87. Dark Sky with Lamp Posts at Full Illumination (11:00 PM).**



**Figure 88. Dark Sky with Lamp Posts with Partial Illumination (11:00 PM).**



**Figure 89. Civil Twilight (8:34 PM).**



**Figure 90. Dusk (8:08 PM).**



**Figure 91. Afternoon (5:00 PM).**





**Figure 92. Solar Noon (1:27 PM).**



**Figure 93. Solar Noon on the Summer Solstice (1:32 PM).**

### *Fog Conditions*

Simulation of UAS image acquisition in foggy weather conditions required more complex modeling than natural lighting conditions. To simulate fog conditions, the research team used the volumetric lighting technique in Blender. Volumetric lighting is a technique in 3D computer graphics to add lighting effects to a rendered scene. This technique enables the viewer to see beams of light shining through the environment. In volumetric lighting, the light cone emitted by the light source is modeled as a transparent object and considered as a container of a “volume.”

This technique has the capability to give the effect of light passing through an actual 3D medium, such as dust, smoke, or fog, that is contained inside its volume.

A classic example of this effect is a search light with a visible halo. In the real world, a halo is caused by particles in the air scattering light. Some of the scattered light is diverted into the eyes in the form of a halo or shaft of light. Blender can simulate this scattering effect by using various volumetric lighting options. The Sky & Atmosphere panel in Blender further enables the user to simulate various properties of real sky and atmosphere (e.g., sunlight scattering from a certain source direction as it crosses through a certain path length of air overhead).

The research team modeled two illumination scenarios for fog conditions: high visibility and low visibility. The sunlight source in the scene was set at a solar elevation of two degrees and a solar azimuth of 73 degrees to simulate an early morning sky at 7:00 AM on May 1<sup>st</sup> (103). For both illumination scenarios, the light intensity was set to zero at the height of UAS image acquisition (i.e., 30 m or 98 ft AGL), and then it increased linearly until reaching a maximum value at the ground surface.

Table 70 shows the fog parameters and visibility conditions for the two simulated fog scenarios. Computation of the maximum range of vertical and horizontal visibility is based on the appearance of a set of artificial targets added to the scene, spaced 10 m (33 ft) horizontally and 2 m (6.6 ft) vertically, and rendered in images taken at set camera distances away from the targets. Referring to the intensity parameter, Blender computes the strength of the ambient lighting from the sun (intensity) in watts per square meter ( $\text{watt/m}^2$ ), which represents the strength of light radiating from each square meter of the simulated scene. For the high and low visibility fog scenarios, the morning sky condition was simulated using a radiating light intensity of  $0.1 \text{ watt/m}^2$  (high visibility) and  $0.01 \text{ watt/m}^2$  (low visibility). The smaller intensity value for the low visibility scenario simulated more light scattering due to the presence of dense fog in the scene, producing a darker, lower visibility scene. Figure 94 and Figure 95 show the visibility of the set of targets in images taken in fog condition for high and low visibility, respectively.

**Table 70. Fog Simulation Conditions.**

Fog Scenario	Radiating Light Intensity ( $\text{watt/m}^2$ )	Fading Condition	Maximum Range for Vertical Visibility (m)	Maximum Range for Horizontal Visibility (m)
High Visibility	0.1	linear	150	More than scene length
Low Visibility	0.01	linear	50	< 50



**Figure 94. Fog Condition with High Visibility.**



**Figure 95. Fog Condition with Low Visibility.**

### *Wet Surface Conditions*

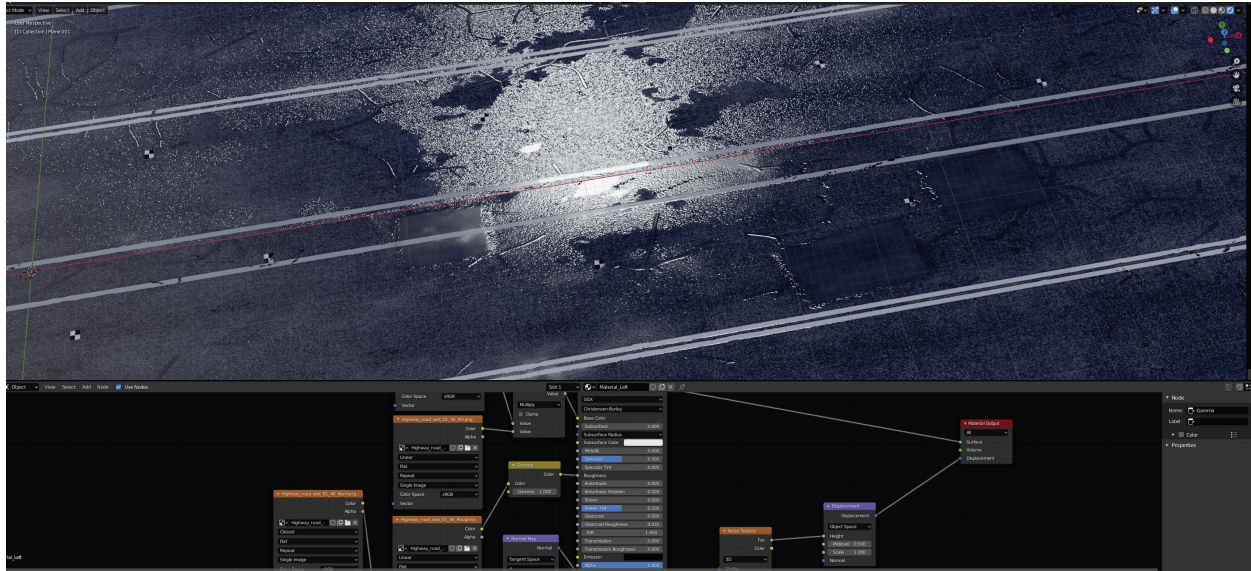
Wet surfaces can alter spectral response patterns of underlying surfaces through absorption, introduce sun glint and specular scattering in areas of ponded water, introduce dynamic surface movement in areas of flowing water, and produce mirror-like reflections of surrounding structures. All these effects can alter scene texture.

To simulate a wet asphalt road, the research team designed a  $310 \times 80$  m ( $1017 \times 262$  ft) texturized mesh model of a flat surface resembling a straight road. The simulation applied a wet look to an asphalt texture applied to the road. This texture includes images related to the base color image of an asphalt road, ambient occlusion map, normal image, roughness image, and mask image. In Blender, a shader editor window combined all these images into a single node tree structure. A glossy shader node with roughness set to zero, when added to the node tree structure, made the road texture appear as a mirror-like surface. The glossy shader was then mixed with the normal asphalt texture. The next step involved darkening the road material (texture) to mimic the real-world effect of refractive mismatch. This effect happens when water molecules are absorbed into a surface, and the result is a smoother surface that gives sharper

reflections but also reduces the number of the scattered rays, thus making the surface appear darker.

Real-world wet roadway surfaces generally contain texture variations, so the simulation added some puddles to the asphalt texture by using a noise texture node. This node includes a black and white map, which in combination with the original asphalt texture using a mix shader, resulted in dark areas on the roadway appearing wetter and light areas appearing drier.

Figure 96 shows the node tree structure designed in the node editor window of Blender software for the simulated wet asphalt road.



**Figure 96. Wet Asphalt Road and Related Node Tree in the Shader Editor Window.**

### *Simulation Scenarios*

The research team fed the simulated image networks through a typical SfM processing workflow using Pix4D to evaluate the effects of suboptimal lighting on 3D reconstruction. In addition, this work examined the impact of low overlap (E60-S60) versus enough overlap for grid flight patterns (E80-S80).

All simulations used a 20 MP 2.5-cm (1-inch) sensor frame Hasselblad camera model in Blender for image rendering, which is the camera carried onboard a DJI Mavic 2 Pro. Rendering applied a 10 mm focal length resulting in a 7.2 mm (0.2 in) GSD at 30 m (98 ft) flight height AGL. The simulation then applied lens distortion and vignetting effects to all image sets using MATLAB code. The research team used Pix4D's standard 3D mapping template and used standard geolocation uncertainty values for image positions based on a single-frequency, nondifferential GNSS such as onboard a DJI Mavic 2 Pro. This process equated to 5 m (16 ft) horizontal and 10 m (33 ft) vertical position uncertainty for image geolocations in Pix4D. Calibration of the internal parameters used the all prior setting in Pix4D. Figure 97 shows the Pix4D processing settings used for sparse (initial) and dense point cloud generation, respectively.

(a) Initial processing settings

Detected Template	No Template Available
Keypoints Image Scale	Full, Image Scale: 1
Advanced: Matching Image Pairs	Aerial Grid or Corridor
Advanced: Matching Strategy	Use Geometrically Verified Matching: no
Advanced: Keypoint Extraction	Targeted Number of Keypoints: Automatic
Advanced: Calibration	Calibration Method: Standard Internal Parameters Optimization: All prior External Parameters Optimization: All Rematch: Auto, yes

(b) Densification settings

Image Scale	multiscale, 1/2 (Half image size, Default)
Point Density	Optimal
Minimum Number of Matches	3
3D Textured Mesh Generation	no
LOD	Generated: no
Advanced: Image Groups	group1
Advanced: Use Processing Area	yes
Advanced: Use Annotations	yes
Time for Point Cloud Densification	05m:11s
Time for Point Cloud Classification	NA
Time for 3D Textured Mesh Generation	NA

**Figure 97. Pix4D Initial Processing and Densification Settings.**

*Evaluation Metrics*

The research team evaluated the influence of suboptimal lighting conditions on the quality of the 3D reconstruction results by examining quality factors at each of the three key stages of the full SfM workflow:

- Stage 1—Keypoint extraction and matching.
- Stage 2—BA and sparse point cloud creation.
- Stage 3—3D point cloud densification.

For Stages 1 and 2, the research team focused on quality factors that were available from the Pix4D processing report and included metrics such as reprojection error, estimated camera position and orientation uncertainty, and checkpoint geolocation error. For the latter, the processing workflow set GCPs as checkpoints and did not use them to constrain the SfM solution during the bundle block adjustment.

For Stage 3, the evaluation of dense point cloud quality consisted of computing cloud-to-cloud distances between the reconstructed 3D densified point cloud created from the rendered imagery of the scene and the point cloud of the 3D mesh model used in the simulation and created from the real-world UAS imagery (referred to as the ground truth point cloud). The mean cloud-to-cloud distance error and standard deviation of the error served as the dense point cloud quality factors, in addition to point density. For wet surface simulations, the ground truth point cloud

that was compared to the simulated dense point clouds was created from the textured mesh of the artificial roadway scene.

Brightness and darkness of the colorized 3D point cloud generated from the SfM procedure comes from the intensity values of 2D pixels in the raw images used to reconstruct the 3D scene. For the analysis, the research team used brightness and darkness indices as follows (104):

$$\tilde{I}_{gray} = \frac{2 \times (0.2126 \times R + 0.7152 \times G + 0.0722 \times B)}{255} - 1 \quad (15)$$

$$\begin{cases} I_b = \tilde{I}_{gray}, I_d = 0 \text{ if } \tilde{I}_{gray} > 0 \\ I_d = |\tilde{I}_{gray}|, I_b = 0 \text{ if } \tilde{I}_{gray} < 0 \end{cases}$$

where:

$I_b$  = brightness index between 0 and 1, with higher values for brighter pixels; and  
 $I_d$  = darkness index between 0 and 1, with higher values for darker pixels.

For each lighting scenario, the research team computed a single overall brightness and darkness index value by calculating the mean of the set of  $I_b$  and  $I_d$  values computed for every single pixel across the entire set of simulated UAS images (105 images for the S80-E80 scenario).

Table 71 shows the overall brightness and darkness indexes for the eight lighting scenarios shown in Table 69. Table 71 also shows brightness and darkness indexes for high visibility fog conditions. Larger brightness index values relative to darkness index values for a specific scene imply a brighter scene overall. For example, the solar noon scene was a bright scene overall because it had a brightness value of 0.487 but a darkness value of 0.281. Larger brightness or darkness values relative to another scene's brightness or darkness index values imply that the scene has more overall scene brightness or scene darkness. Accordingly, the summer solstice solar noon scene was the brightest of all scenes used for the analysis.

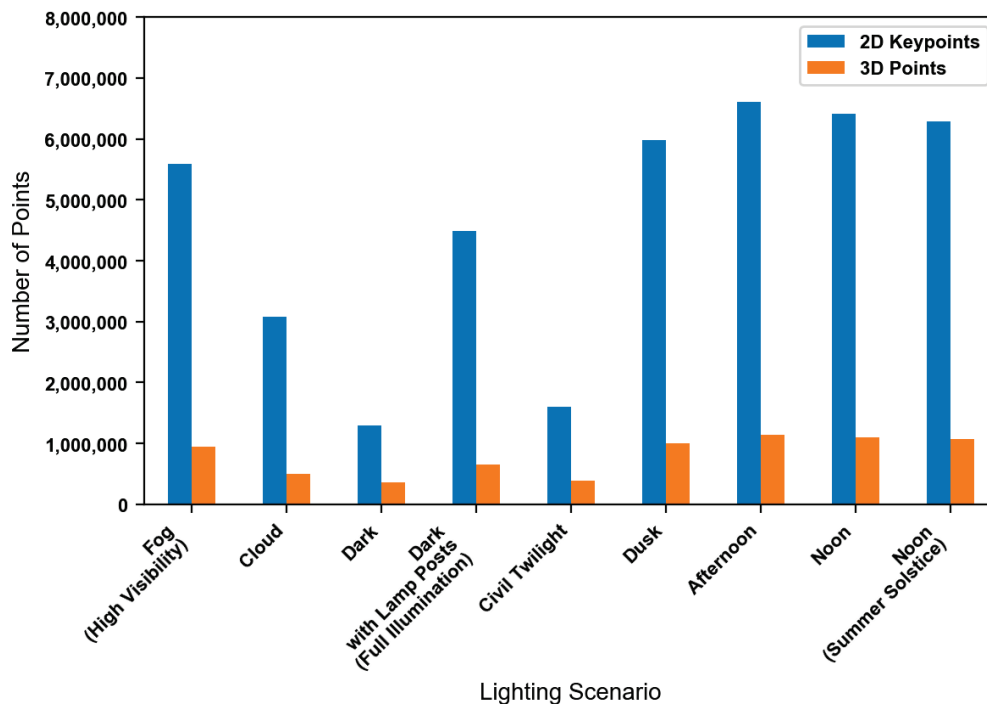
**Table 71. Overall Brightness and Darkness Index Values for Different Scenarios.**

Visibility Scenario	Overall Brightness Index $\bar{I}_b$	Overall Darkness index $\bar{I}_d$
Fog (High Visibility)	0.411	0.084
Cloud	0.000	0.683
Dark	0.000	0.914
Dark with Lamp Posts	0.021	0.546
Civil Twilight	0.000	0.842
Dusk	0.074	0.370
Afternoon	0.286	0.273
Solar Noon	0.487	0.281
Solar Noon (Summer Solstice)	0.532	0.254

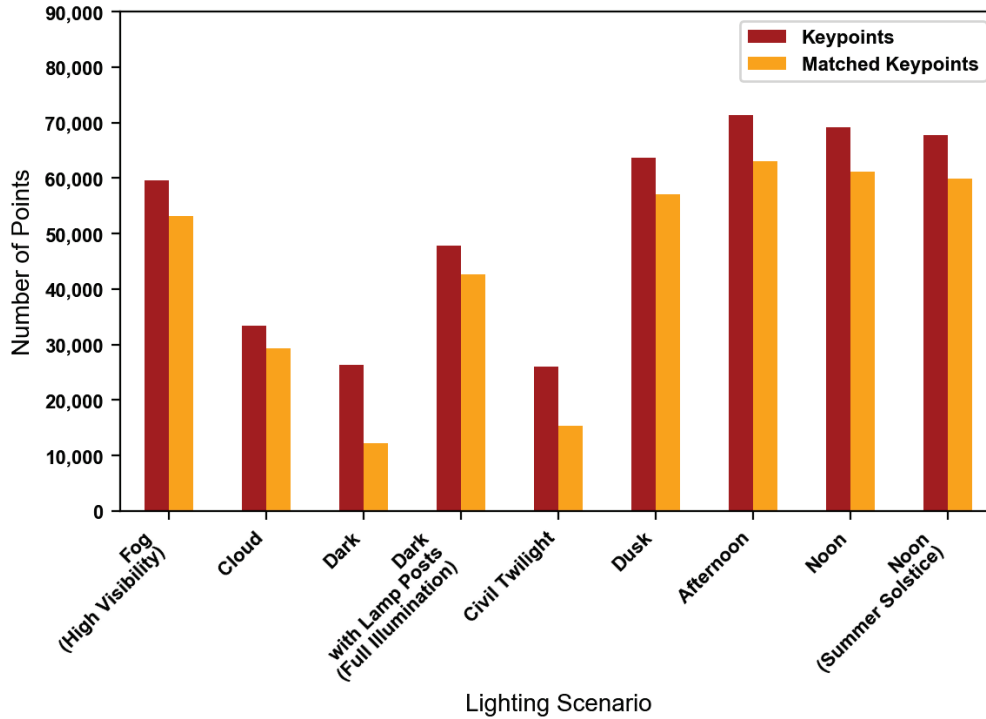
## Results

### *Keypoint Extraction and Matching Quality Factors*

Figure 98 shows the total number of 2D keypoints and 3D points extracted across the entire scene for the eight different lighting scenarios shown in Table 69 plus high visibility fog condition (Table 70). Afternoon sky, followed by noon and dusk, provided the most favorable conditions for keypoint matching. The dark sky and civil twilight scenarios had the lowest number of 2D keypoints, which resulted in a smaller number of 3D points resolved in the sparse point cloud. Full illumination with artificial lamp posts had a reduction compared to natural lighting scenarios, but it resulted in much better keypoint extraction conditions than dark sky or civil twilight. High visibility fog only had a slight reduction in the number of keypoints relative to daytime sky conditions. Cloudy sky, which occurred in the evening, had a large reduction in 2D and 3D keypoints. Figure 99 shows similar patterns for the average number of 2D keypoints and matched keypoints per an image.



**Figure 98. Total Number of 2D Keypoints and 3D Points by Lighting Scenario.**

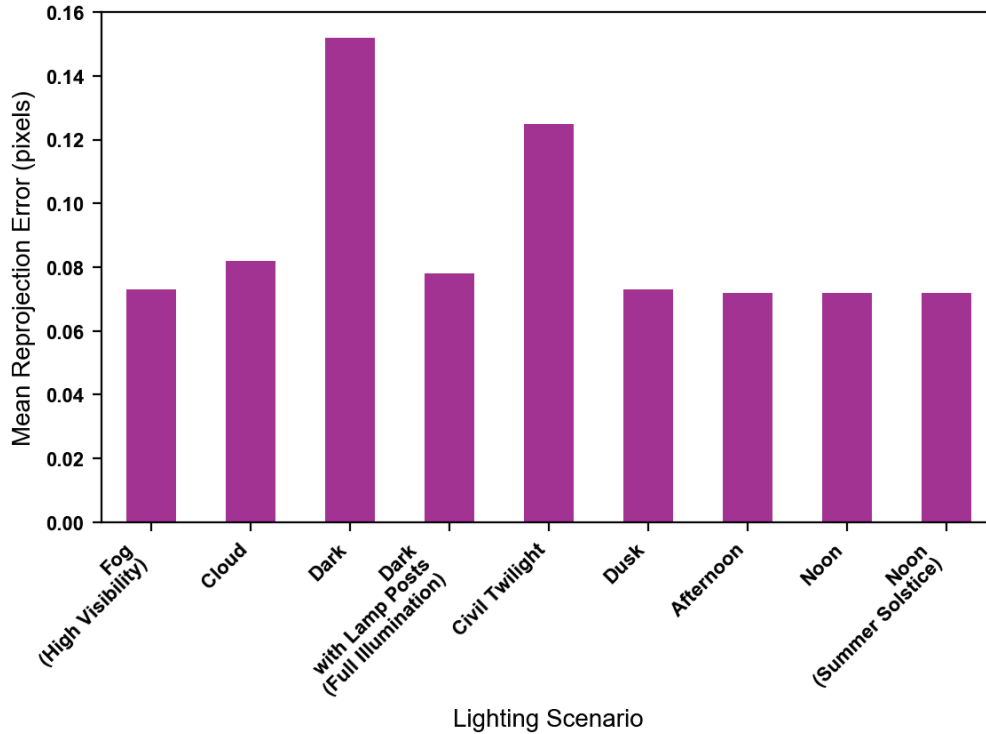


**Figure 99. Average Number of 2D Keypoints and Matched Keypoints per Image.**

### *BA Quality Factors*

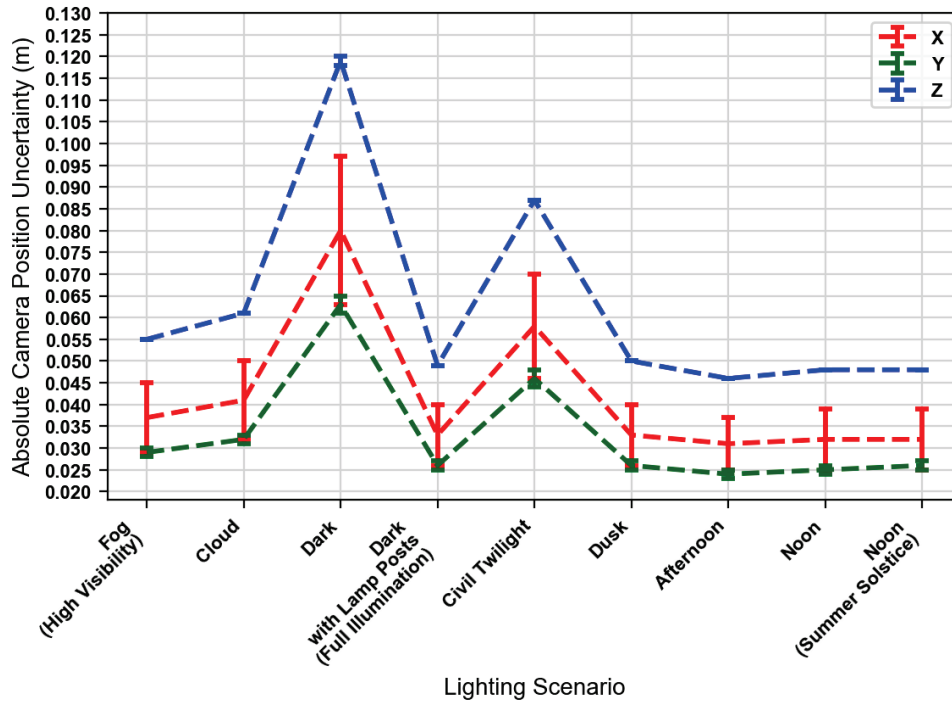
Figure 100 shows mean reprojection error by lighting scenario measured in pixel space. Reprojection errors should be less than 1 pixel. As expected, all lighting scenarios were well below this threshold because the simulation included camera pose information and camera calibration parameters. Nevertheless, the impact was clear. Increasing darkness resulted in a larger mean reprojection error, resulting from reduced keypoint correspondence, with dark sky and civil twilight scenarios having the largest reprojection error.





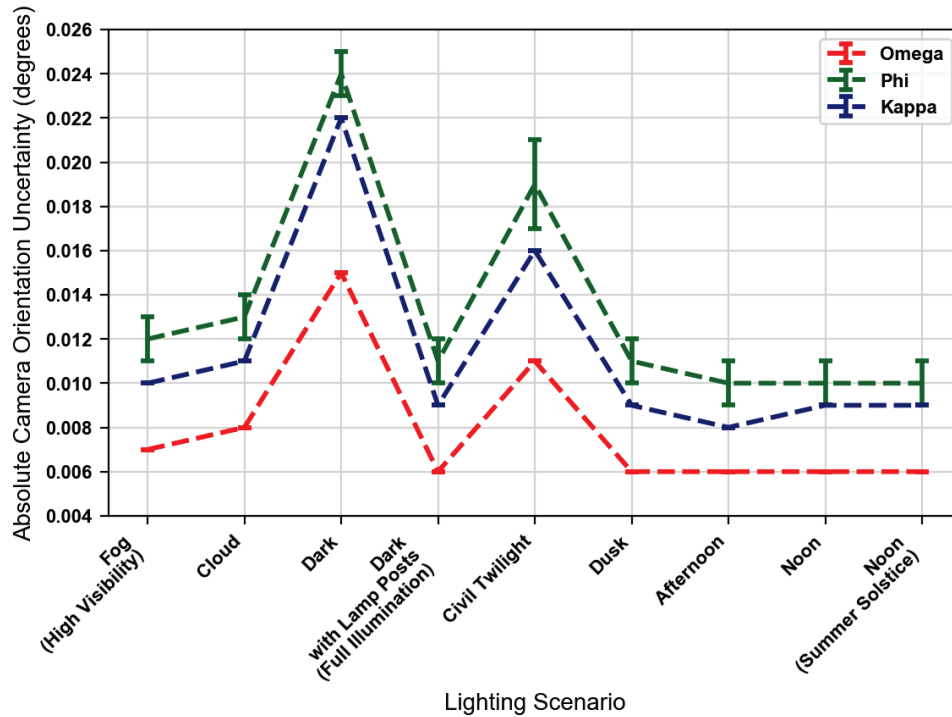
**Figure 100. Mean Reprojection Error.**

Figure 101 and Figure 102 show mean absolute camera position and orientation uncertainties, respectively, based on the BA estimation. Both figures demonstrate the impact of reduced lighting on the estimated position and orientation uncertainties with dark sky and civil twilight causing the largest degradation. Daytime sky conditions had a similar behavior, except for a slight degradation in position and uncertainty for noon and noon at the solstice due to brighter sky conditions potentially saturating some texture or darker shadowing. The Z coordinate had the largest positional uncertainty across all scenarios. The phi and kappa angular values had the largest orientation uncertainty across all scenarios.



Note: The dashed lines are used for overall visualization, not to suggest linear trends between adjacent data points.

**Figure 101. Mean Absolute Camera Position Uncertainty with Error Bars.**

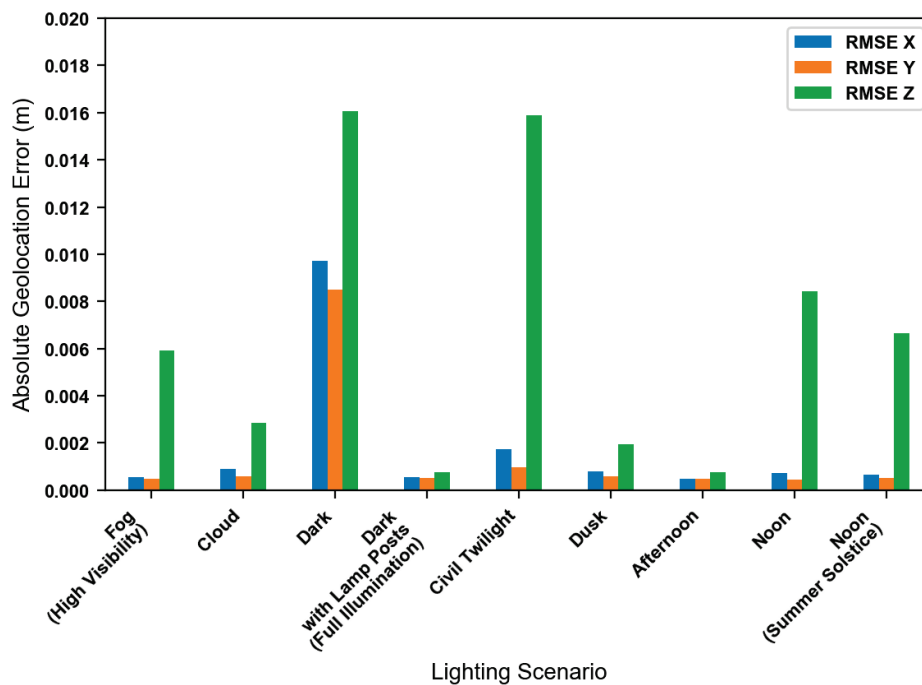


Note: The dashed lines are used for overall visualization, not to suggest linear trends between adjacent data points.

**Figure 102. Mean Absolute Camera Orientation Uncertainty with Error Bars.**

Figure 103 and Figure 104 show the RMSE of the absolute camera geolocation and orientation errors. Dark sky and civil twilight produced the largest error geolocation and orientation errors. Interestingly, solar noon and solar noon solstice conditions produced a noticeable geolocation error, particularly in the Z direction. This error might potentially be due to reduced texture from increased scene brightness, but might also be due to darker shadows in the scene. Noon conditions are generally preferable to shorten length of shadows, but prior research shows this can generate darker shadows in certain areas that can then degrade the SfM point cloud solution for those specific areas (49).

Figure 105 shows the RMSE of the checkpoint error based on the artificial GCPs introduced to the rendered scene. There were larger errors across all coordinates for both dark sky and civil twilight conditions due to reduced lighting. Interestingly, their largest error was in the X direction, which might be related to a larger phi angle orientation error, as shown in Figure 104. Fog and noon solstice conditions had the largest error in the Z direction, which is likely due to a larger absolute camera position error in the Z direction relative to the horizontal components for fog and solstice scenarios, as shown in Figure 103, while the angular phi orientation errors were relatively small compared to dark sky and civil twilight, as shown in Figure 104.



**Figure 103. Absolute Camera Geolocation Error.**

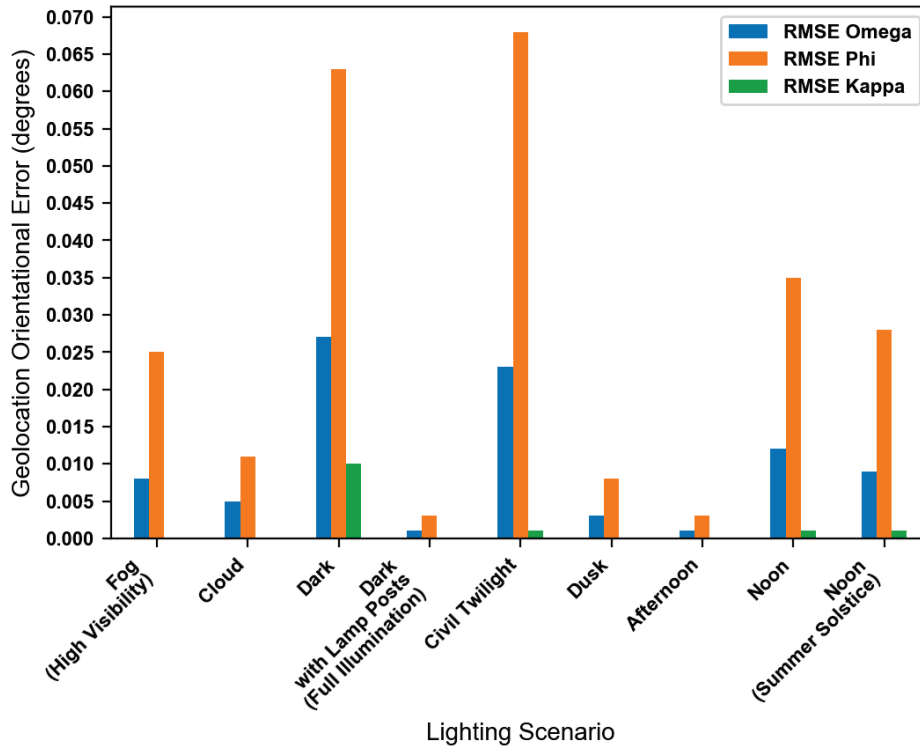


Figure 104. Absolute Camera Orientation Error.

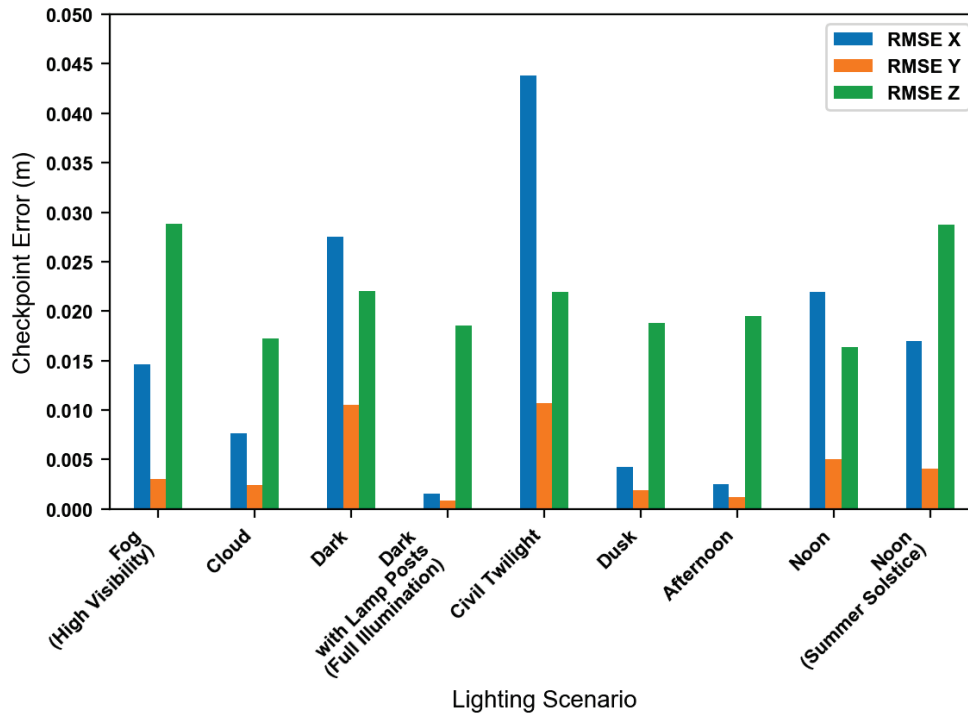


Figure 105. RMSE of the Checkpoint Error.

### *Combined Effect of Overlap Levels and Fog*

Before proceeding with the discussion about dense point cloud quality factors, this section (and the next three sections) examines the combined effect of several factors, including ambient lighting variations, overlap variations, and roadway surface conditions. This section focuses on the combined effect of overlap levels and fog.

Figure 106 shows a derived orthomosaic before densification for the low and high visibility fog scenario at E80-80. Figure 107 shows the total number of 2D keypoints and 3D points reconstructed in the sparse point cloud from matched keypoints for low and high visibility fog at E60-S60 and E80-S80 overlap levels. Low visibility fog resulted in significantly fewer keypoints and 3D points in the sparse point cloud, with an approximate five-time reduction in the number of keypoints and three-time reduction in the number of 3D points compared to high visibility fog. Overlap also played a key role in enhancing the number of keypoints for both low and high visibility fog.

Figure 108 and Figure 109 show the mean absolute camera position and orientation uncertainties (i.e., theoretical standard deviations for the estimated parameter values) estimated from the SfM BA solution for low and high visibility fog at the two overlap scenarios. Error bars shown represent the variation (sigma) of the estimated uncertainty values. A significant increase occurred in uncertainties for low visibility versus high visibility due to the reduction in keypoint correspondence. Both figures show the importance of increasing overlap in suboptimal lighting conditions to improve the BA solution for sparse cloud reconstruction. High visibility fog position and orientation uncertainty at E60-S60 was in the same range as E80-S80 for low visibility.

Figure 110 shows the RMSE of the checkpoint coordinate error for the different fog and overlap scenarios. High overlap resulted in much lower checkpoint errors for both low and high visibility scenarios.



Low Visibility Fog at E80-S80 Overlap



High Visibility Fog at E80-S80 Overlap

**Figure 106. Orthomosaic Showing Low-Visibility Fog and High-Visibility Fog Scenarios at E80-S80 Overlap.**

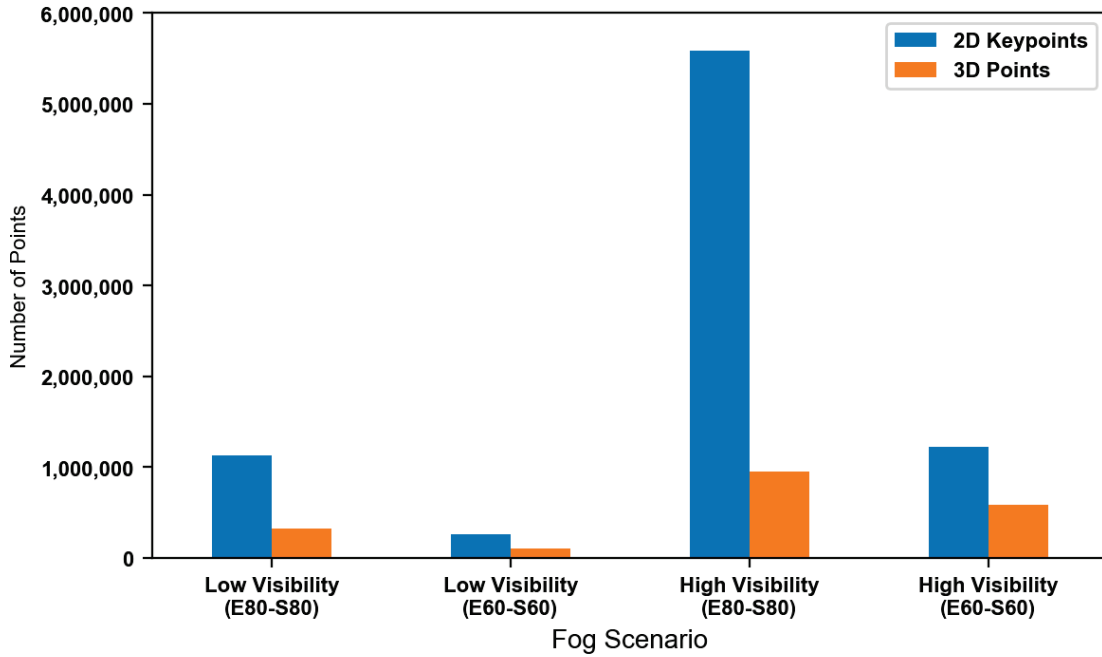
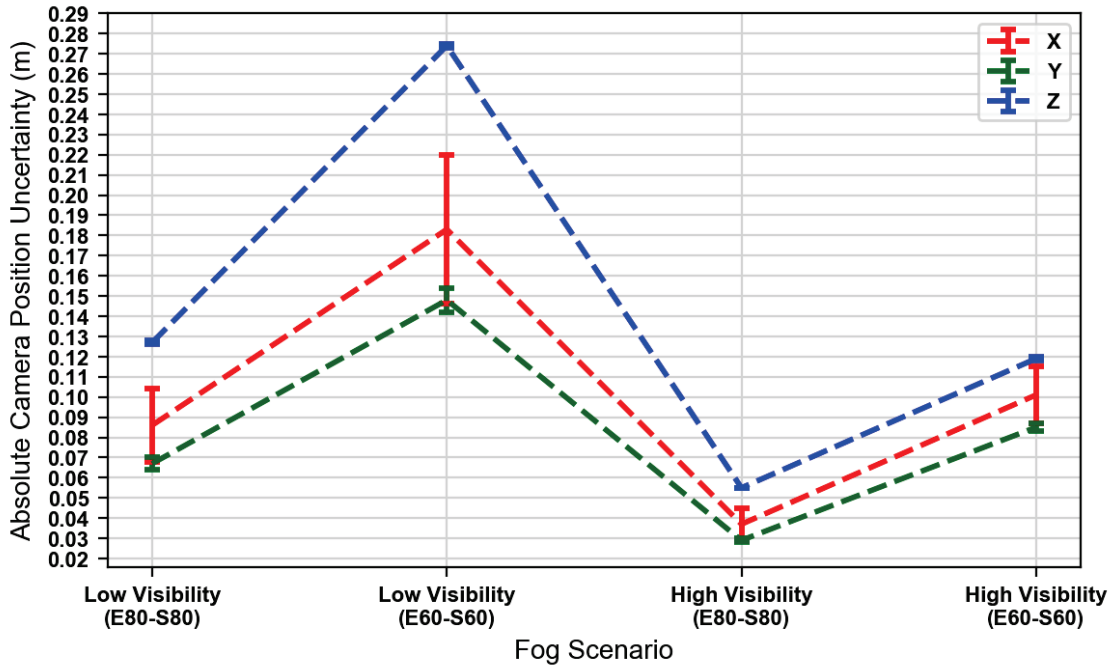
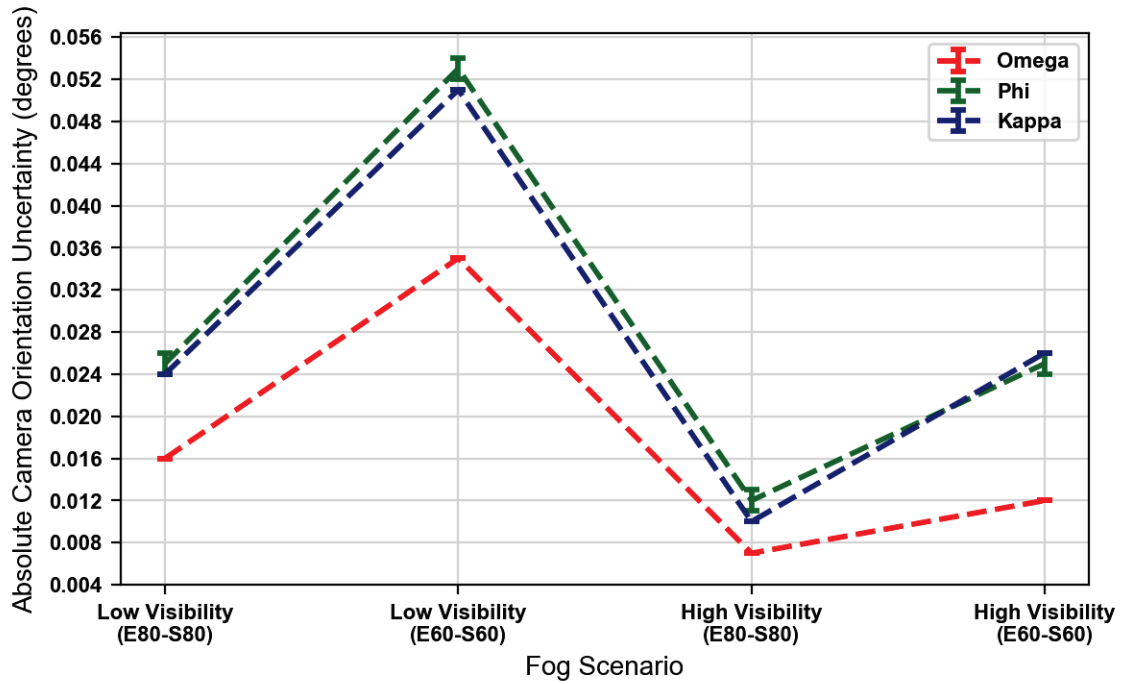


Figure 107. Total Number of 2D Keypoints and 3D Points by Fog and Overlap Scenario.



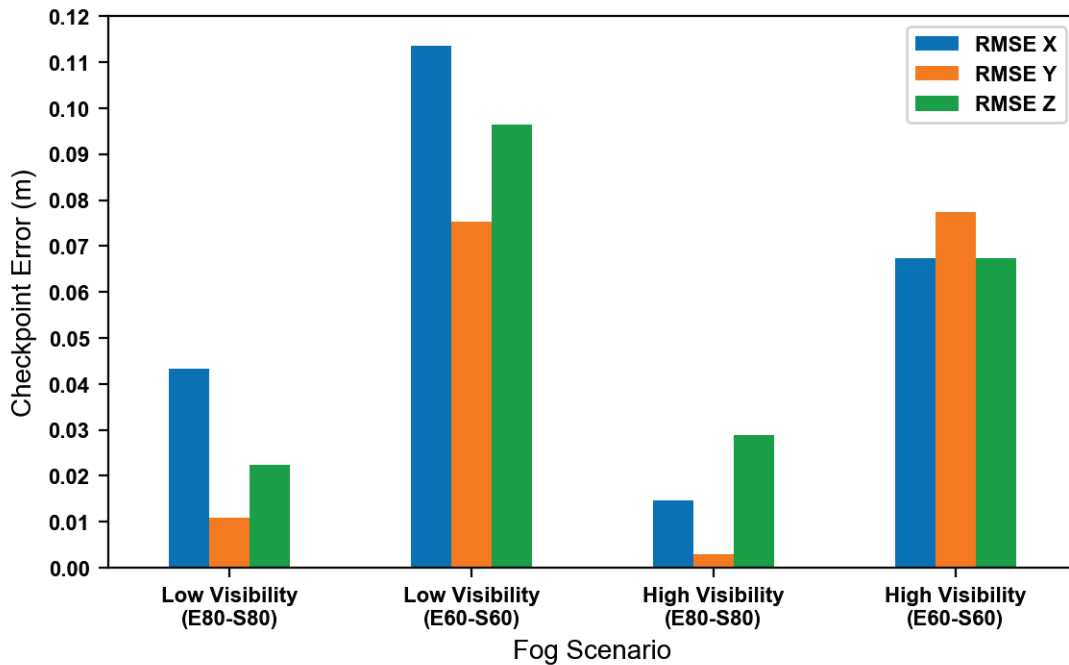
Note: The dashed lines are used for overall visualization, not to suggest linear trends between adjacent data points.

Figure 108. Mean Absolute Camera Position Uncertainties by Fog and Overlap Scenario.



Note: The dashed lines are used for overall visualization, not to suggest linear trends between adjacent data points.

**Figure 109. Mean Absolute Camera Orientation Uncertainties by Fog and Overlap Scenario.**

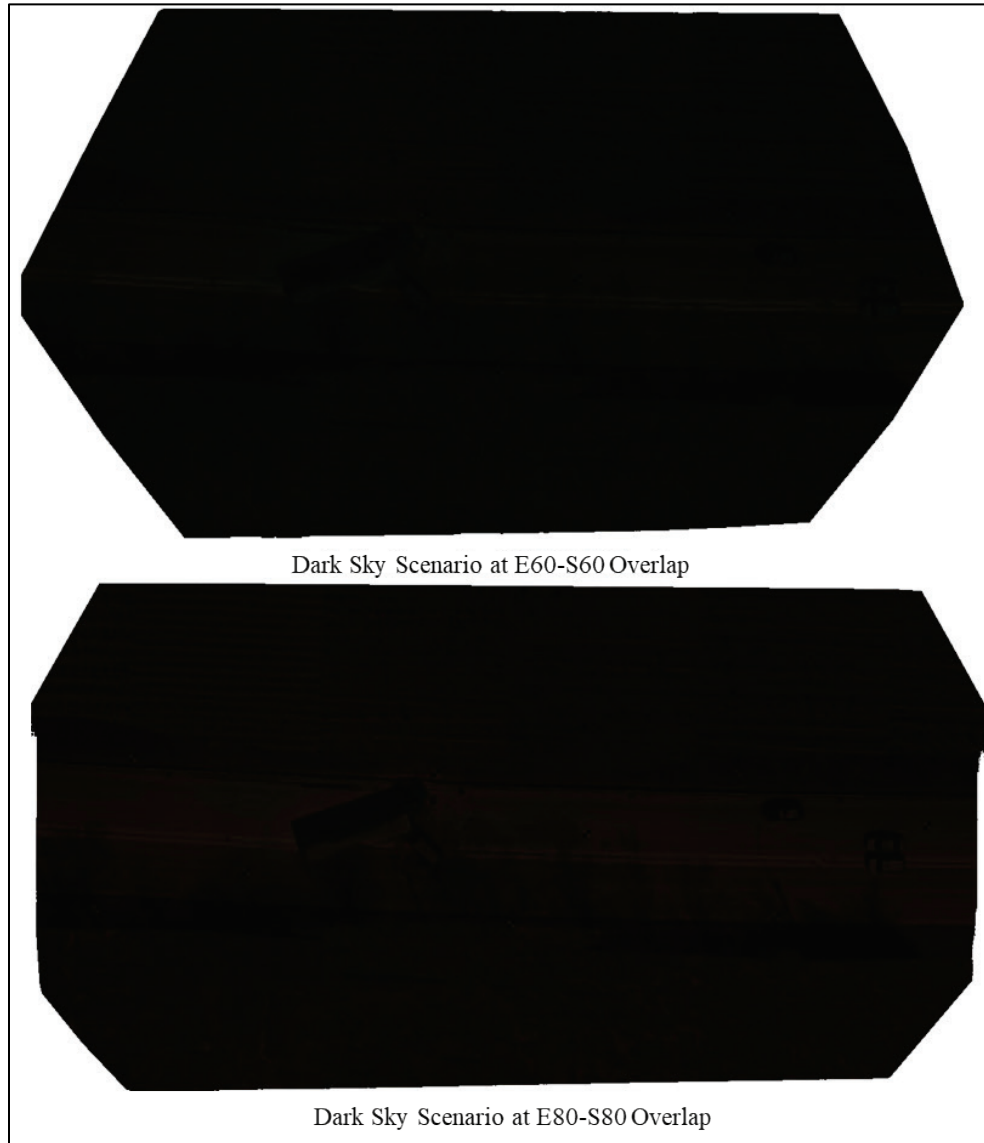


**Figure 110. RMSE of the Checkpoint Error by Fog and Overlap Scenario.**

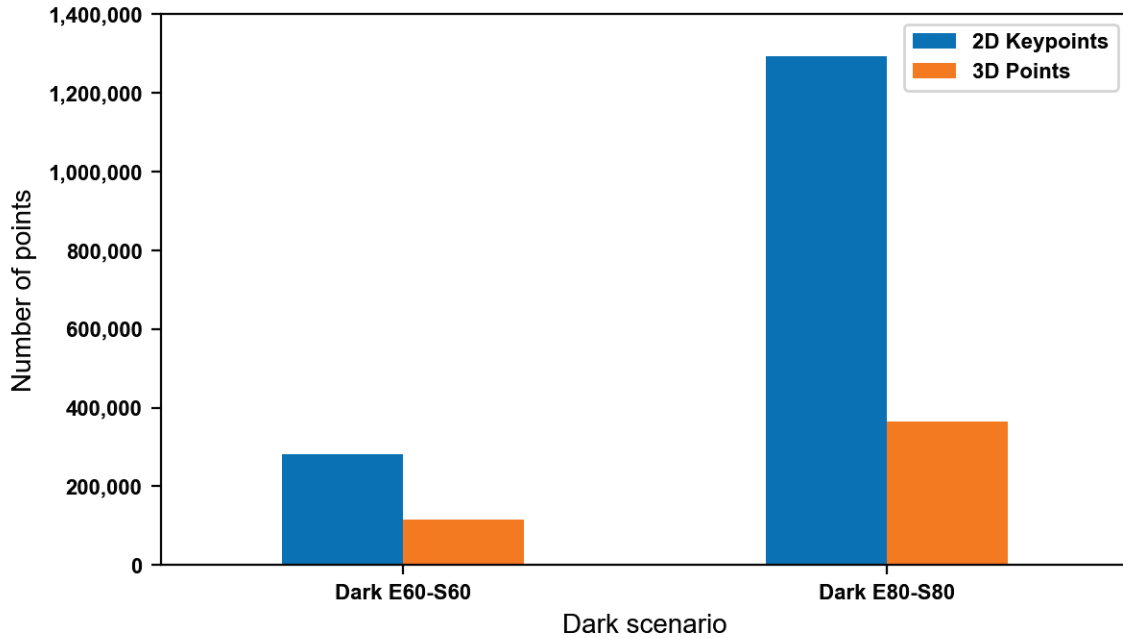


*Combined Effect of Overlap Levels and Dark Sky*

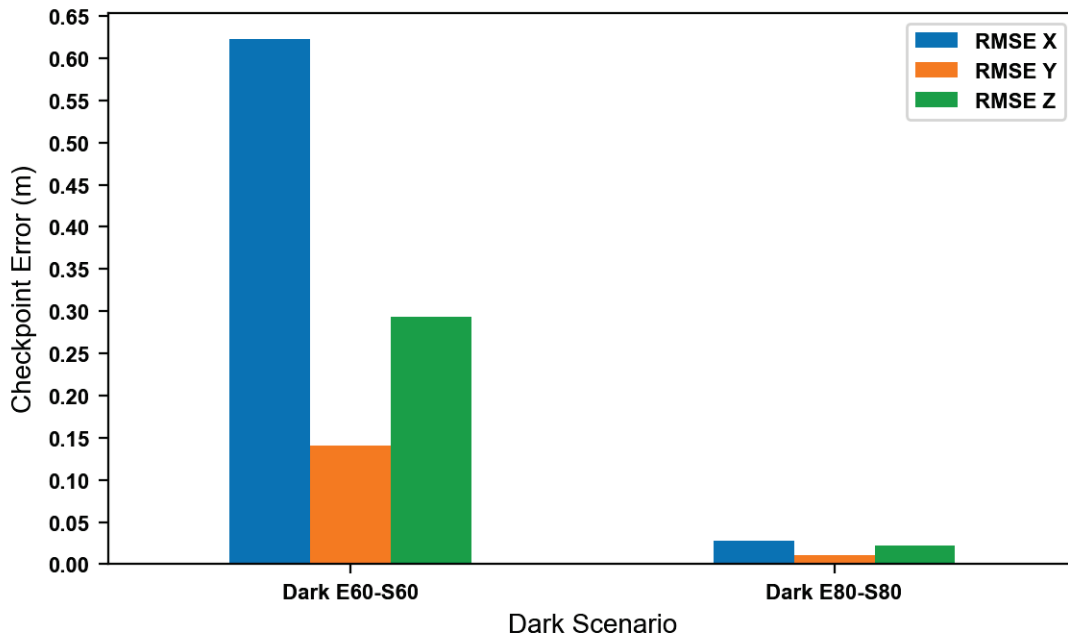
Figure 111 shows a derived orthomosaic before densification for the dark sky scenario at both E60-S60 and E80-S80 overlap levels. Figure 112 shows the total number of 2D keypoints and 3D points reconstructed in the sparse point cloud for low and high overlap levels, assuming a dark sky condition. Figure 113 shows RMSE of the checkpoint coordinate error for low and high overlap scenarios. Both figures illustrate the importance of increasing overlap in severely reduced lighting scenarios to enable sufficient keypoint correspondence and improve SfM 3D reconstruction error of the sparse point cloud.



**Figure 111. Orthomosaic for Dark Sky Scenario at E60-S60 and E80-S80 Overlap Scenarios.**



**Figure 112. Total Number of 2D Keypoints and 3D Points by Overlap Scenario.**



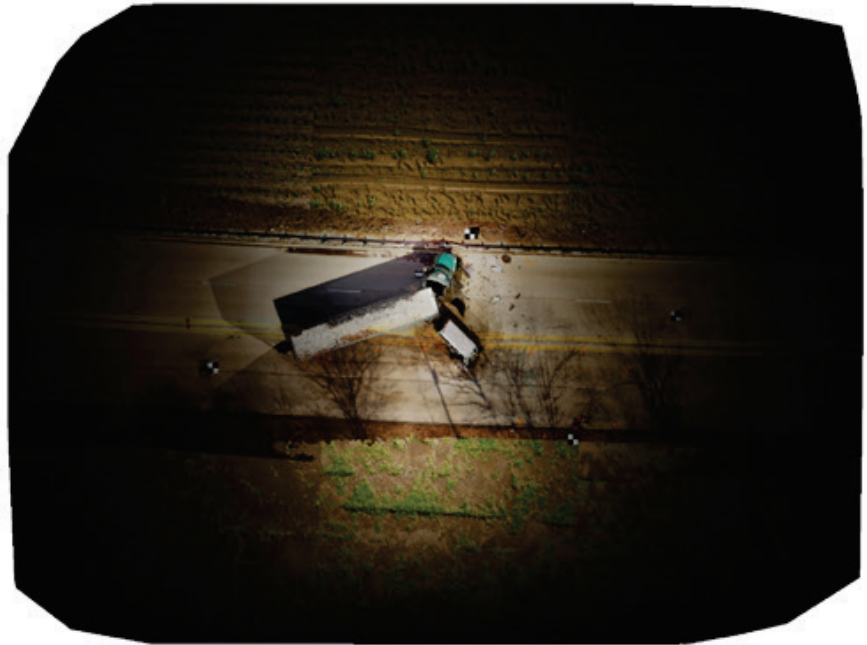
**Figure 113. RMSE of the Checkpoint Error by Overlap Scenario.**

*Differences between Full and Partial Artificial Illumination*

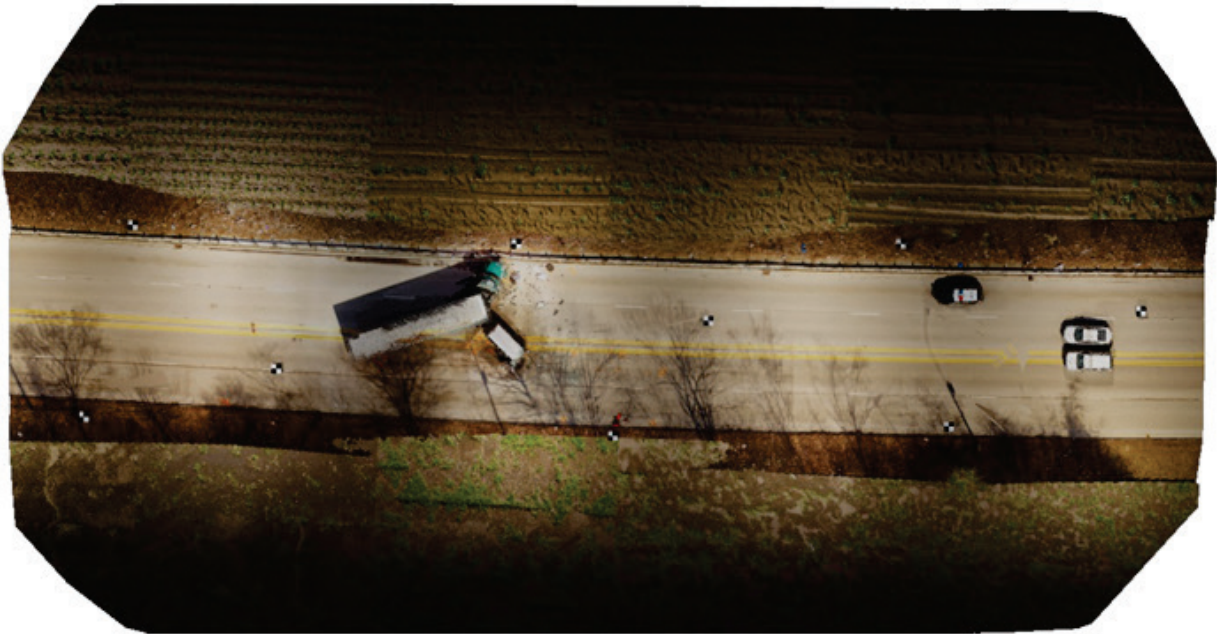
Figure 114 shows a derived orthomosaic before densification for full and partial illumination lamp post scenarios at E80-S80. Pix4D calibrated only 91 out of 105 images (i.e., 86 percent) for the partial illumination scenario compared to 100 percent for full illumination. Mapping of

periphery zones of the crash scene required sufficient artificial lighting under dark sky scenarios. A lack of keypoints on the fringe of the study site for partial illumination caused the reduction in calibrated images for the scene. Figure 115 shows the drop in 2D keypoints and reconstructed 3D points of the sparse point cloud for partial illumination compared to full illumination.

Figure 116 and Figure 117 show the impact of inadequate illumination across the entire scene on the mean absolute position and orientation uncertainty, respectively, estimated from the SfM procedure. Partial illumination had a much larger estimated camera position and orientation uncertainty than full illumination. Similarly, Figure 118 shows a substantial increase in the RMSE of the checkpoint coordinate error measured for partial illumination when compared to full illumination.

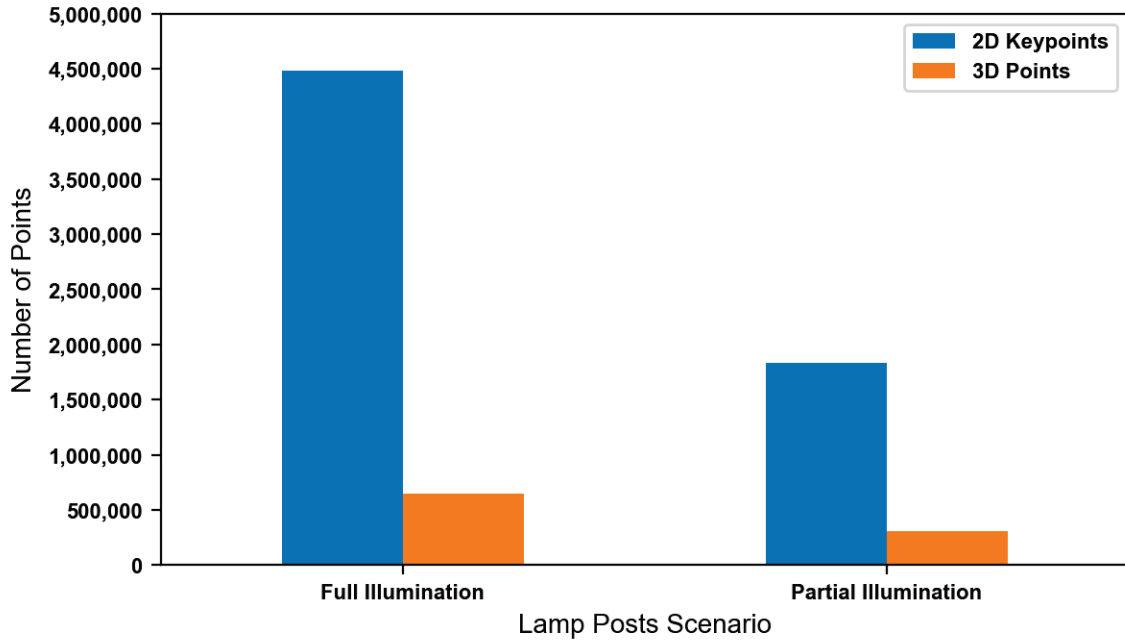


Partial Illumination at E80-S80 Overlap

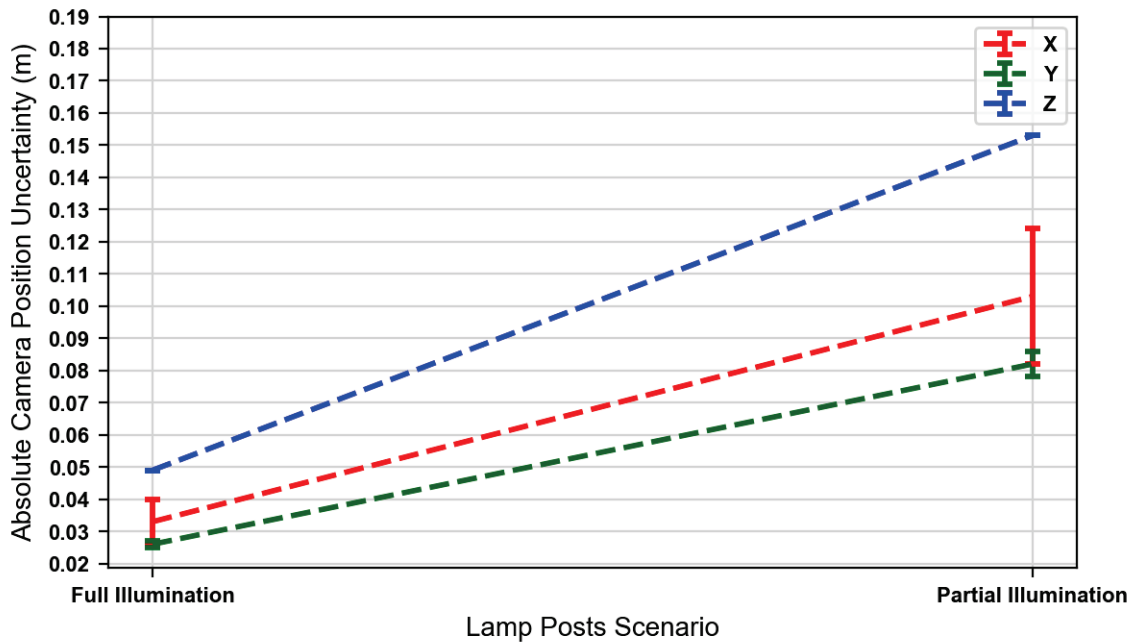


Full Illumination at E80-S80 Overlap

**Figure 114. Orthomosaic for Partial Illumination and Full Illumination Lamp Post Scenarios at E80-S80 Overlap.**

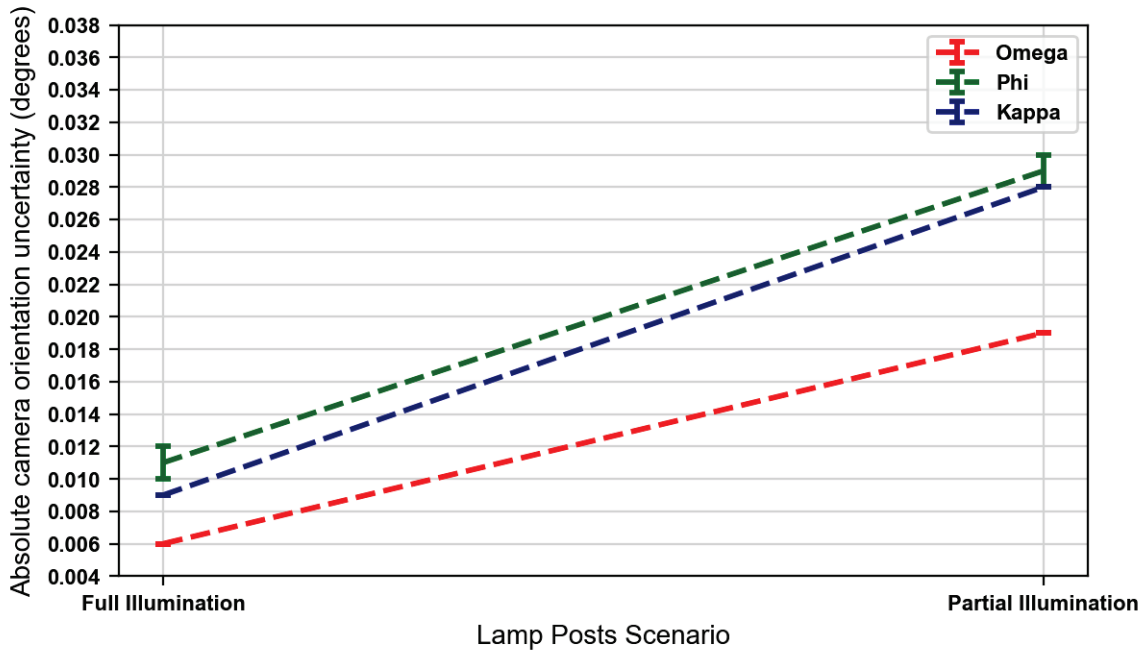


**Figure 115. Total Number of 2D Keypoints and 3D Points by Illumination Scenario.**



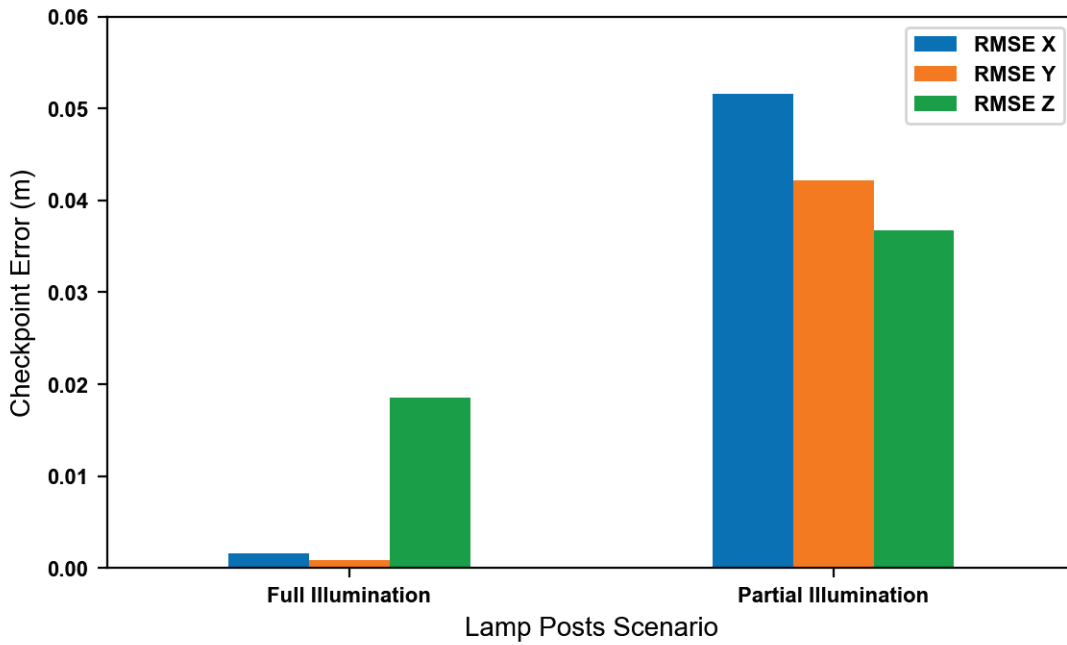
Note: The dashed lines are used for overall visualization, not to suggest linear trends between adjacent data points.

**Figure 116. Mean Absolute Camera Position Uncertainties by Illumination Scenario.**



Note: The dashed lines are used for overall visualization, not to suggest linear trends between adjacent data points.

**Figure 117. Mean Absolute Camera Orientation Uncertainties by Illumination Scenario.**



**Figure 118. RMSE of the Checkpoint Error by Illumination Scenario.**

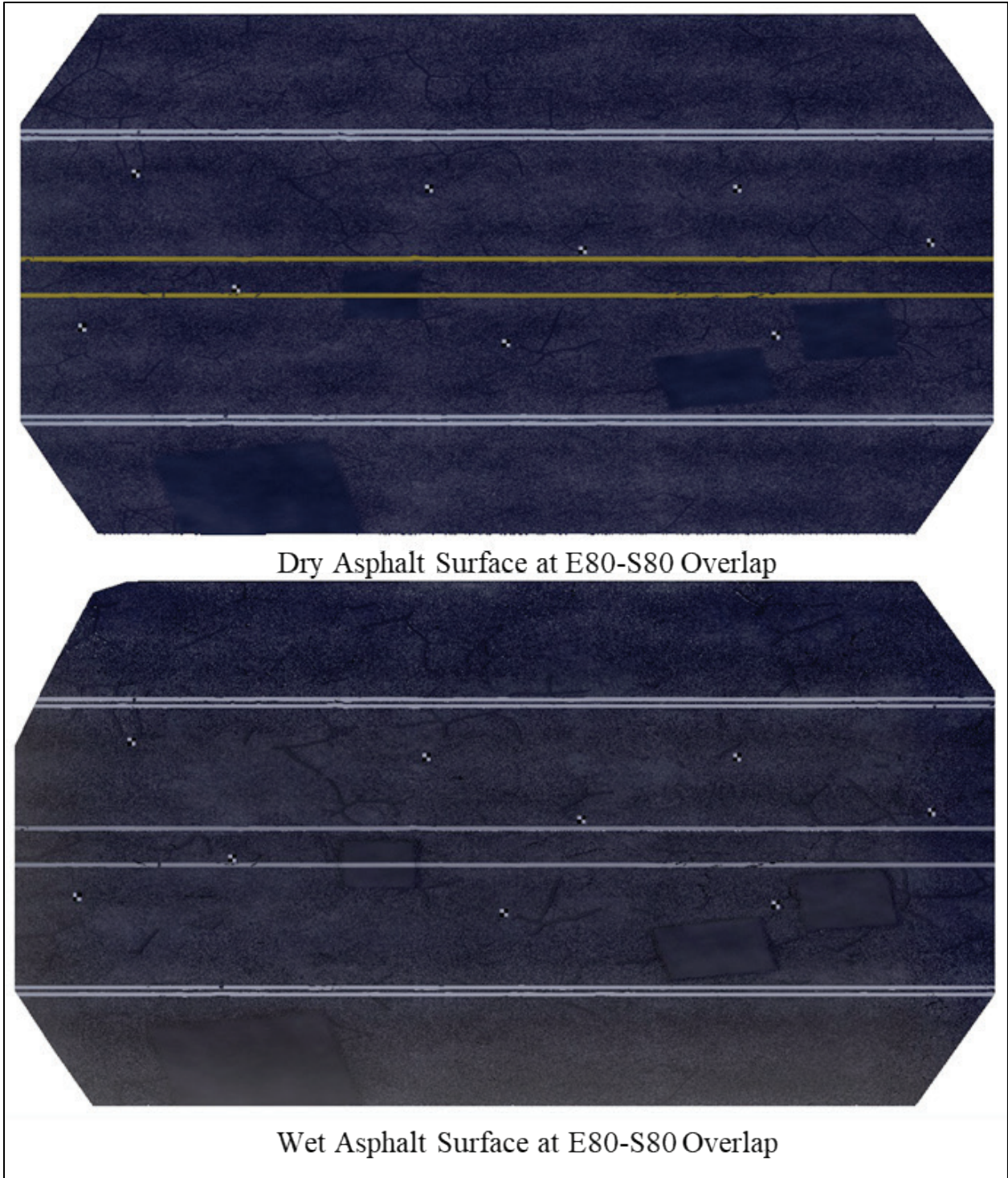
### *Differences between Dry and Wet Surface Conditions*

Figure 119 shows a derived orthomosaic before densification for dry and wet surface scenarios. Although it is hard to tell from these images, the wet surface scenario had more sun glint and specular scattering artifacts because of the simulated water on the asphalt surface.

Figure 120 shows the mean number of 2D keypoints and matched keypoints per image. The wet asphalt surface resulted in more keypoints per image than for the dry asphalt, with a reduction in the number of matched keypoints per image. In Pix4D, keypoints are points of interest (high contrast, interesting texture) on the images that can be easily recognized by the software's feature-matching algorithm. This result suggests that water added unique textures to the scene, increasing the number of potential keypoints, but due to the noisy nature of some of these features, the result might have been a reduction in the number of matched candidates. This impact is shown in Figure 121, which shows a larger mean reprojection error likely due to less precise, reduced matched keypoints.

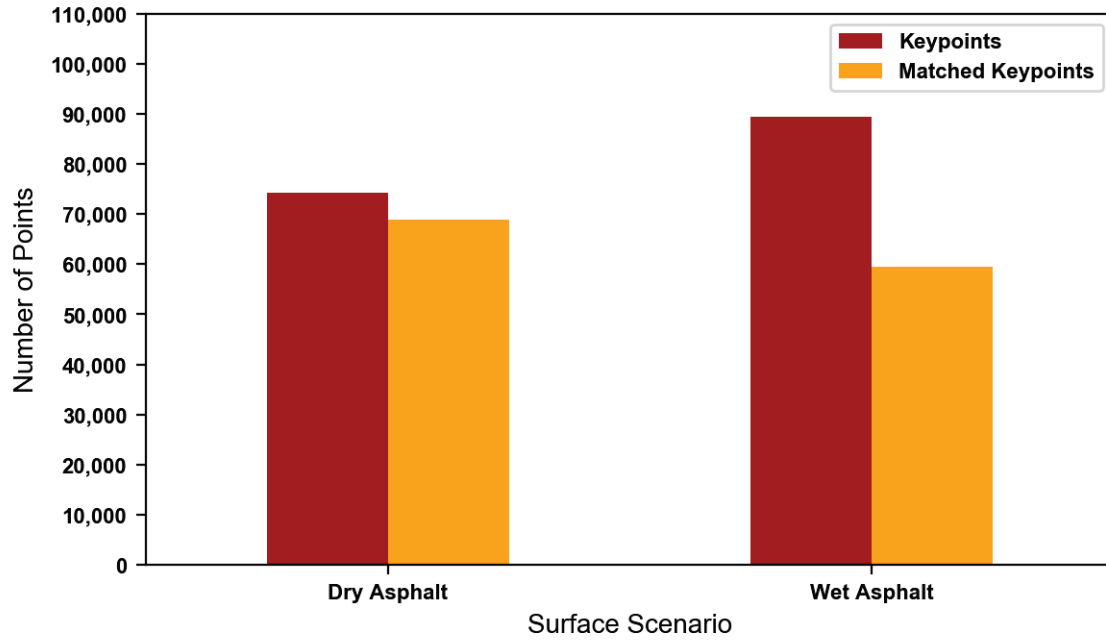
Figure 122 shows that the wet surface condition increased the mean absolute camera position uncertainty based on the matched keypoints used in the BA procedure. The impact on orientation uncertainty was minor (figure not included).

Figure 123 shows differences in mean checkpoint errors for dry and wet surface conditions. Results show only a subtle difference in error between the two scenarios, with the Z component having the largest relative error. A slight reduction in errors occurred for wet surface conditions, possibly because of a slightly enhanced contrast on the targets. Results illustrate the potential robustness of the SfM procedure for maintaining the absolute positional accuracy under wet surface suboptimal conditions. However, readers should note that the simulation conducted here did not replicate other wet surface conditions that could result in more severe effects. Such scenarios include mirror-like reflections of surrounding structures in ponded water, dynamic water flow, or changing scene texture during flight due to variable water absorption or surface drying inducing false matching and parallax.

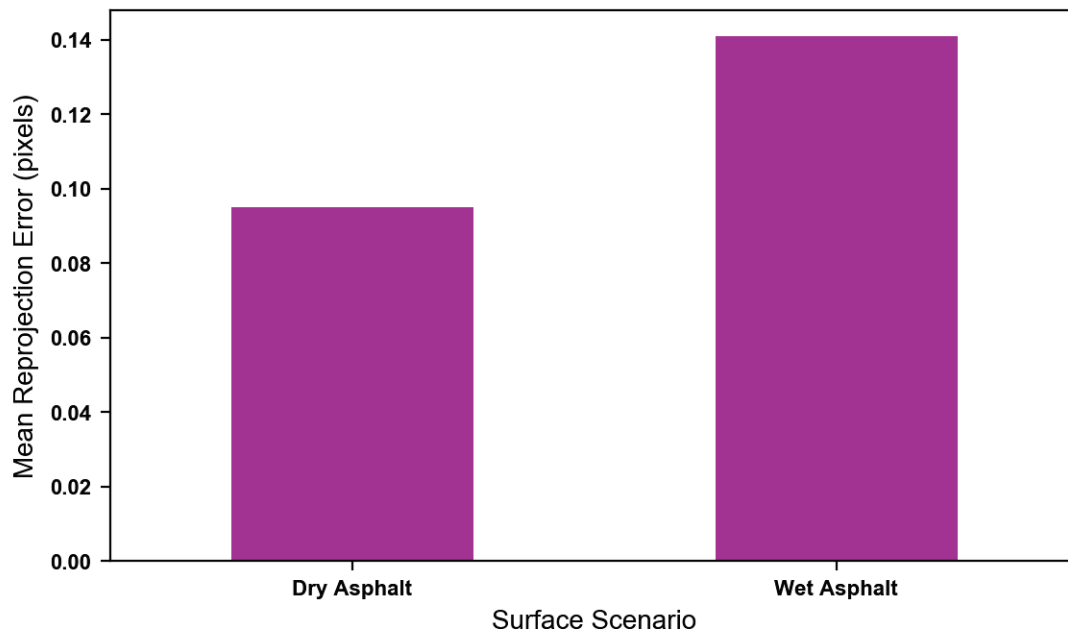


**Figure 119. Orthomosaic for Dry Asphalt Surface and Wet Asphalt Surface at E80-S80.**

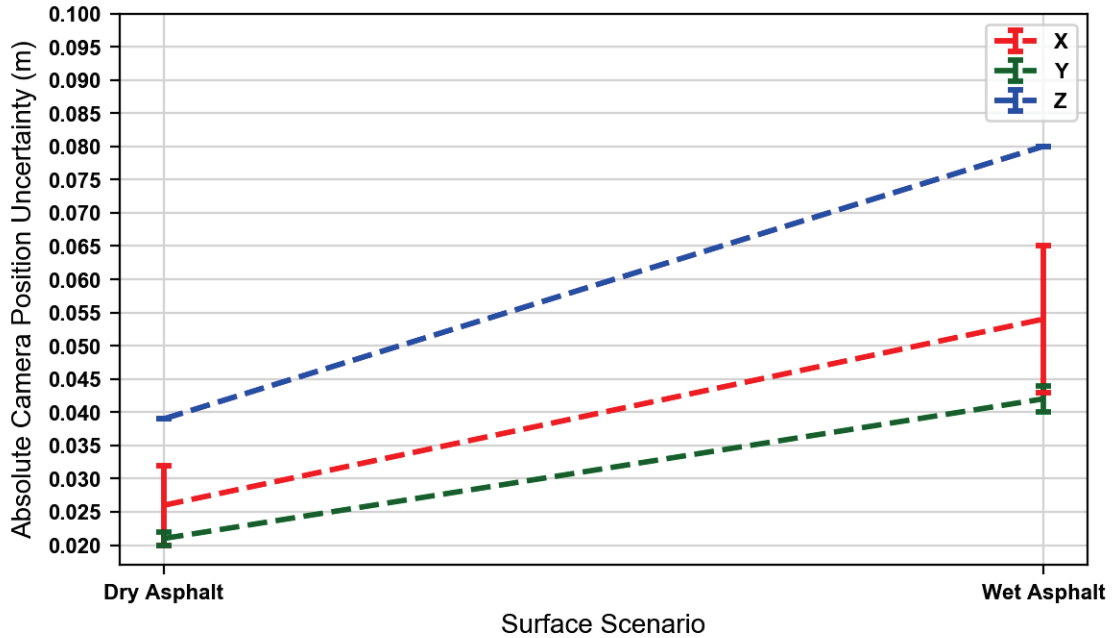




**Figure 120. Mean Number of 2D Keypoints and Matched 2D Keypoints Per Image for Dry and Wet Surface.**

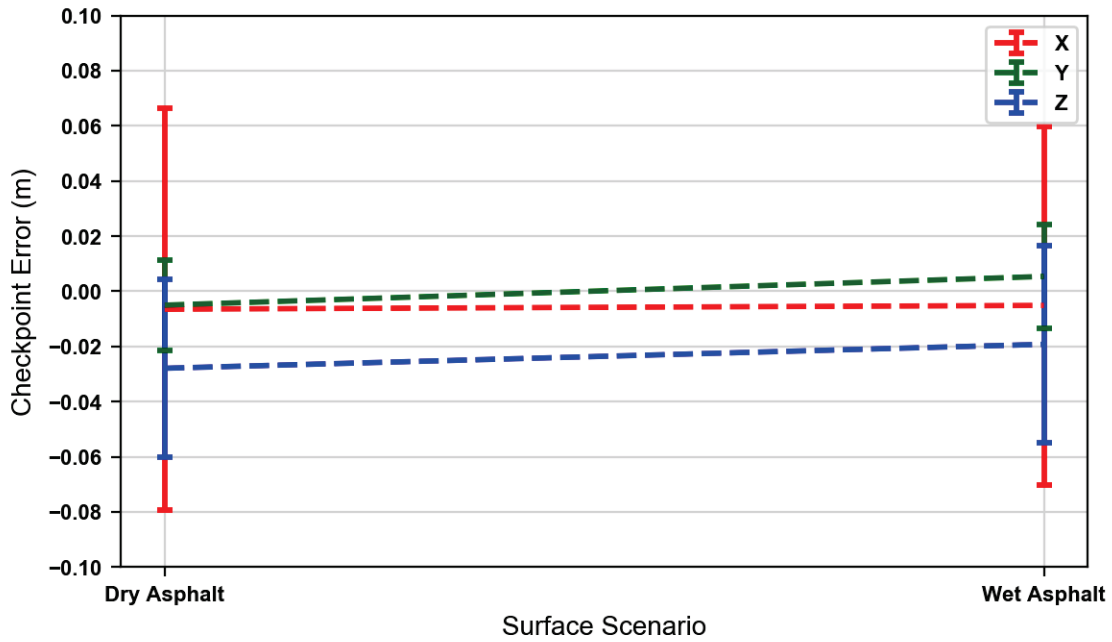


**Figure 121. Mean Reprojection Error for Dry and Wet Surface.**



Note: The dashed lines are used for overall visualization, not to suggest linear trends between adjacent data points.

**Figure 122. Mean Absolute Camera Position Uncertainty for Dry and Wet Surface.**



Note: The dashed lines are used for overall visualization, not to suggest linear trends between adjacent data points.

**Figure 123. Mean Checkpoint Error for Dry and Wet Surface.**

### *Dense Point Cloud Quality Factors*

Figure 124 and Figure 125 show the total number of points in the densified point cloud and average point density, respectively, for the various lighting scenarios, excluding wet surface. Densification shown here is based on the S80-E80 overlap scenario. Differences among scenarios were relatively minor. Interestingly, the two scenarios with the most reduced lighting, dark and civil twilight, and to a lesser degree cloudy sky in the late evening, had the greatest number of points in the densified cloud. Average point density was the lowest for the dark sky scenario.

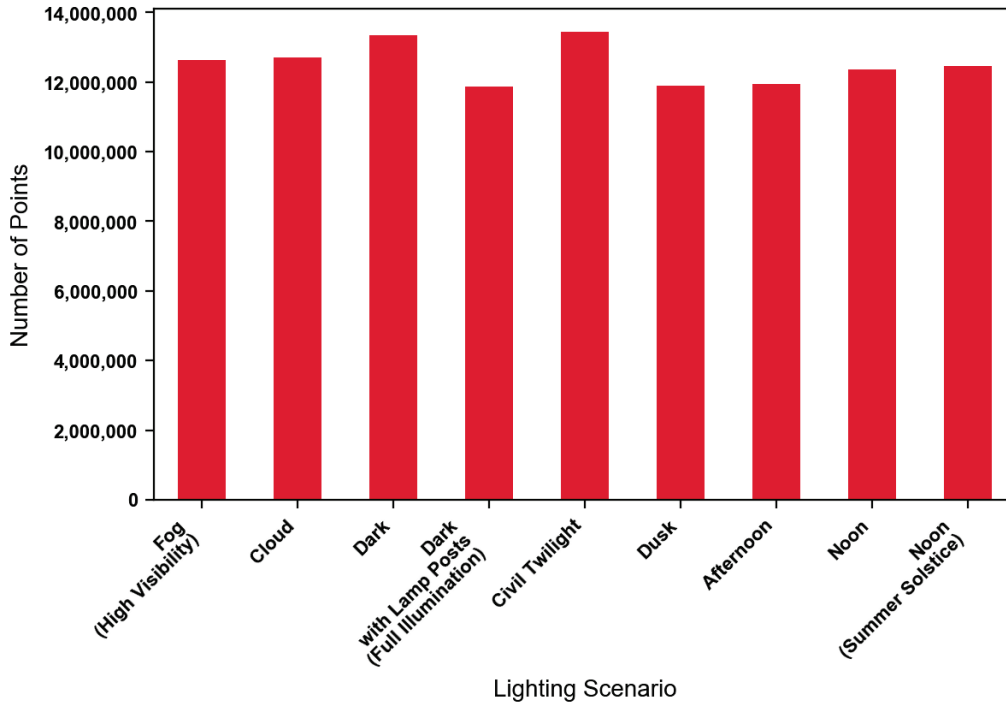
Figure 126 and Figure 127 show the RMSE of the cloud-to-cloud distances for each lighting scenario's densified 3D point cloud based on the total scene and crash scene, respectively, computed relative to the ground truth point cloud. Both scenes show similar patterns, with fog (low visibility) producing the largest RMSE. Dark sky and civil twilight also produced larger RMSE relative to most other scenarios, although they both had more 3D densified points as shown in Figure 124, which may suggest that the additional points generated by densification were noisier (i.e., less precise). Lamp post at full illumination and solar noon had the lowest RMSE suggesting that for those two scenarios, the densification was more precise relative to other scenarios. Partial illumination of the scene with lamp posts resulted in a much larger RMSE relative to full illumination. Results show that artificial lighting scenarios can enable accurate 3D densification if the scene is sufficiently lit to maintain brightness and contrast throughout the area of interest. The caveat would be oversaturation of brightness and places with strong shadowing.

Interestingly, Figure 126 and Figure 127 show that solar noon at the summer solstice had a larger RMSE compared to solar noon on May 1, 2020, indicating that the increase in solar elevation angle (a more directly overhead perspective) on the solstice resulted in noticeable differences in scene brightness. This effect subsequently resulted in Pix4D creating a more variable dense point cloud for the solstice scenario based on the larger RMSE, which may be due to a combination of stronger shadowing in places and increases in brightness-reducing image texture in some locations.

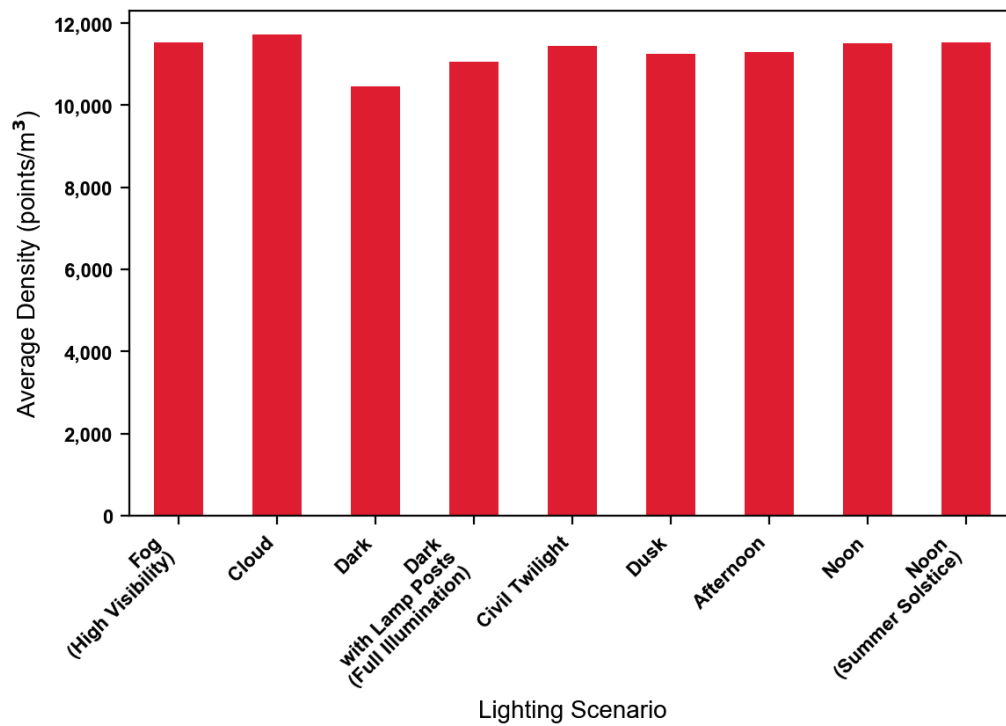
Figure 128 shows the RMSE of the cloud-to-cloud distances for low and high visibility fog under both overlap scenarios. Fog at low visibility and 60 percent overlap had a much larger RMSE relative to 80 percent overlap. Fog at high visibility also showed a substantially degraded RMSE at 60 percent overlap relative to 80 percent overlap.

Dark sky at 60 percent overlap produced a much smaller number of points in the densified point cloud than 80 percent overlap (Figure 129). It also resulted in a larger cloud-to-cloud distance RMSE (not shown in the figure).

Figure 130 shows the total number of densified points for the dry and wet asphalt surface scenarios based on the entire scene. Wet surface conditions generated more densified points relative to dry surface, which resulted in a slightly more detailed, but not noisier point cloud, and lower cloud-to-cloud distance RMSE than the dry surface, as shown in Figure 131. As mentioned, the simulation conducted here did not replicate other wet surface conditions, which could result in more severe effects.



**Figure 124. Total Number of Points in the Densified Point Cloud.**



**Figure 125. Average Point Density.**

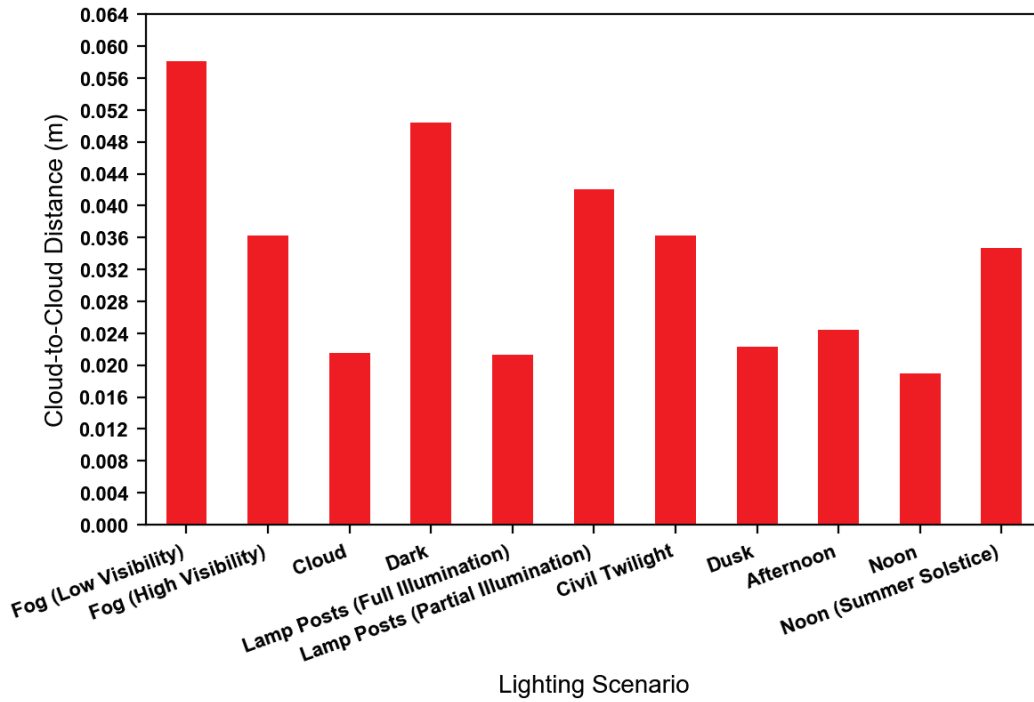


Figure 126. Cloud-to-Cloud Distance RMSE for Total Scene.

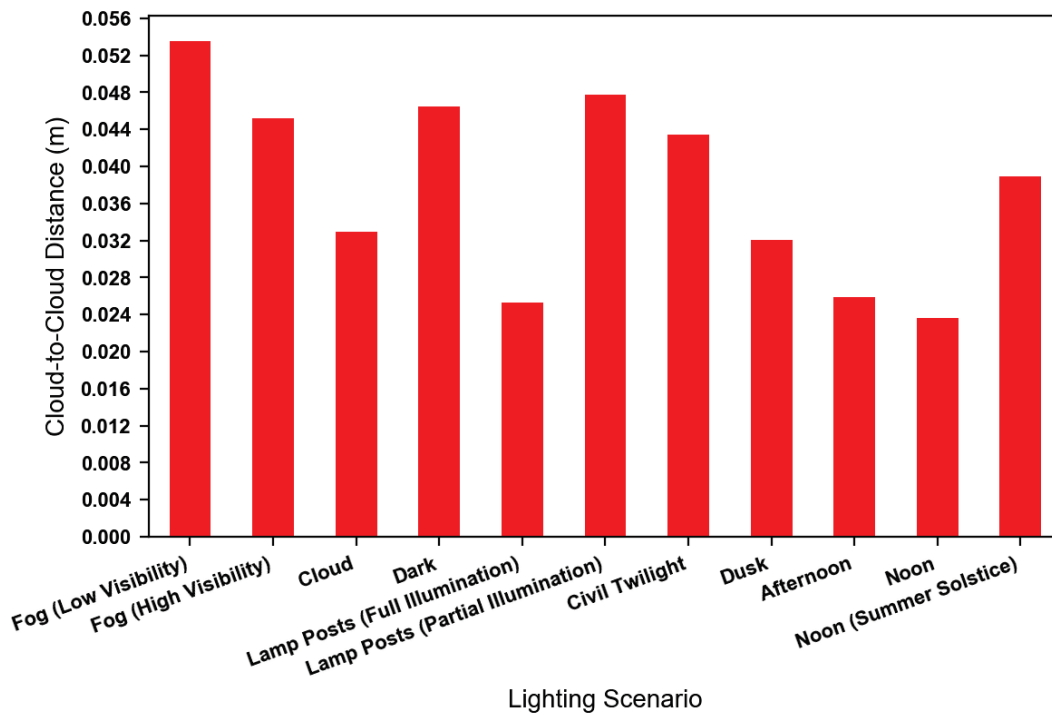
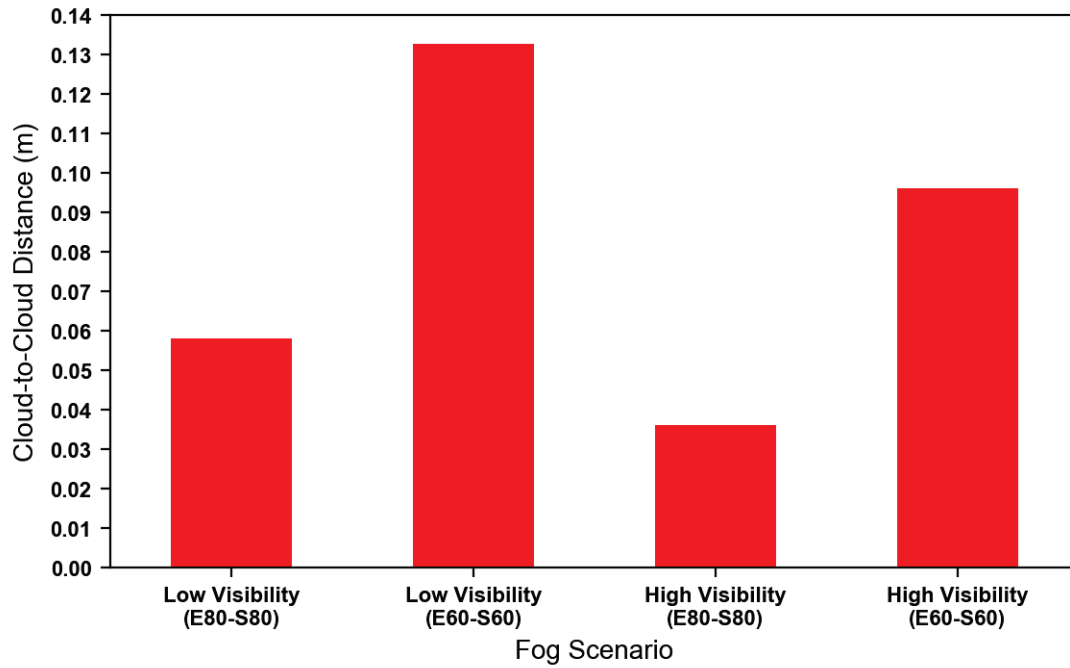
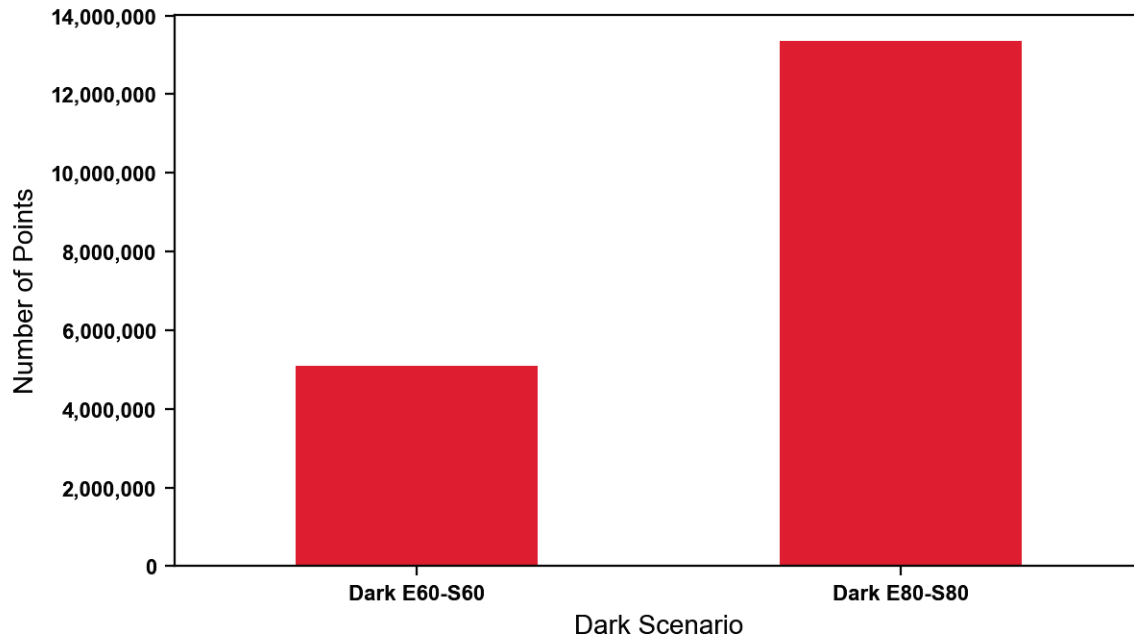


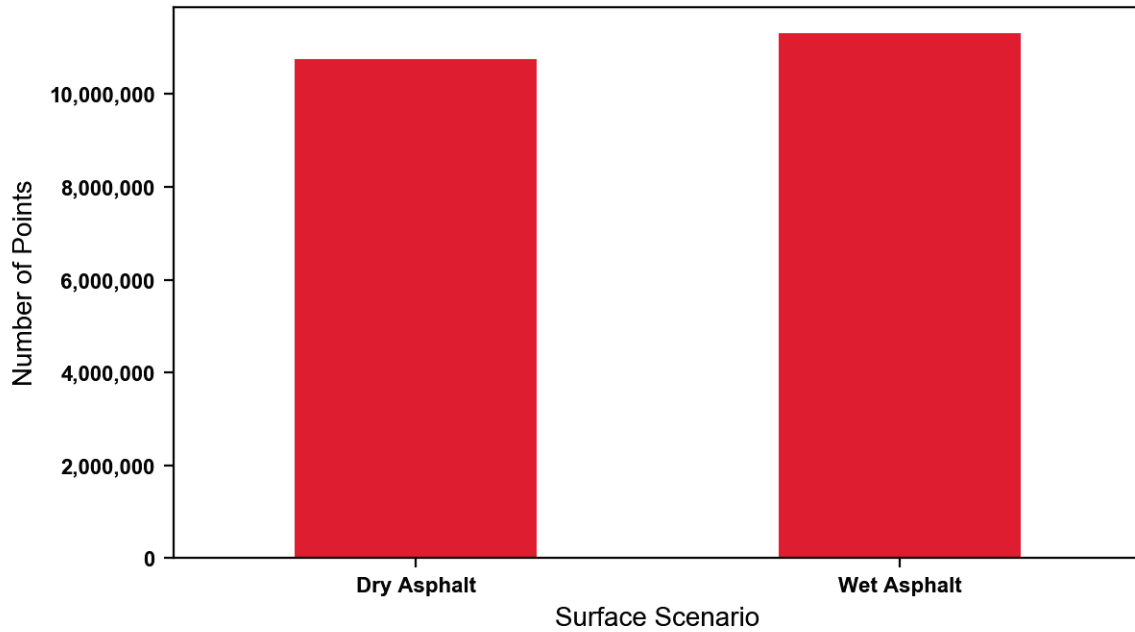
Figure 127. Cloud-to-Cloud Distance RMSE for Crash Scene.



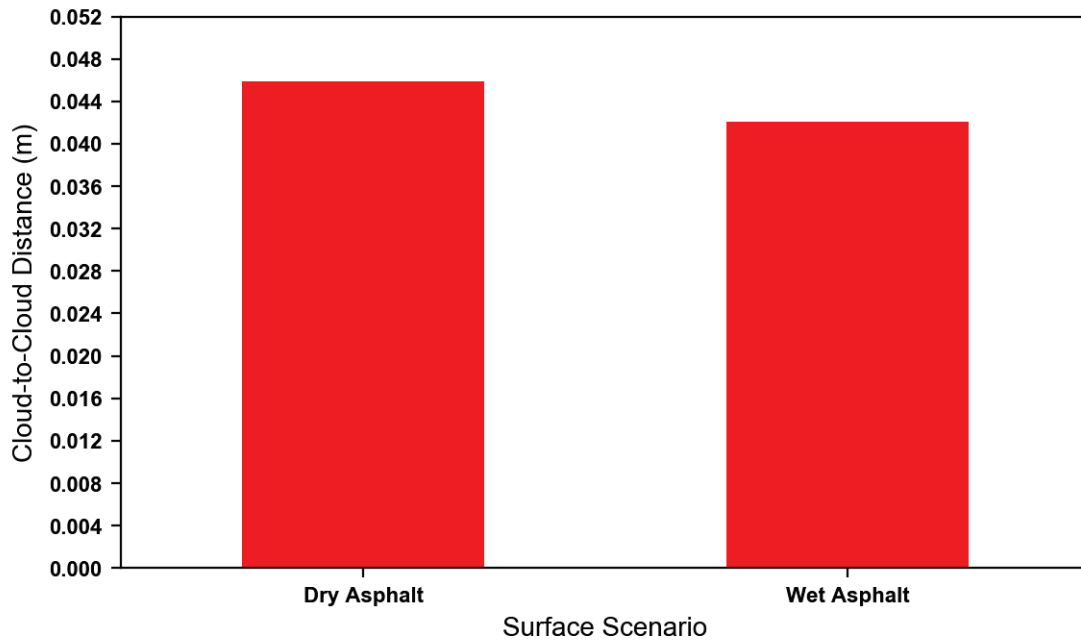
**Figure 128. Cloud-to-Cloud Distance RMSE for Different Fog and Overlap Scenarios.**



**Figure 129. Total Number of Points in Densified Cloud for Dark Sky Scenario by Overlap.**



**Figure 130. Total Number of Points in Densified Point Cloud for Dry and Wet Surface.**

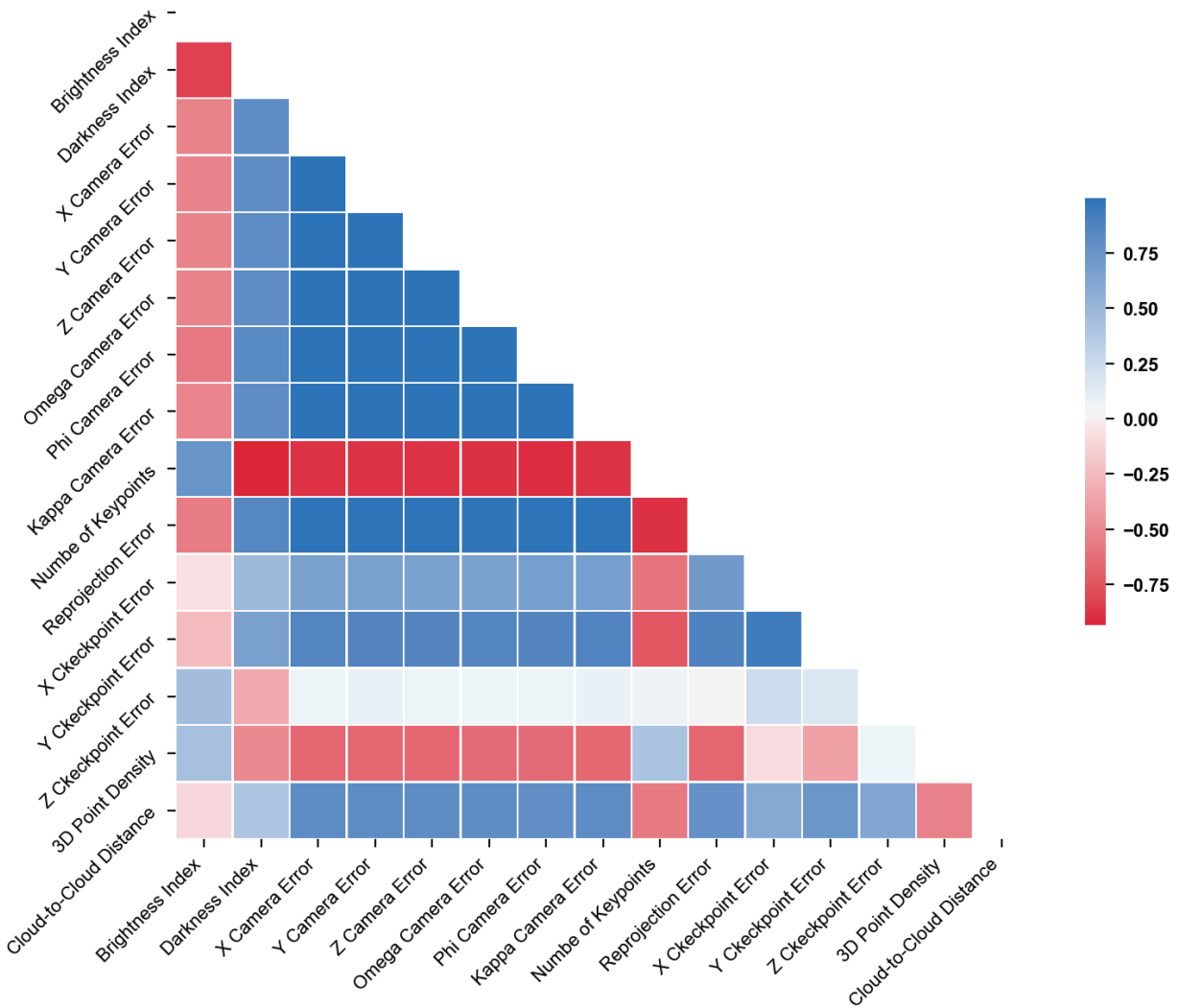


**Figure 131. Cloud-to-Cloud Distance RMSE for Dry and Wet Surface.**

### *Correlation Analysis*

Figure 132 shows the Pearson's correlation coefficient between the various quality factors and the brightness and darkness indexes. In general, the correlation of the brightness index with the

various quality factors had the opposite sign to that of the darkness index. The brightness index was negatively correlated with the darkness index.



**Figure 132. Correlation Coefficient Matrix between Different Quality Factors and Brightness and Darkness Indexes.**

This opposite pattern of correlation held for the mean reprojection error. The brightness index was negatively correlated, but the darkness index was positively correlated. This result indicates that darker scenes, relative to brighter scenes, appeared to degrade more the overall radiometric quality of the imagery in terms of contrast or scene texture.

The brightness index and the darkness index showed opposite sign correlations with the magnitude of the absolute camera’s position and orientation error. The brightness index was negatively correlated, whereas the darkness index was positively correlated, suggesting that brighter scenes aid estimation of camera pose due to more precise keypoint correspondences.



The brightness index and the darkness index showed opposite sign correlations with the horizontal error and vertical errors. The darkness index showed a negative correlation with the vertical error and a positive correlation with the horizontal error. Neither index showed a strong relationship to the checkpoint error.

The 3D point density showed a positive correlation with the brightness index and a negative correlation with the darkness index. This pattern reversed for the cloud-to-cloud distance error, suggesting that darker scenes generate less dense and potentially more noisy densified point clouds.

## Lessons Learned

Major lessons learned from the simulation exercise included the following:

- Keypoint extraction and reprojection errors:
  - Of the various lighting conditions simulated, dark sky and civil twilight scenarios showed the lowest number of 2D keypoints, which resulted in a smaller number of 3D points resolved in the sparse point cloud. (Note: Civil twilight, when the sun is just below the horizon and there is enough natural light to carry out outdoor activities, is the brightest of the three twilight periods.) Afternoon sky provided the most favorable conditions for keypoint matching under the scenarios examined.
  - Full illumination with artificial lamp posts had a reduction in keypoints compared to natural lighting scenarios under daytime and dusk conditions, but it provided much better keypoint extraction conditions than 100 percent cloudy evening sky, civil twilight, or dark sky scenarios. Partial illumination with artificial lamp posts resulted in fewer keypoints and keypoint matches compared to full illumination.
  - Low visibility fog resulted in significantly fewer keypoints and 3D points in the sparse point cloud than high visibility fog. Overlap also played a key role in enhancing the number of keypoints for both low and high visibility fog. Increasing overlap from low (E60-S60) to enough (E80-S80) resulted in a similar increase in keypoint extraction and matching.
  - Wet asphalt surface resulted in more keypoints per image than dry asphalt, with a reduction in matched keypoints per image. This result suggests that the water added more unique textures to the scene, thereby increasing the number of potential keypoints, but due to the noisy nature of some of these features, the number of matched candidates may have been reduced.
  - Increasing darkness resulted in a larger mean reprojection error. Dark sky and civil twilight scenarios produced the largest reprojection error, followed by a 100 percent cloudy sky evening scenario. Wet asphalt showed a larger mean reprojection error than dry asphalt, most likely due to less precise and reduced matched keypoints.
- SfM reconstruction accuracy:
  - Reduced lighting scenarios (i.e., dark sky and civil twilight) showed the largest error in absolute camera position and orientation error. This result is also related to the larger mean reprojection error associated with those scenarios.

- Increased lighting scenarios (i.e., solar noon sky and solar noon solstice conditions) showed an increase in absolute camera position and orientation error, respectively, relative to afternoon sky and dusk, which may be due to stronger shadowing in the scene and reduced texture for areas of overexposure. Local noon conditions shorten the length of shadows, but the result can be darker shadows in certain areas that can degrade the SfM point cloud solution for those areas.
- There was a clear influence of suboptimal lighting conditions on UAS-SfM absolute positional accuracy. Reduced lighting scenarios (i.e., dark sky and civil twilight) resulted in the largest RMSE of checkpoint errors. Solar local noon and solar noon solstice showed a slight increase in checkpoint error relative to afternoon lighting.
- Increasing overlap from E60-S60 to E80-S80 for all scenarios resulted in a substantial decrease in RMSE of checkpoint errors, both horizontally and vertically.
- A substantial increase occurred in the RMSE of the checkpoint coordinate error when measured for partial illumination versus full illumination. Without other ambient background lighting, mapping of periphery zones of the crash scene under dark sky conditions requires sufficient artificial lighting to cover these areas. A lack of keypoints on the fringe of the study site for partial illumination caused a reduction in calibrated images for the scene.
- Wet asphalt and dry asphalt scenarios showed a slight difference in the RMSE of their absolute checkpoint coordinate errors.
- Densification accuracy:
  - Fog (low visibility) produced the largest RMSE of cloud-to-cloud distance errors. Dark sky and civil twilight also produced larger RMSE values relative to most other scenarios, although they both had more 3D densified points.
  - Lamp post at full illumination and solar noon produced the lowest RMSE suggesting that for those two scenarios, the densification was more accurate relative to other scenarios. Partial illumination with lamp posts resulted in a much larger RMSE relative to full illumination.
  - Interestingly, solar noon at the summer solstice exhibited a larger RMSE than solar noon on May 1, 2020, indicating that the subtle increase in solar elevation angle (more directly overhead perspective) on the solstice produced noticeable differences in scene brightness. This factor subsequently resulted in Pix4D creating a more variable dense point cloud for the solstice scenario based on the larger RMSE, which may be due to a combination of stronger shadowing in places and increases in brightness reducing image texture in some locations. Although the differences in RMSE are minor, simulations show the influence of subtle variations in scene lighting on SfM results.
  - Increasing overlap from E60-S60 to E80-S80 for all scenarios resulted in a substantial decrease in the RMSE of cloud-to-cloud distance errors.
  - Wet surface conditions generated more densified points relative to dry surface conditions. RMSE of cloud-to-cloud distance errors was lower for the wet surface scenario than for the dry surface scenario. Results could be different for more extreme wet surface conditions (e.g., mirror-like reflections of surrounding

structures in ponded water, dynamic water flow, or changing scene texture during flight due to variable water absorption or surface drying).

- Correlation analysis:
  - The brightness index was positively correlated and the darkness index was negatively correlated with the number of keypoints, suggesting that midday to afternoon daytime conditions are more favorable than early morning, late evening, or nighttime conditions.
  - The brightness index was negatively correlated and the darkness index was positively correlated with the mean reprojection error, which indicates that darker scenes, relative to brighter, appear to degrade more the overall radiometric quality of the imagery in terms of contrast or scene texture.
  - The brightness index was negatively correlated and the darkness index was positively correlated with the absolute camera's position and orientation error, suggesting that brighter scenes aid in the estimation of camera pose due to an increase in keypoint correspondences.
  - The brightness index was positively correlated and the darkness index was negatively correlated with the 3D point density.
  - The total number of points in the densified point cloud showed a fairly strong positive correlation with the darkness index, which was unexpected. This would need to be investigated further to determine if the result was unique to the simulation environment or if this is a general effect of Pix4D's internal algorithms. In contrast, the average point density showed a negative correlation with the darkness index, suggesting that darker images caused more point spread.
- General lessons learned:
  - The results showed the capability of the full SfM-MVS processing pipeline, as implemented by Pix4D, to reconstruct a scene under a variety of suboptimal lighting scenarios, including severely reduced/dark lighting scenarios. It is worth noting that this work only focused on 3D reconstruction and did not take into consideration orthomosaic image quality for visual inspection.
  - The SfM reconstruction procedure, as implemented by Pix4D, performed well under wet asphalt surface conditions. However, these results cannot be generalized because only one type of wet surface was simulated. The simulation did not include other wet surface conditions (e.g., mirror-like reflections of surrounding structures in ponded water, dynamic water flow).
  - The results clearly showed the importance of increasing overlap for improving UAS-SfM reconstruction under moderate to severe suboptimal lighting conditions. In particular, the results show that increasing overlap from E6-S60 to E80-S80 resulted in a substantial improvement in reconstruction.
  - An environment with balanced ambient, direct lighting is preferable for UAS surveys (e.g., a bright cloudy day). The presence of shadows affects SfM reconstructions. Shadows are shortest at solar noon and flying at that time can help to reduce shadowing in the scene. However, shadows are also strongest at that time, and 3D reconstruction in areas of dark shadowing can be poor.
  - For any particular scene and illumination conditions, the exposure of a digital picture is determined primarily by three camera settings: aperture size, exposure time, and ISO sensitivity. Understanding their relationship for improving or

degrading image quality becomes important when conducting UAS surveys under suboptimal lighting conditions. High dynamic range imaging is another technique that may be viable to improve image quality under adverse scene lighting and exposure conditions. Discussion on the technical considerations of these factors is beyond the scope of this work.

## **SELF-CALIBRATION VERSUS PREFLIGHT CALIBRATION PROCEDURES FOR CONSUMER-GRADE NONMETRIC DIGITAL RGB CAMERAS**

The research team tested self-calibration methods in Pix4D. The experiments used a set of simulated UAS imagery rendered from a 3D model of the crash scene used in previous subtasks, so the simulated data had known camera geometry and lens distortion parameters. The tests compared differences in calibration solutions and SfM reconstruction accuracy for different processing settings implemented with the Pix4D automatic self-calibration procedure. The research team also performed an in-lab camera calibration experiment using a separate commercial SfM photogrammetry software (Agisoft Metashape).

### **General Concepts**

Geometric camera calibration enables the estimation of the internal parameters of the lens and image sensor frame of a camera. Also known as intrinsic or IO parameters, these parameters are needed to correct for lens distortions and to accurately measure the size of an object in world units based on the location of the camera in the scene (*105, 106*). Knowing this information is necessary to accurately relate an image coordinate system to a real-world object coordinate system.

IO parameters that can be determined through calibration include the following (*105, 106*):

- **Calibrated focal length (CFL)**—The focal length that produces an overall mean distribution of lens distortion. For digital cameras, this is typically reported in pixel units for calibration purposes within the SfM software. Focal length is the distance from the focal point on the camera sensor frame to the center of a lens.
- **Principal point location**—The location (X–Y coordinates) of the principal point in pixels. Principal point is the point on the image plane onto which the perspective center of the lens is projected. For a digital camera, the principal point is where the optical axis intersects the image plane, nominally located at the center of the sensor frame. Due to imperfections, it is often not perfectly aligned with the optical center of the lens. Calibration can determine the offset from this location.
- **Radial lens distortion**—The symmetric component of lens distortion that occurs along lines radially away from the principal point. Radial distortion occurs when light rays bend more near the edges of a lens than they do at its optical center. Although the amount may be negligible, this type of distortion is theoretically always present. Compared to more expensive metric-grade digital cameras, consumer-grade digital cameras are generally prone to larger magnitudes of radial distortion.
- **Tangential lens distortion**—The lens distortion that remains after compensation for symmetric radial lens distortion. Sometimes referred to as decentering distortion,

tangential distortion occurs when the physical elements of a lens are not perfectly parallel and aligned with the image plane.

- **Skew coefficient**—Nonzero coefficients that can sometimes be used in calibration to compensate for image axes that are skewed (not perpendicular) within a digital camera.

Using an accurately calibrated camera model with well-known IO and lens distortion parameter values is imperative for any photogrammetric process needed for accurate real-world coordinates or measurements. Errors in camera calibration propagate as inaccuracies of image coordinate measurements, which in turn produce errors in real-world object coordinate measurements.

Poor calibration of the camera model is one of the most significant contributors to systematic errors reported for UAS-SfM generated point clouds and DSMs, largely associated with radial distortion (107, 108). A standard method for correction (calibration) of radial distortion is Brown's distortion model, which also includes components for tangential distortion (109). Unless camera models represent distortion effects accurately, broad-scale deformations (doming or bowling) can manifest, resulting in a systematic increase in vertical error across the scene (108, 110). These errors are most evident on flatter, structure-limited surfaces. This effect is often credited to a lack of strong geometric features within the scene that are important for aiding the automated self-calibration procedures typically implemented in commercial SfM photogrammetry software to resolve accurate distortion values (108). UAS-SfM surveys of roadway corridors, which can be relatively flat and limited in geometric structure, are sometimes prone to this bowl effect error (107). Methods to mitigate this effect include adding oblique angle camera perspectives, using perpendicular flight lines to increase perspective and overlap, and adding GCPs (110, 111). Such techniques seek to aid a SfM software's calibration routine to arrive at a better solution.

Impacts of erroneous camera calibration values, whether for distortion values or internal parameters such as focal length, play a major role in dictating the accuracy and quality of any 3D reconstruction with UAS-SfM. In general, two approaches are used to determine the camera model for SfM processing: pre-calibration and self-calibration.

Pre-calibration is when the user solves for the intrinsic geometry and distortion parameters of the camera before the BA stage in the SfM workflow (108). For metric-grade cameras, this is typically done in a professional lab setting. Values are often provided by the camera manufacturer because it is assumed that the intrinsic geometry remains stable as long as no serious physical impact occurs. Of course, even metric-grade cameras require assessment of their calibration values over time and use. For consumer-grade digital cameras such as those typically used for UAS surveys of crash scenes, a common method for pre-calibration is to use a 2D planar calibration target and acquire images of the target from multiple camera perspectives. A typical example of a 2D calibration target is a black-and-white checkerboard pattern with known, accurately measured dimensions of the squares. The images, along with the known target measurements, are input into the software to solve for the intrinsic parameters and distortion model parameters (108).

An advantage of pre-calibration is that it can be performed in a controlled environment, and the values can be predetermined before flight. These values can then be locked and applied during

the SfM data processing procedure to provide a potentially more stable SfM reconstruction than self-calibration, which relies on the automated feature (keypoint)-matching algorithms (108).

Pre-calibration may be advantageous under certain conditions where scene texture is degraded and can impede the self-calibration algorithms. It can also be advantageous for UAS surveys conducted over flat and geometrically limited scenes, such as roadway corridors, and/or where the UAS imaging network (e.g., single-scale nadir imagery) did not provide enough multiple perspectives with overlap redundancy to provide a rigorous solution. It may also provide a means to initialize parameter values to aid self-calibration routines within SfM software. Finally, for higher-grade metric cameras suitable for UAS use, which are now starting to become available, pre-calibration values provided by the manufacturer or derived by the end user in a lab calibration procedure can be used and locked during SfM processing.

A disadvantage of pre-calibration is that camera parameters can change under actual operating conditions. In addition, pre-calibration is determined from images at close range (e.g., <10 m or 33 ft). A small error resulting from poor calibration at close-range can propagate and scale up as the distance between the camera and the features captured in the images increase.

Self-calibration is when camera calibration parameters are automatically determined during the BA phase of SfM and are constrained by the keypoint extraction and correspondence matches between overlapping images. Use of GCPs and accurate image geolocations can help refine the estimation of camera model parameters in the BA. Self-calibration is by far the most common approach used by commercial SfM photogrammetry software, including Pix4D, for calibration of the camera model onboard the UAS.

A major advantage of self-calibration for UAS surveys conducted with consumer-grade digital cameras is that the parameters are determined at the scale of data acquisition and optimized based on the environment and physical condition of the camera at the time of flight (108).

Self-calibration has some disadvantages. When surveying relatively flat landscapes with a UAS, the self-calibration BA solution relies primarily on changes in two dimensions for parameter optimization unless oblique imagery is included (107, 108). In surveys that only gather single-scale nadir imagery, accurately solving for the entire spectrum of distortion parameters represented in a full Brown-type distortion model with self-calibration is unlikely. Rigorous calibration results for the full spectrum of camera intrinsic and distortion parameters are generally only possible with image networks that are highly redundant with strong convergent geometry (108). As mentioned, certain flight design techniques can help improve image network geometry and self-calibration solutions.

Another disadvantage of self-calibration is its reliance on automated keypoint matches by the SfM software. Under suboptimal conditions, such as poor ambient lighting, or where there are dynamic features in the scene, such as cars moving from image to image, the quality of keypoint extraction and correspondences across images can be degraded. These inaccuracies and spurious matches can potentially affect the effectiveness of the self-calibration procedure.

## Methods

The research team used the UAS image acquisition simulation tool developed in the prior subtasks to generate imagery suitable to test self-calibration methods in Pix4D. As discussed, the simulation introduced nine artificial ground control targets with known coordinates into the artificial scene for use as GCPs for evaluating positional accuracy of the SfM reconstruction and to test their use in improving camera calibration during processing.

The analysis used a simulated dataset rendered at 80 percent endlap and 80 percent sidelap, which resulted in a final image set that consisted of 105 rendered images. All self-calibration experiments in Pix4D used the same set of image renderings. The camera interior geometry and distortion parameters as well as exterior position and orientation of the camera at each image acquisition location were known from the simulation. Figure 133 shows an example orthomosaic created for the crash scene area derived from SfM processing of the simulated set of UAS images.



**Figure 133. Example Orthomosaic of the Crash Scene Derived from Simulated UAS Imagery Using a Textured Mesh Created from Real-World UAS Data.**

### *Self-Calibration Experiment with Pix4D*

The research team used Pix4D version 4.5.6 for the analysis. More specifically, the research team used Pix4D's standard 3D mapping template and standard geolocation uncertainty values for image positions (unless otherwise stated) based on a single-frequency, nondifferential GNSS, such as onboard a DJI Mavic 2 Pro. Calibration of the camera model in Pix4D is performed completely through self-calibration at the SfM BA stage where the sparse point cloud is created. The error minimization is constrained by the keypoint extraction and correspondence matches

between overlapping images. GCPs and accurate image geolocations can also be used to reoptimize the BA solution and in process potentially improve the camera calibration solution.

The research team evaluated six different calibration processing runs, five self-calibrations and one fixed calibration, based on settings that can be implemented in Pix4D's initial processing and calibration stage of the processing workflow:

- **Scenario 1 (Standard Calibration without GCPs).** This run used Pix4D's standard calibration method, which is the default.
- **Scenario 2 (Standard Calibration with GCPs).** This run used the same procedure as Scenario 1, except that four GCPs distributed evenly throughout the artificial scene were used to optimize the solution of the internal camera parameters.
- **Scenario 3 (All Prior Setting without Distortion Values).** This run used the all prior setting in Pix4D, which tells Pix4D to give more weight to the initial camera values in the BA. This condition constrains the self-calibration solution to remain close to the initial camera model values. This run provided focal length and principal point values.
- **Scenario 4 (All Prior Setting with Distortion Values).** This run used the same all prior setting in Pix4D as Scenario 3, except distortion parameter values from the simulation, in addition to focal length and principal point, were provided to Pix4D for the initial parameter values. This process is similar to performing a pre-calibration of a camera and then supplying the values as initial values to be used by Pix4D during self-calibration.
- **Scenario 5 (Fixed Calibration).** This run used the known internal camera parameter and distortion values from the simulation and fixed them during SfM processing in Pix4D.
- **Scenario 6 (Accurate Geolocation).** This run used the accurate geolocation and orientation setting for calibration, which is a setting for images with accurate geolocation and orientation values. Pix4D recommends this setting when using imagery that has been accurately geolocated using RTK/PPK GNSS onboard the UAS. Accurate IMU information can also be used. For this processing run, the exact camera position and orientation values were fed to Pix4D, and the external calibration was set to None. This locked in the external camera position and orientation values during optimization such that Pix4D would only solve for the internal camera parameters. This simulation run provided a comparison of accurate geolocations versus GCPs (i.e., Scenario 2) for aiding calibration and SfM reconstruction.

The calibration solved for the CFL ( $F$ ) and principal point X-Y location ( $C_{0x}$ ,  $C_{0y}$ ). It also used Pix4D's default five parameter lens distortion model, which uses three radial distortion coefficients ( $R_1$ ,  $R_2$ , and  $R_3$ ) and two tangential distortion coefficients ( $T_1$  and  $T_2$ ). The initial camera calibration values used in all processing runs, unless otherwise stated, stemmed from the default camera model values available in Pix4D's camera library for the DJI Mavic 2 Pro Hasselblad camera.

Regarding Scenario 6, one typically does not fully lock the geolocations as done here. Because this was a simulation and the camera positions and orientations were known, locking the geolocation and orientation values of the camera allowed the research team to examine its effect on the calibration of the internal camera parameters. In practice, one processes image geolocations obtained from RTK/PPK GNSS by importing the imagery into Pix4D and assigning them very low positional uncertainty values, down to the horizontal and vertical accuracy of the



RTK/PPK solution. This process allows Pix4D to still optimize the external parameters, but the optimization is heavily weighed by the higher horizontal and vertical accuracy of the image geolocations. Figure 134 shows the initial processing settings for fixed calibration of the camera geolocations with optimization of the external parameters set to none.

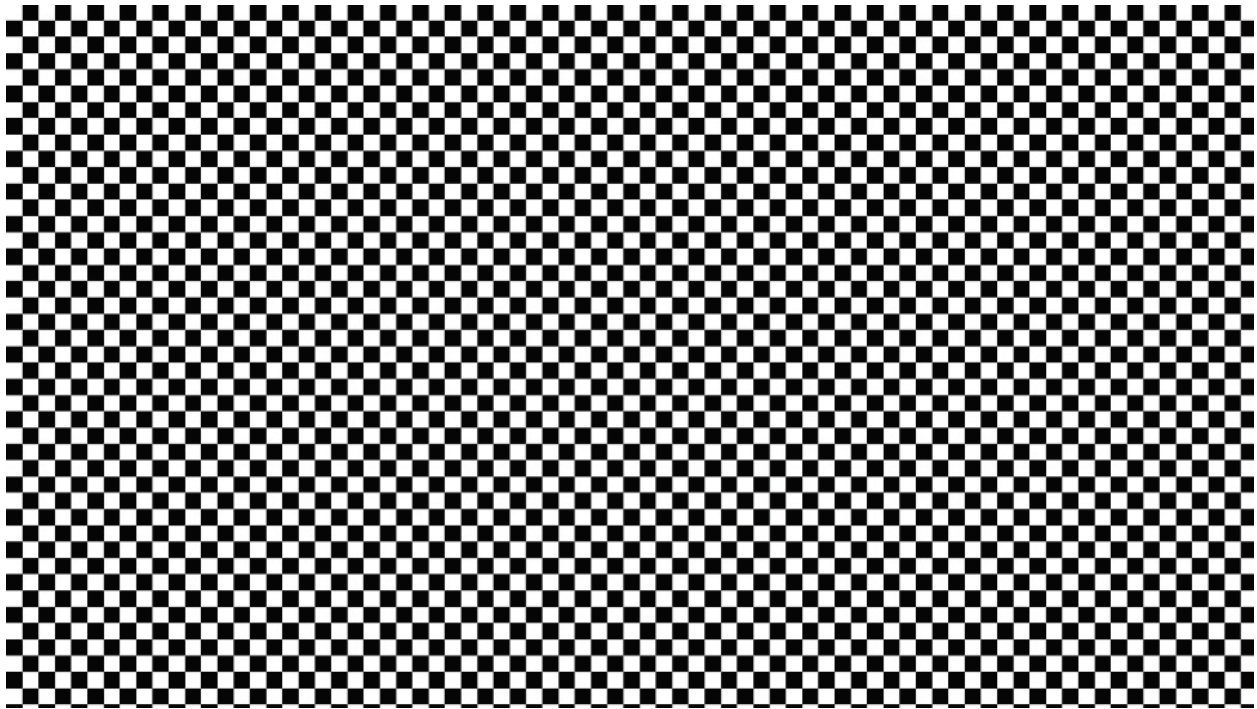
Evaluation of the results for each of the six different processing runs examined differences in the solution of the internal camera calibration parameters, differences in external camera position and orientation values, and checkpoint errors for assessing absolute accuracy of the SfM reconstruction.

Detected Template	No Template Available
Keypoints Image Scale	Full, Image Scale: 1
Advanced: Matching Image Pairs	Aerial Grid or Corridor
Advanced: Matching Strategy	Use Geometrically Verified Matching: no
Advanced: Keypoint Extraction	Targeted Number of Keypoints: Automatic
Advanced: Calibration	Calibration Method: Geolocation Based Internal Parameters Optimization: All External Parameters Optimization: None Rematch: Auto, yes

**Figure 134. Example of Pix4D Initial Processing Settings for Fixed Geolocation with Optimization of External Camera Parameters Set to None.**

*Pre-Calibration Experiment with Metashape*

Metashape includes a method to perform pre-calibration using a checkerboard pattern projected onto a television (TV) screen as a calibration target (Figure 135). It is also possible to use a printed checkerboard pattern, provided it remains flat and all the cells are squares. The lens calibration procedure supports estimation of the full camera calibration matrix, including nonlinear distortion coefficients.



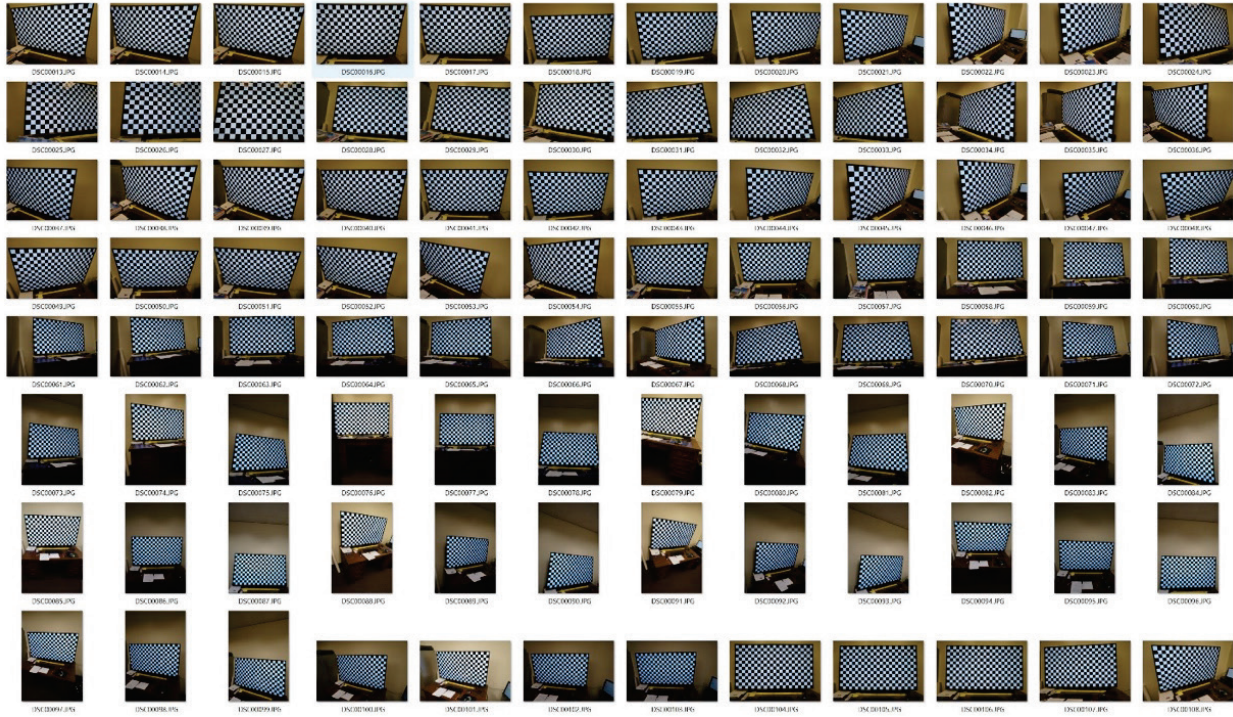
**Figure 135. Digital Calibration Target in Metashape (112).**

The research team used a 24-MP Sony A6500 mirrorless digital camera for the pre-calibration experiment in Metashape. Table 72 lists the camera specifications.

**Table 72. Sony A6500 Camera Specifications.**

<b>Parameter</b>	<b>Value</b>
Sensor Size	23.5×15.6mm
Number of Pixels	6000×4000
Pixel Pitch	3.9 μm
Lens Type	16 mm, fixed, Sony E-mount (E 16 mm F2.8)

The research team gathered a set of calibration images with the camera using Metashape’s digital checkerboard pattern projected onto a 165 cm (65-inch) TV screen. The process resulted in 96 images that captured the checkerboard pattern from a variety of positions and angles (Figure 136). Once acquired, Metashape proceeded with the automatic lens calibration procedure.



**Figure 136. Calibration Images of the Checkerboard Pattern Projected onto a 165-cm (65-inch) TV.**

*Self-Calibration Experiment with Metashape*

The research team also conducted a self-calibration experiment with the Sony A6500 camera using Metashape. The research team gathered a set of images with the A6500 camera of the Early Childhood Development Center (ECDC) building on the TAMUCC campus (Figure 137). This two-story building has a footprint of about 4,300 m<sup>2</sup> (58,300 ft<sup>2</sup>) and is about 9 m (30 ft) in height.

The research team gathered 874 ground-level images of the building. The process entailed walking around the building and acquiring a set of overlapping images from near and far perspectives, including oblique, that covered the entire perimeter of the building. Distances from the camera to the building ranged from 4 m (13 ft) for detailed images and for under the eaves to about 50 m (164 ft) for more encompassing, wider field-of-view images.



**Figure 137. ECDC Building on the TAMUCC Campus.**

The research team performed three different processing runs in Metashape:

- **Self-calibration Run 1.** This run used the standard initial values from Metashape’s camera database for the A6500 camera, which only includes focal length. The run then allowed Metashape to perform a self-calibration procedure during the sparse point cloud generation stage of the SfM processing workflow.
- **Self-calibration Run 2.** This run used the calibration solution from the pre-calibration procedure as the initial parameter values. The run then allowed Metashape to perform its self-calibration procedure.
- **Pre-calibration Run 3.** This run used the camera calibration parameter results from the pre-calibration procedure. Those parameters were then fixed during the sparse point cloud generation stage of the SfM workflow. This process is different from Run 2 above, which used the pre-calibration values as initial values for calibration but still used Metashape’s self-calibration procedure to solve for the parameters.

Additional information about self-calibration in Metashape is available elsewhere (112).

## Results

### *Self-Calibration Experiment in Pix4D*

Figure 138 shows the difference between the initial and optimized internal parameters for the six different self-calibration scenarios. Scenario 1 had the largest deviation between initial versus optimized camera internal parameter values. The initial values stemmed from Pix4D’s default camera library, which uses manufacturer values for the DJI Mavic 2 Pro Hasselblad camera in the simulation. Because the initial values were close in range to the actual values used for the simulated data set, a large deviation from those values after self-calibration indicates a less accurate solution relative to the other five scenarios examined.

Scenario 1 had a 9.5 percent difference between initial and optimized internal camera parameters versus a 2.8 percent relative difference when four GCPs were added to aid calibration (i.e., Scenario 2). This result shows the benefit of adding GCPs to a UAS survey to help reoptimize the self-calibration solution in Pix4D. Most of the difference between Pix4D’s standard self-calibration without GCPs (Scenario 1) versus with GCPs (Scenario 2) resulted from poor estimation of the focal length (Figure 139). Correct focal length estimation is known to be one of the most crucial components in a camera calibration model because small errors can result in highly exaggerated surface point coordinates through photogrammetric reconstruction (108). Scenarios 3, 4, and 6 resulted in similar CFL values. Scenario 5 (fixed calibration) did not solve for this parameter because the values were locked in place.

	Focal Length	Principal Point x	Principal Point y	R1	R2	R3	T1	T2	
<b>(Scenario 1)</b>	Initial Values	4148.830 [pixel] 10.000 [mm]	2732.000 [pixel] 6.585 [mm]	1820.000 [pixel] 4.387 [mm]	0.000	0.000	0.000	0.000	0.000
	Optimized Values	3753.363 [pixel] 9.047 [mm]	2731.417 [pixel] 6.584 [mm]	1819.463 [pixel] 4.385 [mm]	-0.001	0.000	-0.000	0.000	0.000
	Uncertainties (Sigma)	501.657 [pixel] 1.209 [mm]	0.019 [pixel] 0.000 [mm]	0.017 [pixel] 0.000 [mm]	0.000	0.000	0.000	0.000	0.000
<b>(Scenario 2)</b>	Initial Values	4148.830 [pixel] 10.000 [mm]	2732.000 [pixel] 6.585 [mm]	1820.000 [pixel] 4.387 [mm]	0.000	0.000	0.000	0.000	0.000
	Optimized Values	4031.034 [pixel] 9.716 [mm]	2731.401 [pixel] 6.584 [mm]	1819.507 [pixel] 4.386 [mm]	-0.001	0.001	-0.001	0.000	0.000
	Uncertainties (Sigma)	20.230 [pixel] 0.049 [mm]	0.019 [pixel] 0.000 [mm]	0.017 [pixel] 0.000 [mm]	0.000	0.000	0.000	0.000	0.000
<b>(Scenario 3)</b>	Initial Values	4148.830 [pixel] 10.000 [mm]	2732.000 [pixel] 6.585 [mm]	1820.000 [pixel] 4.387 [mm]	0.000	0.000	0.000	0.000	0.000
	Optimized Values	4148.830 [pixel] 10.000 [mm]	2731.433 [pixel] 6.584 [mm]	1819.471 [pixel] 4.386 [mm]	-0.001	0.001	-0.001	0.000	0.000
	Uncertainties (Sigma)	0.108 [pixel] 0.000 [mm]	0.019 [pixel] 0.000 [mm]	0.017 [pixel] 0.000 [mm]	0.000	0.000	0.000	0.000	0.000
<b>(Scenario 4)</b>	Initial Values	4200.000 [pixel] 10.123 [mm]	2782.000 [pixel] 6.706 [mm]	1870.000 [pixel] 4.507 [mm]	-0.001	0.000	0.000	0.000	0.000
	Optimized Values	4200.025 [pixel] 10.123 [mm]	2733.078 [pixel] 6.588 [mm]	1820.648 [pixel] 4.388 [mm]	-0.001	0.001	-0.001	0.000	0.000
	Uncertainties (Sigma)	0.163 [pixel] 0.000 [mm]	0.029 [pixel] 0.000 [mm]	0.025 [pixel] 0.000 [mm]	0.000	0.000	0.000	0.000	0.000
<b>(Scenario 5)</b>	Initial Values	4200.000 [pixel] 10.123 [mm]	2782.000 [pixel] 6.706 [mm]	1870.000 [pixel] 4.507 [mm]	-0.001	0.000	0.000	0.000	0.000
	Optimized Values	4200.000 [pixel] 10.123 [mm]	2782.000 [pixel] 6.706 [mm]	1870.000 [pixel] 4.507 [mm]	-0.001	0.000	0.000	0.000	0.000
	Uncertainties (Sigma)	0.000 [pixel] 0.000 [mm]	0.000 [pixel] 0.000 [mm]	0.000 [pixel] 0.000 [mm]	0.000	0.000	0.000	0.000	0.000
<b>(Scenario 6)</b>	Initial Values	4148.830 [pixel] 10.000 [mm]	2732.000 [pixel] 6.585 [mm]	1820.000 [pixel] 4.387 [mm]	0.000	0.000	0.000	0.000	0.000
	Optimized Values	4149.379 [pixel] 10.001 [mm]	2731.503 [pixel] 6.584 [mm]	1819.505 [pixel] 4.386 [mm]	-0.001	0.001	-0.001	0.000	0.000
	Uncertainties (Sigma)	0.000 [pixel] 0.000 [mm]	0.001 [pixel] 0.000 [mm]	0.001 [pixel] 0.000 [mm]	0.000	0.000	0.000	0.000	0.000

Figure 138. Pix4D Calibration Results for the Six Different Self-Calibration Scenarios.

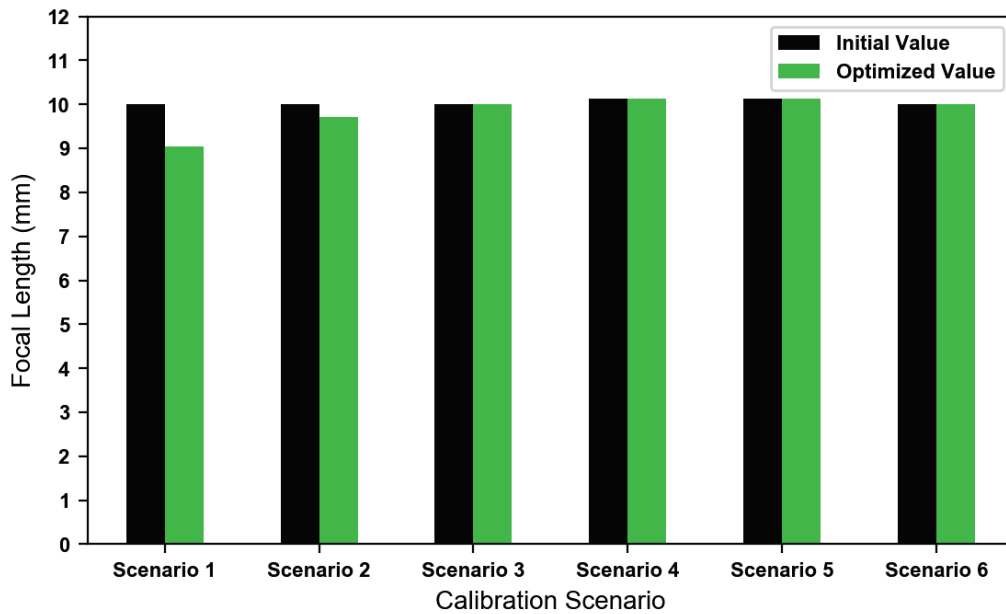
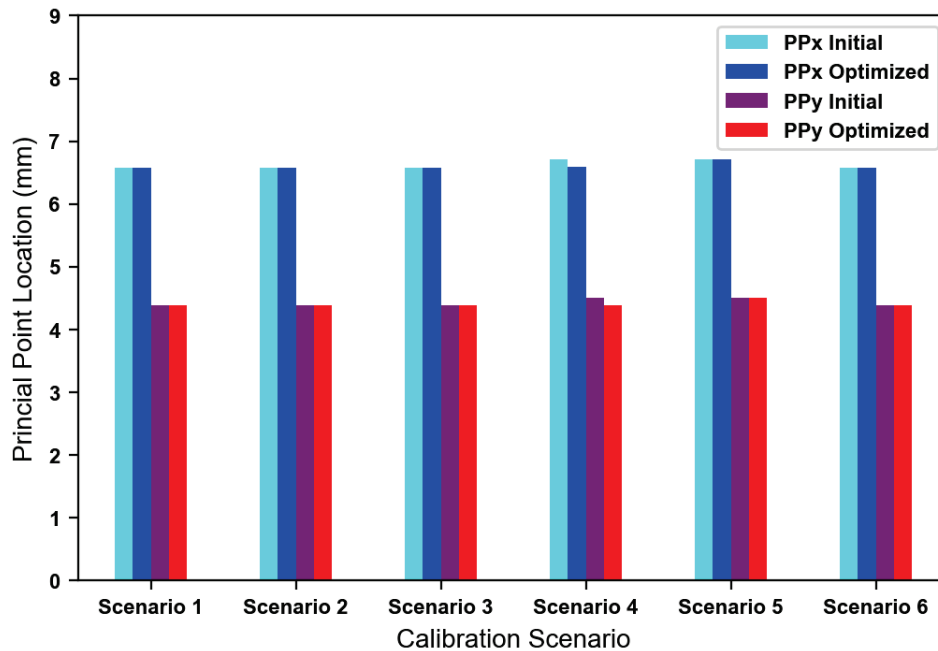


Figure 139. Initial vs. Optimized Focal Length for the Six Calibration Scenarios.

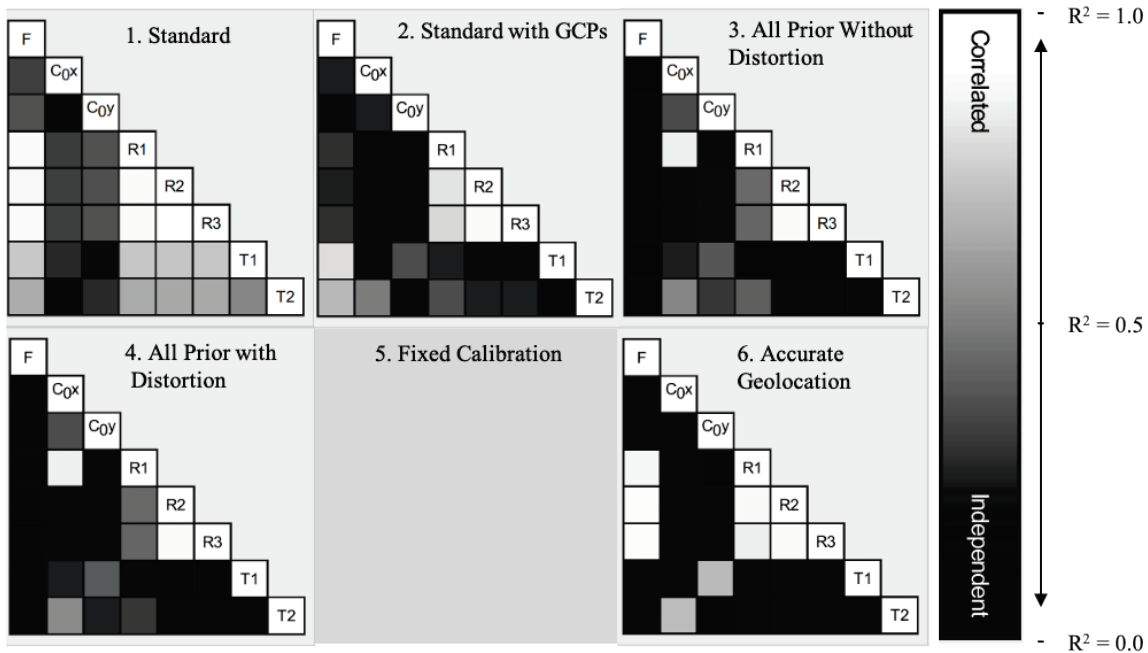
Figure 140 shows differences in initial versus optimized principal point locations. Both Scenario 1 and 2 estimated well the principal point locations. Similarly, all the other scenarios performed well solving for focal length and principal point locations; Scenario 5 (fixed calibration) did not solve for these parameters because the values were locked in place.

As shown in Figure 138, the results for Scenarios 3 and 4 showed the influence of the all prior setting in Pix4D, which weighs the solution based on the initial parameter values. Scenario 3 only used initial values from the default camera library for focal length and principal point location whereas Scenario 4 weighed the solution using the known internal parameter values including distortion from the simulation. Both solutions resulted in optimized values close to the initial values, with no change in focal length but slight changes in the optimized principal point location (Figure 140). Figure 138 shows that Scenario 6 had optimized values close to the initial values for the internal camera parameters without using the all prior setting, which indicates that accurate camera geolocations, such as those obtained from RTK/PPK GNSS, can aid Pix4D in reoptimizing the solutions for the self-calibration values at similar levels as when using GCPs.



**Figure 140. Initial vs. Optimized Principal Point for the Six Calibration Scenarios.**

Figure 141 shows squared correlation coefficient ( $R^2$ ) values between the various camera internal parameters for each of the six processing scenarios reported in the Pix4D quality report. The correlation values were obtained from the covariance matrix resulting from a least-squares estimation procedure that is performed during the SfM BA procedure. The adjustment is constrained by the keypoint matches between overlapping images found by Pix4D’s automated keypoint extraction and detection algorithms. Using all prior settings, GCPs, and accurate geolocations can further constrain the optimization solution.



Note: Symbology used by Pix4D. F = focal length; C<sub>0x</sub> and C<sub>0y</sub> = principal point coordinates; R<sub>1</sub>, R<sub>2</sub>, R<sub>3</sub> = radial distortion coefficients; T<sub>1</sub>, T<sub>2</sub> = tangential distortion coefficients. Lighter colors mean a stronger linear correlation.

**Figure 141. Correlation between Camera Internal Parameters.**

Compared to Scenario 2, Scenario 1 showed a higher correlation between the focal length and the radiation distortion parameters. Scenario 6 showed a similar correlation with radial distortion but a reduced correlation for tangential distortion compared to Scenario 1. Correlation of focal length with radial distortion is a known occurrence, but whether it significantly degrades the SfM solution depends heavily on the accuracy of the optimized internal parameter solutions and EO solution. Scenario 1 would likely produce a worse result than Scenario 6 in terms of reconstruction positional accuracy of the sparse point cloud due to the inaccurate optimized focal length.

Scenarios 3 and 4 showed similar results regarding the correlation between focal length and principal point, which signifies a desired behavior and demonstrates the benefit of the all prior setting aiding self-calibration solutions in Pix4D when acceptable initial internal parameter values are provided.

Ideally, camera internal parameters should be independent. However, some degree of correlation between parameters is expected for most projects. For example, correlation between the radial distortion parameters should be expected because these parameters are bounded by the physical constraints of the lens. Furthermore, finding strong correlation between parameters may sometimes be helpful in detecting certain types of problems with the SfM reconstruction. Examples of situations where correlation between camera internal parameters might occur include the following (113):

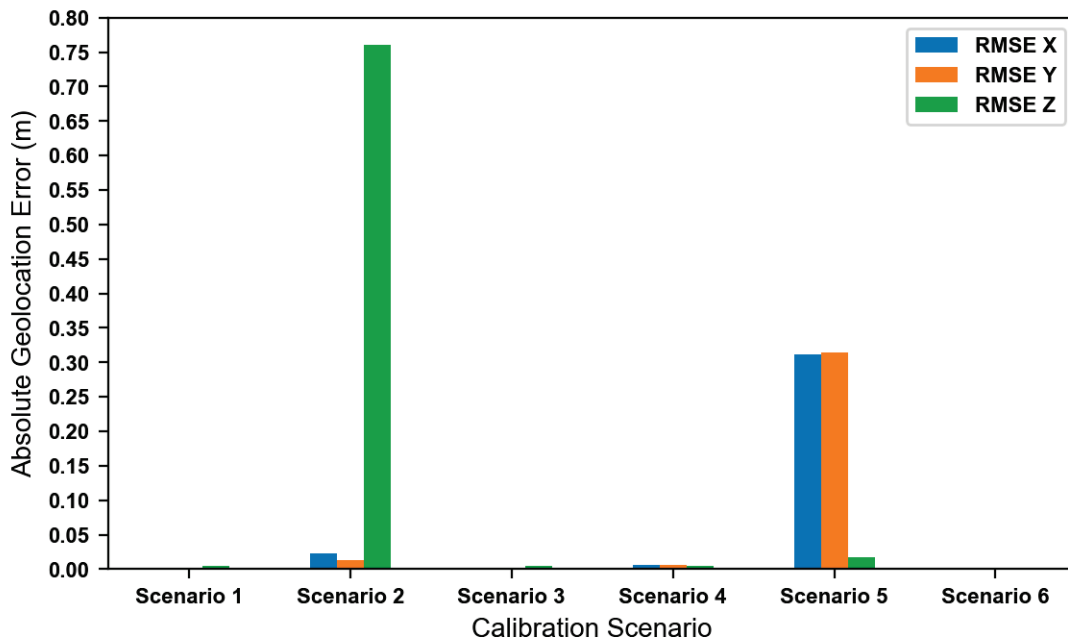
- Uniform data resulting from flat terrain relative to flight heights, GCPs placed in one plane (no height variations), few matched keypoints at the edges of images, and images taken with the same orientation.

- Nadir images in which correlation between the radial distortion parameters and between the two principal point coordinates might occur.
- Oblique images in which correlation between the focal length and the coordinates of the principal point and between the coordinates of the principal point and the tangential distortion parameters might occur.

Strategies to help with decorrelation include the following (113):

- Accurate camera positions (e.g., RTK/PPK GNSS) combined with GCPs.
- Terrain and built environment height variations.
- Keypoint matches at multiple depths and near image edges for oblique images.
- Different camera orientations, such as rotating at the ends of gridded flight rows or using perpendicular flight grids.
- Use of the all prior constraint for internal parameters optimization, assuming decent initial values are provided.

Figure 142 shows the RMSE of the absolute camera geolocation errors for the six different self-calibration processing scenarios. Figure 143 shows the RMSE of the absolute camera orientation errors for the six different self-calibration processing scenarios. Figure 144 and Figure 145 show the mean of the checkpoint error and RMSE of the checkpoint error, respectively, for each of the six different self-calibration scenarios. Figure 146 shows an example of subtle differences in DSMs generated from sparse point clouds created from Scenario 1 (standard calibration) and Scenario 2 (standard calibration with GCPs). The arrows in Figure 146 highlight subtle differences between the two scenarios in regard to reconstruction of the GCP targets located on either side of the crash scene, which were elevated above the ground in the simulation.



**Figure 142. Absolute Camera Geolocation Error for the Six Calibration Scenarios.**



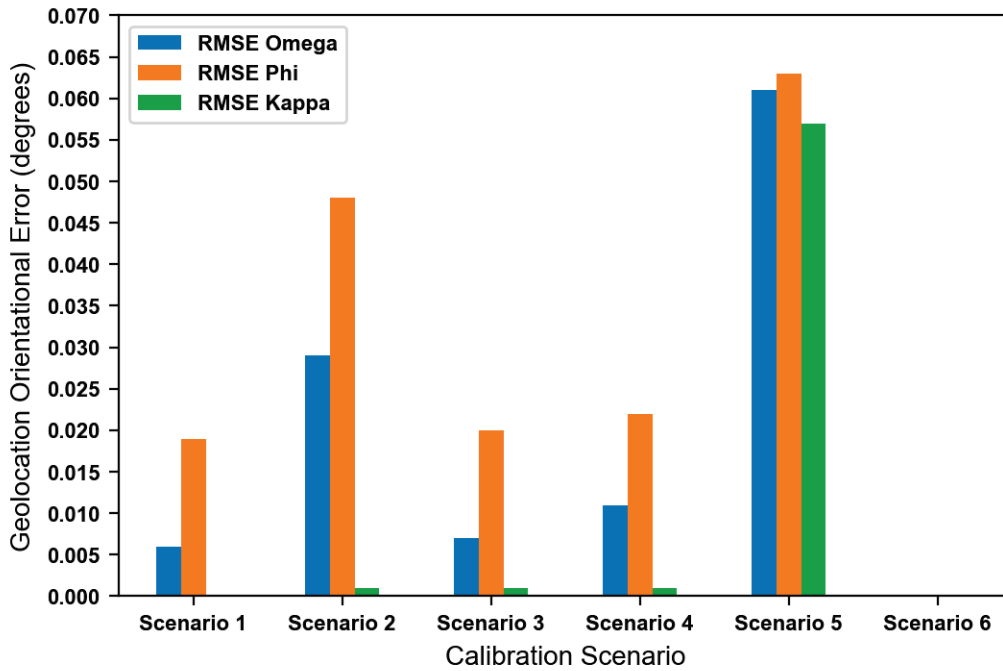
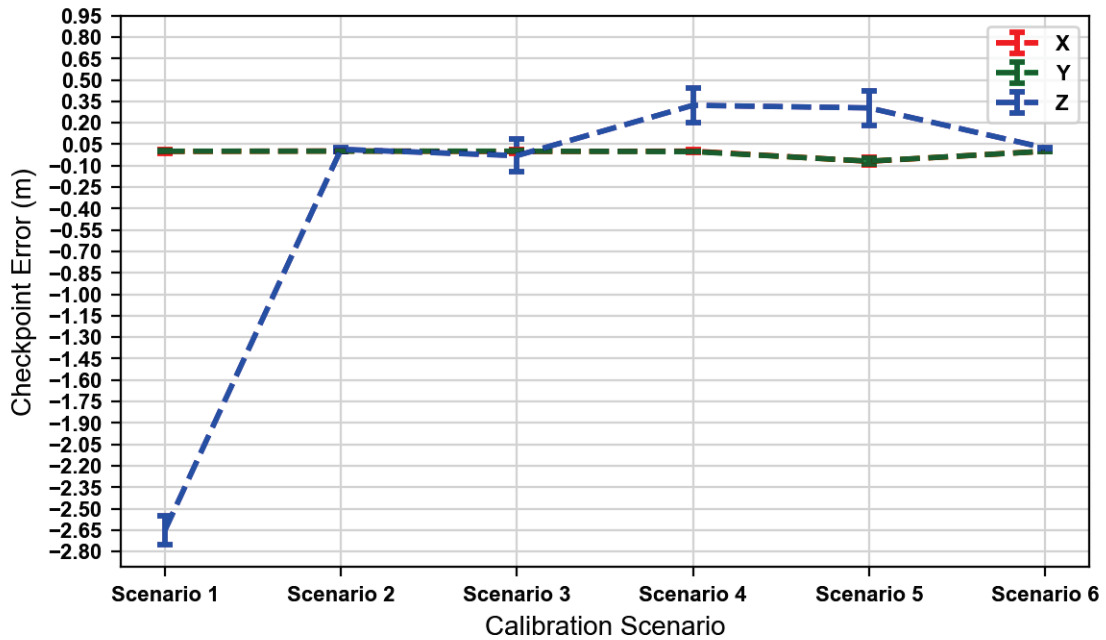
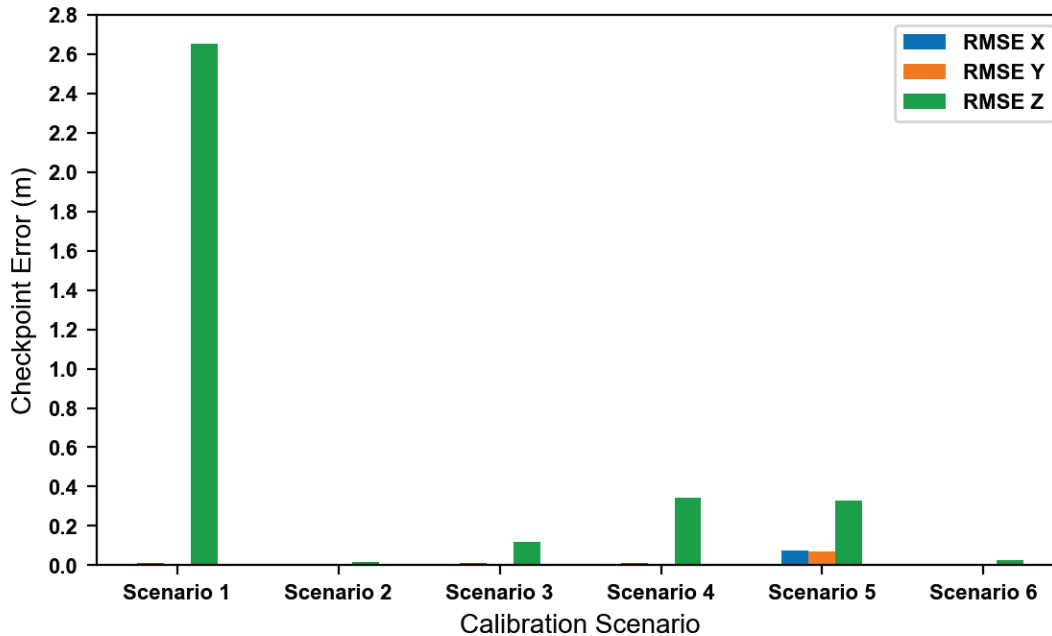


Figure 143. Absolute Camera Orientation Error for the Six Calibration Scenarios.



Note: The dashed lines are used for overall visualization, not to suggest linear trends between adjacent data points.

Figure 144. Mean Checkpoint Error with Error Bars for the Six Calibration Scenarios.



**Figure 145. RMSE of the Checkpoint Error for the Six Calibration Scenarios.**

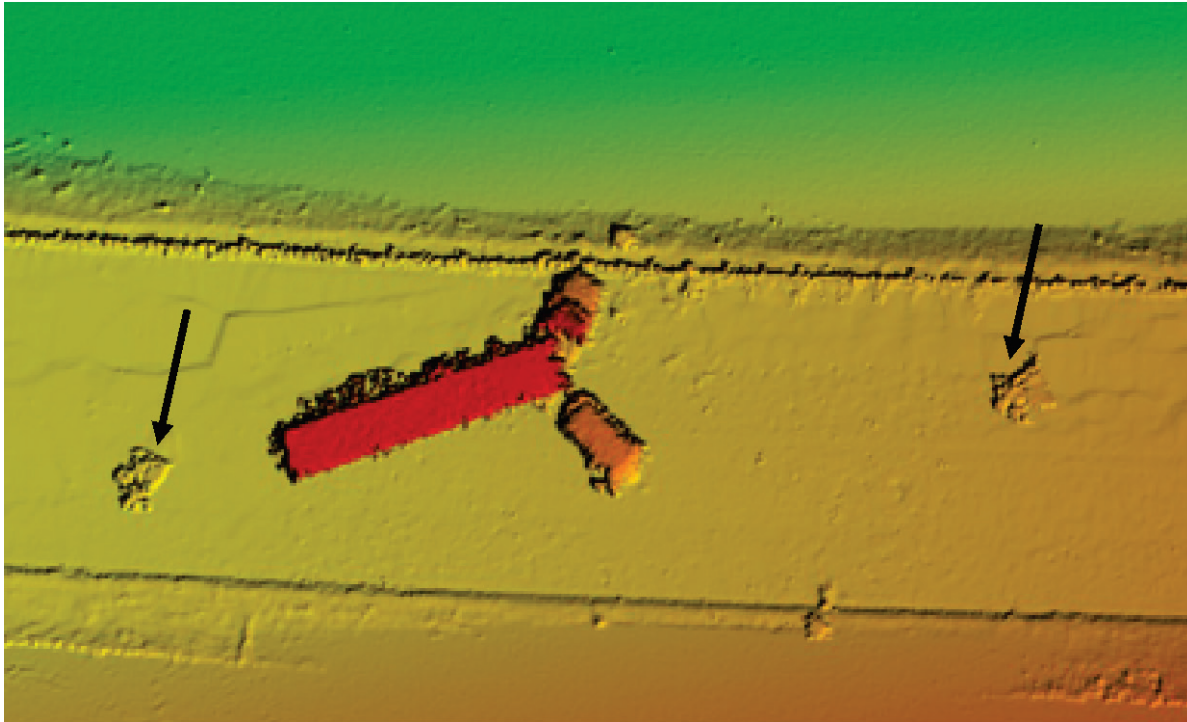
Scenario 1 produced the worst accuracy overall, which resulted from large errors in the Z component. Scenario 2, which used GCPs, had much better positional accuracy overall. This result can be attributed to the inaccurate focal length estimation during self-calibration. It further demonstrates the value in having GCPs to aid self-calibration. In self-calibration, a poorly estimated focal length can result in poor optimization of other distortion coefficients. Proper estimation of focal length becomes even more important when using single-scale nadir only imagery acquired over linear topographies (e.g., flat roadways flown at a single height). The simulated UAS data set used here stems from such conditions.

Scenarios 3 and 4 had a low RMSE for the checkpoint error. Using the all prior setting with realistic initial camera internal parameter values aided the overall SfM reconstruction accuracy. Interestingly, weighing the solution by the leading parameters performed better in terms of positional accuracy than weighing the solution by the leading parameters plus distortion parameters, which suggests that it may be better to apply the all prior setting only to the leading parameters during a self-calibration solution with Pix4D.

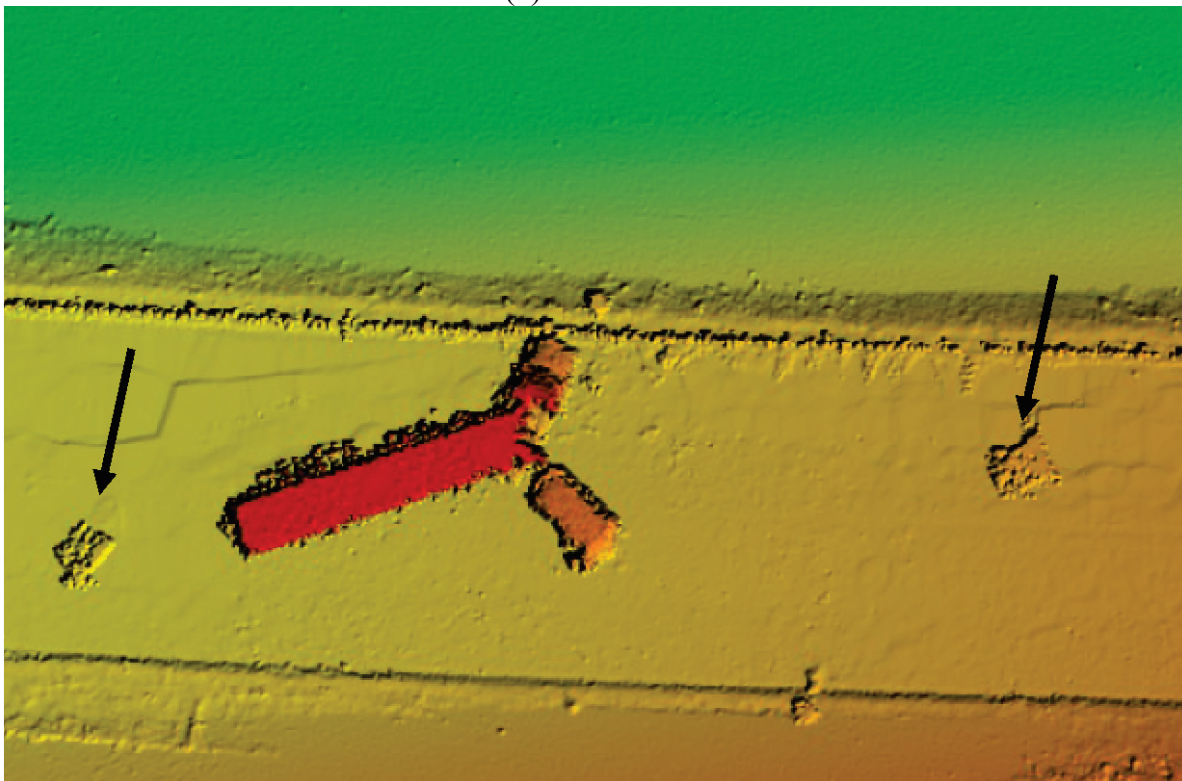
Scenario 5 resulted in the second most erroneous solution, which was derived directly from the more inaccurate estimation of camera external parameters (absolute position and orientation). This result is interesting and further analysis is necessary to understand how Pix4D integrates fixed calibrations into the overall SfM reconstruction.

Scenario 6, along with Scenario 2, resulted in the lowest RMSE overall for checkpoint error. This result shows the benefit of using a UAS integrated with an RTK/PPK-enabled GNSS to provide accurate camera geolocations. It further showed the importance of including GCPs in the reconstruction to aid the calibration when relying on inaccurate geolocations or processing UAS data acquired from imaging networks that are not ideal for self-calibration, such as nadir-only perspectives acquired over relatively flat terrain reliefs.

(a) Scenario 1



(b) Scenario 2



Note: Arrows show subtle differences in reconstruction of the floating GCP targets.

**Figure 146. Digital Surface Models Generated from Scenarios 1 and 2.**

*Pre-Calibration and Self-Calibration Experiments with Metashape*

Table 73 shows the results of the pre-calibration solution for the Sony A6500 camera compared to the self-calibration Run 1 solution. Table 74 shows the results of the pre-calibration solution compared to the self-calibration Run 2 solution.

**Table 73. Camera Calibration Solutions in Metashape for Pre-Calibration and Self-Calibration Run 1.**

Internal Parameters	Pre-Calibration Values	Self-Calibration Values	% Difference
f (pixels)	4057	4048	0.21
cx (pixels)	-41.0	-49.4	20
cy (pixels)	-25.4	-37.0	45
b1	0.507674628	0	100
b2	-0.423222167	0	100
k1	-0.072554524	-0.070862	2.3
k2	0.10468948	0.0958112	8.5
k3	-0.029298207	0.0016151	106
k4	0.027992617	0	100
p1	0.000167368	0.000294991	76
p2	-5.55E-05	-0.000384593	592
p3	15.64511407	0	100
p4	-9.989678266	0	100

Note: Symbology used by Metashape. f = focal length (pixels); cx and cy = principal point coordinates; b1, b2 = affinity and skew (nonorthogonality) transformation coefficients; k1, k2, k3, k4 = radial distortion coefficients; p1, p2, p3, p4 = tangential distortion coefficients.

**Table 74. Camera Calibration Solutions in Metashape for Pre-Calibration and Self-Calibration Run 2.**

Internal Parameters	Pre-Calibration Values	Self-Calibration Values	% Difference
f (pixels)	4057	4049	0.20
cx (pixels)	-41.0	-52.3	27
cy (pixels)	-25.4	-37.7	48
b1	0.507674628	0.507675	0.0
b2	-0.423222167	-0.423222	0.0
k1	-0.072554524	-0.073348	1.1
k2	0.10468948	0.111836	6.
k3	-0.029298207	-0.0357571	22
k4	0.027992617	0.0279926	0.0
p1	0.000167368	1.23E-05	93
p2	-5.55E-05	-6.62E-05	19
p3	15.64511407	15.6451	0.0
p4	-9.989678266	-9.98968	0.0

Note: Symbology used by Metashape. f = focal length (pixels); cx and cy = principal point coordinates; b1, b2 = affinity and skew (non-orthogonality) transformation coefficients; k1, k2, k3, k4 = radial distortion coefficients; p1, p2, p3, p4 = tangential distortion coefficients.

A substantial difference existed for some parameters between optimized camera internal parameters derived from pre-calibration versus self-calibration. Self-calibration Run 1, which used a focal length only as an initial value, provided no solution for affinity and skew coefficients and no solutions for some of the higher-order radial distortion coefficients and

tangential coefficients. By comparison, Self-calibration Run 2 used the optimized values from pre-calibration as the initial parameter values for implementing the self-calibration procedure in Metashape. This process resulted in slightly larger differences for the principal point locations than Run 1. This effect was unexpected, suggesting the Metashape algorithm does not weigh the self-calibration too heavily based on the initial values provided from pre-calibration. Both Run 1 and Run 2 had similar values for the optimized focal length.

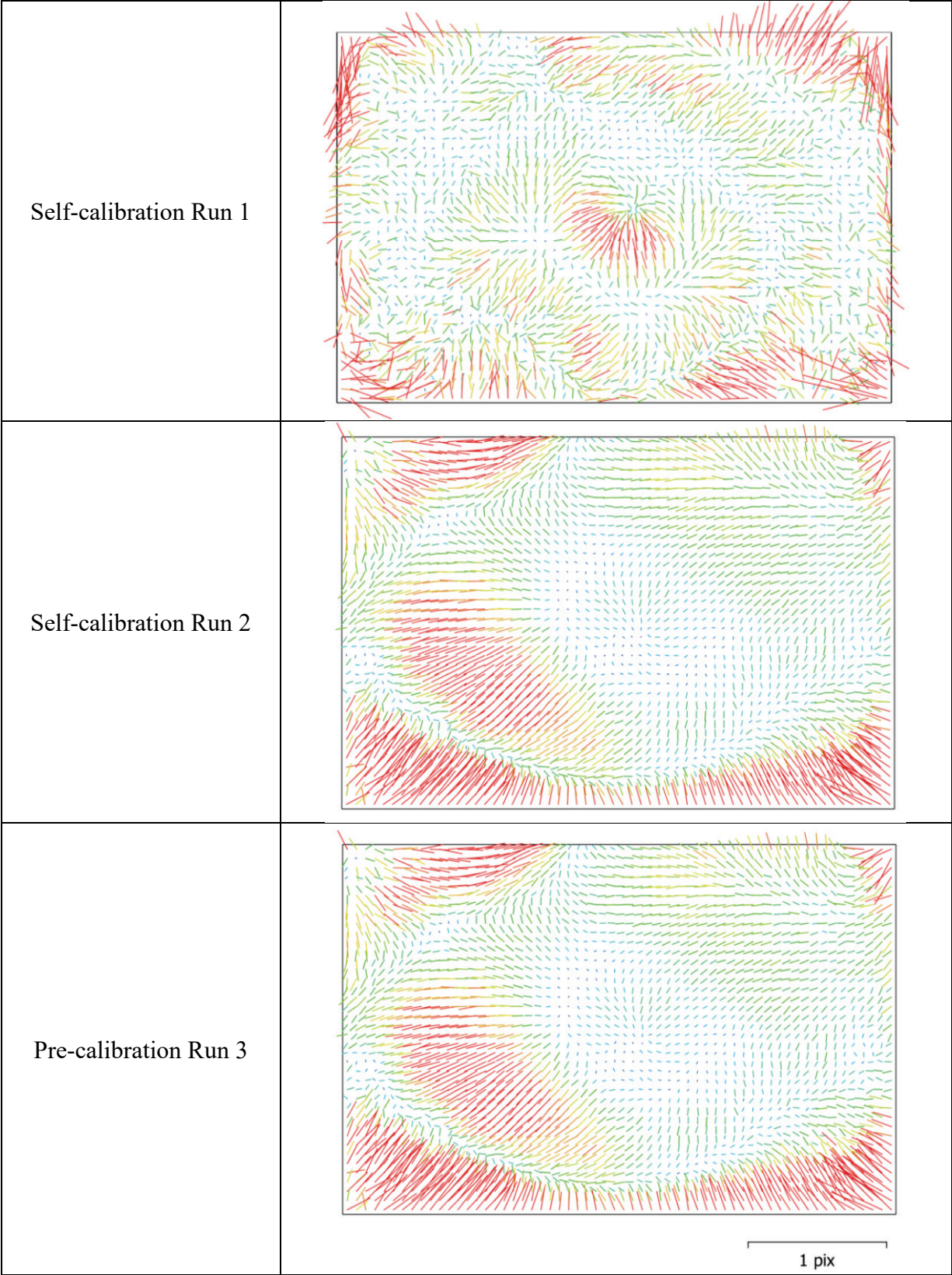
Self-calibration Run 2 produced much closer estimates of distortion and skew coefficient values relative to the pre-calibration result than Run 1. Run 2 derived coefficient solutions for all radial and tangential parameters, whereas Run 1 did not. The results show the potential value in using pre-calibration to set more realistic initial camera internal parameters to aid the self-calibration routine in SfM software.

The results highlighted differences in camera calibration stemming from pre-calibration versus self-calibration approaches. Pre-calibration may be useful in cases where self-calibration does not provide a decent result based on the imaging network geometry or reduced scene texture, such as under suboptimal lighting or weather conditions. It may also prove useful for processing UAS imagery acquired with metric or higher-grade, more stable digital cameras.

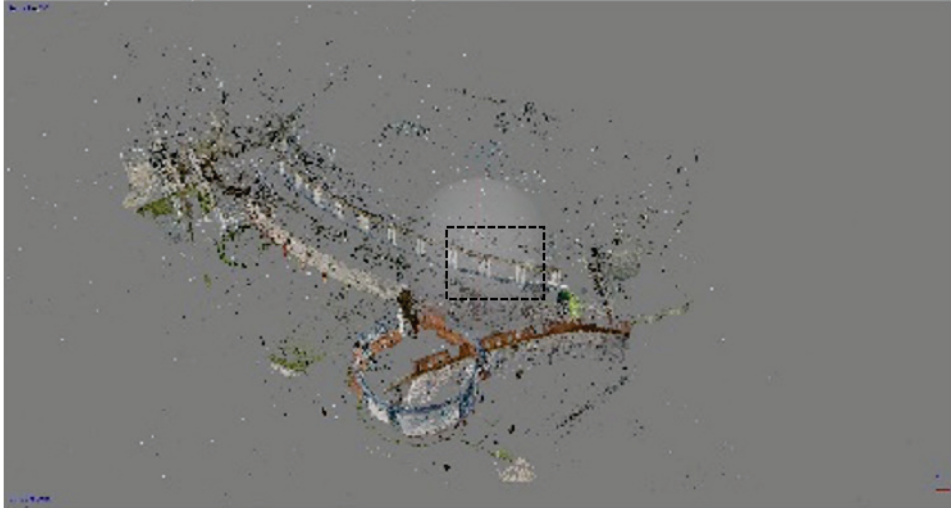
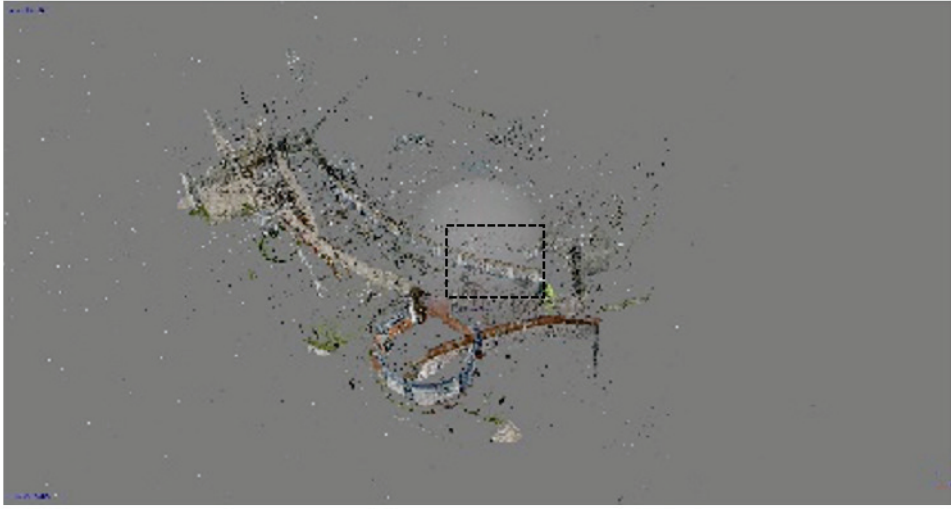
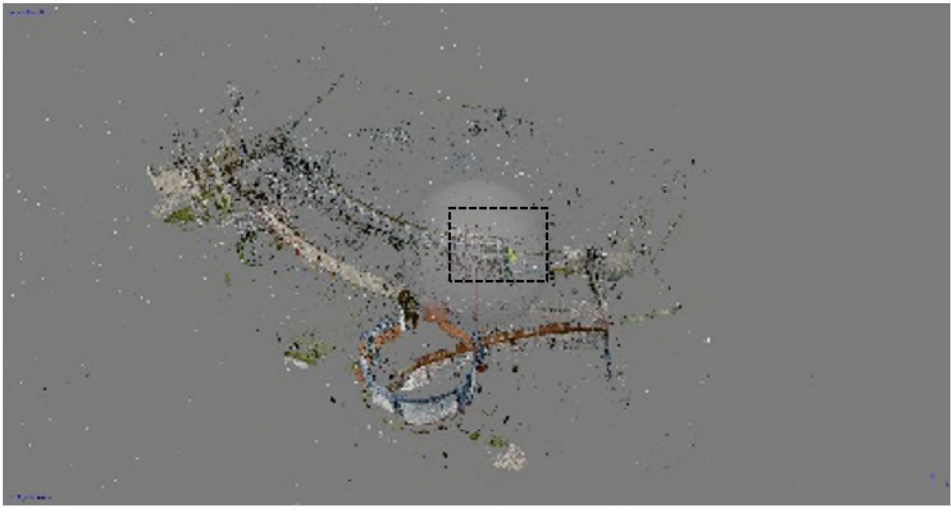
The results show the sensitivity of SfM reconstruction to variations in the optimized camera calibration solutions, which can result from self-calibration approaches, pre-calibration approaches, or a combination between them. It is advisable to monitor the UAS camera's calibration solution over time. As values start to vary, a pre-calibration may prove useful in setting new initial values for use in the SfM software's self-calibration procedure.

Figure 147 shows the estimated camera distortion based on Metashape's calibration solution for the self-calibration and pre-calibration scenarios. The primary observation here is to notice the difference in estimated distortion between self-calibration Run 1 and Run 2 due to the initial parameters provided. Run 2 had a similar distortion to the pre-calibration run.

Figure 148 shows sparse point clouds generated from SfM processing of the set of handheld images gathered for the ECDC building on the TAMUCC campus. The sparse point clouds represent solutions based on self-calibration Run 1, self-calibration Run 2, and pre-calibration Run 3—all processed within Metashape. Run 3 had the calibration values locked during SfM reconstruction based on the values from pre-calibration. The box shown in Figure 148 highlights a region along the backside of the building where noticeable differences in sparse point cloud reconstruction occurred between the different calibration scenarios. This result further illustrates the impact of differing calibration solutions on the point cloud products produced by SfM software.



**Figure 147. Estimated Camera Lens Distortion for Each Calibration Scenario.**

<p>Self-calibration Run 1</p>	
<p>Self-calibration Run 2</p>	
<p>Pre-calibration Run 3</p>	

**Figure 148. Sparse Point Clouds of the ECDC Building on the TAMUCC Campus Generated from the Different Calibration Processing Scenarios with Metashape.**

## Lessons Learned

Major lessons learned from the calibration exercise included the following:

- Self-calibration experiment with Pix4D:
  - Scenario 1 had the largest difference between initial and optimized camera internal parameter values. The initial values came from the manufacturer values for the DJI Mavic 2 Pro Hasselblad camera. The same values were also used for the camera model within Blender to render and simulate imagery. Because the same values were used in the simulation, a large deviation from the initial values after self-calibration indicates a less accurate solution relative to the other five scenarios examined.
  - Scenario 1 had a 9.5 percent difference between initial and optimized internal camera parameters versus a 2.8 percent relative difference when four GCPs were added to aid calibration (i.e., Scenario 2). This finding shows the benefit of adding GCPs to a UAS survey to help optimize the self-calibration solution in Pix4D.
  - Most of the difference between Scenario 1 and Scenario 2 resulted from poor estimation of the focal length. Correct focal length estimation is one of the most crucial components in a camera calibration model because small errors can result in highly exaggerated surface point coordinates through photogrammetric reconstruction.
  - Scenarios 3 and 4 demonstrated the potential benefit of the all prior setting in Pix4D. Both scenarios resulted in optimized values close to the initial values, with no change in focal length but slight changes in the optimized principal point location, which resulted in a better calibration solution than standard self-calibration. Pix4D states that a difference greater than 5 percent between initial and optimized parameter values may indicate a problem with the calibration. In such cases, it is recommended to apply the all prior setting to stabilize the calibration. This setting constrains (i.e., weighs) the solution based on the initial parameter values provided to Pix4D.
  - Scenario 6 showed optimized values close to the initial values for the internal camera parameters without using the all prior setting, which indicates that accurate camera geolocations, such as those obtained from RTK/PPK GNSS, can aid Pix4D in reoptimizing the solutions for the self-calibration values, similar to GCPs. The advantage is that accurate geolocations apply to the entire image set, whereas the influence of GCPs is constrained to the area/boundary defined by the control target network.
  - Some differences existed in correlation levels among parameters. Ideally, the internal parameters should be independent. However, some degree of correlation between parameters is expected for most projects. For example, correlation between the radial distortion parameters is expected because the correlation values are bounded by the physical constraints of the lens.
  - Scenario 1 showed a high correlation between the focal length and radial distortion parameters compared to Scenario 2, which used GCPs. Scenario 1 had issues resolving an accurate focal length, and this problem is reflected in the correlation matrix provided by the Pix4D quality report. Correlation of focal



length to radial distortion is a known occurrence, but the degree to which it degrades the SfM solution depends heavily on the accuracy of the optimized internal parameter solutions (e.g., focal length) and EO solution. Results showed that in this case, this high correlation degraded the absolute positional accuracy of the reconstructed point cloud.

- A strong correlation between two important parameters, focal length and principal point, is an indicator of a potential problem with the reconstruction. In such a scenario, applying the all prior constraint is recommended. Scenarios 3 and 4, which applied the all prior setting to the initial camera internal parameter values used for self-calibration, showed no correlation of distortion values with respect to the focal length or between leading parameters. This effect is desirable and demonstrates the benefit of the all prior setting in aiding self-calibration solutions in Pix4D when good initial internal parameter values are provided.
- Scenario 1 exhibited some vertical distortion effects. Poor calibration of the camera model is a common source of radial distortion for UAS-SfM generated point clouds. Unless camera models accurately represent distortion effects, the result is frequently broad scale deformations, such as doming or bowing. These errors are most evident on flatter, structure-limited surfaces.
- Scenario 2 and Scenario 5 resulted in the largest RMSE for the absolute geolocation error. It appears that adding the GCP coordinates constrained the SfM solution of exterior camera position and forced it to compensate by adjusting camera positions more in the Z component. Fixed-calibration affected the solution of exterior camera position more in the X-Y components. Results were similar for the absolute orientation error.
- Scenario 1 produced the worst absolute SfM reconstruction accuracy on the checkpoint error. Most of this error resulted from the large error in the Z component. Scenario 2, which used GCPs, had a much better positional accuracy. This result further shows the value of having GCPs to aid self-calibration. In self-calibration, a poorly estimated focal length can result in poor optimization of other distortion coefficients. Proper estimation of focal length becomes even more important when using single-scale nadir-only imagery acquired over linear topographies (e.g., flat roadways flown at a single height).
- Scenarios 3 and 4 had a low RMSE for the checkpoint error. Using the all prior setting with realistic initial camera internal parameter values aided the overall SfM reconstruction accuracy. Interestingly, weighing the solution by the leading parameters performed better in terms of positional accuracy than weighing the solution by the leading parameters plus distortion parameters. This finding suggests that it may be better to apply the all prior setting only to the leading parameters during a self-calibration solution with Pix4D.
- Scenario 5 resulted in the second most erroneous solution, which was caused by inaccurate estimation of camera external parameters (absolute position and orientation). More investigation is needed to understand how Pix4D integrates fixed calibrations into the SfM reconstruction.
- Scenario 6, along with Scenario 2, resulted in the lowest RMSE overall for checkpoint error. This result showed the benefit of using a UAS integrated with an RTK/PPK-enabled GNSS to provide accurate camera geolocations. It further

showed the importance of including GCPs in the reconstruction to aid the calibration when relying on inaccurate geolocations or processing UAS data acquired from imaging networks that are not ideal for self-calibration, such as nadir-only perspectives acquired over relatively flat terrain reliefs.

- The results showed the interplay between the optimization of internal camera parameters through self-calibration and external camera parameters (position and orientation) within the SfM BA procedure. The camera calibration values, based on the different self-calibration processing scenarios, affected the 3D reconstruction of camera position and orientation and point cloud accuracy.
- Pre-calibration and self-calibration experiments with Metashape:
  - A substantial difference existed for some parameters between optimized camera internal parameters derived from pre-calibration versus self-calibration. Self-calibration Run 1, which used a focal length only as an initial value, provided no solution for affinity and skew coefficients, and no solutions for some of the higher-order radial distortion coefficients and tangential coefficients. By comparison, Self-calibration Run 2 used the optimized values from pre-calibration as the initial parameter values for implementing the self-calibration procedure in Metashape. This process resulted in slightly larger differences for the principal point locations than in Run 1. This finding was unexpected and suggests that the Metashape algorithm does not weigh the self-calibration too heavily based on the initial values provided from pre-calibration. Both Run 1 and Run 2 had similar values for the optimized focal length.
  - Self-calibration Run 2 produced much closer estimates of distortion and skew coefficient values relative to the pre-calibration result compared to Run 1. Run 2 derived coefficient solutions for all radial and tangential parameters, whereas Run 1 did not. The results show the potential value in using pre-calibration to set more realistic initial camera internal parameters to aid the self-calibration routine in SfM software.
  - The results highlighted differences in camera calibration resulting from pre-calibration (Run 3) versus self-calibration approaches (Runs 1 and 2). Pre-calibration (Run 3) may be useful in cases where self-calibration does not provide a decent result based on the imaging network geometry or reduced scene texture, such as under suboptimal lighting or weather conditions. It may also prove useful for processing UAS imagery acquired with metric or higher-grade, more stable digital cameras.
  - The results showed the sensitivity of SfM reconstruction to variations in the optimized camera calibration solutions, which can result from self-calibration approaches, pre-calibration approaches, or a combination of both. It is advisable to monitor the UAS camera's calibration solution over time. As values start to vary, a pre-calibration may prove useful in setting new initial values for use in the SfM software's self-calibration procedure.

## IMPACT OF SUBOPTIMAL CONDITIONS ON VISUAL IMAGE QUALITY

The research team examined the impact of fog and high wind speed on the visual quality of UAS data. The research team conducted a series of simulation runs to generate synthetic images resulting from reduced visibility due to fog and motion blur. Next, the research team quantified and evaluated UAS image quality degradation and its impact on crash scene reconstruction. The research team focused on feature extraction and matching between images (which are part of SfM Stage 1, as described earlier). A previous section handled fog at two general visibility levels: high visibility and low visibility. This section provides in-depth view by evaluating the effect of different levels of visibility and weather condition on the number of pairwise matches and number of 3D points in the crash scene reconstruction.

### General Concepts

#### *Impact of Fog on Crash Scene Features*

Fog affects the perception of features differently depending on how far away the features (and elements on the surface of the features) are with respect to the point of observation. As the distance from the camera increases, the effect of fog increases. Therefore, to simulate the effect of different levels of fog on imagery captured by a camera it is necessary to have information about the 3D characteristics of the objects depicted on the imagery.

The impact of fog on an image can be simulated by using depth map information and the meteorological optical range (MOR) to estimate the decrease in radiance for each pixel on the image. The depth map is generated by measuring the distance between a pixel on an image and the corresponding real-world object (as represented in a 3D model, e.g., using a 3D point cloud).

The effect of fog on a given pixel based on its associated depth map can be expressed as (114):

$$F(x) = t(x)R(x) + [1 - t(x)]L \quad (16)$$

where:

$F(x)$  = radiance at pixel  $x$  due to fog impact,

$t(x)$  = transmittance at pixel  $x$ ,

$R(x)$  = clear scene radiance at pixel  $x$ , and

$L$  = ambient light in an image.

The radiance received by the camera includes attenuated radiance from the scene and ambient light reflected into the line of sight by atmospheric particles. Particles in the atmosphere absorb or scatter light as it travels from the scene to the camera.

In this section, ambient light is estimated from pixel brightness data. To this end, images are decomposed into hue, saturation, and brightness, and then pixels with the highest brightness are selected to estimate ambient light. Brightness is calculated as follows (115, 116):

$$\text{Brightness} = \left[ \text{Max} \left( \frac{R}{255}, \frac{G}{255}, \frac{B}{255} \right) + \text{Min} \left( \frac{R}{255}, \frac{G}{255}, \frac{B}{255} \right) \right] / 2 \quad (17)$$

According to the Beer-Lambert law, transmittance is a function of the depth map distance associated with a pixel, as follows (117):

$$t(x) = e^{-\beta l(x)} \quad (18)$$

$$l(x) = \sqrt{\frac{f^2 + p(x)^2 + q(x)^2}{f^2}} \text{ depth}(x) \quad (19)$$

where:

$\beta$  = attenuation coefficient,

$l(x)$  = distance obtained from the depth map information of the pixel,

$f$  = focal length,

$p(x)$  = distance of pixel  $x$  from the image center on the width axis,

$q(x)$  = distance of pixel  $x$  from the image center on the height axis, and

$\text{depth}(x)$  = depth information at pixel  $x$ .

MOR is the distance needed to reduce the luminous flux of a collimated beam (i.e., light that emits parallel rays) from a 2700-K color temperature to 5 percent of the original value. MOR varies with the amount of fog (e.g., >50 km [30 mi] for clear weather or 10 m [33 ft] for heavy fog). MOR is related to the attenuation coefficient, as follows (114):

$$MOR = 2.996/\beta \quad (20)$$

where:

MOR = meteorological optical range (m).

Table 75 illustrates the relationship between  $\beta$  and MOR. Fog intensity is often reported in terms of visibility in weather reports. Visibility is a measure of the distance at which a target object can be clearly discerned. Table 75 shows the relationship between MOR and visibility (118). Table 75 also shows a characterization of fog intensity based on commonly used weather condition perceptions (i.e., light fog, moderate fog, thick fog, and dense fog) (119).

**Table 75. Relationship between Attenuation Coefficient, MOR, and Visibility.**

$\beta$	MOR		Visibility (118)		Weather Condition (119)
	(m)	(ft)	(m)	(ft)	
0.003	1000	3281	1000	3281	Light fog
0.005	600	1969	720	2362	Moderate fog
0.01	300	984	420	1378	Thick fog
0.02	150	492	262	860	Thick fog
0.03	100	328	200	656	Thick fog
0.06	50	164	112	367	Dense fog
0.08	37.5	123	87	285	Dense fog
0.10	30	98	72	236	Dense fog
0.12	25	82	65	213	Dense fog
0.14	21.4	70	56	185	Dense fog
0.16	18.7	61	50	163	Dense fog

### *Impact of Wind and Exposure Time on Crash Scene Features*

Motion blur is a smearing effect on an image (e.g., due to long exposure or rapid movement of the camera or objects). Several factors can influence motion blur for cameras onboard UASs, including wind speed and camera exposure time.

For the analysis, the research team assumed the UAS flies on a plane parallel to the image plane without rotational movement. In other words, the simulation assumed a UAS equipped with a perfectly functioning gimbal (120, 121). The simulation assumed wind speeds up to 10 m/s (22 mph) and exposure times between 1/500 and 1/60 seconds.

The distance traveled by a camera while the camera shutter is open can be expressed as:

$$X = VS \times t_{ex} \quad (21)$$

where:

$X$  = distance traveled by the UAS at the time of exposure,  
 $VS$  = UAS speed (m/s), and  
 $t_{ex}$  = exposure time (seconds).

A heterogeneous depth-aware motion flow for individual pixels can be expressed as (122):

$$\delta_{(i,j)} = f \frac{x}{d_{(i,j)}} \quad (22)$$

where:

$f$  = focal length,  
 $d_{(i,j)}$  = depth information at location  $i,j$  in a given image (in pixels), and  
 $\delta_{(i,j)}$  = motion flow at location  $i,j$  in a given image (in pixels).

With respect to the location of the camera, objects closer to the camera experience greater relative motion than objects farther away. As the exposure time increases, the UAS travels a longer distance, and thus, the motion effect is more pronounced. Therefore, to simulate the effect of motion blur on imagery captured by a camera, it is necessary to have information about the 3D characteristics of the objects depicted on the imagery.

Conceptually, the amount of motion blur for each pixel can be expressed as (123):

$$Y = K * C + N \quad (23)$$

where:

$Y$  = matrix representing image with motion blur effect,  
 $*$  = convolution operation,  
 $K$  = heterogeneous motion blur kernel map with different blur kernels for each pixel in  $C$ ,  
 $C$  = matrix representing the original sharp image, and  
 $N$  = additive noise.

## Methods

### *Impact of Fog on Crash Scene Features*

For the simulation, the research team used the same crash scene provided by NUCPS that was used in previous sections. The purpose of the simulation was to analyze the extent to which the degraded visual quality of UAS data due to fog could affect the performance of SfM. Specifically, the research team focused on feature extraction and matching and 3D point cloud reconstruction (i.e., SfM Stages 1 and 2).





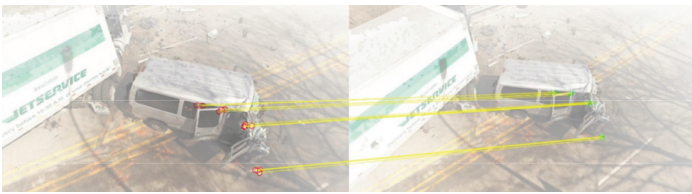
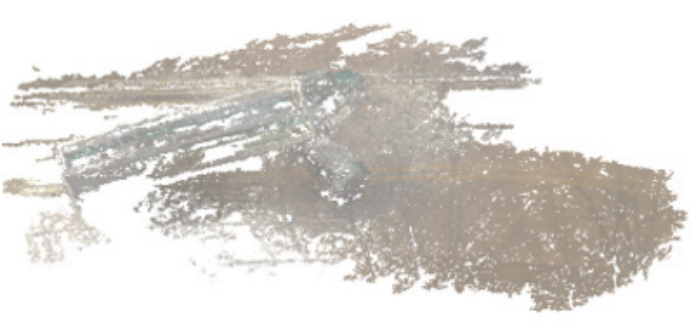
Figure 149 illustrates the workflow to conduct the simulation. After preparing a 3D point cloud, the research team established the association between 3D points in the point cloud and 2D pixels in the collected UAS data. At each camera location, the research team prepared a depth map image by measuring the distance between each 2D pixel and its corresponding point in the 3D point cloud. In order to enhance the depth map quality for simulation, the research team performed a morphological linear interpolation to retrieve the pixel values associated with the gaps in the incomplete depth maps (i.e., filling gaps in the incomplete point cloud) (124). Next, the research team calculated radiance at the 2D pixel level for different fog levels. Finally, the research team used the SfM process to conduct feature extraction and matching for different fog levels, as well as prepare the corresponding 3D point clouds.

For comparison purposes, the research team completed simulation runs for two scenarios:







- **Scenario 1 (Original UAS imagery).** The original crash took place in Illinois in March 2018. UAS data collection began at 11:43 AM and ended at 12:20 PM. The solar elevation at the location of the crash was 48 degrees (125, 126). The corresponding sunlight intensity was around 80,300 lux (127). Although fog at noon is infrequent, simulating fog conditions for the original imagery was important for context.
- **Scenario 2 (Early morning imagery).** The research team reduced the ambient light associated with the original imagery to reflect a hypothetical crash during the early morning hours such that UAS data collection started four hours earlier than the actual crash (i.e., around 7:40 AM). Under this hypothetical scenario, the solar elevation was 20 degrees and the sunlight intensity was around 36,900 lux. With this information, the research team reduced the ambient light associated with the original imagery by 54 percent. It is worth noting that this adjustment had an overall impact on image brightness but could not modify the extent of shadows in the imagery.

### *Impact of Wind on Crash Scene Features*

The research team conducted simulations of UAS data degradation for different wind speeds and exposure time. Similar to the fog simulation, the research used the enhanced depth map and affected each 2D pixel by a convolution process of the kernel function to simulate motion blur. After completing this step, the research team used the SfM process to conduct feature extraction and matching for different wind speed and exposure time values as well as prepare the corresponding 3D point clouds Figure 150 illustrates the corresponding workflow.

<p>Prepare 3D point cloud from original crash scene imagery.</p>	
<p>Prepare depth map by measuring the distance between each 2D pixel and its corresponding point in the 3D point cloud.</p>	
<p>Enhance depth map through a morphological linear interpolation.</p>	
<p>Calculate radiance at the 2D pixel level for different fog levels.</p>	
<p>Use SfM process to conduct feature extraction and matching for different fog levels.</p>	
<p>Use SfM process to prepare sparse 3D point clouds for different fog levels.</p>	

**Figure 149. Workflow to Simulate and Analyze Fog Impacts.**

<p>Prepare 3D point cloud from original crash scene imagery.</p>	
<p>Prepare depth map by measuring the distance between each 2D pixel and its corresponding point in the 3D point cloud.</p>	
<p>Enhance depth map through a morphological linear interpolation.</p>	
<p>Apply motion blur to each 2D pixel for different wind speeds.</p>	
<p>Use SfM process to conduct feature extraction and matching for different wind speed and exposure time values.</p>	
<p>Use SfM process to prepare sparse 3D point clouds for different wind speed and exposure time values.</p>	

**Figure 150. Workflow to Simulate and Analyze Motion Blur Impacts.**



## Results

### *Impact of Fog on Crash Scene Features*

Figure 151 shows sample images of the original UAS crash scene (i.e., Scenario 1). Figure 152 shows a sample of original UAS images with different MOR values. The visual impact of fog was to reduce texture within the imagery by creating a “whiteout” effect. Figure 153 show a sample of simulated early morning images with different MOR values (i.e., Scenario 2). As before, the visual impact of fog was to reduce texture within the imagery. However, because the imagery had a lower ambient light (7:40 AM instead of noon), the images were also darker, therefore reducing the relative impact of the whiteout effect. Darkness became more pronounced as the MOR value decreased.

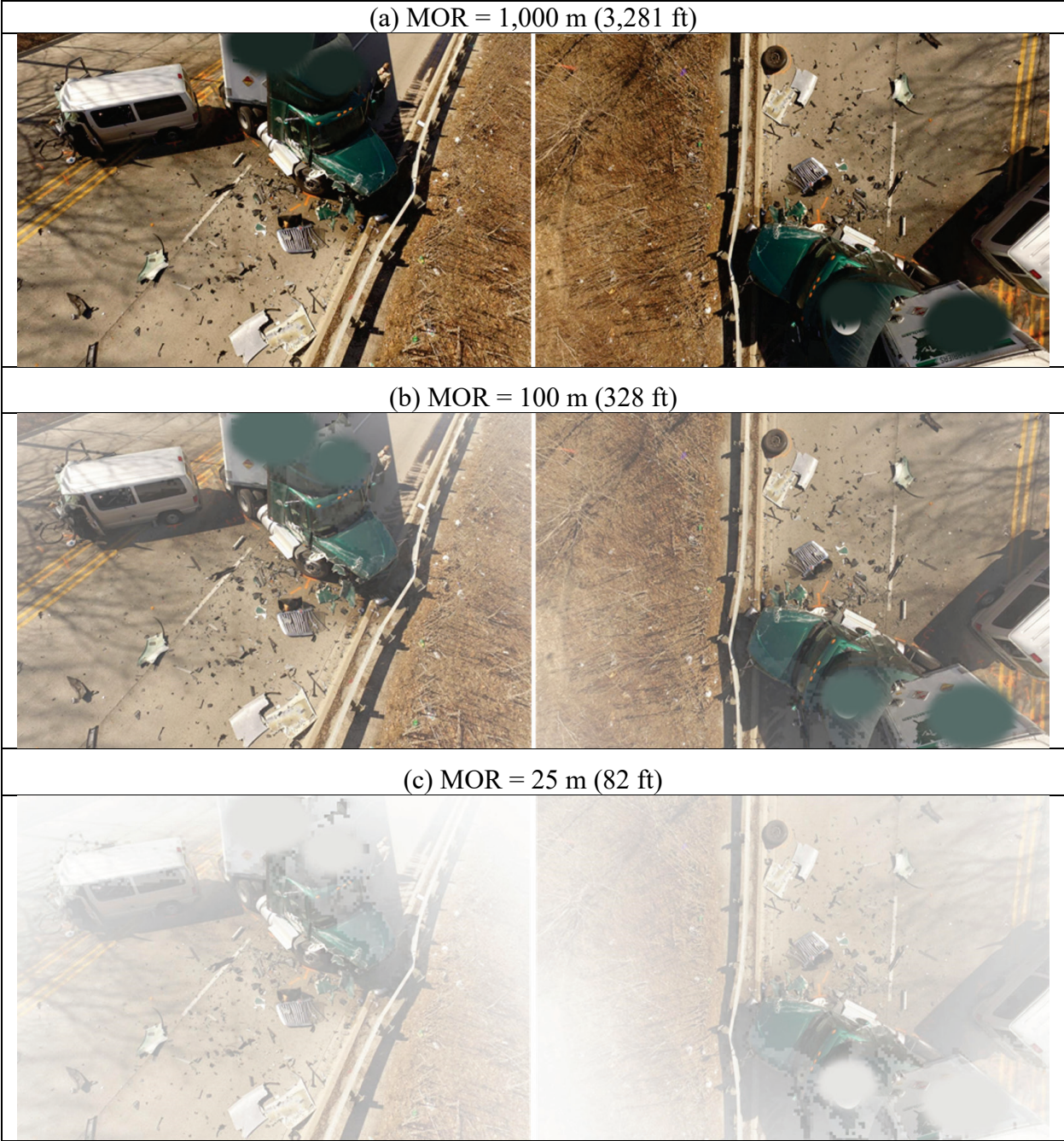


**Figure 151. Original UAS Imagery.**

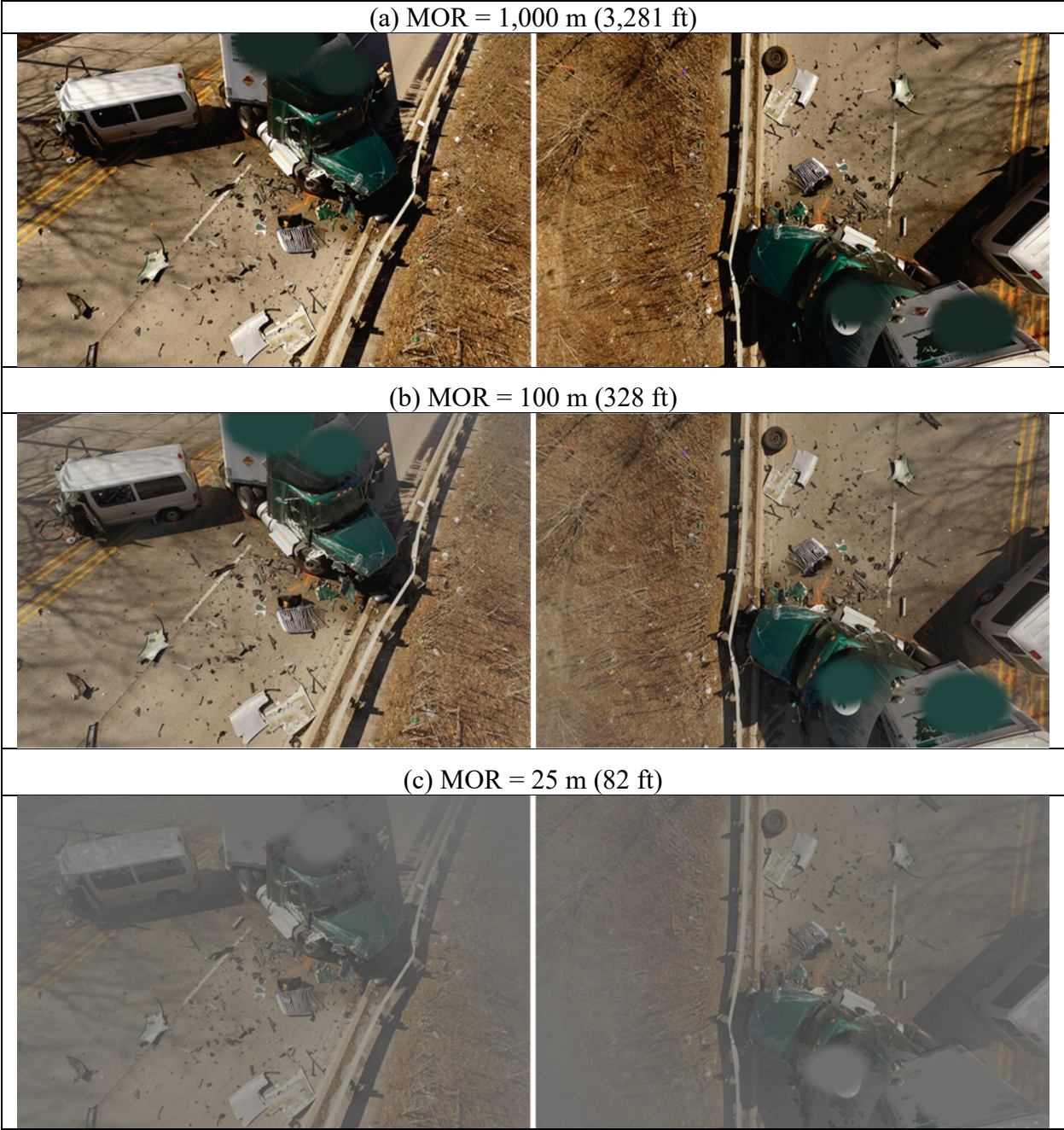
For each MOR value, the research team used the SfM process to extract and match features. To illustrate, Figure 154 shows a sample of matched features associated with the original imagery, for the case where MOR = 1,000 m (3,281 ft). In the figure, each pair of left and right images show the crash scene from two different aerial perspectives. The circles on each image (red on the left image and green on the right image) correspond to matched features. The straight yellow lines connect matched features on the left and right images.

In general, as the MOR values decreased (i.e., as the fog became denser), the number of matched features decreased. Interestingly, the total number of matched features for the early morning imagery did not decrease substantially in relation to the number of matched features for the original imagery. In fact, for many of the images, the number of matched features actually increased, although only slightly.

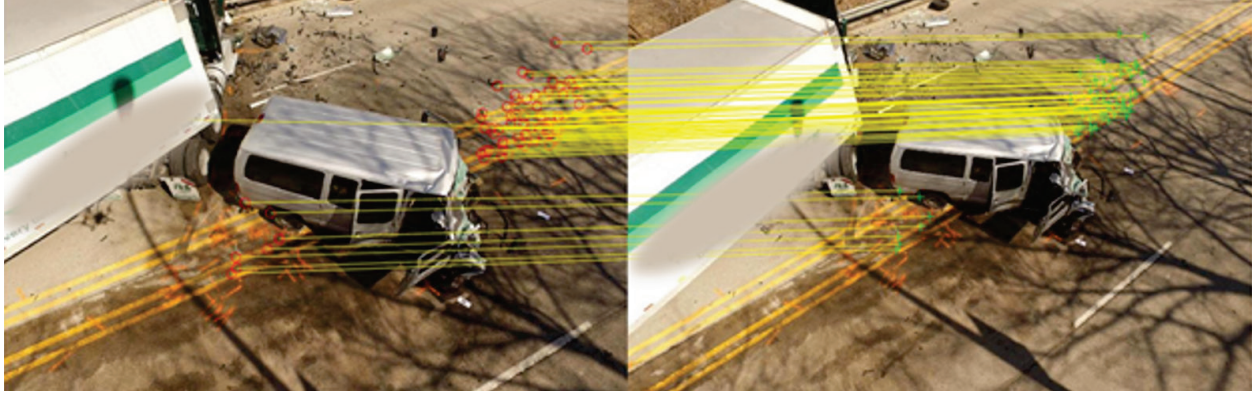
The final step involved the reconstruction of 3D points. Table 76 shows the number of points in the sparse 3D point cloud for each MOR value as well as the corresponding reduction in the number of 3D points with respect to the original UAS imagery. Table 77 shows the number of points in the sparse 3D point cloud for each MOR value as well as the corresponding reduction in the number of 3D points with respect to the early morning imagery.



**Figure 152. Original UAS Imagery with Different MOR Values.**



**Figure 153. Simulated Early Morning Imagery with Different MOR Values.**



**Figure 154. Original UAS Imagery Feature Matching (MOR = 1000 m).**

**Table 76. Number of Points in the 3D Point Cloud (original UAS Imagery).**

MOR (m)	Visibility (m)	Weather Condition	No. Points in 3D Point Cloud Model	Reduction in No. of Points
Clean Image	Clean Image	No fog	81,607	
1000	1000	Light fog	77,656	4.8%
600	720	Moderate fog	75,465	7.5%
300	420	Thick fog	74,457	8.8%
150	262	Thick fog	70,442	14%
100	200	Thick fog	66,522	18%
50	112	Dense fog	49,151	40%
37.5	87	Dense fog	40,116	51%
30	72	Dense fog	28,630	65%
25	65	Dense fog	21,782	73%

**Table 77. Number of Points in the 3D Point Cloud (Early Morning Imagery).**

MOR (m)	Visibility (m)	Weather Condition	No. Points in 3D Point Cloud	Reduction in No. of Points
50000	50000	No fog	78,945	
1000	1000	Light fog	77,110	2.3%
600	720	Moderate fog	75,799	4.0%
300	420	Thick fog	74,595	5.5%
150	262	Thick fog	69,847	12%
100	200	Thick fog	68,393	13%
50	112	Dense fog	50,609	36%
37.5	87	Dense fog	42,273	46%
30	72	Dense fog	32,434	59%
25	65	Dense fog	24,101	69%

As with the number of matched features, the number of points in the 3D point cloud decreased as the MOR values decreased (i.e., as the fog became denser). The reduction in the number of points in the 3D point cloud was relatively small for light or moderate fog levels. Even for thick

fog, the reduction in the number of points in the 3D point cloud was less than 20 percent. For dense fog, the reduction in the number of points in the 3D point cloud became much more pronounced. For the densest fog (i.e., visibility of 65 m [213 ft]), the reduction in the number of 3D points was about 70 percent.

This result indicates that UASs and the SfM process can perform well under foggy weather conditions, but performance will degrade quickly if fog is dense. It is also important to note that overlap plays an important role. As documented in a previous section, a significant improvement in the number of matched feature points and 3D points occurred when the overlap went from E60-S60 to E80-80. For the crash scene in Illinois, the target was a 75 percent overlap. In practice, the crash scene included several passes at different heights and oblique pictures, effectively increasing the overlap level significantly.

The reduction in the number of 3D points as a function of the fog level for the early morning imagery was similar to that for the original imagery. In fact, the number of 3D points assuming no fog was only slightly lower for the early morning imagery compared to the original imagery. Further, for thick or dense fog, the number of points in the 3D point cloud increased for the early morning imagery, although only slightly. This result is not surprising because the type of camera used, corresponding GSD (about 7 mm), and high overlap levels provided multiple feature redundancy opportunities, minimizing the impact of reduced ambient lighting associated with the early morning imagery. As documented in a previous section, the reduction in the number of 3D points increases significantly for darker sky conditions (e.g., during twilight or at dusk).

#### *Impact of Wind on Crash Scene Features*

Figure 155 shows a sample of the simulation outcomes. Each image represents the simulation outcome of UAS data for a specific combination of wind speed and exposure time. For each combination of wind speed and exposure time, the research team used the SfM process to extract and match features. In general, as the simulated blur increased, the blurring effect was more pronounced in the middle section of the images (where the vehicles were) due to the depth-aware motion effect (i.e., objects closer to a camera experience a relatively greater motion). As a result, feature matching was more evident in the top section of the images in situations where the blur was stronger (e.g., due to a longer exposure time of 1/60 or 1/125 seconds). By comparison, feature matching was more evident in the middle section of the images in situations where the blur was weak (e.g., a short exposure time of 1/500 seconds). If the blur was somewhat intermediate (e.g., due to a exposure time of 1/250 seconds), feature matching was more evenly distributed between the top and the middle sections of the images.

(a) wind speed = 10 m/s (22 mph); exposure time = 1/500 s



(b) wind speed = 6 m/s (13 mph); exposure time = 1/125 s



(c) wind speed = 2 m/s (4.5 mph); exposure time = 1/60 s



**Figure 155. Effect of Wind Speed on Motion Blur for Different Exposure Times.**

The research team used Motion System’s VisualSFM to perform a 3D reconstruction and examine the quality of the point cloud models (i.e., model completeness) depending on the degraded quality of UAS data used for the simulation. Table 78 shows the results of the quality degradation analysis for different wind speed and exposure time levels. For each combination, the research team conducted 10 trials to enable the calculation of average and standard deviation metrics. The table also shows the reduction in the number of pairwise matches, the number of points in the sparse 3D point cloud reconstruction, and the quality loss in the reconstruction. The quality loss was measured as the reduction in the number of 3D points in the crash scene reconstruction.

**Table 78. Reduction in the Number of Pairwise Matches and Sparse Point Cloud Points.**

Exposure Time (s)	Wind Speed		Number of Matches after 10 Trials		Reduction in No. of Pairwise Matches	No. Points in Sparse Point Cloud Reconstruction	Quality Loss in Reconstruction
	(m/s)	(mph)	Average	Standard Deviation			
1/60	2	4.5	4	0	95%	Failed	100%
	4	8.9	3	0	96%	Failed	100%
	6	13	0	-	100%	Failed	100%
	8	18	0	-	100%	Failed	100%
	10	22	0	-	100%	Failed	100%
1/125	2	4.5	12	0.7	84%	41,147	50%
	4	8.9	9	0.4	88%	37,240	55%
	6	13	7	0.9	91%	33,333	60%
	8	18	5	0.4	94%	29,509	64%
	10	22	5	0	94%	Failed	100%
1/250	2	4.5	33	2.9	57%	62,677	25%
	4	8.9	25	2.8	68%	60,598	27%
	6	13	24	3.3	69%	58,520	30%
	8	18	21	2.3	73%	56,608	32%
	10	22	22	2.8	72%	54,696	34%
1/500	2	4.5	57	4.1	26%	72,984	12%
	4	8.9	56	2.7	27%	72,402	13%
	6	13	50	3.2	35%	71,820	14%
	8	18	47	2.5	39%	70,823	15%
	10	22	44	1.7	43%	69,825	16%

## Lessons Learned

Major lessons learned from the simulation exercise included the following:

- The results showed a clear effect of fog on the software’s capability to reconstruct 3D points in the sparse point cloud. The number of points in the 3D point cloud decreased as the MOR values decreased (i.e., as the fog became denser). The reduction in the number of points in the 3D point cloud was relatively small for light or moderate fog levels. Even for thick fog, the reduction in the number of points in the 3D point cloud was less than 20 percent. For dense fog, the reduction in the number of points in the 3D point cloud became much more pronounced. For the densest fog (i.e., visibility of 65 m [213 ft]), the reduction in the number of 3D points was about 70 percent. These results indicate that

UASs and the SfM process can perform well under foggy weather conditions, but performance will degrade quickly if fog is dense.

- The reduction in the number of 3D points as a function of the fog level for the early morning imagery (synthetic) was similar to the reduction for the original noon-time imagery. This result is not surprising because the original UAS imagery was the result of a data collection strategy that provided multiple feature redundancy opportunities, thereby minimizing the impact of reduced ambient lighting associated with the early morning imagery.
- The results showed a clear effect of wind speed on the software's capability to reconstruct 3D points in the sparse point cloud. As the wind speed increased, the number of 3D points decreased. This result is consistent with results described previously.
- The results also showed the effect of exposure time on the software's capability to reconstruct 3D points in the sparse point cloud. In general, as the exposure time decreased, there was less motion blur, which resulted in a higher number of 3D points.
- In general, the results confirm the industry practice of not recommending the use of UASs when environmental conditions reach a certain threshold that make the results of the 3D reconstruction insufficient or unreliable.

## **IMPACT OF CAMERA PROPERTIES ON UAS IMAGE QUALITY TO GUIDE CRASH SCENE IMAGING**

The research team examined the impact of UAS speed and exposure time on the software's capability to reconstruct 3D point in a sparse point cloud. The research team conducted a series of simulation runs to generate synthetic images resulting from motion blur and noise due to these camera properties. The research team quantified and evaluated UAS image quality degradation and its impact on crash scene reconstruction. Specifically, the research team focused on feature extraction and matching between images (which are part of SfM Step 1, as described earlier). The research team used the 3D point cloud model that was used as input for the previous subtasks.

The research team also assessed the visual quality of 2D geospatial data products (i.e., orthomosaics) generated from a sample of UAS flight tests, with a specific focus on blurriness and lack of defined edges. Orthomosaic generation is based on orthorectification by removing perspective distortions from images using the DSM. An orthomosaic receives the DSM as input, and the DSM receives the densified point cloud as input. If the point cloud is noisy, the DSM is likely to be noisy, and, therefore, the orthomosaic is also likely to be noisy.

### **Methods**

The research team conducted simulations of UAS data degradation for different UAS speed and exposure time levels. To simulate motion blur, each pixel of each clean image was affected by a convolution process of the kernel function. The simulation process was similar to that used previously. To analyze the impact of different UASs and exposure times on crash scene features, the research team used general feature detection and matching algorithms, including the SIFT algorithm, to extract and match generic image features from both original and simulation datasets.



The maximum flying speed of most UASs is around 20 m/s (45mph) (128). Camera exposure time can vary from 8 to 1/8000 seconds. For the simulation, the research team varied the UAS speed from 5–25 m/s (11–56 mph) and varied the exposure time from 1/60 to 1/4000 seconds.

A common practice for crash reconstructions involves taking pictures while the UAS is stationary. Nevertheless, it was of interest to simulate the movement of a UAS, either because the motion was intentional or there was turbulence. As such, the analysis here complements other analyses described in previous sections.

To evaluate the impact of blurriness and lack of edges on the visual quality of orthomosaics, the research team used the variance of the Laplacian to assess the relative degree of focus of a sample of UAS flight test images (129). The Laplacian of an image highlights regions of rapid intensity change and can be used for edge detection. In general, a high variance of the Laplacian corresponds to a large number of responses (both edge and non-edge). Conversely, a low variance of the Laplacian indicates less response spread, which corresponds to fewer edges, thus suggesting the image is likely blurred. In addition to using the image processing algorithm, the research team visually examined orthomosaic features. The analysis involved completing the following steps on orthomosaics obtained from the Abbott, RELLIS Campus, and Florence flight tests (see Chapter 5):

- Extract a rectangular patch from the original orthomosaic for image processing.
- Convert the orthomosaic patch to grayscale.
- Apply convolution to the orthomosaic patch by using a  $3 \times 3$  Laplacian kernel.
- Compute the variance of the Laplacian and visually examine orthomosaic features.

## Results

Figure 156 illustrates the quality degradation of the images at different UAS speed and exposure time levels. Table 79 shows the relative decrease in the number of points in the 3D point cloud model.

Figure 157, Figure 158, and Figure 159 show the variance of the Laplacian responses in different orthomosaics. In general, orthomosaics from lower altitude flights produced a higher variance, indicating a wide spread of responses (both edge and non-edge) and suggesting an in-focus orthomosaic. When there is lower variance (e.g., flights with higher altitudes or more wind), a relatively smaller spread of responses exists, indicating there are smaller number of edges in the orthomosaic.

(a) UAS speed = 5 m/s (11 mph); exposure time = 1/500 s



(b) UAS speed = 10 m/s (22 mph); exposure time = 1/125 s



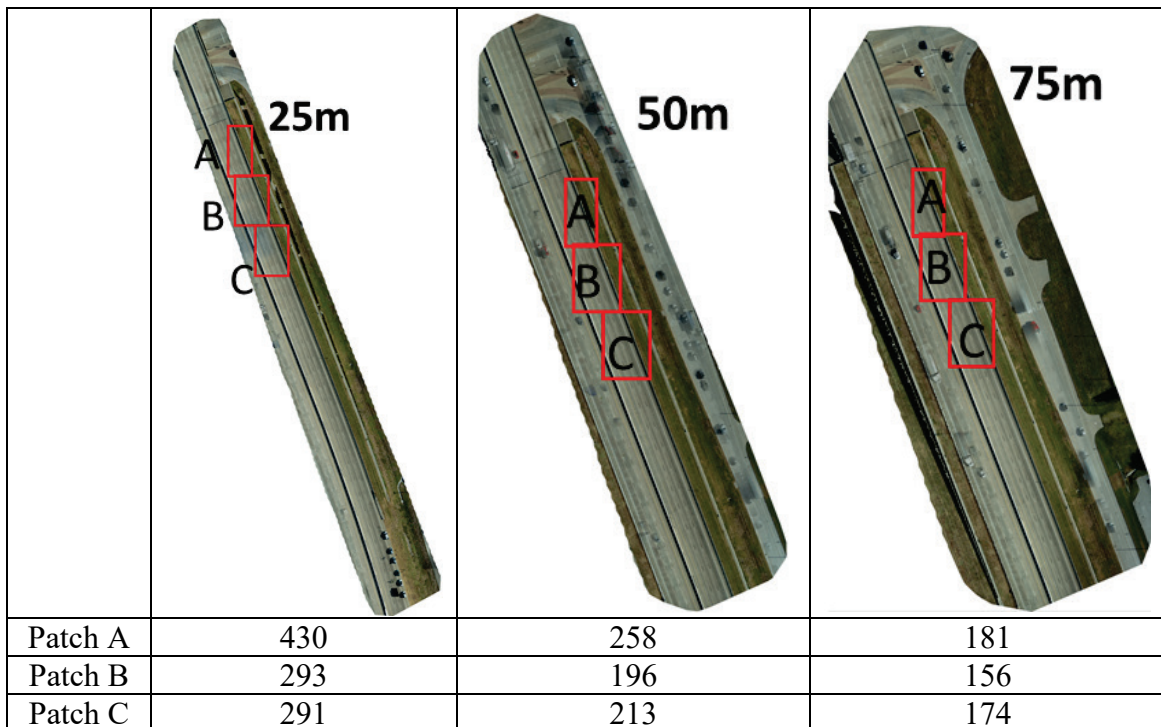
(c) UAS speed = 15 m/s (34 mph); exposure time = 1/60 s




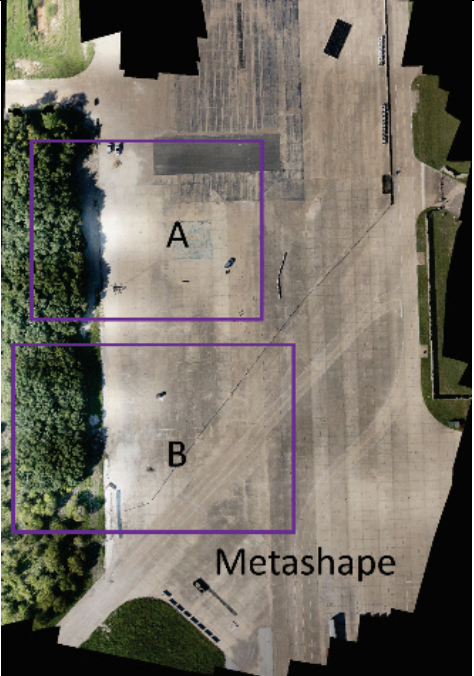
**Figure 156. Image Quality Degradation for Different Exposure Times and UAS Speeds.**

**Table 79. Reduction in the Number of Points in the 3D Point Cloud at Different UAS Speed and Exposure Time Levels.**

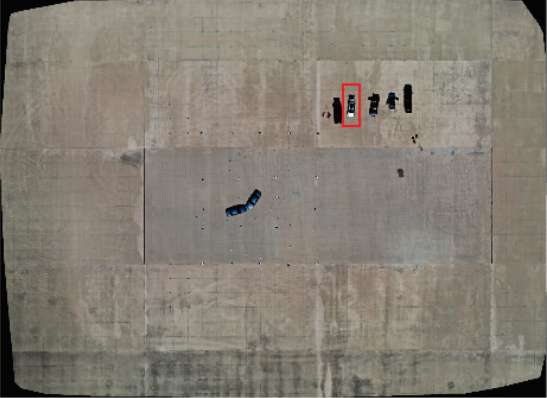
Exposure Time (s)	UAS Speed				
	5 m/s (11 mph)	10 m/s (22 mph)	15 m/s (34 mph)	20 m/s (45 mph)	25 m/s (56 mph)
1/60	23%	Failed	Failed	Failed	Failed
1/125	12%	22%	34%	46%	58%
1/250	6.1%	12%	16%	22%	28%
1/500	1.6%	6.1%	9.8%	12%	13%
1/1000	Negligible	1.6%	3.6%	6.1%	8.6%
1/2000	Negligible	Negligible	0.9%	1.6%	2.4%
1/4000	Negligible	Negligible	Negligible	Negligible	0.6%



**Figure 157. Variance of Laplacian for Orthomosaics Obtained in Abbott, Texas (Flight Altitudes: 25 m, 50 m, and 75 m).**

		
Pix4D	102	148
Metashape	113	172

**Figure 158. Variance of Laplacian for Orthomosaics Obtained at the RELLIS Campus (Orthomosaics Obtained with Pix4D and Metashape).**

		
Flight Date	01/15/2021	03/20/2021
Variance of Laplacian	33	43

**Figure 159. Variance of Laplacian for Orthomosaics Obtained in Florence, Texas (Orthomosaics Obtained from 01/15/2021 and 03/20/2021 Flights).**

## Lessons Learned

Major lessons learned from the simulation exercise included the following:

- The results showed a clear effect of UAS speed on the software's capability to reconstruct 3D points in the sparse point cloud. In general, as the UAS speed increased, the loss in the number of 3D points increased (i.e., the number of 3D points reconstructed decreased).
- The results confirmed the effect of exposure time on the software's capability to reconstruct 3D points in the sparse point cloud. In general, as the exposure time decreased, less motion blur occurred, and the loss in the number of 3D points decreased (i.e., the number of 3D points reconstructed increased).
- The results confirmed the correlation between low-altitude flights and the software's capability to generate in-focus imagery, including orthomosaics.



## CHAPTER 5. FIELD TESTING OF UAS FLIGHT OPERATIONS

### INTRODUCTION

This chapter describes the activities undertaken to collect and process UAS data under a variety of scenarios depicting vehicle crashes. The research team conducted seven flight tests:

- Test 1 (08/09/2020): Crash scene in Abbott, Texas, in conjunction with TxDPS. This crash scene was related to actual fatal crash on IH-35.
- Test 2 (08/25/2020): Simulated crash scene at Phil Hardberger Park in San Antonio, Texas. This test was used to test the functionality of the Mavic 2 Pro UAS.
- Test 3 (09/30/2020): Delivery truck crash test at the Texas A&M REELLIS Campus in College Station, Texas.
- Test 4 (10/07/2020): Passenger car crash test at the Texas A&M REELLIS Campus in College Station, Texas. This test was the first test that included GCPs surveyed by TAMUCC.
- Test 5 (12/07/2020): Delivery truck crash test with nighttime data collection at the Texas A&M REELLIS Campus in College Station, Texas. This test was the first test involving a nighttime run.
- Test 6 (01/15/2021): Simulated passenger car crash test with nighttime data collection at the TxDPS Tactical Training Facility in Florence, Texas.
- Test 7 (03/20/2021): Simulated passenger car crash test with nighttime data collection at the TxDPS Tactical Training Facility in Florence, Texas. This test included GCPs gathered by TAMUCC and TxDOT.

Unfortunately, it was not possible to conduct sample flights at actual fatal crash locations. Given the nature and scope of the data collection the research team was planning, the agencies in charge of approving the use of UASs for specific events (FAA at the federal level and the A&M System at the state level) did not issue approvals for the research team to collect data as originally intended. Nevertheless, the research team completed seven data collection tests, as described above.

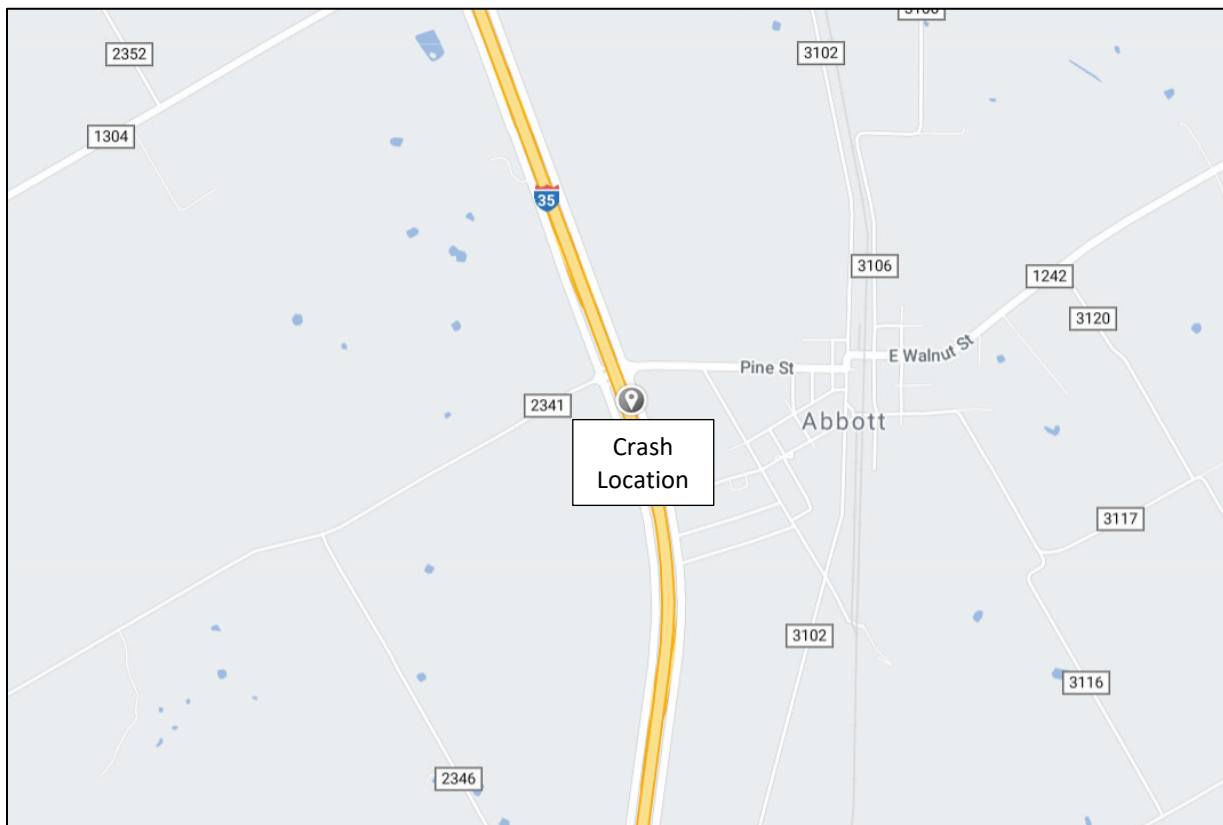
The research team divided the data collection and corresponding analyses into two large groups of activities. The first group (led by research team members at TAMUCC) focused on a systematic assessment of positional accuracies at the test locations, which included surveying GCPs and checkpoints used in all photogrammetry software processing. It also included an in-depth analysis of SfM data and calculations as well as TLS data.

The second group of activities (led by research team members at TTI) focused on typical activities associated with the reconstruction of crashes, leading up to the calculation of relative distances between points that are relevant to the crash reconstruction process.

## TEST LOCATIONS

### Test 1 (08/09/2020): Crash Scene in Abbott, Texas

The research team was invited to attend a TxDPS event to collect UAS data needed in connection with an actual fatal crash on IH-35 in Abbott, Texas (Figure 160). At the end of this event, the research team gathered additional UAS data. The crash, which happened a week earlier, affected all three main lanes in the northbound direction of IH-35. According to the crash report, a passenger vehicle traveling northbound hit the left-hand concrete barrier, bounced back and traversed all main lanes, hit the right-hand guardrail, bounced back and then was struck by a truck traveling in the northbound direction. To facilitate the UAS data collection (which took place on a Sunday morning), TxDOT closed all northbound main lanes. The southbound main lanes and the northbound frontage road remained open to traffic.

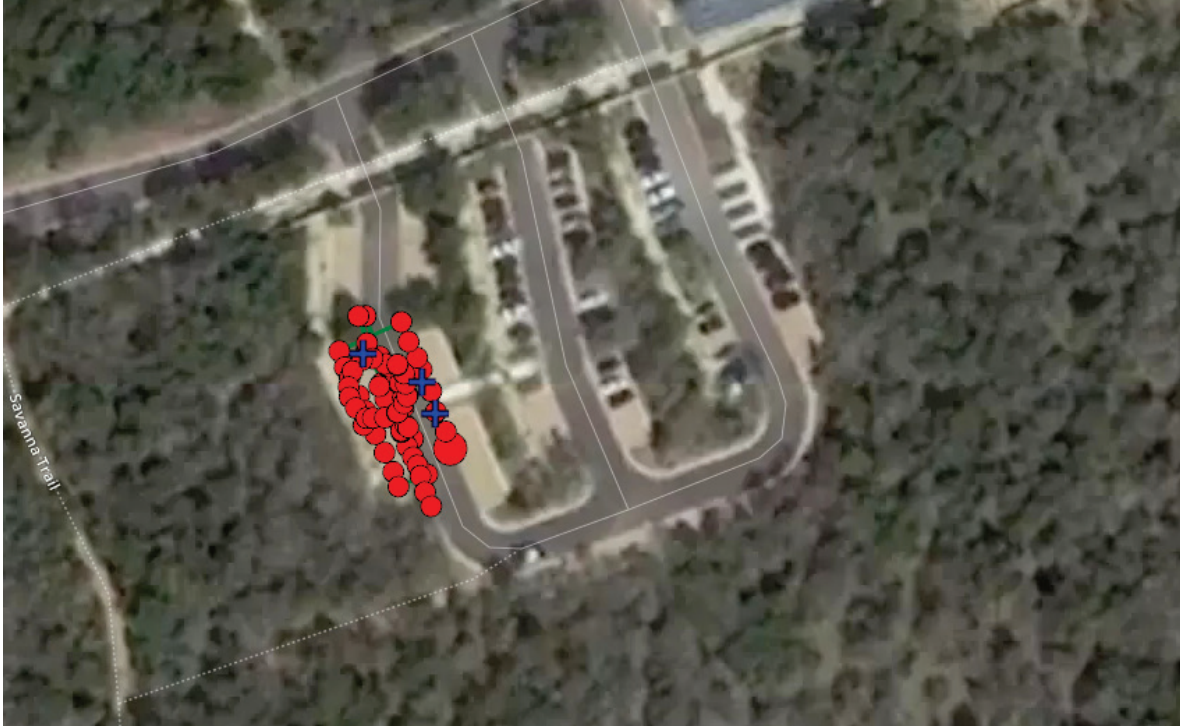


**Figure 160. Test Site Location (08/09/2020).**

### Test 2 (08/25/2020): Simulated Crash at Phil Hardberger Park, San Antonio, Texas

This data collection took place at Phil Hardberger Park in San Antonio, Texas (Figure 161). The purpose was to conduct an initial test of the functionality of the Mavic 2 Pro. The research team placed a vehicle in the parking lot and added some fictitious evidence on the ground using a chalk and traffic cones (Figure 162). This figure also shows a view of the 3D model that was generated using Pix4D.





**Figure 161. Test Site Location (08/25/2020).**



**Figure 162. Vehicle Location (08/25/2020).**

### Test 3 (09/30/2020): Crash Test at the RELLIS Campus, College Station, Texas

This data collection took place at the Texas A&M RELLIS Campus in College Station (Figure 163). A crash test scene took place in which a truck was let go against a guard rail at about 100 km/h (60 mph). The crash resulted in the truck rolling over at the end of the guard rail (Figure 164).

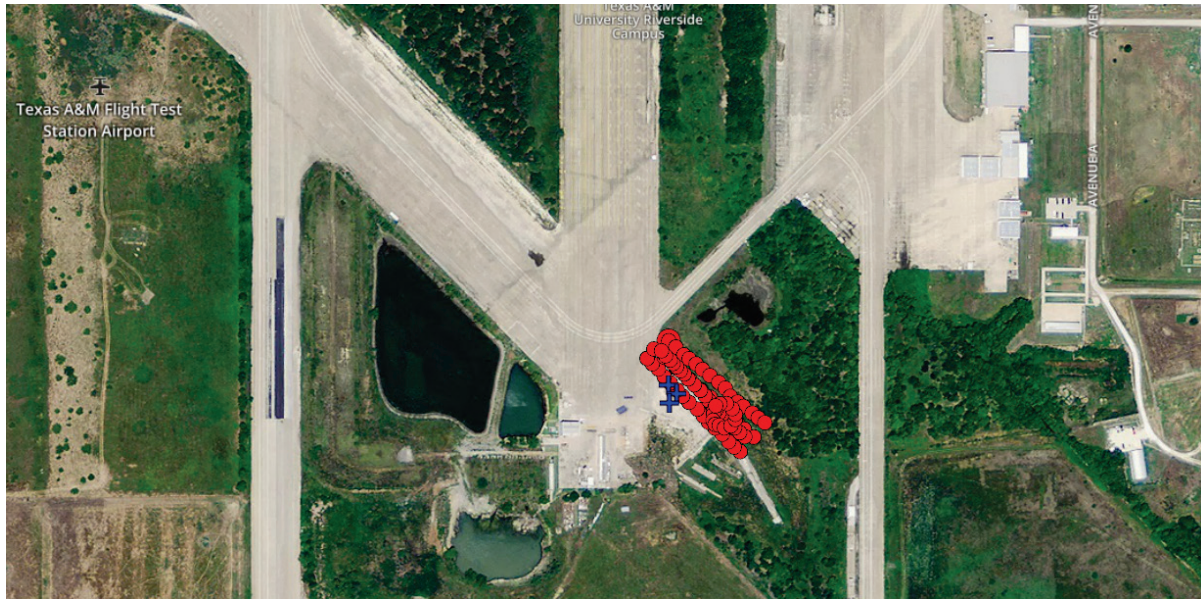


Figure 163. Test Site Location (09/30/2020).

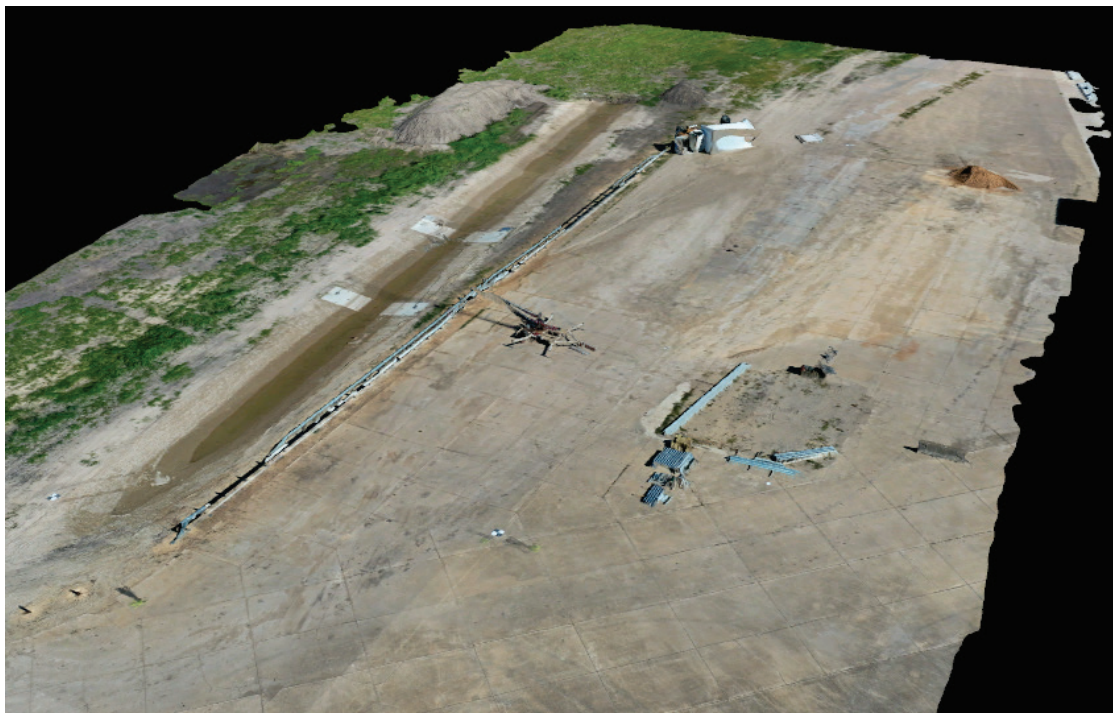


Figure 164. Crash Scene 3D Model (09/30/2020).

#### Test 4 (10/07/2020): Crash Test at The RELLIS Campus, College Station, Texas

This data collection took place at the RELLIS campus in College Station (Figure 165). A crash test scene was performed in which a passenger vehicle was let go against a guard rail at about 100 km/h (60 mph). After the car collided with the guard rail, it bounced back and traversed on the concrete surface until it stopped (Figure 166).

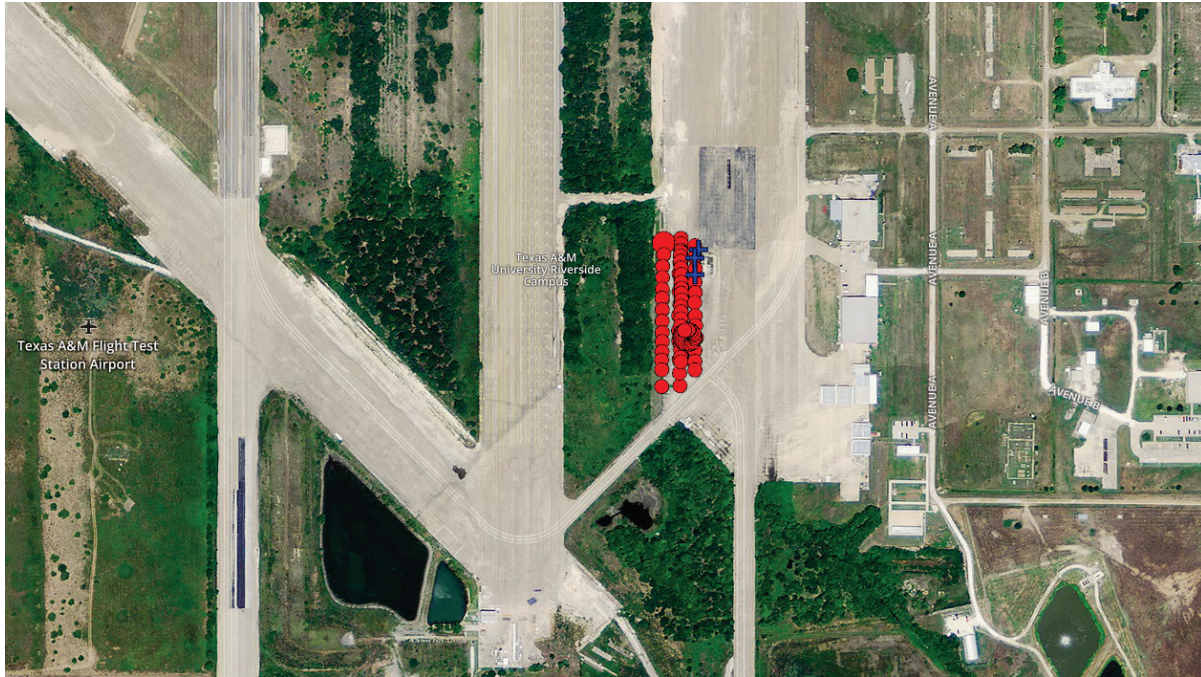


Figure 165. Test Site Location (10/07/2020).

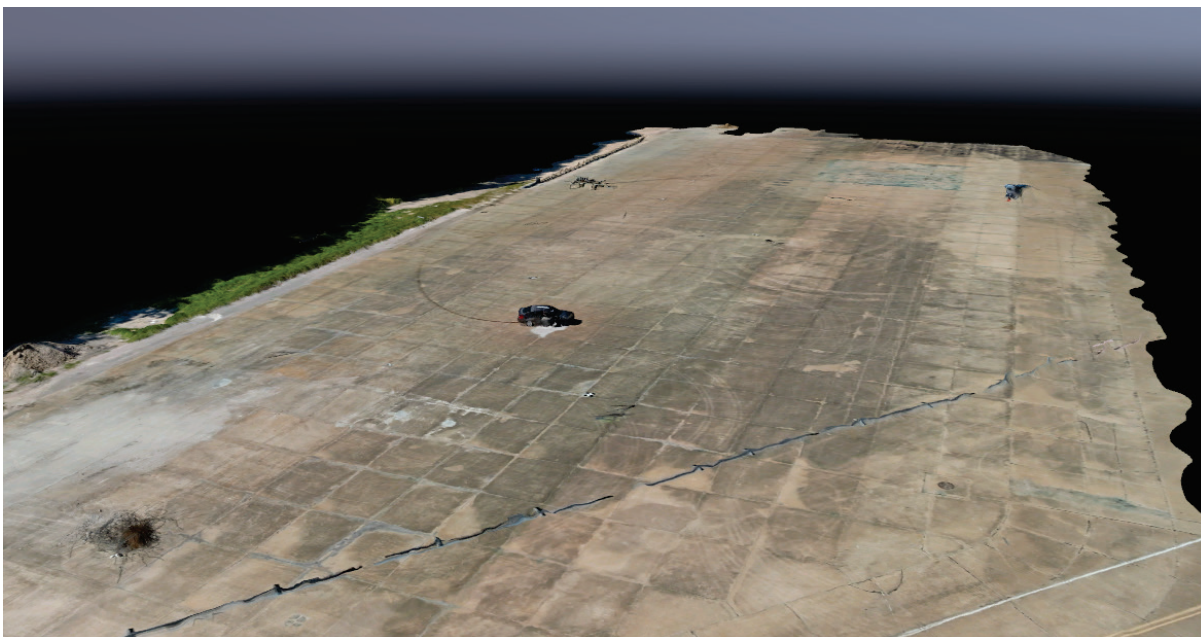


Figure 166. Crash Scene 3D Model (10/07/2020).

**Test 5 (12/07/2020): Delivery Truck Crash Test at the RELLIS Campus, College Station, Texas**

This data collection took place at the RELLIS Campus in College Station (Figure 167). A crash test scene took place in which a delivery truck was let go against a guard rail at about 100 km/h (60 mph). After the collision with the guard rail, the truck rolled over the guard rail (Figure 168).



**Figure 167. Crash Site Location (12/07/2020)**



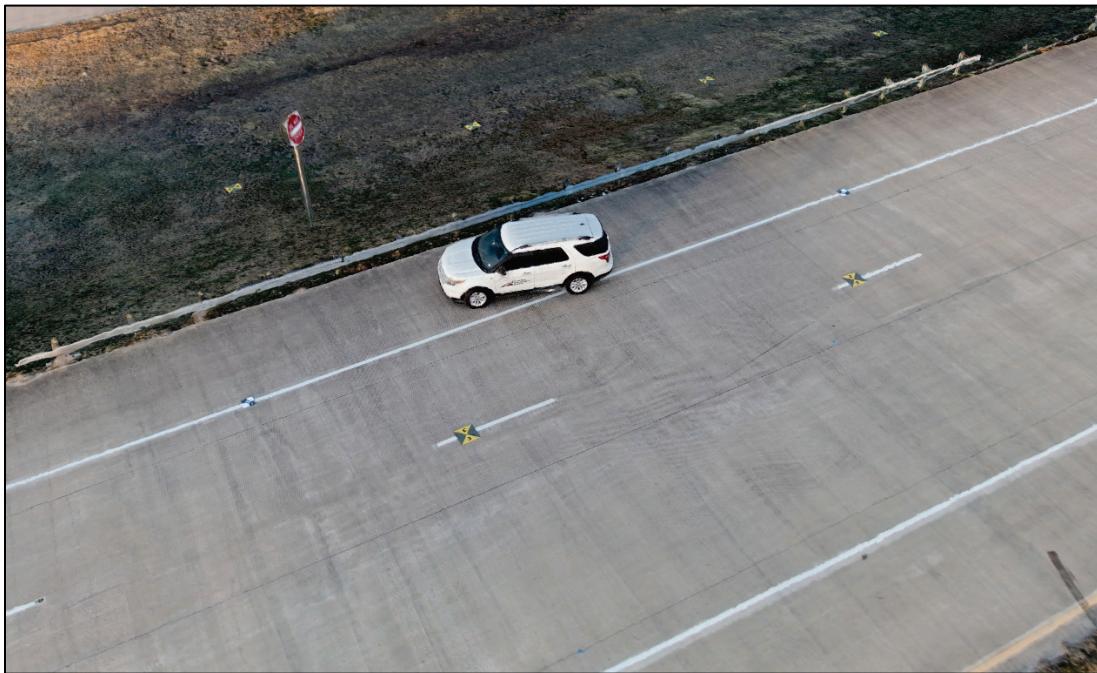
**Figure 168. Crash Scene 3D Model (12/07/2020).**

**Test 6 (01/15/2021): Simulated Passenger Car Crash Test at the TxDPS Tactical Training Facility in Florence, Texas**

This data collection took place at the TxDPS Tactical Training Facility near Florence, Texas (Figure 169). A crash test scene was simulated in which a test vehicle was parked on the right shoulder of a test freeway facility (Figure 170).



**Figure 169. Crash Site Location (01/15/2021)**



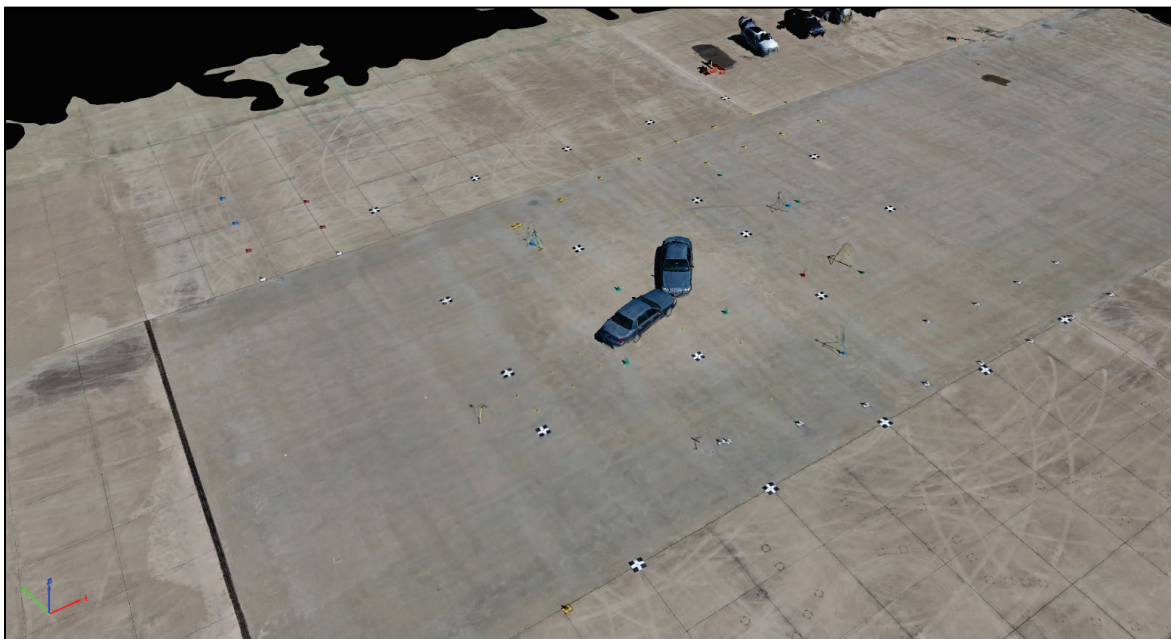
**Figure 170. Crash Scene 3D Model (01/15/2021).**

**Test 7 (03/20/2021): Simulated Passenger Car Crash Test at the TxDPS Tactical Training Facility in Florence, Texas**

This data collection took place at the TxDPS Tactical Training Facility near Florence, Texas (Figure 171). A crash test scene was simulated in which two passenger cars were placed in the middle of a test skid pad (Figure 172).



**Figure 171. Crash Site Location (03/20/2021).**



**Figure 172. Crash Scene 3D Model (03/20/2021).**

## DATA COLLECTION EQUIPMENT

The research team conducted a market analysis of 24 UASs for potential use based on the results of the review of UASs described in Chapter 2. At the time of the review in the early summer of 2020, the Skydio 2 UAS was expected to be available in October 2020. The project schedule required acquisition of two UASs by August 2020, and, consequently, the Skydio UAS was not a feasible option. The research team selected a DJI Mavic 2 Pro and a DJI Matrice 300 RTK. In addition, TAMUCC made available the following equipment for data collection at the various locations: a DJI Phantom 4 RTK UAS, a Wingtra WingtraOne UAS, a RIEGL-VZ geodetic-grade TLS, and a ground-based LiDAR LiBackpack DG50 unit. This last unit was used once during the data collection in Abbott, Texas, but its performance was not acceptable, and it was not used again. A brief description of the equipment used follows.

### DJI Mavic 2 Pro

The Mavic 2 Pro is a small, lightweight quadcopter UAS with a large 2.5-cm (1-inch) CMOS image sensor capable of producing 20-MP imagery (Figure 173). The UAS weighs 0.9 kg (2 lb) and measures 35 cm (14 inches) diagonally with arms extended. The electronic shutter ranges from 8–1/8,000 seconds with a 77-degree field of view. The UAS can operate in wind up to 35 km/h (22 mph) and air temperature from –10–40°C (14–104°F). The Mavic 2 Pro has dual downward-looking LED lights as well as green and red positional LED lights in the front and back. A separate infrared sensor can detect objects above and below the aircraft. The Mavic 2 Pro can be used with a standard controller connected to a smartphone or a smart controller equipped with a built-in display. The research team used a smart controller. The Mavic 2 Pro has a built-in camera and does not support exchangeable payloads. The UAS is not rated for use in rainy conditions. The downward-looking LED lights can be used to take nighttime pictures. The maximum flight time is about 31 minutes in windless conditions.



Figure 173. DJI Mavic 2 Pro.

### DJI Matrice 300 RTK

The Matrice 300 RTK became available in the United States in the summer of 2020 (Figure 174). The quadcopter UAS measures 90 cm (35 inches) diagonally with arms extended, weighs 3.6 kg (7 lb) without batteries, and can carry up to 2.7 kg (6 lb) of additional payload. Payloads can be added to a single downward gimbal or a dual downward gimbal. An upward gimbal can also be added to the top of the UAS. Various cameras and sensors, including thermal and LiDAR, are compatible with the Matrice 300 RTK. The research team selected a Zenmuse H20 camera, which is a dual-camera system with a 20-MP zoom camera and a 12-MP wide camera and laser range finder.



**Figure 174. DJI Matrice 300 RTK.**

The UAS can operate in wind up to 53 km/h (33 mph) and air temperature from  $-16$ – $50^{\circ}\text{C}$  ( $-4$ – $122^{\circ}\text{F}$ ). The Matrice 300 RTK has dual top and bottom auxiliary downlight LEDs in addition to positional LEDs in the front and back. The UAS has a built-in RTK receiver. The UAS has an International Protection 45 ingress protection rating (i.e., protection from low waterpower jets), which enables the aircraft to fly in rainy or snowy conditions. The Matrice 300 RTK uses a smart remote controller that has its own display and does not need a smartphone to work. The maximum flight time is about 55 minutes in windless conditions without any payloads.

The research team also acquired a DJI D-RTK 2™ GNSS mobile station as well as a DJI battery charging station capable of charging up to eight intelligent flight batteries for the Matrice 300 RTK and up to four remote controller or survey base station batteries. DJI states the mobile station can provide centimeter-level real-time differential data capabilities. The research team was unable to replicate this level of positional accuracy during field testing. The finest positional accuracy obtained in the field without the assistance of surveyed ground control points was 3.3 cm (1.3 inches) horizontally and 10 cm (4 inches) vertically.

### **DJI Phantom 4 RTK**

The Phantom 4 RTK is a quadcopter measuring 35 cm (14 inches) diagonally (Figure 175). It can fly up to 58 km/h (36 mph) and up to 6,000 meters above sea level. It has an operating temperature range of  $0$ – $40^{\circ}\text{C}$  ( $32$ – $104^{\circ}\text{F}$ ), and an approximate flying time of 30 minutes. The Phantom 4 RTK includes a 20-MP camera with an electronic shutter ranging from  $8$ – $1/8,000$  seconds.

The research team operated the Phantom 4 RTK in RTK mode by connecting to the TxDOT RTN through a networked transport of RTCM via internet protocol connection. In a typical situation, a user connects the Phantom 4 RTK remote controller to the internet through a Wi-Fi hotspot or a cellular modem connection. The research team used the cellular modem approach with an AT&T SIM card. Regardless of the default WGS84 datum stated in the exchangeable



image file format (EXIF) data of the images, which DJI software populates, the datum is what the RTN uses. In the case of the TxDOT RTN, this is NAD83(2011) with ellipsoid heights.



**Figure 175. DJI Phantom 4 RTK.**

### **Wingtra WingtraOne**

The WingtraOne is a fixed-wing, vertical take-off and landing aircraft powered by two electric motors (Figure 176). Its wingspan is 125 cm (49 inches). The WingtraOne weighs 3.7 kg (8.1 lb) and has a maximum payload weight of 0.8 kg (1.8 lb). It can fly up to 58 km/h (36 mph) for up to an hour. It can fly in wind up to 30 km/h (19 mph) and air temperature from  $-10$ – $40^{\circ}\text{C}$  ( $14$ – $104^{\circ}\text{F}$ ).



**Figure 176. WingtraOne UAS Platform.**

The system includes a GNSS receiver capable of operating in PPK mode. The UAS was integrated with a Sony™ RX1III™ 42-MP digital RGB camera for photogrammetry applications. The camera has a 35-mm lens, full-frame sensor with a leaf shutter mechanism and is considered a higher fidelity photogrammetric camera for UAS mapping operations. Operating at 120 m (400 ft) AGL, which is the standard flying height ceiling for non-waivered FAA Part 107

operations, the camera has a corresponding GSD of 1.5 cm. The flight control software, WingtraPilot™, is integrated with the platform's handheld controller.

### **RIEGL-VZ 2000i TLS**

The research team collected 3D point cloud data for ground truthing and accuracy assessment of UAS-SfM survey products using a RIEGL-VZ 2000i geodetic-grade TLS (Figure 177). The VZ-2000i has an effective range of up to 2 km (1.2 mi) with a laser pulse repetition rate of up to 1200 kHz operating in the near-infrared with a 1500 nm laser wavelength. The scanner is integrated with a Nikon™ D810™ 36-MP digital camera and 20-mm lens for point cloud colorization, and an RTK-enabled GNSS receiver, microelectromechanical systems (MEMS) IMU, and compass for obtaining accurate pose estimation (position and orientation). This equipment includes the capability to connect to the TxDOT RTN to receive a fixed solution correction and perform automatic scan-to-scan registration and georeferencing. The scanner is operated in the field with a laptop connected via Wi-Fi or by the scanner's onboard touch screen module. The latter method was used for data acquisition in this field test.

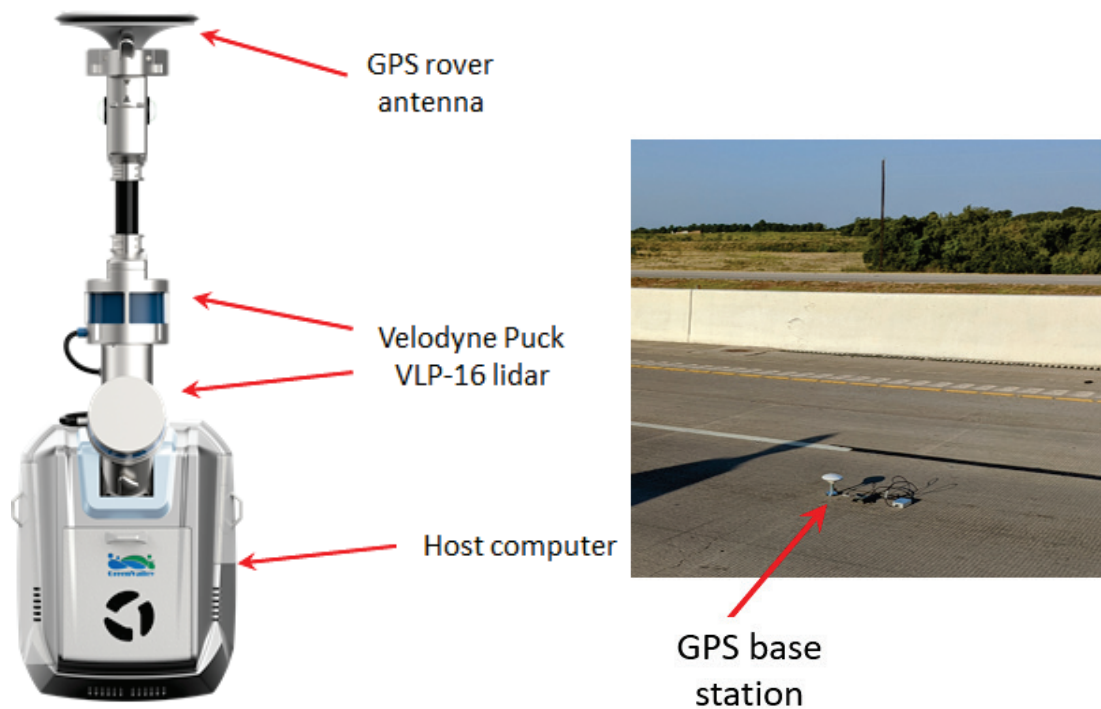


**Figure 177. RIEGL VZ-2000i.**

The RIEGL VZ-2000i TLS uses online waveform processing to convert range measurements to point cloud data and provides multi-echo (i.e., multiple target) detection capability. Multi-echo detection is useful when mapping topography under vegetation or canopy. The system also records the return waveform deviation relative to the outgoing pulse shape (which can help determine how noisy is a detected echo), calibrates amplitude, and calibrates relative reflectance for each point measurement.

### LiBackpack DG50 LiDAR

The research team used a ground-based LiDAR backpack mobile scanner at the Abbott test location. The backpack scanner is a LiBackpack DG50 unit consisting of two Velodyne Puck VLP-16 lidar scanners, an IMU module, and a GNSS module (Figure 178). The unit also includes a base station. The scanner has a range up to 100 m (i.e., 328 ft). The data can be used to generate a high-quality 3D point cloud data based on simultaneous localization and mapping (SLAM).



**Figure 178. LiBackpack DG50 Mobile 3D Mapping System.**

### GNSS Equipment

The team used a pair of survey-grade Septentrio™ NR3™ GNSS receivers that were run in the field by an Allegro 2 data collector running Carlson™ SurvCE™. One antenna was used to record static observations, while the other was tied to the TxDOT RTN and used as a rover to collect ground control data.

## FIELD TESTING—TAMUCC

This section focuses on a systematic assessment of positional accuracies at the test locations, which included surveying GCPs and checkpoints that were used in all photogrammetry software processing. These activities covered the following tests: Test 1, Test 4, Test 5, Test 6, and Test 7.

### Test 1 (08/09/2020): Crash Scene in Abbott, Texas

#### *Data Collection*

At the beginning of August 2020, the research team had just received the Mavic 2 Pro but had not been properly authorized to fly it. The Matrice 300 RTK had not arrived yet, so the research team used the Phantom 4 RTK. The research team used two Septentrio NR3 GNSS receivers. One of the receivers was used to record static observations, while the other one was tied to TxDOT's RTN and used as a rover to collect ground control data. The research team set up the static observation receiver to log GNSS observations for PPK postprocessing of UAS image geolocations (Figure 179). It should be noted that if a solution using the precise ephemerides of the GNSS satellite constellation is needed, the observation length must be at least two hours long for static processing within the National Geodetic Survey (NGS) Online Positioning User Service (OPUS) (130).



**Figure 179. Static Observation GNSS Receiver Being Set Up.**

TxDPS laid out eight aerial control targets. The research team laid out four additional targets in a staggered framework to provide coverage on both sides of the northbound main lanes at the beginning, middle, and end of the survey area while taking advantage of the control target network established by TxDPS. Figure 180 shows the two types of targets used in the survey. The maximum spacing between any one set of targets was about 50 m (164 ft). The research team surveyed the coordinates of each target using the second GNSS receiver (Figure 181). Ten seconds of observations at 1 Hz were recorded for each target, and the average of those observations was stored as the final location for each target. All 12 aerial control targets were used as checkpoints for evaluation of the SfM photogrammetric accuracy.

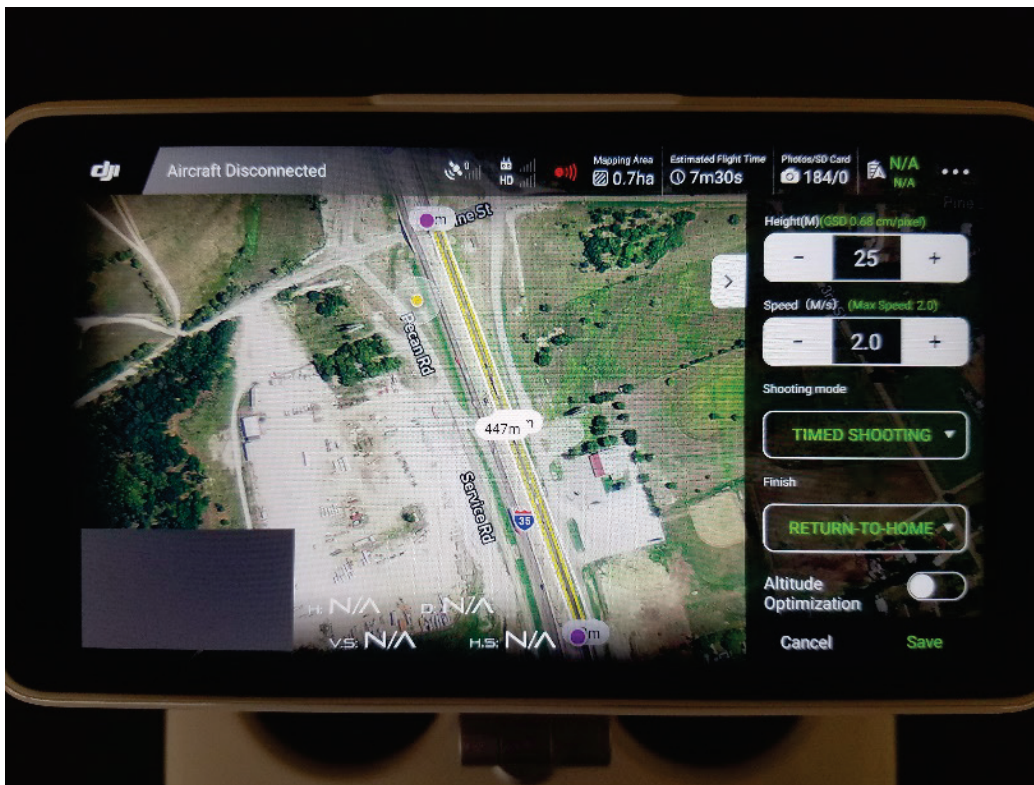


**Figure 180. TxDPS Target (left) and Research Team's Target (right).**



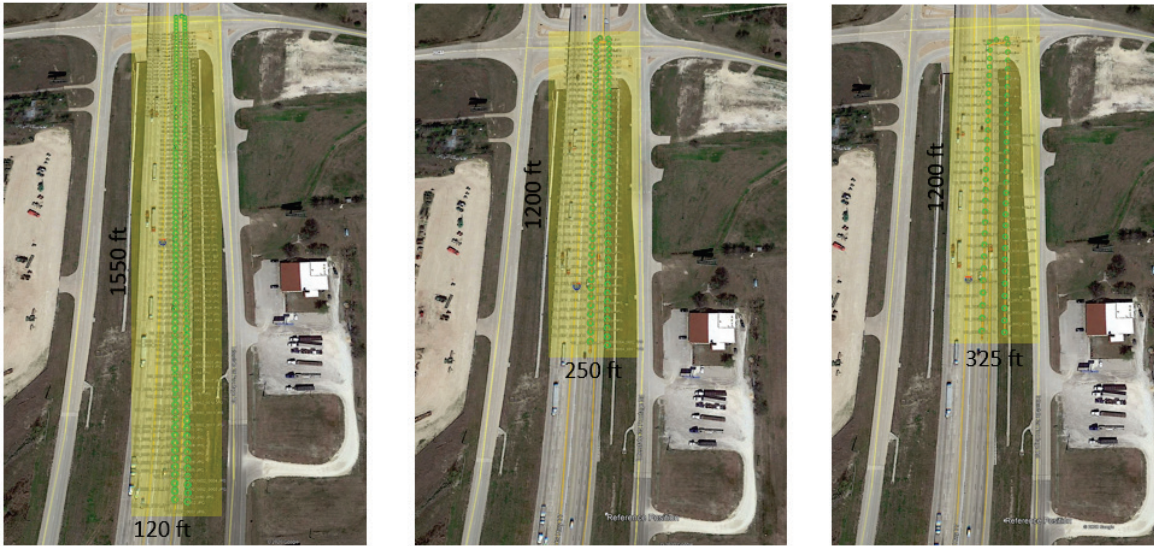
**Figure 181. RTK Surveying of Targets.**

The research team conducted three flights (Figure 182). The flight plan was designed for orthomosaic generation and top-down nadir view topographic mapping. The mission template included two parallel flight lines with 80 percent endlap, 80 percent sidelap, and a nadir camera angle. The flights were modified from the ground control software's recommendations to remove flight lines over southbound main lanes and the northbound frontage road (which were open to traffic). To increase the overlap coverage of the subject area, the research team planned stacked flights at three heights: 25 m (82 ft), 50 m (164 ft), and 75 m (246 ft) AGL. Figure 183 and Figure 184 show the missions. The research team coordinated with TxDPs to ensure there were no airspace conflicts. Immediately after TxDPs completed their flight, the research team received confirmation to deploy and flew the planned three missions. The missions were performed as individual flights, with the UAS landing and batteries being swapped between each flight.

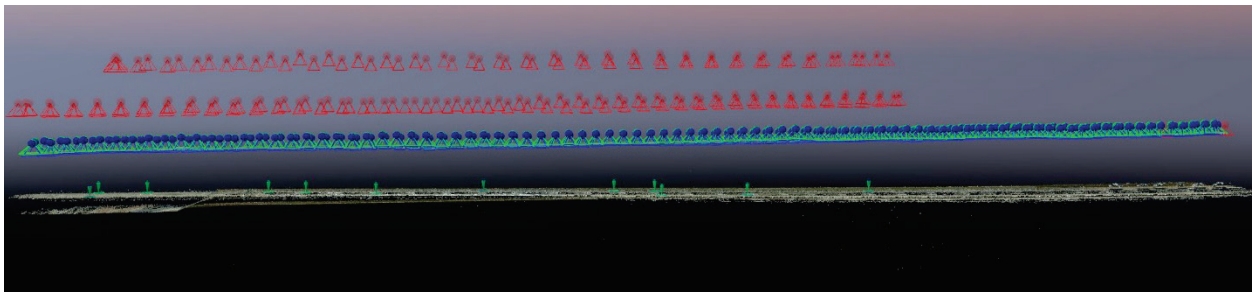


**Figure 182. Example Mission Plan for Low-Altitude Flight.**

Low Flight = 180 images    Medium Flight = 88 images    High Flight = 60 images



**Figure 183. UAS Flight Image Locations.**

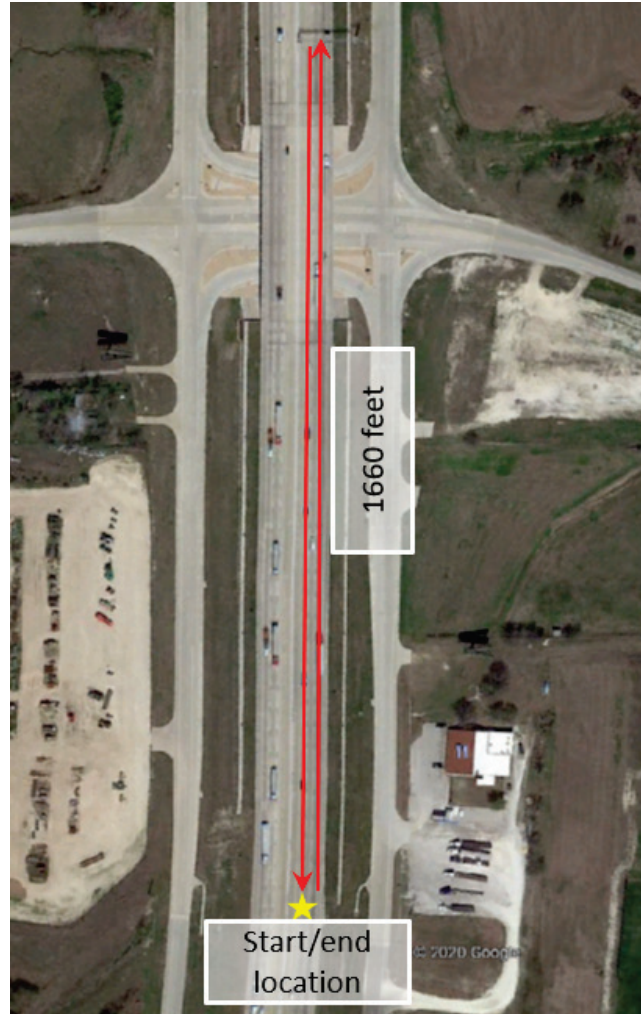


**Figure 184. Profile View of Image Locations with the Low-Altitude Flight in Blue.**

#### *Data Collection Using the LiBackpack DG50 LiDAR*

The research team placed the base station in the middle lane of northbound IH-35. After setting up the backpack's wireless connection to the cellphone web interface, the backpack operator started logging data via the cellphone web user interface. Although the backpack system enables real-time processing, the research team decided to use the postprocessing mode to prevent the backpack computer from overheating (because of the warm weather forecast).

The backpack operator remained still for about three minutes to lock in strong GNSS signals and coarsely determine the IMU's initial attitude and heading. Then the operator walked four times in a figure eight pattern to introduce IMU heading changes, observe heading errors, and allow the heading accuracy to converge. After this step, the operator walked along the planned scanning route along northbound IH-35 and went back to the starting point (Figure 185). Finally, the operator walked four times in a figure eight calibration pattern before remaining still for about three minutes.



**Figure 185. Lidar Field Testing Site near Abbott, Texas.**

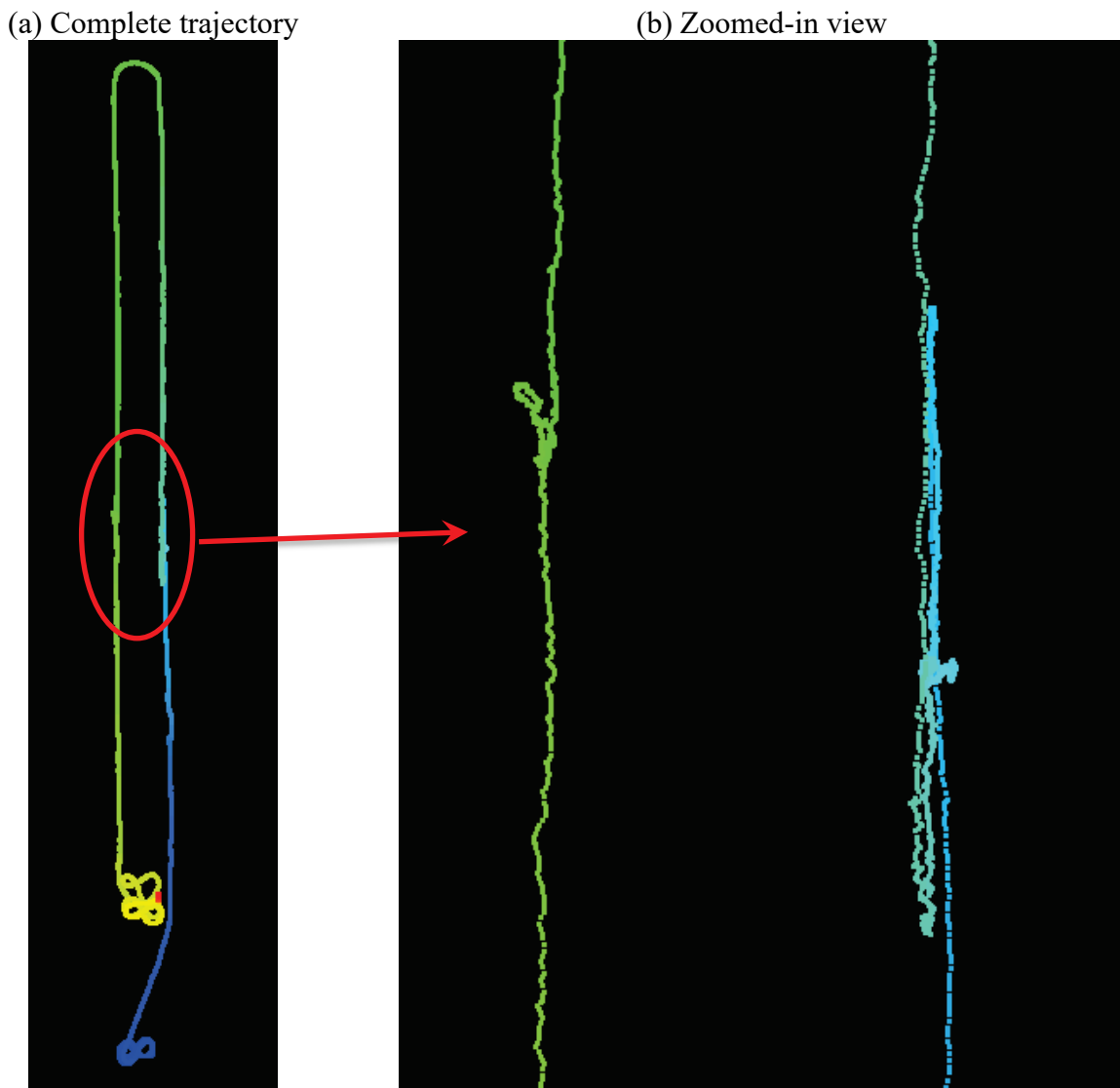
The research team completed the data processing steps below to generate a data point cloud:

- Base station observation processing. Since the GNSS base station was placed at a location with unknown coordinates near the testing site, the base station observation file was loaded into the NGS OPUS interface to obtain its geographic coordinates.
- SLAM processing of point cloud. The most automated and recommended procedure to process lidar and GNSS data is to combine differential GNSS and SLAM, which generates a GNSS trajectory by differential processing and then uses SLAM to obtain point cloud data with precise geographical coordinates. However, processing was not successful using this procedure. The research team consulted the DG50 vendor’s technical support, who recommended processing SLAM first before combining the available GNSS information. Because the point cloud processed using the SLAM mode is subject to error accumulation from the IMU module and LiDAR registration without GNSS calibration, the research team had to deliberately select processing parameters.
- GNSS. In this step, the research team generated a high-accuracy GNSS trajectory by differencing observations between the DG50 unit and the base station.

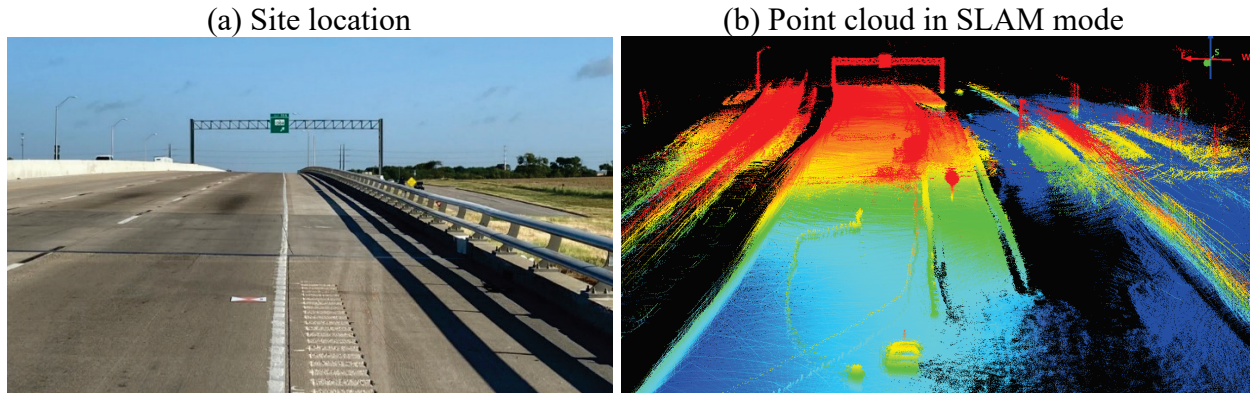


- SLAM results re-optimization with differential GNSS (DGNSS) trajectory. This step was recommended by the vendor's technical support to merge SLAM and DGNSS to optimize the results achieved from the SLAM solution. However, the point cloud could not be optimized with DGNSS information, meaning the resulting point cloud is pure SLAM-based with accumulated errors.

The backpack LiDAR point cloud processed using the SLAM algorithm did not merge high-accuracy GNSS information, resulting in cumulative errors when reconstructing the 3D scene. As Figure 186 shows, the calculated trajectory did not exactly match the trajectory the operator followed. Figure 187 displays a side-by-side comparison between a picture of the testing site and the point cloud (colored by elevation) processed in SLAM mode. Potential reasons the result was not successful include the lack of distinguishing features within the scene and moving vehicles on the northbound frontage road and southbound main lanes that could have confused the SLAM alignment process.



**Figure 186. Testing Trajectory Recovered in SLAM Mode Using the LiBackpack DG50.**



**Figure 187. Field Testing Site and Point Cloud Processed in SLAM Mode.**

### *Data Processing*

The first step in the UAS data processing workflow was to obtain the differentially corrected image locations for each flight via PPK processing. This requires a solution for the coordinates of the GNSS base station setup during the survey. Within OPUS, the research team used the precise ephemerides for the GNSS constellation at the static observation point's location and provided the base station observation file to solve for a static coordinate solution.

The precise ephemerides are usually available within OPUS in two weeks. However, a rapid processing of the base station observations can be performed within OPUS using non-precise ephemerides to obtain a static coordinate solution. For most applications, rapid processing can suffice and differences between precise and non-precise in the static coordinate solution are often negligible (i.e., a few millimeters). The research team used the precise ephemerides because they were available at the time of processing.

Once a static base station's observation coordinate solution was available, the research team used REDtoolbox to perform the PPK processing of the image geolocations. This process required the following inputs (131):

- UAS image set.
- .mrk file (image time stamps and lever arm offsets from UAS).
- RINEX file from the UAS rover.
- RINEX file from the static observation.
- Nav (ephemeris) files from the used constellations.
- Solved OPUS position of the base station.

The output of the PPK software was a .csv text file that contained the coordinates and estimated accuracy of each image. The research team then converted this file to the appropriate coordinate system (i.e., NAD83[2011] Epoch 2010.0 State Plane Texas North Central with NAVD 88 GEOID12B elevations) using the NGS VDatum software (132). This information was then combined with the image orientations from the EXIF data (Table 80). This final text file, along with the image set from each flight, was then imported into the SfM processing software.

**Table 80. Example of Final Image Locations for Import to SfM Software.**

image name	X	Y	Z	Pitch	Roll	Yaw	Accuracy Horz	Accuracy Vert
100_0002_0001.JPG	734188.1613	2024646.458	227.408	0	0	25.9134	0.009	0.017
100_0002_0002.JPG	734186.4961	2024651.341	227.554	0.0927735	0.0373198	21.9133	0.009	0.017
100_0002_0003.JPG	734184.7514	2024655.741	227.508	0.0934729	0.0355319	20.8133	0.009	0.017
100_0002_0004.JPG	734182.9474	2024660.461	227.252	0	0	20.8133	0.009	0.017
100_0002_0005.JPG	734181.0337	2024665.102	227.131	0.0935348	0.0353687	20.7133	0.009	0.017

The research team completed eight SfM processes, including four processes using Pix4Dmapper 4.5.6 and four processes using Metashape version 1.6.3. In total, the research team processed 328 images, including 180 low-altitude images, 88 mid-altitude images, and 60 high-altitude images.

In Pix4D, the research team used the standard workflow and 3D mapping template, including standard calibration. When using accurate image locations, Pix4D recommends using the “Accurate Geolocation and Orientation” calibration method under the initial processing options. This setting is optimized for projects with accurate image geolocations and orientations. The calibration method still requires all images to be geolocated and oriented via the SfM BA, but it weighs more heavily the image geolocations and orientations (if provided) based on the estimated PPK standard deviations for each image’s geolocation. In some scenarios, it can speed up processing or improve processing under low image texture conditions. The research team found the standard calibration to produce more accurate results and used it accordingly. No angular orientation information for the imagery (e.g., from an IMU onboard the UAS) was imported with the PPK corrections during processing. Lack of accurate orientation information is another reason for use of the standard calibration method in Pix4D.

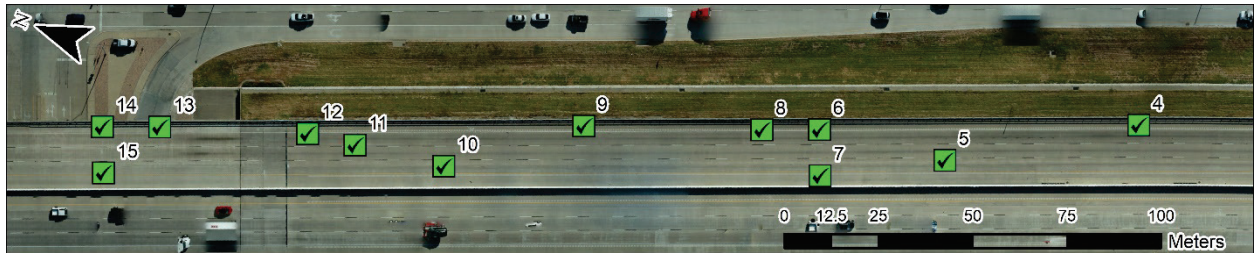
In Metashape, the research team used a slightly modified version of a workflow developed by the United States Geological Survey (USGS) (133, 134). When using Metashape with PPK- or RTK-corrected image geolocations, the user must set the position accuracy estimates under settings in the reference menu. In both cases, the horizontal and vertical accuracy estimates are brought into the software within the image location text file that is output by the PPK software. Like Pix4D, no angular orientation information was input with the imagery.

The research team did not use any of the aerial control targets in the SfM processing to constrain the solutions. All aerial targets were used solely as checkpoints for absolute accuracy assessment. The geolocation of the final products was based entirely upon the image locations from PPK and bundle block solutions from the SfM processing.

### *Results*

The main purpose of the SfM processing experiment was to assess the absolute accuracy of the SfM reconstruction of the roadway (i.e., SfM-derived point cloud) at the three flight altitudes, and all flights combined, based solely on PPK-corrected image geolocations. In addition, the research team examined the difference in accuracy between Pix4D and Metashape using recommended processing workflows. Accuracy analysis was based on the checkpoint residuals, as shown in the quality reports generated for each processing solution within the two software suites. For all processing runs, the research team generated a densified point cloud and orthomosaic, as well as a textured digital mesh for the all-flight combined solution. Figure 188

shows the location of the checkpoints. Checkpoints 4, 5, 9, and 10 were research team targets and the rest were TxDPS targets. Table 81 and Table 82 show the checkpoint accuracy for the combined flights solution from the Pix4D and Metashape quality reports, respectively.



**Figure 188. Checkpoint Locations Overlaid on an Orthomosaic Generated from the Combined Flights Processed with Metashape.**

**Table 81. Checkpoint Residuals for the Combined Flight Solution in Pix4D.**

Check Point Name	Accuracy XYZ [m]	Error X [m]	Error Y [m]	Error Z [m]	Projection Error [pixel]	Verified/Marked
4		-0.029	-0.009	0.062	0.523	27 / 27
5		-0.015	-0.001	0.081	0.493	31 / 31
6		-0.024	0.001	0.101	0.461	31 / 31
7		-0.017	-0.017	0.091	0.493	31 / 31
8		-0.030	0.012	0.085	0.523	30 / 30
9		-0.029	-0.005	0.080	0.472	28 / 28
10		-0.020	-0.007	0.062	0.568	28 / 28
11		-0.015	-0.002	0.064	0.555	29 / 29
12		-0.022	-0.004	0.051	0.613	26 / 26
13		-0.006	-0.003	0.059	0.469	27 / 27
14		-0.019	0.001	0.061	0.281	21 / 21
15		-0.009	-0.009	0.062	0.746	25 / 25
Mean [m]		-0.019645	-0.003492	0.071676		
Sigma [m]		0.007551	0.006690	0.014797		
RMS Error [m]		0.021046	0.007547	0.073188		

**Table 82. Checkpoint Residuals for the Combined Flight Solution in Metashape.**

Label	X error (cm)	Y error (cm)	Z error (cm)	Total (cm)	Image (pix)
4	1.83838	0.187586	-6.10584	6.37935	0.121 (27)
5	1.28809	-0.0140167	-7.64801	7.75574	0.096 (33)
6	1.88571	-0.119748	-10.3798	10.5504	0.265 (31)
7	1.70263	1.18331	-9.07495	9.30881	0.180 (31)
8	2.32661	-1.31729	-9.43075	9.80242	0.127 (31)
9	2.2548	0.460806	-7.75336	8.08772	0.072 (30)
10	2.112	0.674709	-6.10552	6.49562	0.046 (30)
11	1.56437	0.186861	-6.41025	6.60102	0.132 (29)
12	2.23644	0.575071	-5.31577	5.79567	0.088 (27)
13	0.681578	0.840733	-5.08173	5.1957	0.072 (27)
14	1.6447	0.589529	-6.28319	6.52159	0.283 (26)
15	1.55948	1.28217	-5.56955	5.92417	0.077 (26)
<b>Total</b>	<b>1.81434</b>	<b>0.759206</b>	<b>7.2908</b>	<b>7.55143</b>	<b>0.149</b>

As shown in Table 81 and Table 82, accuracy results were similar for both software packages and demonstrate that the absolute accuracy of the UAS-SfM solutions based solely on PPK image geolocation accuracy, without using ground control targets, can compare well to the TxDOT RTN checkpoint location coordinates. In both cases, the largest error, roughly 7.5 cm (2.9 inches), was associated with the Z component. It is important to note that the above accuracies come from the combined flight solution, which combined the three flights to achieve a reasonable amount of image overlap and differing camera perspective within the scene. This variation in perspective and altitude can sometimes aid SfM reconstruction quality.

Table 83 and Table 84 show the accuracy results for the processing solutions at the three different flight altitudes for Pix4D and Metashape, respectively. Some variability existed in the results. Most noticeable is the large deviation in the Z component. Pix4D shows a 12-cm (4.7 inch) RMSE at the mid-altitude flight and Metashape shows a 17 cm (6.7-inch) RMSE at the high-altitude flight. Horizontal errors across all flight altitudes and software solutions remained low and stable with a maximum horizontal error in the X component for Pix4D of 5 cm (2 inches) at the low-altitude flight. Overall, the combined flight solution for both software provided the best balance in errors between horizontal and vertical components.

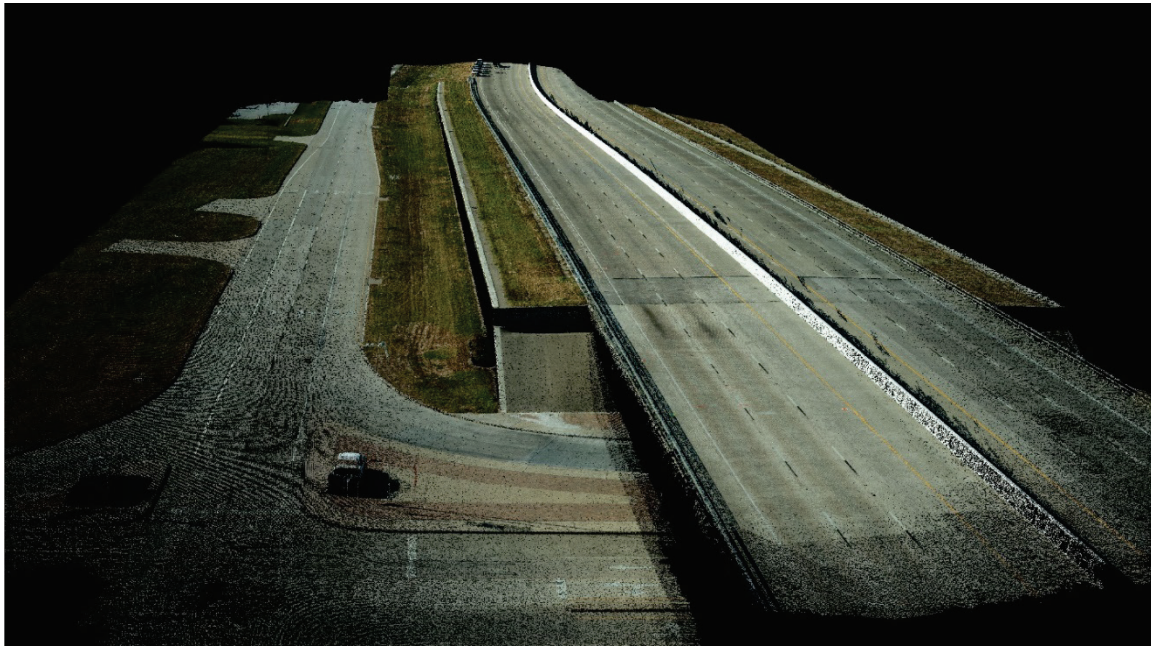
The average final point cloud densities based on the processing settings used were 8,819 points per m<sup>3</sup> for the low-altitude flight, 2,446 points per m<sup>3</sup> for the mid-altitude flight, 832 points per m<sup>3</sup> for the high-altitude flight, and 1,521 points per m<sup>3</sup> for all flights combined. Figure 189 to Figure 194 show examples of UAS-SfM-derived mapping products from the flights conducted.

**Table 83. RMSE of Checkpoint Residuals (Pix4D Solution).**

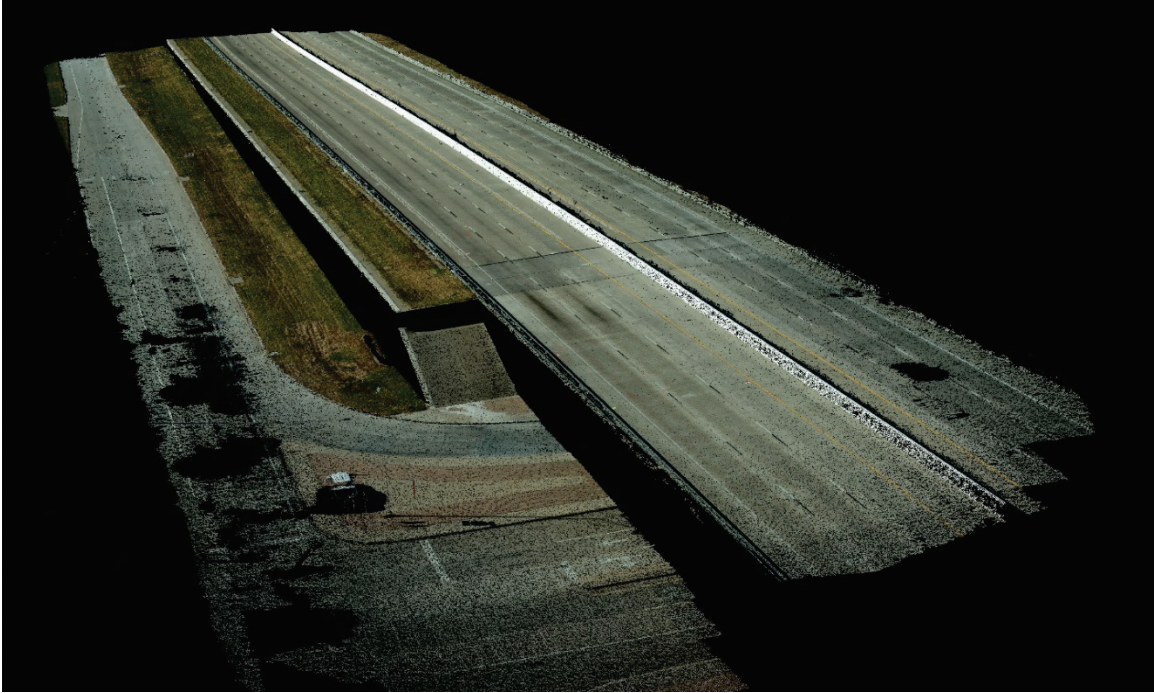
Scenario	X RMSE (cm)	Y RMSE (cm)	Z RMSE (cm)	Average GSD (cm/pixel)
Low-Altitude	4.86	1.75	8.33	0.73
Mid-Altitude	1.05	0.96	12.6	1.08
High-Altitude	3.30	1.19	4.67	1.55
Combined Flights	2.10	0.76	7.32	0.88

**Table 84. RMSE of Checkpoint Residuals (Metashape Solution).**

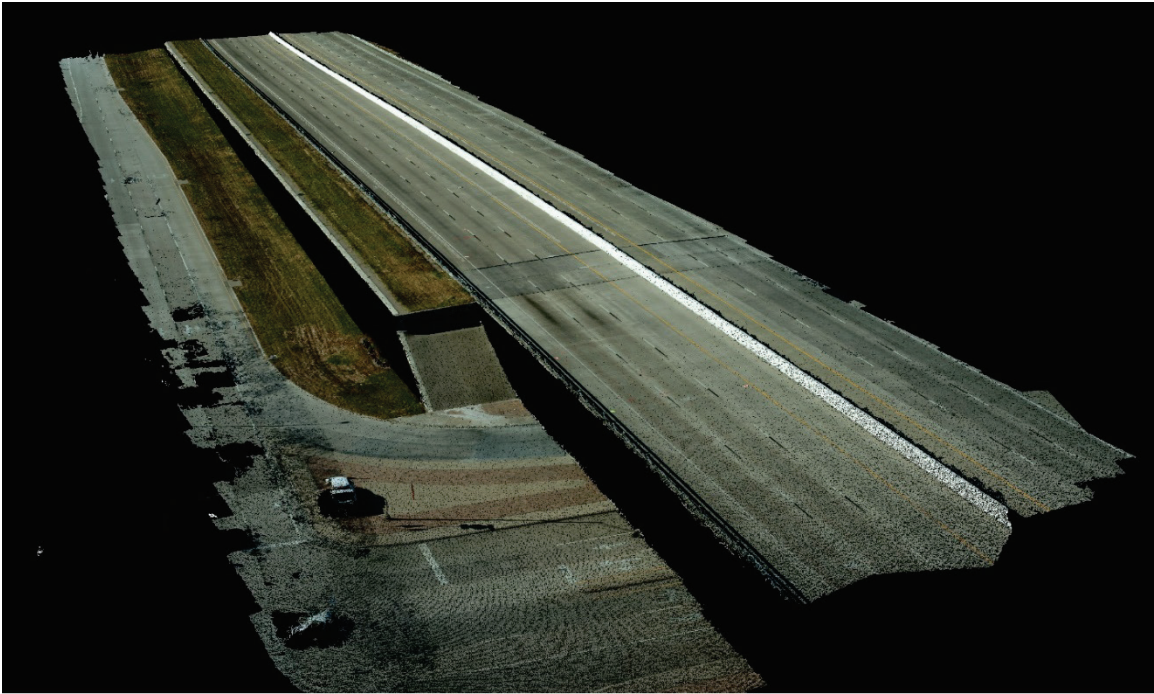
Scenario	X RMSE (cm)	Y RMSE (cm)	Z RMSE (cm)	Average GSD (cm/pixel)
Low-Altitude	2.34	0.98	11.3	0.61
Mid-Altitude	1.10	0.78	4.05	0.94
High-Altitude	3.11	1.07	17.4	1.38
Combined Flights	1.81	0.76	7.29	0.84



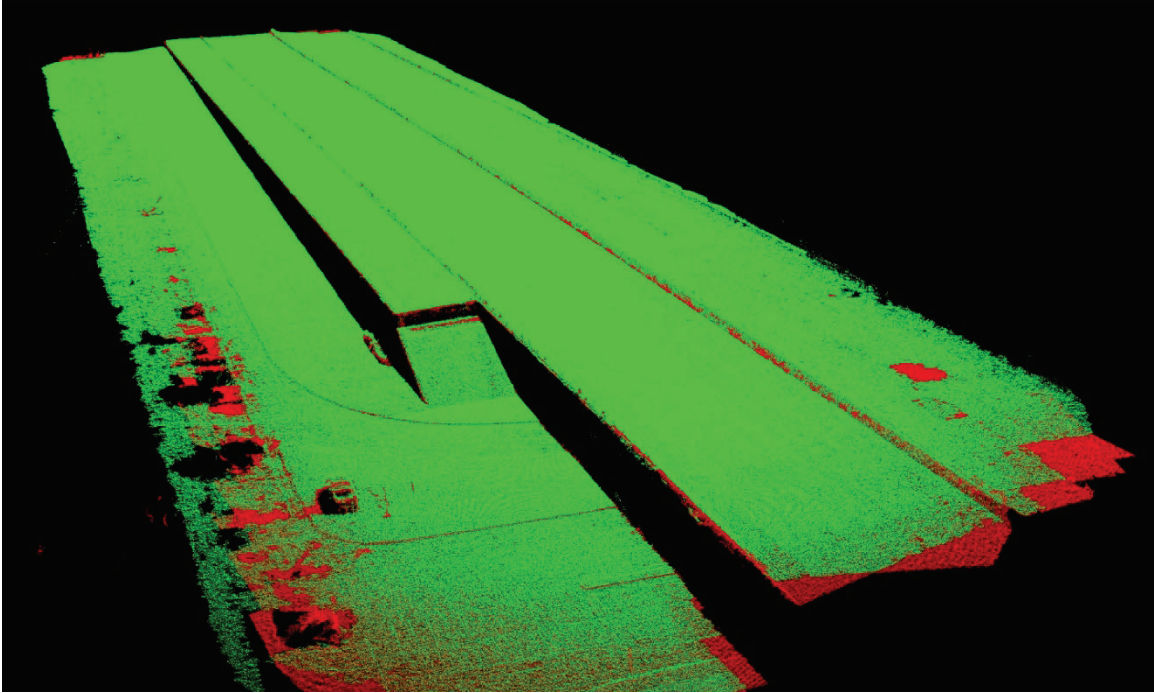
**Figure 189. Point Cloud from Combined Flights Solution Processed in Pix4D.**



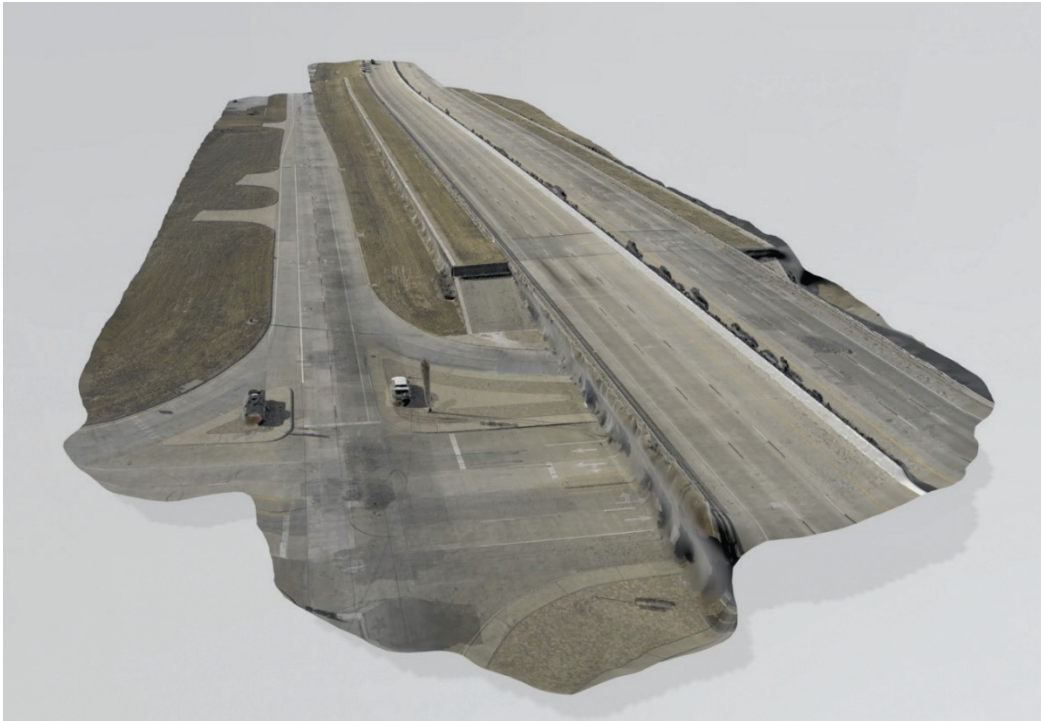
**Figure 190. Point Cloud from Mid-Altitude Flight Processed in Pix4D.**



**Figure 191. Point Cloud from Mid-Altitude Flight Processed in Metashape.**



**Figure 192. Comparison of Point Clouds (Metashape in Red and Pix4D in Green).**



**Figure 193. 3D Mesh Model Generated from Pix4D for the Combined Flight Solution.**





**Figure 194. 3D Mesh Model Generated from Pix4D for the Combined Flight Solution.**

#### **Test 4 (10/07/2020): Crash Test at the RELLIS Campus, College Station, Texas**

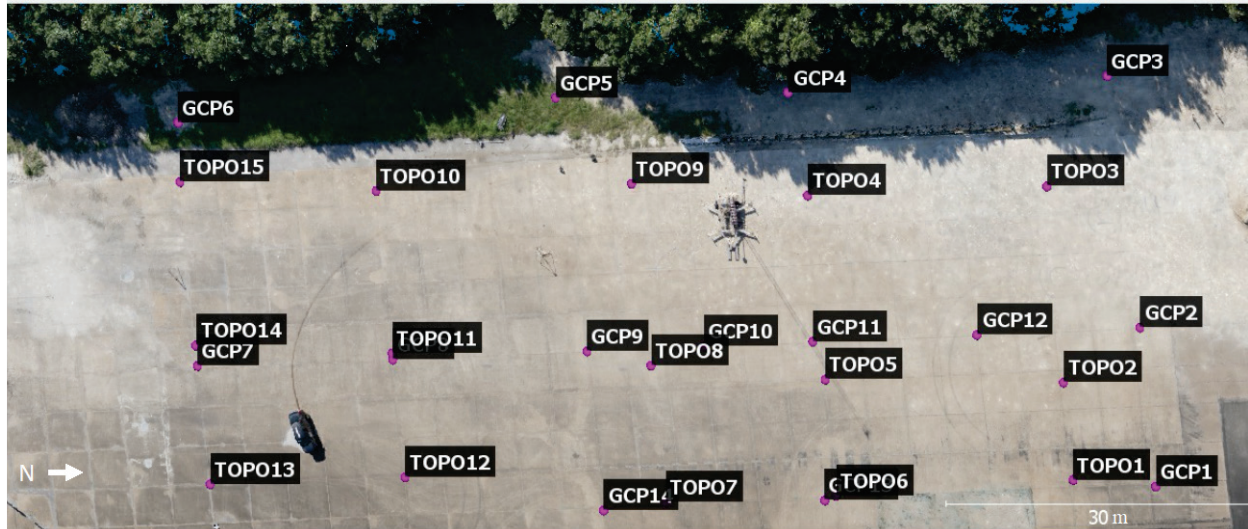
##### *Data Collection*

The procedure followed for Test 4 was similar to that followed for Test 1, with some minor modifications. The research team used the WingtraOne UAS. The research team also collected 3D point cloud data using the RIEGL-VZ 2000i TLS for ground truthing and accuracy assessment of UAS-SfM survey products.

This test assessed the horizontal and vertical accuracy of a UAS-SfM solution (densified 3D point cloud) processed in Pix4D and Metashape using uncontrolled PPK sensor augmentation for image geotags. The research team assessed accuracy relative to aerial control targets, topo points, and TLS 3D point cloud data of the crash scene. The research team set up one of the Septentrio NR3 GNSS receivers on a tripod located nearby to the scene to log static observations for PPK postprocessing of the WingtraOne image geolocations. Over two hours of static observations were collected for processing of the base station coordinate using OPUS. The other GNSS receiver was tied to TxDOT's RTN and used as a rover to collect ground control data.

The research team laid out 14 GCPs in a grid pattern on the parking lot and perimeter of the simulated crash scene, as well as 15 additional topo points on the pavement for accuracy assessment, resulting in 29 control points for accuracy validation (Figure 195). The research team surveyed these points using the second GNSS receiver. For each target, the research team recorded 5–10 seconds of observations at 1 Hz and then averaged the X-Y-Z coordinates. Unless

otherwise noted, the research team used all 14 GCPs and 15 topo points as checkpoints for evaluation of the SfM photogrammetric accuracy.

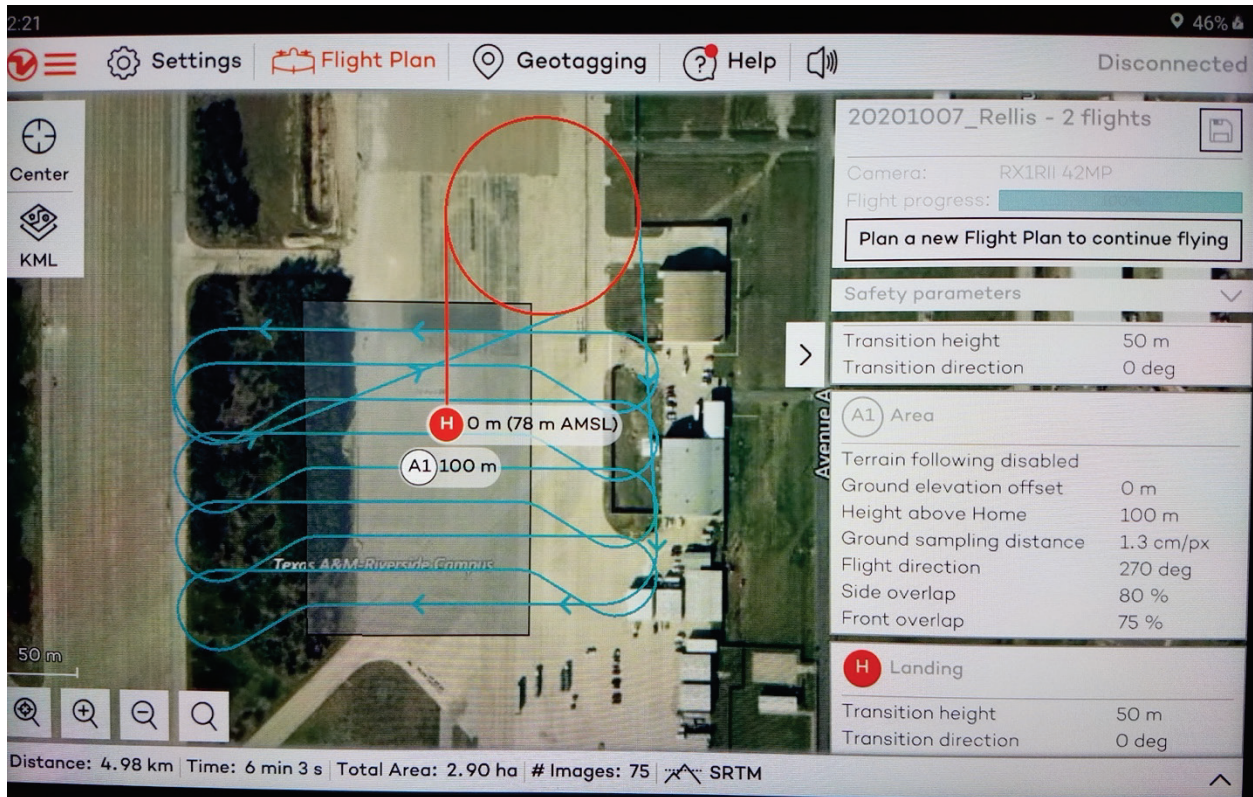


**Figure 195. Test 4 Aerial Control Network for Accuracy Assessment.**

The research team collected ground control data in NAD83(2011) State Plane Texas Central (meters) for X-Y and NAD83(2011) ellipsoid heights for Z. Ellipsoid heights were used to ensure consistent comparison of vertical accuracies relative to the SfM processing workflows using PPK image geotags, which come in NAD83(2011) ellipsoid heights. Although these tags can be converted to NAVD 88 using a hybrid geoid model, the research team’s standard practice is to convert the derived mapping products into NAVD 88 outside of the respective SfM software.

The research team conducted a flight using the WingtraOne in PPK mode. The flight plan was designed for 2.5D topographic mapping using a top-down nadir view perspective. The survey used 75 percent endlap and 80 percent sidelap in a grid flight plan with parallel flight lines (Figure 196). The UAS flew at about 100 m (328 ft) AGL, resulting in an average GSD of about 1.3 cm/pixel (0.51 inches/pixel). Figure 197 shows the level of image detail that was obtained. The flight took six minutes to complete.

The research team acquired TLS data from a series of four tripod scan positions distributed in a rectangular fashion around the crashed vehicle scene. Each scan position was within 30 m (100 ft) from the vehicle. Scans used the VZ-2000i accurate pose (position and orientation) estimation method, which integrates the scanner’s onboard MEMS IMU for orientation and RTK GNSS for georeferencing. Imagery was also acquired at each scan position to colorize the point cloud. Table 85 shows the TLS survey parameters used for data acquisition. Figure 198 shows the four TLS scan positions. The scanner was connected to TxDOT RTN using a cellular network to obtain a fixed position solution at each scan location.



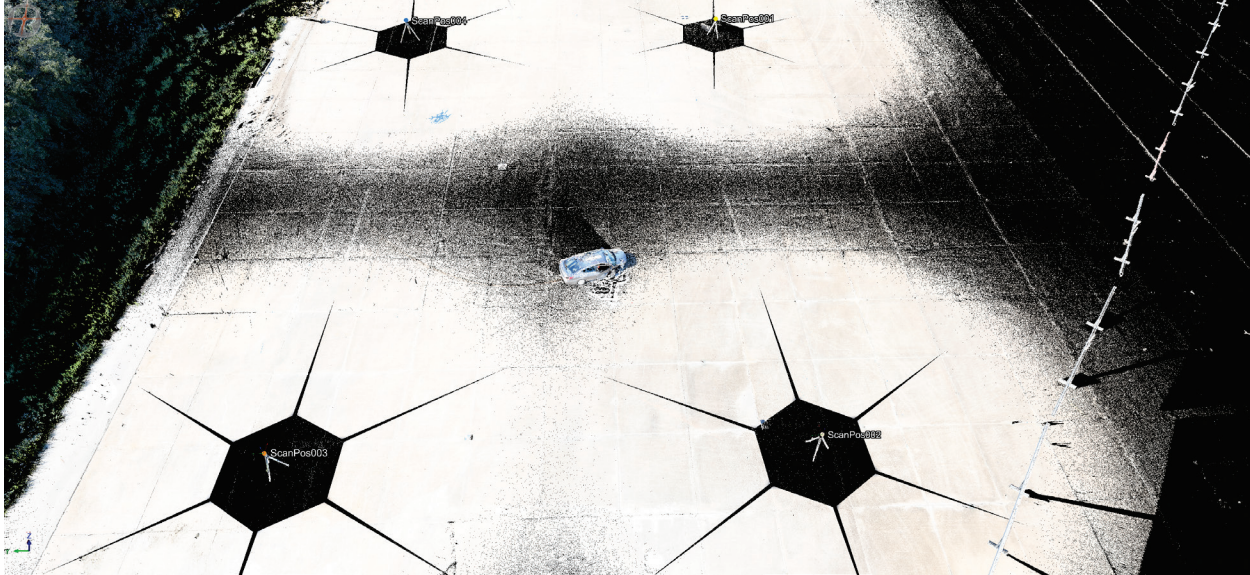
**Figure 196. UAS Flight Design for the WingtraPilot.**



**Figure 197. Zoomed-in View of an Orthomosaic Image Created with the WingtraOne.**

**Table 85. TLS Survey Parameters Used for Each Scan Position.**

Scan Parameters	Values
Laser Pulse Rate	1200 kHz
Stepping Angle	20 millidegrees
Horizontal Field-of-View	360°
Vertical Field-of-View	100° (+60°, -40°)



**Figure 198. Example of a Merged Point Cloud Showing the Four TLS Scan Positions.**

### *Data Processing*

#### WingtraOne PPK Data Processing

The research team obtained the differentially corrected image locations for each flight via PPK processing. This activity involved submitting the RINEX file of the static GNSS base station's observations collected during the flight to OPUS to solve for a static coordinate in the NAD83(2011) datum. As in the case of Test 1, the research team used the precise ephemerides because they were available at the time of processing, and there was not a need to have the data processed and provided sooner.

Once the static base station's observation coordinate was resolved, the research team proceeded with the PPK processing in WingtraHub. The procedure for PPK processing with WingtraHub was different from that used for the Phantom 4 RTK. After completion, WingtraHub generated a .csv file containing the image names, positions, orientations, and accuracies for import into the SfM software. Table 86 shows an example in .csv format for Pix4D.

**Table 86. PPK-Corrected WingtraOne UAS Image Positions.**

	A	B	C	D	E	F	G	H	I
1	# image name	latitude [decimal degrees]	longitude [decimal degrees]	altitude [meter]	omega [degrees]	phi [degrees]	kappa [degrees]	accuracy horizontal [meter]	accuracy vertical [meter]
2	21_03_20_Florence_Flight_01_00002.JPG	30.80853623	-97.75114498	330.3705067	-10.35059287	1.9769006	-1.07884977	0.02	0.03
3	21_03_20_Florence_Flight_01_00003.JPG	30.80868708	-97.7511356	328.3970909	-9.5380805	-3.97642073	-2.88445672	0.02	0.03
4	21_03_20_Florence_Flight_01_00004.JPG	30.80882908	-97.75112927	326.1585669	-4.94298296	-5.49425821	-2.27393208	0.02	0.03
5	21_03_20_Florence_Flight_01_00005.JPG	30.80897472	-97.7511283	324.7390799	-1.88829192	-2.49202675	-1.52363029	0.02	0.03
6	21_03_20_Florence_Flight_01_00006.JPG	30.80912034	-97.75112732	325.3634544	-1.39702982	-3.06067719	-0.68151315	0.02	0.03
7	21_03_20_Florence_Flight_01_00007.JPG	30.80926398	-97.75112488	325.5564937	-3.9744002	-6.35187901	-3.7469592	0.02	0.03
8	21_03_20_Florence_Flight_01_00008.JPG	30.80941084	-97.75112795	325.0678682	-2.23295245	-0.27092659	-3.33789461	0.02	0.03
9	21_03_20_Florence_Flight_01_00009.JPG	30.80955395	-97.75113289	324.419074	0.2474032	-1.13903865	-2.8203405	0.02	0.03
10	21_03_20_Florence_Flight_01_00010.JPG	30.80970438	-97.75113502	324.5584173	3.70991797	20.28904356	-4.97522569	0.02	0.03
11	21_03_20_Florence_Flight_01_00011.JPG	30.80984399	-97.75110736	325.6199344	14.08696168	26.10442395	-26.93456565	0.02	0.03
12	21_03_20_Florence_Flight_01_00012.JPG	30.80997399	-97.75103424	326.7935933	3.08254591	8.74229882	-32.5817061	0.02	0.03
13	21_03_20_Florence_Flight_01_00013.JPG	30.81009667	-97.75094556	326.6724001	-1.63775706	-3.03032379	-34.06299621	0.02	0.03
14	21_03_20_Florence_Flight_01_00014.JPG	30.81001167	-97.75129729	328.8438176	7.44014063	-4.75517404	-178.3855765	0.02	0.03
15	21_03_20_Florence_Flight_01_00015.JPG	30.8098566	-97.75129814	327.9408026	3.56858853	2.06117479	179.670611	0.02	0.03
16	21_03_20_Florence_Flight_01_00016.JPG	30.80971537	-97.75129866	328.0625129	2.7247767	3.02489729	-176.2727291	0.02	0.03
17	21_03_20_Florence_Flight_01_00017.JPG	30.80957442	-97.7512976	328.1161264	2.95349209	2.20128461	-175.4826174	0.02	0.03
18	21_03_20_Florence_Flight_01_00018.JPG	30.80943155	-97.75129727	327.3155548	2.2175949	-0.70878792	-177.6573172	0.02	0.03
19	21_03_20_Florence_Flight_01_00019.JPG	30.8092885	-97.75129868	326.9910297	1.93077204	2.34016836	174.2647808	0.02	0.03
20	21_03_20_Florence_Flight_01_00020.JPG	30.80914659	-97.75130146	326.766221	1.58003085	1.98943753	176.4951483	0.02	0.03
21	21_03_20_Florence_Flight_01_00021.JPG	30.80899857	-97.75130397	326.5442876	0.419533	-1.33013971	174.4379704	0.02	0.03
22	21_03_20_Florence_Flight_01_00022.JPG	30.80885819	-97.7513054	327.2183326	1.42132379	21.24364868	179.262061	0.02	0.03
23	21_03_20_Florence_Flight_01_00023.JPG	30.80871905	-97.75128534	327.3782893	-9.24202975	29.83547716	-154.9135441	0.02	0.04
24	21_03_20_Florence_Flight_01_00024.JPG	30.80858634	-97.7512173	327.6439186	-8.98346132	14.81682446	-139.8049416	0.02	0.03
25	21_03_20_Florence_Flight_01_00025.JPG	30.80847265	-97.75112178	328.6898223	4.82872124	0.13388757	-142.7344536	0.02	0.03
26	21_03_20_Florence_Flight_01_00026.JPG	30.80857974	-97.75146748	329.3522202	-5.66431396	-11.98702734	-111.14972704	0.02	0.03
27	21_03_20_Florence_Flight_01_00027.JPG	30.80872102	-97.75146122	329.3351598	-7.3588913	-10.03942793	2.92136669	0.02	0.03
28	21_03_20_Florence_Flight_01_00028.JPG	30.80886454	-97.75146739	328.3334899	-6.50550582	-0.94731897	6.58627713	0.02	0.03
29	21_03_20_Florence_Flight_01_00029.JPG	30.80900881	-97.75147518	328.1274728	-5.79096051	4.82639185	4.95467208	0.02	0.03
30	21_03_20_Florence_Flight_01_00030.JPG	30.80915217	-97.75147682	327.2940436	-5.37858049	1.48166933	0.88380371	0.02	0.03

**SfM Data Processing**

The research team performed six individual SfM processing runs using the WingtraOne flight data, including five runs in Pix4Dmapper and one run in Metashape:

- Autonomous (i.e., non PPK-corrected) image geotags, 7 GCPs (Pix4D).
- PPK-corrected image geotags, no GCPs (Pix4D).
- PPK-corrected image geotags, no GCPs (Metashape).
- PPK-corrected image geotags, 1 GCP (Pix4D).
- PPK-corrected image geotags, 3 GCPs (Pix4D).
- PPK-corrected image geotags, 5 GCPs (Pix4D).

In Pix4D, the research team used the standard workflow and 3D mapping template. The research team experimented with the “Accurate Geolocation and Orientation” calibration method but observed that differences in accuracy results between the standard calibration method and the accurate geolocation and orientation calibration method were not significant.

In Metashape, the research team used a slightly modified version of a workflow developed by USGS (133, 134). When using Metashape with PPK- or RTK-corrected image geolocations, one must set the position accuracy estimates under settings in the reference menu. Like Pix4D, no angular orientation information is input with the imagery. For both Metashape and Pix4D, the research team brought horizontal and vertical accuracy estimates into the software within the image location text file produced by the PPK software. Angular orientation information for each image was available from the onboard IMU of the WingtraOne UAS. Although not required for SfM processing, the research team entered this information into Pix4D and Metashape along with the PPK-corrected image locations and uncertainties.

For the runs with PPK-corrected image geotags and no control, the research team did not use the aerial targets to constrain the solution in the SfM processing. The research team used the aerial targets as checkpoints for absolute accuracy assessment. The geolocation of the final products was based entirely on the image locations from PPK and bundle block solution.

For the runs with PPK-corrected image geotags and at least one GCP, the research team used the selected GCPs to reoptimize the SfM solution. For the autonomous scenario, the research team used half of the GCPs as control and the remaining half as checkpoints.

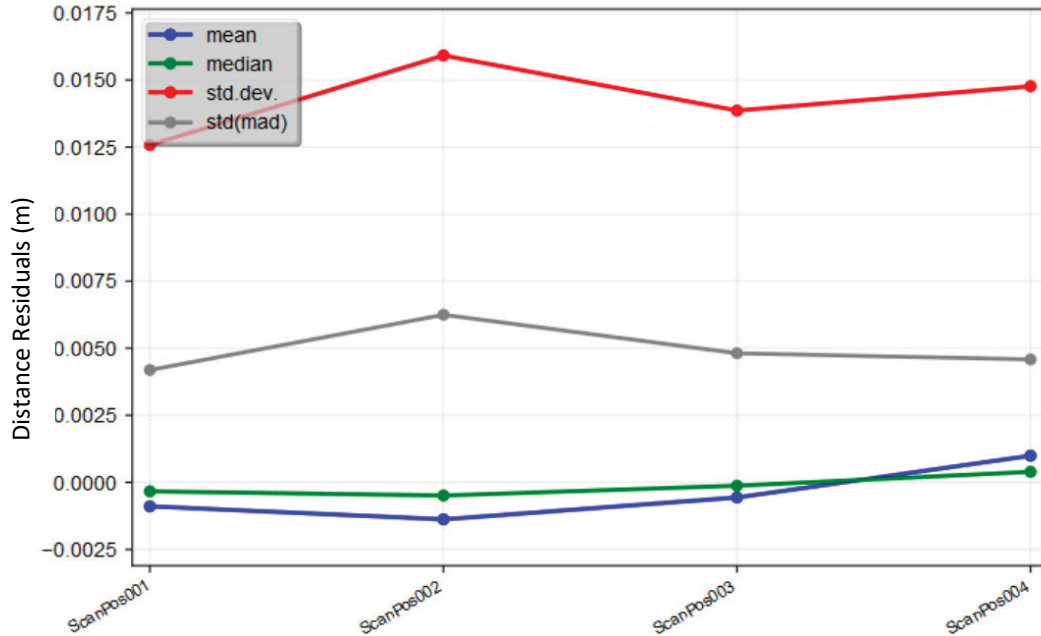
### TLS Data Processing

The research team processed the four TLS scan positions into a merged point cloud using the automatic registration and multi-station adjustment (MSA) tools in RIEGL's RiSCAN™ postprocessing software. This approach uses the estimated scan position and orientation information provided by the scanner's RTK GNSS fixed solution (corrected via the TxDOT RTN) and orientation sensors (IMU and 3-axis magnetometer). Geometric constraints based on cloud-to-cloud overlap were applied to register and adjust the scans in a two-stage process.

The procedure involved extracting a voxel (or 3D pixel) representation of the data and merging (or co-registering) the point clouds from the different scan positions based on optimizing the fit of these voxel representations. The research team then used the MSA tool to perform a fine alignment based on extracted plane patches from all the scan positions. Figure 199 shows an example of the distance residuals of all planar patches per scan position. The MSA tool considers additional sensor measurements such as roll, pitch, and yaw to prevent unwanted tilting of scan positions, and uses the GNSS RTK solution to adjust the absolute position. Although not used here, reflector targets with known coordinates can also be integrated into the solution for fine alignment. After alignment, the procedure provided an estimate of the scan position accuracies, as shown in Table 87.

TLS point cloud data often includes noisy measurements, such as random points floating over the 3D scene, due to interaction of the laser pulse with dust particles or birds flying over the scene during a scan. Some measurements from a limited area of the laser illumination spot on a target, usually related to the edges of an object, typically have a low reflectance, and their location in the point cloud can be more uncertain relative to stronger point returns. In addition, because the scanner has multitarget detection capability, some measured points can be located at a distance between two consecutive targets along the laser transmit path that is less than the TLS's effective range resolution for target separation.

The research team applied a semi-automatic method to reduce point cloud noise. All measured points have additional attributes recorded by the scanner's online waveform processing unit, including calibrated relative reflectance, calibrated amplitude, and pulse shape deviation. Visual inspection of the data revealed that most noisy points on the edges of objects had low relative reflectance values (e.g., <-25 dB). The research team applied a reflectance threshold to filter these points from the point cloud within the scene of interest.



Note: The lines are used for overall visualization, not to suggest linear trends between adjacent data points.

**Figure 199. Example MSA Adjustment Result from a RiSCAN Pro Processing Report.**

**Table 87. TLS Estimated Scan Position Accuracy.**

Scan Position	Horizontal Accuracy (m)	Vertical Accuracy (m)
1	0.014	0.010
2	0.014	0.010
3	0.014	0.010
4	0.014	0.012

Erroneous points located between targets at distances less than the TLS range resolution tend to have higher pulse shape deviation values. Through visual inspection of the data, a pulse shape deviation threshold was determined (e.g., >30, where 0 implies no deviation) and applied to exclude these points from the point cloud. Finally, the research team applied a manual inspection of the cloud for any residual clean up. Figure 200 shows examples of the noise-filtered and colored TLS point cloud for this field test.



**Figure 200. Colorized TLS Scan of the Crashed Vehicle.**

### *Analysis*

The research team evaluated the overall quality of the UAS-based densified 3D point cloud of the reconstructed crash scene and surrounding pavement, absolute horizontal and vertical accuracy of the point cloud measurements with emphasis on the vertical component, and relative accuracy of measurements acquired within the point cloud. The research team completed the following analyses:

- Evaluation of the UAS and TLS point cloud data relative to ground control data.
- Evaluation of the UAS point cloud data relative to TLS point cloud data.
- Relative accuracy evaluation within the UAS point cloud data.
- Accuracy evaluation based on SfM processing reports.

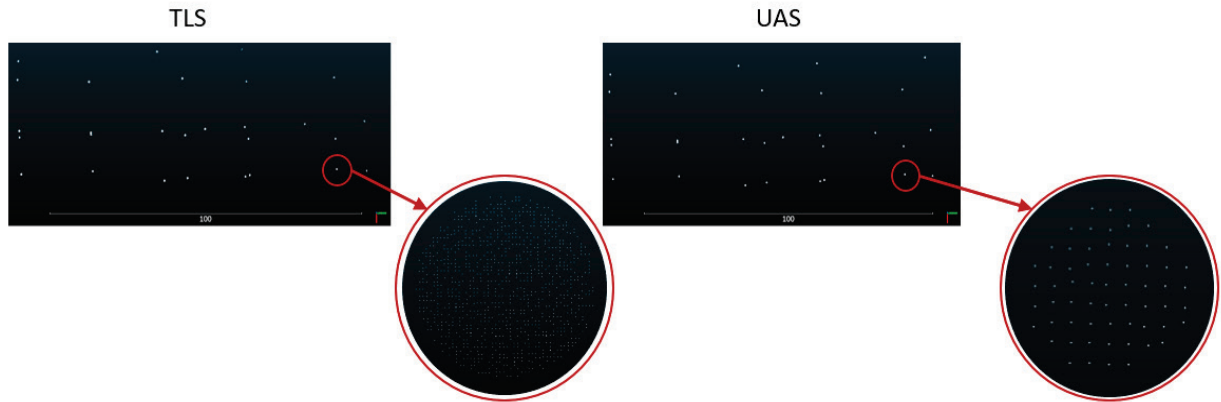
Readers should note that the evaluation procedures and metrics described in this section also apply for subsequent field tests described in this report (i.e., Tests 5, 6, and 7).

### Evaluation of UAS and TLS Point Cloud Data Relative to Ground Control Data

The research team developed a python script to assess the magnitude and statistics of the absolute error vectors in the X-Y-Z components of the UAS and TLS point cloud measurements relative to the RTK GNSS GCPs and topo points collected at the scene. For comparison purposes, the research team also used the *lascontrol* module in LAStools™ (135). The python script completed four activities:

- Using the position of each RTK GNSS observation, found the closest point to that observation within the UAS or TLS point cloud.
- Searched a cluster of points around the closest point within a radius of 25 cm (10 inches) and saved that information in a separate file (Figure 201).
- Generated a triangulated irregular network (TIN) surface from the cluster of points.
- Calculated the distance between the RTK GNSS observation and the generated TIN.





**Figure 201. Example of 25-cm Radius Point Patches Extracted from UAS and TLS Data.**

Evaluation of UAS Point Cloud Data Relative to TLS Point Cloud Data

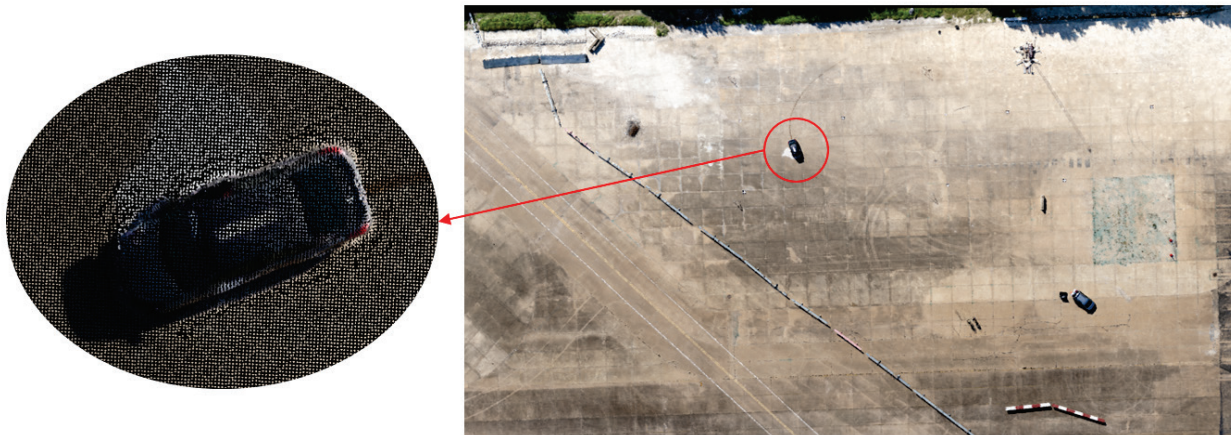
The research team compared the UAS-SfM point cloud and the TLS point cloud by comparing surface roughness values (both pavement and crash scene), point-to-point distance measurements within a region of interest, and cloud-to-cloud distances within a region of interest.

**Surface Roughness.** Similar to the case discussed above, the research team developed a python script to compute the surface roughness (defined as the standard deviation of the Z component) of the pavement and crash scene based on the TLS and UAS point cloud data. The script selected 10,000 seed points equally distributed over the road surface and crash scene from the underlying TLS point cloud. Then, for each seed point, the script extracted circular patches, including neighboring points within a 25-cm radius from the TLS and UAS point clouds, and calculated the standard deviation of the Z component for those points (Figure 202).



**Figure 202. Circular Patches for Computing Surface Roughness (not to scale).**

**Point-to-Point Comparison in Region of Interest.** The research team developed a python script to compare point-to-point distances between UAS and TLS point clouds within a selected region of interest around the crashed vehicle (Figure 203). The script randomly selected 10,000 UAS points from within the region of interest and calculated distances between UAS points and the nearest TLS reference points. The script also measured local variability in surface height (or elevation representation) of the UAS point cloud relative to the TLS point cloud within the region of interest. The script selected 10,000 seed points equally distributed within the region of interest from the underlying TLS point cloud. Then, for each seed point, the script extracted circular patches including neighboring points within a 25-cm radius from the TLS and UAS point clouds and calculated the mean value of all measured Z distances (Figure 202).



**Figure 203. Segmented Car Region of Interest.**

**Cloud-to-Cloud Comparison.** Using CloudCompare, the research team computed cloud-to-cloud distances between the 3D densified point cloud created from the UAS survey and the TLS survey. The mean cloud-to-cloud distance and standard deviation of the distance served as the dense point cloud quality factors. The method worked by searching for the nearest neighbor in the reference cloud (i.e., TLS) for each point of the compared cloud (i.e., UAS) and computing their Euclidean distance.

#### Relative Accuracy Evaluation within UAS Point Cloud Data

The research team performed point cloud measurements to evaluate differences in relative accuracy between the TLS and UAS point cloud data. The research team used identifiable GCPs within the scene to measure triangular geometry, distances, and angles. The research team also compared and evaluated differences in distances and angles between the TLS and UAS point clouds.

#### Evaluation Based on SfM Processing Reports

The research team examined Pix4D SfM processing reports to evaluate differences in the absolute accuracy of the sparse point cloud 3D reconstruction based on the SfM BA process. This activity involved comparing differences in reported RMSE for reconstructed point measurements relative to checkpoints, which were based solely on PPK-corrected image geotags and the addition of GCPs with, and without, PPK-corrected geotags.

## Results

### Evaluation of UAS and TLS Point Cloud Data Relative to Ground Control Data

Table 88, Table 89, and Table 90 provide summarized information about the TLS and UAS-SfM point clouds processed with Metashape and Pix4D based on the entire mapped area, the crashed vehicle scene and surrounding pavement area, and the segmented car scene only, respectively. Figure 204 shows the coverage of the TLS point cloud data based on the entire area scanned. Some differences existed in coverage and average point density between Metashape and Pix4D. Figure 205 show differences in reconstruction between Metashape and Pix4D for the entire mapped area and segmented area of the car scene and surrounding pavement. By comparison, Figure 206 shows the UAS and TLS point clouds for the segmented car scene.

**Table 88. General Information about Point Cloud Data for Entire Scene.**

Metric	TLS	UAS (Metashape)	UAS (Pix4D)
Number of Points	61,577,951	22,597,285	23,814,582
Point Density (per square meter)	1,217	354	347
Point Spacing (meter)	0.03	0.05	0.05
Area Covered (square meter)	50,608	63,788	68,456

**Table 89. General Information about Point Cloud Data for Surrounding Scene.**

Metric	TLS	UAS (Metashape)	UAS (Pix4D)
Number of Points	59,055,046	5,668,241	7,061,069
Point Density (per square meter)	3,022	304	377
Point Spacing (meter)	0.02	0.06	0.05
Area Covered (square meter)	19,540	18,632	18,728

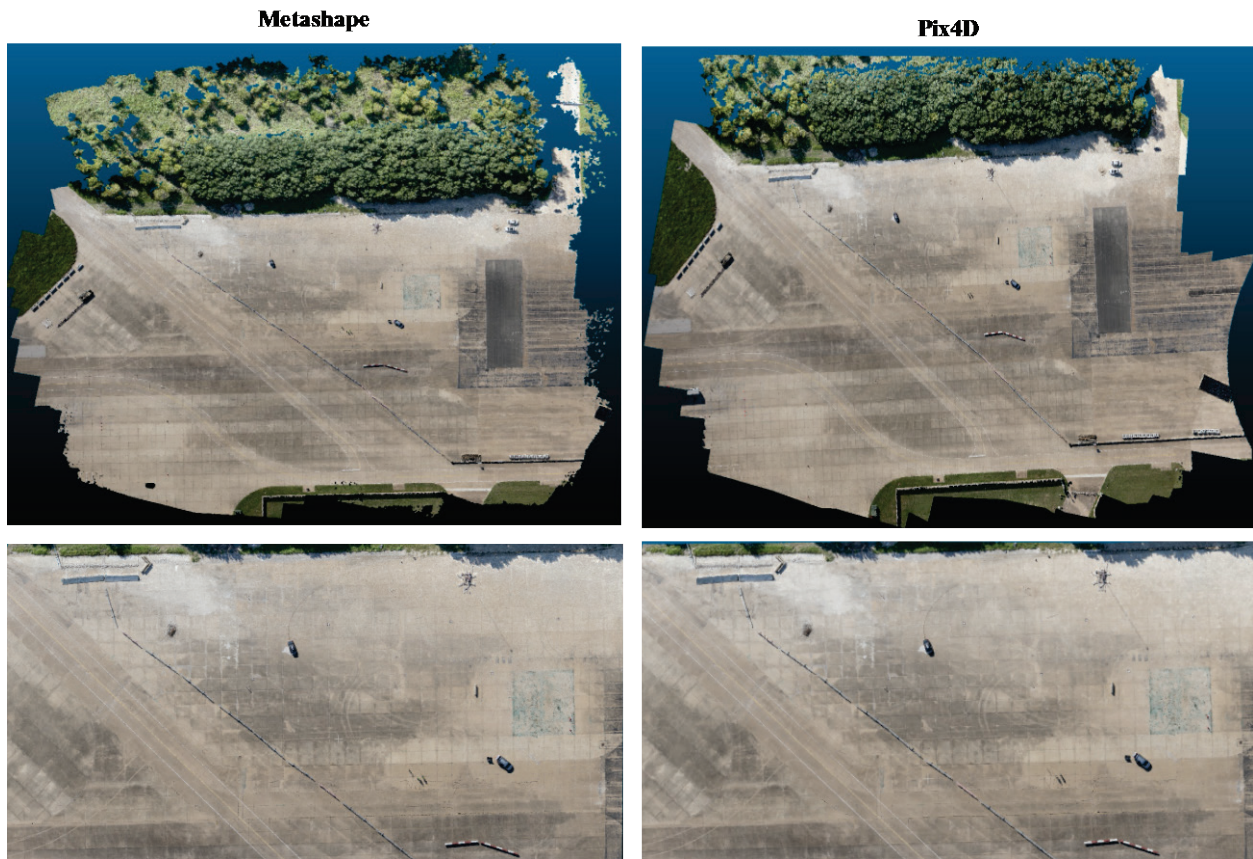
**Table 90. General Information about Point Cloud Data for Car Scene Only.**

Metric	TLS	UAS (Metashape)	UAS (Pix4D)
Number of Points	418,448	17,016	16,012
Point Density (per square meter)	6,538	265	250
Point Spacing (meter)	0.01	0.06	0.06
Area Covered (square meter)	64	64	64



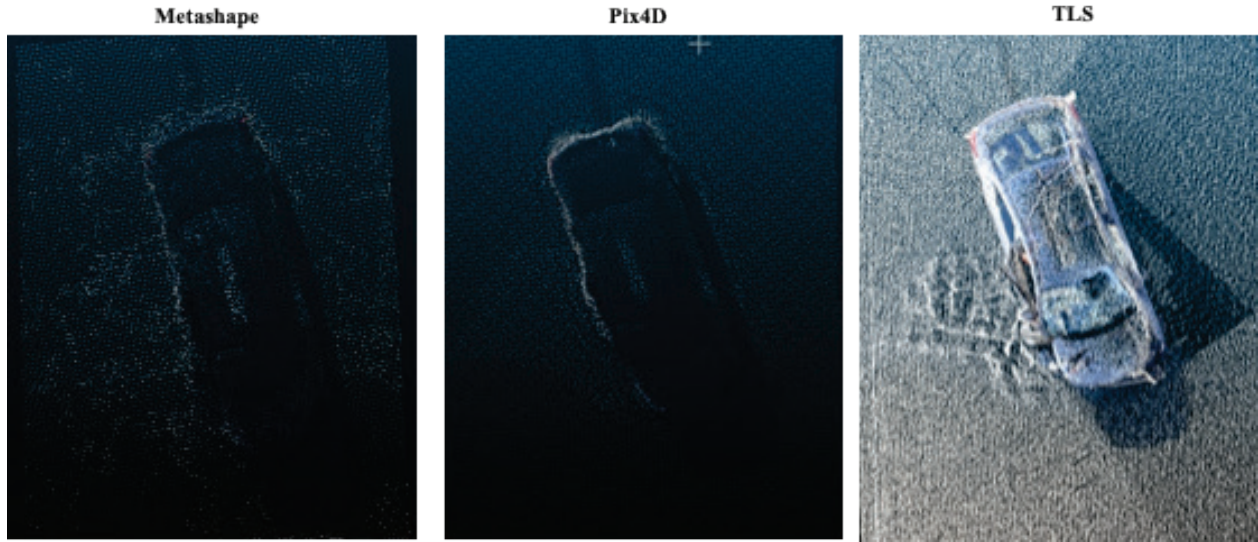
Note: The dashed box represents the approximate area mapped by the UAS.

**Figure 204. Orthometric View of the Entire Scanned Area of the TLS Point Cloud.**



Note: The bottom images show the segmented region of crash scene and surrounding area used for analysis.

**Figure 205. Comparison of UAS Point Cloud Created with Metashape and Pix4D.**



**Figure 206. Comparison of UAS and TLS Point Cloud for Car Scene.**

The research team computed the absolute accuracy of the UAS and TLS point cloud measurements in the Z component relative to the 14 GCPs and 15 topo points. A total of 4 GCPs located on the perimeter of the scene in vegetation were excluded from the TLS computations due to a vertical bias related to vegetation occlusion.

Table 91 and Table 92 show results for the developed method and LAStools, respectively. In general, Pix4D resulted in a more accurate estimate of surface height relative to Metashape. RMSEs for Pix4D ranged from 0.032–0.039 m compared to 0.044–0.049 m for Metashape. The UAS results in Table 91 and Table 92 compared favorably to the TLS data, which is significant, considering that the solution was based solely on PPK-corrected image geotags because no GCPs were used to constrain the SfM solution. Both Pix4D and Metashape provided reconstructions with vertical accuracies at near survey-grade quality with a 3–4 cm (1.2–1.6 inch) mean error.

**Table 91. Magnitude of Surface Height Error Relative to RTK GNSS (Developed Method).**

Metric	TLS	UAS (Metashape)	UAS (Pix4D)
Mean Error Length (m)	0.033	0.048	0.037
STD Error Length (m)	0.016	0.011	0.013
RMSE (m)	0.037	0.049	0.039

**Table 92. Magnitude of Surface Height Error Relative to RTK GNSS (LAStools Method).**

Metric	TLS	UAS (Metashape)	UAS (Pix4D)
Mean Error Length (m)	0.026	0.042	0.029
STD Error Length (m)	0.014	0.017	0.020
RMSE (m)	0.030	0.044	0.032

## Evaluation of UAS Point Cloud Data Relative to TLS Point Cloud Data

**Surface Roughness.** Figure 207 shows surface roughness results estimated from the TLS, UAS (Metashape), and UAS (Pix4D) point clouds. TLS had the smallest mean standard deviation, overall, with a value of 0.4 cm (0.16 inches) compared to 0.7 cm (0.28 inches) for Metashape and 0.9 cm (0.35 inches) for Pix4D. Metashape and Pix4D results show somewhat similar patterns to TLS in terms of capturing areas with more or less surface roughness. However, Pix4D shows more variability (greater surface roughness) across the patches than Metashape.

**Point-to-Point Comparison in the Region of Interest.** Figure 208 shows results for the UAS Metashape and UAS Pix4D point clouds. Table 93 shows point-to-point distance statistics for all coordinate components (X-Y-Z). Pix4D provided a more similar reconstruction to the TLS scan within the region of interest. The mean distance error was lower for Pix4D, 2 cm (0.79 inches) compared to Metashape, 3.5 cm (1.4 inches).

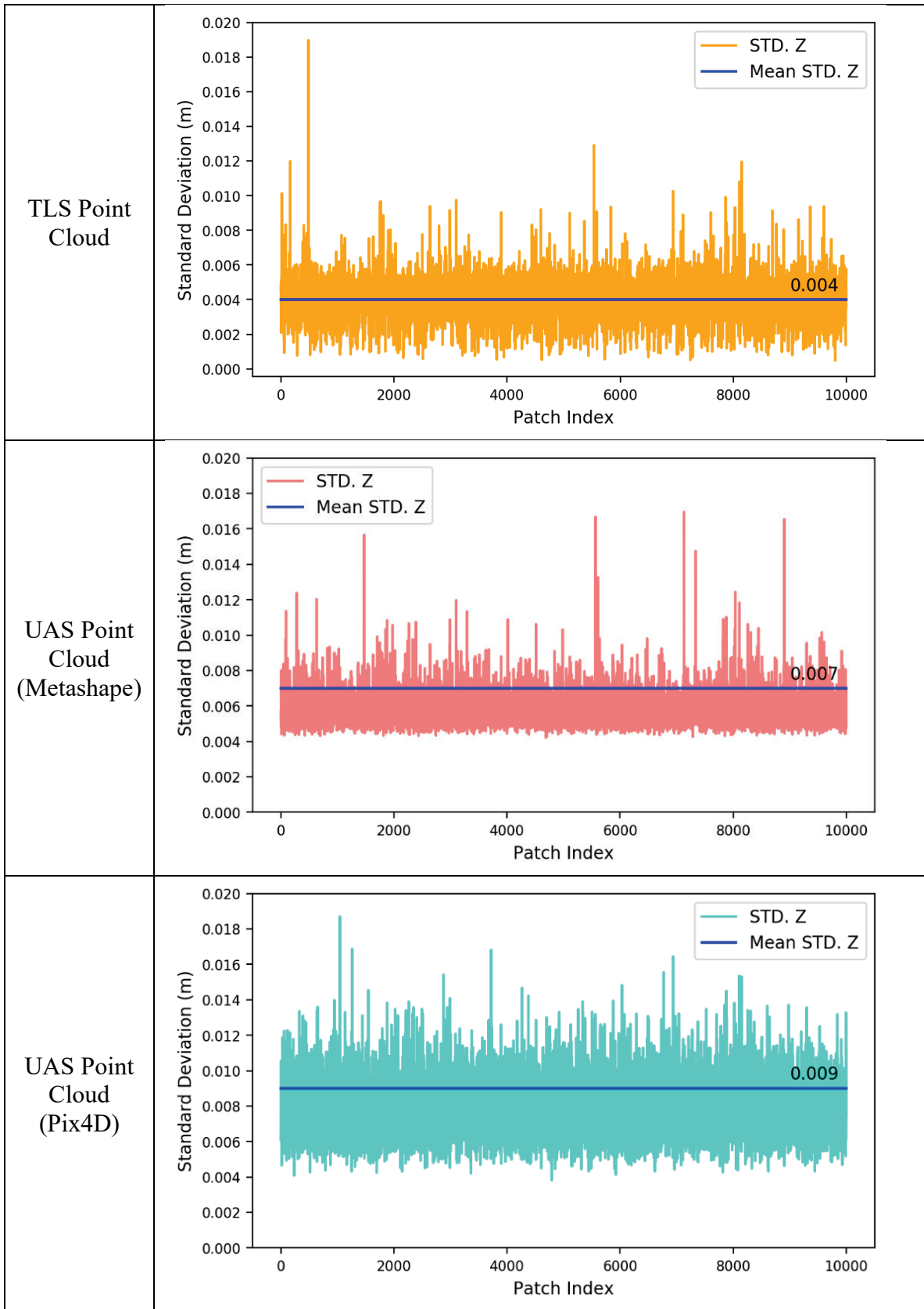
Figure 209 shows the mean distance in the Z component (i.e., mean absolute vertical error) for a respective UAS Metashape point patch and UAS Pix4D point patch relative to a TLS point patch within the region of interest. The two plots show similar patterns across the set of point patches in terms of larger or smaller vertical displacement relative to the TLS cloud. Interestingly, Pix4D shows a slightly higher overall mean distance in the Z component across all patches relative to Metashape.

These plots should be taken as an assessment of vertical measurement variability relative to the TLS data rather than as an overall metric of absolute vertical accuracy. It is important to emphasize that there are places on the vehicle with limited UAS-SfM point coverage due to the nadir perspective of the WingtraOne data collected. Regions with reduced point density or data gaps on the car, when averaged over a 25-cm (10-inch) radius patch, can result in large errors in Z distance, as observed in the plots. A smaller search radius would reduce this effect.

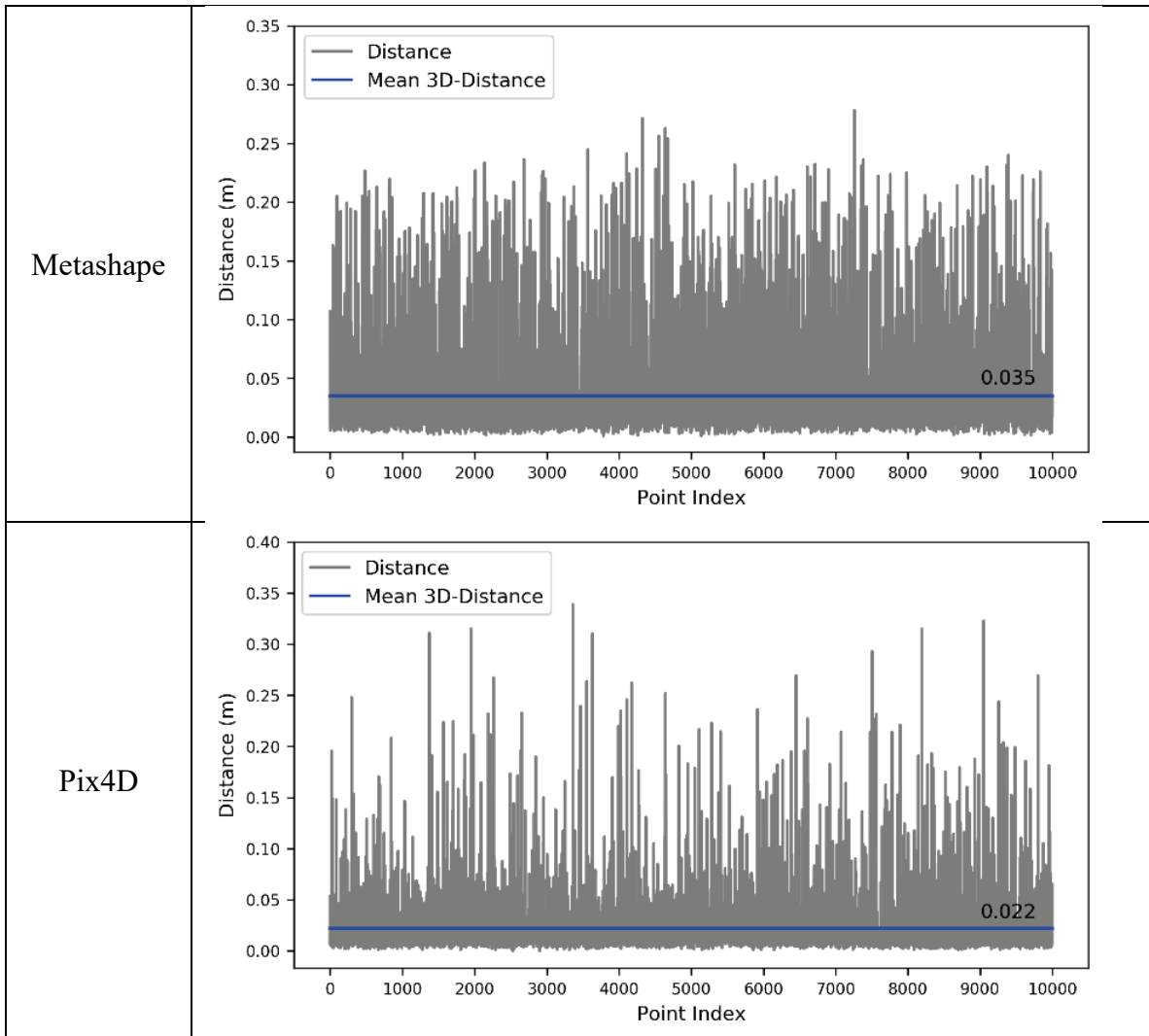
Alternatively, there are places on the vehicle more occluded by the laser pulse but not the UAS (e.g., on the roof of the vehicle). These places could also result in larger mean Z distance error for patches extracted from that region.

**Cloud-to-Cloud Comparison.** Figure 210 shows cloud-to-cloud distances for Metashape and Pix4D computed over a large scene that includes the crash scene and the surrounding area. Figure 211 shows the results for the car segmented scene. When comparing results visually, the patterns are nearly identical based on the color ramp used.

Table 94 summarizes the cloud-to-cloud distance statistics for the densified UAS point clouds in Metashape and Pix4D. Pix4D provided a closer representation of the TLS point cloud in both the large scene and car scene than Metashape. Pix4D also provided less variability in distances overall, specifically for the car scene. These results are significant, considering the difference in cost between a geodetic TLS and a UAS camera.



**Figure 207. Surface Roughness.**

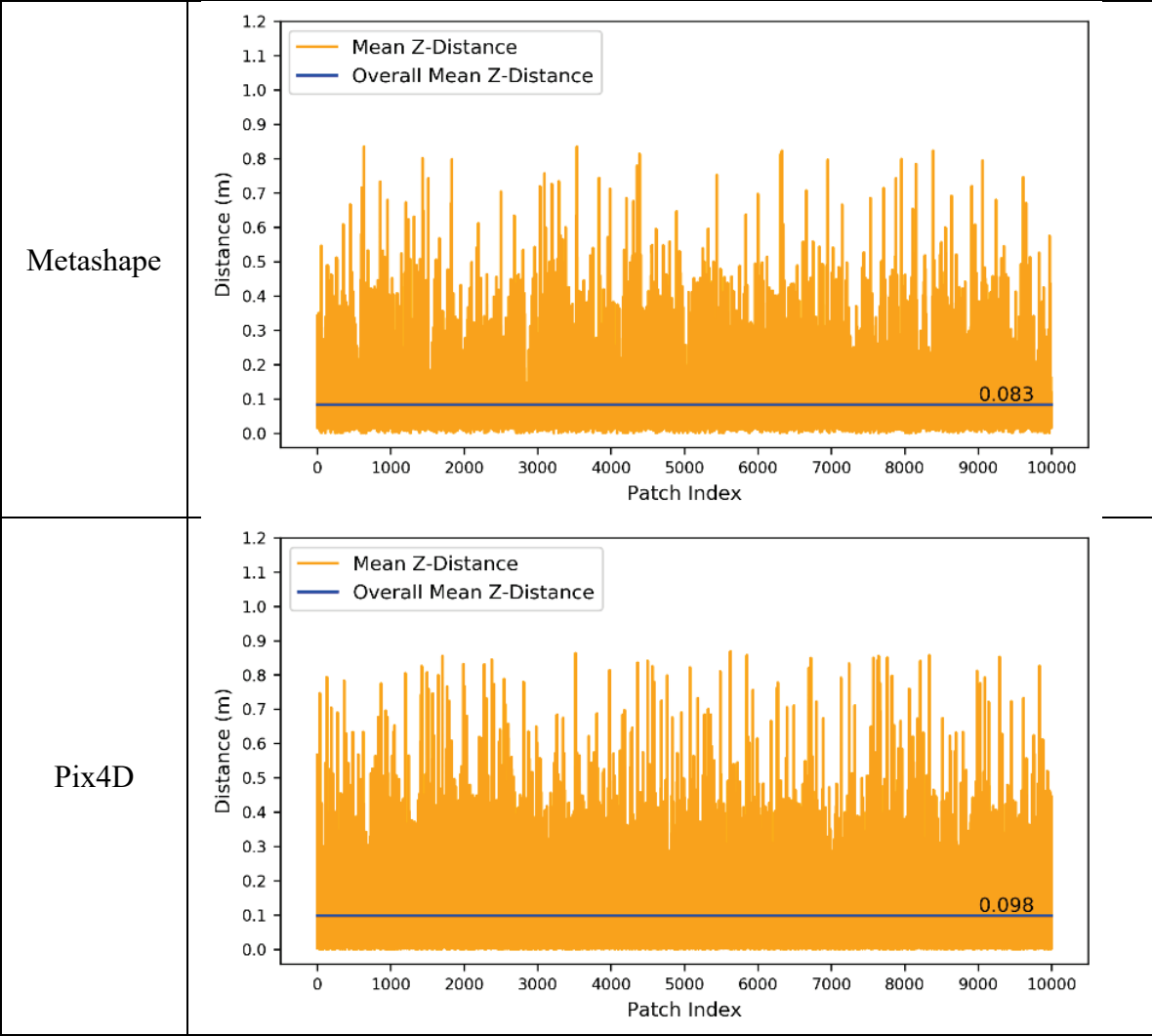


**Figure 208. Distance from UAS Points to TLS Points for Car Segment Region of Interest.**

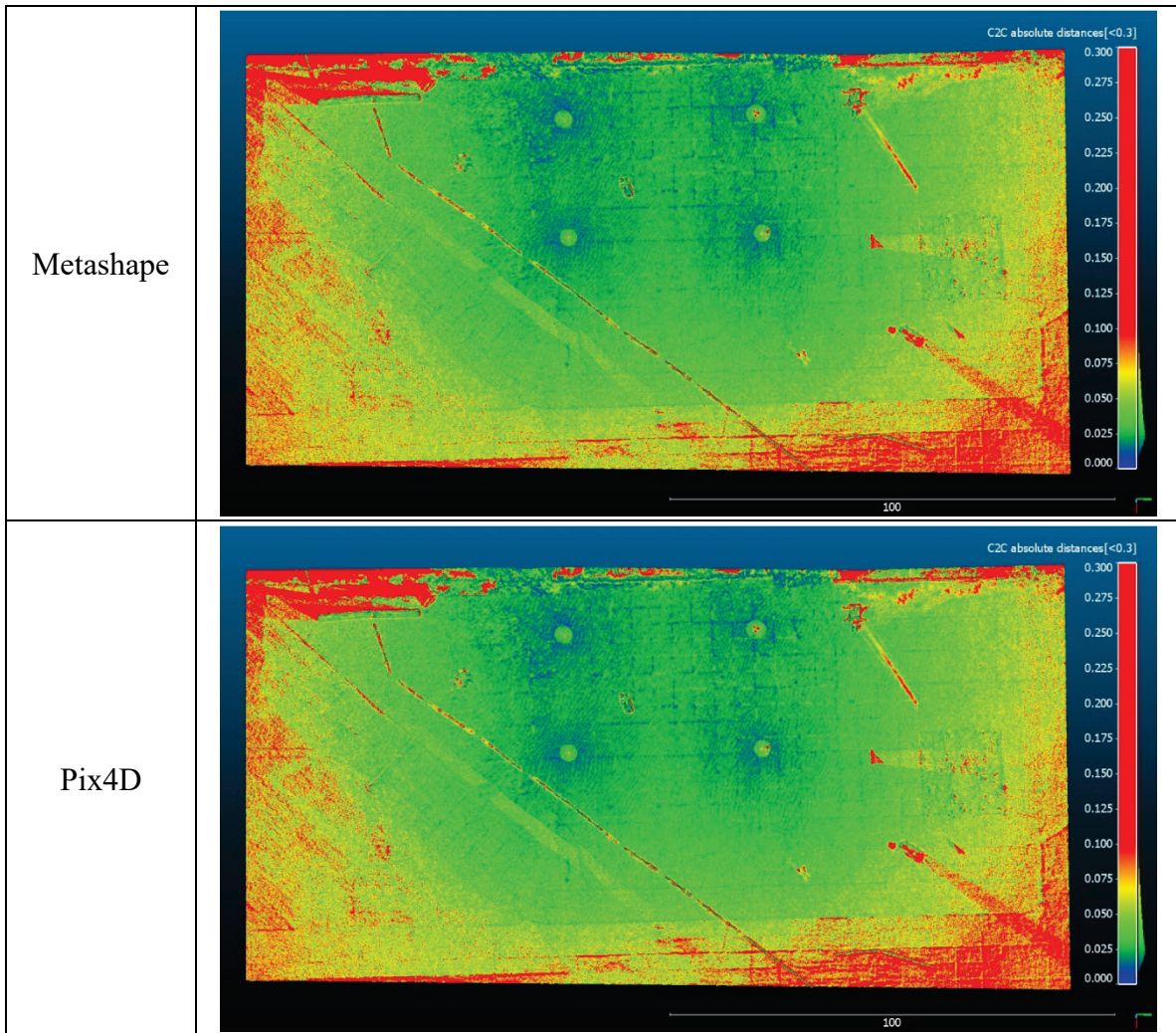
**Table 93. Statistics for Point-to-Point Distance Comparisons.**

Metric	Distance—Metashape (m)				Distance—Pix4D (m)			
	X-Y-Z	X	Y	Z	X-Y-Z	X	Y	Z
Minimum (m)	0.001	0.000	0.000	0.000	0.000	0.000	0.000	0.000
Maximum (m)	0.278	0.240	0.217	0.249	0.339	0.303	0.023	0.315
Mean (m)	0.035	0.013	0.014	0.026	0.022	0.009	0.010	0.014
Standard Deviation (m)	0.040	0.024	0.023	0.031	0.028	0.016	0.017	0.019

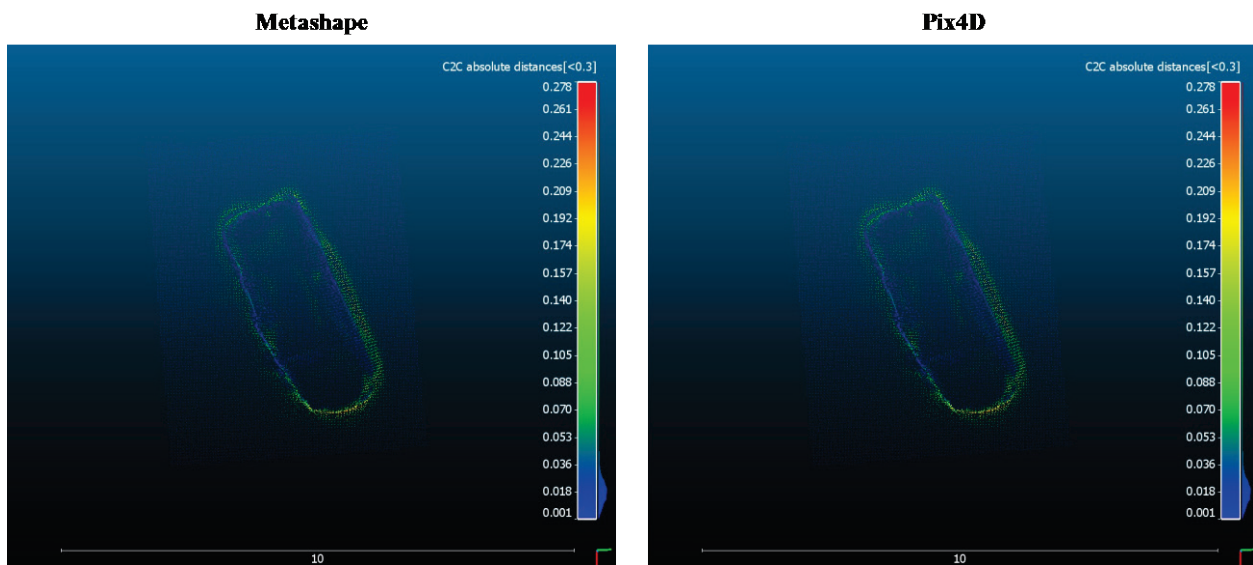




**Figure 209. Mean Distance in Z for UAS Point Patches to TLS Point Patches.**



**Figure 210. Cloud-to-Cloud Distances in Meters for Large Scene (Metashape).**



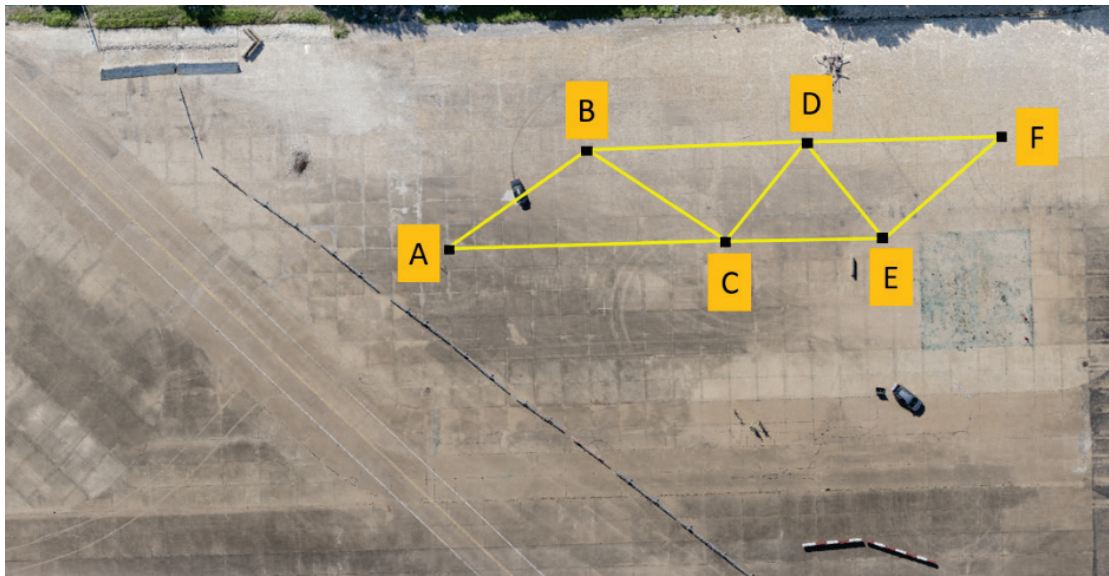
**Figure 211. Cloud-to-Cloud Distances in Meters for Car Scene (Metashape and Pix4D).**

**Table 94. Cloud-to-Cloud Distance Statistics.**

Region of Interest	Distance–Metashape (m)		Distance–Pix4D (m)	
	Mean	Standard Deviation	Mean	Standard Deviation
Large Scene	0.054	0.050	0.046	0.050
Car Scene	0.038	0.040	0.023	0.028

Relative Accuracy Evaluation within UAS Point Cloud Data

Using CloudCompare, the research team compared measurements of distances and angles of triangular facets. The triangular geometry was based on targets (GCPs) identifiable in the scene as shown in Figure 212. Not all targets were distinctly identifiable in the TLS point cloud, so only triangles ABC and BCD were used for TLS comparison.



**Figure 212. Geometry of Triangular Facets in the Scene.**

Table 95 shows distance measurement results. Most distance measurements were within 1 cm or less relative to the respective TLS measurement for both Metashape and Pix4D UAS point clouds. Metashape and Pix4D had equivalent RMSE values of 0.018 m, with Metashape providing a slightly smaller mean error (bias) relative to Pix4D at the expense of a slightly higher standard deviation of the error. Table 95 also shows additional distances measured for triangles CDE and DEF within the UAS point cloud. Results show a close agreement between the Metashape and Pix4D, suggesting consistent accuracy in relative distance measurements.

Table 96 shows angular measurement results. The Metashape UAS point cloud had an RMSE of 0.073 degrees while the Pix4D UAS point cloud had a slightly larger RMSE of 0.088 degrees. Overall, both Metashape and Pix4D resulted in a close agreement to TLS angular measurements with absolute residuals typically in the range of a few hundredths of a degree. Table 96 shows additional angular measurements between triangles CDE and DEF for the two UAS point clouds revealing close, relative agreement between them.

**Table 95. Measured Distances within TLS and UAS Point Clouds.**

Triangle	Segment	TLS (m)	UAS (m)		$ D_{TLS} - D_{UAS} $	
			Metashape	Pix4D	Metashape	Pix4D
ABC	AB	27.568	27.567	27.582	0.001	0.014
	AC	45.424	45.432	45.430	0.008	0.006
	BC	27.684	27.684	27.681	0.000	0.003
BCD	BC	27.684	27.684	27.681	0.000	0.003
	CD	20.887	20.880	20.909	0.007	0.022
	BD	36.597	36.558	36.565	0.039	0.032
CDE	CD		20.880	20.909	Mean, standard deviation, RMSE: 0.009, 0.015, 0.018 (Metashape) 0.013, 0.012, 0.018 (Pix4D)	
	CE		25.947	25.970		
	DE		19.780	19.775		
DEF	DE		19.780	19.775		
	EF		25.220	25.248		
	DF		31.997	32.031		

**Table 96. Measured Angles within TLS and UAS Point Clouds.**

Triangle	Segment	TLS (degree)	UAS (degree)		$ \alpha_{TLS} - \alpha_{UAS} $	
			Metashape	Pix4D	Metashape	Pix4D
ABC	AB	34.785	34.769	34.779	0.016	0.006
	AC	110.596	110.630	110.585	0.034	0.011
	BC	34.618	34.601	34.636	0.017	0.018
BCD	BC	34.521	34.562	34.612	0.041	0.091
	CD	83.206	83.339	83.374	0.133	0.168
	BD	48.685	48.777	48.762	0.092	0.077
CDE	CD		48.501	48.433	Mean, standard deviation, RMSE: 0.056, 0.047, 0.073 (Metashape) 0.062, 0.063, 0.088 (Pix4D)	
	CE		79.256	79.281		
	DE		52.243	52.286		
DEF	DE		52.016	52.020		
	EF		89.801	89.857		
	DF		38.183	38.123		

Evaluation Based on SfM Processing Reports

Table 97 shows the RMSE results for the six processing runs. Contrary to the initial expectations, adding GCPs to the PPK adjustment did not significantly improve the result except for reducing the X component error. Overall, there was minimal gain in accuracy for Pix4D when adding GCPs to the PPK solution, which is interesting considering that the GCPs and checkpoints were both surveyed using RTK corrected via TxDOT RTN at the time of the survey.

Table 98 shows the absolute difference in the RMSE for each processing run relative to the RMSE for the PPK-aided solution with no GCPs in Pix4D. Results show a close agreement in accuracy across all coordinate components. Interestingly, the PPK-aided solution processed in Metashape resulted in a difference of almost 2 cm (0.8 inches) in the Z component with respect

to Pix4D. This observation is only one case study and cannot be generalized or extended to other situations.

**Table 97. Summary of SfM Processing Report Results for Checkpoint Error.**

Processing Run	RMSE X (m)	RMSE Y (m)	RMSE Z (m)
Autonomous Image Geotags, 7 GCPs (Pix4D)	0.012	0.015	0.032
PPK-Corrected Image Geotags, no GCPs (Pix4D)	0.031	0.016	0.028
PPK-Corrected Image Geotags, no GCPs (Metashape)	0.028	0.014	0.046
PPK-Corrected Image Geotags, 1 GCP (Pix4D)	0.013	0.021	0.027
PPK-Corrected Image Geotags, 3 GCPs (Pix4D)	0.010	0.015	0.032
PPK-Corrected Image Geotags, 5 GCPs (Pix4D)	0.011	0.013	0.028

**Table 98. Difference in RMSE between Processing Runs and PPK-Only Solution in Pix4D.**

Processing Run	\Delta RMSE X	\Delta RMSE Y	\Delta RMSE Z
Autonomous Image Geotags, 7 GCPs (Pix4D)	0.019	0.001	0.004
PPK-Corrected Image Geotags, no GCPs (Pix4D)	Reference	Reference	Reference
PPK-Corrected Image Geotags, no GCPs (Metashape)	0.003	0.001	0.018
PPK-Corrected Image Geotags, 1 GCP (Pix4D)	0.018	0.006	0.000
PPK-Corrected Image Geotags, 3 GCPs (Pix4D)	0.021	0.001	0.004
PPK-Corrected Image Geotags, 5 GCPs (Pix4D)	0.021	0.003	0.000

Table 99 through Table 103 below show the detailed error results reported in Pix4D for each processing run. Table 104 shows the checkpoint errors results reported in Metashape for the PPK aided solution.

**Table 99. Pix4D SfM Checkpoint Error (Autonomous GNSS and 7 GCPs).**

Check Point Name	Accuracy XY/Z [m]	Error X [m]	Error Y [m]	Error Z [m]	Projection Error [pixel]	Verified/Marked
GCP2		0.0068	0.0069	-0.0054	0.5810	14 / 14
GCP4		0.0136	-0.0002	0.0454	0.5843	21 / 21
GCP5		-0.0195	0.0184	-0.0357	0.5268	24 / 24
GCP9		-0.0146	-0.0143	-0.0210	0.5650	23 / 23
GCP11		-0.0137	0.0131	-0.0138	0.6304	22 / 22
GCP13		0.0059	0.0241	0.0308	0.4152	21 / 21
GCP14		-0.0026	0.0111	0.0468	0.3746	23 / 23
Mean [m]		-0.003428	0.008441	0.006724		
Sigma [m]		0.011769	0.011759	0.031215		
RMS Error [m]		0.012258	0.014475	0.031931		

**Table 100. Pix4D SfM Checkpoint Error (PPK).**

Check Point Name	Accuracy XY/Z [m]	Error X [m]	Error Y [m]	Error Z [m]	Projection Error [pixel]	Verified/Marked
GCP1		-0.036	-0.030	-0.013	0.543	14 / 14
GCP2		-0.025	-0.018	-0.010	0.599	14 / 14
GCP3		-0.027	-0.018	0.016	0.601	18 / 18
GCP4		-0.008	-0.014	0.056	0.565	21 / 21
GCP5		-0.039	0.014	-0.027	0.490	24 / 24
GCP6		-0.006	0.016	0.018	0.436	20 / 20
GCP7		-0.034	0.014	-0.027	0.603	19 / 19
GCP8		-0.019	0.004	-0.024	0.429	22 / 22
GCP9		-0.042	-0.017	-0.043	0.549	23 / 23
GCP10		-0.036	-0.018	-0.035	0.385	26 / 26
GCP11		-0.043	0.000	-0.030	0.633	22 / 22
GCP12		-0.030	-0.013	-0.026	0.440	18 / 18
GCP13		-0.028	0.013	-0.006	0.414	21 / 21
GCP14		-0.035	0.009	0.004	0.349	23 / 23
<b>Mean [m]</b>		-0.029220	-0.004049	-0.010518		
<b>Sigma [m]</b>		0.011092	0.015097	0.025553		
<b>RMS Error [m]</b>		0.031254	0.015631	0.027633		

**Table 101. Pix4D SfM Checkpoint Error (PPK and 1 GCP).**

Check Point Name	Accuracy XY/Z [m]	Error X [m]	Error Y [m]	Error Z [m]	Projection Error [pixel]	Verified/Marked
GCP1		-0.012	-0.030	0.014	0.542	14 / 14
GCP2		0.002	-0.017	0.013	0.601	14 / 14
GCP3		0.005	-0.015	0.036	0.618	18 / 18
GCP4		0.020	-0.004	0.072	0.564	21 / 21
GCP5		-0.013	0.028	-0.015	0.500	24 / 24
GCP6		0.017	0.036	0.023	0.446	20 / 20
GCP7		-0.014	0.033	-0.017	0.602	19 / 19
GCP8		0.003	0.020	-0.010	0.440	22 / 22
GCP9		-0.020	-0.005	-0.025	0.551	23 / 23
GCP11		-0.019	0.008	-0.009	0.643	22 / 22
GCP12		-0.004	-0.008	-0.003	0.443	18 / 18
GCP13		-0.006	0.020	0.017	0.416	21 / 21
GCP14		-0.015	0.020	0.024	0.355	23 / 23
<b>Mean [m]</b>		-0.004242	0.006575	0.009186		
<b>Sigma [m]</b>		0.012357	0.020319	0.025638		
<b>RMS Error [m]</b>		0.013065	0.021356	0.027234		

**Table 102. Pix4D SfM Checkpoint Error (PPK and 3 GCPs).**

Check Point Name	Accuracy XYZ [m]	Error X [m]	Error Y [m]	Error Z [m]	Projection Error [pixel]	Verified/Marked
GCP1		-0.0047	-0.0211	-0.0170	0.5493	14 / 14
GCP2		0.0061	-0.0080	-0.0149	0.5956	14 / 14
GCP4		0.0202	-0.0043	0.0524	0.5700	21 / 21
GCP5		-0.0114	0.0231	-0.0299	0.4904	24 / 24
GCP7		-0.0069	0.0216	-0.0276	0.6035	19 / 19
GCP8		0.0092	0.0115	-0.0249	0.4310	22 / 22
GCP9		-0.0137	-0.0097	-0.0455	0.5457	23 / 23
GCP10		-0.0074	-0.0096	-0.0381	0.3913	26 / 26
GCP11		-0.0136	0.0088	-0.0335	0.6339	22 / 22
GCP12		0.0002	-0.0036	-0.0299	0.4439	18 / 18
GCP13		0.0018	0.0203	-0.0092	0.4151	21 / 21
<b>Mean [m]</b>		-0.001831	0.002641	-0.019817		
<b>Sigma [m]</b>		0.010096	0.014369	0.024912		
<b>RMS Error [m]</b>		0.010260	0.014610	0.031833		

**Table 103. Pix4D SfM Checkpoint Error (PPK and 5 GCPs).**

Check Point Name	Accuracy XYZ [m]	Error X [m]	Error Y [m]	Error Z [m]	Projection Error [pixel]	Verified/Marked
GCP2		0.0062	0.0056	0.0038	0.5917	14 / 14
GCP4		0.0143	-0.0018	0.0649	0.5710	21 / 21
GCP5		-0.0172	0.0180	-0.0206	0.4996	24 / 24
GCP8		0.0110	0.0007	-0.0165	0.4308	22 / 22
GCP9		-0.0122	-0.0135	-0.0356	0.5486	23 / 23
GCP11		-0.0126	0.0122	-0.0207	0.6355	22 / 22
GCP12		0.0008	0.0049	-0.0146	0.4363	18 / 18
GCP13		0.0071	0.0241	0.0033	0.4193	21 / 21
GCP14		-0.0003	0.0124	0.0113	0.3550	23 / 23
<b>Mean [m]</b>		-0.000309	0.006971	-0.002761		
<b>Sigma [m]</b>		0.010642	0.010605	0.027685		
<b>RMS Error [m]</b>		0.010647	0.012691	0.027822		

**Table 104. Metashape SfM Checkpoint Error (PPK).**

<b>Label</b>	<b>X error (cm)</b>	<b>Y error (cm)</b>	<b>Z error (cm)</b>	<b>Total (cm)</b>	<b>Image (pix)</b>
GCP1	3.31733	2.97293	3.45175	5.63539	0.121 (11)
GCP2	2.06046	1.77859	6.54269	7.0863	0.153 (3)
GCP3	2.59606	1.44045	0.791195	3.07253	0.356 (4)
GCP4	1.24	2.27813	-3.57044	4.41311	0.190 (5)
GCP5	3.27051	-1.05121	4.29157	5.49717	0.194 (3)
GCP6	0.580156	-0.574044	0.825358	1.16074	0.222 (5)
GCP7	3.45345	-0.415283	3.56028	4.97738	0.089 (3)
GCP8	1.65316	-0.0828564	5.25726	5.51168	0.031 (18)
GCP9	3.31634	1.12873	6.51338	7.39569	0.250 (3)
GCP10	3.22003	1.86142	5.25487	6.43794	0.036 (9)
GCP11	3.94406	0.936256	5.79012	7.06807	0.170 (5)
GCP12	2.61412	1.27467	5.07513	5.84939	0.125 (12)
GCP13	2.82804	-0.684018	4.47955	5.34154	0.050 (17)
GCP14	3.17043	-0.57924	3.88504	5.04784	0.055 (8)
<b>Total</b>	<b>2.81609</b>	<b>1.43736</b>	<b>4.56687</b>	<b>5.55452</b>	<b>0.135</b>

**Test 5 (12/07/2020): Delivery Truck Crash Test at the RELLIS Campus, College Station, Texas**

*Data Collection*

The UAS procedure followed for Test 5 was similar to that followed for Test 1, with some modifications. The research team used the Phantom 4 RTK. The research team also collected 3D point cloud data using the RIEGL-VZ 2000i TLS for ground truthing and accuracy assessment of UAS-SfM survey products. The team used a pair of Septentrio NR3 GNSS receivers. One of the receivers was used to record static observations, while the other one was tied to TxDOT’s RTN and used as a rover to collect ground control data. The research team set up the first receiver on a tripod located near the scene to log static observations for PPK postprocessing of the Phantom 4 RTK image geolocations. Over two hours of static observations were collected for processing of the base station coordinate using OPUS.

The team laid out 16 GCPs in a grid pattern along the pavement, ditch, and perimeter of the crash scene, as well as collected 15 additional topo points on the pavement for accuracy assessment, resulting in 31 control points for accuracy validation. The research team surveyed these points using the second GNSS receiver, which received corrections from TxDOT’s RTN. For each target, the research team recorded 5–10 seconds of observations at 1 Hz and then averaged the X-Y-Z coordinates. Unless otherwise noted, the research team used all 16 GCPs and 15 topo points as checkpoints for evaluation of the SfM photogrammetric accuracy.

The research team collected ground control data in NAD83(2011) State Plane Texas Central (meters) for X-Y and NAD83(2011) ellipsoid heights for Z. Ellipsoid heights were used to ensure consistent comparison of vertical accuracies relative to the SfM processing workflows using PPK image geotags, which come in NAD83(2011) ellipsoid heights.



For the flight with the Phantom 4 RTK, which took place at night, the research team used high-beam headlights from two vehicles placed at opposing ends of the scene within 100 m (328 ft) of the crashed vehicle to illuminate the scene. The flight design involved a double grid survey mode, consisting of perpendicular flight lines at an altitude of 25 m (82 ft) with the camera angled 30 degrees from nadir (i.e., 60 degrees with respect to the horizon). Overlap was set at 80 percent endlap and sidelap.

The flight was on autonomous mode with the Phantom 4 RTK flying at 2 m/s. During daylight missions, it is common to set the camera shutter at 1/1000 s or 1/2000 s in shutter priority mode (which holds the exposure time and adjusts both the f-stop and the ISO value). For this test, one of the goals was to assess whether there was enough ambient lighting from the vehicle headlights to enable sufficient SfM reconstruction while the UAS was moving. The research team set the camera shutter at 1/1000 s. Another reason for using the autonomous mode was that, when operating the Phantom 4 RTK in PPK mode, a RINEX file from the UAS for PPK processing is only accessible in connection with an automated mapping mission.

The research team acquired TLS data from a series of seven scan positions distributed around the crashed vehicle scene to ensure adequate coverage of the entire area. Scans used the VZ-2000i accurate pose (position and orientation) estimation method, which integrates the scanner’s onboard MEMS IMU for orientation and RTK GNSS for georeferencing. Imagery for point cloud colorization was not acquired due to nighttime conditions. Table 105 shows the TLS survey parameters used for data acquisition. The scanner was connected to the TxDOT RTN using a cellular network to obtain an RTK GNSS fixed position solution at each scan location.

**Table 105. Test 5 TLS Survey Parameters Used for Each Scan Position.**

<b>Scan Parameters</b>	<b>Values</b>
<b>Laser pulse rate</b>	1200 kHz
<b>Stepping angle</b>	20 millidegrees
<b>Horizontal field-of-view</b>	360°
<b>Vertical field-of-view</b>	100° (+60°, -40°)

*Data Processing*

Phantom 4 RTK PPK Data Processing

The research team obtained the differentially corrected image locations for each flight via PPK processing. This activity involved submitting the RINEX file of the static GNSS base station’s observations collected during the flight to OPUS to solve for a static coordinate in the NAD83(2011) datum. The research team used the precise ephemerides because they were available at the time of processing.

The research team used REDtoolbox to perform PPK corrections. The output was a .csv file that contained the corrected coordinates for each image in NAD83(2011) latitude, longitude, and ellipsoid height and their estimated positional accuracies. The research team imported this file along with the corresponding image set into the SfM processing software.

### SfM Data Processing

For this test, the research team used nighttime data collected with the Mavic 2 Pro and the Matrice 300 RTK in addition to the data collected with the Phantom 4 RTK. In total, the research team processed four UAS flights under different artificial lighting conditions to evaluate the impact of lighting and flight design on densified 3D point cloud quality and accuracy (Table 106). For flights conducted manually, the UAS came to a stop at each photo location to acquire the image.

**Table 106. UAS Flights and SfM Processing Runs.**

	<b>Flight</b>	<b>Time of Survey</b>	<b>Flight Mode</b>	<b>GNSS Mode</b>	<b>Lighting Source</b>
<b>1</b>	Mavic 2 Pro	7:05 PM	Manual	Autonomous	Built-in LEDs
<b>2</b>	Matrice 300 RTK	7:25 PM	Manual	RTK	Built-in LEDs
<b>3</b>	Matrice 300 RTK	7:50 PM	Manual	RTK	Built-in LEDs and spotlight
<b>4</b>	Phantom 4 RTK	8:30 PM	Autonomous	PPK	Vehicle headlights

The research team processed the Mavic 2 Pro flight using Pix4D’s standard workflow and 3D mapping template. The research team used seven GCPs visible in the scene for processing.

For the Matrice 300 RTK flights, the research team used Pix4D’s standard workflow and 3D mapping template with some modifications. Using the standard calibration method, Pix4D could not achieve an adequate number of calibrated images for a useful result. The only way to improve feature matching leading to a usable result, without forced calibration via manually selecting tie points, was by selecting the Accurate Geolocation and Orientation calibration method. The team also evaluated Pix4D solutions with and without GCPs using the RTK-corrected image geotags. The research team used five GCPs in the final SfM processing solution.

For the Phantom 4 RTK flight with PPK-corrected image geotags, the research team used Pix4D’s standard workflow and 3D mapping template with Accurate Geolocation and Orientation calibration. No GCPs were used during SfM processing.

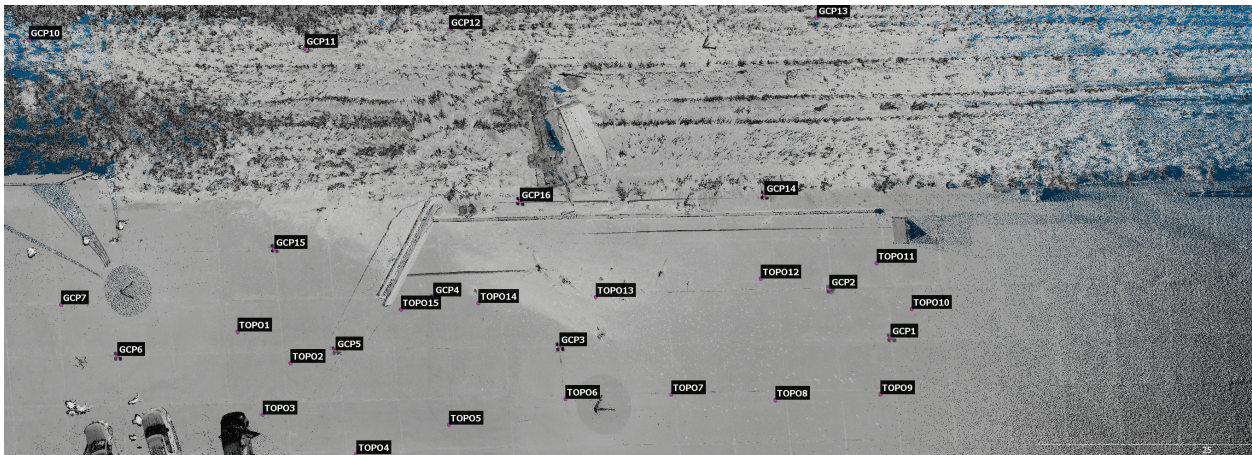
### TLS Data Processing

The research team processed the seven TLS scan positions into a merged point cloud using the automatic registration and MSA tools in RIEGL’s RiSCAN™ postprocessing software. This approach uses the estimated scan position and orientation information provided by the scanner’s RTK GNSS fixed solution (corrected via the TxDOT RTN) and orientation sensors (IMU and 3-axis magnetometer). Geometric constraints based on cloud-to-cloud overlap were applied to register and adjust the scans in a two-stage process. After alignment, the procedure provided an estimate of the scan position accuracies (Table 107).

**Table 107. TLS Estimated Scan Position Accuracy.**

Scan Position	Horizontal Accuracy (m)	Vertical Accuracy (m)
1	0.014	0.014
2	0.014	0.013
3	0.014	0.015
4	0.014	0.013
5	0.014	0.011
6	0.014	0.013
7	0.014	0.013

The research team applied a semi-automatic method to filter point cloud noise based on calibrated reflectance and pulse shape deviation attributes recorded for each point. Manual inspection of the cloud was then performed for any residual clean up. Figure 213 and Figure 214 show examples of the merged and georeferenced TLS point cloud.



**Figure 213. Top-Down View of TLS Point Cloud Showing Ground Control Layout.**



**Figure 214. Oblique View of TLS Point Cloud of Crashed Vehicle.**

## Analysis

The research team evaluated the quality and absolute accuracy of the densified 3D point cloud data generated from the Pix4D SfM processing runs of the four nighttime UAS flights. The research team completed the following analyses:

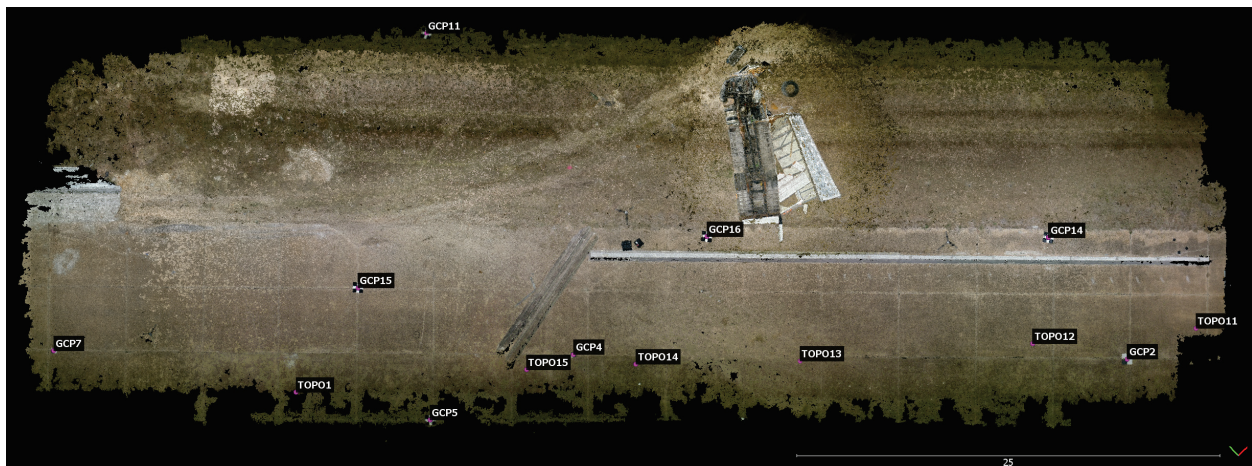
- Evaluation of the UAS and TLS point cloud data relative to ground control data.
- Evaluation of the UAS point cloud data relative to TLS point cloud data.
- Accuracy evaluation based on SfM processing reports.

The Test 4 analysis section above provides additional information about the methods developed and used to evaluate UAS data quality and accuracy.

## Results

### Evaluation of UAS and TLS Point Cloud Data Relative to Ground Control Data

Figure 215 shows the dense point cloud for the Mavic 2 Pro nighttime flight illuminated with built-in LEDs. Overlaid on the point cloud scene are the visible GCPs and topo points. This flight appeared to enable a decent 3D reconstruction of the crashed vehicle scene, including the barricade and nearby perimeter. Point gaps on the edges of the scene with low lighting and in areas of dark shadowing are also evident on the dense point cloud.



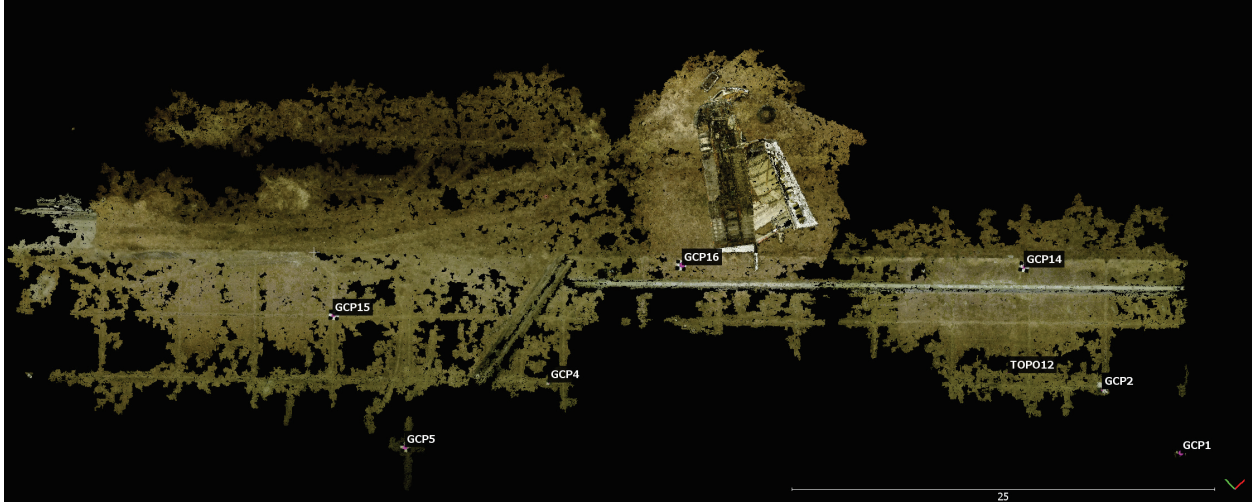
**Figure 215. Mavic 2 Pro with LEDs Dense Point Cloud.**

Table 108 shows vertical accuracy results for the Mavic 2 Pro flight with LEDs and a TLS survey. TLS results are based on all 31 RTK observations and Mavic 2 Pro results are based on a reduced set of RTK observations. The Mavic 2 Pro flight had a vertical RMSE of 2.2 cm (0.87 inches), which was nearly identical to the TLS data and slightly better based on the reduced set of GCPs and topo points used to evaluate the UAS survey. Processing the Mavic 2 Pro flight in Pix4D involved using 7 GCPs during the SfM BA. This result shows that uncorrected GNSS image geotags with sufficient ground control and lighting can enable accurate SfM reconstruction under nighttime conditions within the boundary of your control.

**Table 108. Mavic 2 Pro with LEDs Surface Height Error.**

RTK Observation	Surface	Height Error (m)	
		TLS	UAS (Pix4D)
GCP1	Concrete	0.023	
GCP2	Concrete	0.006	0.008
GCP3	Concrete	0.029	
GCP4	Concrete	0.006	0.013
GCP5	Concrete	0.020	0.030
GCP6	Concrete	0.012	
GCP7	Concrete	0.013	0.008
GCP8	Concrete	0.019	
GCP9	Vegetation	0.073	
GCP10	Vegetation	0.070	
GCP11	Vegetation	0.019	0.060
GCP12	Vegetation	0.032	
GCP13	Vegetation	0.030	
GCP14	Concrete	0.010	0.005
GCP15	Concrete	0.012	0.009
GCP16	Concrete	0.016	0.002
TOPO1	Concrete	0.018	0.035
TOPO2	Concrete	0.009	
TOPO3	Concrete	0.013	
TOPO4	Concrete	0.015	
TOPO5	Concrete	0.021	
TOPO6	Concrete	0.019	
TOPO7	Concrete	0.008	
TOPO8	Concrete	0.016	
TOPO9	Concrete	0.008	
TOPO10	Concrete	0.011	
TOPO11	Concrete	0.014	0.012
TOPO12	Concrete	0.003	0.014
TOPO13	Concrete	0.007	0.014
TOPO14	Concrete	0.016	0.009
TOPO15	Concrete	0.008	0.006
Mean error length		0.019	0.016
Standard deviation error length		0.015	0.015
RMSE		0.024	0.022

Figure 216 shows the dense point cloud for the Matrice 300 RTK nighttime flight illuminated with built-in LEDs. Overlaid on the point cloud scene are the visible GCPs and topo points. In this case, it was possible to reconstruct the main part of the crashed vehicle but there was a much sparser dense point cloud result than the result for the Mavic 2 Pro flight with LEDs. Large gaps in the point cloud data occurred, indicating that Pix4D failed to calibrate some of the images and had low overall feature matching in areas of the scene.



**Figure 216. Matrice 300 RTK with LEDs Dense Point Cloud.**

Table 109 shows vertical accuracy results for the Matrice 300 RTK flight with LEDs and TLS survey. The results only show GCPs and topo points visible in the UAS survey. The Matrice 300 RTK flight had a vertical RMSE of 10 cm (4 inches) relative to 1.4 cm (0.55 inches) for the TLS survey. Although this flight had RTK-corrected image geotags and 5 GCPs were used during SfM processing, vertical accuracy was significantly lower than for the Mavic 2 Pro flight with LEDs.

**Table 109. Matrice 300 RTK with LEDs Surface Height Error.**

RTK Observation	Surface	Height Error (m)	
		TLS	UAS (Pix4D)
GCP1	Concrete	0.023	0.031
GCP2	Concrete	0.006	0.114
GCP4	Concrete	0.006	0.143
GCP5	Concrete	0.020	0.080
GCP14	Concrete	0.010	0.116
GCP15	Concrete	0.012	0.108
GCP16	Concrete	0.016	0.091
TOPO12	Concrete	0.003	0.105
Mean Error Length		0.012	0.098
Standard Deviation Error Length		0.007	0.033
RMSE		0.014	0.103

Figure 217 shows the dense point cloud for the Matrice 300 RTK nighttime flight illuminated with built-in LEDs and a spotlight. Overlaid on the point cloud scene are the visible GCPs and topo points. In this case, it was only possible to reconstruct the crashed vehicle and perimeter in close proximity. This flight had the worst performance overall for reconstruction coverage of the scene compared to the Mavic 2 Pro and Matrice 300 RTK flights with LEDs only.



**Figure 217. Matrice 300 RTK with LEDs and Spotlight Dense Point Cloud.**

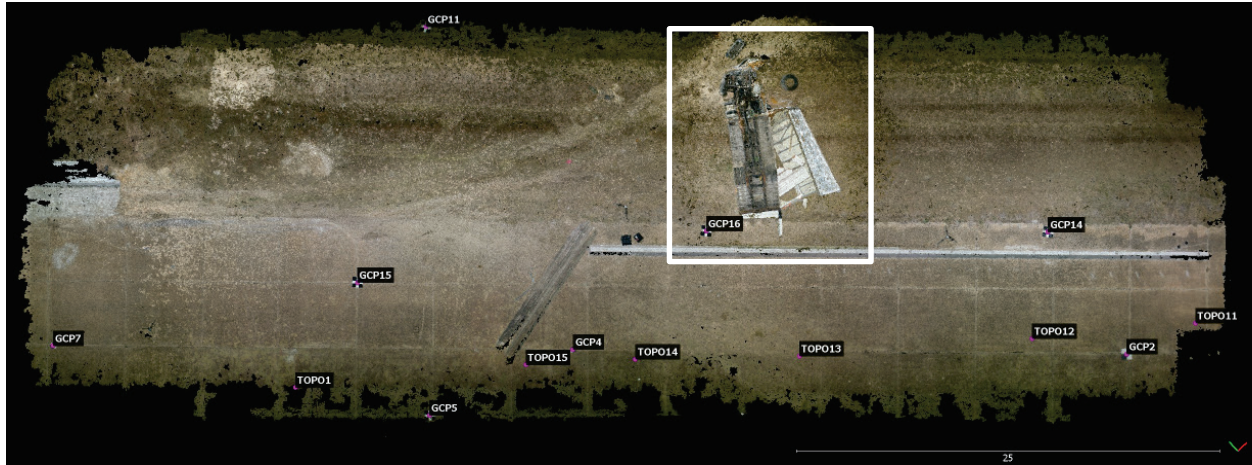
Table 110 shows vertical accuracy results for the Matrice 300 RTK flight with LEDs and a spotlight. The results only show GCPs and topo points that were visible in the UAS survey. The Matrice 300 RTK flight had a vertical RMSE of 0.063 m relative to 0.019 m for the TLS survey. Similar to the Matrice 300 RTK flight with LEDs, this flight also used 5 GCPs during SfM processing. However, vertical RMSE for this flight with the spotlight was worse than the case where only LEDs were used.

**Table 110. Matrice 300 RTK with LEDs + Spotlight Surface Height Error.**

RTK Observation	Surface	Height Error (m)	
		TLS	UAS (Pix4D)
GCP2	Concrete	0.006	0.040
GCP12	vegetation	0.032	0.109
GCP13	vegetation	0.030	0.020
GCP14	Concrete	0.010	0.023
GCP16	Concrete	0.016	0.007
TOPO11	Concrete	0.014	0.204
TOPO12	Concrete	0.003	0.039
Mean Error Length		0.016	0.091
Standard Deviation Error Length		0.011	0.070
RMSE		0.019	0.115

#### Evaluation of UAS Point Cloud Data Relative to TLS Point Cloud Data

**Point-to-Point Comparison in the Region of Interest.** Due to differences in area of coverage for the reconstruction between the flights, the region of interest selected for this analysis focused on the crashed vehicle with densest coverage (Figure 218). Cloud-to-cloud distance comparisons, discussed later, include a larger region of the surrounding barricade and pavement.



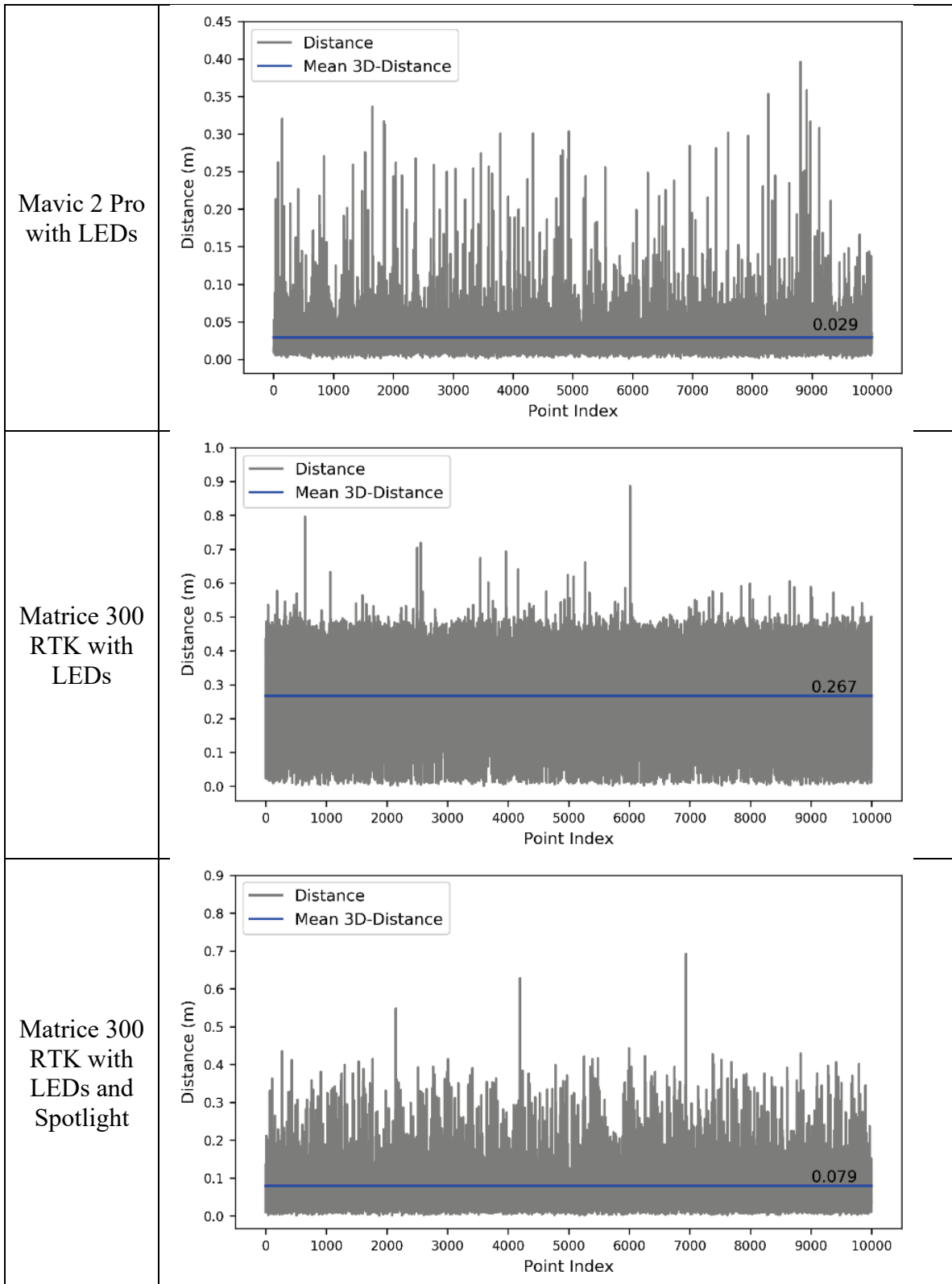
**Figure 218. Region of Interest Overlaid on Mavic 2 Pro with LEDs Point Cloud.**

Figure 219 shows point-to-point 3D distances computed for the Mavic 2 Pro and Matrice 300 RTK flights relative to the TLS survey. For the Mavic 2 Pro flight with LEDs, the mean overall 3D distance offset relative to the TLS point cloud based on 10,000 point measurements was 0.029 m. For the Matrice 300 RTK flights, the 3D distances were considerably greater (i.e., 0.267 m when only LEDs were used and 0.079 m when both LEDs and spotlight were used).

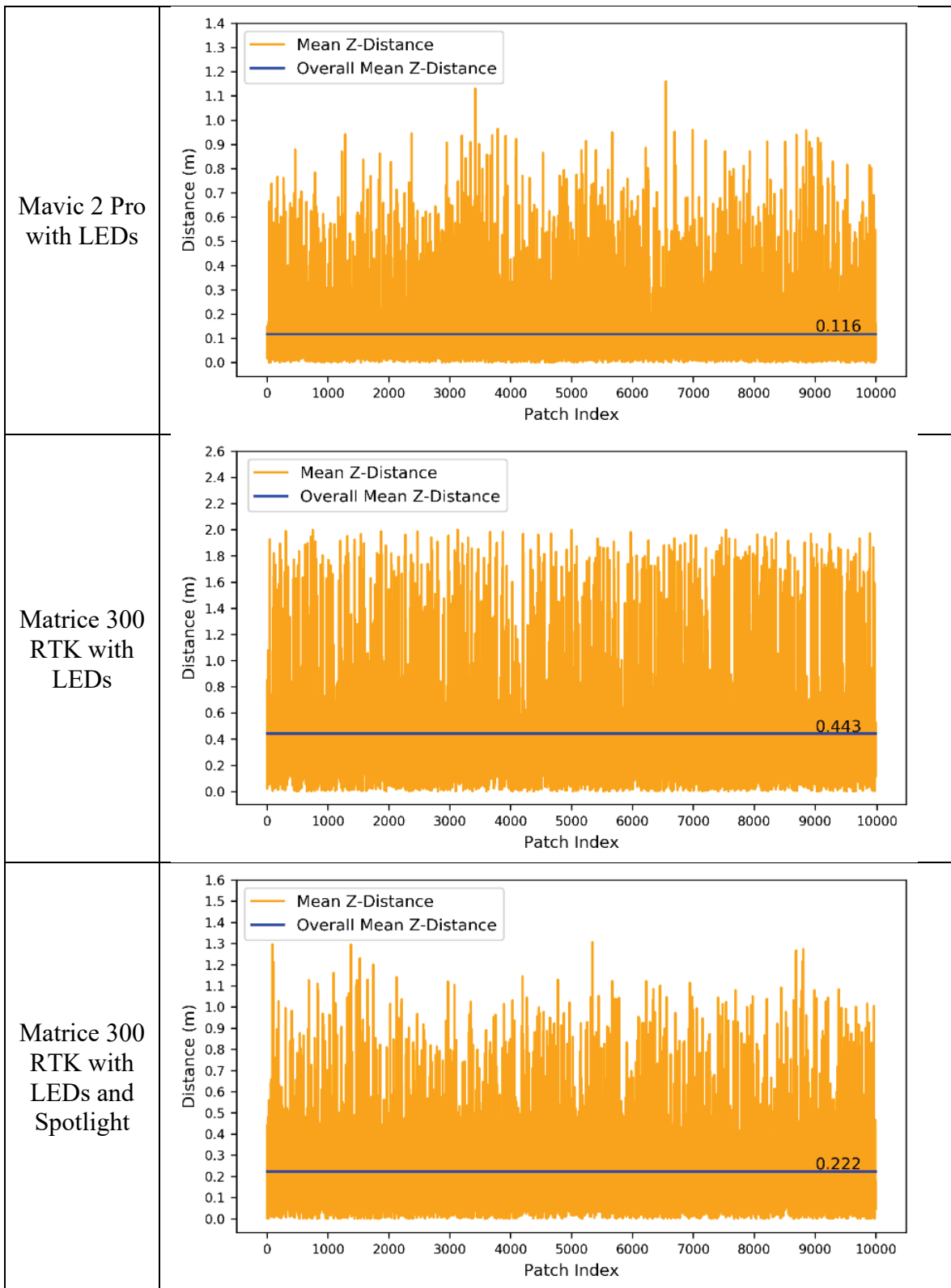
Figure 220 shows the mean distance in the Z component (i.e., mean absolute vertical error) for UAS point patches relative to a TLS point patch within the region of interest. For the Mavic 2 Pro with built-in LEDs, the mean overall Z distance across 10,000 point patches was 0.116 m. For the Matrice 300 RTK flights, the Z distances were considerably greater (i.e., 0.443 m when only LEDs were used and 0.222 m when both LEDs and spotlight were used).

**Cloud-to-Cloud Comparison.** Figure 221 shows cloud-cloud distances computed in CloudCompare for the large region of interest. Figure 222 shows results for the crash scene region of interest.



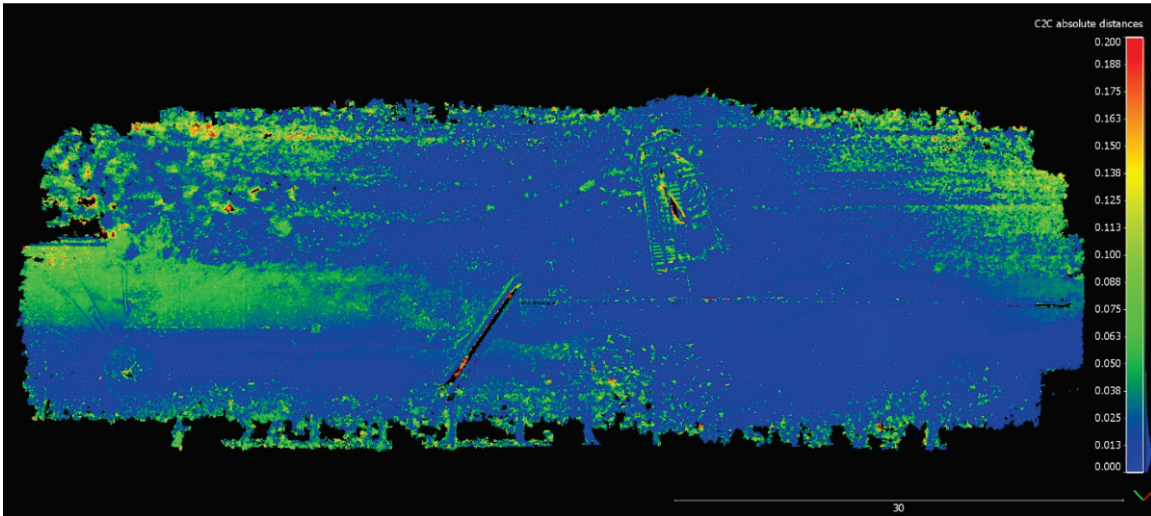


**Figure 219. Distances from Mavic 2 Pro and Matrice 300 RTK Point Sets to TLS Point Set within the Region of Interest.**

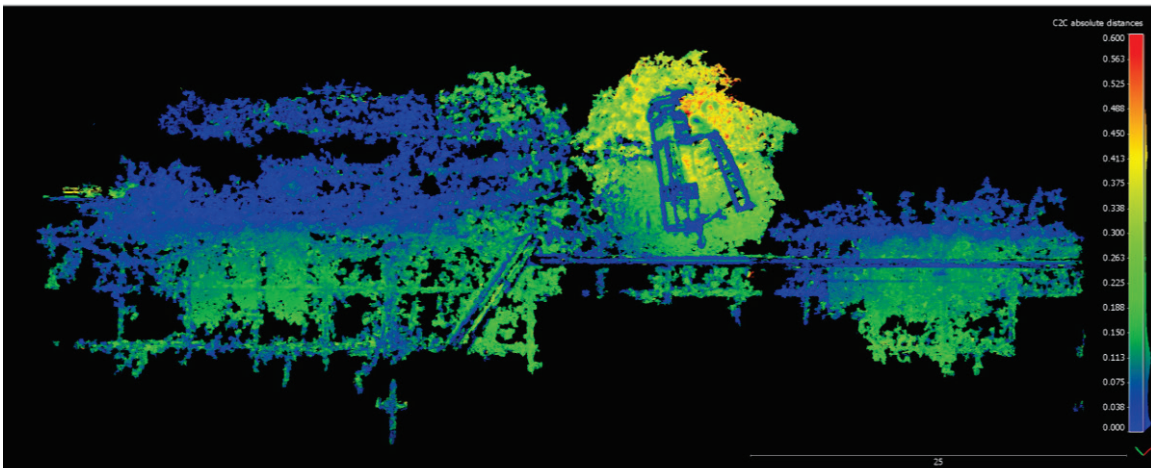


**Figure 220. Mean Distance in Z for UAS Point Patches to TLS Point Patches.**

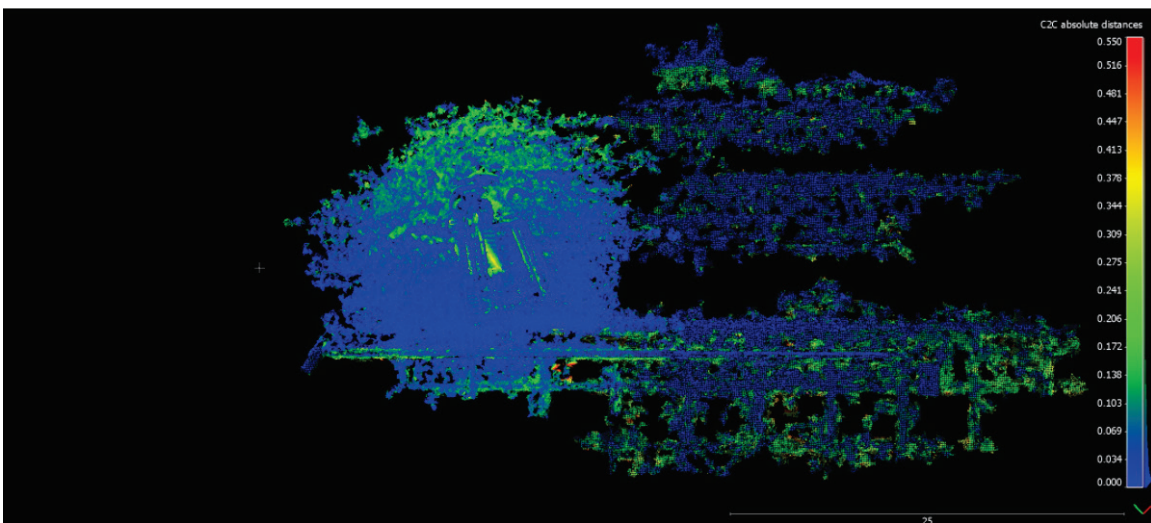
**Mavic 2 Pro with LEDs**



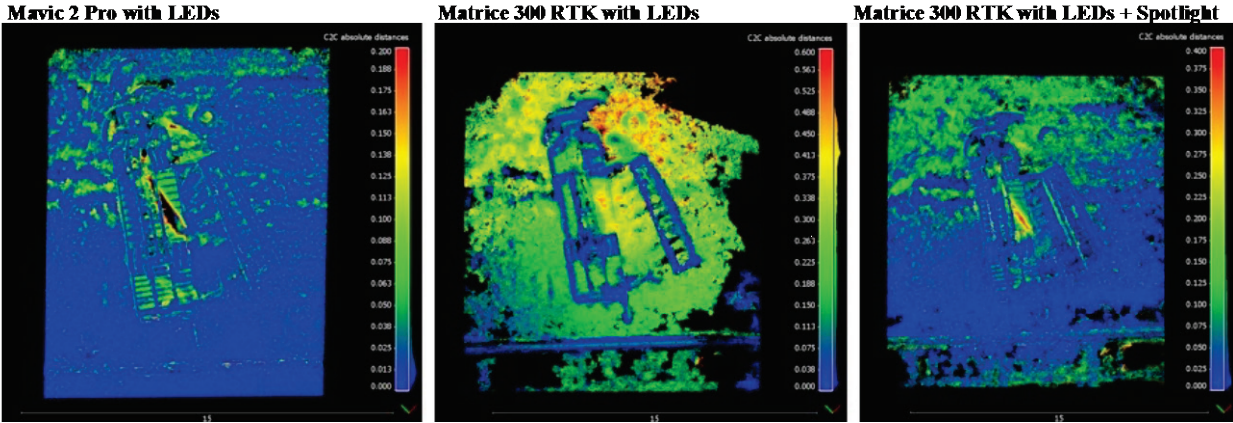
**Matrice 300 RTK with LEDs**



**Matrice 300 RTK with LEDs + Spotlight**



**Figure 221. Cloud-to-Cloud Distances for Large Region of Interest.**



**Figure 222. Cloud-to-Cloud Distances for Crash Scene Region of Interest.**

Table 111, Table 112, and Table 113 summarize cloud-to-cloud distance statistics computed for each of the respective UAS flights with the large scene and crash scene regions of interest. The Mavic 2 Pro flight provided a closer representation of the TLS point cloud in both the large scene and the crash scene than to the Matrice 300 RTK flights. The Mavic 2 Pro also provided less variability in distances overall.

**Table 111. Cloud-to-Cloud Distance Statistics for Mavic 2 Pro with LEDs.**

Region of Interest	Distance (m)		
	Points	Mean	Standard Deviation
Large Scene	18,984,263	0.029	0.031
Crash Scene	3,812,866	0.030	0.033

**Table 112. Cloud-to-Cloud Distance Statistics for Matrice 300 RTK with LEDs.**

Region of Interest	Distance (m)		
	Points	Mean	Standard Deviation
Large Scene	4,801,821	0.195	0.148
Crash Scene	2,826,285	0.268	0.148

**Table 113. Cloud-to-Cloud Distance Statistics for Matrice 300 RTK with LEDs and Spotlight.**











Region of Interest	Distance (m)		
	Points	Mean	Standard Deviation
Large Scene	3,398,200	0.078	0.072
Crash Scene	2,957,232	0.079	0.073

Comparing the Matrice 300 RTK flight with LEDs and flight with LEDs and spotlight, the flight with the spotlight performed better in terms of mean cloud-to-cloud distances and standard deviation of those distances. However, the spotlight degraded reconstruction away from the crashed vehicle scene as evidenced by the reduced number of points.











Evaluation Based on SfM Processing Reports

Table 114, Table 115, and Table 116 show quality check results from the Pix4D processing reports for the Mavic 2 Pro flight and the two Matrice 300 RTK flights, respectively. A comparison of the two Matrice 300 RTK flights (Table 115 and Table 116) to the Mavic 2 Pro flight revealed a significant decrease in the median number of keypoint matches per a calibrated image for the Matrice 300 RTK flight without the spotlight. Also of interest is that the mean GCP RMSE was 0.037 m versus 0.148 m for the Matrice 300 RTK flight with LEDs and with LEDs and spotlight, respectively. This error is based on the five GCPs used to reoptimize the SfM BA during Pix4D processing. In contrast, the checkpoint RMSE behavior was the reverse. Table 117 shows much larger checkpoint errors for the Matrice 300 RTK flight with LEDs than the Matrice 300 RTK flight with LEDs and spotlight (Table 118).











**Table 114. Pix4D Processing Quality Results for Mavic 2 Pro with LEDs.**

 Images	median of 22084 keypoints per image	
 Dataset	175 out of 175 images calibrated (100%), all images enabled	
 Camera Optimization	2.96% relative difference between initial and optimized internal camera parameters	
 Matching	median of 1843.24 matches per calibrated image	
 Georeferencing	yes, 7 GCPs (7 3D), mean RMS error = 0.039 m	

**Table 115. Pix4D Processing Quality Results for Matrice 300 RTK with LEDs.**

 Images	median of 14747 keypoints per image	
 Dataset	119 out of 172 images calibrated (69%), all images enabled, 2 blocks	
 Camera Optimization	3.1% relative difference between initial and optimized internal camera parameters	
 Matching	median of 454.412 matches per calibrated image	
 Georeferencing	yes, 5 GCPs (5 3D), mean RMS error = 0.037 m	

**Table 116. Pix4D Processing Quality Results for Matrice 300 RTK with LEDs + Spotlight.**

 Images	median of 15006 keypoints per image	
 Dataset	89 out of 126 images calibrated (70%), all images enabled, 3 blocks	
 Camera Optimization	4.24% relative difference between initial and optimized internal camera parameters	
 Matching	median of 1570.42 matches per calibrated image	
 Georeferencing	yes, 5 GCPs (5 3D), mean RMS error = 0.148 m	

**Table 117. Checkpoint Errors for Matrice 300 RTK with LEDs.**

Check Point Name	Accuracy XYZ [m]	Error X [m]	Error Y [m]	Error Z [m]	Projection Error [pixel]	Verified/Marked
GCP2		-0.0325	-0.0319	-0.1531	1.3147	5 / 5
GCP3		0.0391	0.0458	-0.1864	1.6623	6 / 6
GCP4		-0.0255	0.0157	-0.1957	1.3247	7 / 8
GCP6		-0.0700	-0.0201	-0.1469	0.8933	5 / 5
GCP7		-0.1092	0.0263	-0.1375	0.8827	3 / 3
GCP12		0.4463	0.3465	-0.9815	0.8830	2 / 2
GCP14		0.0026	-0.0035	-0.1175	0.8071	15 / 15
GCP15		-0.0310	0.0324	-0.1171	1.1154	13 / 13
<b>Mean [m]</b>		0.027467	0.051400	-0.254439		
<b>Sigma [m]</b>		0.163638	0.114268	0.276084		
<b>RMS Error [m]</b>		0.165927	0.125296	0.375448		

**Table 118. Checkpoint Errors for Matrice 300 RTK with LEDs and Spotlight.**

Check Point Name	Accuracy XYZ [m]	Error X [m]	Error Y [m]	Error Z [m]	Projection Error [pixel]	Verified/Marked
GCP2		-0.0034	-0.0168	-0.0231	0.7157	5 / 5
GCP3		-0.0148	-0.0066	-0.0920	0.8443	8 / 8
GCP4		0.0013	0.0182	-0.0950	1.4719	10 / 11
GCP6		0.0594	-0.0103	0.0880	0.8653	5 / 5
GCP7		0.0314	-0.0155	0.0568	1.2641	4 / 4
GCP10		-0.0292	-0.0022	0.0998	0.4312	3 / 3
GCP12		0.0241	-0.0480	0.0785	3.5738	17 / 17
GCP14		0.0223	-0.0249	-0.0298	0.7792	14 / 14
GCP15		0.0073	-0.0179	0.0222	1.0714	9 / 10
<b>Mean [m]</b>		0.010948	-0.013779	0.011717		
<b>Sigma [m]</b>		0.025074	0.016826	0.070914		
<b>RMS Error [m]</b>		0.027360	0.021748	0.071875		

Figure 223 shows orthomosaics and corresponding sparse DSMs before densification for the Mavic 2 Pro flight illuminated with LEDs, the Matrice 300 RTK flight illuminated with LEDs, and the Matrice 300 RTK flight illuminated with LEDs and spotlight.

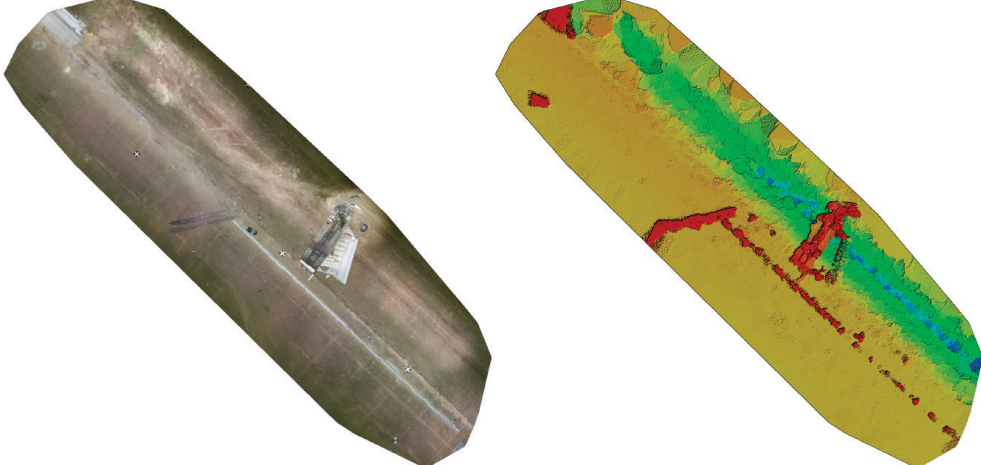
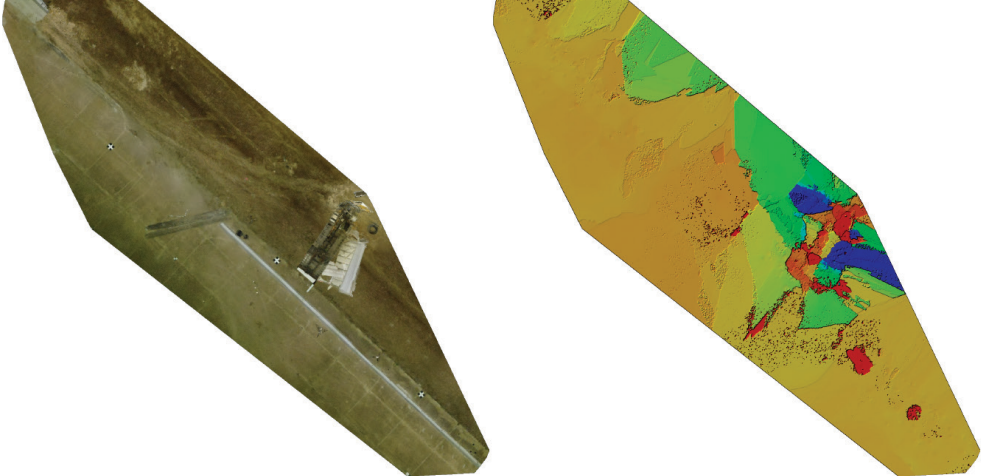
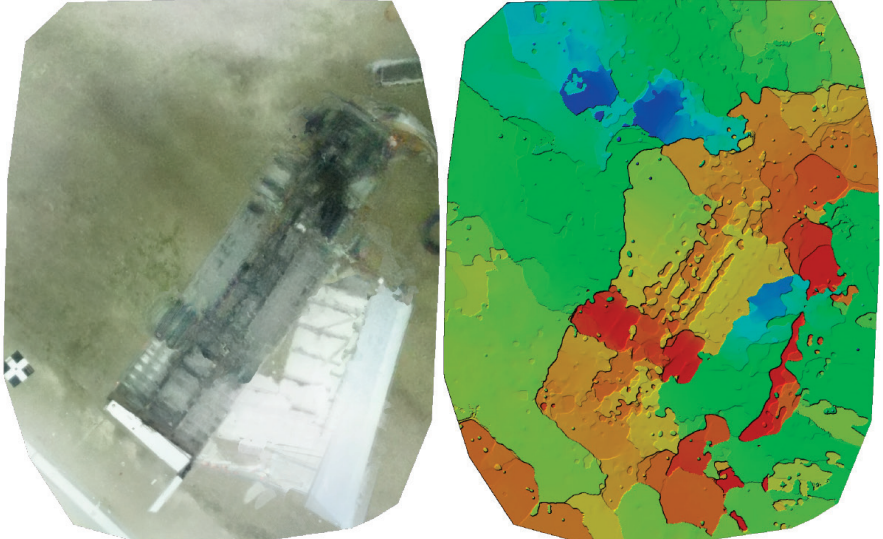
<p>Mavic 2 Pro with LEDs</p>	 <p>The left image is an orthomosaic showing a wide, flat, brownish terrain with a small white structure in the center. The right image is a Digital Surface Model (DSM) of the same area, color-coded by elevation, showing a relatively flat surface with some minor variations in height.</p>
<p>Matrice 300 RTK with LEDs</p>	 <p>The left image is an orthomosaic showing a similar terrain to the Mavic 2 Pro, but with a more detailed view of the white structure. The right image is a DSM showing more pronounced elevation changes, particularly around the structure, with colors ranging from yellow to red.</p>
<p>Matrice 300 RTK with LEDs and Spotlight</p>	 <p>The left image is an orthomosaic showing a very close-up view of the white structure, with a spotlight effect highlighting the details. The right image is a DSM showing significant elevation changes, with a large area of red and orange indicating higher elevations, and green and blue indicating lower elevations.</p>

Figure 223. Orthomosaics and DSMs from Pix4D Processing Report.

### Phantom 4 RTK Autonomous Night Flight

Unfortunately, due to operator error and a previously undiscovered behavior in DJI's Ground Station RTK flight control software, the shutter priority setting was overridden by a camera setting called auto mode that was not explicitly turned off. The research team had assumed that setting the camera to shutter priority would override this setting, but it did not. In auto mode, the camera automatically chooses the exposure time, aperture, and ISO values. Under these conditions, the camera set the shutter at 0.5 seconds with maximum ISO and maximum aperture. Because the UAS was moving at 2 m/s on autonomous flight mode, the result was significant motion blur in the images (Figure 224).



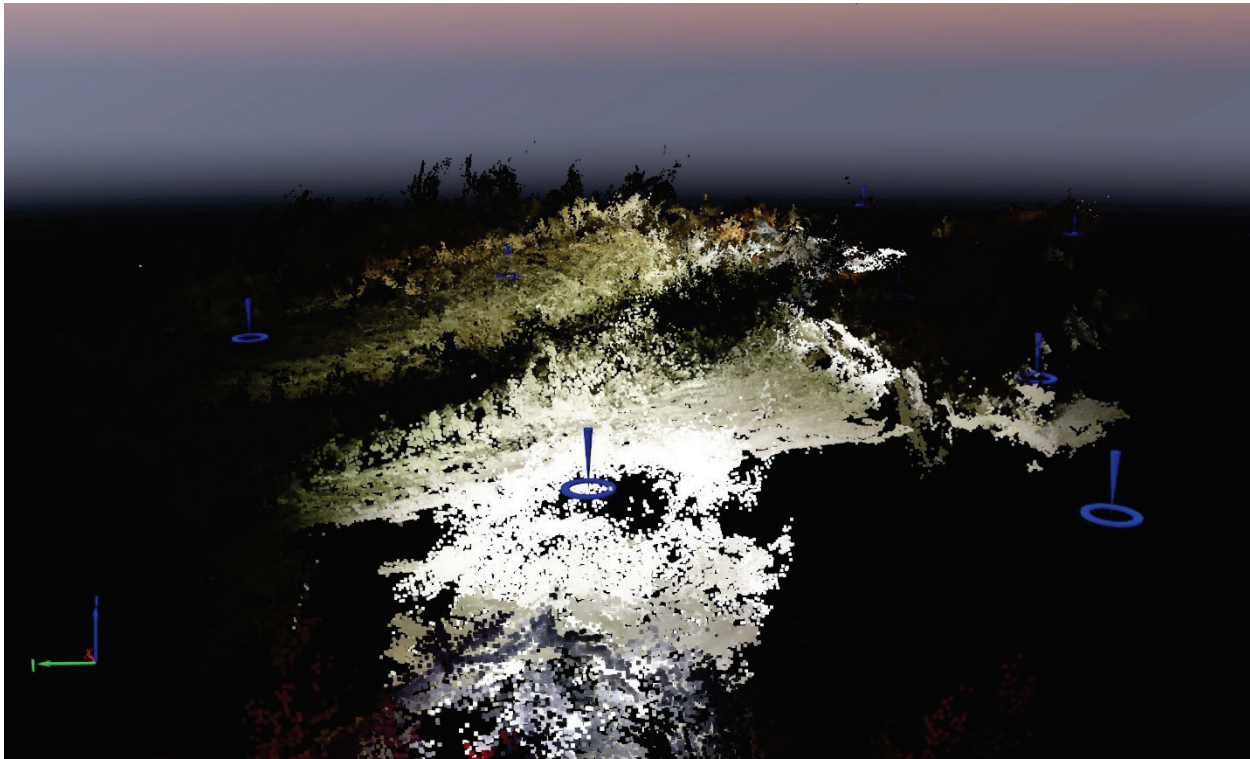
**Figure 224. Image from Phantom 4 RTK Flight Showing Excessive Motion Blur.**

Not surprisingly, Pix4D processing of the flight data failed to provide a meaningful model from the images. As Table 119 shows, only 50 percent of the images were calibrated, and the median number of keypoint matches per calibrated image was about 94. The result was an insufficient number of features for adequate SfM reconstruction, producing an erroneous, meaningless sparse point cloud (Figure 225).



**Table 119. Pix4D Processing Quality Results for Phantom 4 RTK.**

🔍 Images	median of 25740 keypoints per image	✅
🔍 Dataset	133 out of 262 images calibrated (50%), all images enabled, 4 blocks	⚠️
🔍 Camera Optimization	0.58% relative difference between initial and optimized internal camera parameters	✅
🔍 Matching	median of 94.3311 matches per calibrated image	⚠️
🔍 Georeferencing	yes, no 3D GCP	⚠️



**Figure 225. Example of the Poor Sparse Point Cloud Reconstruction Quality in Pix4D.**

**Test 6 (01/15/2021): Simulated Passenger Car Crash Test at the TxDPS Tactical Training Facility in Florence, Texas**

*Data Collection*

The UAS procedure followed for Test 6 was similar to that followed for Test 1, with some modifications. The research team used the Phantom 4 RTK. The research team also collected 3D point cloud data using the RIEGL-VZ 2000i TLS for ground truthing and accuracy assessment of UAS-SfM survey products. The team used a pair of Septentrio NR3 GNSS receivers. One of the receivers was used to record static observations, while the other one was tied to TxDOT’s RTN and used as a rover to collect ground control data. The research team set up the first GNSS receiver on a tripod located near the scene to log static observations for PPK postprocessing of

the Phantom 4 RTK image geolocations. Over two hours of static observations were collected for processing of the base station coordinate using OPUS.

The team laid out 27 GCPs in a grid pattern on the surface of the roadway around the vehicle and on the perimeter of the scene within a vegetated ditch. The research team recorded five seconds of observations at 1 Hz for each target using the second GNSS receiver and then averaged the X-Y-Z coordinates. Ground control data were collected in NAD83(2011) State Plane Texas Central (meters) for X-Y and NAD83(2011) ellipsoid heights for Z. Ellipsoid heights were used to ensure consistent comparison of vertical accuracies relative to the SfM processing workflows using PPK image geotags, which come in NAD83(2011) ellipsoid heights.

The research team conducted two nighttime autonomous mapping missions with the Phantom 4 RTK. Both flights used the same survey design. Headlights from two vehicles placed at opposing ends of the scene within 100 m of the crashed vehicle lit the scene. High beams were used on both vehicles. The flight design involved a double grid survey mode consisting of perpendicular flight lines at an altitude of 25 m with the camera angled 30 degrees from nadir (i.e., 60 degrees with respect to the horizon). Overlap was set at 80 percent endlap and sidelap.

The flight control software, DJI Ground Station RTK, does not provide an option for stopping to take photos during automated flight. For this mission, the UAS speed was 2 m/s. For the first flight, the UAS camera operated in shutter priority mode set to 1/1000 seconds. For the second flight test, the UAS camera had shutter priority mode set to 1/500 seconds.

The research team acquired TLS data from a series of four scan positions distributed around the staged vehicle scene to ensure adequate coverage of the entire scene, including the perimeter and vegetated ditch. Imagery for point cloud colorization was not acquired due to nighttime scan conditions. Table 120 shows the TLS survey parameters used for data acquisition. The scanner was connected to TxDOT RTN using a cellular network to obtain an RTK GNSS fixed position solution at each scan location.

**Table 120. TLS Survey Parameters Used for Each Scan Position.**

Scan Parameters	Values
Laser Pulse Rate	1200 kHz
Stepping Angle	20 millidegrees
Horizontal Field-of-View	360°
Vertical Field-of-View	100° (+60°, -40°)

### *Data Processing*

#### Phantom 4 RTK PPK Data Processing

The research team submitted the RINEX file of the static GNSS base station’s observations collected during the flight to OPUS to solve for a static coordinate in NAD83(2011). The research team used REDtoolbox to perform PPK corrections. The output was a .csv file that contained the corrected coordinates for each image in NAD83(2011) latitude, longitude, and ellipsoid height and their estimated positional accuracies. The research team imported this file along with the corresponding image set into the SfM processing software.

### SfM Data Processing

The research team processed the flight data using Pix4Dmapper. Table 121 shows the two nighttime flight experiments processed. Processing of the data used Pix4D's standard workflow and 3D mapping template with the Accurate Geolocation and Orientation calibration method. No GCPs were used during processing.

**Table 121. UAS Flights and SfM Processing Runs.**

<b>Flight</b>	<b>Time of Survey</b>	<b>Flight Mode</b>	<b>Exposure Time (s)</b>	<b>Lighting Source</b>	
<b>1</b>	Phantom 4 RTK	8:50 PM	Autonomous	1/1000	Vehicle headlights
<b>2</b>	Phantom 4 RTK	9:03 PM	Autonomous	1/500	Vehicle headlights

### TLS Data Processing

The research team processed the four TLS scan positions into a merged point cloud using the MSA tools in RIEGL's RiSCAN. This approach uses the estimated scan position and orientation information provided by the scanner's RTK GNSS fixed solution (corrected via the TxDOT RTN) and orientation sensors. Geometric constraints based on cloud-to-cloud overlap were applied to register and adjust the scans in a two-stage process. After alignment, the procedure provided an estimate of the scan position accuracies (Table 122).

**Table 122. TLS Estimated Scan Position Accuracy.**

<b>Scan Position</b>	<b>Horizontal Accuracy (m)</b>	<b>Vertical Accuracy (m)</b>
<b>1</b>	0.014	0.012
<b>2</b>	0.014	0.015
<b>3</b>	0.014	0.011
<b>4</b>	0.014	0.011

The research team applied a semi-automatic method to filter point cloud noise based on calibrated reflectance and pulse shape deviation attributes recorded for each point. Manual inspection of the cloud was then performed for any residual clean up. Figure 226 and Figure 227 show examples of the merged and georeferenced TLS point cloud.



**Figure 226. Top-Down View of TLS Point Cloud Showing Ground Control Layout.**



**Figure 227. Oblique View of TLS Point Cloud of Staged Vehicle.**

### *Analysis*

The research team completed the following analyses:

- Evaluation of the UAS and TLS point cloud data relative to ground control data.
- Accuracy evaluation based on SfM processing reports.

The Test 4 analysis section above provides additional information about the methods developed and used to evaluate UAS data quality and accuracy.

## Results

### Evaluation of UAS and TLS Point Cloud Data Relative to Ground Control Data

SfM reconstruction of the UAS nighttime flight tests within Pix4D was not feasible (explained further below). For consistency, Table 123 shows the results of the TLS accuracy assessment.

**Table 123. TLS Surface Height Error.**







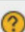

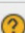

<b>RTK Observation</b>	<b>Surface</b>	<b>Height Error (m)</b>
GCP1	Asphalt	0.008
GCP2	Asphalt	0.031
GCP3	Asphalt	0.029
GCP4	Asphalt	0.043
GCP5	Asphalt	0.041
GCP6	Asphalt	0.046
GCP7	Asphalt	0.043
GCP8	Asphalt	0.021
GCP9	Asphalt	0.043
GCP10	Asphalt	0.044
GCP11	Asphalt	0.046
GCP12	Asphalt	0.069
GCP13	Asphalt	0.052
GCP14	Asphalt	0.041
GCP15	Asphalt	0.030
GCP16	Asphalt	0.028
GCP17	Asphalt	0.021
GCP18	Asphalt	0.033
GCP19	Asphalt	0.040
GCP20	Asphalt	0.039
GCP21	Asphalt	0.052
GCP22	Vegetation	0.024
GCP23	Vegetation	0.025
GCP24	Vegetation	0.028
GCP25	Vegetation	0.045
GCP26	Vegetation	0.035
GCP27	Vegetation	0.041
Mean Error Length		0.037
Standard Deviation Error Length		0.012
RMSE		0.039

## Phantom 4 RTK Autonomous Night Flight







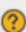



Neither of the tested exposure times enabled the UAS camera to gather enough ambient light for Pix4D software to match a sufficient number of keypoints between images to successfully calibrate the camera. Therefore, no 3D model was reconstructed.

Table 124 and Table 125 show the quality check results from the Pix4D processing reports for the two exposure time options (1/1000 and 1/500 seconds, respectively). For the 1/1000-second scenario, not a single image was calibrated, and the median number of keypoints matched per calibrated image was 1.4. For the 1/500-second scenario, 15 percent of the images were calibrated, indicating a positive impact from the lower exposure time. However, this was not enough for successful reconstruction. The median number of keypoints matched per calibrated image was 6. Figure 228 shows an example of the poor image quality due to insufficient exposure at the 1/500-second exposure time.

**Table 124. Pix4D Processing Quality Results (Shutter: 1/1000 Seconds).**

 Images	median of 26746 keypoints per image	
 Dataset	205 out of 205 images enabled	
 Camera Optimization	not available	
 Matching	median of 1.41887 matches per calibrated image	
 Georeferencing	no GCP	

**Table 125. Pix4D Processing Quality Results (Shutter: 1/500 Seconds).**

 Images	median of 26740 keypoints per image	
 Dataset	31 out of 198 images calibrated (15%), all images enabled	
 Camera Optimization	0.13% relative difference between initial and optimized internal camera parameters	
 Matching	median of 6.02115 matches per calibrated image	
 Georeferencing	yes, no 3D GCP	



**Figure 228. Example Image Acquired at 1/500-Second Exposure Time.**

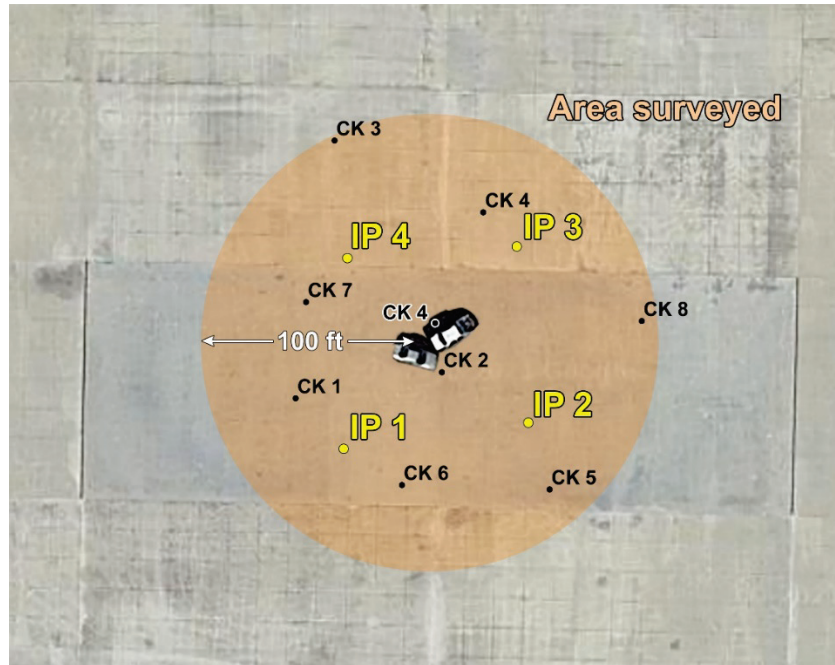
**Test 7 (03/20/2021): Simulated Passenger Car Crash Test at The TxDPS Tactical Training Facility in Florence, Texas**

*Data Collection*

The procedure followed for Test 7 was similar to that followed for Test 1 and Test 4, with some modifications. The research team used the WingtraOne and the Phantom 4 RTK. For this test, the research team operated the Phantom 4 RTK in RTK mode by connecting to the TxDOT RTN. The team operated the platform autonomously for daytime image acquisition and manually for nighttime image acquisition. The research team used the Ground Station RTK flight control software for autonomous mission planning and flight control.

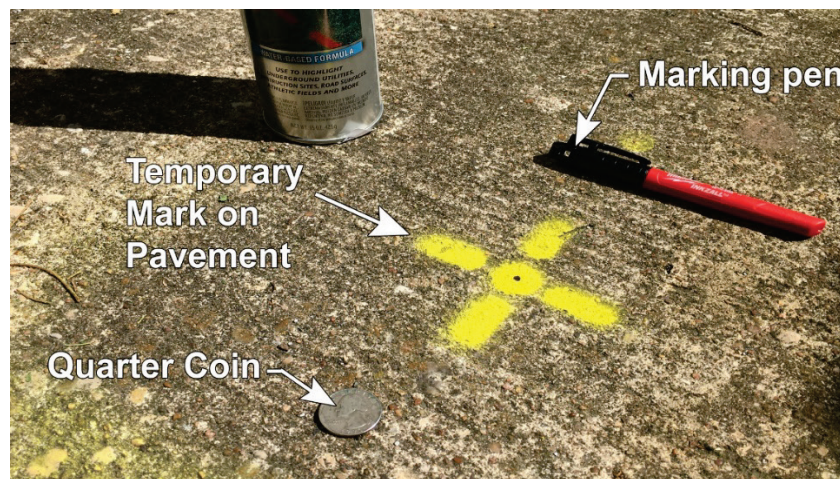
The research team collected 3D point cloud data for ground truthing and accuracy assessment of UAS-SfM survey products using the RIEGL-VZ 2000i TLS. The team also used a pair of survey-grade Septentrio NR3 GNSS receivers. One of the receivers was used to record static observations while the other one was tied to TxDOT's RTN and used as a rover to collect ground control data. The research team set up the first GNSS receiver on a tripod located near the scene to log static observations for PPK postprocessing of the WingtraOne image geolocations. Over two hours of static observations were collected for processing of the base station coordinate using OPUS.

Prior to the research team’s field test, TxDOT surveyors installed four instrument points and eight checkpoints (Figure 229). The surveyors marked each instrument and checkpoint location using yellow marking spray paint, as shown in Figure 230. The surveyors performed a digital level loop through the marked instrument points and checkpoints by holding the GNSS elevation of a set reference mark as the truth take-off elevation. This reference mark elevation was established using the TxDOT RTN and was expected to be at the vertical accuracy provided by the network adjustment. However, the relative difference in leveled elevation from one instrument or checkpoint to another was expected to be much more accurate and precise relative to RTK observations alone.



Note: IP: Instrument Point; CK: Checkpoint

**Figure 229. TxDOT’s Instrument Point and Checkpoint Locations.**



**Figure 230. Marks to Indicate TxDOT’s Instrument Points and Checkpoints.**



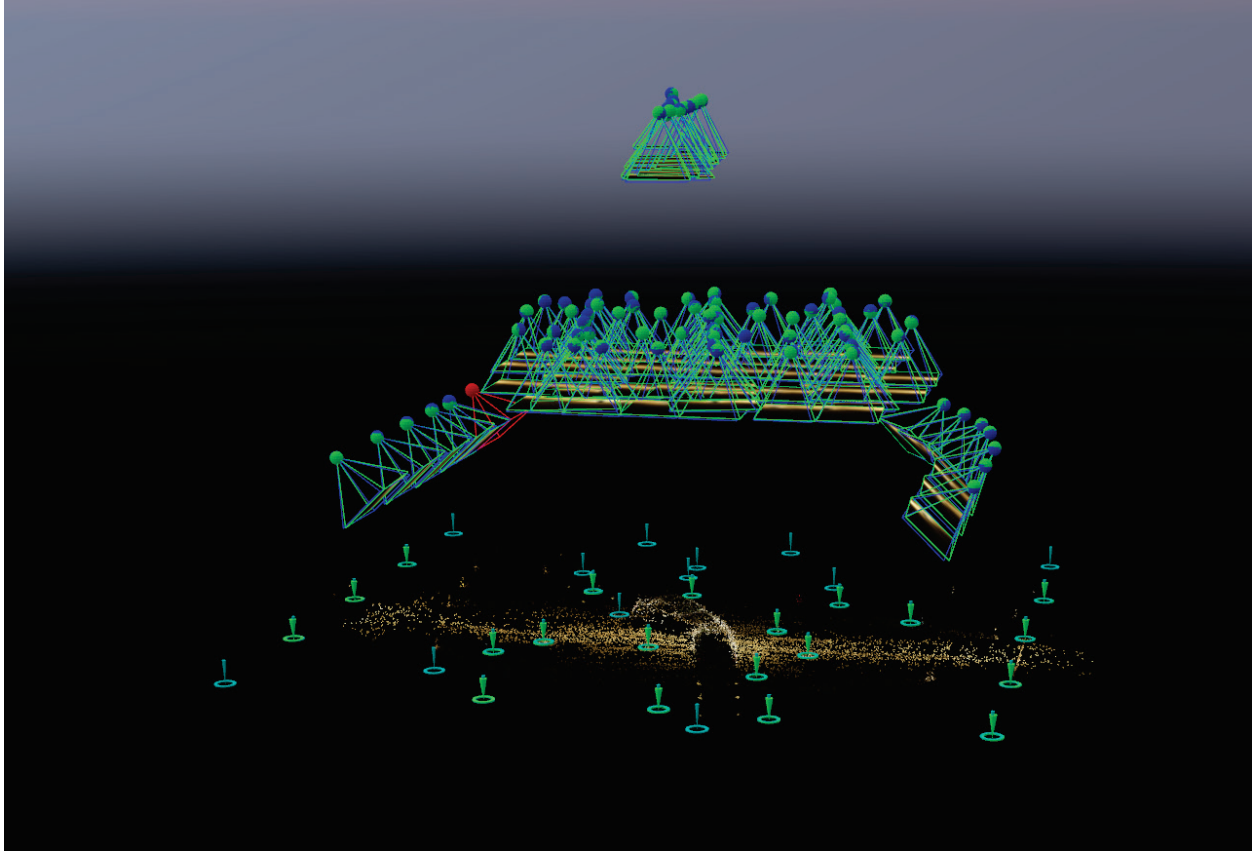
Using a Trimble SX10 total station, the TxDOT surveyors established horizontal coordinates of the instrument points by means of a closed traverse. Checkpoint horizontal coordinates were then measured as side shots from the traverse. TxDOT provided this control in NAD83(2011) State Plane Texas Central for X-Y and NAVD 88 elevation for Z. These coordinates were in U.S. survey ft. The research team used TxDOT's established survey control to georeference the TLS survey data and to assess the accuracy of the UAS-SfM survey data.

The research team laid out 20 GCPs in a grid pattern around the staged crash scene. For each target, the research team recorded 10 seconds of observations at 1 Hz using the second Septentrio GNSS receiver, which was connected to the TxDOT RTN, and then averaged the X-Y-Z coordinates. Unless otherwise noted, the research team used all 20 GCPs as checkpoints for evaluation of the SfM photogrammetric accuracy. Ground control data were collected in NAD83(2011) State Plane Texas Central for X-Y and NAD83(2011) ellipsoid heights for Z.

The research team conducted two daytime flights and one nighttime flight. The first daytime flight was an autonomous survey with the WingtraOne operating in PPK mode. The survey used 80 percent sidelap and 65–75 percent endlap in a gridded flight plan with parallel flight lines. The flight was at 75 m (246 ft) resulting in an average image GSD of 1 cm/pixel (0.4 inches/pixel). The flight took 10 minutes.

The second daytime flight was an autonomous survey with the Phantom 4 RTK operating in RTK mode (via TxDOT RTN). The flight design included a double grid consisting of perpendicular flight lines at an altitude of 25 m, resulting in an average image GSD of 0.85 cm/pixel (0.3 inches/pixel). Overlap was set to 80 percent sidelap and endlap with the camera angled 30 degrees up from nadir (i.e., 60 degrees with respect to the horizon).

The nighttime flight was a manual flight of the Phantom 4 RTK operating in RTK mode (via TxDOT RTN). The scene was illuminated by headlights from two vehicles parked on the northern and southern side of the staged vehicle scene. The manual flight mode enabled the research team to stop at each location and use lower exposure times. The flight plan included a midlevel 15 m (49 ft) altitude image set of high overlap nadir images acquired in parallel flight lines, half of which had the camera orientation perpendicular to the other half. It also included a high-level, 25 m (82 ft) altitude image set flown for an overview of the scene acquired in parallel flight lines, half of which had the camera orientation perpendicular to the other half. Finally, it included a low-level, 8 m (26 ft) altitude set of oblique imagery to better capture the sides of the vehicles. The targeted overlap was 75 percent sidelap and endlap for images acquired at the same height. Figure 231 shows the final camera positions and orientations within Pix4D.



**Figure 231. Camera Positions and Orientations for Phantom 4 RTK Night Flight.**

The research team acquired TLS data from a series of four scan positions distributed in a rectangular fashion around the staged vehicle scene. Each scan position was located within 20 m (65 ft) from the vehicles. Imagery for point cloud colorization was also acquired at each scan position. For registration and georeferencing of each scan position, the research team set up and leveled four fixed-height tripods on the TxDOT-established instrument points (Figure 232). The research team installed a RIEGL 10-cm cylinder target with reflective tape on top of each tripod. These targets are designed specifically for registration and georeferencing of the RIEGL VZ line of scanners and are highly reflective and identifiable in the TLS point cloud. The research team installed an additional fixed-height tripod with a 10-cm cylinder target in the scene to add an additional scanner tie point for scan-to-scan registration. Each target was fine scanned at each scan position for accurate shape fitting within the TLS postprocessing software, RiSCAN PRO.

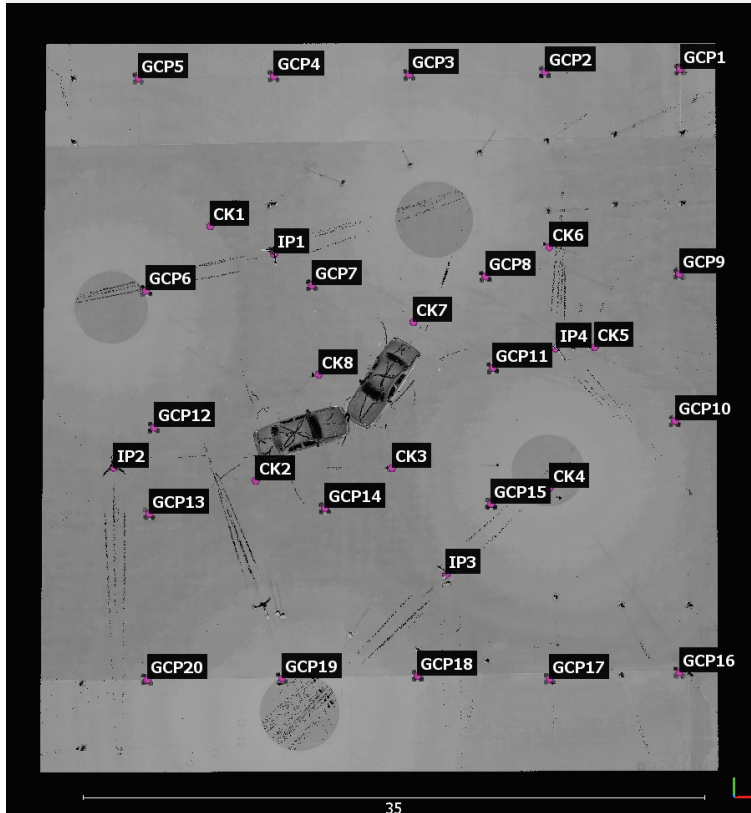
Table 126 shows the TLS survey parameters used for data acquisition at each scan position. Figure 233 shows the GCPs and TxDOT survey control overlaid on the TLS point cloud, colored by intensity. The four scan position locations can be observed in the darker gray circular areas that are visible in the merged scan due to reduced point density there.



**Figure 232. TLS Target Setup on Instrument Points and an Additional Target Tie Point.**

**Table 126. Test 7 TLS Survey Parameters Used for Each Scan Position.**

Scan Parameters	Values
Laser Pulse Rate	1200 kHz
Stepping Angle	20 millidegrees
Horizontal Field-of-View	360°
Vertical Field-of-View	100° (+60°, -40°)



**Figure 233. GCP and TxDOT Survey Control Overlaid on Merged TLS Point Cloud.**

### *Data Processing*

#### TxDOT Survey Control Data Processing

The research team converted the TxDOT control points from U.S. survey ft to meters and from NAVD 88 orthometric heights to NAD83 ellipsoid heights using VDatum and GEOID12B. The reference mark take off elevation was converted to a NAD83 ellipsoid height and the geoid offset computed. That offset was then applied to all the leveled elevation coordinates for the instrument points and checkpoints to convert them to NAD83 ellipsoid heights. The research team used ellipsoid heights to enable a more seamless comparison when processing PPK or RTK corrected image geotags within Pix4D, which are referenced to NAD83 ellipsoid heights.

#### UAS PPK Data Processing

For the WingtraOne UAS PPK survey, the research team submitted the RINEX file of the static GNSS base station's observations collected during the flight to OPUS to solve for a static coordinate in NAD83(2011) datum. This coordinate was then used along with the WingtraOne onboard GNSS observation data to correct the image geotags using PPK processing within the WingtraHub software. The output was a .csv text file containing the corrected coordinates for each image in NAD83(2011) latitude, longitude, and ellipsoid height, as well as the estimated positional accuracies.

For the Phantom 4 RTK flights, images were acquired in RTK mode during flight, so corrections, as previously mentioned, were applied directly to the EXIF image geotags. No further processing was required.

### SfM Data Processing

Table 127 shows the UAS flights processed and evaluated in this test. The research team processed all flight data in Pix4D, and the nighttime flight was also processed in Metashape for comparison.

**Table 127. Test 7 UAS Flights and SfM Processing Runs.**

	<b>Flight</b>	<b>Time of Survey</b>	<b>Flight Mode</b>	<b>GNSS</b>	<b>Lighting Source</b>	<b>SfM Software</b>
<b>1</b>	WingtraOne	1:59 PM	Autonomous	PPK	Sunlight	Pix4D
<b>2</b>	Phantom 4RTK	2:32 PM	Autonomous	RTK	Sunlight	Pix4D
<b>3</b>	Phantom 4 RTK	10:25 PM	Manual	RTK	Vehicle headlights	Pix4D, Metashape

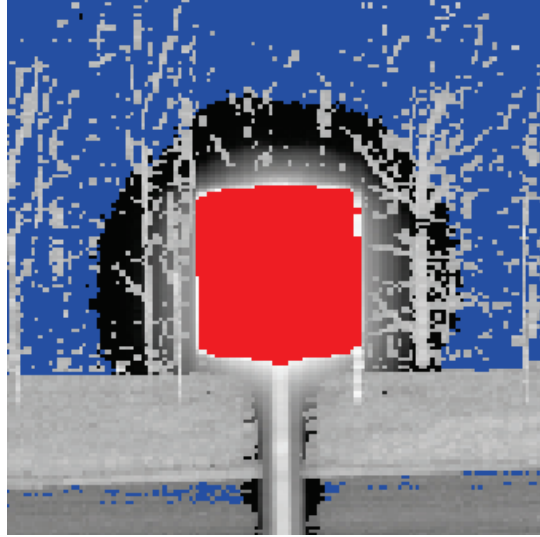
For the WingtraOne PPK daytime flight and the Phantom 4 RTK daytime flight, the research team used Pix4D’s standard workflow and 3D mapping template. The data were processed without GCPs relying solely on the PPK- or RTK-corrected image geotags, respectively. For comparison, the research team also processed the data using four GCPs that were set to the four TxDOT instrument points. For the Phantom 4 RTK night flight, the research team used Pix4D’s standard workflow and 3D mapping template with the Accurate Geolocation and Orientation calibration method. In Metashape, the research team used a slightly modified version of a workflow developed by the USGS (133, 134).

The research team used the TxDOT survey control points and their GCP network as checkpoints to evaluate the absolute accuracy of the SfM BA within the Pix4D or Metashape.

### TLS Data Processing

The research team processed the four TLS scan positions into a merged point cloud using the MSA tools in RIEGL’s RiSCAN PRO. The process occurred in two stages. First, the research team fit 10-cm (4-inch) cylinder shapes to the fine scans of the 10-cm (4-inch) cylinder targets acquired from each scan position (Figure 234 and Figure 235). These fitted shapes were then used as tie points to perform an automatic registration of the scans and merge them together (Figure 236).

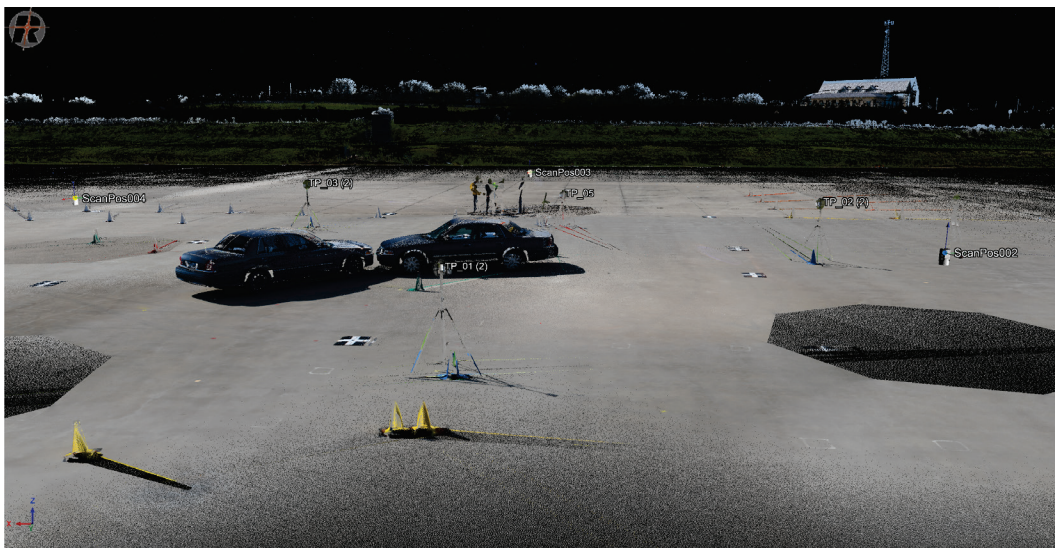
Second, the research team used the MSA tools to georeference the point cloud data and perform a fine adjustment of the scans based on tie points and cloud-to-cloud geometric constraints. To do this, the research team assigned the X-Y-Z coordinates for each of the four TxDOT instrument points to their four respective tie points within the point cloud to establish TLS “control points.” The research team added the tripod rod height plus a 5-cm (2-inch) offset to each TxDOT instrument point Z-value. The 5-cm (2-inch) offset was necessary because RiSCAN assigned coordinates to the center of the 10-cm (4-inch) cylinder target.



**Figure 234. 2D View of Target Fine Scan.**



**Figure 235. Cylinder Shape Fit to a Tie Point Target.**



**Figure 236. Colorized TLS Point Cloud Showing Tie Points and Scan Positions.**

After completing this step, the research team applied the MSA tools to georeference and refine the alignment of the TLS point cloud data. Table 128 shows statistical results from the MSA report based on 16 observations resulting from the four control points observed from four scan positions. The additional tie point not used as control was also used in the adjustment. Table 129 shows MSA statistical results for the single tie point based on four observations from each scan position.

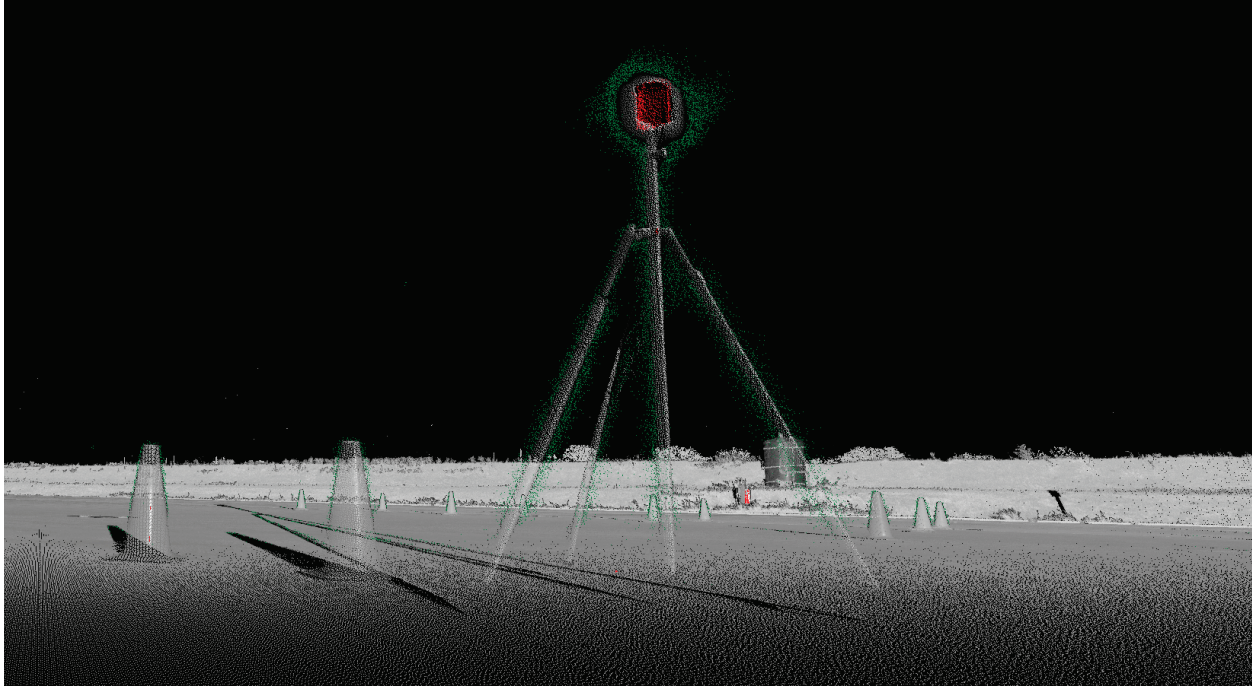
**Table 128. Statistical Results from MSA for Control Points.**

	dX [m]	dY [m]	dZ [m]	dist. [m]
Minimum deviation	-0.0146	-0.0146	-0.0030	0.0030
Maximum deviation	0.0121	0.0087	0.0027	0.0164
Mean deviation	0.0000	-0.0000	0.0000	0.0088
Standard deviation	0.0070	0.0063	0.0016	---
Median abs. dev. (std)	0.0085	0.0073	0.0018	---

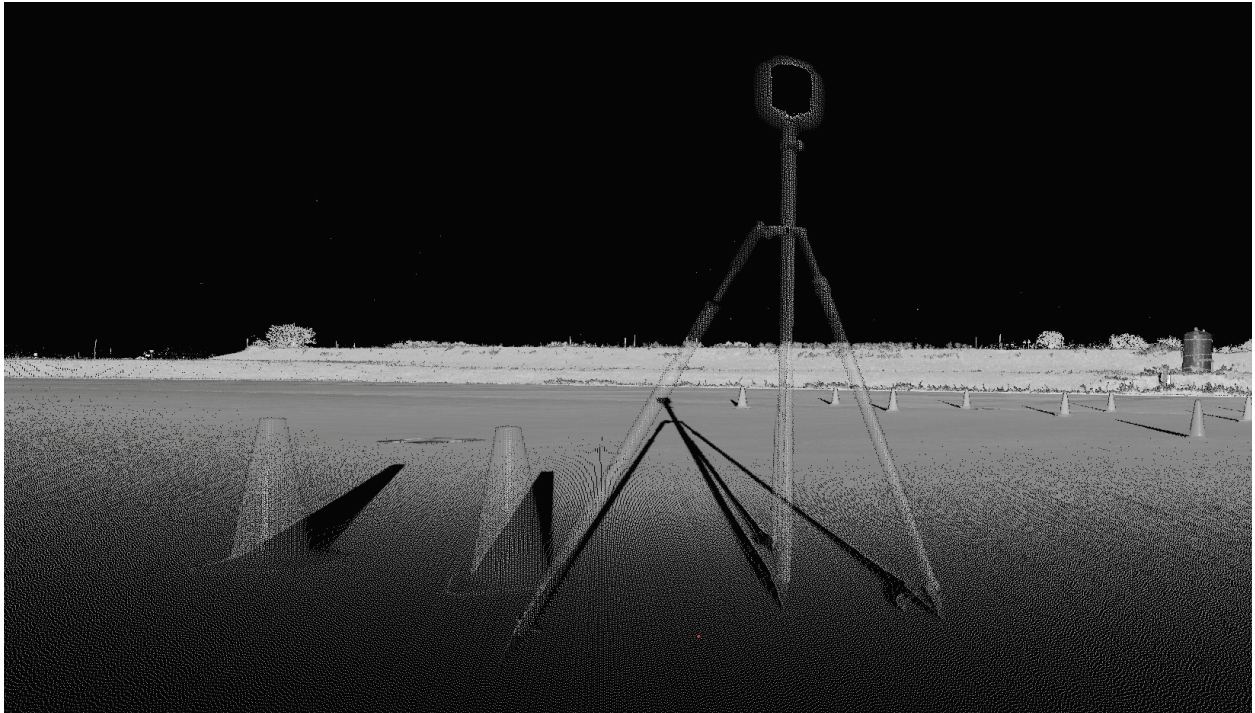
**Table 129. Statistical Results from MSA for Single Tie Point.**

	dX [m]	dY [m]	dZ [m]	dist. [m]
Minimum deviation	-0.0034	-0.0021	-0.0039	0.0011
Maximum deviation	0.0014	0.0081	0.0032	0.0096
Mean deviation	-0.0007	0.0021	-0.0002	0.0044
Standard deviation	0.0019	0.0039	0.0025	---
Median abs. dev. (std)	0.0021	0.0034	0.0028	---

The research team applied a semi-automatic method to rigorously filter point cloud noise based on calibrated reflectance and pulse shape deviation attributes recorded for each point. The research team then performed manual inspection of the cloud for any residual clean up. Figure 237 and Figure 238 show examples of before and after noise filtering, respectively. Figure 239 shows an example view of the staged car scene within the final, colored TLS point cloud.



**Figure 237. Before Noise Filtering.**



**Figure 238. After Noise Filtering.**





**Figure 239. Colorized TLS Point Cloud View of Staged Car Scene.**

### *Analysis*

The research team evaluated the quality and absolute accuracy of the densified 3D point cloud data generated from the Pix4D and Metashape SfM processing. The research team completed the following analyses:

- Evaluation of the UAS and TLS point cloud data relative to ground control data.
- Evaluation of the UAS point cloud data relative to TLS point cloud data.
- Accuracy evaluation based on SfM processing reports.

### *Results*

#### Evaluation of UAS and TLS Point Cloud Data Relative to Ground Control Data

The research team computed the accuracy of the UAS and TLS point cloud measurements in the Z component relative to the 12 TxDOT control points and the 20 GCPs surveyed with RTK GNSS. Table 130 shows vertical accuracy results for the UAS flights relative to TxDOT control. All UAS results were based solely on PPK or RTK image geotags with no GCPs used during SfM processing. The TLS had an RMSE of 6 mm (0.24 inches) and best overall accuracy. The most accurate UAS flight was the Phantom 4 RTK nighttime flight processed in Metashape with an RMSE of 9 mm (0.35 inches). However, this result is based on a limited set of five control points. Pix4D reconstructed more of the scene at night, enabling more control points to be used in its RMSE computation.

Table 131 shows vertical accuracy results relative to the GCPs surveyed using RTK GNSS. All UAS flights increased in RMSE except for the Phantom 4 RTK nighttime flight processed in Pix4D. The TLS survey increased by about 2 cm. This result stems from the point-to-point vertical uncertainty in the RTK GNSS height observations.

**Table 130. Surface Height Error Relative to TxDOT Control.**

Observation	Height Error (m)				
	TLS	WingtraOne PPK Day (Pix4D)	Phantom 4 RTK Day (Pix4D)	Phantom 4 RTK Night (Pix4D)	Phantom 4 RTK Night (Metashape)
Instrument Point 1	0.004	0.023	0.027	0.004	0.022
Instrument Point 2	0.007	0.017	0.014	0.056	
Instrument Point 3	0.005	0.020	0.023	0.007	
Instrument Point 4	0.005	0.017	0.020		
Checkpoint 1	0.007	0.021	0.022	0.012	
Checkpoint 2	0.003	0.013	0.020	0.007	0.014
Checkpoint 3	0.003	0.023	0.017	0.007	0.006
Checkpoint 4	0.013	0.029	0.023	0.019	
Checkpoint 5	0.004	0.019	0.013	0.006	
Checkpoint 6	0.003	0.020	0.019	0.015	
Checkpoint 7	0.003	0.022	0.021	0.002	0.009
Checkpoint 8	0.006	0.026	0.019	0.007	0.014
RMSE	0.006	0.021	0.020	0.019	0.009

**Table 131. Surface Height Error Relative to RTK GNSS GCPs.**

Observation	Height Error (m)				
	TLS	WingtraOne PPK Day (Pix4D)	Phantom 4 RTK Day (Pix4D)	Phantom 4 RTK Night (Pix4D)	Phantom 4 RTK Night (Metashape)
GCP1	0.014	0.023	0.023		
GCP2	0.010	0.023	0.021		
GCP3	0.008	0.017	0.011	0.023	
GCP4	0.013	0.018	0.009	0.020	
GCP5	0.024	0.016	0.009		
GCP6	0.018	0.027	0.013	0.020	
GCP7	0.030	0.045	0.051	0.028	0.047
GCP8	0.039	0.052	0.057	0.042	0.061
GCP9	0.045	0.037	0.051		
GCP10	0.033	0.041	0.041		
GCP11	0.015	0.039	0.029	0.019	
GCP12	0.007	0.025	0.019	0.009	
GCP14	0.018	0.029	0.032	0.018	0.022
GCP15	0.018	0.044	0.041	0.008	
GCP16	0.037	0.033	0.038		
GCP17	0.030	0.033	0.040	0.025	
GCP18	0.024	0.043	0.032	0.009	
GCP19	0.025	0.029	0.033	0.013	
GCP20	0.027	0.040	0.039	0.003	
RMSE	0.025	0.034	0.034	0.017	0.018

## Evaluation of UAS Point Cloud Data Relative to TLS Point Cloud Data

**Surface Roughness.** The research team computed surface roughness using the standard deviation of the Z-values for all points that fell within 25-cm (10-inch) radius circular patches (10,000 in total). These patches were randomly distributed throughout a region of interest that included the staged vehicle scene and GCP control network.

Figure 240 shows surface roughness results generated from Pix4D for the TLS point cloud, the WingtraOne PPK daytime point cloud, and the Phantom 4 RTK daytime point cloud. The mean surface roughness value was 0.2 cm (0.08 inches) for the TLS point cloud, 1.4 cm (0.55 inches) for the WingtraOne point cloud, and 1.2 cm (0.47 inches) for the Phantom 4 RTK point cloud. The TLS point cloud had significantly lower mean standard deviations than the UAS-SfM point clouds, especially over the skid pad surface. Both UAS flights showed similar patterns representing surface height variability, although each point cloud was generated from different cameras and flight designs as well as GNSS correction methods.

**Point-to-Point Comparison in Region of Interest.** The research team evaluated point-to-point differences between the UAS point cloud data and TLS point cloud data. Due to differences in area of coverage for the reconstruction between the daytime and nighttime flights, the region of interest selected for this analysis focused on the staged vehicle scene. Figure 241 shows the region of interest for the TLS point cloud, which was used as a reference for the WingtraOne PPK and Phantom 4 RTK point cloud regions of interest.

First, the research team assessed the daytime UAS flights. Figure 242 shows top-down views of the WingtraOne PPK and Phantom 4 RTK point clouds within the region of interest. Figure 243 shows point-to-point 3D distances computed between the WingtraOne PPK daytime flight and TLS survey, as well as distances computed between the Phantom 4 RTK daytime flight and TLS survey. The mean overall 3D distance offset was 2.4 cm (0.94 inches) for the WingtraOne and 2.2 cm (0.87 inches) for the Phantom 4 RTK.

Figure 244 shows the mean distance in the Z component between respective 25-cm (10-inch) point patches extracted from the WingtraOne and Phantom 4 RTK point clouds and the TLS point cloud within the region of interest. The overall mean Z distance was 7.9 cm (3.1 inches) for the Wingtra and 5.4 cm (2.1 inches) for the Phantom 4 RTK. For visualization purposes, Figure 245 shows example point patches extracted from the daytime Phantom 4 RTK point cloud within the region of interest.

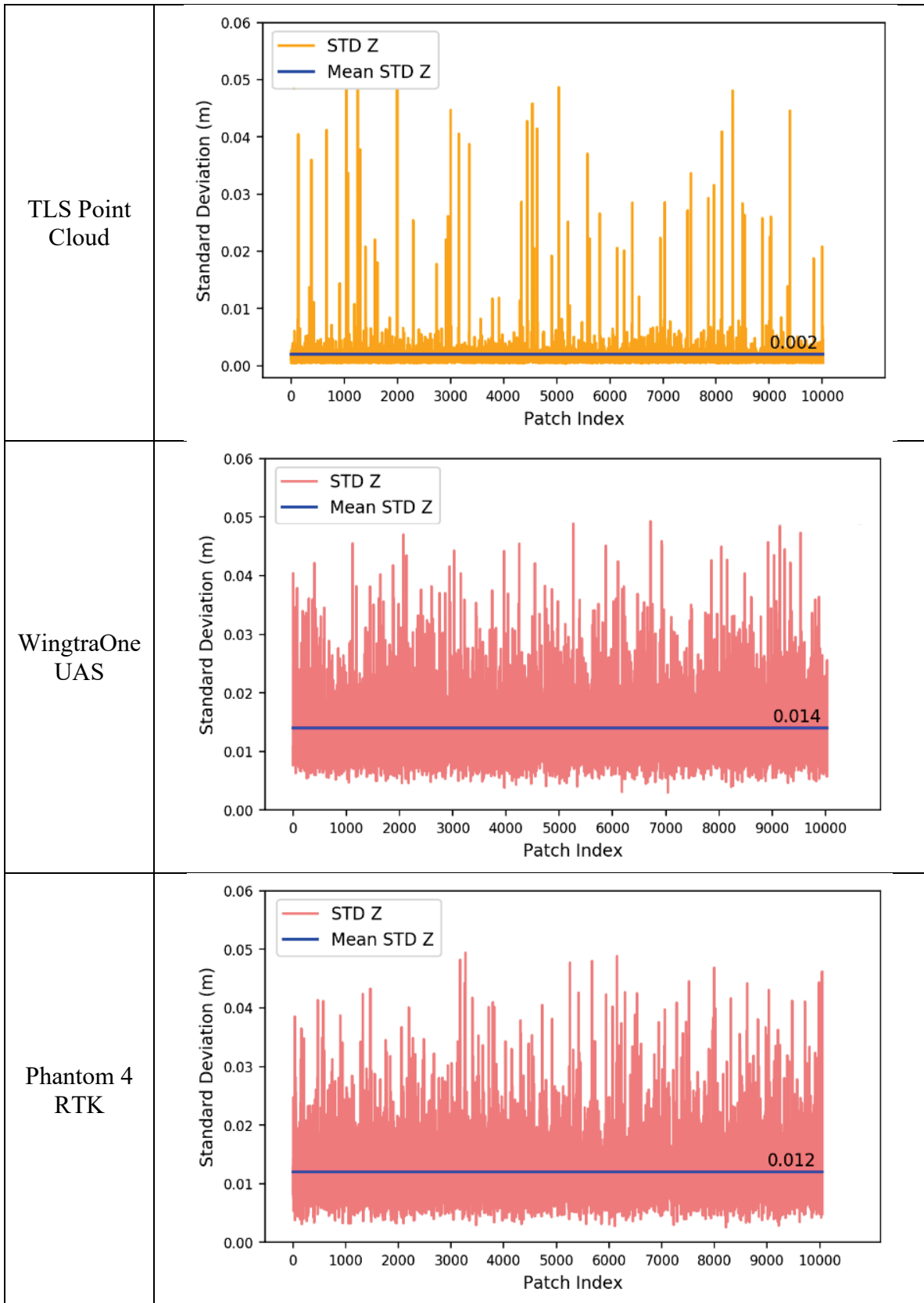


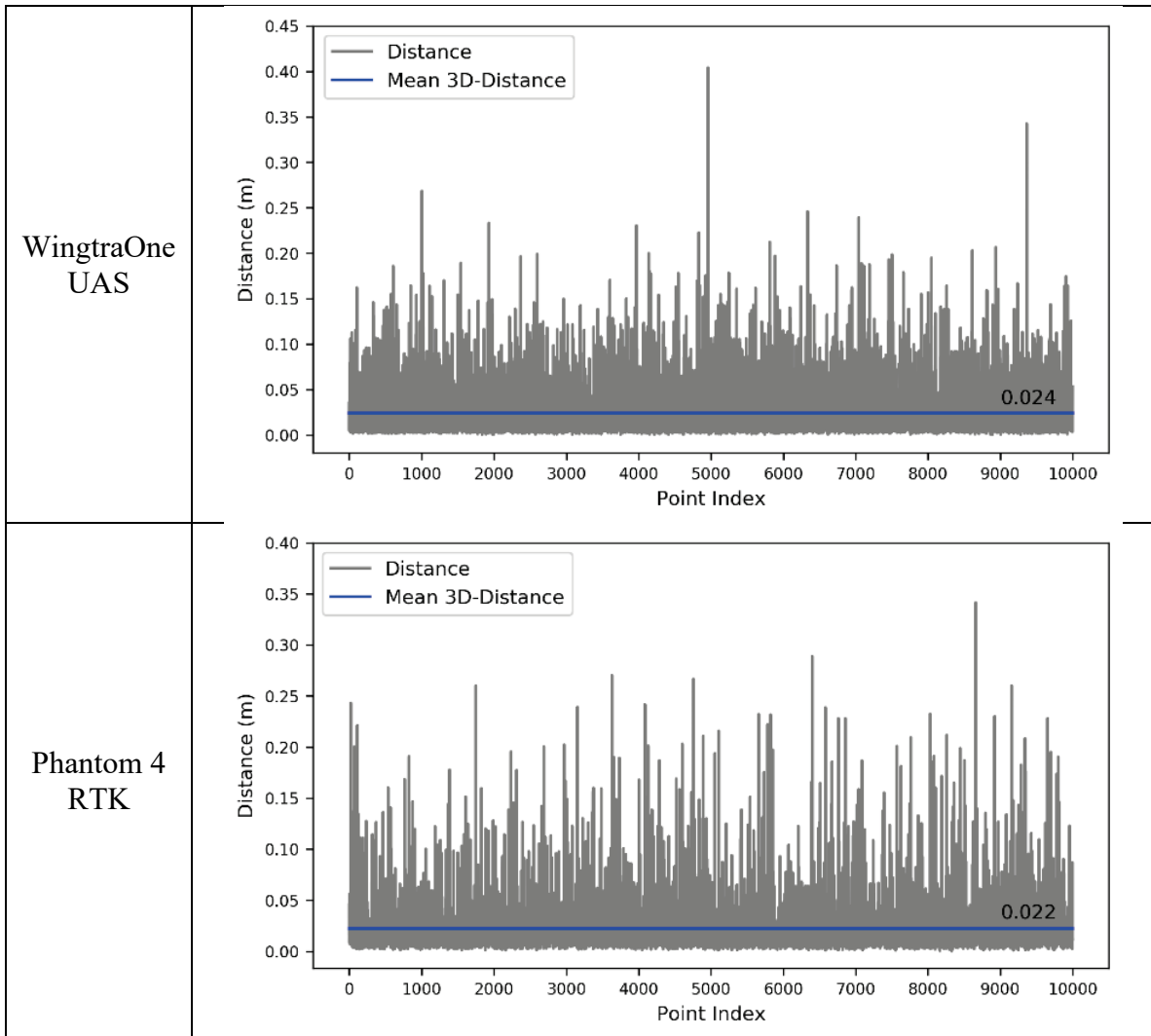
Figure 240. Surface Roughness.



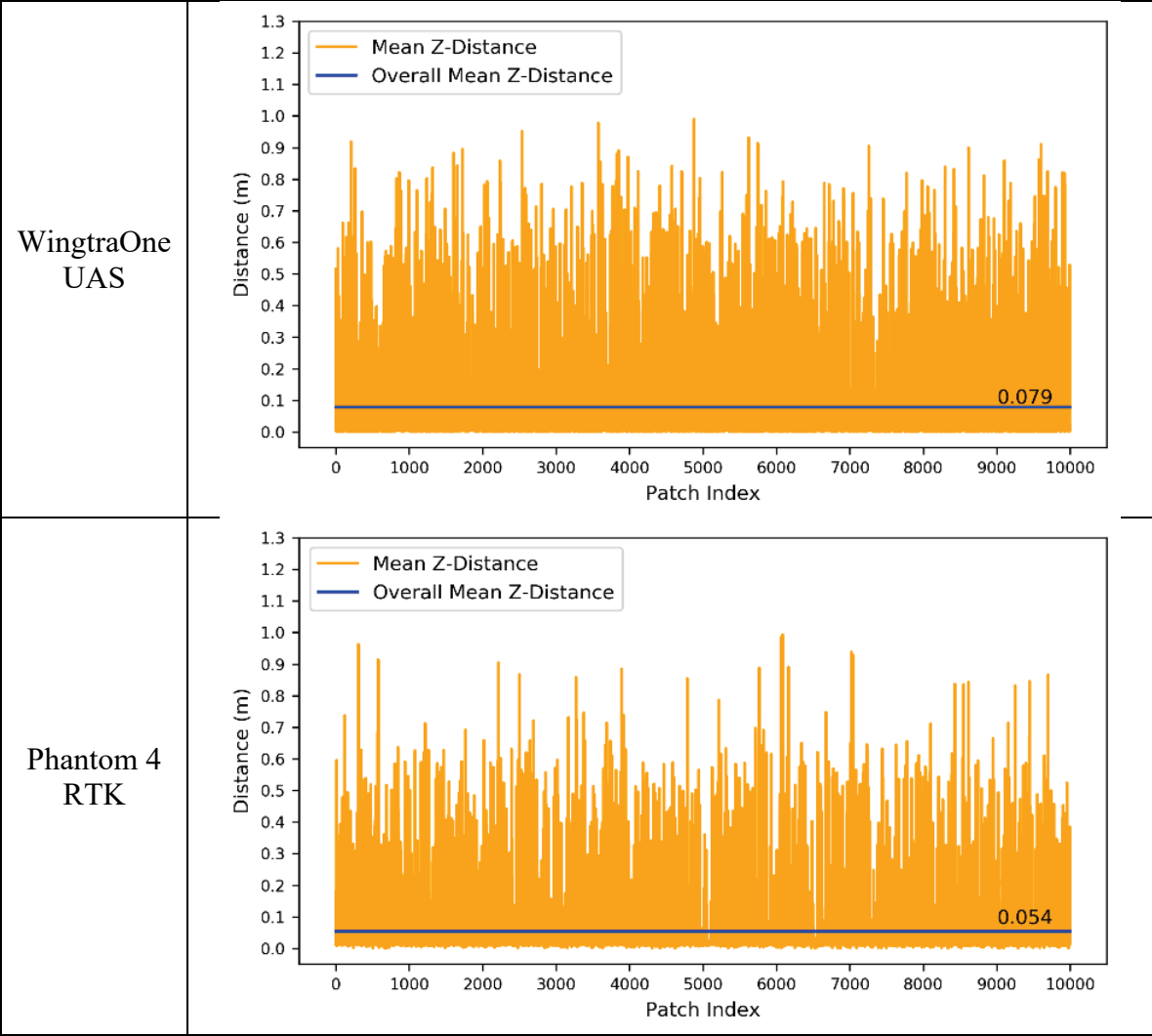
Figure 241. Region of Interest for TLS Point Cloud (Oblique View).

<p>WingtraOne</p>	<p>A top-down view of a point cloud generated by a WingtraOne drone. The two cars from Figure 241 are visible from above, showing their roof and side profiles. The ground is a light gray point cloud. A white crosshair marker is located at the bottom center of the image. A scale bar at the bottom indicates a length of 10 units.</p>
<p>Phantom 4 RTK</p>	<p>A top-down view of a point cloud generated by a Phantom 4 RTK drone. The two cars are visible from above, showing their roof and side profiles. The ground is a light gray point cloud. A white crosshair marker is located at the bottom center of the image. A scale bar at the bottom indicates a length of 10 units.</p>

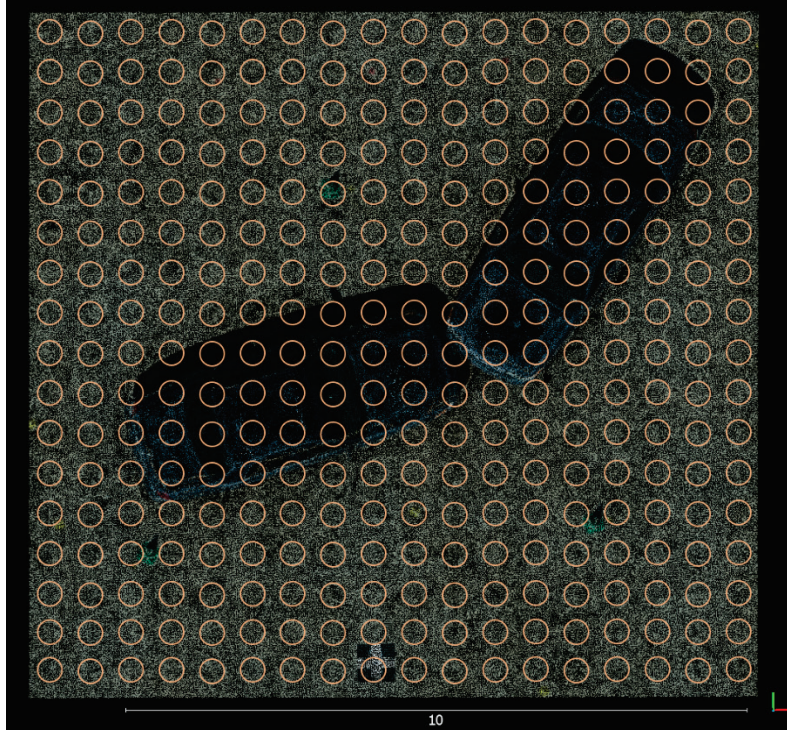
Figure 242 Region of Interest for the UAS Point Clouds (Daytime).



**Figure 243. Distance from UAS Points to TLS Points within the Region of Interest.**



**Figure 244. Mean Distance in Z for UAS Point Patches within the Region of Interest.**



**Figure 245. Point Patches Overlaid on Phantom 4 RTK Point Cloud.**

Next, the research team evaluated the Phantom 4 RTK nighttime flight based on the results obtained with Pix4D and Metashape. Figure 246 shows top-down views of the Phantom 4 RTK point clouds generated from Pix4D and Metashape. Pix4D successfully reconstructed more of the scene than Metashape under low light conditions. Figure 247 shows point-to-point 3D distances computed between the nighttime Pix4D and Metashape point clouds and TLS point cloud. The mean overall 3D distance based on 10,000 random point measurements was 0.018 m for Pix4D and 0.024 m for Metashape. These results are slightly lower than for the daytime flight. Metashape reconstructed less of the scene, but for the points that were reconstructed, distance offsets were within <1 cm (0.4 inches) of the results obtained with Pix4D.

Figure 248 shows the mean distance in the Z component between respective 25-cm (10-inch) point patches extracted from the Pix4D and Metashape point clouds and the TLS point cloud within the region of interest. The overall mean Z distance was 7.7 cm (3.0 inches) for Pix4D and 7.9 cm (3.1 inches) for Metashape. These results show that in places where Metashape reconstructed the scene for the nighttime data acquisition, point-to-point distances and surface height representations were similar to those measured from the Pix4D point cloud. However, Pix4D appears to provide a slightly more accurate reconstruction based on the TLS data. In any case, this result should not be taken as a measure of overall point cloud fidelity in terms of 3D scene representation given there are areas of data gaps in the point cloud results.



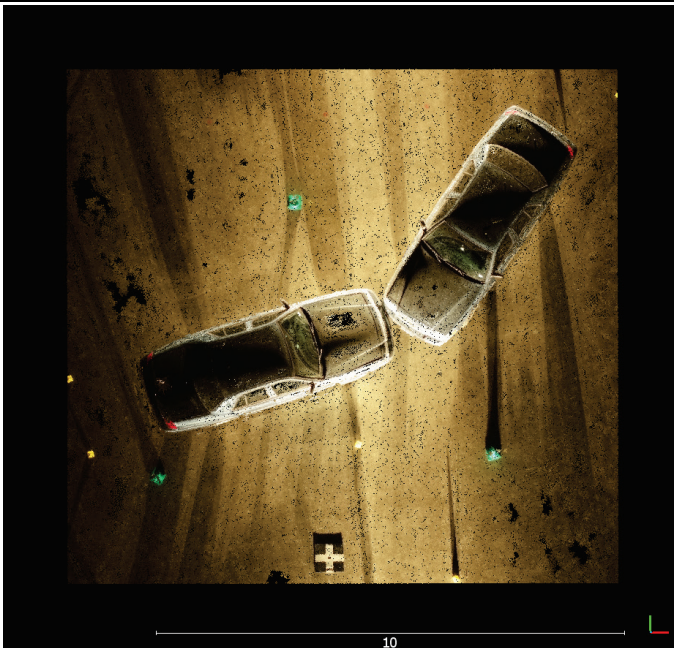

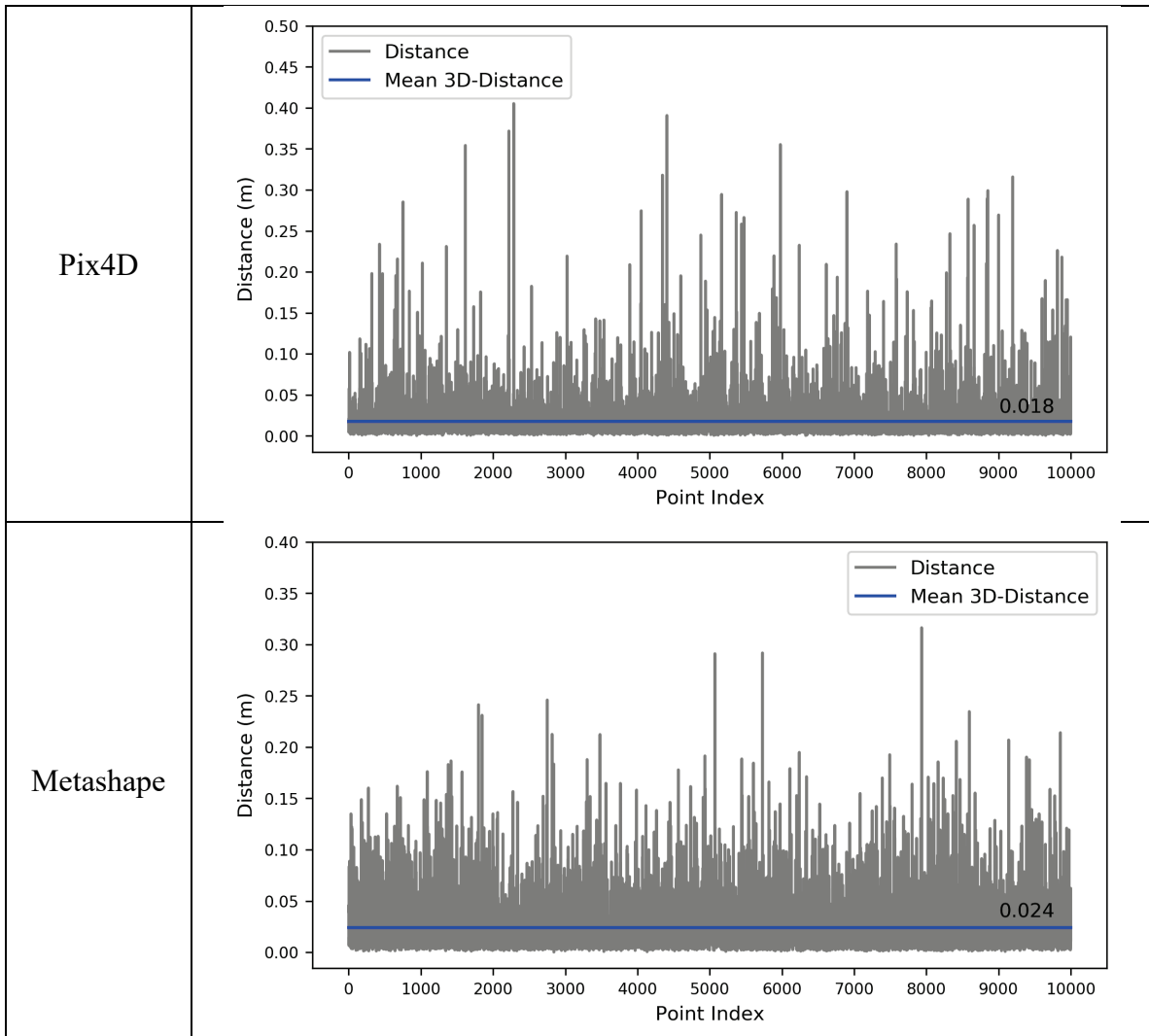
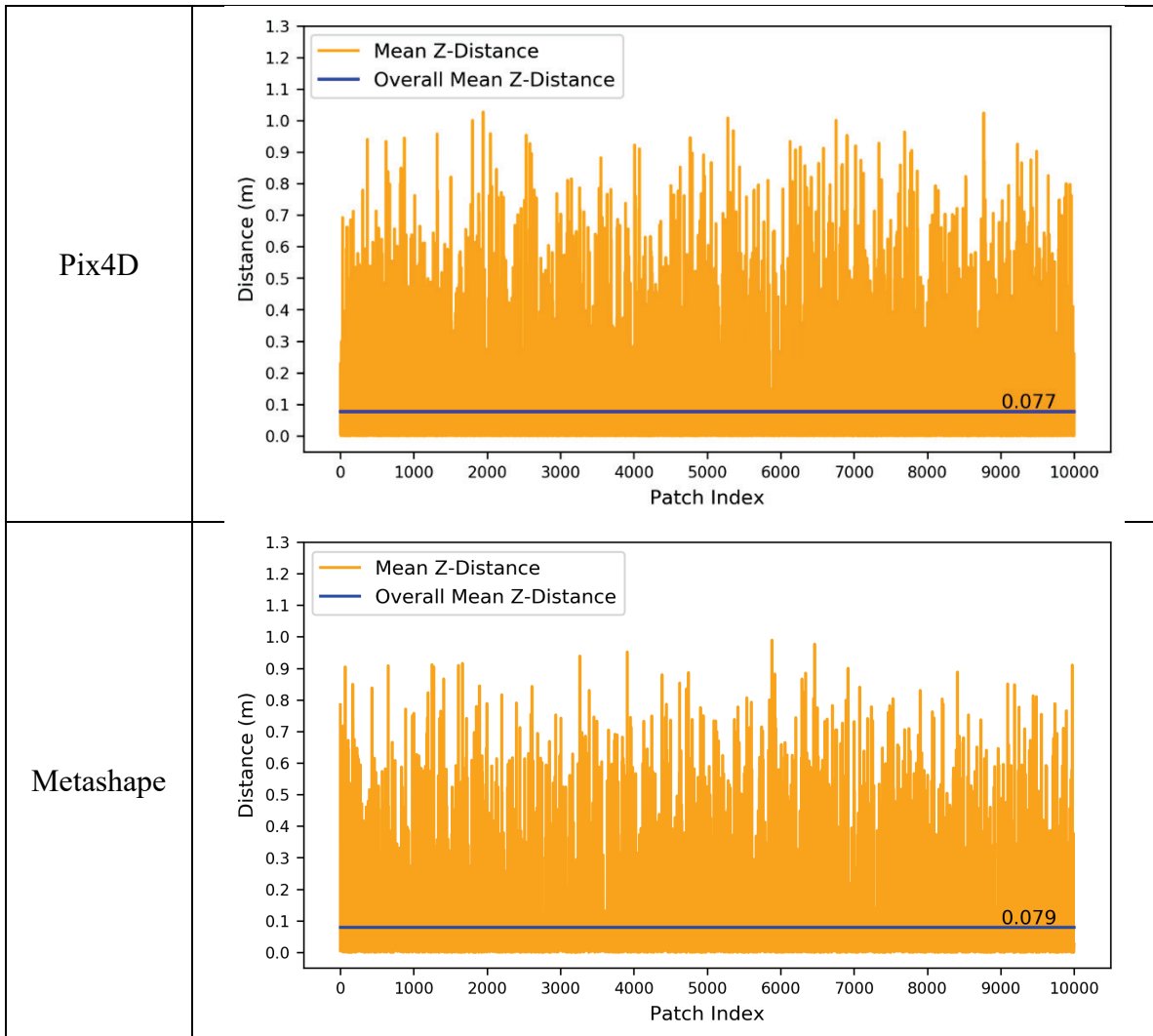
<p>Pix4D</p>	 A point cloud visualization of two cars parked on a road at night, processed by Pix4D. The cars are rendered with a semi-transparent, light-colored mesh. The background shows the road surface and some streetlights. A white crosshair is visible on the road, and a scale bar with the number '10' is at the bottom. A small red and green icon is in the bottom right corner.
<p>Metashape</p>	 A point cloud visualization of the same two cars at night, processed by Metashape. The cars are rendered with a semi-transparent, light-colored mesh. The background shows the road surface and some streetlights. A white crosshair is visible on the road, and a scale bar with the number '10' is at the bottom. A small red and green icon is in the bottom right corner.

Figure 246. Phantom 4 RTK Point Clouds at Night.



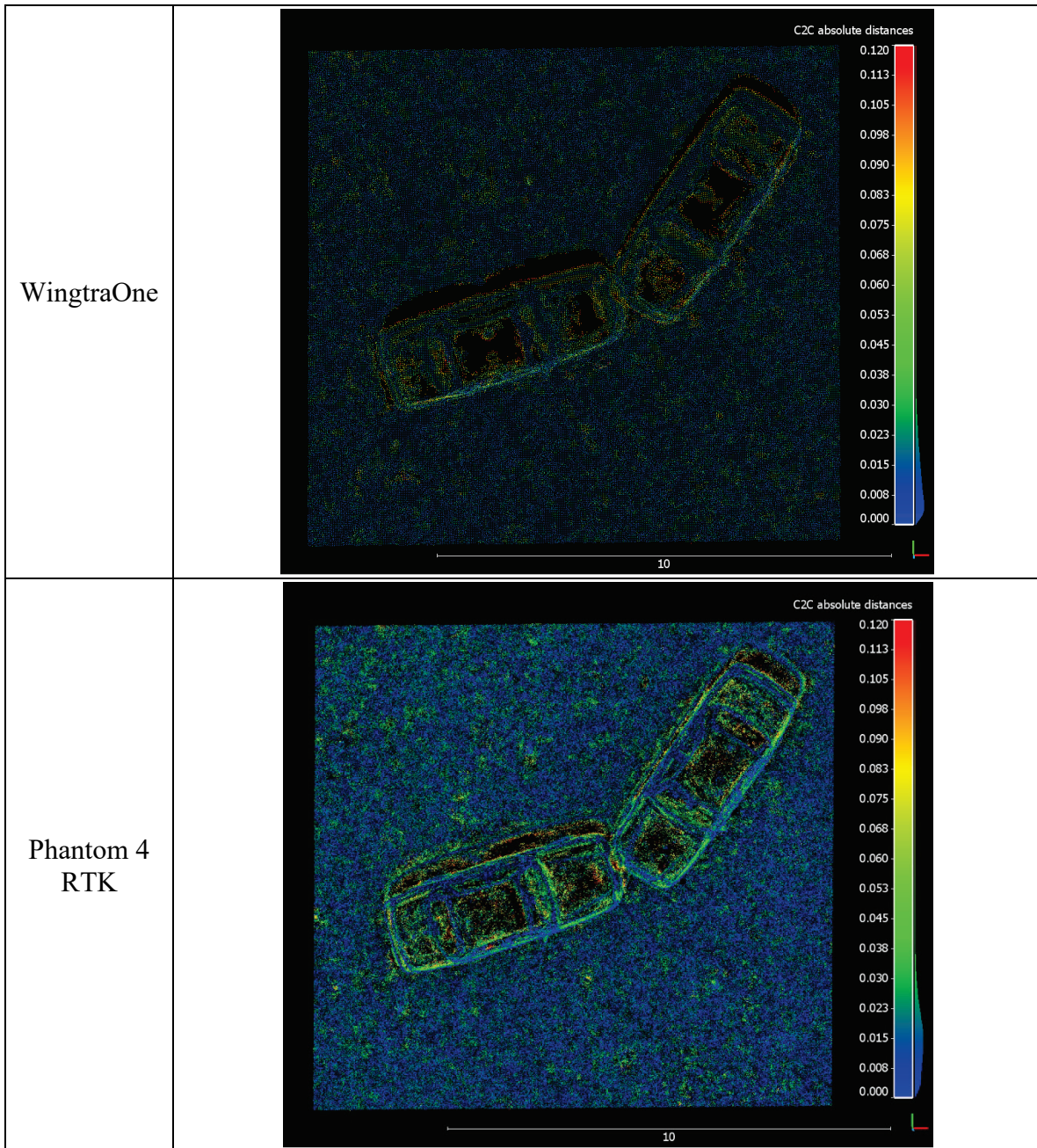
**Figure 247. Distance from Phantom 4 RTK Points to TLS Points within the Region of Interest.**



**Figure 248. Mean Distance in Z for Nighttime Result within the Region of Interest.**

**Cloud-to-Cloud Comparison.** The research team computed the mean and standard deviation of cloud-to-cloud distances between the UAS and TLS point clouds as an indicator of dense point cloud quality. Using CloudCompare, the research team computed distances for a larger region of interest that included the staged vehicle scene and surrounding pavement area encompassing the control network and for a smaller region of interest focused on the staged car scene.

Figure 249 shows cloud-to-cloud distances computed for the WingtraOne and Phantom 4 RTK daytime flights within the car scene region of interest. Differences in image brightness are due to reduced point density in the WingtraOne survey than the Phantom 4 RTK survey.



**Figure 249. Cloud-to-Cloud Distances in Car Scene Region of Interest (Daytime Flights).**

Table 132 and Table 133 show cloud-cloud-distance statistics for the WingtraOne PPK and Phantom 4 RTK daytime flights, respectively, computed for each region of interest. In the large scene, WingtraOne slightly outperformed the Phantom 4 RTK. In the car scene, the Phantom 4 RTK provided a closer 3D representation of the TLS survey than the WingtraOne as evidenced by its lower mean distance and standard deviation. This effect is likely due to the larger number of points reconstructed for the car scene from the Phantom 4 RTK survey as a result of the higher resolution imagery acquired in the flight.

**Table 132. Cloud-to-Cloud (C2C) Distance Statistics for WingtraOne.**

Region of interest	Distance (m)		
	Points	Mean	Standard Deviation
Large Scene	1,551,982	0.014	0.015
Car Scene	131,321	0.023	0.036

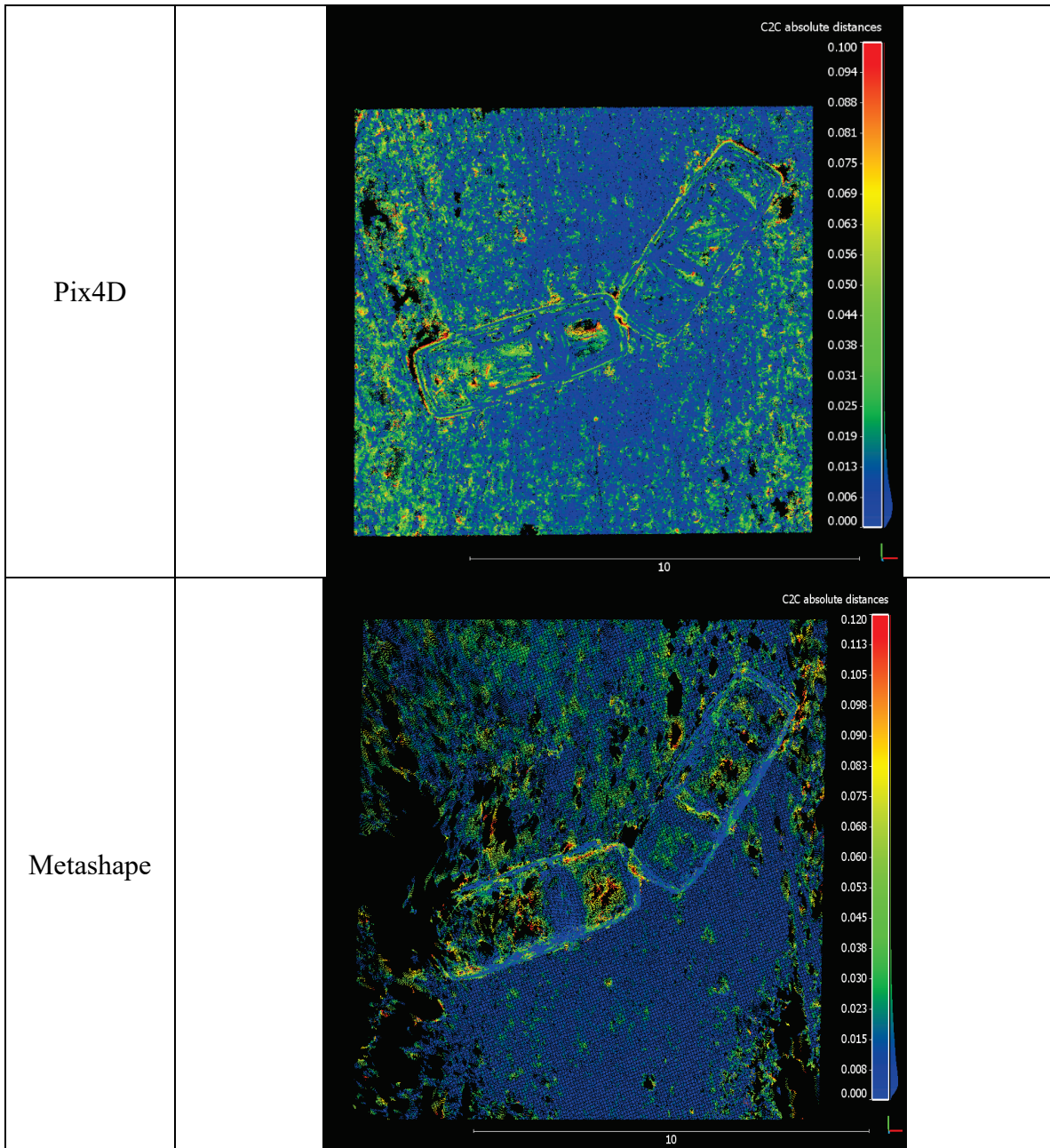
**Table 133. Cloud-to-Cloud (C2C) Distance Statistics for Phantom 4 RTK.**

Region of interest	Distance (m)		
	Points	Mean	Standard Deviation
Large Scene	6,547,520	0.016	0.014
Car Scene	583,092	0.022	0.025

Figure 250 shows cloud-to-cloud distances computed for the Phantom 4 RTK nighttime flight processed in Pix4D and Metashape within the car scene region of interest. Most apparent are the large data gaps in the Metashape point cloud relative to the Pix4D point cloud on the left-hand side of the image, particularly on the pavement. It should be mentioned, however, that the cloud-to-cloud distance statistics are assessed only for those areas of the UAS point cloud with point representation.

Table 134 and Table 135 show cloud-cloud-distance statistics for the Phantom 4 RTK nighttime flight processed in Pix4D and Metashape, respectively, computed for each region of interest. Pix4D and Metashape had similar mean distances for the large scene region of interest, but Pix4D had more variability in distance, as evidenced by its larger standard deviation. This effect may be due to the larger area reconstructed, and greater number of points, resulting in some pockets of noisier points reconstructed on the edges of the scene with low lighting as shown in Figure 251. Differences in how the respective software reconstructed points in areas of shadowing, such as due to occlusion of the vehicle lights from cones on the ground, can also be observed in Figure 251. It appears that in some areas these static shadows aided reconstruction.

In the car scene region of interest, Pix4D outperformed Metashape with a lower mean distance, although both had similar standard deviations. Overall, in areas where reconstruction was successful, both software platforms produced similar results relative to the TLS survey.



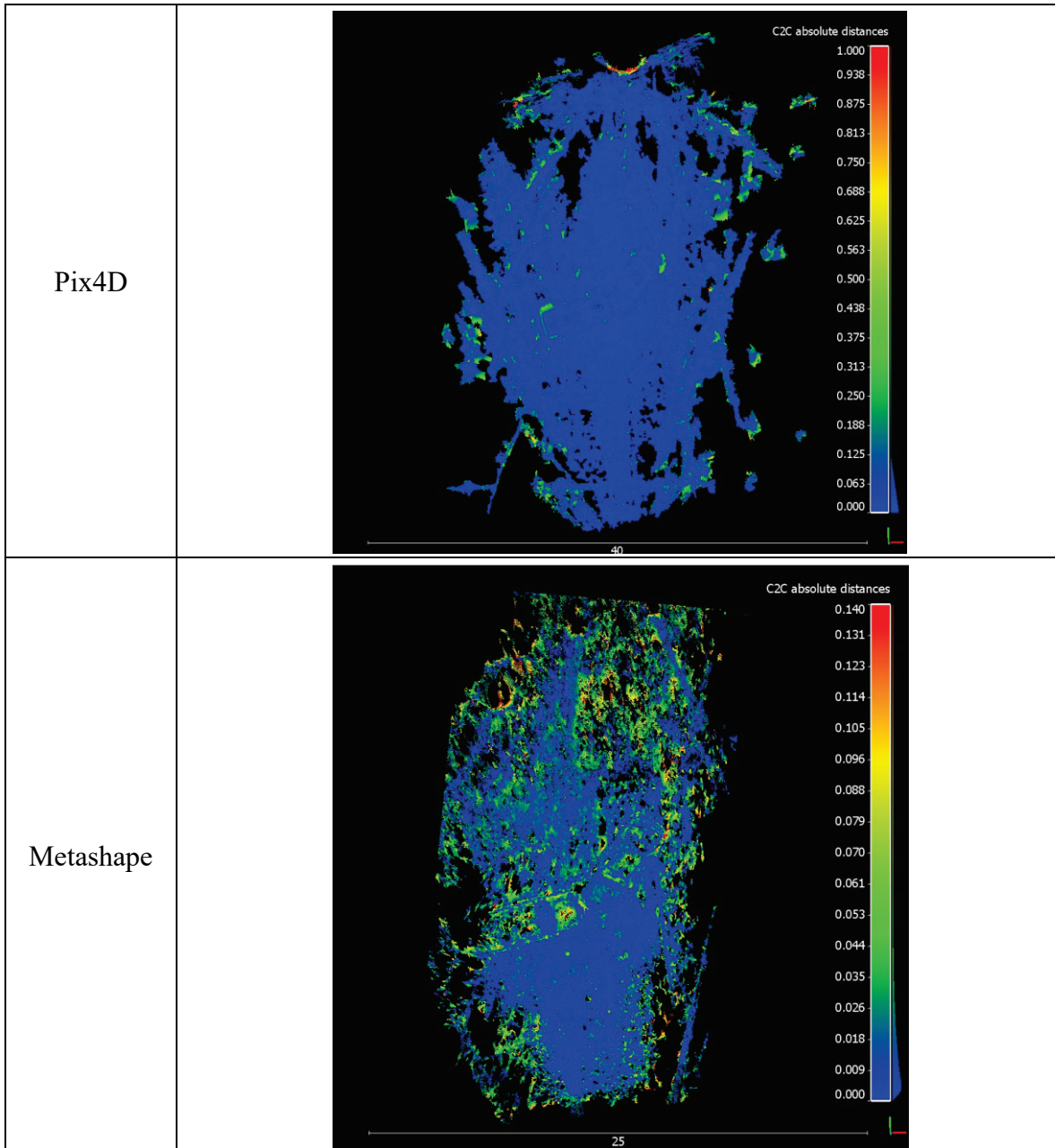
**Figure 250. Cloud-to-Cloud Distances for Phantom 4 RTK Night Flight.**

**Table 134. Cloud-to-Cloud (C2C) Distance Statistics for Phantom 4 RTK (night flight).**

Region of interest	Distance (m)		
	Points	Mean	Standard Deviation
Large Scene	4,202,056	0.029	0.141
Car Scene	1,411,905	0.018	0.027

**Table 135. Cloud-to-Cloud (C2C) Distance Statistics for Phantom 4 RTK (night flight).**

Region of interest	Distance (m)		
	Points	Mean	Standard Deviation
Large Scene	955,750	0.029	0.034
Car Scene	506,315	0.024	0.027



**Figure 251. Cloud-to-Cloud Distances for Phantom 4 RTK Night Flight for Large Region of Interest.**

### Evaluation Based on SfM Processing Reports

Table 136 shows SfM checkpoint errors from the Pix4D processing report for the WingtraOne PPK flight (daytime). Errors are computed relative to the TxDOT control network and the GCP aerial target control network surveyed with RTK GNSS. Table 137 shows checkpoint RMSE broken down by control method. The Z RMSE was 0.9 cm (0.35 inches) when estimated based on the TxDOT control network compared to 2.8 cm (1.1 inches) based on the GCP control network.

Table 138 shows SfM checkpoint errors from the Pix4D processing report for the Phantom 4 RTK daytime flight. Table 139 shows checkpoint RMSE broken down by control method. The Z RMSE was 2.4 cm (0.94 inches) when evaluated based on the TxDOT control network compared to 4.3 cm (1.7 inches) based on the GCP control network.

Table 140 shows SfM checkpoint errors from the Pix4D processing report for the Phantom 4 RTK nighttime flight. Table 141 shows checkpoint RMSE broken down by control method. The Z RMSE was 0.7 cm (0.28 inches) when evaluated based on the TxDOT control network compared to 2.2 cm (0.87 inches) based on the GCP control network.

These results consistently show lower Z RMSE values relative to the TxDOT control network.



**Table 136. Pix4D SfM Checkpoint Error for WingtraOne PPK.**

Check Point Name	Accuracy XYZ [m]	Error X [m]	Error Y [m]	Error Z [m]	Projection Error [pixel]	Verified/Marked
IP2		0.002	-0.010	0.010	0.481	18 / 18
IP3		0.004	-0.013	0.010	0.239	13 / 13
IP4		0.003	-0.014	0.010	0.323	13 / 13
IP1		0.007	-0.007	0.009	0.351	19 / 19
CK1		0.005	-0.010	0.006	0.386	16 / 16
CK8		0.001	-0.012	0.007	0.208	14 / 14
CK2		0.001	-0.007	0.002	0.334	16 / 16
CK3		0.003	-0.010	0.007	0.284	18 / 18
CK4		0.003	-0.012	0.011	0.312	15 / 15
CK5		-0.001	-0.011	0.009	0.304	16 / 16
CK6		-0.004	-0.005	0.011	0.272	18 / 18
CK7		-0.000	-0.012	0.011	0.301	16 / 16
GCP1		-0.001	0.001	0.016	0.384	17 / 17
GCP2		0.007	0.003	0.018	0.251	17 / 17
GCP3		0.013	0.005	0.006	0.232	15 / 15
GCP4		0.013	0.005	0.002	0.241	18 / 18
GCP5		0.018	0.004	-0.008	0.334	19 / 19
GCP6		0.002	-0.009	-0.004	0.228	19 / 19
GCP7		0.005	-0.008	0.047	0.269	18 / 18
GCP8		0.013	-0.007	0.053	0.284	15 / 15
GCP9		0.007	-0.010	0.041	0.250	12 / 12
GCP10		0.015	-0.003	0.035	0.406	12 / 12
GCP11		0.010	-0.006	0.021	0.243	14 / 14
GCP12		0.017	-0.003	0.022	0.252	16 / 16
GCP13		0.007	-0.010	0.022	0.313	12 / 12
GCP14		0.003	-0.006	0.025	0.321	17 / 17
GCP15		-0.002	-0.010	0.031	0.284	15 / 15
GCP16		-0.002	-0.011	0.032	0.328	14 / 14
GCP17		-0.000	-0.009	0.027	0.301	14 / 14
GCP18		0.003	-0.013	0.032	0.245	16 / 16
GCP19		0.005	-0.015	0.020	0.267	16 / 16
GCP20		0.002	-0.013	0.030	0.242	11 / 11
<b>Mean [m]</b>		0.004913	-0.007295	0.017894		
<b>Sigma [m]</b>		0.005716	0.005573	0.014264		
<b>RMS Error [m]</b>		0.007538	0.009180	0.022883		

**Table 137. Checkpoint RMSE for WingtraOne Based on Control Method.**

Control Method	RMSE X (m)	RMSE Y (m)	RMSE Z (m)
TxDOT Control	0.003	0.011	0.009
RTK GCPs	0.009	0.008	0.028

**Table 138. Pix4D SfM Checkpoint Error for Phantom 4 RTK (Daytime).**

Check Point Name	Accuracy XY/Z [m]	Error X [m]	Error Y [m]	Error Z [m]	Projection Error [pixel]	Verified/Marked
IP2		0.006	-0.008	0.023	0.297	36 / 36
IP3		0.006	-0.010	0.025	0.187	25 / 25
IP4		0.006	-0.012	0.027	0.309	31 / 31
IP1		0.010	-0.006	0.024	0.275	19 / 19
CK1		0.008	-0.011	0.024	0.247	18 / 18
CK8		0.005	-0.010	0.026	0.247	24 / 24
CK2		0.005	-0.006	0.021	0.203	22 / 22
CK3		0.006	-0.009	0.024	0.256	22 / 22
CK4		0.006	-0.009	0.027	0.215	27 / 27
CK5		0.001	-0.010	0.024	0.209	37 / 37
CK6		-0.001	-0.005	0.023	0.227	24 / 24
CK7		0.003	-0.011	0.023	0.356	32 / 32
GCP1		0.000	0.003	0.031	0.220	21 / 21
GCP2		0.007	0.004	0.031	0.164	16 / 16
GCP3		0.016	0.006	0.019	0.209	20 / 20
GCP4		0.016	0.003	0.016	0.222	23 / 23
GCP5		0.021	0.005	0.008	0.223	21 / 21
GCP6		0.006	-0.008	0.011	0.216	20 / 20
GCP7		0.009	-0.006	0.061	0.174	18 / 18
GCP8		0.016	-0.006	0.067	0.179	21 / 21
GCP9		0.007	-0.008	0.061	0.177	21 / 21
GCP10		0.017	-0.002	0.052	0.207	20 / 20
GCP11		0.012	-0.005	0.040	0.206	21 / 21
GCP12		0.021	-0.001	0.035	0.233	24 / 24
GCP13		0.010	-0.007	0.034	0.167	20 / 20
GCP14		0.006	-0.003	0.044	0.186	20 / 20
GCP15		-0.001	-0.007	0.046	0.144	17 / 17
GCP16		-0.001	-0.011	0.050	0.299	24 / 24
GCP17		0.002	-0.007	0.047	0.226	20 / 20
GCP18		0.003	-0.011	0.046	0.222	20 / 20
GCP19		0.008	-0.012	0.041	0.233	20 / 20
GCP20		0.006	-0.010	0.050	0.292	28 / 28
<b>Mean [m]</b>		0.007651	-0.005865	0.033780		
<b>Sigma [m]</b>		0.005875	0.005127	0.014783		
<b>RMS Error [m]</b>		0.009646	0.007790	0.036874		

**Table 139. Checkpoint RMSE for Phantom 4 RTK Based on Control Method (Daytime).**

Control Method	RMSE X (m)	RMSE Y (m)	RMSE Z (m)
TxDOT Control	0.006	0.009	0.024
RTK GCPs	0.011	0.007	0.043

**Table 140. Pix4D SfM Checkpoint Error for Phantom 4 RTK (Nighttime).**

Check Point Name	Accuracy XY/Z [m]	Error X [m]	Error Y [m]	Error Z [m]	Projection Error [pixel]	Verified/Marked
IP3		-0.007	0.005	-0.010	0.574	6 / 6
IP1		0.020	-0.007	0.007	0.706	21 / 21
CK8		0.007	-0.004	0.008	0.737	59 / 59
CK2		0.006	0.012	-0.004	0.772	21 / 21
CK3		-0.003	0.001	0.006	0.582	11 / 11
GCP2		0.004	-0.031	0.028	1.057	3 / 3
GCP3		0.029	-0.013	-0.002	0.629	5 / 5
GCP4		0.036	-0.021	-0.005	0.362	4 / 4
GCP6		0.023	-0.001	-0.019	1.190	27 / 27
GCP7		0.015	-0.006	0.042	0.656	51 / 51
GCP8		0.009	-0.014	0.053	0.858	29 / 29
GCP11		0.001	-0.007	0.021	0.808	42 / 42
GCP12		0.034	0.018	0.008	0.985	42 / 42
GCP13		0.016	0.021	-0.002	1.028	36 / 36
GCP14		-0.001	0.013	0.018	0.702	61 / 61
GCP15		-0.019	0.002	0.019	0.590	40 / 42
GCP17		-0.022	0.029	0.006	0.650	3 / 3
GCP18		-0.018	0.014	0.001	0.522	14 / 14
GCP19		-0.003	0.020	-0.003	0.800	11 / 11
GCP20		0.005	0.032	0.004	0.855	9 / 9
<b>Mean [m]</b>		0.006628	0.003075	0.008728		
<b>Sigma [m]</b>		0.016239	0.016257	0.016910		
<b>RMS Error [m]</b>		0.017540	0.016545	0.019030		

**Table 141. Checkpoint RMSE for Phantom 4 RTK Based on Control Method (Nighttime).**

Control Method	RMSE X (m)	RMSE Y (m)	RMSE Z (m)
TxDOT Control	0.010	0.007	0.007
RTK GCPs	0.019	0.019	0.022

Table 142 and Table 143 show GCP errors computed for the WingtraOne PPK and Phantom 4 RTK daytime flights, respectively, processed in Pix4D with the four TxDOT instrument point coordinates used as GCPs to reoptimize the SfM solution. These processing runs still used the PPK- and RTK-corrected image geotags. Table 144 compares the vertical RMSE with and without GCPs for the two respective flights. Checkpoint errors are computed using the TxDOT control points. GCP inclusion improved the vertical RMSE for both flights, reaching 0.3 cm (0.1 inches) for the WingtraOne PPK flight and 0.2 cm (0.08 inches) for the Phantom 4 RTK flight.

**Table 142. GCP Errors for WingtraOne PPK Processed in Pix4D.**

GCP Name	Accuracy XY/Z [m]	Error X[m]	Error Y[m]	Error Z[m]	Projection Error [pixel]	Verified/Marked
IP2 (3D)	0.020/ 0.020	-0.002	0.001	-0.000	0.482	18 / 18
IP3 (3D)	0.020/ 0.020	-0.000	-0.002	0.000	0.239	13 / 13
IP4 (3D)	0.020/ 0.020	-0.001	-0.003	0.000	0.323	13 / 13
IP1 (3D)	0.020/ 0.020	0.003	0.003	-0.000	0.351	19 / 19
<b>Mean [m]</b>		-0.000008	-0.000019	-0.000000		
<b>Sigma [m]</b>		0.001609	0.002435	0.000265		
<b>RMS Error [m]</b>		0.001609	0.002435	0.000265		

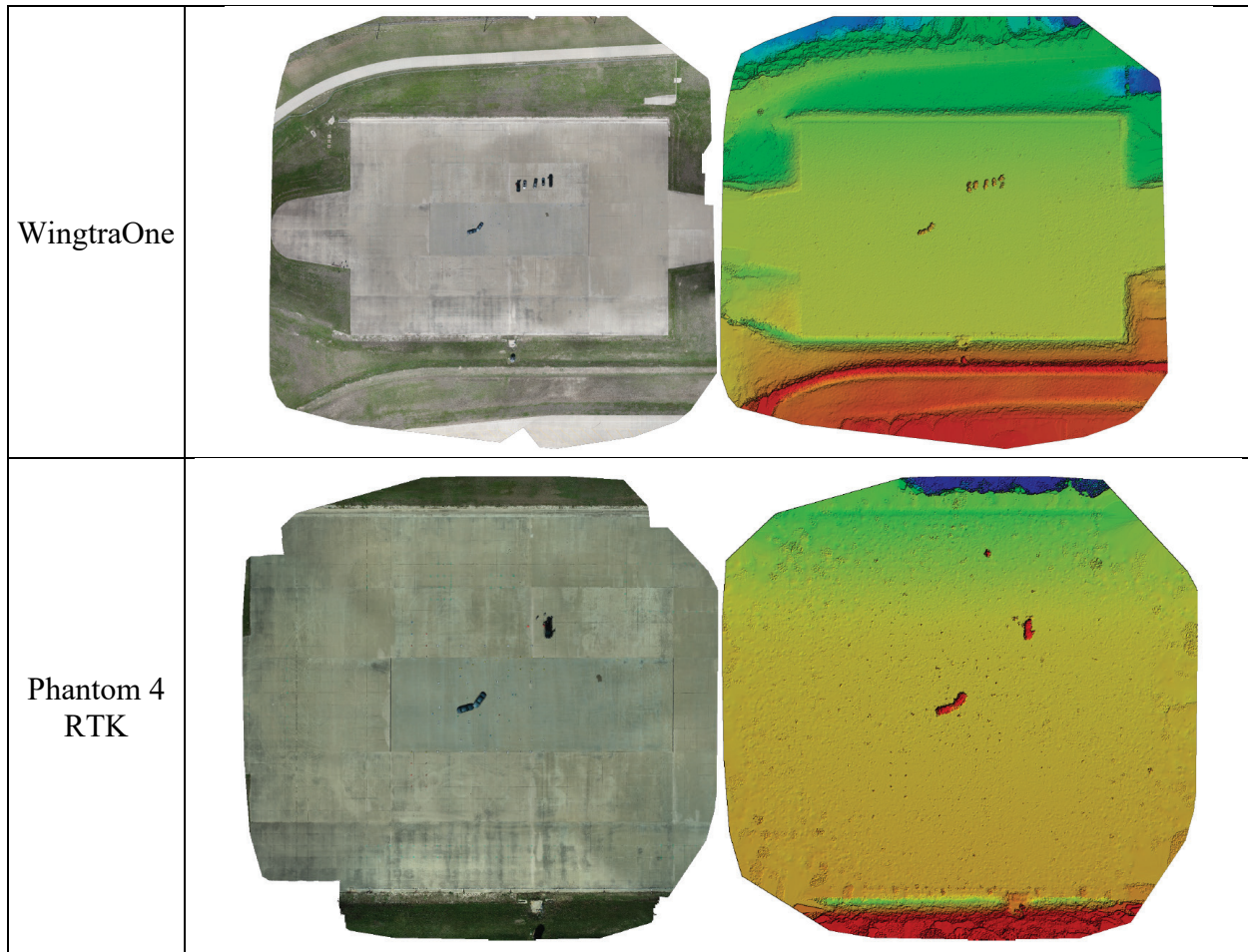
**Table 143. GCP Errors for Phantom 4 RTK Processed in Pix4D (Daytime).**

GCP Name	Accuracy XY/Z [m]	Error X[m]	Error Y[m]	Error Z[m]	Projection Error [pixel]	Verified/Marked
IP2 (3D)	0.020/ 0.020	-0.001	0.001	-0.002	0.297	36 / 36
IP3 (3D)	0.020/ 0.020	-0.001	-0.001	0.001	0.187	25 / 25
IP4 (3D)	0.020/ 0.020	-0.001	-0.003	0.002	0.309	31 / 31
IP1 (3D)	0.020/ 0.020	0.003	0.003	-0.001	0.274	19 / 19
<b>Mean [m]</b>		0.000002	0.000002	-0.000009		
<b>Sigma [m]</b>		0.001495	0.002108	0.001335		
<b>RMS Error [m]</b>		0.001495	0.002108	0.001335		

**Table 144. Vertical RMSE for TxDOT Checkpoints with and without GCPs.**

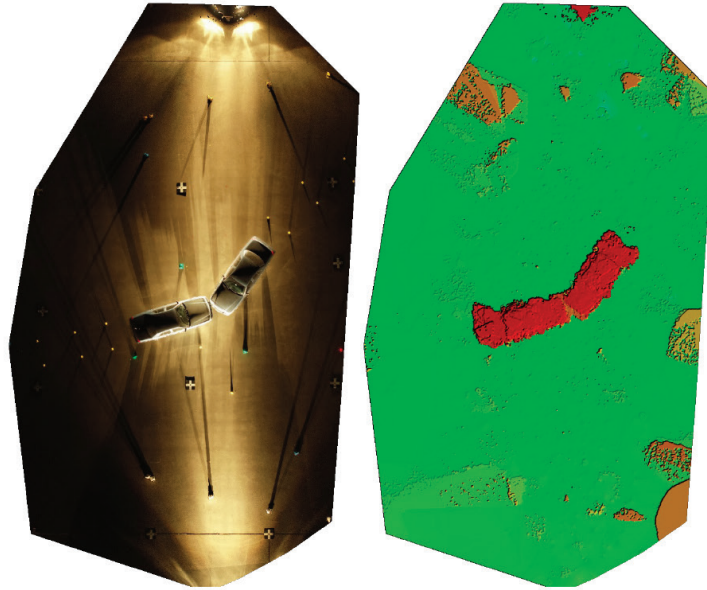
UAS	RMSE Z (m) without GCPs	RMSE Z (m) with GCPs
WingtraOne PPK	0.009	0.003
Phantom 4 RTK	0.024	0.002

For visualization of Pix4D mapping products, Figure 252 shows an orthomosaic and DSM created before densification from the WingtraOne PPK and Phantom 4 RTK daylight flights.

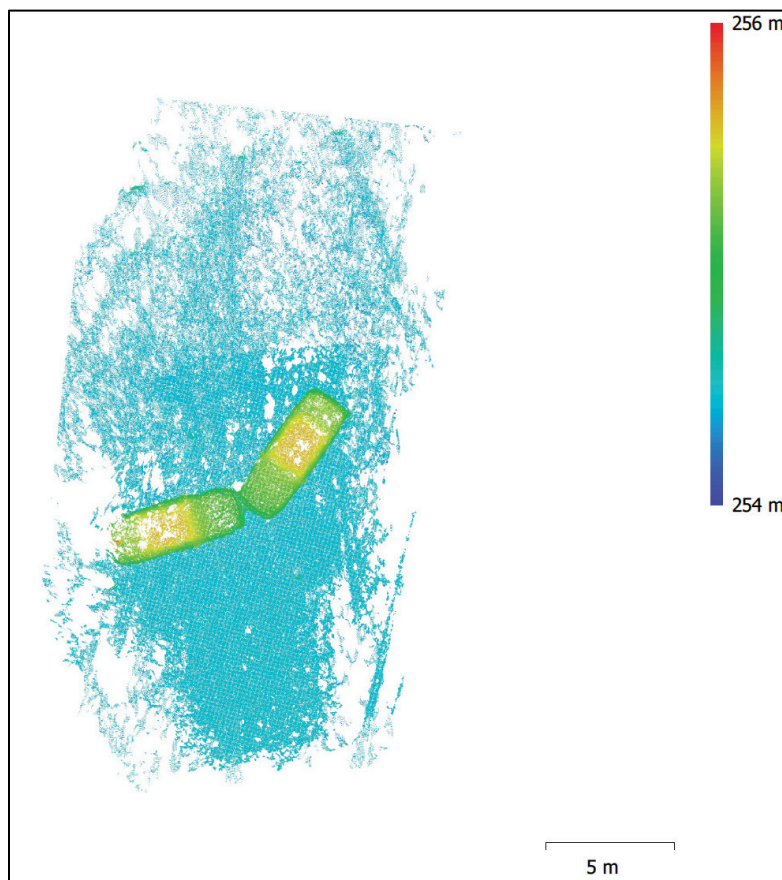


**Figure 252. Orthomosaics and DSMs from Pix4D Processing Report.**

Figure 253 shows an orthomosaic and DSM created from the Phantom 4 RTK nighttime flight processed in Pix4D. For comparison, Figure 254 shows an example DSM created from processing of the flight data in Metashape. Table 145 shows the checkpoint errors from the Metashape processing report.



**Figure 253. Phantom 4 RTK Orthomosaic and DSM from Pix4D Processing Report.**



**Figure 254. DSM from Metashape Processing Report for Phantom 4 RTK Night Flight.**

**Table 145. Checkpoint Errors from Metashape Report for Phantom 4 RTK Night Flight.**

<b>Label</b>	<b>X error (cm)</b>	<b>Y error (cm)</b>	<b>Z error (cm)</b>	<b>Total (cm)</b>	<b>Image (pix)</b>
IP3	0.186973	-1.38997	0.803778	1.61649	0.616 (8)
IP1	0.443965	0.709427	-1.87957	2.05747	1.111 (20)
CK8	0.792114	0.279545	-1.24567	1.50243	0.495 (8)
CK2	0.265715	-0.583436	-0.239758	0.68446	0.713 (8)
CK3	0.93248	-0.859733	0.0136508	1.2684	0.439 (5)
GCP2	1.21043	-3.65778	4.9517	6.27406	2.350 (3)
GCP3	1.69722	1.07662	-0.380596	2.04561	0.942 (4)
GCP4	0.925976	0.734014	1.14745	1.64707	0.911 (4)
GCP6	0.0143121	0.370418	-0.110633	0.386851	1.651 (13)
GCP7	0.561779	0.273626	-5.11501	5.15304	0.597 (34)
GCP8	0.948977	-0.21415	-5.27414	5.36311	0.809 (22)
GCP11	1.06413	-0.83587	-1.76416	2.22336	0.994 (37)
GCP12	-1.93211	-0.674561	-2.36019	3.12387	0.844 (18)
GCP13	-0.894725	-0.708861	-0.510029	1.25026	1.170 (29)
GCP14	0.448772	-1.28965	-1.77997	2.24341	0.586 (57)
GCP15	1.90747	-1.2148	-1.8112	2.89735	0.872 (39)
GCP17	0.293998	-1.38736	1.77122	2.26901	0.974 (3)
GCP18	0.61045	-1.19344	-0.308876	1.37562	0.807 (14)
GCP19	-0.320719	-0.792263	0.52008	1.00051	0.984 (9)
GCP20	-1.20801	-3.53867	-1.66699	4.09394	1.250 (4)
<b>Total</b>	<b>0.993634</b>	<b>1.41814</b>	<b>2.3177</b>	<b>2.89312</b>	<b>0.917</b>

## FIELD TESTING—TTI

This section focuses on an assessment of positional accuracies, distances (and their accuracies), and general lessons learned in connection with the use of UASs for crash reconstruction activities. The activities described in this section covered the use of the Mavic 2 Pro and Matrice 300 RTK UASs for the following tests: Test 2, Test 3, Test 4, Test 5, Test 6, and Test 7. For the analysis, the research team used GCPs and corresponding coordinate data, as described in the previous section.

For each test, the research team conducted several runs. For each run, the research team processed a variety of scenarios, including UAS flights under various conditions (e.g., UAS equipment, and time of day) and different ground control levels (i.e., standalone GNSS, onboard RTK, base station RTK, Google elevation data, and surveyed GCPs). For SfM processing, the research team used Pix4Dmapper 4.5.6. Table 146 provides a list of all the tests, runs, and scenarios completed. Table 147 provides a summary of results for each scenario, including image calibration percentages, number of keypoints per image, and absolute and relative geolocation errors. Table 148 shows deltas associated with the locations of five points for each scenario. Table 149 shows deltas associated with relative distances between these five points.





**Table 146. Tests, Runs, and Scenarios Completed.**

Date	Location	Run	Scenario	Equipment	Camera Resolution	Start Time	Georeferencing	Ground Control Points	Additional Light Source
8/25/2020	San Antonio	1	1a	Mavic 2 Pro	20 MP	8:30 AM	Standalone GNSS	None	
8/25/2020	San Antonio	1	1b	Mavic 2 Pro	20 MP	8:30 AM	Standalone GNSS	Google Elevation Data	
9/30/2020	RELLIS	1	1a	Mavic 2 Pro	20 MP	4:30 PM	Standalone GNSS	None	
9/30/2020	RELLIS	1	1b	Mavic 2 Pro	20 MP	4:30 PM	Standalone GNSS	Google Elevation Data	
9/30/2020	RELLIS	2	1a	Matrice 300 RTK	12 MP	3:11 PM	On-board RTK	None	
9/30/2020	RELLIS	2	1b	Matrice 300 RTK	12 MP	3:11 PM	On-board RTK	Google Elevation Data	
9/30/2020	RELLIS	2	1c	Matrice 300 RTK	12 MP and 20 MP (zoom)	3:11 PM	On-board RTK	None	
9/30/2020	RELLIS	2	1d	Matrice 300 RTK	12 MP and 20 MP (zoom)	3:11 PM	On-board RTK	Google Elevation Data	
9/30/2020	RELLIS	3	1a	Matrice 300 RTK	12 MP	2:45 PM	Base Station RTK	None	
9/30/2020	RELLIS	3	1b	Matrice 300 RTK	12 MP	2:45 PM	Base Station RTK	Google Elevation Data	
9/30/2020	RELLIS	3	1c	Matrice 300 RTK	12 MP and 20 MP (zoom)	2:45 PM	Base Station RTK	None	
9/30/2020	RELLIS	3	1d	Matrice 300 RTK	12 MP and 20 MP (zoom)	2:45 PM	Base Station RTK	Google Elevation Data	
10/7/2020	RELLIS	1	1a	Mavic 2 Pro	20 MP	5:23 PM	Standalone GNSS	None	
10/7/2020	RELLIS	1	1b	Mavic 2 Pro	20 MP	5:23 PM	Standalone GNSS	Google Elevation Data	
10/7/2020	RELLIS	1	1c	Mavic 2 Pro	20 MP	5:23 PM	Standalone GNSS	Surveyed	
10/7/2020	RELLIS	2	1a	Matrice 300 RTK	12 MP	4:00 PM	Standalone GNSS	None	
10/7/2020	RELLIS	2	1b	Matrice 300 RTK	12 MP	4:00 PM	Standalone GNSS	Google Elevation Data	
10/7/2020	RELLIS	2	1c	Matrice 300 RTK	12 MP	4:00 PM	Standalone GNSS	Surveyed	
10/7/2020	RELLIS	2	1d	Matrice 300 RTK	12 MP and 20 MP (zoom)	4:00 PM	Standalone GNSS	None	
10/7/2020	RELLIS	2	1e	Matrice 300 RTK	12 MP and 20 MP (zoom)	4:00 PM	Standalone GNSS	Google Elevation Data	
10/7/2020	RELLIS	2	1f	Matrice 300 RTK	12 MP and 20 MP (zoom)	4:00 PM	Standalone GNSS	Surveyed	
10/7/2020	RELLIS	3	1a	Matrice 300 RTK	12 MP	3:16 PM	On-board RTK	None	
10/7/2020	RELLIS	3	1b	Matrice 300 RTK	12 MP	3:16 PM	On-board RTK	Google Elevation Data	
10/7/2020	RELLIS	3	1c	Matrice 300 RTK	12 MP	3:16 PM	On-board RTK	Surveyed	
10/7/2020	RELLIS	3	1d	Matrice 300 RTK	12 MP and 20 MP (zoom)	3:16 PM	On-board RTK	None	
10/7/2020	RELLIS	3	1e	Matrice 300 RTK	12 MP and 20 MP (zoom)	3:16 PM	On-board RTK	Google Elevation Data	
10/7/2020	RELLIS	3	1f	Matrice 300 RTK	12 MP and 20 MP (zoom)	3:16 PM	On-board RTK	Surveyed	
10/7/2020	RELLIS	3	1g	Matrice 300 RTK	20 MP	3:16 PM	On-board RTK	None	
10/7/2020	RELLIS	3	1h	Matrice 300 RTK	20 MP	3:16 PM	On-board RTK	Google Elevation Data	
10/7/2020	RELLIS	3	1i	Matrice 300 RTK	20 MP	3:16 PM	On-board RTK	Surveyed	
12/7/2020	RELLIS	1	1a	Mavic 2 Pro	20 MP	7:05 PM	Standalone GNSS	None	Built-in LEDs
12/7/2020	RELLIS	1	1b	Mavic 2 Pro	20 MP	7:05 PM	Standalone GNSS	Google Elevation Data	Built-in LEDs
12/7/2020	RELLIS	1	1c	Mavic 2 Pro	20 MP	7:05 PM	Standalone GNSS	Surveyed	Built-in LEDs
12/7/2020	RELLIS	2	1a	Matrice 300 RTK	12 MP	5:15 PM	On-board RTK	None	
12/7/2020	RELLIS	2	1b	Matrice 300 RTK	12 MP	5:15 PM	On-board RTK	Surveyed	
12/7/2020	RELLIS	2	1c	Matrice 300 RTK	12 MP and 20 MP (zoom)	5:15 PM	On-board RTK	None	
12/7/2020	RELLIS	2	1d	Matrice 300 RTK	12 MP and 20 MP (zoom)	5:15 PM	On-board RTK	Surveyed	
12/7/2020	RELLIS	3	1a	Matrice 300 RTK	12 MP	7:25 PM	On-board RTK	None	Built-in LEDs
12/7/2020	RELLIS	3	1b	Matrice 300 RTK	12 MP	7:25 PM	On-board RTK	Surveyed	Built-in LEDs
12/7/2020	RELLIS	3	1c	Matrice 300 RTK	12 MP and 20 MP (zoom)	7:25 PM	On-board RTK	None	Built-in LEDs
12/7/2020	RELLIS	3	1d	Matrice 300 RTK	12 MP and 20 MP (zoom)	7:25 PM	On-board RTK	Surveyed	Built-in LEDs

**Table 146. Tests, Runs, and Scenarios Completed (Continued).**

Date	Location	Run	Scenario	Equipment	Camera Resolution	Start Time	Georeferencing	Ground Control Points	Additional Light Source
12/7/2020	RELLIS	4	1a	Matrice 300 RTK	12 MP	7:50 PM	On-board RTK	None	Built-in LEDs and Spotlight
12/7/2020	RELLIS	4	1b	Matrice 300 RTK	12 MP	7:50 PM	On-board RTK	Surveyed	Built-in LEDs and Spotlight
12/7/2020	RELLIS	4	1c	Matrice 300 RTK	12 MP and 20 MP (zoom)	7:50 PM	On-board RTK	None	Built-in LEDs and Spotlight
12/7/2020	RELLIS	4	1d	Matrice 300 RTK	12 MP and 20 MP (zoom)	7:50 PM	On-board RTK	Surveyed	Built-in LEDs and Spotlight
1/15/2021	Florence	1	1a	Mavic 2 Pro	20 MP	8:15 PM	Standalone GNSS	None	Built-in LEDs
1/15/2021	Florence	1	1b	Mavic 2 Pro	20 MP	8:15 PM	Standalone GNSS	Google Elevation Data	Built-in LEDs
1/15/2021	Florence	1	1c	Mavic 2 Pro	20 MP	8:15 PM	Standalone GNSS	Surveyed	Built-in LEDs
1/15/2021	Florence	2	1a	Mavic 2 Pro	20 MP	9:20 PM	Standalone GNSS	None	Built-in LEDs and Tower Lights
1/15/2021	Florence	2	1b	Mavic 2 Pro	20 MP	9:20 PM	Standalone GNSS	Google Elevation Data	Built-in LEDs and Tower Lights
1/15/2021	Florence	2	1c	Mavic 2 Pro	20 MP	9:20 PM	Standalone GNSS	Surveyed	Built-in LEDs and Tower Lights
1/15/2021	Florence	3	1a	Matrice 300 RTK	12 MP and 20 MP (zoom)	5:30 PM	Base Station RTK	None	
1/15/2021	Florence	3	1b	Matrice 300 RTK	12 MP and 20 MP (zoom)	5:30 PM	Base Station RTK	Surveyed	
1/15/2021	Florence	4	1a	Matrice 300 RTK	12 MP and 20 MP (zoom)	5:45 PM	On-board RTK	None	
1/15/2021	Florence	4	1b	Matrice 300 RTK	12 MP and 20 MP (zoom)	5:45 PM	On-board RTK	Surveyed	
1/15/2021	Florence	5	1a	Matrice 300 RTK	12 MP and 20 MP (zoom)	6:45 PM	Base Station RTK	None	Built-in LEDs
1/15/2021	Florence	5	1b	Matrice 300 RTK	12 MP and 20 MP (zoom)	6:45 PM	Base Station RTK	Surveyed	Built-in LEDs
1/15/2021	Florence	6	1a	Matrice 300 RTK	12 MP and 20 MP (zoom)	7:30 PM	On-board RTK	None	Built-in LEDs
1/15/2021	Florence	6	1b	Matrice 300 RTK	12 MP and 20 MP (zoom)	7:30 PM	On-board RTK	Surveyed	Built-in LEDs
3/20/2021	Florence	1	1a	Mavic 2 Pro	20 MP	11:00 AM	Standalone GNSS	None	
3/20/2021	Florence	1	1b	Mavic 2 Pro	20 MP	11:00 AM	Standalone GNSS	Surveyed TAMUCC	
3/20/2021	Florence	1	1c	Mavic 2 Pro	20 MP	11:00 AM	Standalone GNSS	Surveyed TxDOT	
3/20/2021	Florence	1	1d	Mavic 2 Pro	20 MP	11:00 AM	Standalone GNSS	Google Elevation Data	
3/20/2021	Florence	2	1a	Mavic 2 Pro	20 MP	8:20 PM	Standalone GNSS	None	Built-in LEDs
3/20/2021	Florence	2	1b	Mavic 2 Pro	20 MP	8:20 PM	Standalone GNSS	Surveyed TAMUCC	Built-in LEDs
3/20/2021	Florence	2	1c	Mavic 2 Pro	20 MP	8:20 PM	Standalone GNSS	Surveyed TxDOT	Built-in LEDs
3/20/2021	Florence	3	1a	Matrice 300 RTK	12 MP and 20 MP (zoom)	4:00 PM	Standalone GNSS	None	
3/20/2021	Florence	3	1b	Matrice 300 RTK	12 MP and 20 MP (zoom)	4:00 PM	Standalone GNSS	Surveyed TAMUCC	
3/20/2021	Florence	3	1c	Matrice 300 RTK	12 MP and 20 MP (zoom)	4:00 PM	Standalone GNSS	Surveyed TxDOT	
3/20/2021	Florence	4	1a	Matrice 300 RTK	12 MP and 20 MP (zoom)	3:45 PM	Standalone GNSS	None	
3/20/2021	Florence	4	1b	Matrice 300 RTK	12 MP and 20 MP (zoom)	3:45 PM	Standalone GNSS	None	
3/20/2021	Florence	5	1a	Matrice 300 RTK	12 MP and 20 MP (zoom)	12:55 PM	Base Station RTK	None	
3/20/2021	Florence	5	1b	Matrice 300 RTK	12 MP and 20 MP (zoom)	12:55 PM	Base Station RTK	Surveyed TAMUCC	
3/20/2021	Florence	5	1c	Matrice 300 RTK	12 MP and 20 MP (zoom)	12:55 PM	Base Station RTK	Surveyed TxDOT	
3/20/2021	Florence	6	1a	Matrice 300 RTK	12 MP and 20 MP (zoom)	1:25 PM	On-board RTK	None	
3/20/2021	Florence	6	1b	Matrice 300 RTK	12 MP and 20 MP (zoom)	1:25 PM	On-board RTK	Surveyed TAMUCC	
3/20/2021	Florence	6	1c	Matrice 300 RTK	12 MP and 20 MP (zoom)	1:25 PM	On-board RTK	Surveyed TxDOT	
3/20/2021	Florence	6	1d	Matrice 300 RTK	12 MP and 20 MP (zoom)	1:25 PM	On-board RTK	Surveyed TxDOT(ft)	
3/20/2021	Florence	6	1e	Matrice 300 RTK	12 MP and 20 MP (zoom)	1:25 PM	On-board RTK	Surveyed TxDOT(ft)	
3/20/2021	Florence	7	1a	Matrice 300 RTK	12 MP and 20 MP (zoom)	9:15 PM	On-board RTK	None	Built-in LEDs and Spotlight
3/20/2021	Florence	7	1b	Matrice 300 RTK	12 MP and 20 MP (zoom)	9:15 PM	On-board RTK	Surveyed TAMUCC	Built-in LEDs and Spotlight
3/20/2021	Florence	7	1c	Matrice 300 RTK	12 MP and 20 MP (zoom)	9:15 PM	On-board RTK	Surveyed TxDOT	Built-in LEDs and Spotlight

Table 147. Summary of Results for Each Scenario.

Date	Location	Run	Scenario	Average GSD (mm)	Total Images	Calibrated Images	Calibration (%)	Initial vs. Optimized Internal Camera Parameters	2D Keypoints for BA	3D Points for BA	Mean RMS Error for GCPs (m)	GCP RMS Error X,Y,Z (m)	Absolute Geolocation RMS Error X,Y,Z (m)	3D Densified Points	Average Density (per m3)	Total Time (min)
8/25/2020	San Antonio	1	1a	3	66	65	98%	3.27%	630,054	221,437	n.d.	n.d	0.223, 0.356, 0.656	5,869,328	151,330	43.30
8/25/2020	San Antonio	1	1b	3	66	65	98%	3.27%	630,035	221,435	0.056	-0.053, 0.064, -0.000	0.876, 1.157, 33.154	5,873,767	150,512	37.53
9/30/2020	RELLIS	1	1a	6.8	89	89	100%	1.81%	2,232,769	697,022	n.d.	n.d	0.294, 0.398, 2.239	13,554,908	10,264	55.05
9/30/2020	RELLIS	1	1b	6.8	89	89	100%	1.81%	2,232,764	697,019	0.124	0.253, 0.153, 0.053	1.085, 2.407, 33.308	13,547,678	10,239	67.68
9/30/2020	RELLIS	2	1a	11.6	82	82	100%	6.65%	1,145,146	369,820	n.d.	n.d.	0.236, 0.215, 0.525	6,569,292	3,039	29.42
9/30/2020	RELLIS	2	1b	11.6	82	82	100%	6.65%	1,145,130	369,817	0.059	0.112, 0.110, 0.014	0.318, 1.277, 56.847	6,562,376	3,027	48.92
9/30/2020	RELLIS	2	1c	6.2	164	136	82%	8.19%	1,574,816	551,901	n.d.	n.d.	0.604, 0.591, 2.582	6,717,016	6,247	47.03
9/30/2020	RELLIS	2	1d	6.3	164	136	82%	7.95%	1,577,008	552,578	0.075	0.202, 0.105, 0.009	0.500, 1.477, 58.268	6,723,159	6,155	91.95
9/30/2020	RELLIS	3	1a	12.2	79	79	100%	6.02%	1,078,500	361,532	n.d.	n.d.	0.224, 0.495, 1.084	6,316,276	2,736	30.08
9/30/2020	RELLIS	3	1b	12.2	79	79	100%	6.02%	1,078,582	361,489	0.115	0.082, 0.190, 0.144	0.860, 1.058, 25.073	6,315,326	2,750	48.67
9/30/2020	RELLIS	3	1c	5.6	158	132	83%	5.43%	1,437,602	513,699	n.d.	n.d.	0.371, 0.713, 1.179	7,548,401	7,855	62.57
9/30/2020	RELLIS	3	1d	5.6	158	132	83%	5.66%	1,442,105	515,446	0.147	0.074, 0.108, 0.345	0.984, 1.246, 25.134	6,805,443	7,013	88.22
10/7/2020	RELLIS	1	1a	7.86	80	80	100%	3.99%	1,682,213	477,295	n.d.	n.d	0.300, 0.869, 2.145	10,269,808	4,619	26.22
10/7/2020	RELLIS	1	1b	7.9	80	80	100%	3.42%	1,683,971	478,049	0.099	0.151, 0.145, 0.018	1.324, 2.722, 34.334	10,276,440	4,622	27.33
10/7/2020	RELLIS	1	1c	7.9	80	80	100%	3.16%	1,683,277	477,810	0.015	0.007, 0.013, 0.027	0.446, 3.367, 7.915	10,252,130	4,595	28.08
10/7/2020	RELLIS	2	1a	10.6	74	74	100%	6.73%	855,858	274,278	n.d.	n.d	0.462, 0.562, 1.532	5,394,527	1,883	14.20
10/7/2020	RELLIS	2	1b	10.6	74	74	100%	6.75%	856,598	274,277	0.183	0.254, 0.335, 0.000	0.482, 0.731, 30.901	5,391,931	1,875	15.25
10/7/2020	RELLIS	2	1c	10.1	74	74	100%	6.95%	855,863	274,158	0.053	0.020, 0.024, 0.134	1.263, 1.316, 32.349	5,395,228	1,820	16.08
10/7/2020	RELLIS	2	1d	8.7	148	148	100%	5.05%	2,249,924	708,508	n.d.	n.d.	1.013, 1.469, 3.293	12,595,708	5,320	30.17
10/7/2020	RELLIS	2	1e	8.6	148	148	100%	4.97%	2,249,115	708,121	0.181	1.489, 0.359, 0.002	1.722, 0.869, 30.881	12,598,157	5,450	38.57
10/7/2020	RELLIS	2	1f	8.7	148	148	100%	5.09%	2,248,561	708,004	0.044	0.015, 0.018, 0.118	1.219, 1.371, 1.760	12,575,635	5,279	35.78
10/7/2020	RELLIS	3	1a	9.0	99	99	100%	6.04%	1,110,197	343,181	n.a	n.a.	0.136, 0.143, 1.014	7,447,350	3,529	18.82
10/7/2020	RELLIS	3	1b	9.0	99	99	100%	6.06%	1,109,724	343,123	0.072	0.071, 0.042, 0.130	0.932, 0.471, 1.752	7,457,780	3,525	17.15
10/7/2020	RELLIS	3	1c	9.0	99	99	100%	6.13%	1,115,902	338,670	0.041	0.028, 0.019, 0.082	0.167, 0.143, 1.070	7,506,196	3,498	16.67
10/7/2020	RELLIS	3	1d	7.3	198	198	100%	4.44%	3,155,313	975,329	n.a	n.a.	0.136, 0.149, 1.015	22,581,532	13,263	42.72
10/7/2020	RELLIS	3	1e	7.3	198	198	100%	4.44%	3,125,107	981,564	0.047	0.056, 0.054, 0.059	0.933, 0.471, 1.854	22,479,335	13,175	43.73
10/7/2020	RELLIS	3	1f	7.3	198	198	100%	4.52%	3,168,068	980,829	0.035	0.025, 0.024, 0.061	0.172, 0.149, 1.083	22,713,457	13,190	43.53
10/7/2020	RELLIS	3	1g	3.7	99	99	100%	2.82%	1,947,950	689,888	n.a	n.a.	0.153, 0.153, 1.194	16,106,257	44,852	40.57
10/7/2020	RELLIS	3	1h	3.7	99	99	100%	2.95%	1,990,656	704,916	0.099	0.058, 0.066, 0.186	0.900, 0.513, 1.717	16,895,743	41,675	39.28
10/7/2020	RELLIS	3	1i	3.7	99	99	100%	2.99%	1,920,120	689,803	0.023	0.015, 0.017, 0.040	0.149, 0.169, 1.085	16,999,826	41,514	37.72
12/7/2020	RELLIS	1	1a	2.4	175	175	100%	3.16%	405,879	146,728	n.a.	n.a.	0.282, 0.316, 0.539	3,656,452	174,577	32.28
12/7/2020	RELLIS	1	1b													
12/7/2020	RELLIS	1	1c													
12/7/2020	RELLIS	2	1a	8.7	85	85	100%	6.24%	853,788	320,675	n.a.	n.a.	0.341, 0.146, 0.588	5,396,681	5,343	21.62
12/7/2020	RELLIS	2	1b	8.6	85	85	100%	6.40%	846,903	319,353	0.036	0.043, 0.019, 0.047	0.336, 0.189, 0.586	5,377,303	5,329	17.62
12/7/2020	RELLIS	2	1c	5.5	170	136	80%	5.02%	1,239,811	474,889	n.a.	n.a.	0.416, 0.321, 0.533	6,606,186	10,800	44.25
12/7/2020	RELLIS	2	1d	5.5	170	163	95%	5.04%	1,211,757	467,432	0.038	0.082, 0.019, 0.028	0.351, 0.241, 0.794	8,097,860	11,043	28.55
12/7/2020	RELLIS	3	1a	4.7	86	74	86%	5.07%	39,613	16,953	n.a.	n.a.	0.019, 0.025, 0.041	90,460	24,140	5.58
12/7/2020	RELLIS	3	1b	5.1	86	82	95%	2.43%	20,396	9,687	0.040	n.a.	0.227, 0.101, 0.701	6,187	22,465	3.40
12/7/2020	RELLIS	3	1c	3.9	172	98	56%	89.89%	51,002	22,835	n.a.	n.a.	0.014, 0.018, 0.042	91,626	36,886	12.55
12/7/2020	RELLIS	3	1d	4.1	172	135	78%	1.86%	66,216	30,248	0.066	n.a.	0.168, 0.150, 0.773	193,255	26,280	n.a.

**Table 147. Summary of Results for Each Scenario (Continued).**

Date	Location	Run	Scenario	Average GSD (mm)	Total Images	Calibrated Images	Calibration (%)	Initial vs. Optimized Internal Camera Parameters	2D Keypoints for BA	3D Points for BA	Mean RMS Error for GCPs (m)	GCP RMS Error X,Y,Z (m)	Absolute Geolocation RMS Error X,Y,Z (m)	3D Densified Points	Average Density (per m3)	Total Time (min)
12/7/2020	RELLIS	4	1a	5.8	62	34	54%	4.49%	33,523	14,163	n.a.	n.a.	0.011, 0.012, 0.022	194,768	14,055	3.03
12/7/2020	RELLIS	4	1b													
12/7/2020	RELLIS	4	1c	4.8	126	52	41%	4.45%	256,157	101,973	n.a.	n.a.	0.010, 0.010, 0.019	1,118,644	93,205	11.18
12/7/2020	RELLIS	4	1d													
1/15/2021	Florence	1	1a	2.0	332	326	98%	3.48%	1,036,760	402,809	n.a.	n.a.	0.419, 0.265, 0.572	10,575,461	453,202	61.95
1/15/2021	Florence	1	1b													
1/15/2021	Florence	1	1c	2.0	332	326	98%	3.45%	949,873	361,936	0.009	0.010, 0.006, 0.014	0.984, 1.428, 9.053	10,598,858	445,316	126.27
1/15/2021	Florence	2	1a	2.2	343	343	100%	2.84%	5,559,319	1,971,998	n.a.	n.a.	0.785, 0.337, 0.633	31,107,669	413,423	119.32
1/15/2021	Florence	2	1b	2.2	343	343	100%	2.84%	5,555,271	1,970,577	0.149	0.932, 0.899, 0.154	0.803, 1.357, 7.484	31,087,370	414,906	130.03
1/15/2021	Florence	2	1c	2.2	343	343	100%	2.84%	5,558,805	1,971,680	0.003	0.006, 0.003, 0.002	2.078, 1.439, 9.510	30,729,631	422,769	160.02
1/15/2021	Florence	3	1a	7.8	190	190	100%	4.35%	3,514,121	1,116,328	n.a.	n.a.	0.074, 0.049, 0.362	15,727,505	9,485	65.55
1/15/2021	Florence	3	1b	7.8	190	190	100%	4.41%	3,445,424	1,091,974	0.023	0.013, 0.037, 0.030	0.078, 0.053, 0.356	15,965,133	9,670	45.18
1/15/2021	Florence	4	1a	7.6	164	164	100%	4.62%	2,792,727	905,998	n.a.	n.a.	0.745, 0.229, 1.572	13,925,477	9,355	62.68
1/15/2021	Florence	4	1b	7.6	164	164	100%	4.58%	2,716,842	878,850	0.037	0.009, 0.009, 0.102	0.508, 0.473, 1.280	14,084,914	9,190	42.60
1/15/2021	Florence	5	1a	3.9	726	395	54%	155.79%	88,668	31,488	n.a.	n.a.	0.019, 0.016, 0.088	67,528	25,994	57.28
1/15/2021	Florence	5	1b													
1/15/2021	Florence	6	1a	3.1	640	352	55%	10.80%	133,887	49,103	n.a.	n.a.	0.022, 0.025, 0.229	1,319,785	250,962	43.27
1/15/2021	Florence	6	1b													
3/20/2021	Florence	1	1a	5.7	75	75	100%	2.83%	556,372	161,356	n.a.	n.a.	3.810, 1.996, 5.315	3,818,649	7,164	21.47
3/20/2021	Florence	1	1b	7.0	75	75	100%	2.58%	544,643	157,252	0.013	0.008, 0.005, 0.030	4.558, 2.190, 6.792	3,855,037	3,758	27.70
3/20/2021	Florence	1	1c	7.0	75	75	100%	2.71%	550,225	159,208	0.007	0.006, 0.004, 0.014	4.507, 2.258, 6.735	3,853,493	3,808	25.52
3/20/2021	Florence	1	1d	7.0	75	75	100%	2.85%	554,172	161,475	0.024	0.047, 0.023, 0.008	5.669, 1.746, 4.825	3,848,587	3,837	23.72
3/20/2021	Florence	2	1a	3.1	297	284	95%	0.42%	151,286	63,148	0.001	n.a.	0.448, 0.541, 0.661	1,816,314	398	n.a.
3/20/2021	Florence	2	1b	4.2	297	284	95%	0.42%	151,286	63,148	0.001	0.001, 0.002, 0.000	0.448, 0.541, 0.661	1,796,430	13,958	n.a.
3/20/2021	Florence	2	1c	3.1	297	284	95%	0.42%	151,286	63,148	0.001	0.001, 0.002, 0.000	0.448, 0.541, 0.661	1,796,104	14,056	n.a.
3/20/2021	Florence	3	1a	7.2	132	132	100%	4.95%	797,464	253,831	n.a.	n.a.	0.208, 0.221, 0.546	3,786,807	3,416	31.12
3/20/2021	Florence	3	1b	7.3	132	132	100%	4.93%	797,665	253,902	0.020	0.013, 0.008, 0.047	0.467, 1.154, 3.815	3,788,322	3,363	34.30
3/20/2021	Florence	3	1c	7.3	132	132	100%	4.94%	797,530	253,917	0.012	0.004, 0.009, 0.026	0.466, 1.145, 3.848	3,784,433	3,374	37.77
3/20/2021	Florence	4	1a	6.3	296	295	99%	92.33%	2,483,973	694,766	n.a.	n.a.	0.985, 1.311, 0.454	3,221,580	3,255	79.52
3/20/2021	Florence	4	1b	6.0	348	346	99%	3.19%	2,495,363	707,229	n.a.	n.a.	0.722, 0.364, 1.103	7,111,394	3,755	83.20
3/20/2021	Florence	5	1a	7.2	136	136	100%	4.58%	789,659	250,648	n.a.	n.a.	0.018, 0.015, 0.032	3,441,712	3,114	26.27
3/20/2021	Florence	5	1b	7.2	136	136	100%	4.56%	765,498	243,647	0.032	0.027, 0.023, 0.050	0.073, 0.061, 0.145	10,905,719	4,562	n.a.
3/20/2021	Florence	5	1c	7.2	136	136	100%	4.71%	767,372	244,160	0.028	0.020, 0.031, 0.035	0.076, 0.057, 0.165	10,877,958	4,603	64.65
3/20/2021	Florence	6	1a	7.2	134	134	100%	4.43%	794,646	252,256	n.a.	n.a.	0.028, 0.028, 0.046	3,432,680	3,142	21.40
3/20/2021	Florence	6	1b	7.2	134	134	100%	4.43%	803,628	254,157	0.024	0.024, 0.016, 0.036	0.123, 0.040, 0.170	11,036,359	4,568	63.63
3/20/2021	Florence	6	1c	7.2	134	134	100%	4.50%	803,150	254,191	0.019	0.016, 0.019, 0.035	0.123, 0.039, 0.183	10,998,375	4,589	62.02
3/20/2021	Florence	6	1d	7.2	134	134	100%	4.50%	808,591	253,734	0.028	0.009, 0.020, 0.057	0.136, 0.044, 26.123	3,565,060	91	23.33
3/20/2021	Florence	6	1e	7.2	134	134	100%	4.29%	802,478	252,928	0.026	0.008, 0.018, 0.054	0.190, 0.040, 0.232	3,713,546	3,350	24.67
3/20/2021	Florence	7	1a	2.4	1108	119	10%	18.08%	5,007	1,982	n.a.	n.a.	10.741, 13.170, 0.709	1,983	69,140	36.02
3/20/2021	Florence	7	1b													
3/20/2021	Florence	7	1c													

**Table 148. Deltas Associated with the Location of Five Points for Each Scenario.**

Date	Location	Run	Scenario	P1 Ref. Delta XY (m)	P1 Ref. Delta Z (m)	P1 Ref. Delta (m)	P2 Ref. Delta XY (m)	P2 Ref. Delta Z (m)	P2 Ref. Delta (m)	P3 Ref. Delta XY (m)	P3 Ref. Delta Z (m)	P3 Ref. Delta (m)	P4 Ref. Delta XY (m)	P4 Ref. Delta Z (m)	P4 Ref. Delta (m)	P5 Ref. Delta XY (m)	P5 Ref. Delta Z (m)	P5 Ref. Delta (m)
8/25/2020	San Antonio	1	1a	1.279	-6.837	6.956	1.287	-6.955	7.073	1.296	-7.156	7.272	1.291	-7.228	7.342	1.290	-6.398	6.527
8/25/2020	San Antonio	1	1b	0.000	0.000	0.000	0.000	0.000	0.000	0.000	0.000	0.000	0.000	0.000	0.000	0.000	0.000	0.000
9/30/2020	RELLIS	1	1a	1.111	-6.201	6.300	1.129	-5.263	5.383	0.897	-5.592	5.664	0.917	-5.170	5.251	1.000	-4.462	4.573
9/30/2020	RELLIS	1	1b	0.178	-0.170	0.246	0.336	-0.130	0.361	0.283	-0.078	0.294	0.210	-0.105	0.234	0.483	-0.003	0.483
9/30/2020	RELLIS	2	1a	0.287	-29.564	29.565	0.273	-29.008	29.009	0.265	-29.162	29.163	0.266	-28.886	28.887	0.267	-28.509	28.510
9/30/2020	RELLIS	2	1b	0.000	0.000	0.000	0.000	0.000	0.000	0.000	0.000	0.000	0.000	0.000	0.000	0.000	0.000	0.000
9/30/2020	RELLIS	2	1c	0.712	-30.746	30.754	1.023	-30.504	30.521	0.659	-30.348	30.355	0.838	-30.223	30.235	1.086	-30.117	30.137
9/30/2020	RELLIS	2	1d	0.038	-0.021	0.044	0.134	0.030	0.137	0.061	0.044	0.075	0.059	0.066	0.089	0.168	0.103	0.197
9/30/2020	RELLIS	3	1a	0.900	1.240	1.532	1.074	1.811	2.106	0.874	1.720	1.929	0.954	1.955	2.175	1.089	2.371	2.609
9/30/2020	RELLIS	3	1b	0.109	-0.655	0.664	0.093	-0.093	0.132	0.125	-0.175	0.215	0.065	0.058	0.087	0.138	0.496	0.515
9/30/2020	RELLIS	3	1c	0.935	1.239	1.552	0.977	1.610	1.883	0.908	1.679	1.909	0.918	1.956	2.161	0.957	2.382	2.567
9/30/2020	RELLIS	3	1d	0.087	-0.750	0.755	0.289	0.469	0.551	0.111	-0.192	0.222	0.070	0.093	0.117	0.105	0.528	0.538
10/7/2020	RELLIS	1	1a							1.828	-7.736	7.949				1.723	-8.711	8.880
10/7/2020	RELLIS	1	1b	0.812	26.399	26.411	1.024	26.491	26.511	0.998	26.463	26.482	0.893	26.476	26.491	0.835	26.451	26.464
10/7/2020	RELLIS	1	1c	0.044	0.052	0.068	0.028	-0.061	0.067	0.011	-0.037	0.039	0.023	-0.034	0.041	0.023	-0.003	0.023
10/7/2020	RELLIS	2	1a							1.410	-31.750	31.781				1.216	-31.829	31.852
10/7/2020	RELLIS	2	1b	0.787	-0.930	1.219	1.138	-0.981	1.503	1.060	-0.940	1.417	0.949	-0.936	1.333	0.899	-0.899	1.271
10/7/2020	RELLIS	2	1c	0.007	0.156	0.156	0.024	-0.031	0.039	0.019	-0.001	0.019	0.012	0.073	0.074	0.006	0.085	0.085
10/7/2020	RELLIS	2	1d							2.114	-29.413	29.489				2.119	-29.719	29.794
10/7/2020	RELLIS	2	1e	1.011	-1.127	1.514	0.989	-1.064	1.453	0.952	-1.077	1.437	0.855	-1.063	1.364	0.817	-1.111	1.379
10/7/2020	RELLIS	2	1f	0.005	0.114	0.114	0.029	-0.066	0.072	0.005	-0.046	0.046	0.006	-0.005	0.008	0.003	0.014	0.014
10/7/2020	RELLIS	3	1a	0.040	0.227	0.231	0.090	0.149	0.174	0.057	0.158	0.168	0.034	0.133	0.137	0.027	0.165	0.167
10/7/2020	RELLIS	3	1b	0.955	-0.841	1.273	0.934	-0.904	1.300	0.962	-0.888	1.309	0.967	-0.904	1.323	0.965	-0.889	1.312
10/7/2020	RELLIS	3	1c	0.006	0.104	0.104	0.023	0.016	0.028	0.006	0.043	0.043	0.013	0.016	0.021	0.017	0.057	0.059
10/7/2020	RELLIS	3	1d	0.032	0.102	0.107	0.086	0.146	0.169	0.064	0.144	0.158	0.042	0.140	0.146	0.033	0.139	0.143
10/7/2020	RELLIS	3	1e	0.965	-1.099	1.463	0.966	-0.973	1.371	0.957	-1.013	1.394	0.971	-1.037	1.421	0.973	-1.036	1.421
10/7/2020	RELLIS	3	1f	0.017	-0.039	0.043	0.010	0.007	0.012	0.005	0.012	0.013	0.011	0.000	0.011	0.015	0.005	0.015
10/7/2020	RELLIS	3	1g	0.071	0.034	0.079	0.074	0.235	0.246	0.067	0.216	0.226	0.072	0.200	0.213	0.079	0.189	0.205
10/7/2020	RELLIS	3	1h	0.996	-0.925	1.359	0.945	-0.877	1.290	0.964	-0.889	1.311	0.987	-0.921	1.350	0.999	-0.931	1.366
10/7/2020	RELLIS	3	1i	0.000	0.000	0.000	0.000	0.000	0.000	0.000	0.000	0.000	0.000	0.000	0.000	0.000	0.000	0.000
12/7/2020	RELLIS	1	1a															
12/7/2020	RELLIS	1	1b															
12/7/2020	RELLIS	1	1c															
12/7/2020	RELLIS	2	1a	0.113	-0.046	0.122	0.086	0.030	0.091	0.075	-0.043	0.087	0.025	-0.030	0.039	0.141	0.066	0.156
12/7/2020	RELLIS	2	1b	0.000	0.000	0.000	0.000	0.000	0.000	0.000	0.000	0.000	0.000	0.000	0.000	0.000	0.000	0.000
12/7/2020	RELLIS	2	1c	0.114	-0.066	0.132	0.056	0.046	0.072	0.085	-0.040	0.094	0.031	0.012	0.033	0.155	0.145	0.213
12/7/2020	RELLIS	2	1d	0.013	-0.023	0.027	0.039	0.069	0.079	0.041	0.047	0.062	0.034	0.001	0.034	0.058	0.085	0.103
12/7/2020	RELLIS	3	1a															
12/7/2020	RELLIS	3	1b							0.255	-0.148	0.295				0.137	0.039	0.143
12/7/2020	RELLIS	3	1c															
12/7/2020	RELLIS	3	1d							0.242	0.056	0.248				0.041	0.035	0.054

**Table 148. Deltas Associated with the Location of Five Points for Each Scenario (Continued).**

Date	Location	Run	Scenario	P1 Ref. Delta XY (m)	P1 Ref. Delta Z (m)	P1 Ref. Delta (m)	P2 Ref. Delta XY (m)	P2 Ref. Delta Z (m)	P2 Ref. Delta (m)	P3 Ref. Delta XY (m)	P3 Ref. Delta Z (m)	P3 Ref. Delta (m)	P4 Ref. Delta XY (m)	P4 Ref. Delta Z (m)	P4 Ref. Delta (m)	P5 Ref. Delta XY (m)	P5 Ref. Delta Z (m)	P5 Ref. Delta (m)
12/7/2020	RELLIS	4	1a															
12/7/2020	RELLIS	4	1b															
12/7/2020	RELLIS	4	1c															
12/7/2020	RELLIS	4	1d															
1/15/2021	Florence	1	1a	1.332	-8.640	8.742	1.320	-9.046	9.142	1.328	-9.013	9.110				1.338	-8.690	8.792
1/15/2021	Florence	1	1b															
1/15/2021	Florence	1	1c	0.057	0.067	0.088	0.014	-0.024	0.028	0.029	-0.013	0.031				0.046	0.052	0.069
1/15/2021	Florence	2	1a	2.688	-9.995	10.350	2.869	-9.486	9.910	2.964	-9.628	10.074				2.669	-9.953	10.305
1/15/2021	Florence	2	1b	1.683	-1.881	2.524	1.726	-2.076	2.700	1.805	-2.000	2.694				1.668	-1.909	2.535
1/15/2021	Florence	2	1c	0.027	-0.040	0.048	0.006	-0.032	0.033	0.010	-0.039	0.040				0.024	-0.051	0.057
1/15/2021	Florence	3	1a	0.040	0.100	0.108	0.033	0.099	0.104	0.051	0.097	0.110				0.045	0.090	0.101
1/15/2021	Florence	3	1b	0.031	-0.011	0.033	0.023	-0.018	0.030	0.044	0.009	0.045				0.028	-0.027	0.039
1/15/2021	Florence	4	1a	0.731	-1.389	1.569	0.615	-1.234	1.379	0.580	-1.186	1.320				0.742	-1.408	1.591
1/15/2021	Florence	4	1b	0.000	0.000	0.000	0.000	0.000	0.000	0.000	0.000	0.000				0.000	0.000	0.000
1/15/2021	Florence	5	1a															
1/15/2021	Florence	5	1b															
1/15/2021	Florence	6	1a															
1/15/2021	Florence	6	1b															
3/20/2021	Florence	1	1a	0.900	0.774	1.187	3.218	0.135	3.221	0.820	1.087	1.362	5.523	0.739	5.572	4.758	0.337	4.769
3/20/2021	Florence	1	1b	0.017	-0.019	0.025	0.006	0.002	0.007	0.012	0.007	0.014	0.006	0.007	0.009	0.008	0.004	0.009
3/20/2021	Florence	1	1c	0.000	0.000	0.000	0.000	0.000	0.000	0.000	0.000	0.000	0.000	0.000	0.000	0.000	0.000	0.000
3/20/2021	Florence	1	1d	0.967	-1.830	2.070	0.956	-1.885	2.113	0.989	-1.819	2.070	1.018	-1.853	2.114	0.995	-1.871	2.119
3/20/2021	Florence	2	1a	2.975	-6.973	7.581	2.943	-6.999	7.592	3.172	-6.972	7.660	2.979	-7.057	7.660	2.967	-6.998	7.601
3/20/2021	Florence	2	1b	2.976	-6.971	7.580	2.942	-6.997	7.590	3.161	-6.961	7.645	2.978	-7.074	7.675	2.967	-7.003	7.605
3/20/2021	Florence	2	1c	2.975	-6.974	7.582	2.941	-7.002	7.594	3.161	-6.962	7.646	2.978	-7.072	7.673	2.966	-7.005	7.607
3/20/2021	Florence	3	1a	1.156	3.859	4.028	1.223	3.872	4.060	1.160	3.970	4.136	1.240	3.984	4.173	1.263	3.965	4.161
3/20/2021	Florence	3	1b	0.007	0.006	0.009	0.012	0.063	0.064	0.012	0.039	0.041	0.003	0.022	0.022	0.016	0.056	0.058
3/20/2021	Florence	3	1c	0.009	-0.030	0.031	0.006	0.027	0.028	0.004	-0.003	0.005	0.006	-0.007	0.009	0.013	0.029	0.032
3/20/2021	Florence	4	1a															
3/20/2021	Florence	4	1b															
3/20/2021	Florence	5	1a	0.078	0.167	0.184	0.097	0.179	0.204	0.033	0.156	0.159	0.138	0.150	0.204	0.157	0.166	0.229
3/20/2021	Florence	5	1b	0.024	0.010	0.026	0.042	0.012	0.043	0.030	0.027	0.041	0.041	0.000	0.041	0.047	0.033	0.058
3/20/2021	Florence	5	1c	0.053	-0.029	0.060	0.023	-0.003	0.023	0.028	0.019	0.034	0.053	-0.022	0.058	0.044	0.020	0.049
3/20/2021	Florence	6	1a	0.107	0.193	0.221	0.148	0.215	0.261	0.090	0.188	0.208	0.182	0.191	0.264	0.165	0.202	0.261
3/20/2021	Florence	6	1b	0.011	0.009	0.014	0.029	0.050	0.058	0.006	0.042	0.042	0.039	-0.003	0.039	0.041	0.056	0.070
3/20/2021	Florence	6	1c	0.024	-0.010	0.026	0.025	0.038	0.046	0.010	0.015	0.018	0.049	-0.015	0.051	0.047	0.028	0.055
3/20/2021	Florence	6	1d	0.022	-0.019	0.029	0.014	0.025	0.029	0.017	0.005	0.018	0.036	-0.024	0.043	0.027	-0.002	0.027
3/20/2021	Florence	6	1e	0.014	-0.019	0.023	0.010	0.008	0.013	0.013	-0.016	0.021	0.039	-0.048	0.062	0.025	-0.017	0.030
3/20/2021	Florence	7	1a															
3/20/2021	Florence	7	1b															
3/20/2021	Florence	7	1c															

**Table 149. Deltas Associated with Distances between Five Points for Each Scenario.**

Date	Location	Run	Scenario	Distance Checkpoint A-B (m)	P3 Checkpoint Delta X (m)	P3 Checkpoint Delta Y (m)	P3 Checkpoint Delta Z (m)	P3 Checkpoint Delta (m)	P5 Checkpoint Delta X (m)	P5 Checkpoint Delta Y (m)	P5 Checkpoint Delta Z (m)	P5 Checkpoint Delta (m)	Distance P3-P5 (m)	Delta Distance P3-P5 (m)	Delta Distance Checkpoint A-B (m)	Norm. Delta Distance Checkpoint A-B (mm/m)
8/25/2020	San Antonio	1	1a										13.435	0.020		
8/25/2020	San Antonio	1	1b										13.415	0.000		
9/30/2020	RELLIS	1	1a										49.980	0.604		
9/30/2020	RELLIS	1	1b										49.984	0.608		
9/30/2020	RELLIS	2	1a										49.374	-0.002		
9/30/2020	RELLIS	2	1b										49.376	0.000		
9/30/2020	RELLIS	2	1c										48.959	-0.417		
9/30/2020	RELLIS	2	1d										49.172	-0.204		
9/30/2020	RELLIS	3	1a										49.585	0.209		
9/30/2020	RELLIS	3	1b										49.585	0.209		
9/30/2020	RELLIS	3	1c										49.429	0.053		
9/30/2020	RELLIS	3	1d										49.537	0.161		
10/7/2020	RELLIS	1	1a	36.571	-0.647	1.721	-7.717	7.933	0.619	-1.633	-8.684	8.857	36.484	-0.101	0.087	2.387
10/7/2020	RELLIS	1	1b	36.571	-0.880	0.498	26.482	26.501	0.726	-0.453	26.478	26.492	36.521	-0.064	0.050	1.380
10/7/2020	RELLIS	1	1c	36.571	-0.010	-0.004	-0.018	0.021	-0.008	-0.008	0.024	0.027	36.583	-0.002	0.011	0.312
10/7/2020	RELLIS	2	1a	36.571	-0.981	1.030	-31.731	31.763	0.998	-0.731	-31.802	31.826	36.272	-0.313	0.299	8.187
10/7/2020	RELLIS	2	1b	36.571	-0.828	0.683	-0.921	1.414	0.831	-0.389	-0.872	1.266	36.278	-0.307	0.294	8.028
10/7/2020	RELLIS	2	1c	36.571	-0.017	-0.011	0.018	0.027	0.017	-0.022	0.112	0.116	36.605	0.020	0.034	0.921
10/7/2020	RELLIS	2	1d	36.571	-2.041	-0.583	-29.394	29.471	2.039	0.592	-29.692	29.767	36.560	-0.025	0.012	0.318
10/7/2020	RELLIS	2	1e	36.571	0.776	0.542	-1.058	1.420	-0.777	-0.235	-1.084	1.354	36.264	-0.321	0.308	8.411
10/7/2020	RELLIS	2	1f	36.571	-0.014	0.003	-0.027	0.031	0.014	-0.022	0.041	0.049	36.591	0.006	0.019	0.529
10/7/2020	RELLIS	3	1a	36.571	0.046	0.008	0.177	0.183	-0.016	-0.018	0.192	0.194	36.582	-0.003	0.011	0.294
10/7/2020	RELLIS	3	1b	36.571	-0.825	0.519	-0.869	1.306	0.843	-0.509	-0.862	1.308	36.562	-0.023	0.010	0.267
10/7/2020	RELLIS	3	1c	36.571	-0.016	0.010	0.062	0.064	0.025	-0.012	0.084	0.089	36.573	-0.012	0.002	0.057
10/7/2020	RELLIS	3	1d	36.571	0.053	0.000	0.163	0.171	-0.022	-0.024	0.166	0.169	36.596	0.011	0.025	0.673
10/7/2020	RELLIS	3	1e	36.571	-0.819	0.520	-0.994	1.389	0.839	-0.532	-1.009	1.416	36.583	-0.002	0.012	0.329
10/7/2020	RELLIS	3	1f	36.571	-0.016	0.007	0.031	0.035	0.025	-0.017	0.032	0.044	36.581	-0.004	0.010	0.269
10/7/2020	RELLIS	3	1g	36.571	-0.013	0.074	0.235	0.246	0.013	-0.100	0.216	0.239	36.597	0.012	0.025	0.692
10/7/2020	RELLIS	3	1h	36.571	-0.797	0.565	-0.870	1.308	0.806	-0.626	-0.904	1.363	36.632	0.047	0.060	1.653
10/7/2020	RELLIS	3	1i	36.571	-0.011	0.007	0.019	0.023	0.011	-0.021	0.027	0.036	36.585	0.000	0.014	0.372
12/7/2020	RELLIS	1	1a													
12/7/2020	RELLIS	1	1b													
12/7/2020	RELLIS	1	1c													
12/7/2020	RELLIS	2	1a	63.466	-0.130	-0.027	-0.007	0.133	-0.244	0.052	0.012	0.250	63.756	0.178	0.290	4.577
12/7/2020	RELLIS	2	1b	63.466	-0.059	-0.052	0.036	0.086	-0.103	0.043	-0.054	0.124	63.578	0.000	0.112	1.770
12/7/2020	RELLIS	2	1c	63.466	-0.144	-0.051	-0.004	0.153	-0.246	0.104	0.091	0.282	63.787	0.209	0.321	5.062
12/7/2020	RELLIS	2	1d	63.466	-0.048	-0.013	0.083	0.097	-0.160	0.053	0.031	0.171	63.645	0.067	0.179	2.825
12/7/2020	RELLIS	3	1a													
12/7/2020	RELLIS	3	1b	63.466	-0.003	0.197	-0.112	0.227	0.014	-0.029	-0.015	0.036	63.573	-0.005	0.107	1.685
12/7/2020	RELLIS	3	1c													
12/7/2020	RELLIS	3	1d	63.466	0.172	0.020	0.092	0.196	-0.086	0.006	-0.019	0.088	63.421	-0.157	0.045	0.706

**Table 149. Deltas Associated with Distances between Five Points for Each Scenario (Continued).**

Date	Location	Run	Scenario	Distance Checkpoint A-B (m)	P3 Checkpoint Delta X (m)	P3 Checkpoint Delta Y (m)	P3 Checkpoint Delta Z (m)	P3 Checkpoint Delta (m)	P5 Checkpoint Delta X (m)	P5 Checkpoint Delta Y (m)	P5 Checkpoint Delta Z (m)	P5 Checkpoint Delta (m)	Distance P3-P5 (m)	Delta Distance P3-P5 (m)	Delta Distance Checkpoint A-B (m)	Norm. Delta Distance Checkpoint A-B (mm/m)
12/7/2020	RELLIS	4	1a													
12/7/2020	RELLIS	4	1b													
12/7/2020	RELLIS	4	1c													
12/7/2020	RELLIS	4	1d													
1/15/2021	Florence	1	1a	23.479	-0.757	1.104	-8.982	9.081	0.772	-1.071	-8.628	8.728	23.469	-0.028627	0.010	0.444
1/15/2021	Florence	1	1b													
1/15/2021	Florence	1	1c	23.479	-0.014	-0.015	0.018	0.027	-0.045	0.046	0.114	0.131	23.539	0.044	0.060	2.543
1/15/2021	Florence	2	1a	23.479	-2.170	2.032	-9.597	10.047	1.950	-1.795	-9.891	10.240	23.701	0.205	0.221	9.427
1/15/2021	Florence	2	1b	23.479	-1.807	-0.026	-1.969	2.673	1.638	0.239	-1.847	2.480	23.650	0.155	0.171	7.275
1/15/2021	Florence	2	1c	23.479	-0.006	0.002	-0.008	0.010	-0.037	0.020	0.011	0.043	23.522	0.027	0.043	1.836
1/15/2021	Florence	3	1a	23.479	0.001	0.062	0.128	0.142	-0.044	0.046	0.152	0.165	23.523	0.027	0.043	1.846
1/15/2021	Florence	3	1b	23.479	-0.022	0.050	0.040	0.068	-0.005	0.038	0.035	0.052	23.506	0.011	0.027	1.154
1/15/2021	Florence	4	1a	23.479	-0.399	0.434	-1.155	1.297	0.555	-0.464	-1.346	1.528	23.323	-0.172	0.156	6.653
1/15/2021	Florence	4	1b	23.479	-0.002	0.011	0.031	0.033	-0.014	0.012	0.062	0.065	23.496	0.000	0.016	0.689
1/15/2021	Florence	5	1a													
1/15/2021	Florence	5	1b													
1/15/2021	Florence	6	1a													
1/15/2021	Florence	6	1b													
3/20/2021	Florence	1	1a	20.688	-0.103	0.807	1.073	1.347	2.155	-4.241	0.332	4.769	16.713	-3.973	3.975	192.126
3/20/2021	Florence	1	1b	20.688	0.001	-0.004	-0.007	0.008	0.006	-0.004	-0.001	0.007	20.678	-0.008	0.010	0.498
3/20/2021	Florence	1	1c	20.688	-0.010	-0.008	-0.014	0.019	0.007	0.004	-0.005	0.009	20.686	0.000	0.002	0.105
3/20/2021	Florence	1	1d	20.688	-0.762	0.634	-1.833	2.084	0.809	-0.585	-1.876	2.125	20.710	0.025	0.022	1.080
3/20/2021	Florence	2	1a	20.688	-2.698	1.676	-6.986	7.674	2.703	-1.235	-7.003	7.607	21.079	0.394	0.392	18.926
3/20/2021	Florence	2	1b	20.688	-2.698	1.655	-6.975	7.659	2.702	-1.236	-7.008	7.612	21.060	0.374	0.372	17.974
3/20/2021	Florence	2	1c	20.688	-2.697	1.656	-6.976	7.660	2.700	-1.239	-7.010	7.613	21.059	0.373	0.371	17.930
3/20/2021	Florence	3	1a	20.688	-0.708	0.918	3.956	4.122	0.740	-1.025	3.960	4.157	20.578	-0.108	0.110	5.309
3/20/2021	Florence	3	1b	20.688	-0.006	0.003	0.025	0.026	0.005	-0.012	0.051	0.053	20.680	-0.005	0.007	0.362
3/20/2021	Florence	3	1c	20.688	-0.009	-0.004	-0.017	0.020	0.003	-0.008	0.024	0.025	20.680	-0.006	0.008	0.379
3/20/2021	Florence	4	1a													
3/20/2021	Florence	4	1b													
3/20/2021	Florence	5	1a	20.688	0.010	-0.034	0.142	0.146	-0.136	0.070	0.161	0.222	20.778	0.092	0.090	4.330
3/20/2021	Florence	5	1b	20.688	-0.033	0.012	0.013	0.037	-0.040	0.000	0.028	0.049	20.732	0.046	0.044	2.126
3/20/2021	Florence	5	1c	20.688	-0.036	-0.018	0.005	0.041	-0.037	-0.002	0.015	0.040	20.703	0.018	0.016	0.750
3/20/2021	Florence	6	1a	20.688	0.080	-0.004	0.174	0.192	-0.157	-0.014	0.197	0.252	20.707	0.021	0.019	0.926
3/20/2021	Florence	6	1b	20.688	-0.009	-0.002	0.028	0.029	-0.034	-0.002	0.051	0.061	20.704	0.018	0.016	0.777
3/20/2021	Florence	6	1c	20.688	-0.019	-0.012	0.001	0.022	-0.040	0.004	0.023	0.046	20.708	0.022	0.020	0.958
3/20/2021	Florence	6	1d	20.688	-0.027	-0.005	-0.009	0.029	-0.014	-0.013	-0.007	0.021	20.690	0.004	0.002	0.107
3/20/2021	Florence	6	1e	20.688	-0.023	-0.007	-0.030	0.038	-0.016	-0.006	-0.022	0.028	20.694	0.008	0.006	0.300
3/20/2021	Florence	7	1a													
3/20/2021	Florence	7	1b													
3/20/2021	Florence	7	1c													



## **Test 2 (08/25/2020): Simulated Crash at Phil Hardberger Park, San Antonio, Texas**

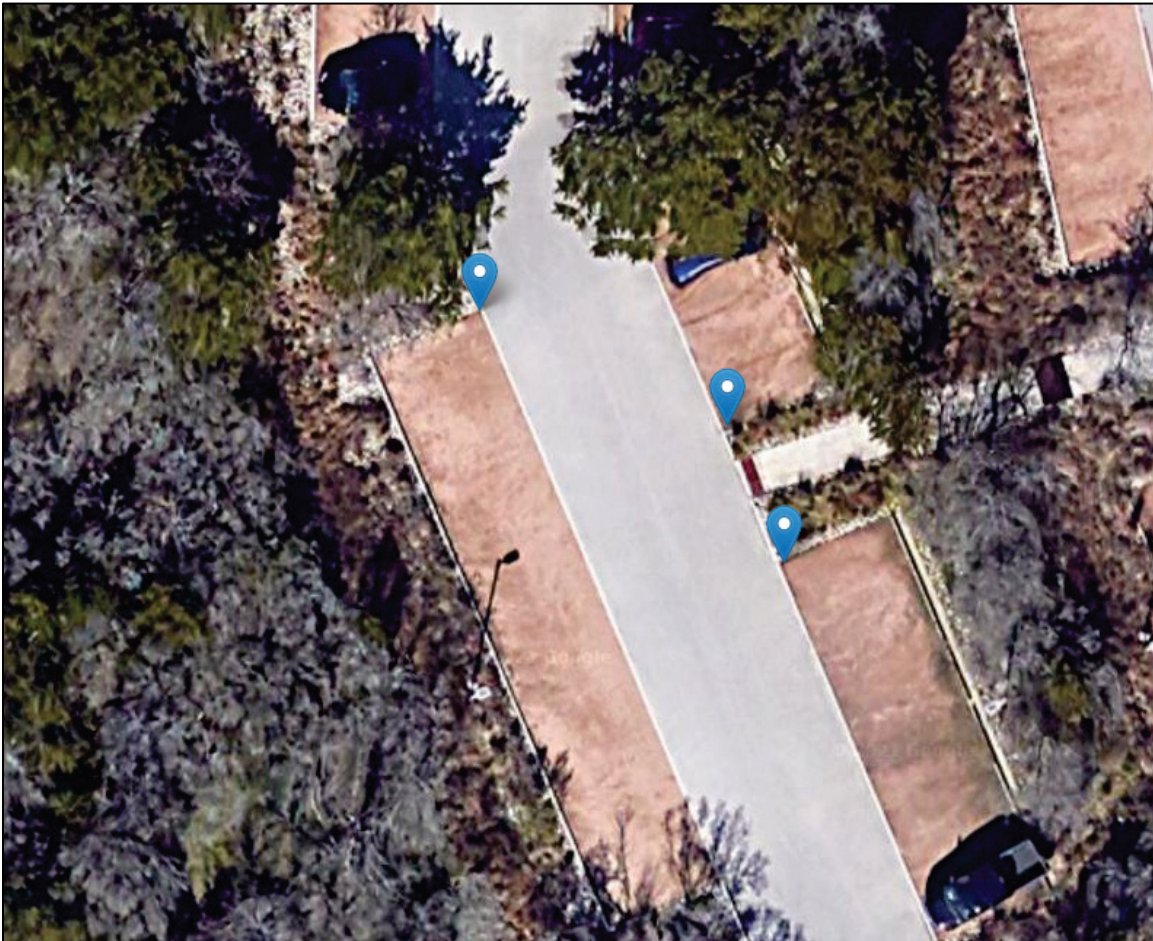
### *Data Collection*

The equipment used for this data collection test was the Mavic 2 Pro. The test run followed a diamond capture protocol, as described in Chapter 2. The research team used three different heights: 21 m (70 ft) for the survey grid pass, 32 m (105 ft) for the overview pass, and 11 m (35 ft) for the evidence pass.

### *Data Processing*

The purpose of Test 2 was to conduct an initial test of the functionality of the Mavic 2 Pro. The research team had just received the UAS from the vendor, and it was critical to assess whether the Mavic 2 Pro was fully functional and could be used for subsequent data collection activities.

The research team gathered Google elevation data for three points, as shown in Figure 255. The research team also identified five points for the analysis, as shown in Figure 256.



**Figure 255. Google Elevation Data Point Locations (08/25/2020).**



**Figure 256. Point Locations (08/25/2020).**

There was only one run for this test, labeled as Run 1: Mavic 2 Pro (GNSS standalone mode). The scenarios processed were as follows:

- Scenario 1a (standalone, i.e., no GCPs).
- Scenario 1b (Google elevation data): For this scenario, the research team used Google elevation data points as GCPs in Pix4D.

### *Results*

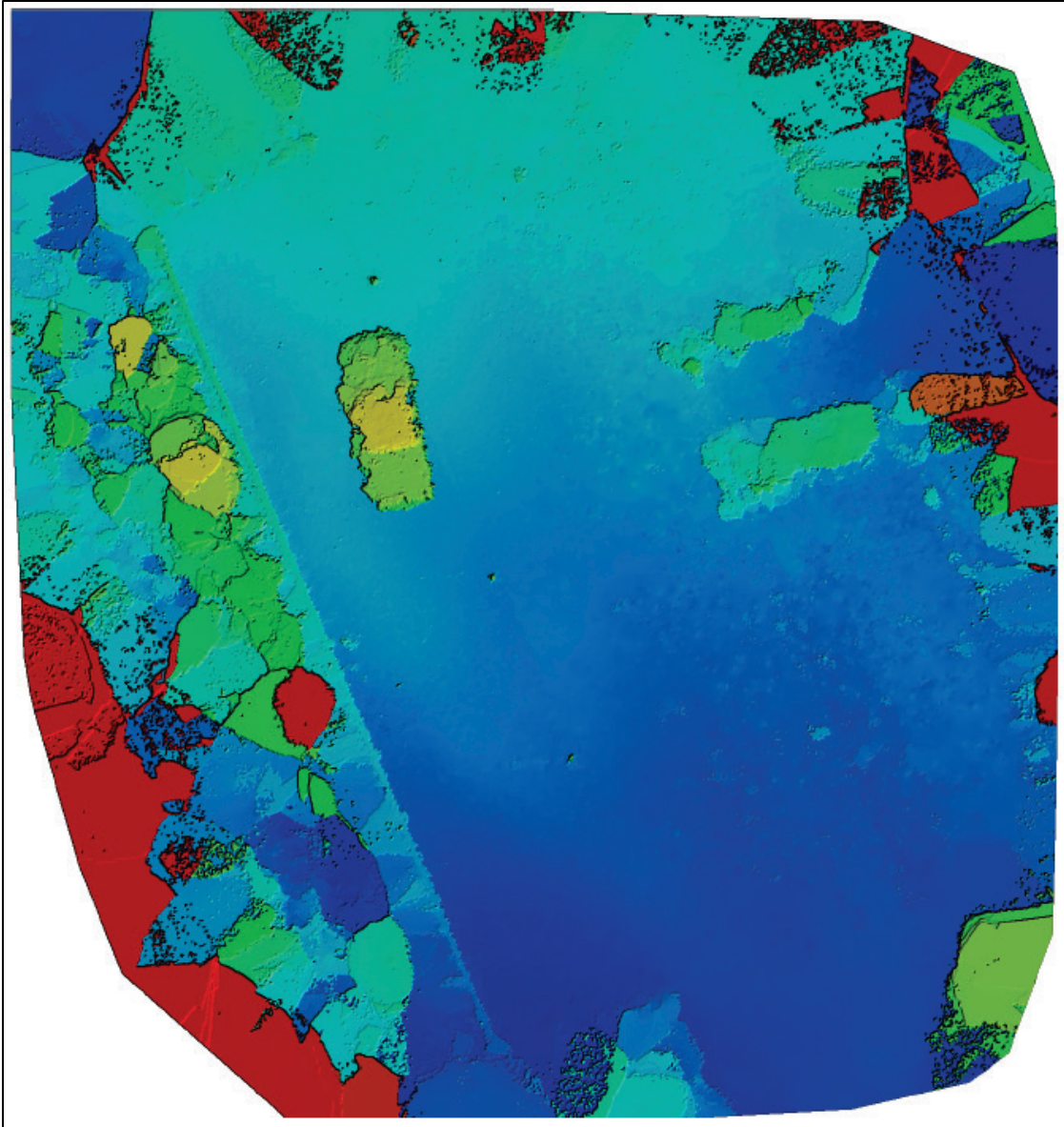
A review of the scenarios and corresponding results, as shown in Table 146, Table 147, and Table 148 (Note: Table 149 does not apply because the test did not include surveyed GCPs), yields the following observations:

- The Mavic 2 Pro performed as expected. The research team was able to gather all the imagery needed, run the three SfM stages in Pix4D, build a usable 3D model, prepare orthomosaics and DSMs, obtain coordinates of critical points, and measure distances between those points. The test did not include GCPs, so all measurements were based on standalone GNSS data. In the case of the second scenario, the research team used Google elevation data and used the corresponding coordinates as GCPs in Pix4D.
- For each scenario, the average GSD was 3 mm. There were 630,000 2D keypoints and 221,000 3D points for the BA process. After densification, the result was a 3D densified model containing 5.9 million points. This level of detail is adequate for crash reconstruction applications. It is worth noting that the scene had adequate natural light illumination and had adequate texture. There were some trees, but they were located away from the central part of the scene and therefore did not affect the SfM process. As a result, there were no gaps in the point clouds, mesh, orthomosaic, or DSM.

- The number and density of oblique images (taken at an angle of 60 degrees with respect to the horizon) were adequate to develop a 3D model of the vehicle and had a sufficient level of detail for typical crash reconstruction efforts.
- The orthomosaic and DSM were visually similar for both scenarios. Figure 257 shows the orthomosaic and Figure 258 shows the DSM.



**Figure 257. Orthomosaic (08/25/2020)**



Note: Blue represents lower elevations, red represents higher elevations.

**Figure 258. Digital Surface Model (08/25/2020).**

- The X-Y-Z coordinates of all five points (in standalone GNSS mode) were 7.3 m (24 ft) off (i.e., 1.3 m [4.3 ft] to the northwest and 7.2 m [24 ft] lower) compared to the scenario in which Google elevation data were used as GCPs. Because the test did not include surveyed GCPs and information about the reliability and accuracy of the Google elevation data is not publicly available, it was not possible to provide any quantifiable statement of positional accuracy.
- Distances between the five points used in the analysis (Figure 256) ranged from 4.3 m (14 ft) between Points 3 and 4 to 20 m (67 ft) between Points 1 and 4. The calculated distances were similar in both scenarios and varied from 0.5 cm (0.2 inches) for the distance between Points 3 and 4 to 2.5 cm (1 inch) for the distance between Points 1 and 3, which was 16 m (52 ft). The test did not include physical distance measurements

in the field or surveyed GCPs from which distances could be calculated. Nevertheless, the small variation in calculated distances was sufficiently promising in relation to the use of the Mavic 2 Pro for subsequent tests.

### **Test 3 (09/30/2020): Crash Test at the RELLIS Campus, College Station, Texas**

#### *Data Collection*

The research team completed three runs that followed a diamond capture protocol, as described in Chapter 2:

- Run 1: Mavic 2 Pro (GNSS standalone mode). This run involved the Mavic 2 Pro in GNSS standalone mode. The heights for this run were 37 m (120 ft) for the survey grid pass, 55 m (180 ft) for the overview pass, and 18 m (60 ft) for the evidence pass. The height for the round of oblique images was 15 m (50 ft).
- Run 2: Matrice 300 RTK (onboard RTK mode). This run involved the Matrice 300 RTK, using the onboard RTK mode. The heights for this run were 37 m (120 ft) for the survey grid pass, 55 m (180 ft) for the overview pass, and 18 m (60 ft) for the evidence pass. The height for the round of oblique images was 15 m (50 ft).
- Run 3: Matrice 300 RTK (RTK base station mode). This run also involved the Matrice 300 RTK, but this time it was connected to the RTK base station. The heights for this run were 37 m (120 ft) for the survey grid pass, 55 m (180 ft) for the overview pass, and 18 m (60 ft) for the evidence pass. The height for round of oblique images was 15 m (50 ft).

#### *Data Processing*

This test was the first test at the RELLIS Campus and the first one that involved the Matrice 300 RTK. The test did not include surveyed GCPs, although some runs involved using Google elevation data. The test included three daytime runs. The first run involved the Mavic 2 Pro in GNSS standalone mode. The second run involved the Matrice 300 RTK in onboard RTK mode. The third run involved the Matrice 300 RTK in base station RTK mode. In the case of the Matrice 300 RTK, the scenarios included wide-angle images and zoomed-in images, both in combination and separately.

The research team gathered Google elevation data for three points, as shown in Figure 259. The research team also identified five points for the analysis, as shown in Figure 260.



**Figure 259. Google Elevation Data Point Locations (09/30/2020).**



**Figure 260. Scene's Manual Point Locations (09/30/2020).**

The research team processed the following runs and scenarios:

- Run 1: Mavic 2 Pro (GNSS standalone mode):
  - Scenario 1a (standalone, i.e., no GCPs).
  - Scenario 1b (Google elevation data).
- Run 2: Matrice 300 RTK (Onboard RTK mode):
  - Scenario 1a (wide-angle images only, no GCPs).
  - Scenario 1b (wide-angle images only, Google elevation data).
  - Scenario 1c (wide-angle and zoomed images, no GCPs).
  - Scenario 1d (wide-angle and zoomed images, Google elevation data).
- Run 3: Matrice 300 RTK (RTK base station mode):
  - Scenario 1a (wide-angle images, no GCPs).
  - Scenario 1b (wide-angle images, Google elevation data).
  - Scenario 1c (wide-angle and zoomed images, no GCPs).
  - Scenario 1d (wide-angle and zoomed images, Google elevation data).

### *Results*

A review of the scenarios and corresponding results, as shown in Table 146, Table 147, and Table 148 (Note: Table 149 does not apply because the test did not include surveyed GCPs), yields the following observations:

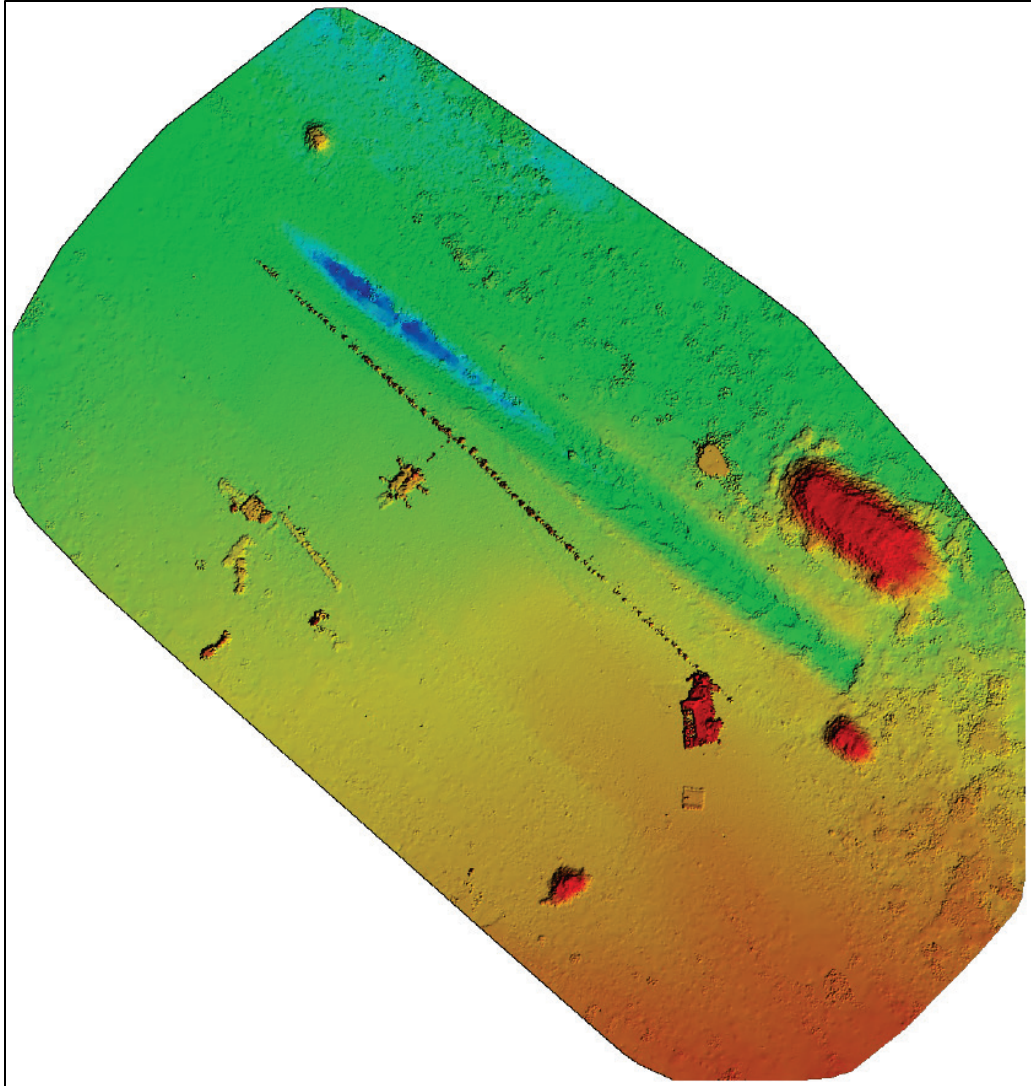
- In general, the Mavic 2 Pro and the Matrice 300 RTK performed as expected. For most scenarios, the research team was able to gather all the imagery needed, run the three SfM stages in Pix4D, build usable 3D models, prepare orthomosaics and DSMs, obtain coordinates of critical points, and measure distances between those points. Nevertheless, using two different UAS platforms (even though they came from same manufacturer) involved different routines and steps before and during data collection and during data processing.
- For the Mavic 2 Pro, the average GSD was 6.8 mm (0.27 inches). There were 2.2 million 2D keypoints and 697,000 3D points for the BA process. After densification, the result was a 3D densified model containing 13.5 million points. For the Matrice 300 RTK, the average GSD varied from 5.6 mm to 12.2 mm. Lower values were associated with zoomed-in 20-MP images and higher values were associated with wide-angle 12-MP images. In general, there were no gaps in the point clouds, mesh, orthomosaic, or DSM.
- The camera calibration percentage was lower for scenarios that used wide-angle and zoom-in images in combination (83 percent) than for scenarios that only used wide-angle images (100 percent). It is possible the reason is related to endlap considerations. For this test, the endlap was 80 percent. However, this endlap was based on wide-angle images. The zoom factor was 5× with respect to the wide-angle images, which means the effective endlap for zoomed-in images was probably very low.
- The number and density of oblique images (taken at an angle of 60 degrees with respect to the horizon) were adequate to develop 3D models of the vehicle having a sufficient level of detail for typical crash reconstruction efforts.

- The orthomosaic and the DSM were visually similar for all scenarios. Figure 261 shows the orthomosaic for Run 1, Scenario 1a. Figure 262 shows the DSM for the same scenario.



**Figure 261. Orthomosaic for Run 1, Scenario 1a (09/30/2020).**





Note: Blue represents lower elevations and red represents higher elevations.

**Figure 262. Digital Surface Model for Run 1, Scenario 1a (09/30/2020).**

- There was a significant difference in absolute coordinates for the five points used during the analysis (Figure 260) depending on the scenario considered. Although no surveyed GCPs were used, a preliminary assessment of the results suggested that Run 2, Scenario 1a (i.e., Matrice 300 RTK, with wide-angle images and Google elevation data) could be used as a reference scenario for the analysis. However, the results did not offer a conclusive answer as to the reliability or accuracy of individual X-Y-Z points. The delta X, Y, and Z (i.e., the difference between X, Y, and Z values for any point and the corresponding values for the reference location) were positive in some cases but were negative in other cases. In general, scenarios that involved a standalone GNSS mode resulted in offsets that were much larger (up to 30 m [98 ft]) than scenarios that involved the use of Google elevation data.
- Distances between the five points used in the analysis (Figure 260) ranged from 15 m (49 ft) between Points 2 and 5 to 49.5 m (162 ft) between Points 3 and 5. Calculated distances between pairs of points were somewhat similar across scenarios, but there were

noticeable differences in some cases. For example, for the scenario that involved the Mavic 2 Pro in standalone GNSS mode, calculated distances varied from 19 cm (7.5 inches) for the calculated distance between Points 1 and 3, which was 15.8 m (52 ft), to 63 cm (25 inches) for the calculated distance between Points 1 and 5, which was 49 m (161 ft). By comparison, for the scenario that involved the Matrice 300 RTK using Google elevation data, the corresponding calculated distances were 8 cm (3.2 inches) for the calculated distance between Points 1 and 3, which was 15.5 m (50.9 ft), and 20 cm (7.9 inches) for the calculated distance between Points 1 and 5, which was 48.1 m (158 ft).

#### **Test 4 (10/07/2020): Crash Test at The RELLIS Campus, College Station, Texas**

##### *Data Collection*

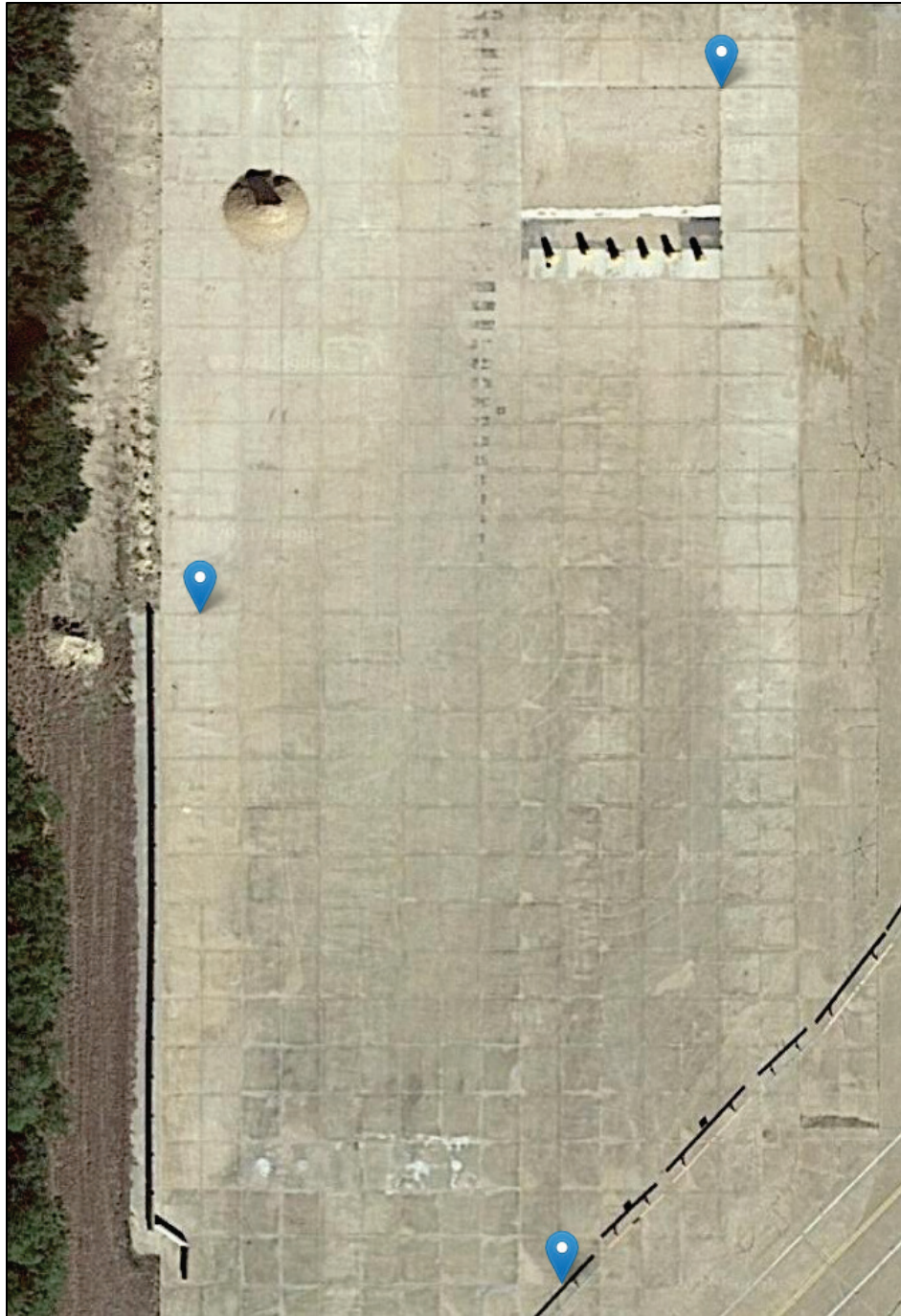
The research team completed three runs:

- Run 1: Mavic 2 Pro (GNSS standalone mode). This run involved the Mavic 2 Pro. The heights for this run were 70 m (230 ft) for the survey grid pass, 105 m (345 ft) for the overview pass, and 35 m (115 ft) for the evidence pass.
- Run 2: Matrice 300 RTK (GNSS standalone mode). This run involved the Matrice 300 RTK in standalone GNSS mode. The heights for this run were 64 m (210 ft) for the survey grid pass, 96 m (315 ft) for the overview pass, and 32 m (105 ft) for the evidence pass.
- Run 3: Matrice 300 RTK (onboard RTK mode). This run involved the Matrice 300 RTK, this time using the onboard RTK mode. The heights for this run were 55 m (180 ft) for the survey grid pass, 82 m (270 ft) for the overview pass, and 27 m (90 ft) for the evidence pass.

##### *Data Processing*

This test was the second test at the RELLIS Campus, and the first one that involved the use of surveyed GCPs. The test included three daytime runs. The first run involved the Mavic 2 Pro in GNSS standalone mode. The second run involved the Matrice 300 RTK in GNSS standalone mode. The third run involved the Matrice 300 RTK in onboard RTK mode. The scenarios covered a wide range of combinations of ground control (i.e., standalone mode, TAMUCC GCPS, and Google elevation data). In the case of the Matrice 300 RTK, the scenarios included wide-angle images and zoomed-in images, both in combination and separately.

The research team gathered Google elevation data for three points, as shown in Figure 263. The research team also selected five points for the analysis, including GCPs surveyed by TAMUCC, as shown in Figure 264.



**Figure 263. Google Elevation Data Point Locations (10/07/2020).**



**Figure 264. Scene's Manual Point Locations (10/07/2020).**

The research team processed the following runs and scenarios:

- Run 1: Mavic 2 Pro (GNSS standalone mode):
  - Scenario 1a (no GCPs).
  - Scenario 1b (Google elevation data).
  - Scenario 1c (TAMUCC-surveyed GCPs).
- Run 2: Matrice 300 RTK (GNSS Standalone Mode):
  - Scenario 1a (wide-angle images only, no GCPs).
  - Scenario 1b (wide-angle images only, Google elevation data).
  - Scenario 1c (wide-angle images only, TAMUCC-surveyed GCPs).
  - Scenario 1d (wide-angle and zoomed images, no GCPs).
  - Scenario 1e (wide-angle and zoomed images, Google elevation data).
  - Scenario 1f (wide-angle and zoomed images, TAMUCC-surveyed GCPs).
- Run 3: Matrice 300 RTK (Onboard RTK mode):
  - Scenario 1a (wide-angle images, no GCPs).
  - Scenario 1b (wide-angle images, Google elevation data).
  - Scenario 1c (wide-angle images, TAMUCC-surveyed GCPs).
  - Scenario 1d (wide-angle and zoomed images, no GCPs).
  - Scenario 1e (wide-angle and zoomed images, Google elevation data).
  - Scenario 1f (wide-angle and zoomed images, TAMUCC-surveyed GCPs).
  - Scenario 1g (zoomed images, no GCPs).
  - Scenario 1h (zoomed images, Google elevation data).
  - Scenario 1i (zoomed images, TAMUCC-surveyed GCPs).

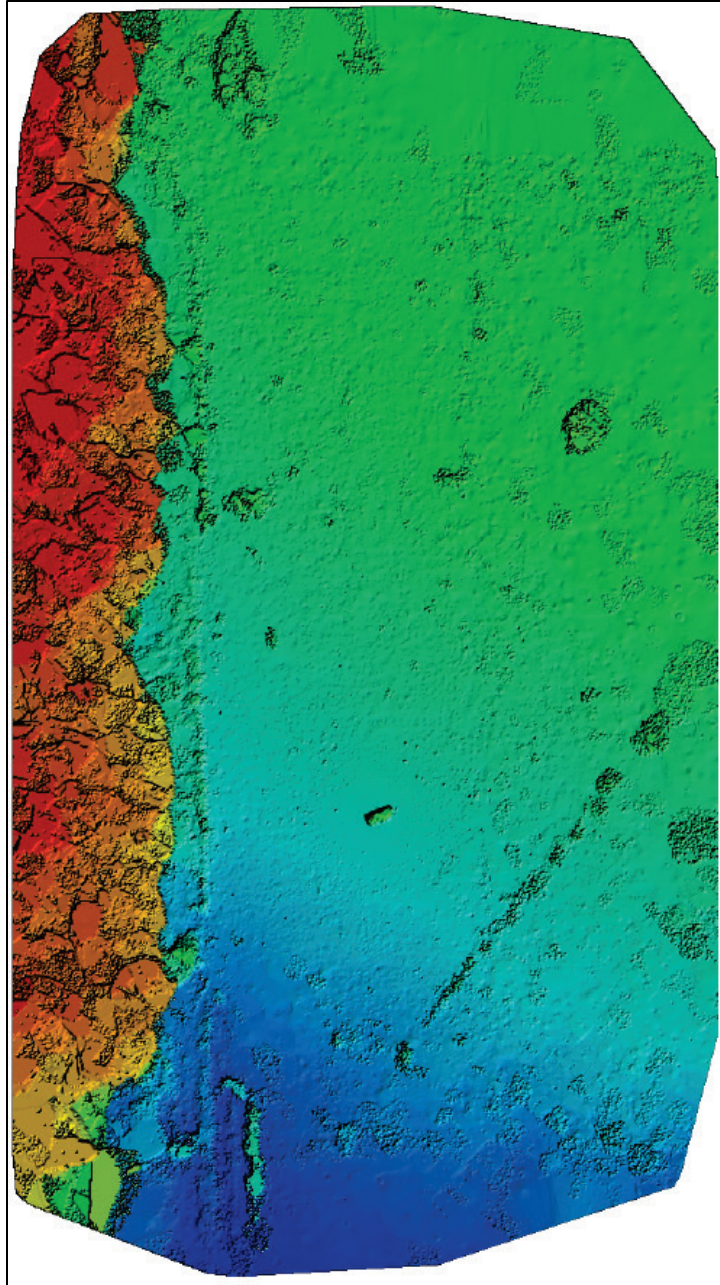
### *Results*

A review of the scenarios and corresponding results, as shown in Table 146, Table 147, Table 148, and Table 149, yields the following observations:

- In general, the Mavic 2 Pro and the Matrice 300 RTK performed as expected. For most scenarios, the research team was able to gather all the imagery needed, run the three SfM stages in Pix4D, build usable 3D models, prepare orthomosaics and DSMs, obtain coordinates of critical points, and measure distances between those points. Nevertheless, using two different UAS platforms (even though they came from the same manufacturer) involved different routines and steps before and during data collection and during data processing. Some of the results were not only different but also somewhat unexpected, particularly when GCPs were not used.
- For the Mavic 2 Pro, the average GSD was 7.9 mm (0.31 inches). There were 1.7 million 2D keypoints and 478,000 3D points for the BA process. After densification, the result was a 3D densified model containing 10.2 million points. For the Matrice 300 RTK, the average GSD varied from 3.7–10.6 mm (0.15–0.42 inches), with the lower value being associated with zoomed-in 20-MP images and the higher value being associated with wide-angle 12-MP images. The scene had adequate natural light illumination and had adequate surface texture. In general, there were no gaps in the point clouds, mesh, orthomosaic, or DSM.
- The number and density of oblique images (taken at an angle of 60 degrees with respect to the horizon) were adequate to develop 3D models of the vehicle having a sufficient level of detail for typical crash reconstruction efforts.
- The orthomosaic and the DSM were visually similar for all the scenarios. Figure 265 shows the orthomosaic for Run 1, Scenario 1a. Figure 266 shows the DSM for the same scenario.



**Figure 265. Orthomosaic (10/07/2020).**



Note: Blue represents lower altitudes, red represents higher altitudes.

**Figure 266. Digital Surface Model (10/07/2020).**

- There was a significant difference in absolute coordinates for the five points used during the analysis (Figure 264), depending on the UAS and ground control used. A preliminary assessment of the results obtained for the various scenarios indicated that Run 3, Scenario 1i (i.e., Matrice 300 RTK, onboard RTK mode, with zoomed images, and with TAMUCC-surveyed GCPs) produced calculated coordinates that were closest to the surveyed GCP coordinates. The research team used this scenario as an additional reference scenario for the analysis. Some of the observations include:

- When used in standalone GNSS mode, the Mavic 2 Pro produced coordinates that were up to 8.9 m (29 ft) off (i.e., 1.7 m [5.6 ft] to the northwest and 8.7 m [29 ft] lower) in comparison to the reference scenario. Interestingly, when the scenario was modified to include Google elevation data, the offset worsened. In this case, the coordinates were up to 26 m [85 ft] off (i.e., 0.8 m [2.6 ft] to the northwest and 26 m [85 ft] higher) when compared to the reference scenario.
- When used in standalone GNSS mode, the Matrice 300 RTK produced coordinates that were up to 32 m (105 ft) off (i.e., 1.4 m [4.6 ft] to the northwest and 32 m [105 ft] lower) in comparison to the reference scenario. Using Google elevation data resulted in coordinates that were 1.4 m (4.6 ft) off (i.e., 1 m [3.3 ft] to the northwest and 1 m [3.3 ft] lower) when compared to the reference scenario.
- For both UASs, using the TAMUCC GCPs for SfM processing produced coordinates that were 3–5 cm (1.2 – 2.0 inches) off in comparison to the surveyed coordinates.
- Distances between the five points used in the analysis (Figure 264) ranged from 12.4 m (40.7 ft) between Points 2 and 3 to 48.5 m (159 ft) between Points 2 and 5. The calculated distances were similar in all scenarios, except for a scenario that involved the Matrice 300 RTK and Google elevation data. In most cases, calculated distances varied from 0.1 cm for the distance between Points 1 and 3, which was 33.4 m (110 ft), to 4 cm (1.6 inches) for the distance between Points 1 and 2, which was 45.4 m (149 ft). For the scenario that involved the Matrice 300 RTK and Google elevation data, calculated distances varied from 11 cm (4.3 inches) for the distance between Points 2 and 3, which was 12.2 m (40 ft), to 43 cm (17 inches) for the distance between Points 2 and 5, which was 48.5 m (159 ft).

## **Test 5 (12/07/2020): Delivery Truck Crash Test at the RELLIS Campus, College Station, Texas**

### *Data Collection*

The research team completed four runs:

- Run 1: Mavic 2 Pro (GNSS standalone mode, nighttime). This run involved the Mavic 2 Pro during nighttime and using its built-in LEDs. This run did not follow a diamond capture protocol described in Chapter 2 because of the difficulty viewing objects at a high altitude. In the field, the research team lowered the UAS until objects appeared to be visible on the remote controller screen. The heights for this run were three passes at 9 m (30 ft), two passes at 15 m (50 ft), and 18 m (60 ft) for the last pass. Obliques were captured at 9 m (30 ft).
- Run 2: Matrice 300 RTK (onboard RTK mode, daytime). This run involved the Matrice 300 RTK following the diamond capture protocol described in Chapter 2. The heights for this run were 34 m (110 ft) for the survey grid pass, 50 m (165 ft) for the overview pass, and 17 m (55 ft) for the evidence pass.
- Run 3: Matrice 300 RTK (onboard RTK mode, nighttime, built-in LEDs). This run involved the Matrice 300 RTK, but this time it was a nighttime run using the UAS built-in LEDs. The run followed the diamond capture protocol, with heights at 15 m (50 ft) for the survey grid pass, 23 m (75 ft) for the overview pass, and 8 m (25 ft) for the evidence



pass. Obliques were captured at 11 m (35 ft). In the field, the amount of illumination from the Matrice 300 RTK's built-in LEDs appeared to be sufficient to capture imagery at higher altitudes than for the Mavic 2 Pro. However, as described below, the SfM process failed even though objects were visible on the remote controller screen.

- Run 4: Matrice 300 RTK (onboard RTK mode, nighttime, built-in LEDs, and spotlight). In addition to the built-in LEDs, illumination included using the additional spotlight that was onboard the UAS. The run followed the diamond capture protocol, with heights at 15 m (50 ft) for the survey grid pass, 23 m (75 ft) for the overview pass, and 8 m (25 ft) for the evidence pass. Obliques were captured at 11 m (35 ft).

### *Data Processing*

This test was the third test at the RELLIS Campus, and the first one that involved nighttime runs. The test included one daytime run using the Matrice 300 RTK. The other three runs were nighttime runs: one run for the Mavic 2 Pro and two runs for the Matrice 300 RTK. The scenarios covered a wide range of combinations of ground control (i.e., standalone mode, TAMUCC GCPS, and Google elevation data). In the case of the Matrice 300 RTK, the scenarios covered the use of wide-angle images and zoomed-in images. For the nighttime runs, the experiments included built-in LEDs for both Mavic 2 Pro and Matrice 300 RTK as well as built-in LEDs and a supplemental spotlight for the Matrice 300 RTK.

The research team gathered Google elevation data for three points. The research team selected five points for the analysis, including GCPs surveyed by TAMUCC, as shown in Figure 267.



**Figure 267. Scene's Manual Point Locations (12/07/2020).**

The research team processed the following runs and scenarios:

- Run 1: Mavic 2 Pro (GNSS standalone mode, nighttime):
  - Scenario 1a (no GCPs).
  - Scenario 1b (Google elevation data).

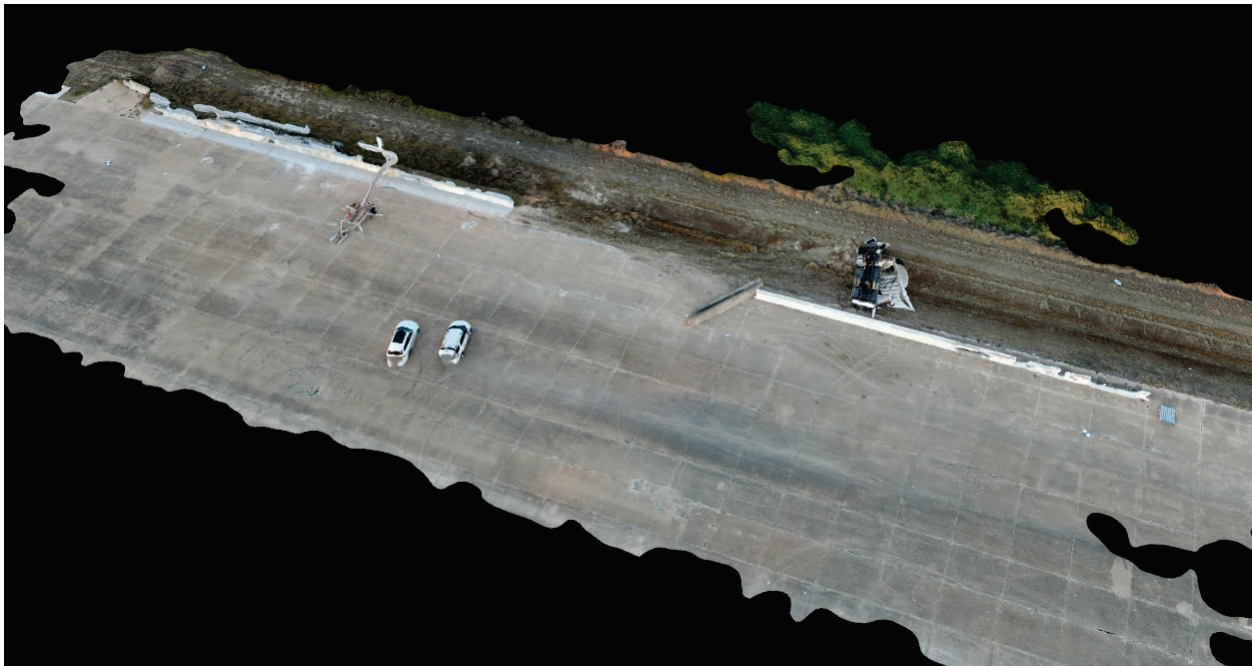
- Scenario 1c (TAMUCC-surveyed GCPs).
- Run 2: Matrice 300 RTK (onboard RTK mode, daytime):
  - Scenario 1a (wide-angle images only, no GCPs).
  - Scenario 1b (wide-angle images only, TAMUCC-surveyed GCPs).
  - Scenario 1c (wide-angle and zoomed images, no GCPs).
  - Scenario 1d (wide-angle and zoomed images, TAMUCC-surveyed GCPs).
- Run 3: Matrice 300 RTK (onboard RTK Mode, nighttime, built-in LEDs):
  - Scenario 2a (wide-angle images only, no GCPs).
  - Scenario 2b (wide-angle images only, TAMUCC-surveyed GCPs).
  - Scenario 2c (wide-angle and zoomed images, no GCPs).
  - Scenario 2d (wide-angle and zoomed images, TAMUCC-surveyed GCPs).
- Run 4: Matrice 300 RTK (onboard RTK Mode, nighttime, built-in LEDs and spotlight)
  - Scenario 3a (wide-angle images only, no GCPs).
  - Scenario 3b (wide-angle images only, TAMUCC-surveyed GCPs).
  - Scenario 3c (wide-angle and zoomed images, no GCPs).
  - Scenario 3d (wide-angle and zoomed images, TAMUCC-surveyed GCPs).

## *Results*

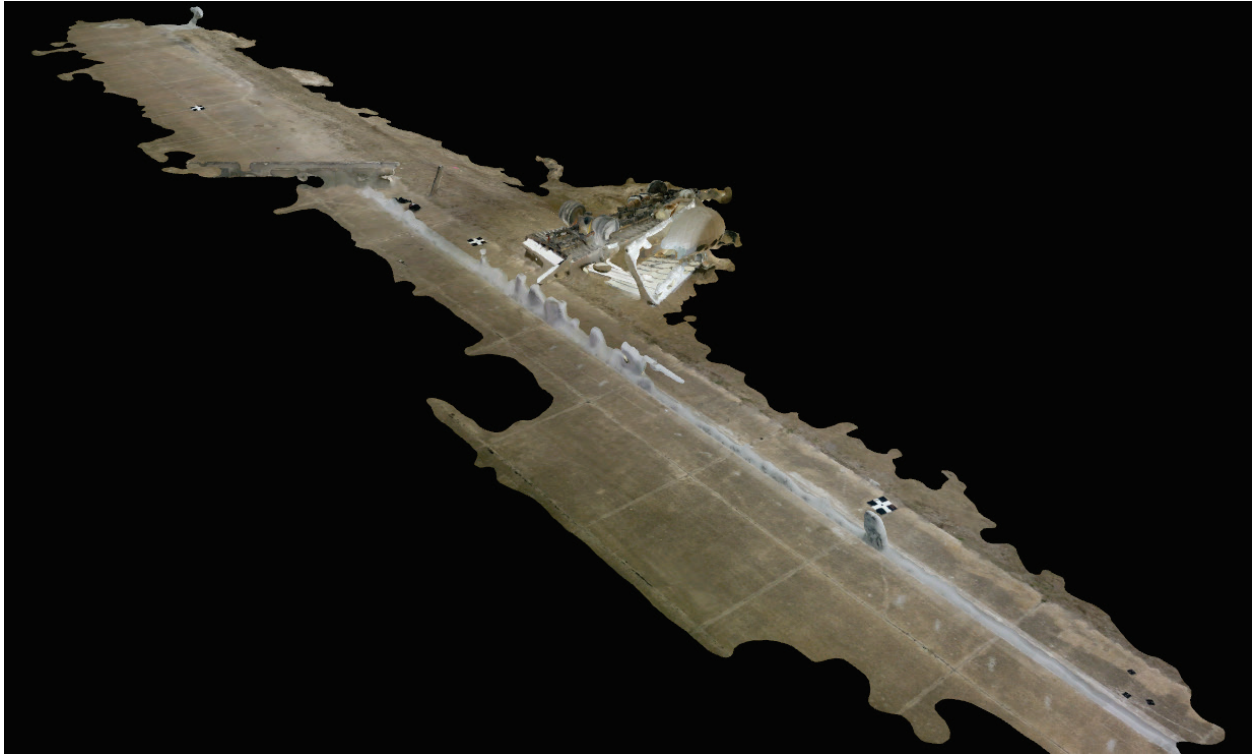
A review of the scenarios and corresponding results, as shown in Table 146, Table 147, Table 148, and Table 149, yields the following observations:

- The research team was able to complete all daytime scenarios for the Matrice 300 RTK (Figure 268). Some gaps occurred, probably because of the lack of scene texture.
- It was not possible to complete the SfM process for any of the 11 nighttime scenarios. The Mavic 2 Pro nighttime runs models performed better than the Matrice 300 RTK models. Camera calibration achieved 100 percent for the Mavic 2 Pro nighttime scenario. The average GSD was 2.4 mm (0.094 inches). However, as Figure 269 shows, the vehicle and only part of the rest of the scene were reconstructed. Several reasons are possible, including lack of adequate lighting and lack of texture. The model had 406,000 2D keypoints and 150,000 3D points, which were considerably lower than for daytime runs in previous tests. Similarly, none of the nighttime scenarios with the Matrice 300 RTK produced adequate results. Other nighttime scenarios exhibited a similar behavior.
- Orthomosaics and DSMs varied depending on several factors, including area covered and time of day. As an illustration, Figure 270 shows the orthomosaic for Run 1, Scenario 1a (i.e., Mavic 2 Pro, nighttime) and the orthomosaic for Run 2, Scenario 1a (i.e., Matrice 300 RTK, daytime). Figure 271 shows the DSMs associated with both scenarios.
- For the Matrice 300 RTK, in addition to the built-in LEDs, some nighttime runs involved the use of the supplemental spotlight. While the spotlight brightened images, there was no evidence that the spotlight improved SfM processing. The main reason is that the spotlight projected a narrow light beam, and the camera compensated for the increase in brightness by reducing the exposure time. Images showed a well-lit circle in the middle, but the rest of the image was considerably darker than similar images that only used the built-in LEDs. As a result:
  - Scenarios that used the spotlight resulted in a worse camera calibration percentage (41–54 percent) than scenarios that only used the built-in LEDs (56–86 percent).

- The number of 2D keypoints and 3D points were lower when using the spotlight. When using built-in LEDS only, the number of 2D keypoints ranged from 39,000 to 51,000, while 3D points ranged from 17,000 to 22,000. When the spotlight was added, the number of 2D keypoints decreased to 33,000 and the number of 3D points decreased to 14,000. These numbers were when using wide-angle images. When zoomed-in images were included, the numbers increased considerably (over 250,000 2D keypoints and 100,000 3D points), but the numbers were not enough to produce an acceptable model.
- The only runs that produced usable coordinates for the five points were daytime runs using the Matrice 300 RTK. For these runs, there was a significant difference in absolute coordinates for the five points used during the analysis (Figure 267), depending on the ground control used. A preliminary assessment of the results obtained for the various scenarios indicated that Run 2, Scenario 1b (i.e., Matrice 300 RTK, onboard RTK mode, and with TAMUCC-surveyed GCPs) produced calculated coordinates that were closest to the surveyed GCP coordinates. The research team used this scenario as an additional reference scenario for the analysis. When used in onboard RTK mode without GCPs, the Matrice 300 RTK produced coordinates that were 10–25 cm (3.9–9.8 inches) off compared to the reference scenario. Using GCPs reduced the offset to about 3–12 cm (1.1–4.7 inches).
- Distances between the five points used in the analysis (Figure 267) ranged from 12.2 m (40 ft) between Points 1 and 3 to 73.5 m (241 ft) between Points 1 and 5. The calculated distances were somewhat similar in all scenarios, although there were variations depending on the ground control used. When used in onboard RTK mode without GCPs, distances between points were 4–21 cm (1.6–8.3 inches) off compared to the reference scenario. Using GCPs reduced the offset considerably to about 1–2 cm (0.4–0.8 inches).



**Figure 268. Run 2, Scenario 1a Model (12/07/2020).**



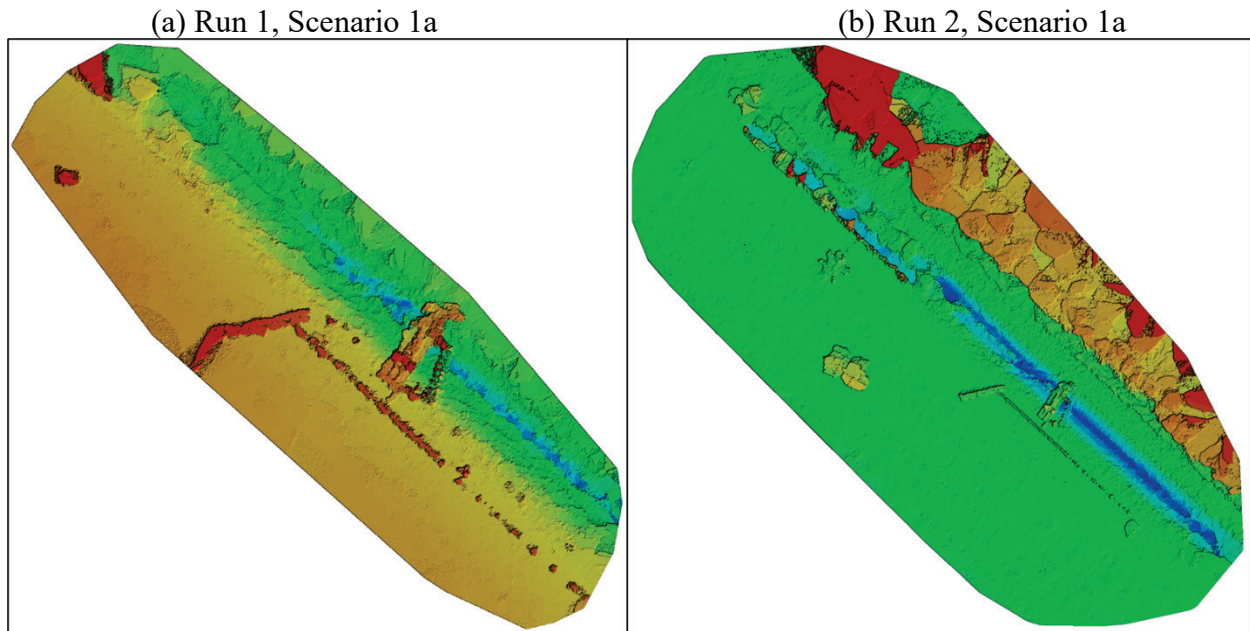
**Figure 269. Mavic 2 Pro Nighttime Run Model (12/07/2020).**

(a) Run 1, Scenario 1a

(b) Run 2, Scenario 1a



**Figure 270. Orthomosaic: Mavic 2 Pro Night Model vs. Matrice 300 RTK (12/07/2020).**



Note: Blue represents lower altitudes, red represents higher altitudes.

**Figure 271. Digital Surface Model: Mavic 2 Pro Night Model vs. Matrice 300 RTK (12/07/2020).**

**Test 6 (01/15/2021): Simulated Passenger Car Crash Test at the TxDPS Tactical Training Facility in Florence, Texas**

*Data Collection*

The research team completed six runs:

- Run 1: Mavic 2 Pro (GNSS standalone mode, nighttime, built-in LEDs). This run involved the Mavic 2 Pro during nighttime and using its built-in LEDs. This run did not follow the diamond capture protocol because of low visibility (i.e., difficult to view objects at a high altitude). The heights for this run were two passes at 12 m (40 ft), two passes at 9 m (30 ft), and one 15 m (50 ft) pass. Obliques were captured at 11 m (35 ft).
- Run 2: Mavic 2 Pro (GNSS standalone mode, nighttime, built-in LEDs and high-mast lights). This run also involved the Mavic 2 Pro with its built-in LEDs, but this time, light from two nearby high-mast lights was added. These lights are similar to those commonly installed at freeway interchanges. The heights for this run were two passes at 6 m (20 ft), two passes at 9 m (30 ft), and one pass at 12 m (40 ft). Obliques were captured at 11 m (35 ft).
- Run 3: Matrice 300 RTK (base station RTK, daytime). This run involved the Matrice 300 RTK connected to its base station. The run followed the diamond capture protocol, with heights at 52 m (170 ft) for the survey grid pass, 78 m (255 ft) for the overview pass, and 26 m (85 ft) for the evidence pass. Two rounds of obliques were captured, one at 20 m (65 ft) with the camera at 60 degrees, and the other one at 14 m (45 ft) with the camera at 50 degrees.

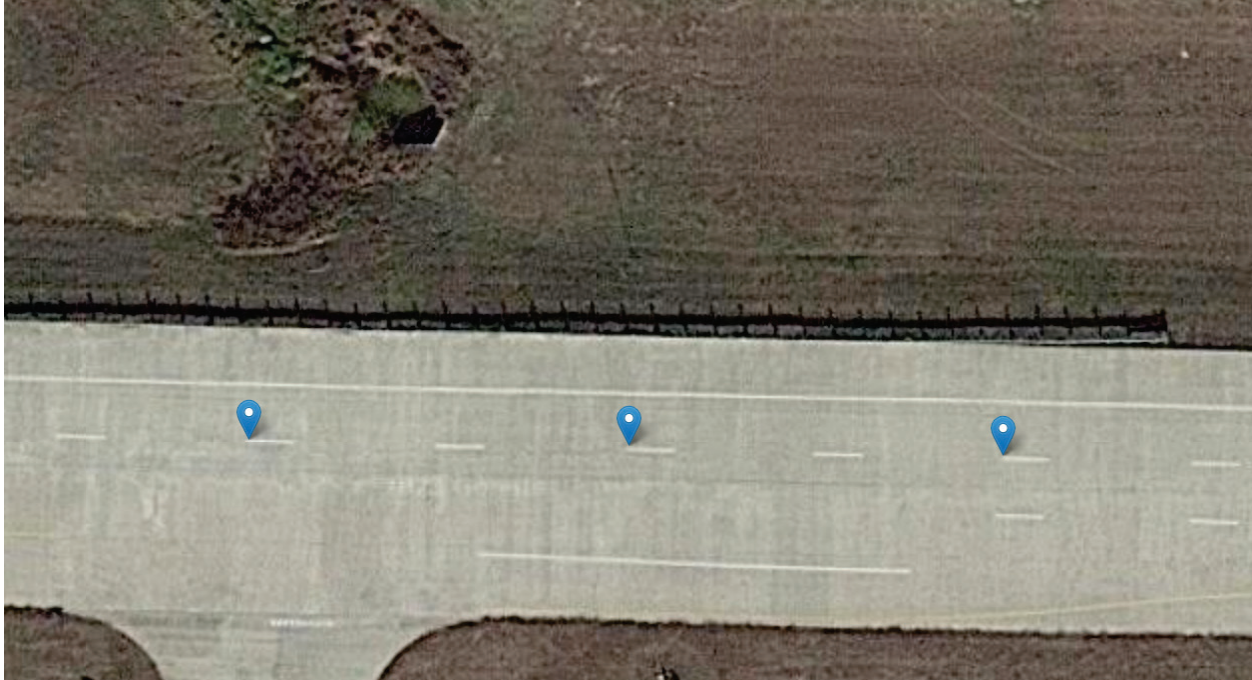
- Run 4: Matrice 300 RTK (onboard RTK mode, daytime). This run also involved the Matrice 300 RTK (onboard RTK mode). It followed the diamond capture protocol, with heights at 52 m (170 ft) for the survey grid pass, 78 m (255 ft) for the overview pass, and 26 m (85 ft) for the evidence pass. Two rounds of obliques were captured, one at 20 m (65 ft) with the camera at 60 degrees, and the other one at 14 m (45 ft) with the camera at 50 degrees.
- Run 5: Matrice 300 RTK (base station, nighttime, built-in LEDs). This run involved the Matrice 300 RTK during nighttime connected to the base station and using its built-in LEDs. Heights included two passes at 12 m (40 ft), two passes at 9 m (30 ft), and one pass at 15 m (50 ft). Obliques were taken at 35 ft.
- Run 6: Matrice 300 RTK (onboard RTK, nighttime, built-in LEDs). This run involved the Matrice 300 RTK during nighttime using its built-in LEDs, but this time in onboard RTK mode. Heights included two passes at 40 ft, two passes at 30 ft, and one pass at 50 ft. Obliques were taken at 11 m (35 ft).

### *Data Processing*

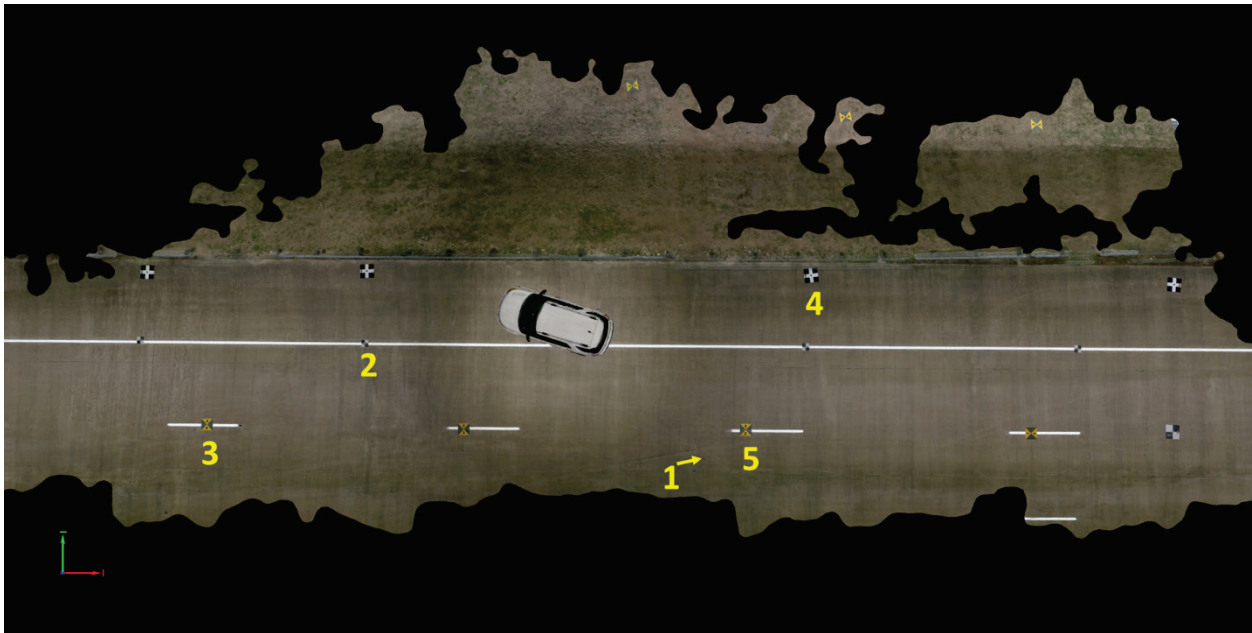
This test was the first test at the TxDPS Tactical Training Facility in Florence, Texas. Like other previous tests, it involved the use of surveyed GCPs. The test included two nighttime runs using the Mavic 2 Pro, as well as daytime and nighttime runs using the Matrice 300 RTK. The scenarios covered a wide range of combinations of ground control (i.e., standalone mode, TAMUCC GCPS, and Google elevation data). In the case of the Matrice 300 RTK, the scenarios included wide-angle images and zoomed-in images (in combination, since previous tests did not suggest any specific advantage to using only wide-angle images or zoomed-in images separately). For the nighttime runs, the experiments included built-in LEDs for both Mavic 2 Pro and Matrice 300 RTK as well as built-in LEDs and high-mast lights for the Mavic 2 Pro.

For the nighttime runs, the research team gathered two images at each location to address the issue of blurriness that was observed in previous tests that involved nighttime data collection.

The research team gathered Google elevation data for three points, as shown in Figure 272. The research team also identified five points, including GCPs surveyed by TAMUCC, to compare the location accuracy of the different scenarios (Figure 273).



**Figure 272. Google Elevation Data (01/15/2021).**



**Figure 273. Scene's Manual Point Locations (01/15/2021).**

The research team processed the following runs and scenarios:

- Run 1: Mavic 2 Pro (GNSS standalone mode, nighttime, built-in LEDs)
  - Scenario 1a (no GCPs)
  - Scenario 1b (Google elevation data)
  - Scenario 1c (TAMUCC-surveyed GCPs)

- Run 2: Mavic 2 Pro (GNSS standalone mode, nighttime, built-in LEDs and high-mast lights)
  - Scenario 1a (no GCPs)
  - Scenario 1b (Google elevation data)
  - Scenario 1c (TAMUCC-surveyed GCPs)
- Run 3: Matrice 300 RTK (base station RTK, daytime)
  - Scenario 1a (no GCPs)
  - Scenario 1b (TAMUCC-surveyed GCPs)
- Run 4: Matrice 300 RTK (onboard RTK mode, daytime)
  - Scenario 1a (no GCPs)
  - Scenario 1b (TAMUCC-surveyed GCPs)
- Run 5: Matrice 300 RTK (base station, nighttime, built-in LEDs)
  - Scenario 1a (no GCPs)
  - Scenario 1b (TAMUCC-surveyed GCPs)
- Run 6: Matrice 300 RTK (onboard RTK, nighttime, built-in LEDs)
  - Scenario 1a (no GCPs)
  - Scenario 1b (TAMUCC-surveyed GCPs)

### *Results*

A review of the scenarios and corresponding results, as shown in Table 146, Table 147, Table 148, and Table 149, yields the following observations:

- The Matrice 300 RTK performed as expected during daytime runs. For most scenarios, the research team was able to gather all the imagery needed, run the three SfM stages in Pix4D, build usable 3D models, prepare orthomosaics and DSMs, obtain coordinates of critical points, and measure distances between those points. At night, the built-in LEDs were insufficient for the Matrice 300 RTK. Although the UAS captured images, the amount of ambient light was not enough for Pix4D to identify an adequate number of matching points. The number of calibrated images was low (54–64 percent of images were calibrated) producing unsatisfactory results (Figure 274).

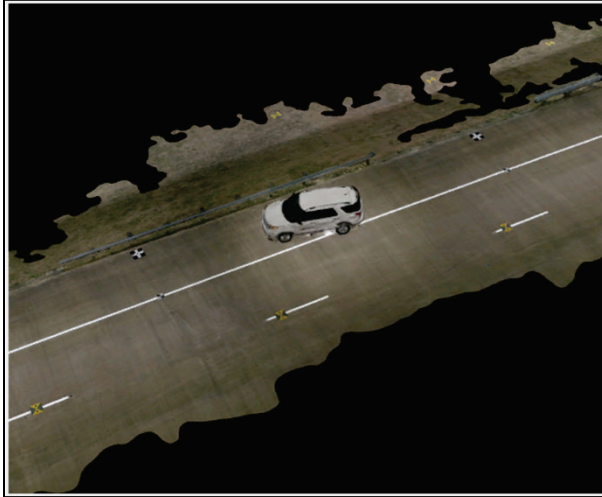




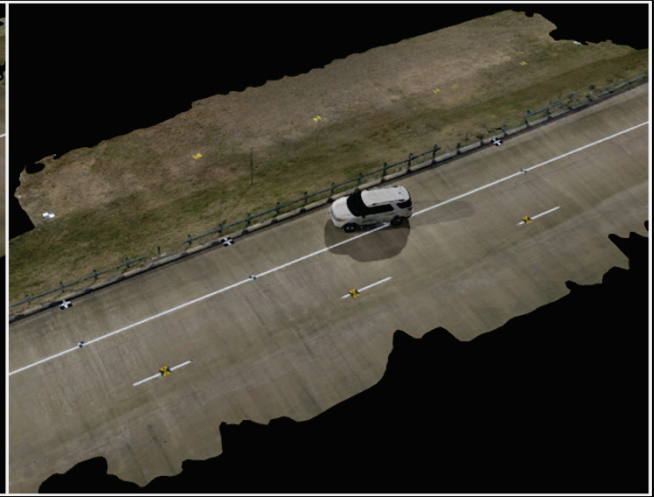
**Figure 274. Matrice 300 RTK Night Model (01/15/2021).**

- The Mavic 2 Pro performed well at night using its built-in LEDs (in standalone GNSS mode). All the images were calibrated, and all the data products were successfully completed. The average GSD was 2.2 mm (0.087 inches). The result was over 1 million 2D keypoints and 403,000 3D points for the BA process. After densification, the result was a 3D densified model containing 10.6 million points. Using the built-in LEDs and high-mast lights, the result was 5.6 million 2D keypoints and 2.0 million 3D points for the BA process. After densification, the result was a 3D densified model containing 31.1 million points. Using the high-mast lights produced better results, particularly on the side of the scene where the high-mast lights were located, as shown in Figure 275. Interestingly, no satisfactory results were obtained with the Mavic 2 Pro at night when using Google elevation data (Figure 276). The cause of this behavior could not be positively established, but it is probably related to a mismatch of images and the corresponding Google elevation data points.
- For the Matrice 300 RTK, the average GSD varied from 7.6–7.8 mm (0.30–0.31 inches). There were 2.8 million 2D keypoints and 905,000 3D points for the BA process. After densification, the result was a 3D densified model containing 1.1 million points.
- The number and density of oblique images (taken at an angle of 60 degrees with respect to the horizon) were adequate to develop 3D models of the vehicle having a sufficient level of detail for typical crash reconstruction efforts.
- Orthomosaics and DSMs varied depending on the scenario. As an illustration, Figure 277 shows the orthomosaic for a nighttime run with the Mavic 2 Pro. Figure 278 shows the DSM. Figure 279 shows the orthomosaic for a daytime run with the Matrice 300 RTK. Figure 280 shows the orthomosaic.

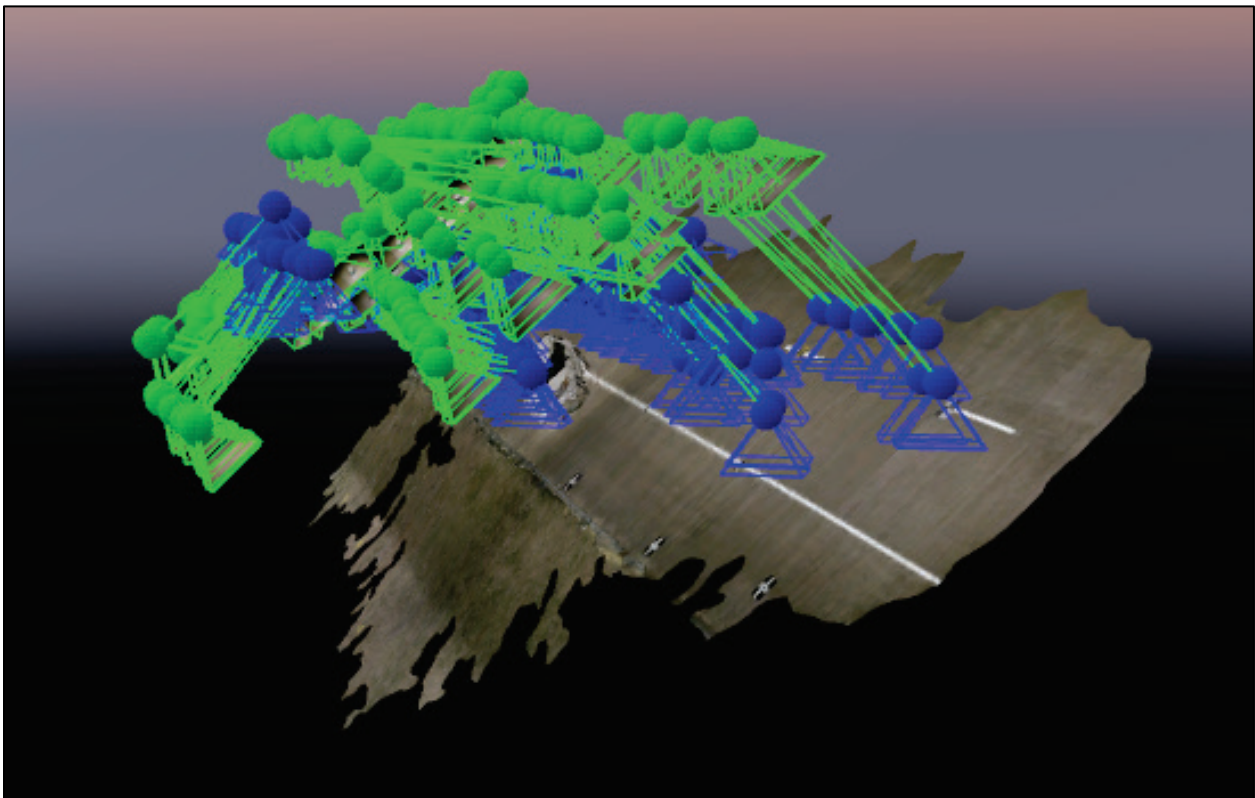
(a) Built-in LEDs



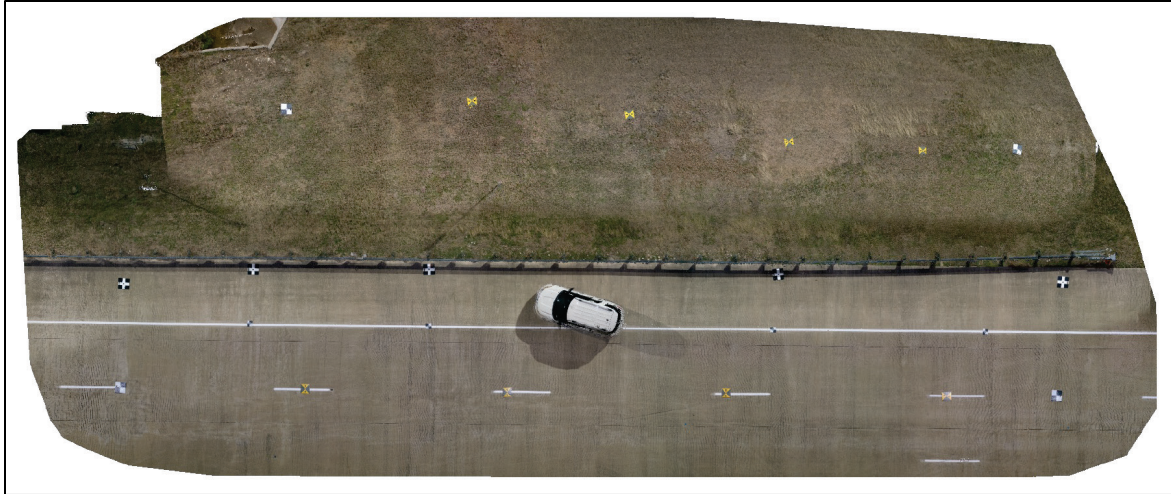
(b) Built-in LEDs and high-mast lights



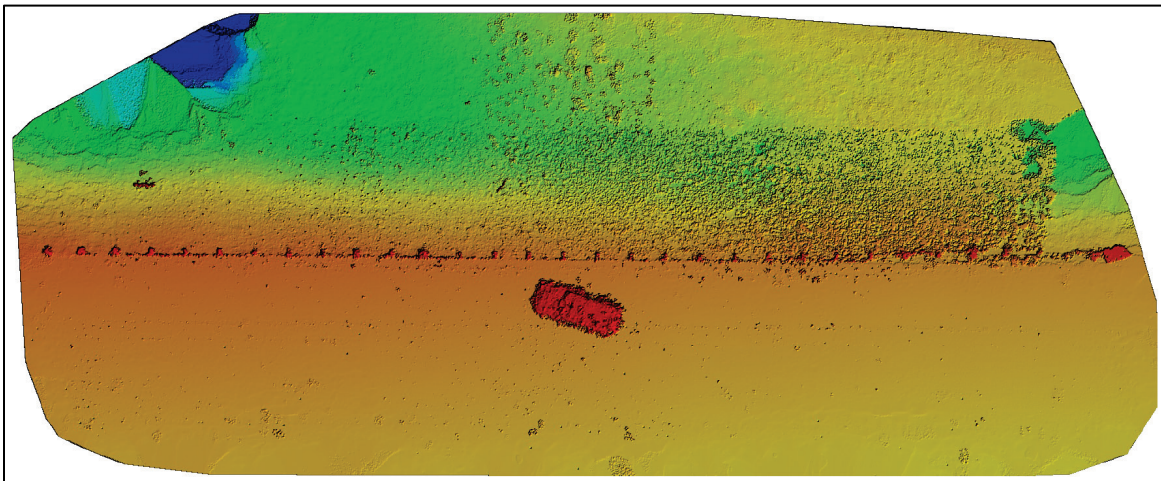
**Figure 275. Mavic 2 Pro Scene with Built-In LEDs and High-Mast Lights (01/15/2021).**



**Figure 276. Nighttime Mavic 2 Pro Model with Google Elevation Data (01/15/2021).**

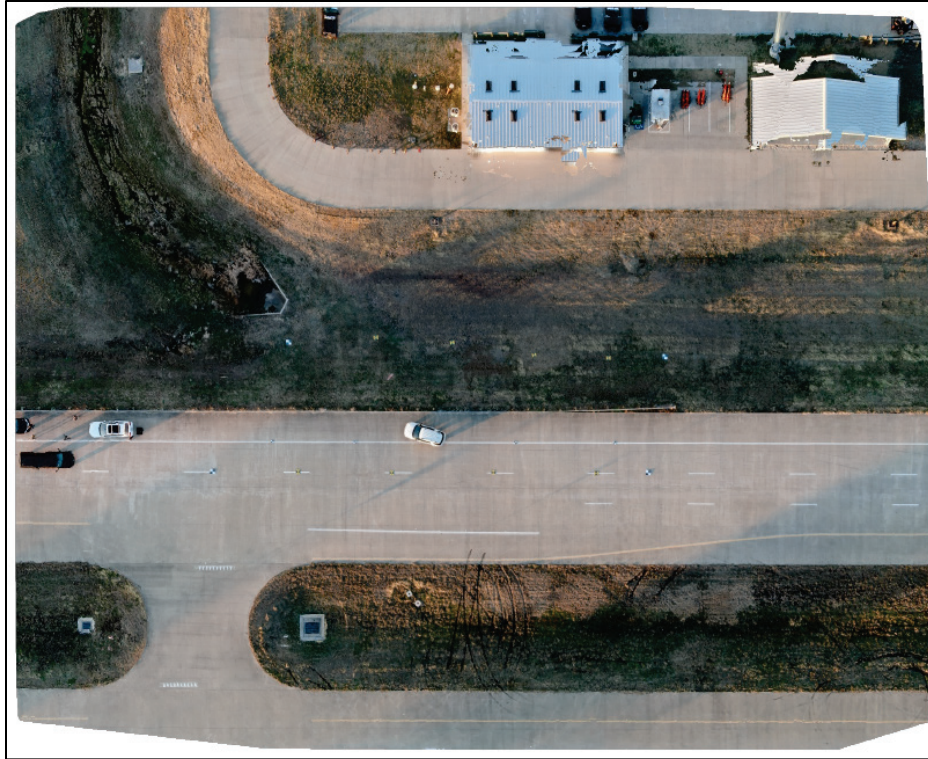


**Figure 277. Nighttime Orthomosaic (01/15/2021).**

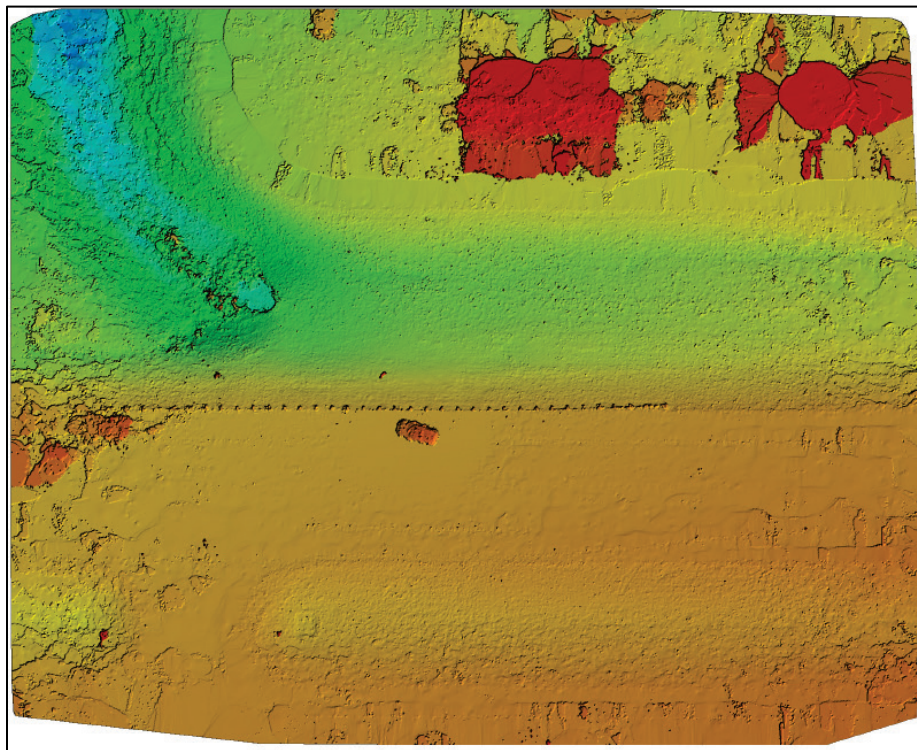


Note: Blue represents lower elevations. Red represents higher elevations.

**Figure 278. Nighttime Digital Surface Model (01/15/2021).**



**Figure 279. Daytime Orthomosaic (01/15/2021)**



Note: Blue represents lower altitude, red represents higher altitude.

**Figure 280. Daytime Digital Surface Model (01/15/2021).**

- There was a significant difference in absolute coordinates for the five points used during the analysis (Figure 273), depending on the UAS and ground control used. A preliminary assessment of the results obtained for the various scenarios indicated that Run 3, Scenario 1i (i.e., Matrice 300 RTK, onboard RTK mode, and with TAMUCC-surveyed GCPs) produced calculated coordinates that were closest to the surveyed GCP coordinates. The research team used this scenario as an additional reference scenario for the analysis. Some of the observations include:
  - When used in standalone GNSS mode, the Mavic 2 Pro produced coordinates that were 8 m (26 ft) off (i.e., 1.4 m [4.6 ft] to the northwest and 8.7 m [29 ft] lower) in comparison to the reference scenario.
  - When used in standalone GNSS mode, the Matrice 300 RTK produced coordinates that were up to 10.3 m (33.8 ft) off (i.e., 2.7 m [8.9 ft] to the northwest and 9.9 m [32 ft] lower) in comparison to the reference scenario. Using Google elevation data resulted in coordinates that were 2.5 m (8.2 ft) off (i.e., 1.7 m [5.6 ft] to the northwest and 1.9 m [6.2 ft] lower) when compared to the reference scenario.
  - For both UASs, using the TAMUCC GCPs produced coordinates that were 3–7 cm (1.2–2.8 inches) off when compared to the surveyed coordinates.
- Distances between the five points used in the analysis (Figure 264) ranged from 2.2 m (7.2 ft) between Points 2 and 5 to 23.5 m (77.1 ft) between Points 3 and 5. The calculated distances were similar in all scenarios except for the scenarios that involved the Mavic 2 Pro or the Matrice 300 RTK in standalone GNSS mode. For the cases where TAMUCC GCPs were used, calculated distances typically varied from 1–4 cm (0.4–1.6 inches). Note: Point 4, which was a suitable checkpoint for the nighttime Mavic 2 Pro run, was not available for the daytime Matrice 300 RTK runs. The reason is that Point 4 was set on the ground after the Matrice 300 RTK runs had taken place.

### **Test 7 (03/20/2021): Simulated Passenger Car Crash Test at the TxDPS Tactical Training Facility in Florence, Texas**

#### *Data Collection*

The research team carried out seven runs during this test. There were two nighttime runs. As in a previous test, the research team gathered two images at each location for these nighttime runs. In addition, this test involved two sets of GCPs, one set prepared by TxDOT and a second set prepared by TAMUCC.

- Run 1: Mavic 2 Pro (GNSS standalone mode, daytime). This run involved the Mavic 2 Pro in standalone mode. It followed the diamond capture protocol, with heights of 55 m (180 ft) for the survey grid pass, 73 m (240 ft) for the overview pass, and 27 m (90 ft) for the evidence pass. Oblique images were taken at 9 m (30 ft) and 14 m (45 ft).
- Run 2: Mavic 2 Pro (GNSS standalone mode, nighttime, built-in LEDs). This run also involved the Mavic 2 Pro, this time relying on its built-in LEDs during the nighttime. The heights for this run were several passes at 11 m (35 ft) and several passes at 15 m (50 ft). Oblique images were at 11 m (35 ft) and 15 m (50 ft).
- Run 3: Matrice 300 RTK (standalone GNSS, daytime). This run involved the Matrice 300 RTK in standalone GNSS mode. It followed the diamond capture protocol, with heights

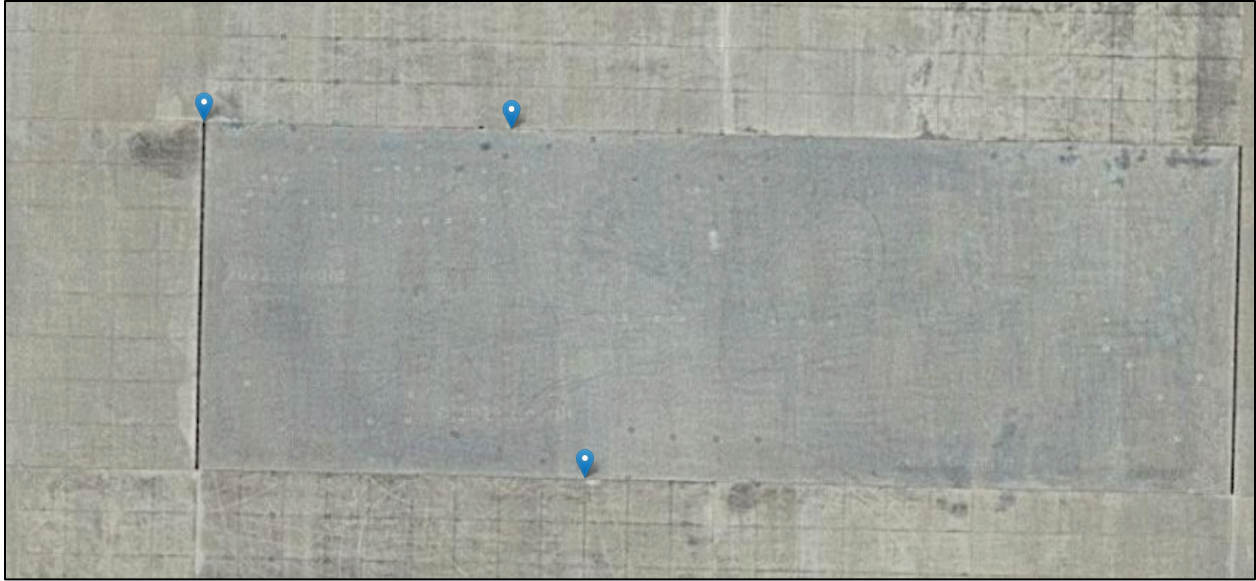
- at 52 m (170 ft) for the survey grid pass, 73 m (240 ft) for the overview pass, and 29 m (95 ft) for the evidence pass. Oblique images were taken at 9 m (30 ft) and 14 m (45 ft).
- Run 4: Matrice 300 RTK (standalone GNSS, autopilot, daytime). This run also involved the Matrice 300 RTK during the daytime, but this time the flight followed a basic autopilot flight plan that consisted of several passes throughout the scene at 46 m (150 ft).
  - Run 5: Matrice 300 RTK (base station RTK, daytime). This run involved the Matrice 300 RTK during the daytime connected to the base station. It followed the diamond capture protocol, with heights at 52 m (170 ft) for the survey grid pass, 73 m (240 ft) for the overview pass, and 29 m (95 ft) for the evidence pass. Oblique images were taken at 9 m (30 ft) and 14 m (45 ft).
  - Run 6: Matrice 300 RTK (onboard RTK, daytime). This run involved the Matrice 300 RTK during the daytime, using the onboard RTK mode. It followed the diamond capture protocol, with heights at 52 m (170 ft) for the survey grid pass, 73 m (240 ft) for the overview pass, and 29 m (95 ft) for the evidence pass. Oblique images were taken at 9 m (30 ft) and 14 m (45 ft).
  - Run 7: Matrice 300 RTK (onboard RTK, nighttime, built-in LEDs and spotlight). This run involved the Matrice 300 RTK during the nighttime, using the onboard RTK mode and built-in LEDs, as well as the spotlight for the oblique images. The heights for this run were several passes at 11 m (35 ft) and several passes at 15 m (50 ft). Oblique images were at 11 m (35 ft) and 12 m (40 ft).

### *Data Processing*

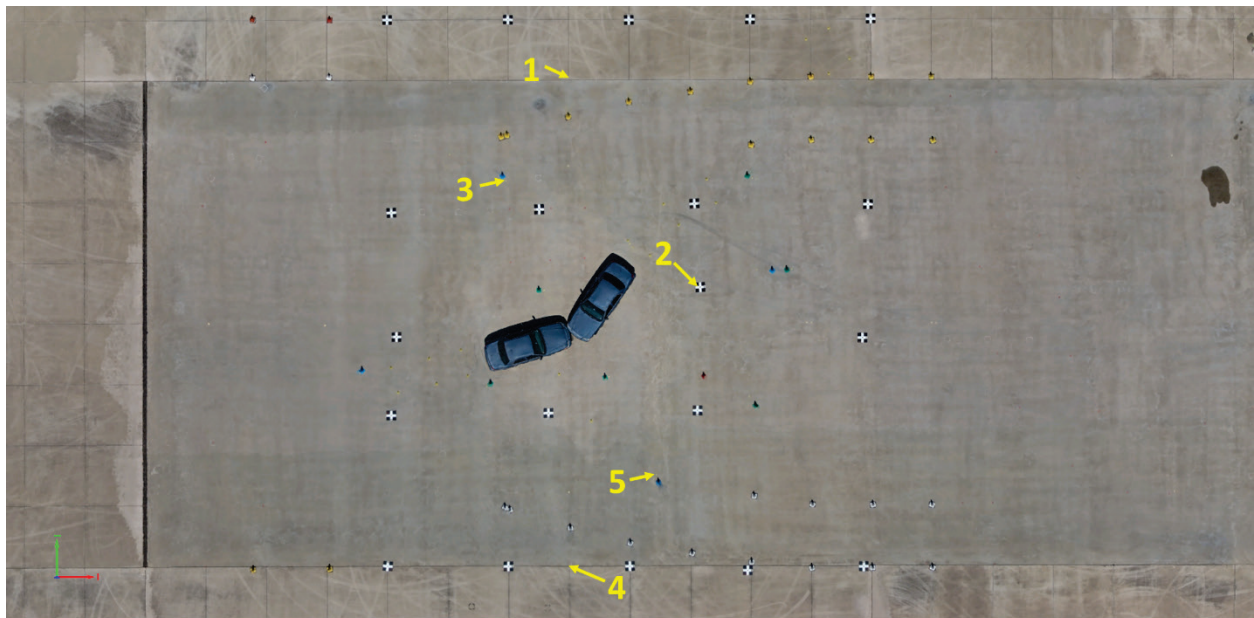
This test was the second test at the TxDPS Tactical Training Facility at Florence, Texas. It involved GCPs prepared by TxDOT and TAMUCC. The test included a large number of daytime and nighttime runs under a variety of UAS, ground control, and lighting conditions.

Test 6 was conducted at a location that mimics a typical divided highway with luminaire poles, but Test 7 was conducted at a skid pad location that is uniquely designed to test driving conditions on flooded surfaces. This skid pad location did not have high-mast lights. Another difference between the Test 6 and Test 7 locations was the pavement surface. Both surfaces were concrete surfaces. However, the skid pad was considerably smoother than a typical concrete pavement. This additional smoothness resulted in a lack of texture that added significant challenges to the SfM photogrammetry process. All runs were conducted on a dry surface because the water pipes that feed the skid pad area were not operational during the day of the test.

The research team gathered Google elevation data for three points, as shown in Figure 281. The research team also identified five points for the analysis, including GCPs surveyed by TAMUCC and TxDOT, as shown in Figure 282.



**Figure 281. Google Elevation Data (03/20/2021).**



**Figure 282. Scene's Manual Point Locations (03/20/2021).**

The research team processed the following runs and scenarios:

- Run 1: Mavic 2 Pro (GNSS standalone mode, daytime):
  - Scenario 1a (no GCPs).
  - Scenario 1b (TAMUCC-surveyed GCPs).
  - Scenario 1c (TxDOT-surveyed GCPs).
  - Scenario 1d (Google elevation data).
- Run 2: Mavic 2 Pro (GNSS standalone mode, nighttime, built-in LEDs):
  - Scenario 1a (no GCPs).

- Scenario 1b (TAMUCC-surveyed GCPs).
- Scenario 1c (TxDOT-surveyed GCPs).
- Run 3: Matrice 300 RTK (standalone GNSS, daytime):
  - Scenario 1a (no GCPs).
  - Scenario 1b (TAMUCC-surveyed GCPs).
  - Scenario 1c (TxDOT-surveyed GCPs).
- Run 4: Matrice 300 RTK (standalone GNSS, autopilot, daytime):
  - Scenario 1a (not including obliques) (standalone GNSS, automated flight plan).
  - Scenario 1b (including obliques) (standalone GNSS, automated flight plan).
- Run 5: Matrice 300 RTK (base station RTK, daytime):
  - Scenario 1a (no GCPs).
  - Scenario 1b (TAMUCC-surveyed GCPs).
  - Scenario 1c (TxDOT-surveyed GCPs).
- Run 6: Matrice 300 RTK (onboard RTK, daytime):
  - Scenario 1a (no GCPs).
  - Scenario 1b (TAMUCC-surveyed GCPs).
  - Scenario 1c (TxDOT-surveyed GCPs).
- Run 7: Matrice 300 RTK (onboard RTK, nighttime, built-in LEDs and spotlight):
  - Scenario 1a (no GCPs).
  - Scenario 1b (TAMUCC-surveyed GCPs).
  - Scenario 1c (TxDOT-surveyed GCPs).

## *Results*

A review of the scenarios and corresponding results, as shown in Table 146, Table 147, Table 148, and Table 149, yields the following observations:

- In general, the Mavic 2 Pro and the Matrice 300 RTK performed as expected. For most scenarios, the research team was able to gather all the imagery needed, run the three SfM stages in Pix4D, build usable 3D models, prepare orthomosaics and DSMs, obtain coordinates of critical points, and measure distances between those points. Processing some of the runs was challenging because of a combination of factors, including nighttime lighting and an extremely smooth surface.
- The average GSD was about 7 mm (0.28 inches) for the Mavic 2 Pro daytime run. There were 550,000 2D keypoints and 160,000 3D points for the BA process. After densification, the result was a 3D densified model containing 3.9 million points. GSD was about 3 mm (0.12 inches) for the nighttime run. There were 151,000 2D keypoints and 63,000 3D points for the BA process. After densification, the result was a 3D densified model containing 1.8 million points.
- For the Matrice 300 RTK daytime runs, the average GSD ranged from 6.0–7.2 mm (0.24–0.28 inches). There were 800,000 2D keypoints and 250,000 3D points for the BA process. After densification, the result was 3D densified models containing 3–11 million points.
- For the daytime runs, the number and density of oblique images were adequate to develop 3D models of the vehicles, having a sufficient level of detail for typical crash reconstruction efforts.



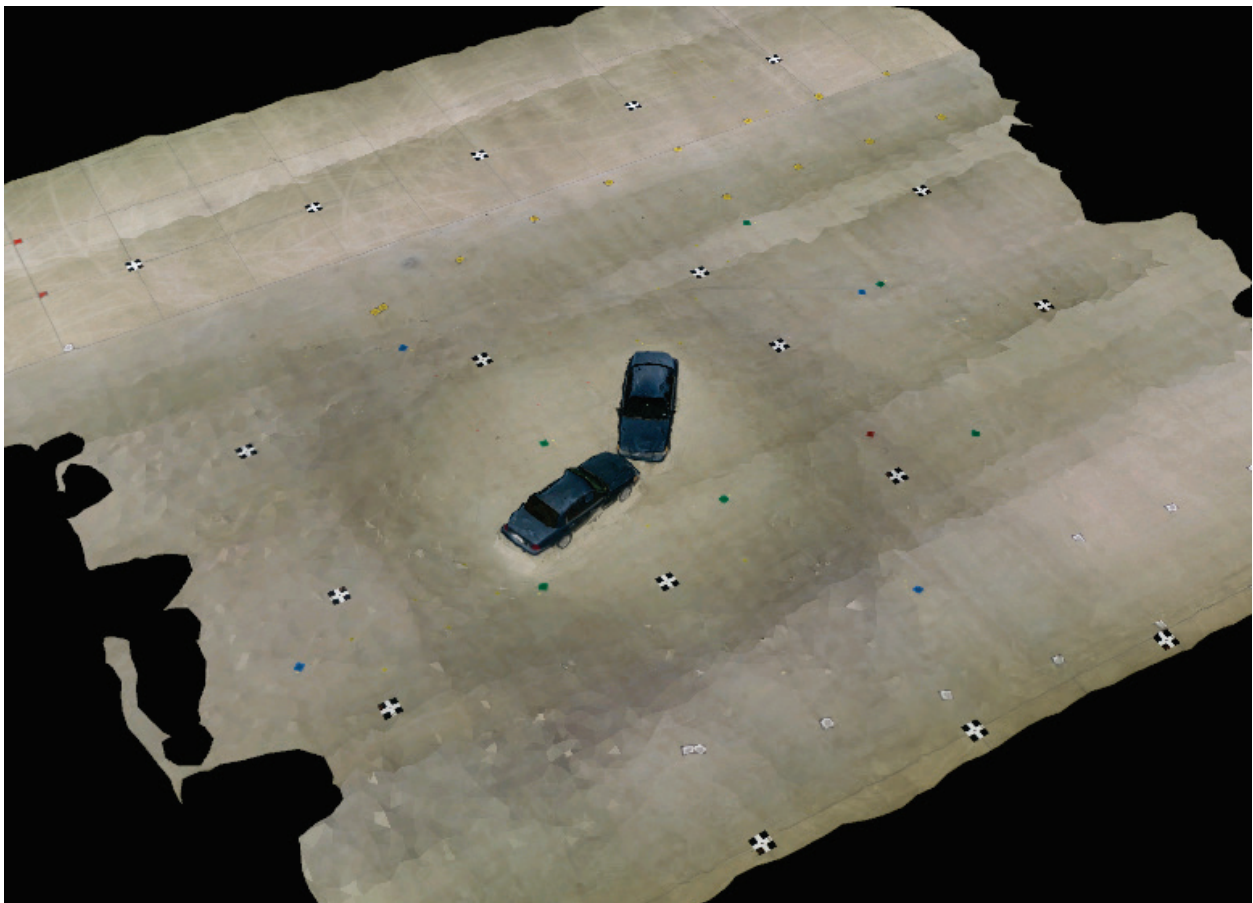
- For the Matrice 300 RTK nighttime run, it was not possible to build a workable model. The camera calibration percentage was only 10 percent. There were 5,000 2D keypoints and less than 2,000 3D points for the BA process. The research team gathered double images and a second round of oblique images (with the first round at 60 degrees and the second round at 45 degrees). The research team also experimented with a variety of settings in Pix4D, but the result was not substantially better.
- For the Mavic 2 Pro nighttime run, it was possible to build a workable model, but the quality was not enough to be able to extract coordinates or measure distances reliably. After experimenting with a variety of settings in Pix4D, the camera calibration percentage reached 95 percent, but the number of 2D keypoints was only 151,000 and the number of 3D points was only 63,000.
- There was a significant difference in absolute coordinates for the five points used during the analysis (Figure 282), depending on the UAS and ground control used. A preliminary assessment of the results obtained for the various scenarios indicated that Run 1, Scenario 1c (i.e., Mavic 2 Pro, TxDOT-surveyed GCPs) produced calculated coordinates that were closest to the surveyed TxDOT GCP coordinates. The research team used this scenario as an additional reference scenario for the analysis. Some of the observations include:
  - For daytime runs, when used in standalone GNSS mode, the Mavic 2 Pro produced coordinates that were 1.2–5.6 m (3.9–18 ft) off compared to the reference scenario. When used in standalone GNSS mode, the Matrice 300 RTK produced coordinates that were about 4 m (13 ft) off compared to the reference scenario.
  - For both UASs, using TAMUCC or TxDOT GCPs produced coordinates that were 1–5 cm (0.4–2 inches) off compared to those of the reference scenario.
- Distances between the five points used in the analysis (Figure 282) ranged from 7.4 m (24 ft) between Points 1 and 3 to 30.5 m (100 ft) between Points 1 and 4. The calculated distances were similar in all scenarios. In most cases, calculated distances varied from 0.5–11 cm (0.2–4.3 inches). However, larger offsets were not necessarily correlated with longer distances.
- There was not a significant difference between TAMUCC GCP-derived point coordinates and TxDOT GCP-derived coordinates. Similar consideration applies to distances between points. This result is consistent with observations made earlier in the chapter regarding differences between both sets of GCPs.

Processing the nighttime runs in Pix4D was challenging. Whether using the built-in LEDs or supplemental lighting, nighttime SfM processing depends heavily on the type and characteristics of the surface texture. In this case, the situation became more challenging because the two vehicles were of the same type, shape, and color. To arrive at the model shown in Figure 283, the research team experimented with the following settings in Pix4D (136):

- Initial processing options:
  - Keypoint image scale: Rapid (to enable a lower image scale).
  - Matching image pairs: Custom.
    - Triangulation of image location option: On (typically used if images have geolocation and it is possible to match images that are connected by a triangle).

- Use distance option: Off (option is typically On if the relative distance between images is uniform).
    - Matching strategy: Geometrically verified matching (typically used to discard geometrically inconsistent matches, e.g., when many similar features are present).
  - Point cloud and mesh options:
    - Point cloud densification:
      - Image scale setting:  $\frac{1}{4}$  (quarter image size, fast) (fewer points are computed than with the default half-image size, but more points are computed in areas with features that cannot be easily matched).
      - Multiscale option: On (to enable additional 3D points to be computed on multiple image scales).
      - Point density setting: Low (Fast) (typically used to generate low-density point clouds).

It was also necessary to remove several images and manually recalibrate cameras that Pix4D had calibrated incorrectly (137). Figure 284 shows the camera views both before and after applying the changes in Pix4D.



**Figure 283. Mavic 2 Pro Nighttime Model (03/20/2021).**

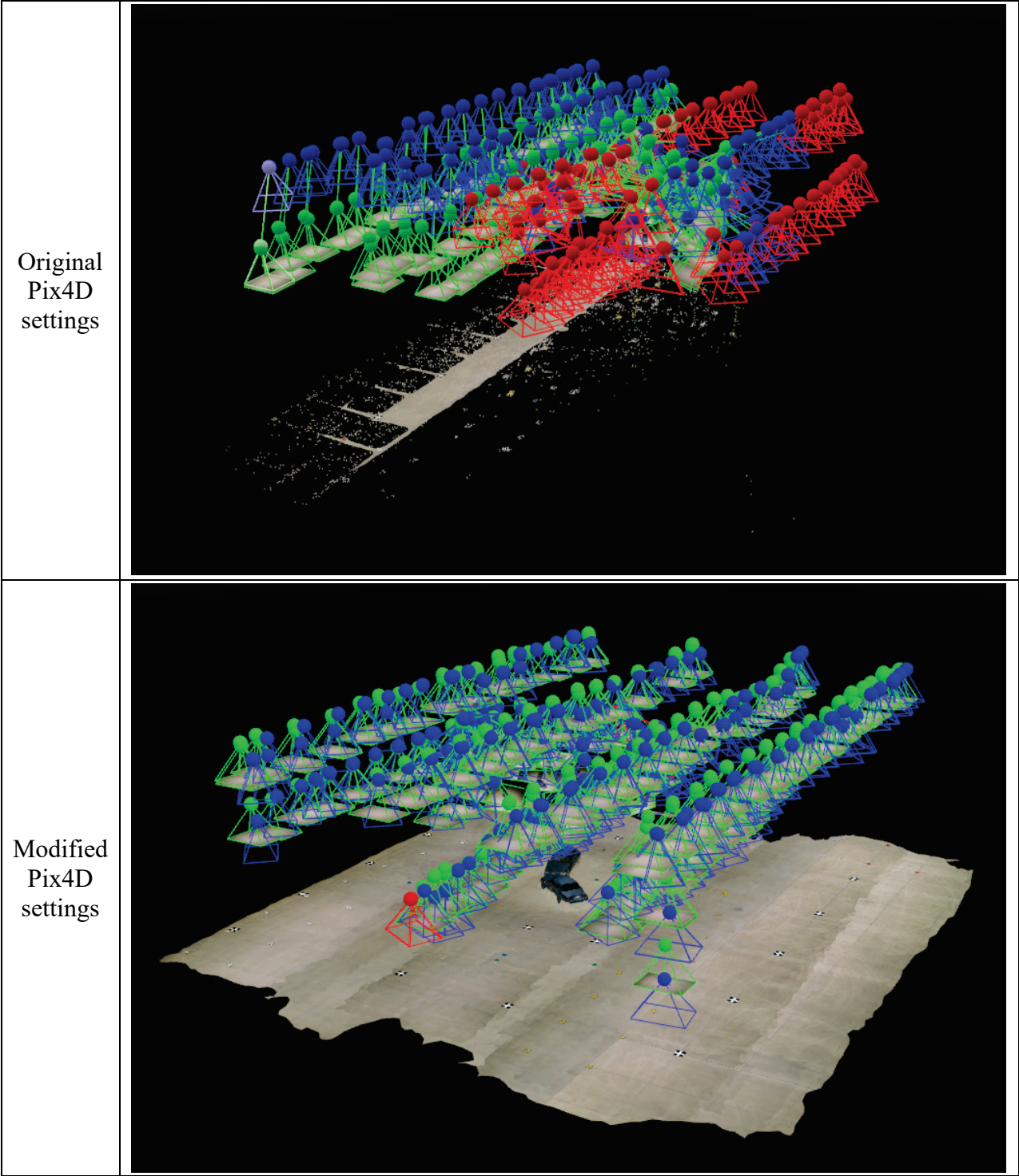


Figure 284. Ray Cloud Views for Mavic 2 Pro Nighttime Run.

## General Trends

The previous sections provided detailed observations and lessons learned for each test and the corresponding runs and scenarios. This section provides a summary of high-level trends and lessons learned from all the tests, runs, and scenarios combined. For the analysis, the research team focused on the following topics:

- Impact of ground control on SfM results and distances between points.
- Coordinate system settings in Pix4D.
- Effect of calibration method in Pix4D.
- Effect of scale constraint in Pix4D.

### *Impact of Ground Control on SfM Results and Distances between Points*

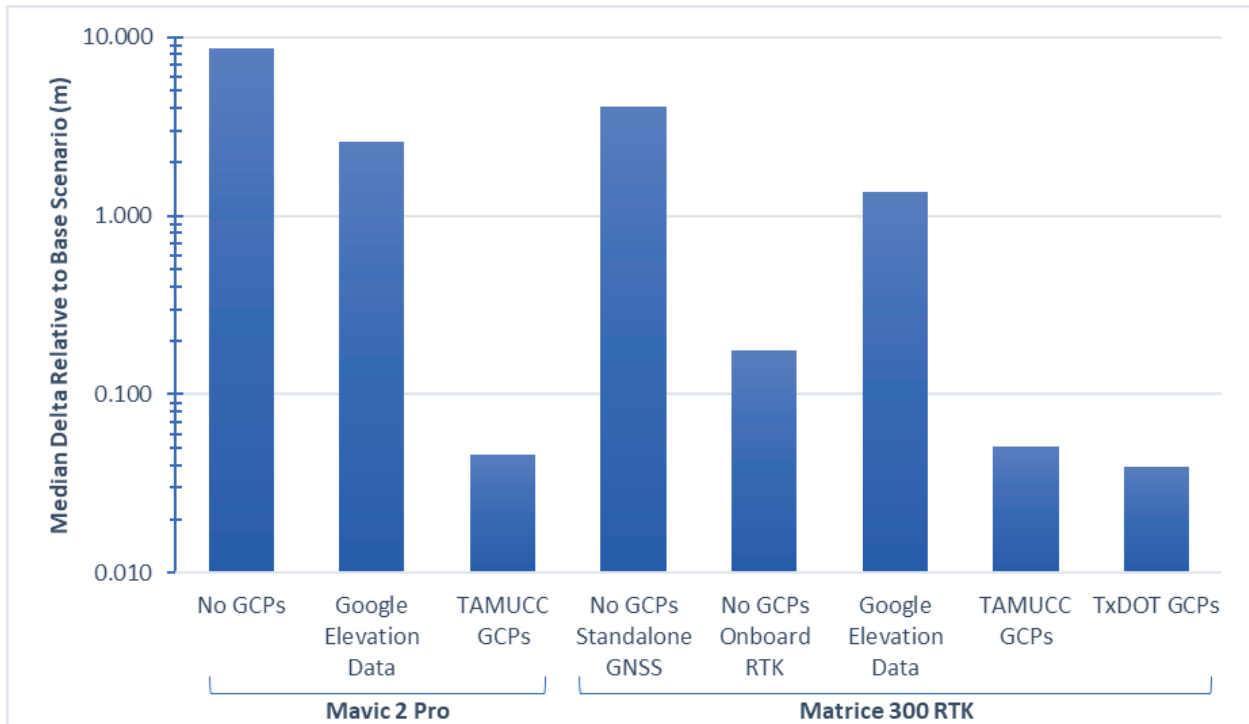
Not surprisingly, using surveyed GCPs had a positive impact on the SfM process and therefore the positional accuracy of point locations and distances between points. To quantify this impact, the research team completed three analyses. The first analysis involved comparing point location deltas with respect to the reference scenario that was used for each test. The second analysis was similar except the deltas were calculated with respect to surveyed checkpoint locations. The third analysis involved comparing deltas of distances between points using coordinates of checkpoints.

### Deltas with Respect to Reference Scenarios

For each test, the reference scenario was the closest to the actual coordinates (if GCPs were used) or the scenario that exhibited the lowest errors within the Pix4D environment. Figure 285 shows 3D distance deltas for each scenario relative to the corresponding reference scenario. For completeness, the figure shows the number of data points per category along with several metrics: median, average, minimum, and maximum. The bar chart shows median values.

Overall, the largest deltas corresponded to scenarios that did not include any GCPs. In standalone GNSS mode, the Mavic 2 Pro had a median delta of 8.7 m (28 ft) compared to 4.1 m (13 ft) for the Matrice 300 RTK. Notice the range of deltas for both UASs (i.e., 3.2–10.2 m [10–33 ft] for the Mavic 2 Pro and 0.11–32 m [0.35–104 ft] for the Matrice 300 RTK). Readers should also note the substantial decrease in delta values when onboard RTK was activated for the Matrice 300 RTK.

Using Google elevation data helped to reduce deltas for both the Mavic 2 Pro and the Matrice 300 RTK. For the Mavic 2 Pro, the median delta decreased from 8.7 m (28 ft) to 2.6 m (8.5 ft). For the Matrice 300 RTK, the median delta decreased from 4.1 m (13 ft) to 1.3 m (4.3 ft). Using Google elevation data also had a positive impact on delta variability. Using surveyed GCPs had a dramatic impact on the magnitude of the deltas and their variability. For both UASs, the median delta decreased to about 5 cm (2 inches) when using TAMUCC GCPs and to less than 4 cm (1.6 inches) when using TxDOT GCPs.



Metric	Mavic 2 Pro			Matrice 300 RTK				
	No GCPs	Google Elevation Data	TAMUCC GCPs	No GCPs		Google Elevation Data	TAMUCC GCPs	TxDOT GCPs
				Standalone GNSS	Onboard RTK			
Count	15	14	18	18	34	25	48	15
Median (m)	8.681	2.613	0.046	4.112	0.175	1.349	0.051	0.039
Average (m)	7.686	10.396	0.040	13.174	0.347	1.366	0.072	0.035
Min (m)	3.222	2.097	0.013	0.106	0.099	1.303	0.019	0.021
Max (m)	10.160	26.472	0.054	31.817	1.465	1.429	0.219	0.045

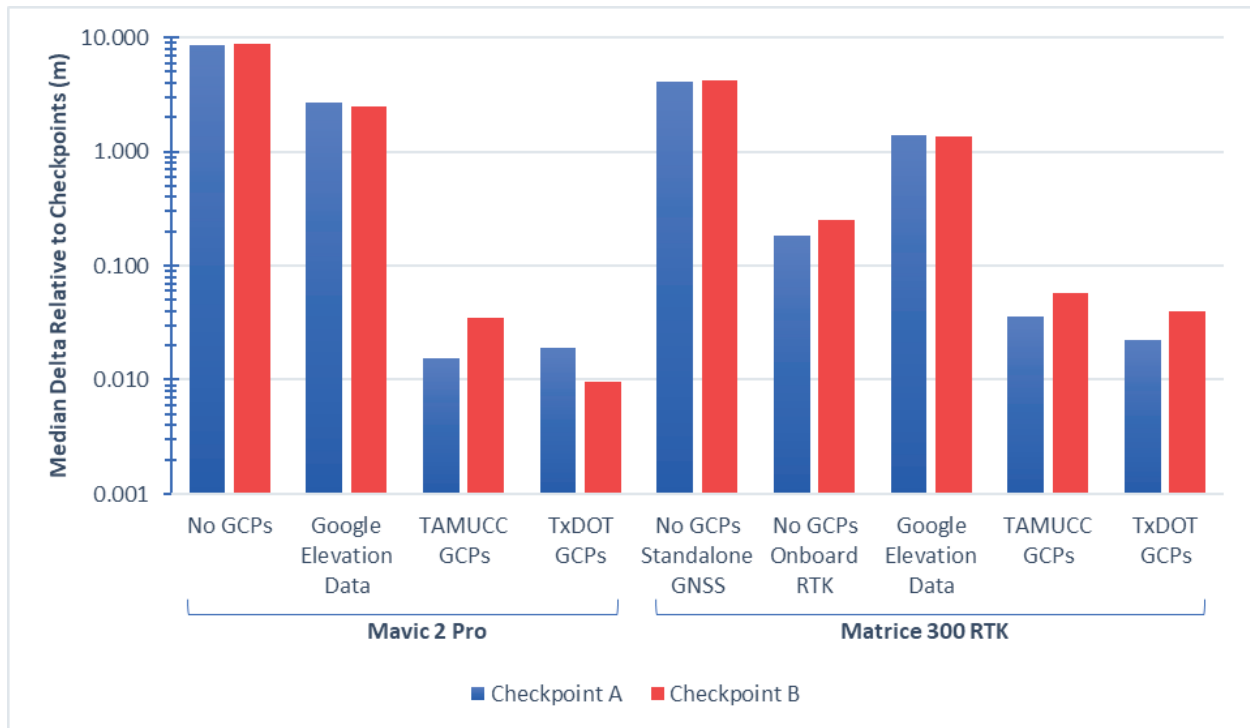
**Figure 285. 3D Distance Deltas with Respect to Base Scenario Coordinates.**

Deltas with Respect to Surveyed Checkpoints

The research team obtained similar results when calculating 3D distance deltas with respect to surveyed checkpoint locations. In this case, the number of data points was lower than the analysis above because only Points 3 and 5 (which corresponded to two surveyed checkpoints labeled A and B) were used for this part of the analysis. Figure 286 shows these deltas grouped by checkpoint, UAS, and type of scenario.

The results were similar for both Checkpoint A and Checkpoint B. For example, for Checkpoint A, the largest deltas corresponded to scenarios that did not include any GCPs. In standalone GNSS mode, the Mavic 2 Pro had a median delta of 8.5 m (28 ft) compared to 4.1 m (13 ft) for the Matrice 300 RTK. The median delta decreased to 0.18 m (0.59 ft) when onboard RTK was activated for the Matrice 300 RTK. Using Google elevation data helped to reduce deltas for both the Mavic 2 Pro and the Matrice 300 RTK. For the Mavic 2 Pro, the median delta decreased from 8.5 m (28 ft) to 2.7 m (8.9 ft). For the Matrice 300 RTK, the median delta decreased from 4.1 m (13 ft) to 1.4 m (4.6 ft). For the Mavic 2 Pro, the median delta decreased to

1.6 cm (0.63 inches) when using TAMUCC GCPs and 1.9 cm (0.75 inches) when using TxDOT GCPs. For the Matrice 300 RTK, the median delta decreased to 3.6 cm (1.4 inches) when using TAMUCC GCPs and 2.2 cm (0.87 inches) when using TxDOT GCPs.



Metric		Checkpoint A					Checkpoint B				
		No GCPs		Google Elevation Data	TAMUCC GCPs	TxDOT GCPs	No GCPs		Google Elevation Data	TAMUCC GCPs	TxDOT GCPs
		GNSS	Onboard RTK				GNSS	Onboard RTK			
Mavic 2 Pro	Count	4		3	4	1	4		3	4	1
	Median (m)	8.507		2.673	0.016	0.019	8.793		2.480	0.035	0.009
	Average (m)	7.100		10.419	0.017	0.019	8.149		10.366	0.052	0.009
	Minimum (m)	1.347		2.083	0.008	0.019	4.769		2.125	0.007	0.009
	Maximum (m)	10.047		26.501	0.027	0.019	10.240		26.492	0.131	0.009
Matrice 300 RTK	Count	5	7	5	14	3	5	7	5	14	3
	Median (m)	4.122	0.183	1.389	0.036	0.022	4.157	0.250	1.354	0.057	0.040
	Average (m)	13.129	0.339	1.367	0.070	0.028	13.227	0.416	1.341	0.074	0.037
	Minimum (m)	0.142	0.133	1.306	0.023	0.020	0.165	0.169	1.266	0.036	0.025
	Maximum (m)	31.763	1.297	1.420	0.227	0.041	31.826	1.528	1.416	0.171	0.046

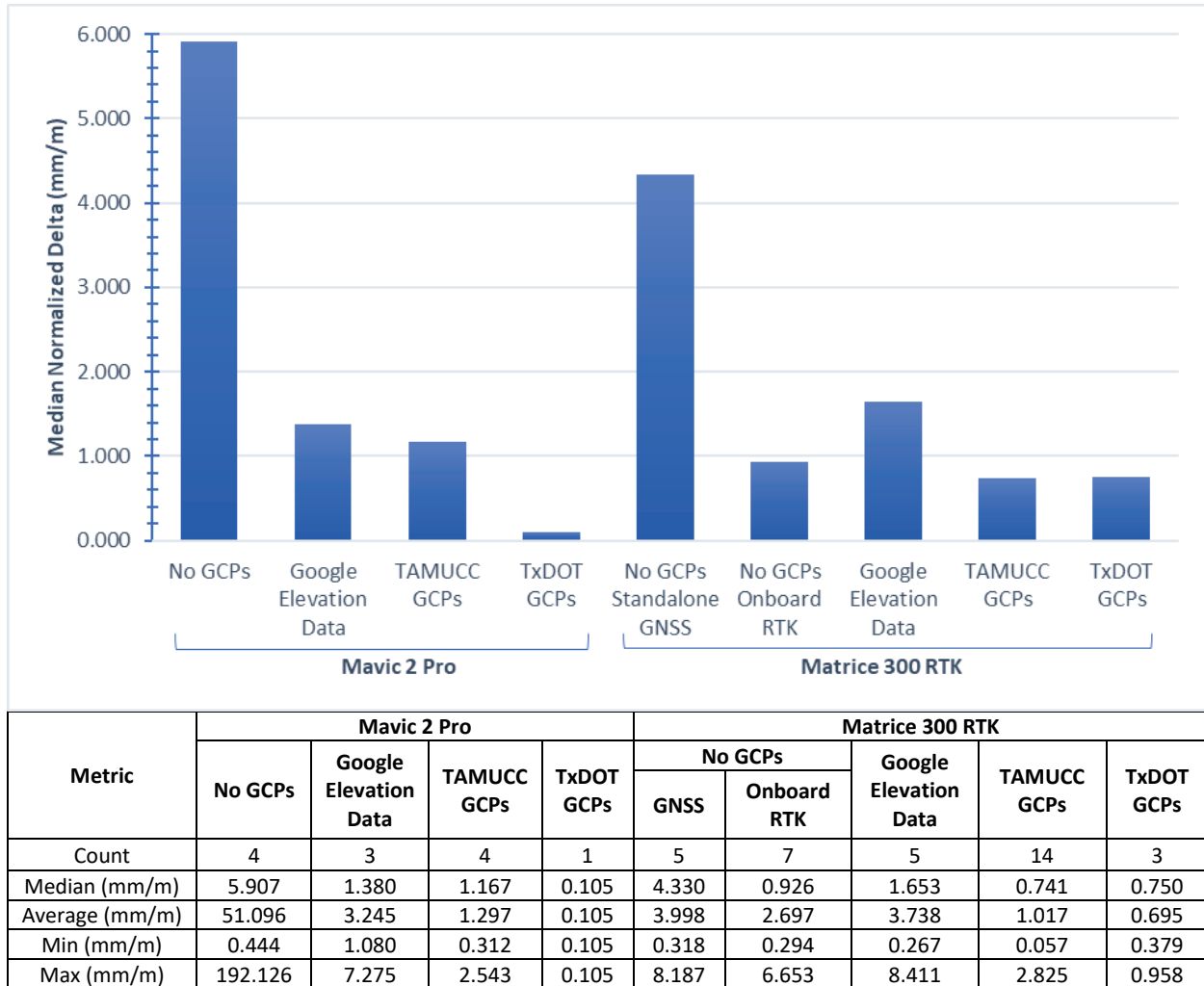
**Figure 286. 3D Distance Deltas with Respect to Surveyed Checkpoint Coordinates.**

Deltas with Respect to Distances between Points

The analysis involved comparing deltas associated with 3D distances between surveyed Checkpoints A and B and the corresponding distances between tie points using calculated coordinates in Pix4D. Because distances between the points were different for each test, the research team normalized deltas by dividing each delta (in mm) by the corresponding distance (in m) between the surveyed points.

As Figure 287 shows, the largest 3D distance deltas occurred for the Mavic 2 Pro in standalone GNSS mode, followed by the Matrice 300 RTK in standalone GNSS mode (5.9 mm/m

[0.071 inches/ft] and 4.3 mm/m [0.052 inches/ft], respectively). Using Google elevation data resulted in a decrease in delta to about 1.4 mm/m (0.017 inches/ft) for the Mavic 2 Pro and 1.7 mm/m (0.020 inches/ft) for the Matrice 300 RTK. Using TAMUCC GCPs, the median delta decreased to 1.2 mm/m (0.014 inches/ft) for the Mavic 2 Pro and 0.74 mm/m (0.0089 inches/ft) for the Matrice 300 RTK. Deltas were lower when using TxDOT GCPs (although the sample size was too small).



**Figure 287. Normalized 3D Distance Deltas with Respect to Distance between Checkpoints A and B.**

### Coordinate System Settings in Pix4D

It is critical to correctly identify all coordinate system parameters for each step in the SfM process, particularly when using distinct kinds of ground control, all of which involve different hardware, software, and business processes. In the case of Pix4D, the software requires the user to select imagery, GCP, and output coordinate systems. By default, Pix4D assigns the GCP and output coordinate systems to be the same as that associated with the imagery. If the GCP and output coordinate systems are different from that of the imagery, it becomes critical to document and, if necessary, transform coordinate system parameters before use.

The research team used the following coordinate system for the imagery during the data collection phase:

- Datum: NAD83(2011).
- Horizontal coordinates: State Plane Texas Central (meters).
- Vertical coordinates: Geoid height above GRS80 ellipsoid: 0 meters.

This coordinate system was also the coordinate system used for the TAMUCC GCPs and output coordinate system in Pix4D.

The TxDOT GCPs were in the following coordinate system:

- Datum: NAD83(2011).
- Horizontal coordinates: State Plane Texas Central (U.S. survey ft).
- Vertical coordinates: NAVD 88 GEOID12B.

In this case, the research team first converted the GCPs coordinates from U.S. survey ft to meters, and then converted the vertical coordinates from NAVD 88 GEOID12B to NAD83 ellipsoid height (m). Completing this conversion prior to importing the GCP data into Pix4D was necessary because Pix4D does not provide direct support for NAVD 88 GEOID12B.

The Google elevation data were in the following coordinate system:

- Datum: World Geodetic System 1984 (WGS 84).
- Horizontal coordinates: WGS 84.
- Vertical coordinates: MSL EGM96 Geoid.

In this case, the research team selected these coordinate system parameters directly in Pix4D.

### *Effect of Calibration Method in Pix4D*

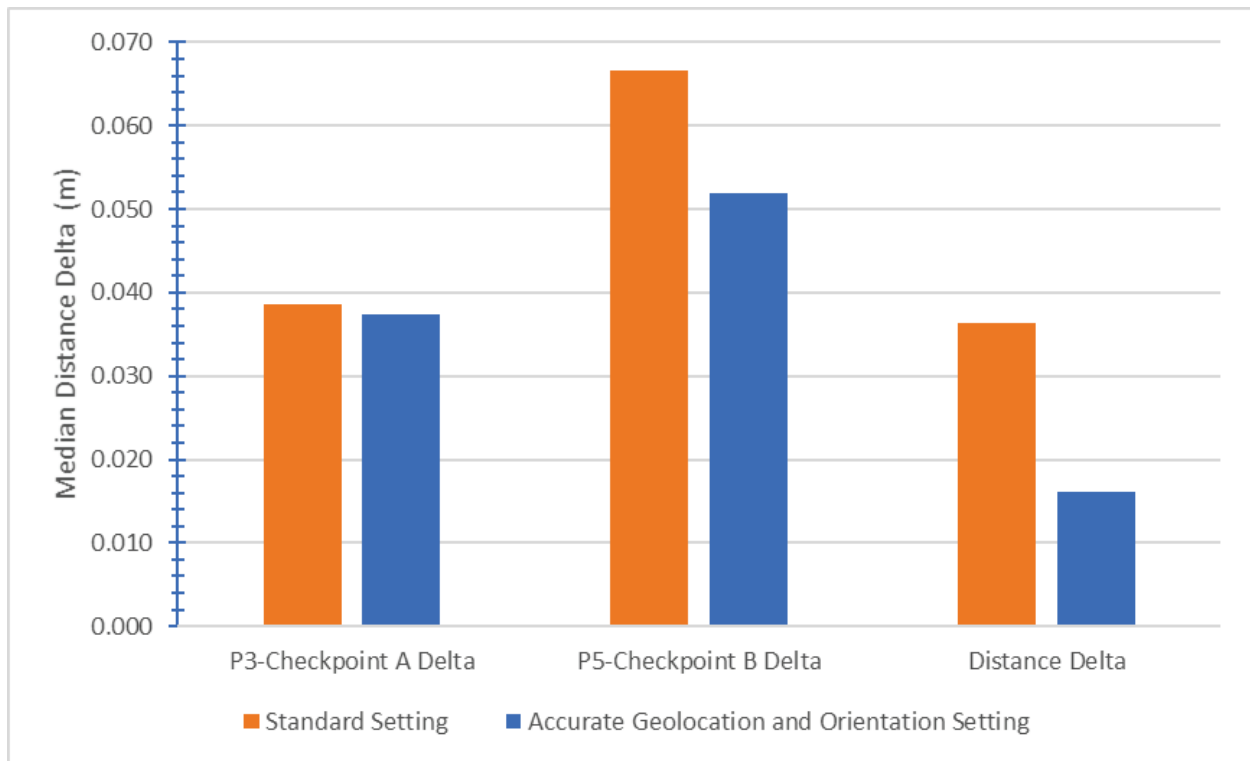
By default, Pix4D uses a standard workflow setting to complete image calibrations during initial processing. When images have accurate geolocations (e.g., by using RTK or PPK GNSS methods), Pix4D recommends using the accurate geolocation and orientation calibration method. This calibration method still requires images to be geolocated and oriented via the SfM BA, but it weighs more heavily the image geolocations based on the ground control parameters associated with each image.

Initially, the research team used the standard workflow for all the runs. However, results improved in several cases when the research team used the accurate geolocation and orientation calibration method. In some instances, using the standard calibration method, Pix4D could not achieve an adequate number of calibrated images for a useful result. The only way to ensure feature matching led to a usable result was by selecting the accurate geolocation and orientation calibration method. To assess this effect, the research team compared coordinates of two specific points in Pix4D (P3 and P5) against the corresponding coordinates of surveyed checkpoints (Checkpoint A and Checkpoint B, respectively), both with the standard setting and the accurate geolocation and orientation setting. The research team also calculated distances between points



P3 and P5 and compared those distances against the corresponding distances between Checkpoint A and Checkpoint B.

Figure 288 shows the results of the analysis. For both points P3 and P5, using the accurate geolocation and orientation setting decreased the delta between the locations of those points and the corresponding checkpoint locations. For Point 3, the median delta decreased from 3.9 cm to 3.7 cm. For Point 5, the median offset decreased from 6.7 cm to 5.2 cm. There was also a decrease in distance deltas by using the accurate geolocation and orientation setting instead of the standard setting. When compared against the distance between Checkpoints A and B, the median distance between Points P3 and P5 decreased from 3.6 cm to 1.6 cm.



Metric	Standard Setting			Accurate Geolocation and Orientation Setting		
	P3-Checkpoint A Delta (m)	P5-Checkpoint B Delta (m)	Distance Delta (m)	P3-Checkpoint A Delta (m)	P5-Checkpoint B Delta (m)	Distance Delta (m)
Median	0.039	0.067	0.036	0.037	0.052	0.016
Average	0.058	0.072	0.049	0.049	0.071	0.041
Minimum	0.022	0.038	0.003	0.022	0.036	0.002
Maximum	0.172	0.124	0.112	0.097	0.171	0.179

**Figure 288. Effect of Using the Accurate Geolocation and Orientation Setting in Pix4D.**

#### *Effect of Scale Constraint in Pix4D*

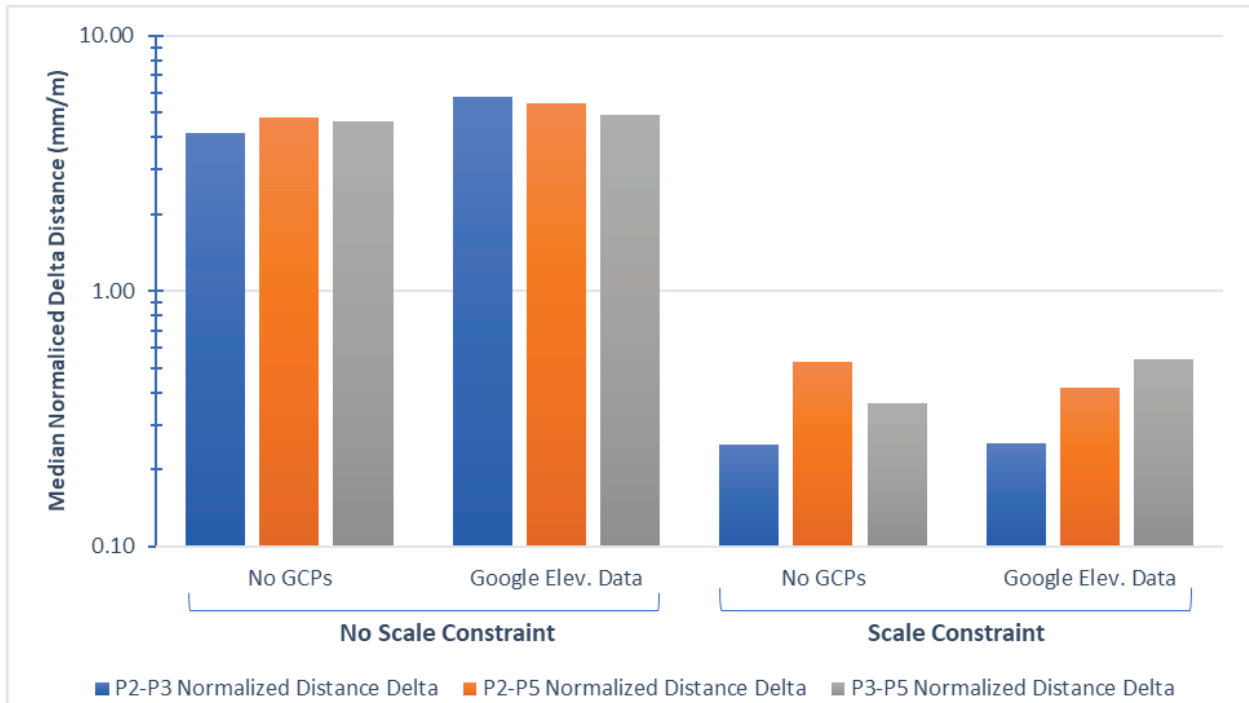
A recommended practice for crash reconstructions using UASs is to measure distances between targets in the field and use those distances for scaling purposes during the SfM process. The research team used surveyed checkpoints for most of the field tests, which made it unnecessary

to measure distances in the field. Nevertheless, it was of interest to evaluate the impact of using the scale constraint function in Pix4D.

In general, using the scale constraint had a negligible impact on the SfM process for scenarios that involved the use of surveyed GCPs. As described above, the research team used the Accurate Geolocation and Orientation calibration method for these scenarios, which gave more weight to the ground control parameters associated with each image.

The impact was significant for standalone GNSS and Google elevation data scenarios. To quantify this impact, the research team calculated distances between surveyed GCPs and applied these distances using the scale constraint in Pix4D. As mentioned previously, the positional accuracy of the surveyed GCPs was centimeter-level, with 1–2 cm (0.4–0.8 inch) RMSE values, which made distances between GCPs reliable. Depending on the GCPs used, this positional accuracy level could translate to a linear uncertainty of 0.3–0.5 mm/m (0.0036–0.006 inches/ft).

Figure 289 shows normalized distance deltas between pairs of GCPs and corresponding tie points within the Pix4D environment, both without and with the scale constraint. The sample size was small. Nevertheless, Figure 289 shows that, without the scale constraint applied, the median delta of the normalized distances was 4–5 mm/m (0.048–0.06 inches/ft), but this delta decreased to 0.3–0.5 mm/m (0.0036–0.006 inches/ft) after applying the scale constraint, therefore confirming the benefit of using the scale constraint method for crash reconstructions using UASs.



		No Scale Constraint			Scale Constraint		
		P2-P3 Normalized Distance Delta	P2-P5 Normalized Distance Delta	P3-P5 Normalized Distance Delta	P2-P3 Normalized Distance Delta	P2-P5 Normalized Distance Delta	P3-P5 Normalized Distance Delta
No GCPs	Count	7	7	7	7	7	7
	Median (mm/m)	4.17	4.79	4.61	0.25	0.53	0.36
	Average (mm/m)	30.69	31.22	30.99	0.80	1.11	0.90
	Minimum (mm/m)	0.10	0.58	0.32	0.11	0.18	0.02
	Maximum (mm/m)	191.29	190.92	191.56	3.72	4.22	4.09
Google Elevation Data	Count	4	4	4	4	4	4
	Median (mm/m)	5.78	5.47	4.91	0.25	0.42	0.54
	Average (mm/m)	7.75	14.71	4.90	0.33	0.39	0.51
	Maximum (mm/m)	18.70	46.30	8.41	0.76	0.65	0.92

**Figure 289. Deltas for Distances between Points with and without Scale Constraint.**

### Nighttime Settings in Pix4D

Several nighttime flights were not successful. The number of 2D keypoints and corresponding 3D points for the BA process was low, typically because the images were blurry or because there was not enough detail or texture in the images. Using the supplemental spotlight on the Matrice 300 RTK had a negative effect because the spotlight created a bright circle in the middle of the image, and the camera compensated for the increase in brightness by reducing the exposure time. As a result, images were brighter where the spotlight projected its narrow light beam but were darker elsewhere. Consequently, the number of 2D keypoints and 3D points was lower when using the spotlight.

The research team had a mixed experience illuminating nighttime scenes using onboard LED lights. In several cases, it was necessary to use supplemental lighting (e.g., from vehicle headlights or high-mast lights). The research team also experimented with techniques such as lowering the UAS altitude and taking double pictures at each location where the UAS stopped. Flying the UAS on autonomous mode at night did not work because the camera was not sensitive enough to take reliable pictures while moving, and the remote controller software was not optimized for nighttime operations.

Nighttime SfM processing was particularly challenging in situations when there was not enough surface texture. During the data collection at the TxDPS Tactical Training Facility near Florence, Texas, an additional challenge was that the two vehicles used during the test were of the same type, shape, and color. With the Matrice 300 RTK nighttime run, it was not possible to build a workable model. With the Mavic 2 Pro, it was possible to build a workable model, but the quality was not enough to be able to extract coordinates or measure distances reliably. To arrive at the workable model, it was necessary to change several settings in Pix4D, remove several images, and manually recalibrate several cameras that Pix4D had calibrated incorrectly.

## CHAPTER 6. CONCLUSIONS AND RECOMMENDATIONS

### CONCLUSIONS

TxDOT has a strategic interest in the use of UASs to support a variety of initiatives, including traffic incident management. Several challenges exist for the effective use of UASs for this type of application. Operational challenges include current and evolving regulations, limitations in platform endurance, difficulty operating UASs along interstate highways and urban corridors, and suboptimal environmental conditions such as high winds, rain, low ambient lighting, or fog.

This research documented key challenges and developed and tested procedures for data collection and processing. The research included a review of historical crash data trends in Texas to establish correlations with environmental factors, simulation of the effect of environmental factors on the quality of photogrammetric data collected with UASs, field tests of UAS-based crash data collection activities under a variety of conditions, development of recommendations and guidelines for UAS operations under suboptimal environmental conditions, and development of recommendations for updates of the TxDOT *Unmanned Aircraft System (UAS) Flight Operations and User's Manual (4)*.

#### Crash Data Analysis

The research team gathered and processed 10 years (2010 to 2019) of crash data. The data included all the records from the crash, unit, primary person, and person tables. The research team prepared a series of figures and charts to develop a high-level understanding of crash locations and trends. In general:

- The number of crashes increased statewide until about 2016, and then it remained roughly at the same level. Statewide, the increase was about 40 percent from 2010 to 2016, which corresponds to an annual growth rate of about 6 percent.
- All five metro areas followed the overall statewide trend. However, crashes in the Austin, Dallas, Houston, and San Antonio areas increased faster than the statewide trend. The Houston area experienced the fastest growth in the number of crashes of all five metro areas. By comparison, crashes in the Fort Worth area increased more slowly than the statewide trend. Fort Worth was the only metro area that experienced a steady decline in crashes since 2016.
- The number of fatal crashes increased statewide until 2016, at which point there was a steady decline.
- All metro areas showed a decrease in the number of fatal crashes from 2016 to 2019.
- Overall, from 2010 to 2019, fatal crashes in all metro areas grew faster than the statewide trend, except Houston, which had a trend similar to the statewide trend.

The research team conducted a high-level statistical analysis to determine potential correlations between a variety of factors and fatal crashes. Light condition was not a strong predictor of whether a crash would be a fatal crash. Nevertheless, the research team conducted a more detailed analysis to identify trends and patterns that could be of interest. With respect to daylight versus nighttime crashes, the analysis revealed that more nonfatal crashes occurred during

daylight hours than during nighttime hours and that more fatal crashes occurred during nighttime hours than during daylight hours. More precisely, less than a third of nonfatal crashes occurred during nighttime hours compared to more than half of fatal crashes. Overall:

- Statewide, daylight fatal crashes increased by about 12 percent from 2010 to 2019. However, daylight fatal crashes increased from 2010 to 2016, but then began to decrease.
- All five metro areas followed a trend similar to the statewide trend. However, daylight fatal crashes increased faster in all metro areas than the statewide trend. Daylight fatal crashes were about 45 percent higher in the Dallas area and about 52 percent higher in the Austin area.
- Statewide, nighttime fatal crashes increased by about 20 percent from 2010 to 2019. During the same period, nighttime fatal crashes increased faster in Austin, Dallas, and San Antonio than the statewide trend. Nighttime fatal crashes increased slower in Fort Worth and Houston than the statewide trend.
- From year to year, there were wide variations in the number of fatal crashes in each of the metro areas, but the variations were wider for nighttime fatal crashes than for daylight fatal crashes. With the information available at this point, it is not clear why there were such wide yearly variations in the number of fatal crashes.

The research team also examined weather conditions. In general:

- Some 91 percent of fatal crashes in Texas from 2010–2019 occurred under clear or cloudy weather conditions. Only 8.8 percent of fatal crashes occurred under any kind of inclement weather. This percentage was lower than the corresponding percentage for all crashes in the state (i.e., 10 percent).
- The most common weather condition, both statewide and for each metro area, was rain. Between 5.7 and 6.9 percent of fatal crashes in the state occurred under rainy weather conditions. This percentage was lower than the corresponding percentage for all crashes in the state (i.e., between 9 and 10 percent).
- All other weather conditions combined were associated with roughly 2 percent of fatal crashes. This percentage was higher than the corresponding percentage for all crashes in the state (i.e., less than 1 percent).
- No consistent trend was observed regarding geographic location with respect to weather conditions and fatal crashes. For example, the lowest percentage for rain was in Houston (5.7 percent), but the highest percentage for fog was in San Antonio (1 percent).

A review of surface conditions revealed the following:

- Some 88 percent of fatal crashes in Texas from 2010–2019 occurred under dry surface conditions. Only 12 percent of fatal crashes occurred under any kind of abnormal surface conditions. This percentage was lower than the corresponding percentage for all crashes in the state (i.e., 14 percent).
- The most common abnormal surface condition both statewide and for each metro area was wet. Between 9.1 and 11 percent of fatal crashes in the metro areas occurred under wet surface conditions. This percentage was lower than the corresponding percentage for all crashes in the metro areas (i.e., between 13 and 14 percent).

- All other abnormal surface conditions combined were associated with between 0.2 and 1.6 percent of fatal crashes. This percentage was lower than the corresponding percentage for all crashes in the state (i.e., less than 2 percent).
- No consistent trend was observed regarding geographic location with respect to surface conditions and fatal crashes. For example, the lowest percentage for wet surfaces was in Houston (9.1 percent), but the percentage for ice was higher in Austin (0.4 percent) than in Dallas (0.2 percent).

### **Simulations to Assess Impacts of Suboptimal Environmental Conditions**

The focus of the analysis was the typical nonmetric RGB digital cameras (e.g., 20-MP, 2.5-cm [1-inch] CMOS sensor, global shutter) used for surveying crash scenes with UASs. The simulation and tests covered the following areas:

- Impact of wind speed and direction on UAS flight operations.
- Impact of aerial imaging network design on 3D crash scene reconstructions using commercial SfM software.
- Impact of ambient lighting and low visibility on UAS-SfM reconstructions.
- self-calibration versus preflight calibration procedures for consumer-grade nonmetric digital RGB cameras.
- Impact of suboptimal conditions on visual image quality.
- Impact of camera properties on UAS image quality to guide crash scene imaging.

#### *Impact of Wind Speed and Direction on UAS Flight Operations*

The research team used a SITL environment to analyze the impacts of wind speed, direction, and turbulence on the endurance of the mission, safety of the craft, and flight design for SfM mapping missions. Metrics included average 3D error, standard deviation, battery use, and flight time. Major lessons learned from the simulation exercise included the following:

- The average 3D error and corresponding standard deviation between planned waypoints and the actual camera trigger locations increased as the wind speed increased. The magnitude of the impact varied significantly as a function of the turbulence level. Specifically, as the turbulence level increased, the impact on the 3D error became more noticeable at lower speeds. The results were similar for the standard deviation.
- Wind direction played a lesser role on the average 3D error and corresponding standard deviation than turbulence. However, the impact of wind direction increased as the wind speed and turbulence increased.
- The total flight time (or time to complete a mission) was less sensitive to changes in wind speed, direction, and turbulence conditions than the average 3D error and standard deviation. The effect due to differences between headwind and tailwind conditions was more noticeable for higher speeds and turbulence levels.
- Battery use was also less sensitive to changes in wind speed, direction, and turbulence conditions than the average 3D error and standard deviation.

The simulations confirmed the accepted practice of operating UASs if the wind is no more than 30 mph and under light to moderate turbulence levels. As wind conditions depart from the ideal

zero-speed, no-turbulence wind scenario, there is an impact on equipment performance measured in terms of positional accuracy, required flight time, and battery use.

### *Impact of Aerial Imaging Network Design on 3D Crash Scene Reconstructions*

The analysis focused on the influence of different amounts of overlap on automated keypoint matching, BA results, densified point cloud quality, flight time, and processing time using simulated data generated from a real-world crash scene. Additional simulations examined how random perturbations to camera position and orientation provided by onboard GNSS and IMU components, respectively, impacted SfM crash scene reconstruction results under high wind conditions. Major lessons learned from the simulation exercise included the following:

- Sidelap and endlap were positively correlated with keypoint extraction. A sharp rise in the number of keypoints at 90 percent endlap for lower sidelap scenarios shows that the endlap can be used to maintain a high number of keypoints (which is desirable) for flight lines oriented along roadway corridors. Increasing keypoints can be beneficial under suboptimal lighting conditions to help ensure there are sufficient keypoint correspondences for reconstruction.
- Higher endlap or sidelap percentages increased the average number of images observed for a keypoint used to reconstruct a 3D point in the sparse point cloud. The higher the image number on which a 3D point is visible, the more observations and constraints there are in the BA (which is desirable).
- Sidelap and endlap were negatively correlated with the uncertainty associated with estimated camera geolocation and orientation, demonstrating the direct benefit of overlap on improving reconstruction of accurate camera position and orientation (also known as camera pose). This process can be beneficial in adverse weather, such as wind speed, where input positional uncertainty may be high.
- Reconstruction of the Z coordinate for camera geolocations and checkpoint locations showed a larger error than that for horizontal X-Y coordinates. This result is expected given that GNSS image geolocation uncertainty tends to be greater in the Z-dimension.
- Variation in overlap directly affected point densification. The total number of points and point density increased with overlap because of the increase in the number of images and coverage of the scene from multiple camera perspectives. Regardless, all overlap scenarios produced dense point clouds.
- As expected, simulation of the effect of high wind on Pix4D processing by perturbing the input image geolocation and orientation values increased the error associated with absolute camera geolocation and checkpoints. Simulation results also showed that geolocation and orientation perturbation increased the estimated uncertainty of camera position and orientation during the BA phase in Pix4D.

### *Impact of Ambient Lighting and Low Visibility on UAS-SfM Reconstructions*

The simulation included low lighting (typical of early morning or late in the day); bright-lighting (e.g., midday); low visibility from mist, fog, or clouds; artificial lighting; and wet surfaces after rainfall events. These conditions represent various levels of overall scene darkness and brightness-producing conditions more favorable or less favorable to under or overexposure within the scene. Major lessons learned from the simulation exercise included the following:



- Keypoint extraction and reprojection errors:
  - Of the various lighting conditions simulated, dark sky and civil twilight scenarios showed the lowest number of 2D keypoints. This process resulted in a smaller number of 3D points resolved in the sparse point cloud.
  - Full illumination with artificial lamp posts produced fewer keypoints than daytime and dusk conditions, but many more keypoints than 100 percent cloudy evening sky, civil twilight, or dark sky scenarios. Partial illumination with artificial lamp posts produced fewer keypoints than full illumination.
  - Low visibility fog resulted in significantly fewer keypoints and 3D points in the sparse point cloud than high visibility fog. Overlap also played a key role in enhancing the number of keypoints for both low and high visibility fog.
  - Wet asphalt surface resulted in more keypoints per image than dry asphalt, but fewer matched keypoints per image.
  - Increasing darkness resulted in a larger mean reprojection error. Dark sky and civil twilight scenarios produced the largest reprojection error, followed by a 100 percent cloudy sky evening scenario.
- SfM reconstruction accuracy:
  - Reduced lighting scenarios (i.e., dark sky and civil twilight) showed the largest error in absolute camera position and orientation error.
  - Increased lighting scenarios (i.e., solar noon sky and solar noon solstice conditions) showed an increase in absolute camera position and orientation error, respectively, relative to afternoon sky and dusk. This effect may be due to stronger shadowing in the scene and reduced texture for areas of overexposure.
  - Reduced lighting scenarios (i.e., dark sky and civil twilight) resulted in the largest RMSE of checkpoint errors. Solar local noon and solar noon solstice showed a slight increase in checkpoint error relative to afternoon lighting.
  - Increasing overlap for extreme reduced lighting scenarios (low visibility fog and dark sky) resulted in a reduction in RMSE of checkpoint errors, both horizontally and vertically.
  - There was a substantial increase in the RMSE of the checkpoint coordinate error measured for partial illumination than full illumination.
  - Wet asphalt and dry asphalt scenarios showed a slight difference in the RMSE of absolute checkpoint coordinate errors.
- Densification accuracy:
  - Fog (low visibility) produced the largest RMSE of cloud-to-cloud distance errors. Dark sky and civil twilight also produced larger RMSE values relative to most other scenarios, although they both had more 3D densified points.
  - Lamp post at full illumination and solar noon produced the lowest RMSE suggesting that for those two scenarios, the densification was more accurate relative to other scenarios. Partial illumination with lamp posts resulted in a much larger RMSE relative to full illumination.
  - Increasing overlap for all scenarios resulted in a substantial decrease in the RMSE of cloud-to-cloud distance errors.
  - RMSE of cloud-to-cloud distance errors was lower for the wet surface scenario than the dry surface scenario. Results could be different for more extreme wet

surface conditions (e.g., mirror-like reflections of surrounding structures in ponded water or dynamic water flow).

- The 3D point density showed a positive correlation with the amount of brightness in an image (measured as a brightness index) and a negative correlation with the amount of darkness in an image (measured as a darkness index). This pattern reversed for the cloud-to-cloud distance error, suggesting that darker scenes generate less dense and potentially more noisy densified point clouds. An unexpected result, which needs to be investigated further, is that the total number of points in the densified point cloud showed a fairly strong positive correlation with the darkness index.

### *Self-Calibration versus Preflight Calibration Procedures for Consumer-Grade Nonmetric Digital RGB Cameras*

The research team evaluated the following scenarios to compare differences in calibration solutions and SfM reconstruction accuracy for different processing settings implemented with the Pix4D automatic self-calibration procedure:

- Scenario 1 (standard calibration without GCPs).
- Scenario 2 (standard calibration with GCPs).
- Scenario 3 (all prior setting without distortion values).
- Scenario 4 (all prior setting with distortion values).
- Scenario 5 (fixed calibration).
- Scenario 6 (accurate geolocation).

Major lessons learned from this calibration exercise included the following:

- Scenario 1 had the largest difference between initial and optimized camera internal parameter values, a high correlation between the focal length and radial distortion parameters, and the worst absolute SfM reconstruction accuracy on the checkpoint error, indicating a less accurate solution relative to the other five scenarios. Lower differences for Scenario 2 show the benefit of adding GCPs to improve the self-calibration solution.
- Scenarios 3 and 4 resulted in optimized values close to the initial values, with no change in focal length but slight changes in the optimized principal point location. They also showed no correlation of distortion values with respect to the focal length or between leading parameters, as well as a low RMSE for the checkpoint error. This demonstrates the benefit of the all prior setting when acceptable initial internal parameter values are provided.
- Scenario 5 resulted in the second most erroneous solution, resulting from the more inaccurate estimation of camera external parameters (absolute position and orientation).
- Scenario 6 showed optimized values close to the initial values for the internal camera parameters. Along with Scenario 2, Scenario 6 resulted in the lowest RMSE for checkpoint error, highlighting the benefit of using UASs integrated with an RTK/PPK-enabled GNSS to provide accurate camera geolocations.

The research team also performed a pre-calibration experiment using Metashape. The research team evaluated the following scenarios:

- Self-calibration Run 1 (standard initial camera values, followed by a self-calibration procedure during the sparse point cloud generation stage).
- Self-calibration Run 2 (calibration solution from the pre-calibration procedure as initial parameter values, followed by a self-calibration procedure).
- Pre-calibration Run 3 (calibration parameter results from the pre-calibration procedure, which were then locked during the sparse point cloud generation stage).

Major lessons learned from this calibration exercise included the following:

- With respect to the pre-calibration procedure, Run 1 provided no solution for affinity and skew coefficients, and no solutions for some of the higher-order radial distortion coefficients and tangential coefficients. Run 2 produced slightly larger differences for the principal point locations than Run 1, suggesting the Metashape algorithm does not weigh the self-calibration too heavily based on the initial values provided from pre-calibration. Both Run 1 and Run 2 had similar values for the optimized focal length.
- With respect to the pre-calibration procedure, Run 2 produced much closer estimates of distortion and skew coefficient values than Run 1, highlighting the potential value in using pre-calibration to set more realistic initial camera internal parameters to aid the self-calibration routine in SfM software.
- These results highlight that pre-calibration may be useful in cases where self-calibration does not provide a decent result based on the imaging network geometry or reduced scene texture and in cases where UASs are equipped with metric-grade cameras. The results also show the sensitivity of SfM reconstruction to variations in optimized camera calibration solutions, which can result from self-calibration, pre-calibration, or a combination of both.

### *Impact of Suboptimal Conditions on Visual Image Quality*

The research team examined the impact of fog and high wind speed on the visual quality of UAS data. The research team conducted a series of simulation runs to generate synthetic images resulting from reduced visibility due to fog and motion blur. Then, the research team quantified and evaluated UAS image quality degradation and its impact on crash scene reconstruction. The research team focused on feature extraction and matching between images. Major lessons learned from the simulation exercise included the following:

- The results showed a clear effect of fog on the software's capability to reconstruct 3D points in the sparse point cloud. The number of points in the 3D point cloud decreased as the fog became denser. The reduction in the number of points in the 3D point cloud was small for light or moderate fog levels. Even for thick fog, the reduction in the number of points in the 3D point cloud was less than 20 percent. For dense fog, the reduction in the number of points in the 3D point cloud became much more pronounced. For the densest fog (i.e., visibility of 65 m [213 ft]), the reduction in the number of 3D points was about 70 percent. These results indicate that UASs and the SfM process can perform well under foggy weather conditions, but performance will degrade quickly if fog is dense.
- The reduction in the number of 3D points as a function of the fog level for the simulated early morning imagery was similar to that for the original noon-time imagery. This result is not surprising considering that the original UAS imagery was the result of a data

collection strategy that provided multiple feature redundancy opportunities, minimizing the impact of reduced ambient lighting associated with the early morning imagery.

- The results showed a clear effect of wind speed on the software's capability to reconstruct 3D points in the sparse point cloud. In general, as the wind speed increased, the number of 3D points decreased.
- The results also showed a clear effect of exposure time on the software's capability to reconstruct 3D points in the sparse point cloud. In general, as the exposure time decreased, there was less motion blur, which resulted in a higher number of 3D points.

### *Impact of Camera Properties on UAS Image Quality to Guide Crash Scene Imaging*

The research team examined the impact of UAS speed and exposure time on the software's capability to reconstruct 3D points in a sparse point cloud. The research team conducted a series of simulation runs to generate synthetic images resulting from motion blur and noise due to these camera properties. The research team quantified and evaluated UAS image quality degradation and its impact on crash scene reconstruction. Specifically, the research team focused on feature extraction and matching between images. Major lessons learned from the simulation exercise included the following:

- The results showed a clear effect of UAS speed on the software's capability to reconstruct 3D points in the sparse point cloud. In general, as the UAS speed increased, the loss in the number of 3D points increased (i.e., the number of 3D points reconstructed decreased).
- The results confirmed the effect of exposure time on the software's capability to reconstruct 3D points in the sparse point cloud. In general, as the exposure time decreased, there was less motion blur and the loss in the number of 3D points decreased (i.e., the number of 3D points reconstructed increased).
- The results confirmed the correlation between low-altitude flights and the software's capability to generate in-focus imagery, including orthomosaics.

### **Field Tests of UAS-Based Data Collection Activities**

The research team conducted seven flight tests:

- Test 1 (08/09/2020): Crash scene in Abbott, Texas, in conjunction with TxDPS. This crash scene was related to a fatal crash in IH-35.
- Test 2 (08/25/2020): Simulated crash scene at Phil Hardberger Park in San Antonio, Texas. This test was used to test the functionality of the Mavic 2 Pro.
- Test 3 (09/30/2020): Delivery truck crash test at the RELLIS Campus in College Station, Texas.
- Test 4 (10/07/2020): Passenger car crash test at the RELLIS Campus. This test was the first test that included GCPs surveyed by TAMUCC.
- Test 5 (12/07/2020): Delivery truck crash test with nighttime data collection at the RELLIS Campus. This test was the first test involving a nighttime run.
- Test 6 (01/15/2021): Simulated passenger car crash test with nighttime data collection at the TxDPS Tactical Training Facility in Florence, Texas.

- Test 7 (03/20/2021): Simulated passenger car crash test with nighttime data collection at the TxDPS Tactical Training Facility. This test included GCPs gathered by TAMUCC and TxDOT.

Unfortunately, it was not possible to conduct sample flights at actual fatal crash locations. It was also not possible to conduct sample flights under adverse environmental conditions such as fog or rain. Given the nature and scope of the data collection the research team was planning, the agencies in charge of approving the use of UASs for specific events (FAA at the federal level and the A&M System at the state level) did not issue approvals for the research team to collect data as originally intended. Nevertheless, the research team completed seven data collection tests that complemented and confirmed results from the various simulation exercises.

The research team divided the data collection and corresponding analyses into two large groups of activities. The first group (led by research team members at TAMUCC) focused on a systematic assessment of positional accuracies and 3D reconstruction fidelity at the test locations, which included surveying GCPs and checkpoints that were used in all photogrammetry software processing. It also included an in-depth analysis of SfM point cloud data and calculations, as well as TLS data. The second group of activities (led by research team members at TTI) focused on typical activities associated with the reconstruction of crashes, leading up to the calculation of relative distances between points that are relevant to the crash reconstruction process.

Major lessons learned from the field tests are grouped into the following categories:

- Impact of ground control on SfM results and distances between points.
- Impact of processing software on SfM results.
- Selection of coordinate system settings in Pix4D.
- Effect of calibration method in Pix4D.
- Effect of scale constraint in Pix4D.
- Effect of nighttime settings in Pix4D.
- Impact of UAS platform on SfM results.

#### *Impact of Ground Control on SfM Results and Distances between Points*

Not surprisingly, using surveyed GCPs had a positive impact on the SfM process and therefore on the positional accuracy of point locations and distances between points. To quantify this impact, the research team completed three analyses. The first analysis involved comparing differences in coordinates (or deltas) between various points and those points associated with the reference scenario used for each test. The second analysis was similar, except the deltas were with respect to surveyed checkpoint locations. The third analysis involved comparing deltas of distances between points using coordinates of checkpoints.

For each test, the reference scenario was the closest to the actual coordinates (if GCPs were used) or the scenario that exhibited the lowest errors within the Pix4D environment. Overall, the largest deltas corresponded to scenarios that did not include any GCPs. In standalone GNSS mode, the Mavic 2 Pro had a median delta of 8.7 m compared to 4.1 m for the Matrice 300 RTK.

Readers should also note the substantial decrease in delta values when onboard RTK was activated for the Matrice 300 RTK.

Using Google elevation data helped to reduce deltas for both the Mavic 2 Pro and the Matrice 300 RTK. For the Mavic 2 Pro, the median delta decreased from 8.7 m to 2.6 m. For the Matrice 300 RTK, the median delta decreased from 4.1 m to 1.3 m. Using Google elevation data also had a positive impact on delta variability. Using surveyed GCPs had a dramatic impact on the magnitude of the deltas and their variability. For both UASs, the median delta decreased to about 5 cm when using TAMUCC GCPs and to less than 4 cm when using TxDOT GCPs.

The research team obtained similar results when calculating deltas with respect to surveyed checkpoint locations. In this case, the number of data points was lower than the analysis above because only points that had been surveyed were used for the analysis. The analysis involved comparing deltas associated with distances between two surveyed checkpoints and the corresponding distances between tie points using calculated coordinates in Pix4D. Because distances between the points were different for each test, the research team normalized deltas by dividing each delta (in mm) by the corresponding distance (in m) between the surveyed points.

The largest deltas occurred for the Mavic 2 Pro in standalone GNSS mode, followed by the Matrice 300 RTK in standalone GNSS mode (5.9 mm/m [0.071 inches/ft] and 4.3 mm/m [0.052 inches/ft], respectively). Using Google elevation data resulted in a decrease in delta to about 1.4 mm/m (0.017 inches/ft) for the Mavic 2 Pro and 1.7 mm/m (0.02 inches/ft) for the Matrice 300 RTK. Using TAMUCC GCPs, the median delta decreased to 1.2 mm/m (0.014 inches/ft) for the Mavic 2 Pro and 0.74 mm/m (0.0089 inches/ft) for the Matrice 300 RTK. Deltas were lower than these values when using TxDOT GCPs (although the sample size was too small to generalize results).

Results with the WingtraOne PPK and Phantom 4 RTK field tests consistently demonstrated that use of PPK- or RTK-corrected image positions and no GCPs can provide near survey-grade SfM surface height measurements (i.e., Z coordinates). Compared to autonomous GNSS, PPK or RTK GNSS sensor augmentation onboard the UAS can reduce the need to install a dense ground control network within a mapped scene where high absolute georeferencing accuracy is required. However, it is always recommended to include GCPs as checkpoints for accuracy validation.

#### *Impact of Processing Software on SfM Results*

The research team used Pix4D and Metashape to process UAS imagery. Results with both software platforms were similar in terms of the number of 2D and 3D points generated and level of reconstruction achieved. Positional accuracies as well as derived distances and angular measurements were also similar. For most of the flights for which the research team used both Pix4D and Metashape, a comparison between TLS-based 3D point clouds and the corresponding 3D point clouds generated with Pix4D and Metashape revealed minor differences between these two platforms, although there was a closer agreement between the TLS-based 3D point clouds and the Pix4D-generated 3D point clouds. In one case that involved a nighttime flight with the Phantom 4 RTK, Pix4D successfully reconstructed more of the scene than Metashape. The mean overall 3D distance based on 10,000 random point measurements was 1.8 cm (0.71 inches) for Pix4D and 2.4 cm (0.94 inches) for Metashape. Metashape reconstructed less of the scene, but

for the points that were reconstructed, distance offsets were within <1 cm (0.4 inches) of the results obtained with Pix4D.

### *Selection of Coordinate System Settings in Pix4D*

It is critical to correctly identify all coordinate system parameters for each step in the SfM process, particularly when using distinct kinds of ground control, all of which involve different hardware, software, and business processes. In the case of Pix4D, the software requires the user to select imagery, GCP, and output coordinate systems. By default, Pix4D assigns the GCP and output coordinate systems to be the same as that associated with the imagery. If the GCP and output coordinate systems are different from that of the imagery, it becomes critical to document and, if necessary, transform coordinate system parameters before use.

The research team used the following coordinate system for the imagery during the data collection phase:

- Datum: NAD83(2011).
- Horizontal coordinates: State Plane Texas Central (meters).
- Vertical coordinates: Geoid height above GRS80 ellipsoid: 0 meters.

This coordinate system was also the coordinate system used for the TAMUCC GCPs and output coordinate system in Pix4D.

The TxDOT GCPs were in the following coordinate system:

- Datum: NAD83(2011).
- Horizontal coordinates: State Plane Texas Central (U.S. survey ft).
- Vertical coordinates: NAVD 88 GEOID12B.

In this case, the research team first converted the GCPs coordinates from U.S. survey ft to meters, and then converted the vertical coordinates from NAVD 88 GEOID12B to NAD83 ellipsoid height (m). This conversion prior to importing the GCP data into Pix4D was necessary because Pix4D does not provide direct support for NAVD 88 GEOID12B.

The Google elevation data were in the following coordinate system (used for the simulated GCPs in Pix4D):

- Datum: World Geodetic System 1984 (WGS 84).
- Horizontal coordinates: WGS 84.
- Vertical coordinates: MSL EGM96 Geoid.

In this case, the research team selected these coordinate system parameters directly in Pix4D.

### *Effect of Calibration Method in Pix4D*

By default, Pix4D uses a standard workflow setting to complete image calibrations during initial processing. When images have accurate geolocations (e.g., by using RTK or PPK GNSS), Pix4D recommends using the Accurate Geolocation and Orientation calibration method. This

calibration method still requires images to be geolocated and oriented via the SfM BA, but it weighs more heavily the image geolocations based on the ground control parameters associated with each image.

Initially, the research team used the standard workflow for all the runs, which is the recommended practice. However, other calibration methods should be evaluated if the standard calibration method does not produce satisfactory results. For example, results improved in several cases that had RTK or PPK-corrected image positions when the research team used the accurate geolocation and orientation calibration method. For some nighttime flights, using the standard calibration method, Pix4D could not achieve an adequate number of calibrated images for a useful result. The only way to ensure feature matching led to a usable result was by selecting the accurate geolocation and orientation calibration method.

To assess this effect, the research team compared coordinates of two specific points in Pix4D against the corresponding coordinates of surveyed checkpoints, both with the standard calibration setting and the accurate geolocation and orientation setting. The research team also calculated distances between the points and compared those distances against the corresponding distances between the checkpoints.

For both sample points, using the accurate geolocation and orientation setting decreased the 3D distance delta between those points and the corresponding checkpoint locations. For the first point, the median delta decreased from 3.9 cm (1.5 inches) to 3.7 cm (1.4 inches). For the second point, the median delta decreased from 6.7 cm (2.6 inches) to 5.2 cm (2.1 inches). There was also a decrease in 3D distance deltas by using the standard workflow instead of the Accurate Geolocation and Orientation setting. When compared against the distance between the checkpoints, the median distance between the sample points decreased from 3.6 cm (1.4 inches) to 1.6 cm (0.63 inches).

#### *Effect of Scale Constraint in Pix4D*

A recommended practice for crash reconstructions using UASs is to measure distances between targets in the field and use those distances for scaling purposes during the SfM process. The research team used surveyed checkpoints for most of the field tests, which made it unnecessary to measure distances in the field. Nevertheless, it was of interest to evaluate the impact of using the scale constraint function in Pix4D.

Using the scale constraint had a negligible impact on the SfM process for scenarios that involved the use of surveyed GCPs. As described above, the research team used the Accurate Geolocation and Orientation calibration method for these scenarios, which gave more weight to the ground control parameters associated with each image.

The impact was significant for standalone GNSS and Google elevation data scenarios. To quantify this impact, the research team calculated distances between surveyed GCPs and applied these distances using the scale constraint in Pix4D. Without the scale constraint, the median delta of the normalized distances was 4–5 mm/m (0.048–0.06 inches/ft), but this delta decreased to 0.3–0.5 mm/m (0.0036–0.006 inches/ft) after applying the scale constraint, therefore confirming the benefit of using the scale constraint method for crash reconstructions using UASs.



### *Effect of Nighttime Settings in Pix4D*

Several nighttime flights were not successful. The number of 2D keypoints and corresponding 3D points for the BA process was low, typically because the images were blurry or because there was not enough detail or texture in the images. Using the supplemental spotlight on the Matrice 300 RTK was not always successful because the camera compensated for the increase in brightness by reducing the exposure time. As a result, images were brighter where the spotlight projected its narrow light beam but were darker elsewhere. For many images, the number of 2D keypoints and 3D points was lower when using the spotlight. Nevertheless, for one of the tests at the RELLIS Campus, the spotlight resulted in more keypoints matched around the crashed vehicle than the scenario where only the built-in LEDs were used.

The research team had a mixed experience illuminating nighttime scenes using onboard LED lights. In several cases, it was necessary to use supplemental lighting (e.g., from vehicle headlights or high-mast lights). The research team also experimented with techniques, such as lowering the UAS altitude and taking double pictures at each location where the UAS stopped. Flying the UAS on autonomous mode at night did not work because the camera was not sensitive enough to take reliable pictures while moving at a set exposure time, and the remote controller software was not optimized for nighttime operations (e.g., allowing the platform to slow down or stop and take pictures using a higher exposure time to reduce motion blur while increasing exposure). The research team did not experiment with a camera bracketing technique, but this technique is an option to gather UAS images at night. The technique involves capturing a sequence of pictures with different camera settings and returning the UAS to the ground to decide on the most favorable settings before conducting the actual data collection flight.

Whether using the built-in LEDs or supplemental lighting, nighttime SfM processing depends heavily on the type and characteristics of the surface texture, including the presence or absence of shadows. The data collection at the TxDPS Tactical Training Facility near Florence, Texas, where two passenger cars were placed in the middle of a test skid pad, clearly illustrates this challenge. The situation was even more challenging because the two vehicles were of the same type, shape, and color. With the Matrice 300 RTK nighttime run, it was not possible to build a workable model. With the Mavic 2 Pro, it was possible to build a workable model, but the quality was not good enough to be able to extract coordinates or measure distances reliably. To arrive at the workable model, it was necessary to change several settings in Pix4D, remove several images, and manually recalibrate several cameras that Pix4D had calibrated incorrectly.

### *Impact of UAS Platform on SfM Results*

The research team used several hardware platforms during the field tests, including four UAS platforms (Mavic 2 Pro, Matrice 300 RTK, Phantom 4 RTK, and WingtraOne PPK) and two LiDAR units (RIEGL-VZ geodetic-grade TLS LiBackpack DG50). The Mavic 2 Pro is a consumer-level UAS. The Matrice 300 RTK, Phantom 4 RTK, and WingtraOne UASs are survey-level (or professional-level) UASs. The RIEGL-VZ is a geodetic-level TLS. The LiBackpack DG50 unit is a backpack LiDAR scanner. The LiBackpack DG50 unit was used once during the data collection in Abbott, Texas, but its performance was not acceptable and was not used again.

To assist with ground control, the research team used a pair of survey-grade Septentrio NR3 GNSS receivers. In addition, differential corrections were possible via the RTK (or PPK) capability integrated with the Matrice 300 RTK, Phantom 4 RTK, and WingtraOne.

All the UASs performed well in meeting the normal data collection requirements associated with crash reconstructions. From this perspective, the surveying-level UASs (i.e., the Matrice 300 RTK, Phantom 4 RTK, and WingtraOne) did not perform better than the consumer-level UAS. However, the field tests went well beyond the minimum requirements associated with crash reconstructions, which enabled the research team to document the capabilities and limitations associated with each of the platforms more thoroughly. In general:

- In standalone GNSS mode, provided the metric of interest is relative distances between objects (as is the case in most crash reconstructions), it is sufficient to use a consumer-level UAS such as the Mavic Pro in conjunction with a tool such as Google elevation data. It is increasingly common for public safety agencies to use this type of platform.
- In standalone GNSS mode, the Matrice 300 RTK produced slightly more accurate results than the Mavic 2 Pro. If only used in standalone GNSS mode, the significant increase in price for the Matrice 300 RTK would not be justified unless the platform is used with additional payloads (which were not tested during the research). When using the onboard RTK option on the Matrice 300 RTK, the result was a significant increase in positional accuracy (about 20 cm), but this increase did not match the positional accuracy obtained with GCPs (3–4 cm). It also did not match the positional accuracy obtained with the Phantom 4 RTK or the WingtraOne (which has an onboard PPK GNSS), both of which compared favorably to the results obtained when using GCPs.
- When using GCPs, all the UAS-SfM solutions produced accuracy levels that compared favorably to TxDOT RTN checkpoint location coordinates. This finding is important because it highlights the potential for using relatively low-cost UAS platforms when these platforms are used in conjunction with appropriate hardware and software platforms to ensure adequate geolocation results. However, accuracy outside of the boundary of the control cannot be trusted because it tends to degrade away from the control network.
- UAS-SfM solutions based solely on RTK or PPK image geolocation accuracy, without using ground control targets, can provide accuracy levels that compare favorably to TxDOT RTN checkpoint location coordinates. In one of the field tests, the research team obtained a vertical error of about 7.5 cm. In another field test, RMSEs ranged from 3.2–4.9 cm when using PPK. When compared to TxDOT-leveled control, RMSEs were down to 2.0 cm vertically for both PPK and RTK solutions, with the latter based on the TxDOT RTN. One RTK nighttime flight had a vertical RMSE of 0.9 cm relative to TxDOT control. This result compared favorably to TLS data, which is significant, considering that the UAS-SfM solution was based solely on PPK- or RTK-corrected image geotags because no GCPs were used to constrain the SfM solution.
- Readers should note that not all RTK- or PPK-enabled UAS implementations are equal in terms of survey accuracy. Implementations must consider factors such as distance to the base station, range of the RTK source, and/or area of the RTN network coverage and cellular signal. Additional factors include quality of the camera and workflows for RTK or PPK GNSS data processing and SfM data processing. Effectiveness of RTK or PPK-only solutions also rely heavily on the UAS platform's capability to tag and synchronize

time at camera exposure with the GNSS time and account for lever arm offsets between the GNSS and camera reference point.

## RECOMMENDATIONS

Based on the results and lessons learned from the literature review, simulations, and field tests, the research team makes the following recommendations:

**Establish and implement a program to use UAS-based platforms to support traffic incident management activities.** A major benefit of using UASs to improve TIM practices, including clearing a crash scene or fatal crash scene reconstruction, is the ability to replace traditional forensic “feet on the ground” surveying methods using a total station or TLS with a method that involves the use of photogrammetric techniques. The research demonstrated the feasibility of using low-cost UASs and SfM software for this purpose. Only acquiring UASs without the support of SfM software seems appealing as a first phase but doing so would significantly limit the capability and value that a UAS-based platform can offer to support TIM activities. Under these conditions, UASs could only be used to capture pictures and video files.

**Focus on low-cost, consumer-level UASs to support TIM activities.** The research demonstrated that it is not necessary to acquire more expensive, surveying-level UAS platforms to achieve the accuracy levels that are typically required for crash reconstructions. In conjunction with low-cost consumer-level UASs, the research team recommends using a suitable commercially available SfM photogrammetry software platform.

**Focus on the metro districts first for the implementation of UAS-based programs to support TIM activities.** The total number of fatal crashes at the five metro area counties (i.e., Bexar, Dallas, Harris, Tarrant, and Travis) accounts for a third of all fatal crashes in the state. Further, fatal crashes in all metro areas (except Houston) are growing faster than the statewide trend. It therefore makes strategic sense to first focus on the metro districts to begin a UAS implementation.

**Begin the UAS implementation with small pilot programs but concurrently develop a strategic plan that involves a potentially large fleet of UASs.** This strategic plan should address factors such as use cases, funding levels, training needs, information technology requirements, and UAS equipment maintenance and replacement needs. As a reference, TxDPS manages a large (and growing) UAS fleet and uses a commercial web-based platform to plan missions, track the maintenance of its UAS fleet, and store relevant information such as pilot information, flight logs, and NOTAMs. TxDPS also uses the platform for training activities, video streaming, and tracking UASs during flight operations. This commercial platform is not cheap. However, TxDPS has found this platform to be beneficial and cost effective for managing its UAS fleet.

**Monitor the evolution of the UAS market as well as federal and state laws and regulations governing the use of UASs for public use.** One of the reasons the research team used DJI UASs was the reality of the UAS marketplace in 2020. However, this marketplace may experience significant changes in the next few years because of government regulations that encourage the increased availability of competitive UAS products from vendors other than DJI.

**Establish a program to test and certify UAS equipment and related software.** Many similarities exist across commercially available UAS and SfM hardware and software platforms. However, the research found differences in hardware and software performance with respect to critical aspects of the UAS-based data collection and data processing workflows that produced significant differences in the quality and reliability of the end results. In several cases, the only way the research team became aware of a potential issue was through systematic experimentation because the available documentation and vendor-provided feedback were insufficient. In other cases, the research results pointed to discrepancies with respect to vendor-stated hardware or software performance levels. Establishing a rigorous testing and certification program will have several benefits, including the capability to anticipate and prevent problems that otherwise might not be apparent to users until they have already spent a significant amount of time and resources using the platforms.

**Develop and implement a comprehensive UAS-SfM training program.** For developing this program, the research team recommends covering all the typical activities associated with the use of UASs and SfM software, including UAS pilot certifications, use of SfM software, file management, validation of data quality and survey accuracy, and UAS fleet management. This program should include both hands-on data collection and data processing activities. It is critical to keep in mind that data processing skills (such as those required to use SfM software effectively) and foundational knowledge (such as an understanding of GNSS principles, coordinate systems, and datums) are usually more demanding and therefore more difficult to transfer than the operation of the UAS equipment. UAS fleet management training should include all aspects of the UAS fleet lifecycle, including day-to-day operations, data log requirements, and regular maintenance needs.

**Partner with public safety agencies throughout the state to encourage the use of UAS-SfM platforms for traffic incident management, including crash reconstructions.** TxDPS has an ongoing training program for TxDPS officers. The research team recommends examining the feasibility of using or adapting the TxDPS training program to support the needs of other public safety agencies throughout the state. The research team also recommends exploring funding mechanisms, such as Section 402 traffic safety funds, to support these initiatives (138).

**Examine the feasibility of using UAS-based platforms for other applications at TxDOT.** The research team conducted simulations and field tests of UASs of several types, capabilities, and costs. The research included a detailed assessment of accuracy levels (both locations and distances) and operational procedures under a variety of scenarios. The primary focus was crash reconstructions. However, it is increasingly clear that UAS-based platforms can be used for a wide range of applications. Examples of documented UAS applications or opportunities that have been mentioned recently include (139):

- Structures: Bridge inspections, high mast lighting inspections, retaining wall inspections, tunnel inspections.
- Operations and safety: Site monitoring, emergency response and incident management including crash reconstructions, search and rescue, route management, mud slide assessments, and snow avalanche management.

- Construction: Estimates and bidding, topographic surveys and elevations, construction monitoring, inspections and quality control, land surveying, break-line surveys, quantities, surface validations, work zone traffic monitoring, and as-builts.
- Maintenance: Roadside condition assessment, pavement inspections, vegetation management, overhead sign inspections, rockfall hazard mapping, and slope failures.
- Planning and design: Vehicle counting, traffic volumes, site analysis, land surveys, geotechnical investigations, and environmental assessments.
- Utilities: Utility investigations, utility design verifications, utility relocation monitoring, utility inspections, and utility as-builts.

Several of these applications involve hardware and/or software platforms beyond the configurations that were tested in this research, and it would be strategic to conduct thorough assessments of their capabilities, limitations, and implementation costs. For example, several UASs can carry additional sensors, such as multispectral sensors, thermal cameras, or miniaturized LiDAR sensors. LiDAR has certain advantages relative to SfM for collecting accurate elevation and dense 3D point cloud data, especially for topographic mapping over vegetated surfaces. However, it is not always clear to what degree UAS-based LiDAR may be preferable to other platforms.

In recent decades, ground penetrating radar (GPR) has been used to detect and document pavement layers, bridges, and underground utilities. Thermal sensors have been used to detect and assess subsurface delamination in reinforced concrete bridge decks. It is also common to use electromagnetic induction (EMI) instruments to find underground utilities. However, conducting subsurface investigations using these technologies can be expensive and time consuming. Recently, there have been experiments mounting GPR, EMI, and thermal sensors on UASs to detect underground features and assess subsurface conditions. If feasible, the potential for more thorough, affordable investigations could result in substantial time and economic benefits, not just during the early phases of project delivery, but also for roadway and roadside asset management after construction.

Integration of UAS-SfM data products with other data products during planning, design, and construction is an area that has enormous potential. TxDOT is rapidly moving from 2D design and construction (where the plan of record is based on plan views, profiles, and cross sections) to workflows that rely on 3D information. The industry is evolving to 3D and building information modeling (BIM) workflows that enable projects to be designed and built in such a way that a 3D product is the document of record, and this document carries from design to construction. Some 3D and BIM applications are also extending this functionality to operations and maintenance phases, in effect projecting those applications throughout the entire lifecycle of the project.

In this environment, UAS-SfM platforms could be used in several ways. For example, they can provide periodic recordings of the physical progress of a construction project in the form of 3D products that can be compared against the original design (which is also in a 3D or BIM platform). Adding a project schedule will extend this functionality to the time domain, in effect enabling schedule-based quality control during construction. After the project is finished, operations and maintenance crews could use UAS-SfM platforms to create 3D products that document how the roadway and roadside environments evolve through time, enabling

comprehensive near real-time comparisons with previous records at a fraction of the cost to accomplish the same goal with traditional techniques.

## REFERENCES

1. D. Turner, A. Lucieer and C. Watson. An Automated Technique for Generating Georectified Mosaics from Ultra-High Resolution Unmanned Aerial Vehicle (UAV) Imagery, Based on Structure from Motion (SfM) Point Clouds. *Remote Sensing*, Vol. 4, Issue 5, 2012, pp. 1392–1410.
2. A. S. Woodget, P. E. Carbonneau, F. Visser and I. P. Maddock. Quantifying Submerged Fluvial Topography Using Hyperspatial Resolution UAS Imagery and Structure from Motion Photogrammetry. *Earth Surface Processes and Landforms*, Vol. 40, Issue 1, 2015, pp. 47–64.
3. I. Colomina and P. Molina. Unmanned Aerial Systems for Photogrammetry and Remote Sensing: A Review. *ISPRS Journal of Photogrammetry and Remote Sensing*, Vol. 92, 2014, pp. 79–97.
4. *Unmanned Aircraft System (UAS) Flight Operations and User's Manual*. Texas Department of Transportation, Austin, Texas, April 2021. Available at <https://ftp.dot.state.tx.us/pub/txdot-info/avn/uas/user-manual.pdf>. Accessed 06/30/2021.
5. 14 CFR Part 107, Small Unmanned Aircraft Systems. Available at <https://ecfr.io/Title-14/pt14.2.107>. Accessed 06/30/2021.
6. Advisory Circular 00-1.1B, *Public Aircraft Operations—Manned and Unmanned*. U.S. Department of Transportation, Federal Aviation Administration, Washington, D.C., September 21, 2018. Available at [https://www.faa.gov/regulations\\_policies/advisory\\_circulars/index.cfm/go/document.information/documentID/1034871](https://www.faa.gov/regulations_policies/advisory_circulars/index.cfm/go/document.information/documentID/1034871). Accessed 06/30/2021.
7. 14 CFR 47, *Aircraft Registration*. Available at <https://ecfr.io/Title-14/Part-47>. Accessed 06/30/2021.
8. *FAADroneZone*. Webpage. U.S. Department of Transportation, Federal Aviation Administration. Available at <https://faadronezone.faa.gov>. Accessed 06/30/2021.
9. Integrated Airman Certification and Rating Application (IACRA). Federal Aviation Administration, U.S. Department of Transportation. Available at <https://iacra.faa.gov/IACRA/default.aspx>. Accessed 06/30/2021.
10. 84 FR 3856, *Operation of Small Unmanned Aircraft Systems Over People*. Available at <https://www.federalregister.gov/documents/2019/02/13/2019-00732/operation-of-small-unmanned-aircraft-systems-over-people>. Accessed 06/30/2021.
11. 86 FR 4314, *Operation of Small Unmanned Aircraft Systems Over People*. Available at <https://www.federalregister.gov/documents/2021/01/15/2020-28947/operation-of-small-unmanned-aircraft-systems-over-people>. Accessed 06/30/2021.
12. 84 FR 72438, *Remote Identification of Unmanned Aircraft Systems*. Available at <https://www.federalregister.gov/documents/2019/12/31/2019-28100/remote-identification-of-unmanned-aircraft-systems>. Accessed 06/30/2021.
13. 86 FR 4390, *Remote Identification of Unmanned Aircraft*. Available at <https://www.federalregister.gov/documents/2021/01/15/2020-28948/remote-identification-of-unmanned-aircraft>. Accessed 06/30/2021.
14. Part 107 Waiver. U.S. Department of Transportation, Federal Aviation Administration. Available at [https://www.faa.gov/uas/commercial\\_operators/part\\_107\\_waivers/](https://www.faa.gov/uas/commercial_operators/part_107_waivers/). Accessed 06/30/2021.

15. *Part 107 Waivers Issued*. U.S. Department of Transportation, Federal Aviation Administration. Available at [https://www.faa.gov/uas/commercial\\_operators/part\\_107\\_waivers/waivers\\_issued/](https://www.faa.gov/uas/commercial_operators/part_107_waivers/waivers_issued/). Accessed 06/30/2021.
16. Advisory Circular 107-2, *Small Unmanned Aircraft Systems*. U.S. Department of Transportation, Federal Aviation Administration, Washington, D.C., June 21, 2016. Available at [https://www.faa.gov/uas/resources/policy\\_library/media/AC\\_107-2\\_AFS-1\\_Signed.pdf](https://www.faa.gov/uas/resources/policy_library/media/AC_107-2_AFS-1_Signed.pdf). Accessed 06/30/2021.
17. Texas Government Code, Title 4, Chapter 423, Use of Unmanned Aircraft. Available at <https://statutes.capitol.texas.gov/Docs/GV/htm/GV.423.htm>. Accessed 06/30/2021.
18. *UAS Flight Plan*. Texas Department of Transportation, Austin, Texas, 2020. Available at <https://ftp.dot.state.tx.us/pub/txdot-info/avn/uas/flight-plan.pdf>. Accessed 06/30/2021.
19. *UAS Flight Pre-Approval Form*. Texas Department of Transportation, Austin, Texas, 2020. Available at <https://ftp.dot.state.tx.us/pub/txdot-info/avn/uas/flight-pre-approval.pdf>. Accessed 06/30/2021.
20. *Unmanned Aerial Systems*. Texas A&M University, Department of Environmental Health and Safety, College Station, Texas, 2020. Available at <https://ehs.tamu.edu/programs/unmanned-aerial-systems/>. Accessed 06/30/2021.
21. *Instructions: Preparing for UAS Flights at Texas A&M University*. Texas A&M University, Department of Environmental Health and Safety, College Station, Texas, 2020. Available at [https://ehs.tamu.edu/media/1602054/guide\\_uas-flight-request-instructions\\_v5\\_web.pdf](https://ehs.tamu.edu/media/1602054/guide_uas-flight-request-instructions_v5_web.pdf). Accessed 06/30/2021.
22. Texas A&M University System Regulation 24.01.07, Unmanned Aircraft System (UAS). Texas A&M University System, College Station, Texas, May 2017. Available at <https://policies.tamus.edu/24-01-07.pdf>. Accessed 06/30/2021.
23. *UAS Flight Authorization Application*. Texas A&M University, Department of Environmental Health and Safety, College Station, Texas, 2020. Available at <https://www.tamus.edu/business/risk-management/uas/uas-flight-authorization-app/>. Accessed 06/30/2021.
24. Texas Government Code Title 4 Chapter 423, Use of Unmanned Aircraft. Available at <https://statutes.capitol.texas.gov/Docs/GV/htm/GV.423.htm>. Accessed 01/31/2020.
25. Visualize It: See FAA UAS Data on a Map. Federal Aviation Administration, Washington, D.C., undated. Available at <https://faa.maps.arcgis.com/apps/webappviewer/index.html?id=9c2e4406710048e19806ebf6a06754ad>. Accessed 06/30/2021.
26. Aeronautical Charts. SkyVector, 2021. Available at <https://skyvector.com/>. Accessed 06/30/2021.
27. Fly Safe GEO Zone Map. DJI, 2021. Available at <https://www.dji.com/flysafe/geo-map>. Accessed 06/30/2021.
28. Qualified Entities Program (QEP). DJI, 2021. Available at <https://enterprise-insights.dji.com/qualified-entities-program>. Accessed 06/30/2021.
29. Matrice 300 RTK. DJI, 2021. Available at <https://www.dji.com/matrice-300>. Accessed 06/30/2021.



30. UAS Data Exchange (LAANC). Federal Aviation Administration, Washington, D.C., 2021. Available at [https://www.faa.gov/uas/programs\\_partnerships/data\\_exchange/](https://www.faa.gov/uas/programs_partnerships/data_exchange/). Accessed 06/30/2021.
31. AirMap, 2021. Available at <https://www.airmap.com/>. Accessed 06/30/2021.
32. Airports Participating in LAANC. Federal Aviation Administration, Washington, D.C., 2021. Available at [https://www.faa.gov/uas/programs\\_partnerships/data\\_exchange/laanc\\_facilities/#all](https://www.faa.gov/uas/programs_partnerships/data_exchange/laanc_facilities/#all). Accessed 06/30/2021.
33. What is the National Spatial Reference System? National Ocean Service, National Oceanic and Atmospheric Administration, Silver Spring, Maryland, 2021. Available at <https://oceanservice.noaa.gov/facts/nsrs.html>. Accessed 06/30/2021.
34. Global Positioning System. Texas Department of Transportation, Austin, Texas, 2021. Available at <https://www.txdot.gov/inside-txdot/division/information-technology/gps.html>. Accessed 06/30/2021.
35. *TxDOT Survey Manual*. Texas Department of Transportation, Austin, Texas, April 2016. Available at <https://onlinemanuals.txdot.gov/txdotmanuals/ess/ess.pdf>. Accessed 06/30/2021.
36. OPUS: Online Positioning User Service. National Geodetic Survey National Oceanic and Atmospheric Administration, Silver Spring, Maryland, 2021. (<https://geodesy.noaa.gov/OPUS/>). Accessed 06/30/2021.
37. Aerial Metrics Maptools. Aerial Metrics, undated. Available at <https://www.aerial-metrics.com/aerial-metrics-software>. Accessed 06/30/2021.
38. Step 1. Before Starting a Project > 1. Designing the Image Acquisition Plan > a. Selecting the Image Acquisition Plan Type. Pix4D, 2020. Available at <https://support.pix4d.com/hc/en-us/articles/202557459>. Accessed 06/30/2021.
39. DroneSense, 2021. Available at <https://dronesense.com/>. Accessed 06/30/2021.
40. M. J. Westoby, J. Brasington, N. F. Glasser, M. J. Hambrey and J. M. Reynolds. Structure-from-Motion Photogrammetry: A Low-Cost, Effective Tool for Geoscience Applications. *Geomorphology*, Vol. 179, 2012, pp. 300–314.
41. M. J. Starek, T. Davis, D. Prouty and J. Berryhill. Small-Scale UAS for Geoinformatics Applications on an Island Campus. *Ubiquitous Positioning Indoor Navigation and Location Based Service (UPINLBS)*, IEEE, 2014, pp. 120–127.
42. R. K. Slocum and C. E. Parrish. Simulated Imagery Rendering Workflow for UAS-Based Photogrammetric 3D Reconstruction Accuracy Assessments. *Remote Sensing*, Vol. 9, Issue 4, 2017.
43. M. Pashaei, M. J. Starek, H. Kamangir and J. Berryhill. Deep Learning-Based Single Image Super-Resolution: An Investigation for Dense Scene Reconstruction with UAS Photogrammetry. *Remote Sensing*, Vol. 12, Issue 11, 2020.
44. D. G. Lowe. Distinctive Image Features from Scale-Invariant Keypoints. *Int. Journal of Computer Vision*, Vol. 60, Issue 2, pp. 91–110.
45. H. Shum, Q. Ke, and Z. Zhang. Efficient Bundle Adjustment with Virtual Key Frames: A Hierarchical Approach to Multi-Frame Structure from Motion. *Proceedings. 1999 IEEE Computer Society Conference on Computer Vision and Pattern Recognition (Cat. No PR00149)*, IEEE Computer Society Conference, Vol. 2, 1999, pp. 538–543.

46. S. Harwin and A. Lucieer. Assessing the Accuracy of Georeferenced Point Clouds Produced via Multi-View Stereopsis from Unmanned Aerial Vehicle (UAV) Imagery. *Remote Sensing*, Vol. 4, Issue 6, 2012, pp. 1573–1599.
47. F. Remondino, M. G. Spera, E. Nocerino, F. Menna and F. Nex. State of the Art in High Density Image Matching. *The Photogrammetric Record*, Vol. 29, Issue 146, 2014, pp. 144–166.
48. Z. Zhu, C. Stamatopoulos and C. S. Fraser. Accurate and Occlusion-robust Multi-view Stereo. *ISPRS Journal of Photogrammetry and Remote Sensing*, Vol. 109, 2015, pp. 47–61.
49. F. Javadnejad. *Small Unmanned Aircraft Systems (UAS) for Engineering Inspections and Geospatial Mapping*. Oregon State University, 2017.
50. D. Bolkas. Assessment of GCP Number and Separation Distance for Small UAS Surveys with and without GNSS-PPK Positioning. *Journal of Surveying Engineering*, Vol. 145, Issue 3, 2019.
51. J. M. G. Rangel, G. R. Gonçalves and J. A. Pérez. The Impact of Number and Spatial Distribution of GCPs on the Positional Accuracy of Geospatial Products Derived from Low-Cost UASs. *International Journal of Remote Sensing*, Vol. 39, Issue 21, 2018, pp. 7154–7171.
52. E. Sanz-Ablanedo, J. Chandler, J. Rodríguez-Pérez and C. Ordóñez. Accuracy of Unmanned Aerial Vehicle (UAV) and SfM Photogrammetry Survey as a Function of the Number and Location of Ground Control Points Used. *Remote Sensing*, Vol. 10, Issue 10, 2018.
53. G. Jozkow and C. Toth. Georeferencing Experiments with UAS Imagery. *ISPRS Annals of the Photogrammetry, Remote Sensing and Spatial Information Sciences*, Vol. 2, Issue 1, 2014, pp. 25–29.
54. P. E. Carbonneau and J. T. Dietrich. Cost-Effective Non-Metric Photogrammetry from Consumer-Grade sUAS: Implications for Direct Georeferencing of Structure from Motion Photogrammetry. *Earth Surface Processes and Landforms*, Vol. 42, Issue 3, 2017, pp. 473–486.
55. American Society for Photogrammetry and Remote Sensing (ASPRS), Positional Accuracy Standards for Digital Geospatial Data, November 2014. Available at [https://www.asprs.org/wp-content/uploads/2015/01/ASPRS\\_Positional\\_Accuracy\\_Standards\\_Edition1\\_Version10\\_0\\_November2014.pdf](https://www.asprs.org/wp-content/uploads/2015/01/ASPRS_Positional_Accuracy_Standards_Edition1_Version10_0_November2014.pdf). Accessed 06/30/2021.
56. M. W. Smith and D. Vericat. From Experimental Plots to Experimental Landscapes: Topography, Erosion and Deposition in Sub-humid Badlands from Structure-from-Motion Photogrammetry. *Earth Surface Processes and Landforms*, Vol. 40, Issue 12, 2015, pp. 1656–1671.
57. M. J. Starek and J. Giessel. Fusion of UAS-Based Structure-from-Motion and Optical Inversion for Seamless Topo-Bathymetric Mapping. *2017 IEEE International Geoscience and Remote Sensing Symposium (IGARSS)*, 2017, pp. 2999–3002.
58. M. Naumann, M. Geist, R. Bill, F. Niemeyer and G. Grenzdörffer. Accuracy Comparison of Digital Surface Models Created by Unmanned Aerial Systems Imagery and Terrestrial Laser Scanner. *International Archives of the Photogrammetry, Remote Sensing and Spatial Information Sciences*, Vol. 40, 2013, pp. 281–286.

59. M. Schwind and M. J. Starek. How to Produce High-quality 3D Point Clouds: Structure-from-Motion Photogrammetry. *GIM International-The Worldwide Magazine for Geomatics*, Vol. 31, Issue 10, 2017, pp. 36–39.
60. M. J. Starek, M. Gingras and G. Jeffress. Application of Unmanned Aircraft Systems for Coastal Mapping and Resiliency. *Sustainable Development Goals Connectivity Dilemma: Land and Geospatial Information for Urban and Rural Resilience*, 2019, pp. 109–125.
61. J. C. Leachtenauer and R. G. Driggers. *Surveillance and Reconnaissance Imaging Systems: Modeling and Performance Prediction*. Artech House: Norwood, Massachusetts, USA, 2001.
62. What is the Relative and Absolute Accuracy of Drone Mapping. Pix4D, 2021. Available at <https://support.pix4d.com/hc/en-us/articles/202558889>. Accessed 06/30/2021.
63. M. A. Fonstad, J. T. Dietrich, B. C. Courville, J. L. Jensen and P. E. Carbonneau. Topographic Structure from Motion: A New Development in Photogrammetric Measurement. *Earth Surface Processes and Landforms*, Vol. 38, Issue 4, 2013, pp. 421–430.
64. J. Bullock, R. Hainje, A. Habib, D. Horton, and D. Bullock. Public Safety Implementation of Unmanned Aerial Systems for Photogrammetric Mapping of Crash Scenes. *Transportation Research Record: Journal of the Transportation Research Board*, Vol. 2673, Issue 7, 2019, pp. 567–574.
65. J. S. Cerreta, S. S. Burgess and J. Coleman. UAS for Public Safety Operations: A Comparison of UAS Point Clouds to Terrestrial LiDAR Point Cloud Data Using a FARO Scanner. *International Journal of Aviation, Aeronautics, and Aerospace*, Vol. 7, Issue 1, 2020.
66. Manual on Classification of Motor Vehicle Traffic Crashes. *ANSI D.16-2017, American National Standards Institute and Association of Traffic Safety Information Professionals*, Nolensville, Tennessee, 2017. Available at <https://www.transportation.gov/sites/dot.gov/files/docs/resources/government/traffic-records/304331/ansid16-2017.pdf>. Accessed 06/30/2021.
67. Fatality Analysis Reporting System (FARS). *National Highway Traffic Safety Administration*, Washington, D.C., 2020. Available at <https://www-fars.nhtsa.dot.gov/Main/index.aspx>. Accessed 06/30/2021.
68. Crash Records Information System. Texas Department of Transportation, Austin, Texas, 2020. Available at <https://cris.dot.state.tx.us/public/Query/app/public/query/advanced>. Accessed 06/30/2021.
69. *Traffic Incident Management*. Report No. FHWA-OP-04-052, Federal Highway Administration, Washington, D.C., 2004. Available at [https://ops.fhwa.dot.gov/aboutus/one\\_pagers/tim.htm](https://ops.fhwa.dot.gov/aboutus/one_pagers/tim.htm). Accessed 06/30/2021.
70. M. Karlaftis, S. Latoski, N. Richards, and K. Sinha. ITS Impacts on Safety and Traffic Management: An Investigation of Secondary Crash Causes. *ITS Journal—Intelligent Transportation Systems Journal: Technology, Planning, and Operations*, Vol. 5, Issue 1, 1999, pp. 39–52. Available at <https://www.tandfonline.com/doi/abs/10.1080/10248079908903756>. Accessed 06/30/2021.

71. J. Bullock, R. Hainje, A. Habib, D. Horton, and D. Bullock. Public Safety Implementation of Unmanned Aerial Systems for Photogrammetric Mapping of Crash Scenes. *Transportation Research Record: Journal of the Transportation Research Board*, Vol. 2673, Issue 7, 2019, pp. 567–574.
72. D. Gettinger. *Public Safety Drones*, 3<sup>rd</sup> Edition. Center for the Study of the Drone, Bard College, New York, March 2020. Available at <https://dronecenter.bard.edu/files/2020/03/CSD-Public-Safety-Drones-3rd-Edition-Web.pdf>. Accessed 06/30/2021.
73. 15 CFR 744. Addition of Entities to the Entity List, Revision of Entry on Entity List, and Removal of Entities from the Entity List. Federal Register, Vol. 85, No. 246, December 22, 2020.
74. Unmanned Aerial Systems. Colorado Department of Transportation, Denver, Colorado, November 2016. Available at <https://www.codot.gov/business/process-improvement/strategy-3-peaks-1/technology/unmanned-aerial-systems>. Accessed 06/30/2021.
75. C. Stevens and T. Blackstock. Demonstration of Unmanned Aircraft Systems Use for Traffic Incident Management (UAS-TIM). Report PRC 17-69F, Transportation Policy Research Center, Texas A&M Transportation Institute, College Station, Texas, December 2017. Available at <https://static.tti.tamu.edu/tti.tamu.edu/documents/PRC-17-69-F.pdf>. Accessed 06/30/2021.
76. Operational Evaluation of Unmanned Aircraft Systems for Crash Scene Reconstruction. Operational Evaluation Report, Report No. AOS-17-0078, Johns Hopkins University, National Institute of Justice, January 2017. Available at <https://www.ncjrs.gov/pdffiles1/nij/grants/251628.pdf>. Accessed 06/30/2021.
77. Look What's New on the Accident Investigation Team: Drones. The Washington Post, August 2018. Available at [https://www.washingtonpost.com/national/health-science/look-whats-new-on-the-accident-investigation-team-drones/2018/08/17/210fad38-a091-11e8-8e87-c869fe70a721\\_story.html](https://www.washingtonpost.com/national/health-science/look-whats-new-on-the-accident-investigation-team-drones/2018/08/17/210fad38-a091-11e8-8e87-c869fe70a721_story.html). Accessed 06/30/2021.
78. R. K. Slocum, W. Wright, C. Parrish, B. Costa, M. Sharr and T. A. Battista. Guidelines for Bathymetric Mapping and Orthoimage Generation Using sUAS and SfM, An Approach for Conducting Nearshore Coastal Mapping. *NOAA Technical Memorandum NOS NCCOS 265*. Silver Spring, Maryland, 2019. Available at <https://doi.org/10.25923/07mx-1f93>. Accessed 06/30/2021.
79. K. E. Joyce, S. Duce, S. M. Leahy, J. Leon and S. W. Maier. Principles and Practice of Acquiring Drone-Based Image Data in Marine Environments. *Marine and Freshwater Research*, Vol. 70, Issue 7, 2019, pp. 952–963.
80. B. H. Wang, D. B. Wang, Z. A. Ali, B. T. Ting and H. Wang. An Overview of Various Kinds of Wind Effects on Unmanned Aerial Vehicle. *Measurement and Control*, Vol. 52, Issues 7–8, 2019, pp. 731–739.
81. J. Siqueira. Modeling of Wind Phenomena and Analysis of Their Effects on UAV Trajectory Tracking Performance. West Virginia University, 2017.
82. A. I. Hentati, L. Krichen, M. Fourati and L. C. Fourati. Simulation Tools, Environments and Frameworks for UAV Systems Performance Analysis. *2018 14th International Wireless Communications & Mobile Computing Conference (IWCMC)*, 2018, pp. 1495–1500.

83. A. S. Biradar. *Wind Estimation and Effects of Wind on Waypoint Navigation of UAVs*. Master's Thesis, Arizona State University, 2014.
84. H. M. Qays, B. A. Jumaa and A. D. Salman. Design and Implementation of Autonomous Quadcopter using SITL Simulator. *Iraqi Journal of Computers, Communication and Control & Systems Engineering*, Vol. 20, Issue 1, 2020, pp. 1–16.
85. ArduPilot/MissionPlanner GitHub source code. Available at <https://github.com/ArduPilot/MissionPlanner>. Accessed 06/30/2021.
86. ZHU Training Page at National Weather Service. Available at [https://www.weather.gov/media/zhu/ZHU\\_Training\\_Page/turbulence\\_stuff/turbulence2/turbulence.pdf](https://www.weather.gov/media/zhu/ZHU_Training_Page/turbulence_stuff/turbulence2/turbulence.pdf). Accessed 06/30/2021.
87. L. S. Seregina, R. Haas, K. Born and J. G. Pinto. Development of a Wind Gust Model to Estimate Gust Speeds and Their Return Periods. *Tellus A: Dynamic Meteorology and Oceanography*, Vol. 66, 2014, pp. 1–15.
88. M. Pepe, L. Fregonese and M. Scaioni. Planning Airborne Photogrammetry and Remote-Sensing Missions with Modern Platforms and Sensors. *European Journal of Remote Sensing*, Vol. 51, Issue 1, 2018, pp. 412–436.
89. E. Seifert, S. Seifert, H. Vogt, D. Drew, J. Van Aardt, A. Kunneke and T. Seifert. Influence of Drone Altitude, Image Overlap, and Optical Sensor Resolution on Multi-View Reconstruction of Forest Images. *Remote Sensing*, Vol. 11, Issue 10, 2019.
90. E. Falkner and D. Morgan. *Aerial Mapping: Methods and Applications*, 2nd ed. CRC Press: Boca Raton, Florida, USA, 2002.
91. J. L. Carrivick, M. W. Smith and D. J. Quincey. *Structure from Motion in the Geosciences*. John Wiley & Sons, 2016.
92. D. C. Brown. Decentering Distortion of Lenses. *Photogrammetric Engineering and Remote Sensing*, 1966.
93. *CloudCompare Version 2.6.1 User Manual*. CloudCompare, undated. Available at <https://www.danielgm.net/cc/doc/qCC/CloudCompare%20v2.6.1%20-%20User%20manual.pdf>. Accessed 06/30/2021.
94. T. Lillesand, R. W. Kiefer and J. Chipman. *Remote Sensing and Image Interpretation*. John Wiley & Sons, 2015.
95. O. García-Feal. Advanced Fluid Visualisation with DualSPHysics and Blender, *11<sup>th</sup> International SPHERIC Workshop*, 2016.
96. J. T. Kajiya. The Rendering Equation. *Proceedings of the 13th Annual Conference on Computer Graphics and Interactive Techniques*, 1986.
97. D. Biedermann, M. Ochs and R. Mester. CONGRATS: Realistic Simulation of Traffic Sequences for Autonomous Driving. *2015 International Conference on Image and Vision Computing New Zealand (IVCNZ)*, 2015.
98. J. Parrón. Millimeter-Wave Scene Simulation Using Blender. *Proceedings of XXV Simposium Nacional de Union Cientifica Internacional de Radio, URSI 2010*, 2010.
99. M. Ouza, M. Ulrich and B. Yang. A Simple Radar Simulation Tool for 3D Objects Based on Blender. *2017 18th International Radar Symposium (IRS)*, 2017.
100. M. P. Fairclough. Systems and Methods for the Real-time and Realistic Simulation of Natural Atmospheric Lighting Phenomenon. *U.S. Patent No. 7,710,418*. 2011.
101. J. Allworth. Development of a High Fidelity Simulator for Generalised Photometric Based Space Object Classification using Machine Learning. *Proceedings of the 70th International Astronautical Congress*, 2019.

102. A. D. Cornetto and J. Suway. Validation of the Cycles Engine for Creation of Physically Correct Lighting Models. No. 2019-01-1004. *SAE Technical Paper*, 2019.
103. NOAA Solar Calculator. Global Monitoring Laboratory, Earth System Research Laboratories. Available at <https://www.esrl.noaa.gov/gmd/grad/solcalc/>. Accessed 06/30/2021.
104. M. Anderson, R. Motta, S. Chandrasekar and M. Stokes. Proposal for a Standard Default Color Space for the Internet—sRGB. *Color Imaging Conference 1996*, 1996.
105. P. R. Wolf, B. A. Dewitt and B. E. Wilkinson. *Elements of Photogrammetry with Applications in GIS*, 4th Edition, McGraw-Hill, 2014.
106. What is Camera Calibration? Matlab, 2020. Available at <https://www.mathworks.com/help/vision/ug/camera-calibration.html>. Accessed 06/30/2021.
107. M. R. James and S. Robson. Mitigating Systematic Error in Topographic Models Derived from UAV and Ground-based Image Networks. *Earth Surface Processes and Landforms*, Vol. 39, Issue 10, 2014, pp. 1413–1420.
108. D. Griffiths and H. Burningham. Comparison of Pre- and Self-Calibrated Camera Calibration Models for sUAS-derived Nadir Imagery for a SfM Application. *Progress in Physical Geography: Earth and Environment*, Vol. 43, Issue 2, 2019, pp. 215–235.
109. J. G. Fryer and D. C. Brown. Lens Distortion for Close-Range Photogrammetry. *Photogrammetric Engineering and Remote Sensing*, Vol. 52, Issue 1, 1986, pp. 51–58.
110. V. Tournadre, M. Pierrot-Deseilligny and P. H. Faure. UAV Linear Photogrammetry. *The International Archives of Photogrammetry, Remote Sensing and Spatial Information Sciences*, Vol. 40, Issue 3, 2015, pp. 327–333.
111. C. Wu. Critical Configurations for Radial Distortion Self-Calibration. *2014 IEEE Conference on Computer Vision and Pattern Recognition (CVPR)*, 2014, pp. 25–32.
112. Agisoft. Agisoft Metashape User Manual: Standard Edition, Version 1.5, Agisoft LLC, 2019.
113. Internal Camera Parameters Correlation. Pix4D, 2019. Available at <https://support.pix4d.com/hc/en-us/articles/115002463763>. Accessed 06/30/2021.
114. M. Hahner, D. Dai, C. Sakaridis, J. Zaech, and L. Van Gool. Semantic Understanding of Foggy Scenes with Purely Synthetic Data. *2019 IEEE Intelligent Transportation Systems Conference (ITSC)*, 2019, pp. 3675–3681.
115. R. T. Tan. Visibility in Bad Weather from a Single Image. *2008 IEEE Conference on Computer Vision and Pattern Recognition*, 2008, pp. 1–8.
116. K. He, J. Sun, and X. Tang. Single Image Haze Removal Using Dark Channel Prior. *IEEE Transactions on Pattern Analysis and Machine Intelligence*, Vol. 33, Issue 12, 2010, pp. 2341–2353.
117. C. Sakaridis, D. Dai, and L. Van Gool. Semantic Foggy Scene Understanding with Synthetic Data. *International Journal of Computer Vision*, Vol. 126, Issue 9, 2018, pp. 973–992.
118. W. M. F. Wauben. Visibility Chain at Regional Civil Airports in the Netherland. *R&D Information and Observation Technology*, Royal Netherlands Meteorological Institute, 2012.
119. D. Deshpande and V. Kale. Analysis of the Atmospheric Visibility Restoration and Fog Attenuation Using Gray Scale Image. *Proc. Satellite Conference ICSTSD 2016*

- International Conference on Science and Technology for Sustainable Development*, Kuala Lumpur, Malaysia, 2016, pp. 32–37.
120. M. Gašparović and L. Jurjević. Gimbal Influence on the Stability of Exterior Orientation Parameters of UAV Acquired Images. *Sensors*, Vol. 17, Issue 2, 2017.
  121. J. Windau and L. Itti. Multilayer Real-time Video Image Stabilization. *2011 IEEE/RSJ International Conference on Intelligent Robots and Systems*, 2011, pp. 2397–2402.
  122. O. Whyte, J. Sivic, A. Zisserman, and J. Ponce. Non-uniform Deblurring for Shaken Images. *International Journal of Computer Vision*, Vol. 98, Issue 2, 2012, pp. 168–186.
  123. D. Gong, J. Yang, L. Liu, Y. Zhang, I. Reid, C. Shen, A. Van Den Hengel, and Q. Shi. From Motion Blur to Motion Flow: A Deep Learning Solution for Removing Heterogeneous Motion Blur. *2017 IEEE Conference on Computer Vision and Pattern Recognition*, 2017, pp. 2319–2328.
  124. I. Granado, N. Sirakov and F. Muge. A Morphological Interpolation Approach—Geodesic Set Definition in Case of Empty Intersection. *Computational Imaging and Vision*, Vol. 18, 2002. Available at [https://doi.org/10.1007/0-306-47025-X\\_9](https://doi.org/10.1007/0-306-47025-X_9). Accessed 06/30/2021.
  125. Sun Path Chart. University of Oregon Solar Radiation Monitoring Laboratory, 2007. Available at <http://solardat.uoregon.edu/SunChartProgram.html>. Accessed 06/30/2021.
  126. Sun Position. SunEarthTools, 2021. Available at [https://www.sunearthtools.com/dp/tools/pos\\_sun.php?lang=en](https://www.sunearthtools.com/dp/tools/pos_sun.php?lang=en). Accessed 06/30/2021.
  127. Natural Sunlight Intensity. First Rays, 2021. Available at <https://firstrays.com/natural-sunlight-intensity/>. Accessed 06/30/2021.
  128. A. Fotouhi, M. Ding, and M. Hassan. Understanding Autonomous Drone Maneuverability for Internet of Things Applications. *2017 IEEE 18th International Symposium on A World of Wireless, Mobile and Multimedia Networks (WoWMoM)*, 2017, pp. 1–6.
  129. R. Bansal, G. Raj, and T. Choudhury. Blur Image Detection using Laplacian Operator and Open-CV. *2016 International Conference System Modeling and Advancement in Research Trends (SMART)*, 2016.
  130. OPUS: Online Positioning User Service. National Geodetic Service, National Oceanic and Atmospheric Administration, Washington, D.C., 2020. Available at <https://geodesy.noaa.gov/OPUS/>. Accessed 06/30/2021.
  131. REDtoolbox GNSS Postprocessing and Geotagging Software. REDcatch GmbH, 2021. Available at <https://www.redcatch.at/redtoolbox/>. Accessed 06/30/2021.
  132. Vertical Datum Transformation. National Oceanic and Atmospheric Administration, Washington, D.C., undated. Available at <https://vdatum.noaa.gov/welcome.html>. Accessed 06/30/2021.
  133. *Unmanned Aircraft Systems Data Post-Processing. Structure-from-Motion Photogrammetry*. United States Geological Survey, March 2017. Available at <https://uas.usgs.gov/nupo/pdf/PhotoScanProcessingDSLRLMar2017.pdf>. Accessed 06/30/2021.
  134. Agisoft PhotoScan Workflow. United States Geological Survey, March 2017. Available at <https://uas.usgs.gov/nupo/pdf/USGSAgisoftPhotoScanWorkflow.pdf>. Accessed 06/30/2021.
  135. lascontrol. Rapidlasso GmbH, undated. Available at <https://rapidlasso.com/lastools/lascontrol/>. Accessed 06/30/2021.

136. Menu Process > Processing Options... > 1. Initial Processing > Matching. Pix4D, 2020. Available at <https://support.pix4d.com/hc/en-us/articles/205433155-Menu-Process-Processing-Options-1-Initial-Processing-Matching>. Accessed 06/30/2021.
137. How to Manually Calibrate Uncalibrated Cameras in the RayCloud. Pix4D, 2020. Available at <https://support.pix4d.com/hc/en-us/articles/202560189-How-to-manually-calibrate-uncalibrated-Cameras-in-the-rayCloud>. Accessed 06/30/2021.
138. *Traffic Safety Program Manual*. Texas Department of Transportation, Austin, Texas, 2020. Available at [http://onlinemanuals.txdot.gov/txdotmanuals/tfc/manual\\_notice.htm](http://onlinemanuals.txdot.gov/txdotmanuals/tfc/manual_notice.htm). Accessed 06/30/2021.
139. Workshop 1008—Application of Unmanned Aerial Systems (UAS) for Condition Assessment of Highway Assets. TRB 100th Annual Meeting. Transportation Research Board, Washington, D.C., 2021. Available at <https://annualmeeting.mytrb.org/OnlineProgram/Details/15173>. Accessed 06/30/2021.



## APPENDIX. VALUE OF RESEARCH

This appendix summarizes the procedure and calculations to estimate the value of research (VOR) associated with this research. The research team considered two types of benefits: economic (or quantitative) and qualitative.

### QUANTITATIVE BENEFITS

The research team followed a conservative approach for the estimation of potential benefits. As mentioned, UASs have considerable potential for implementation in a variety of areas. However, it would first be necessary to establish the technical feasibility of using UASs for some of those areas to produce a reliable measure of benefit. Because the research included statistics on the number of fatal crashes and focused on crash reconstructions, using fatal crashes to estimate the potential benefit of using UASs became feasible when combined with commonly used methodologies to estimate road user costs.

For the estimation of benefits, the research team made the following assumptions:

- UASs are used to assist in fatal crash reconstructions at the five metro districts, more specifically at the urban counties that account for most crashes in each of the five metro districts. Using UASs for fatal crash reconstructions at nonmetro districts is technically feasible, but the corresponding benefit is not included in the calculations here.
- UASs are used to assist in daylight and nighttime fatal crash reconstructions under clear or cloudy weather conditions (i.e., not under inclement weather). The average number of fatal crashes per metro district per year meeting this criterion is 187. This number is based on a 10-year trend between 2010 and 2019.
- Full implementation takes place after 10 years. This means that during the first year of implementation, only 10 percent of qualifying fatal crashes are reconstructed using UASs. During the second year of implementation, the number increases to 20 percent. During the 10th year, the number increases to 100 percent.
- The economic benefits are the result of faster crash reconstructions by using UASs, resulting in lower road user costs. Realistically, this calculation depends on several factors, most of which pertain to the specific highway and traffic conditions when a fatal crash occurs. Factors the research team considered included annual average daily traffic (AADT), directional factor, peak-hour factor, free flow travel time, normal travel time, crash event travel time, total duration of congestion because of the crash, and percentage of trucks. The calculation also depends on economic factors, such as the time value for passenger cars and the time value for trucks.
- Drivers save time because UASs are used to reconstruct crashes instead of using a traditional methodology. For the analysis, the research team considered three scenarios of time savings per fatal crash event: 15 minutes, 30 minutes, and 60 minutes. The research team also considered five hypothetical highway corridors, each one with a different AADT (5,000, 10,000, 25,000, 50,000, and 100,000), to account for typical traffic volumes on urban highway corridors in Texas. These AADT values correspond to the 19th, 29th, 55th, 71st, and 83rd percentiles, respectively. The research team also assumed typical directional and peak-hour factors.

- The discount rate is 7 percent, which is a rate frequently used for economic evaluations of public-sector investments. The research team also assumed a 10-year horizon for the evaluation of economic benefits.
- After full implementation, the annual cost of labor (assuming a dedicated full-time equivalent crew consisting of one pilot and one observer per district), UAS equipment purchase and replacement, computers, SfM software, and maintenance is \$223,000 per district (or \$1,115,000 for the five metro districts). This cost is for the entire county and includes both fatal crashes on state and local highways. It is assumed that state and local agencies have agreements in place where a single UAS crew can serve both state and local highways.

Figure 290 shows the VOR calculation for the case where AADT = 25,000 and the time saved by using UASs is 15 minutes per driver. The figure shows that the economic benefit after full implementation is \$2,839,675/year. When compared to the research investment of \$732,544, the result suggests that the research investment can be recouped at the end of the second year of implementation (when the implementation has increased to 20 percent). For this scenario, the cost-benefit ratio (CBR) is 13:1 over 10 years. If the full implementation could happen from the beginning (although not a realistic scenario), the payback period would be just two months.


Table 150 shows the summary of VOR calculations for all the scenarios considered. In general, as the amount of traffic increases, the anticipated annual net benefits increase and the corresponding CBR increases. Similarly, as the amount of time savings increases, the anticipated annual net benefits increase and the corresponding CBR increases. Assuming AADT = 25,000, which corresponds to the 55th percentile, Table 150 shows CBR values that vary from 13:1 to 65:1 over 10 years.

## **QUALITATIVE BENEFITS**

Based on the experience reported by other agencies throughout the country on the use of UASs for traffic incident management, in particular crash reconstructions, and the results of the simulations and field tests during the research, the research team anticipates the following benefits if UASs are used systematically in Texas for this type of application:

- Faster clearing of fatal crash scenes. In addition to lower road user costs (as documented above), clearing fatal crash scenes faster can result in benefits such as lower risk of secondary crashes, lower emissions, and lower frustration levels for motorists.
- Daylight and nighttime data collection. With supplemental lighting (and, in some instances, built-in LEDs), UASs are increasingly used to collect reliable data at night. Several agencies have also reported success using UASs in mild to moderate rain or snow conditions.

The benefits of using UASs can increase dramatically if the feasibility of using UASs can be established or confirmed for other applications. As mentioned in Chapter 6, examples of reported UAS applications or opportunities include areas such as structures, construction, maintenance, planning and design, and utilities. For each of these areas, the potential exists for quantitative and qualitative benefits.

	<b>Project #</b>	0-7063		
	<b>Project Name:</b>	Guidance for the Use of UAS during Suboptimal Environmental Conditions		
	<b>Agency:</b>	TTI/TAMUCC	<b>Project Budget</b>	\$ 732,544
	<b>Project Duration (Yrs)</b>	1.7	<b>Exp. Value (per Yr)</b>	\$ 2,839,675
<b>Expected Value Duration (Yrs)</b>		0	<b>Discount Rate</b>	7%
<b>Economic Value</b>				
<b>Total Savings:</b>	\$ 14,885,669	<b>Net Present Value (NPV):</b>		\$ 9,219,425
<b>Payback Period (Yrs):</b>	1.789838	<b>Cost-Benefit Ratio (CBR, \$1 : \$___):</b>		\$ 13

Years	Expected Value
0	\$0
1	\$283,968
2	\$567,935
3	\$851,903
4	\$1,135,870
5	\$1,419,838
6	\$1,703,805
7	\$1,987,773
8	\$2,271,740
9	\$2,555,708
10	\$2,839,675

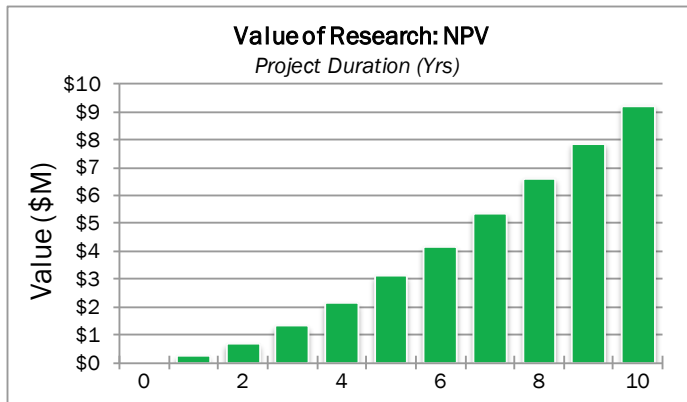


Figure 290. VOR Calculation (Case: 25,000 AADT and 15 Minutes Saved per Driver).

Table 150. Summary of VOR Calculations.

AADT	Time Saved per Driver (min)	Annual Economic Savings	Annual Implementation Cost	Annual Net Benefits	CBR after 10 Years
5,000	15	\$790,935	\$1,115,000	-\$324,065	-1
	30	\$1,581,870	\$1,115,000	\$466,870	2
	60	\$3,163,740	\$1,115,000	\$2,048,740	9
10,000	15	\$1,581,870	\$1,115,000	\$466,870	2
	30	\$3,163,740	\$1,115,000	\$2,048,740	9
	60	\$6,327,475	\$1,115,000	\$5,212,475	23
25,000	15	\$3,954,675	\$1,115,000	\$2,839,675	13
	30	\$7,909,345	\$1,115,000	\$6,794,345	30
	60	\$15,818,690	\$1,115,000	\$14,703,690	65
50,000	15	\$7,909,345	\$1,115,000	\$6,794,345	30
	30	\$15,818,690	\$1,115,000	\$14,703,690	65
	60	\$31,637,385	\$1,115,000	\$30,522,385	135
100,000	15	\$15,818,690	\$1,115,000	\$14,703,690	65
	30	\$31,637,385	\$1,115,000	\$30,522,385	135
	60	\$63,274,765	\$1,115,000	\$62,159,765	275

